Pores, porosity and pore size distribution of some Draupne Formation and Colorado Group shales and kerogens.

Nykky Allen BSc MSc

A thesis submitted to Newcastle University in partial fulfilment of the requirements for the degree of Doctor of Philosophy in the Faculty of Science

School of Civil Engineering and Geosciences

Newcastle University

January 2014

Declaration

I hereby certify that the work described in this thesis is my own work, except where otherwise acknowledged and has not been submitted previously for a degree at this, or any other University

Nykky Allen

Acknowledgements

First and foremost I would like to thank my supervisors Andrew Aplin and Mark Thomas for their guidance and support throughout my studies. Without their endless patience and understanding during the difficult times, I would not have been able to complete a PhD. I would also like to thank the industrial sponsors of the Shale Gas Canada Consortium, who provided the research funding for my work.

In addition, I am eternally grateful to Xuebo Zhao and Jon Bell for the hours of technical assistance and hands-on experimental training given to me in the laboratory. I would also like to thank the past and present members of the NCRL research group for their friendship and assistance, including Apipong Putkam, Thomas Rexer, and Eliza Mathia. Special thanks also go to my close friend and ally Mohammed Bello Adamu.

I would also like to give thanks to all of the technical staff who have aided me during my studies, including Bernie Bowler, Phil Green, Ian Harrison and Rob Hunter. Special thanks go to Maggie White for her many hours of assistance with X-ray crystallographic determination.

Most importantly, I would like to dedicate this PhD thesis to my wife and family. Words cannot capture or convey my feelings of gratitude for your immeasurable support. It is no secret that the last 5 years have been the most difficult and gruelling slog of my life, and there have been many times when I just wanted to run away. Without your encouragement to continue, persist and never give up, I would not be here today with a PhD.

From the bottom of my heart, thank you.

Abstract

Organic rich shales are an important source of natural gas, where significant amounts of gas can be stored in the pore system of shales. The pore systems of organic rich shales are both highly variable and poorly understood, and within this context, the overall research aim is to characterise and investigate the pore system of organic rich shales and isolated kerogens, and to examine the relationship between shale pore structure and gas storage. The research focussed on two case studies: 1) the Draupne Formation (DF) of the North Sea, and 2) the Colorado Group (CG) of the Western Canada Sedimentary Basin of Canada. The DF shales have a range of thermal maturities, from immature to late oil window, allowing the effect of maturity on pore structure to be examined. The CG group shales are both immature and iso-mature, allowing the pore structure of pre-oil window kerogen and shale to be investigated. The geochemistry of the shales and isolated kerogen samples was characterised using TOC, Rock-Eval, Pyrolysis GC-MS, FT-IR, ^{13}C-NMR, Elemental Analysis. The pore structure of the isolated kerogens and shales was investigated using 1) Electron microscopy, 2) Mercury intrusion porosimetry, and 3) low pressure gas adsorption methods, including nitrogen at -78^{o}C and CO_2 at 0^{o}C. The gas storage capacity of the shales was determined using high pressure methane at 30^{o}C and up to 1 MPa.

In the Draupne Formation sample suite, thermal maturity has a significant influence on the pore structure, with organic matter content and mineralogy having a secondary role. Mercury intrusion porosimetry indicates that the pore size distribution of the shales is dominated by pores < than 100 nm in size, and that the proportion of mesopores increases with maturity, at the expense of micropore content. The gas sorption pore volumes of both the isolated kerogens and shales exhibit a strong negative correlation to maturity, with the TOC normalised pore volumes strongly decreasing with increasing maturity. The negative correlation with maturity is also repeated with the Dubinin-Radushkevic (D-R) micropore volumes and the BET surface areas of the kerogens and shales. The absence of shale minerals in the kerogen concentrates indicates that the negative correlation between pore structure and maturity is controlled by the organic matter, and shale matrix mineralogy is a secondary influence on pore structure in this sample suite.

In the Colorado Group case study, mineralogy is the primary influence on the pore structure of the shales, with organic matter content having a secondary role. The mercury intrusion porosimetry of the shale indicates that the pore size distribution is dominated by sub-100 nm pores, and the pore size distribution is constant, with no change across the sample suite. The gas sorption pore volumes of the isolated CG kerogens are almost identical to the isolated DF kerogens, suggesting that Type II algal kerogens have similar gas sorption pore volumes. For the CG shales, the sorption pore volume correlates strongly with illite content. The correlation is positive, with a correlation coefficient of R^2 = 0.97. This indicates pore volume is primarily located in the shale mineral matrix, and organic matter content is secondary in the CG sample suite. This strong positive illite content is also observed in the D-R micropore volumes of the shales, indicating that illite is microporous. The N_2 BET surface area also reflects this strong positive correlation to illite, with a R^2 = 0.90.

Contents

Chapter 2: Materials and Methods

Chapter 3: Geochemical analysis of organic rich shales and isolated kerogens

Chapter 4: Porous structure of organic rich shales

Chapter 5: Porous structure of kerogen

List of Figures

Chapter 1

Chapter 2

Chapter 3

Chapter 4

Chapter 5

Chapter 6

List of Tables

Chapter 1

Chapter 2

Chapter 3

Chapter 4

Chapter 5

Chapter 6

Chapter 1: The pore structure of organic rich shales and kerogens

1.1 Introduction to gas storage in shale pores

1.1.1 Shale gas

Shale gas is the methane-dominated natural gas that can be produced from a shale. The term "gas shale" is applied to a very fine grained sedimentary rock that stores natural gas in its pore system (Law and Curtis, 2002; Bustin *et al.*, 2008). The existence of shale gas has been known for many years; the first recorded production of shale gas was in 1821 from the laterally extensive Devonian shales of the Eastern USA (Vanorsdale, 1987). This 1821 production was sourced from the Dunkirk shale in Chautauqua County, and was used to light the nearby small town of Fredonia (Curtis, 2002).

Historically, shale gas accumulations have been overlooked or ignored due to being expensive and technically challenging to exploit (Curtis, 2002). However, over the last decade interest in shale gas dramatically increased, especially in North America (Chareonsuppanimit *et al*., 2012). In the year 2005, there were over 35,000 producing gas shale wells in the United States (Bustin, 2005). Since then, the shale gas exploration activity has increased rapidly in other regions of the world (Jarvie, 2011; Littke *et al*., 2011). The success of shale gas is due to the recent application of advanced drilling and shale fracturing strategies (Hill and Nelson, 2000; Jarvie *et al.*, 2007).

There are general, and sometimes wide, definitions of what constitutes a gas shale, from "true" shales (fine-grained fissile mudstones comprised mainly of clay minerals), such as the Antrim shale, through to non-fissile mudstones, siltstones and even tight sands, such as the Lewis shale (Bustin, 2005; Bustin *et al*., 2008). Some definitions of a gas shale specify that a portion of the natural gas must be stored in the pore system by adsorption (Bustin, 2005). Most gas bearing shale formations are Palaeozoic and Mesozoic in geological age (Curtis, 2002).

Shale gas is generated in-situ from well preserved hydrogen-rich kerogen and bitumen in organic rich shales. The hydrogen content of kerogen is a controlling factor in the amount of gas that can be formed (Hunt, 1996). The shale gas is stored in the pore system of the shale, and is not subject to the processes of diffusion or migration (Bustin, 2005). Shale gas is a variable mixture of hydrocarbon and non-hydrocarbon gases. Shale gas is primarily methane, with lesser amounts of other gases, such as heavier hydrocarbons, N_2, and CO_2 (Bustin, 2005). The chemical composition of a shale gas mixture will depend on its origin (thermogenic vs biogenic) and geochemical type (i.e. wet gas vs dry gas), Jarvie *et al*., (2007). Shale gas can be associated with hydrocarbon liquid condensates. When shale gas is produced from a well, the reduction in pressure and temperature may cause C_6 (and above) hydrocarbons to condense at the hydrocarbon dew point in to a liquid phase. These "gas condensates" are often more valuable than the shale gas itself, especially in the USA, and are a key exploration target (World Energy Council, 2012). For example, as of the first quarter of 2012, typical Marcellus shale wet gas prices in the USA were about 70% higher than the equivalent dry shale gas (World Energy Council, 2012).

Shale gas can be derived from both thermogenic and biogenic origins (Curtis, 2002; Jenkins and Boyer, 2008). Thermogenic shale gas forms in organic rich sediments that have been buried to great depths and subjected to intense thermal maturation (Bowker, 2007). Thermogenic shale gas can form by the direct maturation of kerogen to gas, and/or the secondary cracking of oil to gas (Braun and Rothman, 1975; Jarvie *et al.*, 2007). Conversely, biogenic shale gas forms at shallow burial depths where the temperature conditions are mild (as high temperatures can sterilise the shale of microbes). Biogenic gas can be formed from both thermally mature and immature organic matter (Rokosh *et al*., 2009); examples of thermally mature kerogen generating biogenic gas have been observed, where the present day temperature regime is mild enough to be conducive to microbial life (Rokosh *et al*., 2009). Biogenic shale gas is a waste by-product of methanogenic bacterial decomposition of kerogen. Accumulation of biogenic gas requires the ground water percolating through the shale formation to be continually replenished with the necessary key nutrients. Biogenic gas formation is usually recent; shale gas from the Antrim Shale has been generated in the last 20, 000 years (Martini *et al*., 2003).

1.1.2. The shale gas system

Shale gas is termed "unconventional" because the shale gas petroleum system has a different geological framework to that of the conventional petroleum system (Hill *et al*., 2007). A standard conventional petroleum system consists of: 1) Source rock, 2) Reservoir rock, 3) Seal, 4) Overburden, 5) Thermal Maturation, 6) Migration, and 7) Trap formation (Magoon and Dow, 1994).

However, in the shale gas petroleum system, the shale acts as the source rock, the trap, and the reservoir simultaneously (Martini *et al.*, 1998; Hill *et al.*, 2007; Bernard *et al*., 2010; Glorioso and Rattia, 2012). The shale gas is generated and is stored within the tight pore systems of the shale. The gas is not expelled from the source rock, and there is no migration into a nearby permeable reservoir rock (Curtis, 2002; Bowker, 2007; Hill *et al.*, 2007). A schematic diagram of the conventional petroleum system and the unconventional shale gas system is presented in Figure 1.1:

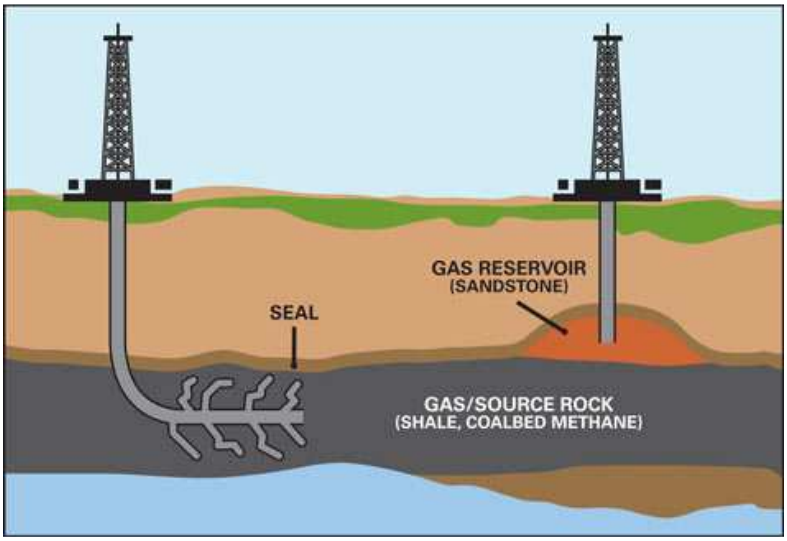

Figure 1.1: Shale gas petroleum systems do not involve migration or a trap (after www.shalegas.co.uk)

Shale gas is stored within the nanometre-scale pore structure of the shale (Chalmers and Bustin, 2007), and no separate reservoir rock is required (the shale is both source and reservoir). Shale may act as a flow barrier because of the low permeability (Amann-Hildenbrand *et al*., 2012) and high capillary entry pressure associated with the tight porosity (Hill *et al.*, 2007; Aplin and Macquaker, 2011); this means that gas shales are essentially self-sealing, with negligible gas leakage over geological time (Curtis, 2002).

The storage of gas in low permeability shales results in specialised drilling and well completion techniques being required to produce the gas (Jarvie *et al.*, 2007). These include horizontal drilling and multi-stage hydraulic fracturing, also known as "fracking" (Hill and Nelson, 2000). Artificially induced fractures are an integral part of the shale gas extraction process because shale fracture permeability is at least eight orders of magnitude higher than shale matrix permeability (Gutierrez *et al*., 2000). Less than 10% of shale-gas wells can be successfully completed without some form of reservoir stimulation (Curtis, 2002). A shale gas reservoir may need to re-fractured several times to extend the productive life of a gas well and sustain the economic rate of production (Walser and Pursell, 2008; Cramer, 2008).

The optimal zone in the shale gas petroleum system (the "fairway") occurs when both high gas-in-place (GIP) and high production efficiency exist together (Curtis, 2002; Jenkins and Boyer, 2008; Bernard *et al*., 2010). Whilst gas shale systems vary considerably, empirical observations have shown that certain geochemical and petrophysical characteristics are usually present in the best USA shale gas provinces (Curtis, 2002; Hill *et al.*, 2007; Jarvie *et al*., 2007; Jenkins and Boyer, 2008; Bernard *et al*., 2010; Hartwig *et al.*, 2010; Hao *et al*., 2013):

- Organic rich, TOC >2%
- High maturity (Ro > 1.2%)
- High silica or carbonate content (> 40%)
- Low clay content (<30%)
- Wide regional extent (on the km scale)
- Thick shale units (> 50m)
- Low total porosity (< 15%) and very low permeability (<100 nD)

Mineralogy is a fundamental property in all successful gas shales. High silica/carbonate content, coupled with low clay mineral content, leads to shale brittleness (Bowker, 2007). The success of fracking depends on the shale brittleness, and brittleness depends upon the mineralogy (Jarvie *et al.*, 2007; Bernard *et al*., 2010).

1.1.3. Phase occurrence of gas in the shale pore system

Gas is stored in three phases within the pore structure of shales (Curtis, 2002; Ross and Bustin, 2008; Bernard *et al*., 2010):

- Free gas
- Adsorbed gas
- Dissolved gas

The free gas phase is the bulk phase of shale gas, where the individual gas molecules are separated, are in constant random motion and continuously colliding with each other. The free gas phase will expand to completely fill the space that it is confined in the inter-granular porosity and fracture network. The amount of gas in the free gas phase is dependent on the temperature, pressure and level of gas saturation of the shale sequence.

The adsorbed gas phase consists of gas molecules that are bound on to surfaces by weak forces of attraction (Gregg and Sing, 1982). One (or several) condensed layers of gas molecules can form at the solid-gas interface of the pore's internal surface (Amann-Hildenbrand, *et al*., 2012). The adsorbed gas molecules are in equilibrium with the free gas phase. Gas adsorption is reversible, and the surface-bound gas molecules can leave the surface and re-enter the free gas phase. The adsorption of gas is influenced by the temperature and pressure conditions of the shale sequence (Ross and Bustin, 2007).

The dissolved gas phase consists of low molecular weight gas molecules being dissolved in to a reservoir fluid (such as oil and formation water). Temperature and pressure influence the amount of dissolution of gas in reservoir fluids, with the gas being evolved out of solution when the temperature and pressure are reduced.

The partition of the gas between these three phases of gas storage is determined by the shale's physical properties (e.g. the geochemistry, petrophysics), the reservoir conditions (depth, temperature, pressure, moisture/water saturation), and the chemical composition of the gas itself (alkanes, N_2, CO_2 ; Montgomery *et al*., 2005; Pollastro *et al*., 2003).

1.1.4 Gas In Place (GIP) in shale pore systems

Gas In Place (GIP) is the maximum amount of gas stored in the pore system of a gas bearing shale. There must be a sufficient GIP stored within the shale pores to be an economic shale-gas play (Curtis, 2002; Bowker, 2007; Jenkins and Boyer, 2008). The GIP is estimated during the appraisal stage of the gas shale exploration. The GIP is dependent on both the 1) total amount of hydrocarbons generated and retained, and 2) the partition of gas between the three phases of storage.

The GIP of a gas shale is determined by calculating the amount of gas that is stored in each of the three phases exhibited in gas shales, and then summing the amounts to arrive at the total GIP (Ambrose *et al*., 2010).

$$GIP = G_f + G_a + G_d$$

(Equation 1.1)

Where G_f = free gas, G_a = adsorbed gas, G_d = dissolved gas

The free gas component is determined by firstly making a 3-D volumetric assessment of the shale formation; i.e. the Area x Net Thickness of the shale unit. Once the total available volume of the shale formation is determined, the volume of the free gas component in the pores is calculated from the petrophysical properties of the shale. These include:

- Total porosity, ϕ (unit-less decimal number between 0 and 1)
- Gas saturation of pore space, S_g (unit-less decimal number between 0 and 1), where $S_g = 1-S_w-S_o$ (S_w= water saturation, and S_o = oil saturation).
- Gas formation volume factor, B_g (cm^3 / cm^3). The ratio of the volume a fixed amount of gas occupies under reservoir conditions, over the volume the same amount of gas occupies under surface pressure and temperature conditions.
- Bulk density, ρ_b (in g cm^{-3}). The bulk density of the shale is incorporated in the equation to allow the volume of gas in the gas saturated pores to be normalized to a volume of gas per unit of shale (i.e. $1/\rho_b$ = 1/g cm^{-3} = cm^3 of gas per gram of shale).

The amount of gas stored in the free gas is calculated from these petrophysical parameters, using the reservoir engineering equation of Ambrose *et al*., (2010):

$$G_f = 32.0368 \frac{\phi(1 - S_w - S_o)}{\rho_b B_g}$$

(Equation 1.2)

The 32.0368 coefficient is used to convert the gas units from $cm^3\ g^{-1}$ to scf ton^{-1} (as 1 $cm^3 g^{-1}$ = 32.0368 scf ton^{-1}). (N.B. It is also noteworthy that 1 mmol g^{-1} = 22.4 $cm^3\ g^{-1}$ at STP, and that 1 mmol g^{-1} = 711.42 scf ton^{-1}, Zhang *et al.*, 2012; Ji *et al*., 2012).

The quantity of gas in the adsorbed phase is determined from the gas adsorption isotherm measurement of the shale (Ross and Bustin, 2007). Under the correct conditions, a dominant proportion of the total gas in shale sequences may be stored in the adsorbed state (Ross and Bustin, 2007; Chareonsuppanimit *et al*., 2012). Gas adsorption isotherms for shales are often interpreted using the Langmuir equation (Langmuir, 1916). Typically, gas shales generate a Type I isotherm, which closely fits the Langmuir isotherm model (Ross and Bustin, 2007). A typical gas adsorption isotherm for shale is presented in Figure 1.2:

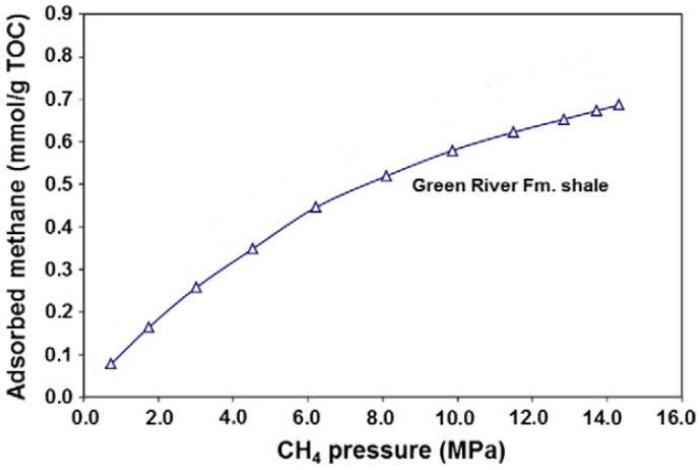

Figure 1.2: Methane gas adsorption isotherm (Type I) for shale (after Zhang *et al*., 2012).

Shales often have relatively small gas adsorption uptakes (~ 0.1 mmol g^{-1}), when compared to the adsorption capacities of other carbon-rich materials (i.e. activated carbons; Chareonsuppanimit *et al*., 2012). For example, Wickramaratne and Jaroniec (2013) measured the low pressure CO_2 adsorption uptakes of two activated carbons to be 4.55 and 8.05 $mmolg^{-1}$. Unfortunately, the small adsorption uptakes of shale samples can often be close to the limits of experimental accuracy for the equipment, and caution must be used when extrapolating the gas adsorption isotherm data from the small experimental sample scale up to the large regional reservoir scale. Small errors in the measured adsorption capacity may result in significant errors in the predicted Gas In Place when scaled up to reservoir scales (Ross and Bustin, 2007).

1.2 Characterisation of pores, porosity and gas storage

1.2.1 Definition of a porous system

Pores and porosity are the primary location for natural gas storage in gas bearing shales (Bustin *et al.*, 2008). Shale pores are voids that are located: 1) between grains and particles (interparticle pores), and 2) inside grains and particles (intraparticle pores), Loucks *et al*., (2009). Pores can have different shapes (e.g. cylindrical, conical, and slit-shaped; Marsh, 1987), and different sizes (millimetre to nanometre diameters), and they can be categorised as either open (O) or closed (C). Open pores (O) are connected to adjacent pores by a network of transport porosity, and closed pores (C) are pockets of porosity that are completely isolated (i.e. gas cannot enter or escape closed pores).

A universally accepted nomenclature for categorising the shale pore system is yet to be agreed upon in the shale literature. There are conflicting terminologies in usage for shale pores in the same pore size range (Chalmers and Bustin, 2012; Loucks *et al*., 2012). The International Union of Pure and Applied Chemistry (IUPAC) system of pore classification is outlined by Rouquerol *et al*., (1994) and is promoted by the coal bed methane and shale gas adsorption community (Clarkson and Bustin, 1996; Prinz *et al*., 2004; Ross and Bustin; 2009; Kang *et al*., 2010; Chalmers and Bustin, 2012; and references therein). Conversely, the non-gas adsorption community, especially those researchers utilising electron microscopy, sedimentological and petrophyiscal techniques, prefer to use terminology based on the “nanometre sized pores = nanopore” concept (Kausik *et al*., 2011; Javadpour *et al*., 2012; Glorioso and Rattia, 2012; Loucks *et al*., 2012; and references therein).

The IUPAC classification scheme (Rouquerol *et al*., 1994) is based on grouping pores into categories termed: 1) macropores, 2) mesopores, and 3) micropores (see Table 1.1). These categories are based on the differing behaviour of adsorbed gas in these three pore ranges. The micropores are subdivided into three categories (see Table 1.2). In the IUPAC classification, the macropores (> 50 nm) behave as transport porosity that allows access to the smaller pores in the interior of the geological sample. Their surface area is very low, but they can represent a significant proportion of the overall pore volume. The mesopores (2 – 50 nm) can also act as transport pores to the smaller microporosity. More importantly, mesopores are subject to the capillary condensation effect, and are responsible for the hysteresis loops observed in the adsorption-desorption isotherms of porous materials. The micropores (< 2nm) play a significant role in the storage of gas in porous materials and are the primary sites for gas adsorption (Ross and Bustin, 2009). Micropores have the largest internal surface area available for gas adsorption (Amann-Hildenbrand *et al*., 2012).

The "Nanopore" classification scheme (i.e. Loucks *et al*., 2009; Javadpour *et al*., 2012) is based on the definition of shale pores that are less than 1 μm (1000 nm) as being termed "nanopores" (Loucks *et al*., 2012). There have been several variations on the "Nanopore" classification scheme in the recent literature, and the most recent attempt to gather all the definitions into one scheme was proposed by Loucks *et al.* (2012). They extended the pore classification scheme proposed by Choquette and Pray (1970) for carbonate rocks, and included the "nanopore" and "picopore" sub-categories. The Loucks *et al.*, (2012) scheme is reported in Table 1.3.

The "Nanopore" classification scheme and the IUPAC classification scheme are compared in Figure 1.3. The main difference is that the "Nanopore" classification scheme of Loucks *et al*., (2012) sub-divides the large "macropore" pore range of the IUPAC classification scheme into more manageable sub-units. The argument of Loucks *et al*., (2012) is that because many mudrock pores commonly range from a few nanometres to several micrometres in diameter, it is useful to have well-defined pore categories for the sub-micrometre range. They argue that whilst the IUPAC system is suitable for synthetic materials (such as zeolites), the IUPAC system is not well suited for the pore structures present in shales and mudrocks.

The pore classification scheme used in this study will be the IUPAC system, as reported in Rouquerol *et al*., (1994). Whilst the arguments for the "Nanopore" scheme have significant merit (Kausik *et al*., 2011; Javadpour *et al*., 2012; Loucks *et al*., 2012), the IUPAC system is well established (unlike the "Nanopore" scheme, which is still in transit). The other important reason why the IUPAC system will be adopted in this study is that much of the data presented will be of gas adsorption in nature, and the usage of the IUPAC system allows the gas adsorption data generated in this study to be directly compared to data available in the published literature. In Figure 1.3, an IUPAC based representation of the different pore categories present in shale is reported.

Table 1.1: IUPAC classification of pores (Rouquerol *et al*., 1994)

IUPAC Pore Classification	Width
Macropores	> 50 nm
Mesopores	2 – 50 nm
Micropores	< 2nm

Table 1.2: IUPAC classification of Micropores (Rouquerol *et al*., 1994)

IUPAC Micropore Classification	Width
Super-Micropores	1.4 – 2.0 nm
Micropores	0.7 – 1.4 nm
Ultra-Micropores	< 0.7 nm

Table 1.3: Loucks *et al*. (2012) classification of pores based on < 1 μm = "nanopores"

Loucks *et al*. (2012) Pore Classification	Width
Macropores	256 mm - 4 mm
Mesopores	4 mm - 62.5 μm
Micropores	62.5 μm - 1 μm
Nanopores	1 μm - 1 nm
Picopores	< 1 nm

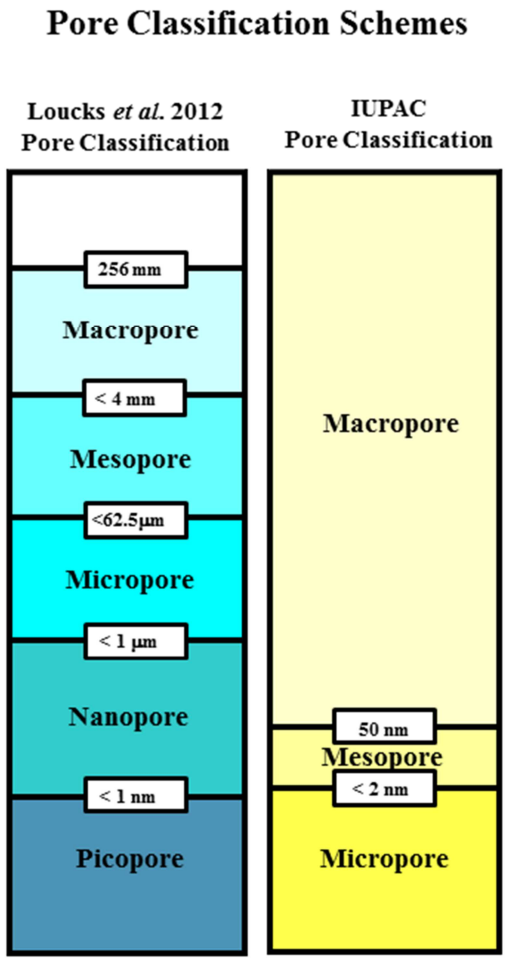

Figure 1.3: The IUPAC and the Nanopore classification schemes are compared. The IUPAC system "macropore" category is subdivided into smaller groups in the "Nanopore" scheme (after Loucks *et al*., 2012)

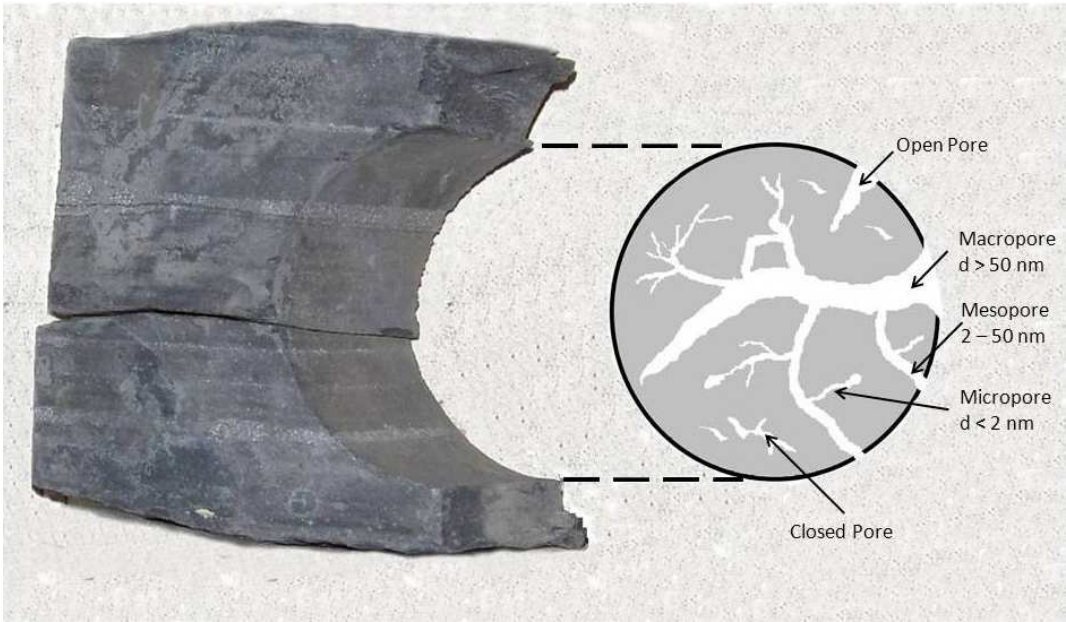

Figure 1.4: A schematic representation of the pore structure in shales. The open pores, closed pores, and transport porosity and pore size distribution can be seen.

Porosity (ϕ) is defined as the ratio of the volume of the voids, V_v, (the pore spaces between grains), to the total (bulk) volume, V_b, of a sample, where V_g is the grain/skeletal volume. The porosity can be expressed as:

$$\emptyset = \frac{V_v}{V_b} = \frac{V_b - V_g}{V_b}$$

(Equation 1.3)

It has been well established that the total porosity of mudstones decreases with increasing effective stress, such as mechanical compaction (Skempton, 1970; Dewhurst *et al.*, 1998).

1.2.2 Methods used to characterise pores and porosity in geological materials

The pore structure and porosity of shales and kerogen concentrates exhibit a wide range of sizes and shapes (Loucks *et al.*, 2012). No one technique or method in isolation can fully analyse the large range of pore structures present in these geological materials. The characterisation of pore structure and porosity is therefore undertaken using a combination of experimental techniques that are used in conjunction.

The size of pore that can be detected depends on the experimental technique used to investigate the pore structure (Bustin *et al.*, 2008). The pore detection ranges of common experimental techniques are shown in Figure 1.5:

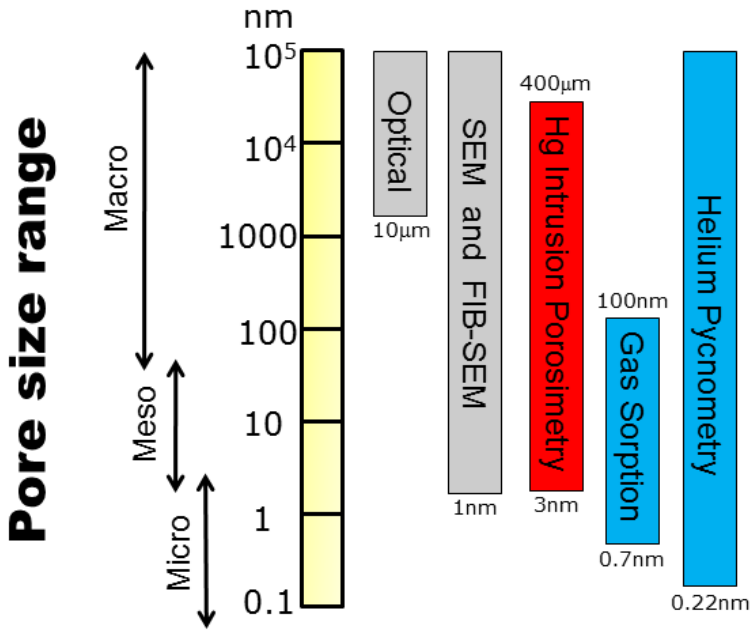

Figure 1.5: The pore ranges covered by common pore characterisation techniques (after Bustin *et al.*, 2008)

1.2.3 Pore characterisation using scanning electron microscopy

Scanning electron microscopy is a widely used experimental technique for generating high magnification images of surfaces (Reimer, 1998: Egerton, 2005). The SEM scans a beam of high energy (typically between 1 and 30 kV) electrons over the surface of a specimen to produce an image (Egerton, 2005). The SEM can produce levels of magnification that are far beyond what is possible with an optical microscopy (Reimer, 1998). Light has a maximum magnification limit of around x2000 and a resolution limit of 200 nm (Smolyaninov, 2008), due to the wavelength of light waves (~ 700 nm to 400 nm). In contrast, electron beams under vacuum have a much shorter wavelength than light (about 100,000 times), and allow the SEM to magnify surfaces up to about 500 000 times, with an image resolution up to 1 nm (Dufek, 2007).

The SEM records images of samples by raster scanning a focused electron beam across the sample surface, and interpreting the signals that are emitted from each scan point (Egerton, 2005). To obtain SEM images of samples, they need to be mounted on to a specimen holder (called a “stub”), and loaded in to the SEM sample chamber. The sample chamber is a high vacuum environment, to prevent gas molecules interfering with the flight path of the electron beam (Egerton, 2005).

Once the sample is loaded in to the chamber, the SEM generates a beam of incident electrons using an “electron gun” (Egerton, 2005). An electron gun can either be a heated filament of tungsten wire (thermionic emission) or a negatively charged tungsten tip surrounded by a positively charged anodic ring (field emission). The high energy primary electrons are emitted from the electron gun in to the high vacuum of the sample chamber, and focussed in to an electron beam using electrostatic condenser lenses (Reimer, 1998; Egerton, 2005).

The beam is focussed in to a small probe spot (0.4 nm to 5 nm in diameter). The beam passes through electrostatic deflector plates that very accurately control the position of the electron beam spot on the sample surface (Reimer, 1998; Egerton, 2005). This control allows the beam to be deflected in any direction, and the electron beam is raster scanned across a rectangular area of interest. A schematic diagram of a scanning electron microscope is shown in Figure 1.6:

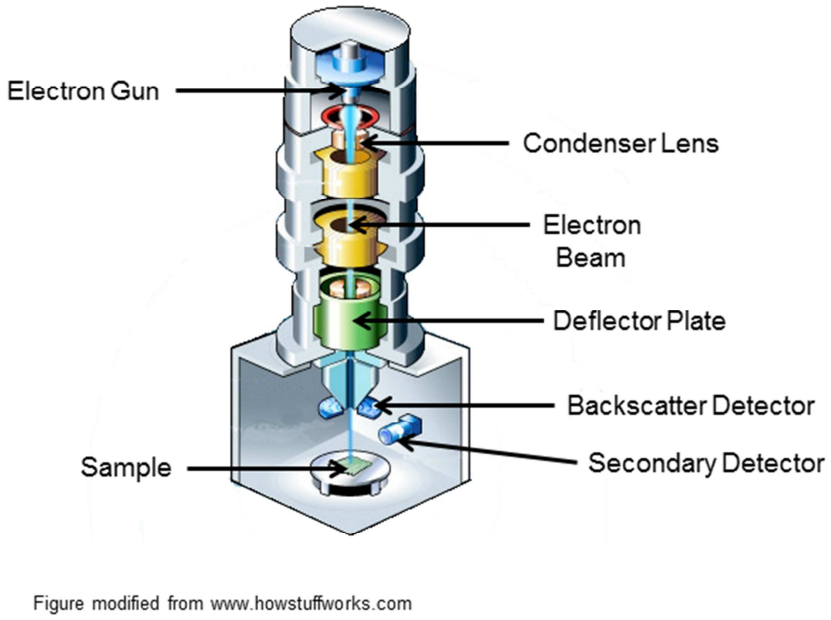

Figure 1.6: A schematic diagram of a scanning electron microscope.

When the high energy primary electrons of the beam come in to contact with the sample surface, the electrons transfer energy to the atoms at or near to the sample surface. This energy is lost by absorption in to the sample and by random back scattering of primary electrons away from the surface (Joy *et al*., 1986; Bozzola and Russell, 1999). The surface atoms that absorb energy are stimulated in to emitting other forms of electromagnetic radiation. These can include, low energy secondary electrons, infra-red heat radiation, visible light radiation (cathodoluminescence) and X-ray radiation. The emitted radiation is detected and these signals are amplified and interpreted to give information about topography and composition of the surface (Joy *et al*., 1986).

The most common detection mode in SEM is secondary electron imaging (SEI), where the low energy secondary electron signal radiation from the surface is detected and used to construct the image (Reimer, 1998). This mode gives information about any topography present on the sample surface. Another signal that is commonly detected during SEM is the back scattered electron (BSE) signal (Reimer, 1998). The BSE is generated by the high energy primary electrons that are randomly scattered back from the surface. The intensity of the reflected electron beam is strongly proportional to the atomic number of the phase under the beam (the higher the mass, the more intense the reflected beam). Therefore BSE images can provide useful information about the elemental distribution of atoms in the surface (Reimer, 1998). Another important signal that is commonly detected is the X-rays generated by the ionisation of surface atoms. The X-rays have discrete wavelengths that are characteristic of the atomic element emitting it, and this allows identification of atomic elements in the sample surface (Bozzola and Russell, 1999).

1.2.4 Pore characterisation using FIB-SEM

The nanometre scale pore structure of shale samples can be investigated using high-resolution images generated by the Focused Ion Beam (FIB) scanning electron microscopy (FIB-SEM) technique. The FIB-SEM technique is a modification of the standard SEM technique that can be used to improve the quality of the mudstone surface prior to high-resolution SEM imaging (Loucks *et al*., 2009).

Standard petrographical preparation of mudstone thin-sections involves grinding and polishing the surface with fine grit and power (Loucks *et al*. 2009). Unfortunately this produces surface irregularities because of differences in hardness of the component grains in the mudstone matrix. A relatively rough surface (on the nanometre scale) is produced by mechanical polishing due to fine grained particles being plucked from the surface. The indentations left behind can be easily misinterpreted as naturally occurring pores. An example of the difference in quality of the "polish" is shown in Figure 1.7, where a sample of Barnett shale was prepared using standard petrographical methods (image A), and a sample of the same shale was prepared using FIB milling:

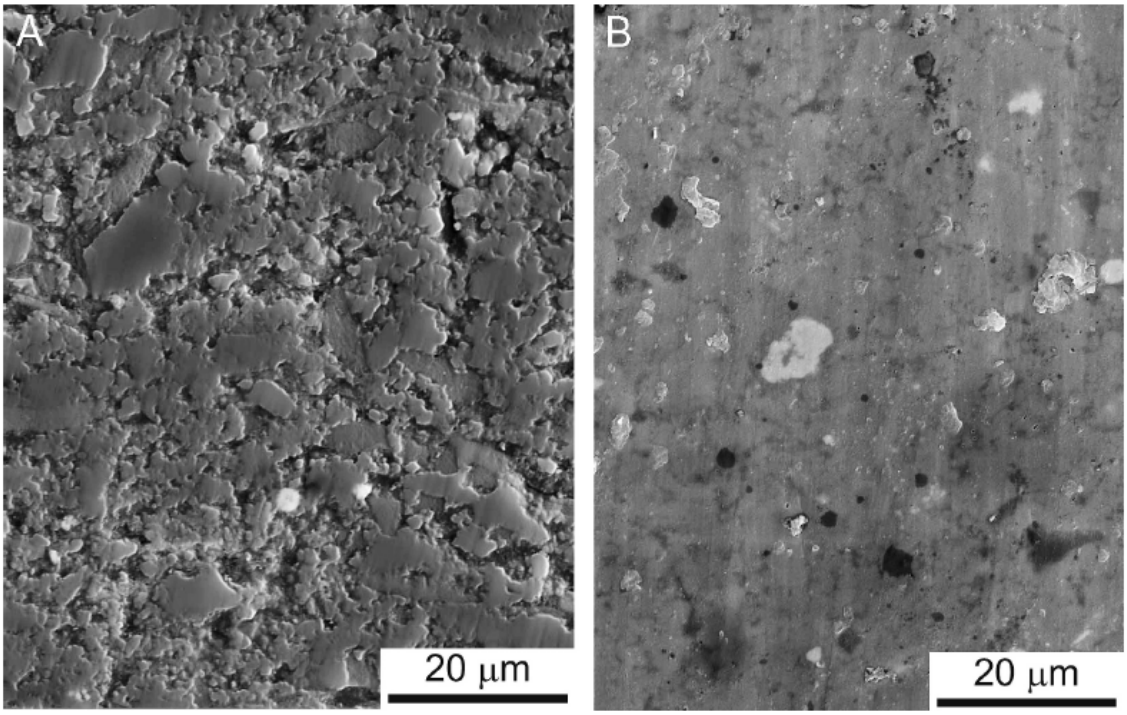

Figure 1.7: The difference in the quality of the surface "polish" can be seen between A) the mechanically polished using standard petrographical techniques, and B) the FIB milling technique (after Loucks *et al*., 2009).

The FIB uses a high energy focused beam of gallium ions (Ga^{+}) to mill material away from the sample (an Argon ion beam can also be used). In a liquid metal ionisation source (LMIS), liquid gallium is heated and then wetted onto a tungsten needle. At the tip of the needle, the gallium atoms become charged, and then are field-emitted from the source. The high energy gallium ions are accelerated and focussed in to a beam by an electrostatic condenser lens.

The gallium ion beam scans the sample surface and mills material away, at a rate depending on the beam current. Once milled the material leaves the surface and enters the vacuum. The ion beam generates secondary electrons in the same way that an electron beam does, and can therefore be used to generate an image, allowing for precision positioning and scanning of the beam to mill material away from specific areas. The ion beam can be used to mill away a trench of material, exposing a surface of material from within the bulk, and therefore exposing any pores which exist in the bulk. Once a surface has been exposed, it can be imaged with the conventional SEM beam in the FIB-SEM.

The main disadvantages of the FIB-SEM technique are that: 1) the images captured are of a very small area, and that this area may not be representative of the whole sample, and 2) the images only provide a qualitative visual qualitative representation, thus hindering a numerical/statistical analysis of the data.

1.2.5 Pore characterisation using mercury intrusion porosimetry

Mercury intrusion porosimetry (MIP) is a long established pore characterisation method that was first implemented by Ritter and Drake (1945). It is based on the earlier theoretical work of Washburn (1921), which is itself based on the Young-Laplace equation from the nineteenth century work of Laplace (1806). The MIP technique is able to measure a wide range of pore sizes, from the smallest nanometre scale up to the (relatively) large millimetre scale. This represents a pore size range of over five orders of magnitude, which is a distinct advantage over other pore characterisation techniques. For example, pore characterisation using gas sorption has a maximum detectable pore diameter size of ~ 100 nm (Diamond, 1970; Lowell and Shields, 1981; Westermarck, 1998; Groen *et al*., 2003; Lubda *et al*., 2005; Klobes *et al*., 2006; Bustin *et al*., 2008; Chalmers and Bustin, 2012; Kuila and Prasad, 2012). Low pressure gas adsorption methods are not able to measure the internal pore volume of pores with diameters in the micrometre or millimetre scale (Westermarck, 1998).

The MIP technique is based on the non-wetting properties of liquid mercury. A non-wetting fluid is defined as having a surface contact angle greater than 90^{o} for the solid surface of interest. For the vast majority of solid materials, liquid mercury is non-wetting, and will not spontaneously intrude the pores of that solid unless an external pressure is applied (Ritter and Drake, 1945; Diamond, 1970).

During mercury intrusion porosimetry, the porous sample is enclosed in a vacuum chamber of known volume (a “penetrometer”). The sample is subjected to a vacuum, to remove entrapped air from the pores, as this air can produce a resistant back pressure that impedes the intrusion of mercury. Once under vacuum, the liquid mercury is then forced in to the pores of a solid using a programme of increasing pressure. Each pressure step increase allows an additional incremental volume of mercury to be forced into the pore structure of the sample (Sing, 2004).

The step-wise increasing pressure programme generates a mercury intrusion curve, as shown in Figure 1.8:

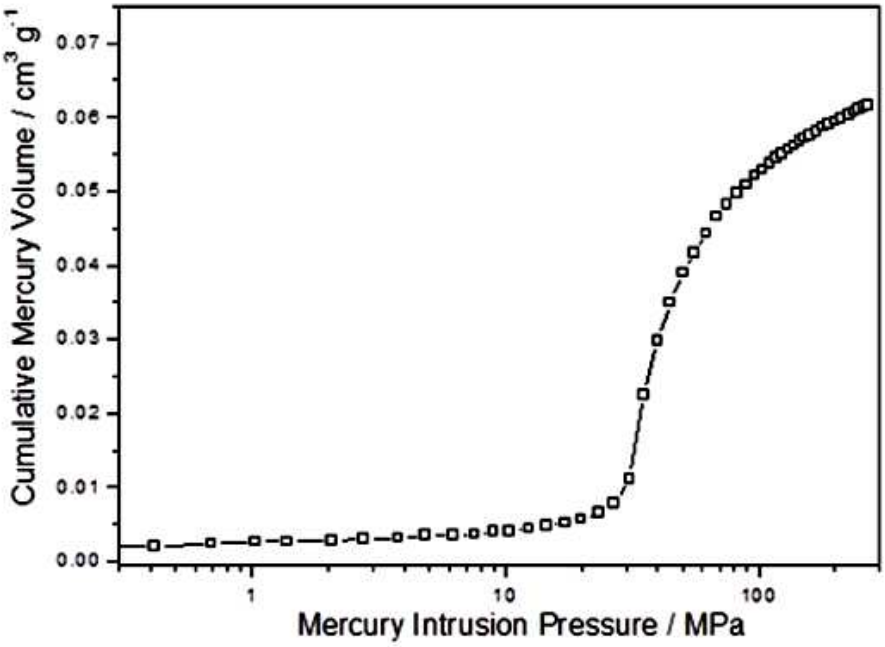

Figure 1.8: The MIP intrusion curve is plotted on a base 10 logarithmic scale because MIP can detect a pore size range that is over several orders of magnitude (Denoyel *et al.*, 2004)

Mercury intrusion porosimetry measures the largest pore throats first (at low pressure), and as pressure increases, the pore size detected becomes ever smaller (Westermarck, 2000). The pressure required to intrude mercury into the pores is inversely proportional to the size of the pores.

The minimum pore size that the MIP technique can detect is dependent on the maximum pressure that can be generated by the porosimeter equipment. Commercially available MIP porosimeters can often reach pressures of up to 60 000 psi, however the equipment used during this study had a maximum pressure of 39 000 psi (268 MPa). At this pressure, the smallest pores accessible are 3 nm in size. This means that there is an overlap between the pore size range accessible to mercury intrusion porosimetry and gas sorption (Westermarck, 2000).

The maximum pore throat size that can be detected by a modern MIP porosimeter is around 400 μm (Giesche, 2006). It is only mercury intrusion porosimetry that can be used to investigate these larger macropores (Ritter and Drake, 1945; Rootare and Prenzlow, 1967; Fischer and Guapp, 2004; Giesche, 2006), as the maximum pore size detectible by gas sorption is around 100 nm to 300 nm (Diamond, 1970; Lowell and Shields, 1981; Westermarck *et al*., 1998, Groen *et al*., 2003; Lubda *et al*., 2005).

It is important to emphasise that the MIP technique only measures the diameter of the pore "throats" (the constriction at the entrance to the pore), and not the diameter of the pore body. Unfortunately, this means that a large pore with a tight constriction at the entrance is misinterpreted as having a small pore volume. Furthermore, if there are several pore throat entrances to one pore body, liquid mercury will pass through the largest pore throat constriction first (as this will require the least pressure to do so; Conner *et al.*, 1986). In this situation, the pore volume is attributed to the diameter of the largest pore throat, which may not be representative of the other pore throats.

The pore throat diameter (d) cannot be directly obtained from the experimental MIP data, and needs to be calculated using the Washburn equation (Washburn, 1921; Ritter and Drake, 1945; Giesche, 2006). The Washburn equation is defined as:

$$d = \frac{-4\gamma \operatorname{Cos} \theta}{P}$$

(Equation 1.4)

where d = pore throat diameter (m), γ = surface tension of mercury (usual taken to be 0.485 N m^{-1}), P = mercury intrusion pressure (Pa), and θ = contact angle between the solid surface and the liquid mercury (by convention, agreed to be 141° for geological materials).

The Washburn equation is based on two assumptions: 1) that the pores are all the same shape (cylindrical, and thus having a circular cross section), and 2) that the pores are both unconnected and non-intersecting (Washburn, 1921; Conner *et al.*, 1986). The assumption of cylindrical pores is used to keep the mathematics of the equation simple (Washburn, 1921). Although these two assumptions do not represent reality (because pores generally have variable 3D geometries, and are usually highly interconnected), the experimental error in the total pore volume has been found to be negligible (Rootare and Prenzlow, 1967), and the experimentally measured pore size distribution is very close to the true distribution of a known calibration sample (Ritter and Drake, 1945).

1.2.6 Data analysis and interpretation of mercury intrusion porosimetry results

Mercury intrusion porosimetry is now routinely used to characterise the pore structure and total porosity of geological materials (Diamond, 1970; Fischer and Guapp, 2004; Cranganu *et al.*, 2009). MIP is able to determine:

1) Bulk density
2) Total and Hg-macropore volume
3) Total porosity
4) Pore surface area
5) Pore size distribution

1) Bulk density: The bulk density (ρ_b) of a sample can be directly determined from the MIP data. The bulk density is defined as the ratio of the total mass of the solid to the total volume of the sample. It includes all the pore spaces and voids in the sample. The bulk density of shale is usually around 2.2 to 2.5 gcm^{-3}.

The bulk density (g cm^{-3}) is simply the ratio of the known sample dry mass (M_s) in grams, to the known bulk volume (V_b) in cm^3, where the bulk volume (V_b) is calculated from:

$$V_b = V_{pen} - V_{Hg}$$

(Equation 1.5)

which becomes

$$V_b = V_{pen} - \left[\frac{\left(M_s + M_{pen} + M_{Hg}\right) - \left(M_s + M_{pen}\right)}{\rho_{Hg}}\right]$$

(Equation 1.6)

where: V_{pen} = volume of empty penetrometer (cm^3), V_{Hg} = volume of liquid mercury (cm^3), M_s = dry mass of sample (g), M_{pen} = mass of empty penetrometer (g), M_{Hg} = mass of liquid mercury (g), and ρ_{Hg} = density of mercury (g cm^{-3}), taken by convention to be 13.54 g cm^{-3}.

2) Total and Hg-macropore volume: The total pore volume is the sum of the internal volumes of all the voids in a porous material. It is the maximum pore space present, and it includes both the open pores (that are accessible to probe molecules), and closed pores (which are "blind" pores that are completely isolated and inaccessible).

Total pore volume is calculated from (Leon, 1998):

$$V_{total} = \frac{1}{\rho_b} - \frac{1}{\rho_g}$$

(Equation 1.7)

Where: V_{total} = Total pore volume (cm g^{-1}), ρ_b = bulk density (g cm^{-3}) and ρ_g = grain density (g cm^{-3}).

The Hg-macropore volume is the pore volume that is measurable with mercury intrusion porosimetry, but is not measurable by gas adsorption analysis (Webb & Orr, 1997). The Hg-macropore volume is the volume of pores with diameters greater than 100 nm. Mercury intrusion porosimetry has a wider pore detection range (3 nm – 400 000 nm = 400 μm) than gas adsorption (~ 0.4 nm to ~ 100 nm), and can therefore fill more of the available pore volume than is possible using gas adsorption (Westermarck, 2000).

3) Total porosity: Mercury intrusion porosimetry can be used to determine the total porosity of porous samples. Total porosity (ϕ) is defined as the unit-less ratio of the volume of the voids (the pore spaces between grains), to the total volume of a sample. It is often represented as a percentage value. Total porosity cannot be measured directly from MIP, but is determined from both the bulk and grain densities of the sample.

The grain density (ρ_g) is defined as the ratio of mass of the grains of the sample only to the volume of these grain particles, and does not include the volumes of the pore spaces between the grains. The grain density of shales is usually around a value of 2.65 gcm^{-3}. The grain density (ρ_g) is usually determined using Archimedes' principle of fluid displacement, using a water bottle pycnometer technique. A more accurate method for determining the grain density (also known as the "skeletal" density) is to use helium pycnometry. This gives a more accurate value of the grain density, but requires expensive and sophisticated gas sorption equipment.

Mercury intrusion porosimetry determines the total porosity (ϕ) of the shale from the bulk density (ρ_b) and the grain density (ρ_g):

$$\emptyset = 1 - \frac{\rho_b}{\rho_g}$$

(Equation 1.8)

Where bulk density (ρ_b) and the grain density (ρ_g) are in g cm^{-3}.

4) Pore surface area: The internal surface area of a porous solid can be determined using mercury intrusion porosimetry, using the R-P equation proposed by Rootare and Prenzlow (Rootare and Prenzlow; 1967, Huismane, 1983; Westermarck, 2000; Giesche, 2006):

$$A = \frac{-1}{\gamma \cos\theta} \int_0^{V_{max}} P \, dV$$

(Equation 1.9)

where A = surface area (m^2), P = mercury intrusion pressure (Pa), V = volume of mercury intruded at pressure P (m^3), γ = mercury surface tension (N m^{-1}), and θ = mercury contact angle. Surface area is usually quoted in units of m^2 g^{-1}, so the surface area needs to be normalised for sample mass. The equation is applied by integrating the area under the mercury intrusion curve, between the defined limits of zero mercury volume, and the maximum mercury volume intruded, at the upper limit of the pressure range desired. This is reported in Figure 1.9:

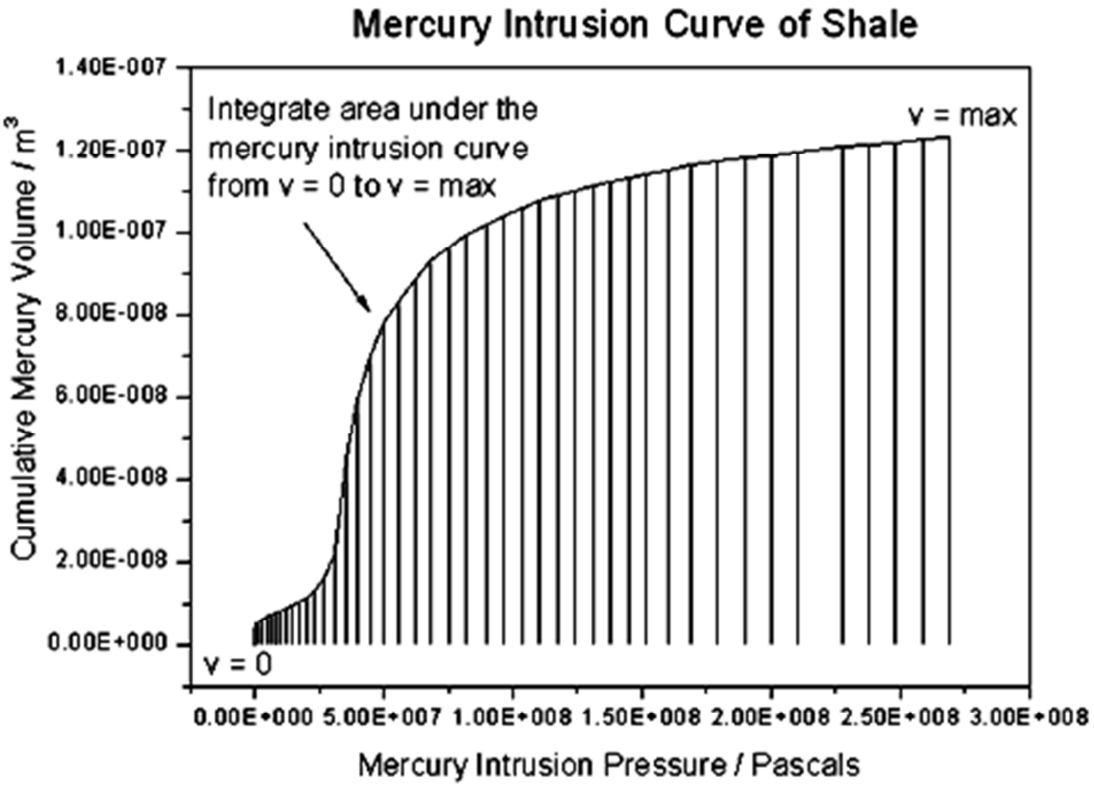

Figure 1.9: The surface area is obtained by integrating the area under the MIP intrusion curve, between the integral limits.

5) Pore Size Distribution (PSD): Mercury intrusion porosimetry can be used to determine the pore size distribution ($\phi_{\%}$). The PSD is calculated from the cumulative porosity (ϕ_{cum}) and the total porosity (ϕ):

$$\phi_{\%} = \frac{\phi_{cum}}{\phi} \cdot 100\%$$

(Equation 1.10)

where the cumulative porosity (ϕ_{cum}) is calculated from the total porosity (ϕ), the cumulative mercury intruded (σ), in $cm^3\ g^{-1}$, up to that pressure step, the mass of the sample (m), and the bulk volume of the sample (V_b):

$$\phi_{cum} = \phi - \frac{(\sigma . m)}{V_b}$$

(Equation 1.11)

The relative pore size distribution ($\phi_{\%}$) is then plotted against a base 10 logarithmic scale of the pore diameter, giving a pore size distribution graph, as shown in Figure 1.10:

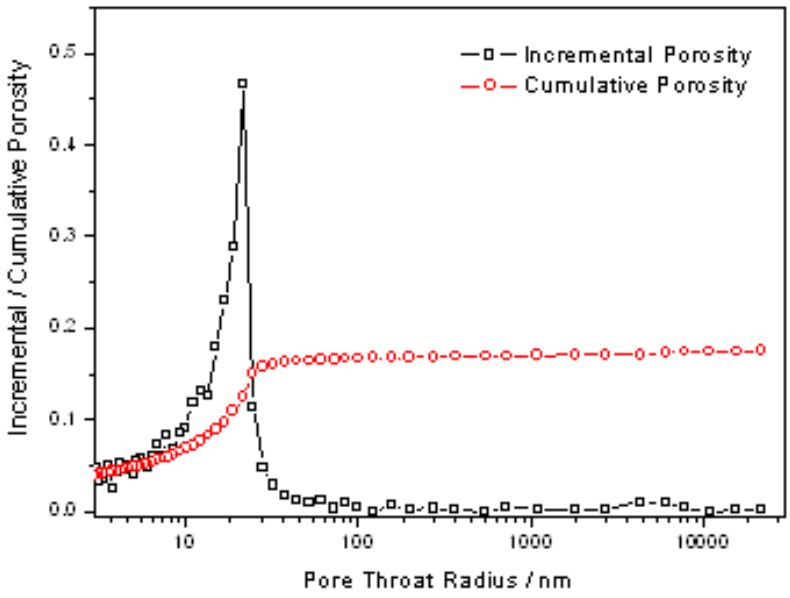

Figure 1.10: The pore size distribution of a typical shale rock sample.

1.2.7 Advantages, disadvantages and limitations of mercury intrusion porosimetry

Mercury intrusion porosimetry has established itself as the standard experimental technique for characterising a wide variety of porous materials; everything from pharmaceutical tablets and sintered ceramic filters, to building cements and petroleum reservoir core samples. This is because MIP has the advantage of being significantly faster than gas sorption techniques (Westermarck, 2000), and generates quantitative pore data (unlike the qualitative pore images from SEM micrograph). MIP porosimeters are also relatively simple equipment to operate and the subsequent data analysis and interpretation is straight forward.

A major limitation of mercury intrusion porosimetry is the assumption that all porous materials are rigid, and that the pore shape or size is not changed during the high pressure intrusion of liquid mercury. It is possible that extremely high applied pressures (39 000 psi = 2680 bar) may compress or distort the sample, causing pores to close (or open), generating inaccurate porosity measurements (Westermarck, 2000).

Another problem with MIP is the use of standard values of surface tension and contact angle, and the assumption that all porous materials have similar contact properties. This may not always be appropriate, as the contact angle of mercury can vary depending on the surface roughness of the porous sample. In high precision work, determination of the true contact angle should be considered (Westermarck, 2000).

Mercury intrusion porosimetry can also sometimes overestimate the amount of smaller pores present in a porous sample (Auvinet and Bouvard, 1989). The measured pore size distribution of a sample can be falsely skewed towards the smaller pores, because MIP measures the pore throat constriction, not the actual pore body (Dees and Polderman 1981; Allen, 1997). This problem occurs because the intrusion cycle of mercury porosimetry involves a sequential increase in applied pressure. Each pressure corresponds to a particular pore throat constriction diameter. At each pressure step, it is not possible to know if all the pores in the sample corresponding to that pressure are being measured. Some pores will not be measured at their correct pressure, because they are located behind narrower pores that require a larger pressure that has not yet been achieved. These inaccessible large pores are only detected after the mercury has intruded the smaller pores that are shielding them, causing these larger pores to be inaccurately assigned as smaller pores. This problematic effect has been termed “shadowing” (Conner *et al.*, 1986; Rigby *et al.*, 2011). Shadowing leads to a false skewing of the pore size distribution towards smaller pores.

1.2.8 Pore characterisation using gas adsorption analysis.

Gas sorption occurs when a gas molecule interacts with the surface of a solid substance. This interaction occurs at the interface between the solid phase and the gaseous phase, and causes the gas molecule to adhere to the surface due to physical or chemical forces.

The term “sorption” is used to describe the multi-step process leading to a gas molecule interacting with a surface (McBain, 1909). Sorption is used to describe the process of a gas molecule in the bulk gas phase diffusing towards a solid, followed by absorption into pores of the solid’s bulk phase, followed by the interaction with the surface of the solid, leading to adsorption.

The following terminology is associated with adsorption science (Gregg and Sing, 1982):

- Absorption: The penetration of a gaseous molecule into the bulk phase of the solid.
- Adsorption: The interaction of a gaseous molecule with a surface site causing binding to the adsorbent surface.
- Desorption: The release of the adsorbate from the adsorbent surface back into the bulk gaseous phase.
- Adsorbent: The solid substance onto which the adsorptive binds.
- Adsorptive: The gas phase molecule.
- Adsorbate: A molecular species that has been adsorbed, producing the adsorbed phase.

Adsorption is an exothermic process, and the release of heat energy during adsorption of a gas molecule is due to the reduction of the disorder (entropy) of the adsorbate gas on the surface relative to the bulk gas phase (Gregg and Sing, 1982). Adsorption can be subdivided into two types: physisorption and chemisorption (Toth, 2002). The difference between them is a result of the nature of the force of attraction between the adsorbate and the surface. There is also a difference between them in the quantity of heat energy released during adsorption (Rouquerol *et al.*, 1999).

The formation of a physical attraction between the solid surface atoms and the adsorbate gas results in physisorption. A weak electrostatic attraction between the adsorbate and atoms in the solid surface is the cause of physisorption (Gregg and Sing, 1982). Although the attraction is weak, it acts over a relatively long range from the surface. The long range nature of physisorption means that multilayers of adsorbate gas molecules can form on the surface (Rouquerol *et al.*, 1999). The electrostatic attraction is due to weak intermolecular forces (most notably London's dispersion forces). The weak strength means that a relatively small amount of heat energy is released during adsorption as a result of physisorption. Physisorption is reversible, and the chemical identity of the molecule remains intact (Do, 1998).

The formation of a chemical bond between the solid surface atoms and the adsorbate gas results in chemisorption (Gregg and Sing, 1982). The chemical bond is strong, but localised to a very short range from the surface (Rouquerol *et al*., 1999).The short range nature of chemisorption means that only monolayers of adsorbate gas form. The chemical bond requires activation energy to form, but once formed, it results in a larger amount of heat energy being released than with physisorption (Rouquerol *et al*., 1999). Chemisorption is usually irreversible, as a covalent bond is formed between the adsorbate gas and the surface, usually resulting in the chemical identity of the molecule being permanently altered (Do, 1998).

1.2.9 Adsorption Isotherms

The pores, porosity and gas storage potential of geological materials has long been investigated using gas adsorption isotherms (Sevenster, 1959; Ettinger *et al*., 1966; Gan *et al*., 1972; Lu *et al*., 1995; Bae and Bhatia, 2006; Chalmers and Bustin, 2007; Busch *et al*., 2008; Ross and Bustin, 2009; Clarkson *et al*., 2013). An isotherm is a measurement of the amount of gas adsorbed onto a surface (or into a pore), as a function of pressure (under the experimental conditions of fixed temperature). An example of an adsorption isotherm is shown in Figure 1.11:

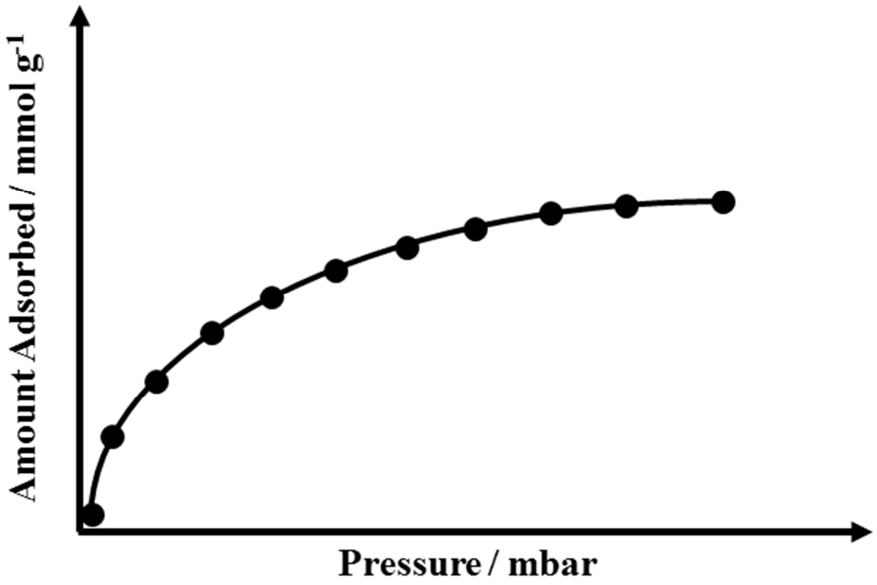

Figure 1.11: Schematic representation of an adsorption isotherm, showing how the amount of gas sorbed changes at each pressure step.

The temperature needs to be held constant throughout the analysis because both temperature and pressure are controlling factors in determining the change in gas amount sorbed onto the surface.

The isotherm is generated by setting the gas pressure to a constant set-point and allowing the amount of adsorbed gas on the surface to reach equilibrium and become constant. This can be seen in Figure 1.12:

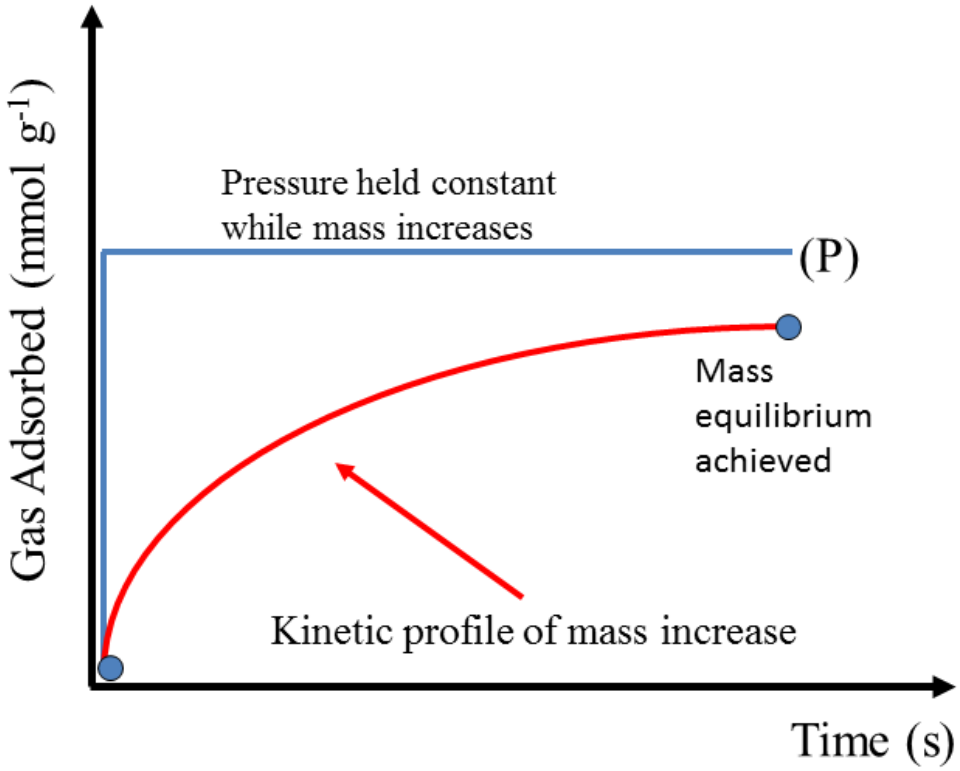

Figure 1.12: Schematic diagram of isothermal mass change due to pressure.

Once equilibrium has been reached the gas pressure is changed to the next set-point, and the amount of adsorbed gas on the surface will also change, in accordance with Le Chatelier's principle. If this process is undertaken several times, a gas adsorption isotherm is generated (Figure 1.13):

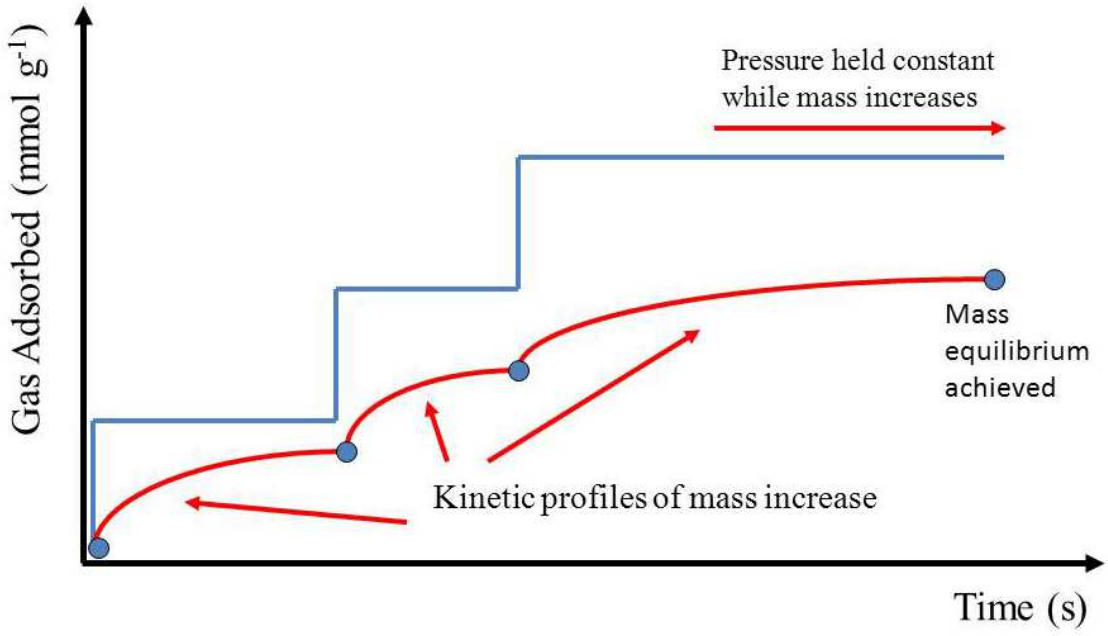

Figure 1.13: Multiple isothermal mass changes due to pressure result in an isotherm.

Adsorption isotherms can be categorised based on their shape; the IUPAC classification scheme recognises six distinct types (Sing *et al*., 1985). The majority of gas adsorption isotherms for geological materials in the published scientific literature can be described as Type I or Type II (Ross and Bustin, 2009; Clarkson *et al*., 2013). The remaining isotherm categories, which are known as Type III, Type IV, V and VI, shall not be discussed here so as to keep this chapter relevant to geological materials. The characteristics of Type I and II isotherms are reported in Figure 1.14:

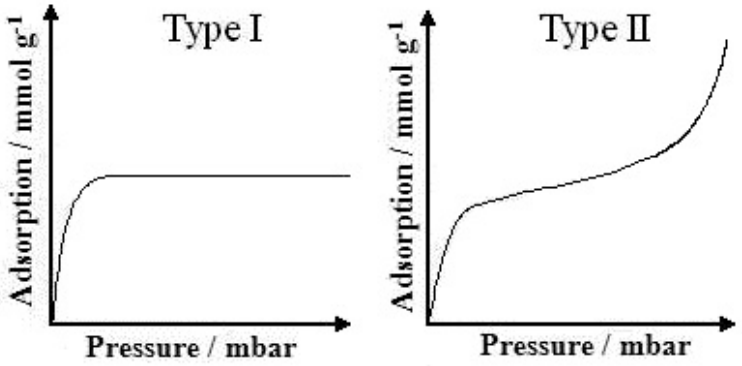

Figure 1.14: The two IUPAC isotherms types observed in geological materials (Sing *et al*., 1985).

Type I isotherms are generated by gas sorption in microporous materials. It is a concave curve (relative to the pressure axis), and it is due to an initial rapid uptake of gas at low relative pressure (over a small change in pressure). Type I isotherms usually reach a plateau at relatively low relative pressures (around about ~0.1 p/p^o), (where relative pressure is signified by the p/p^o symbol). This behaviour indicates that all the microporosity has been filled with gas and no more gas sorption can occur: the plateau region will extend all the way up to $p/p^o = 1$. Gas adsorption in microporous materials is enhanced due to the overlap of Polanyi energy fields from the very closely spaced pore walls (Toth, 2002).

The plateau of Type I isotherms is useful, because the total pore volume of the microporous sample can be calculated by extrapolating the plateau back until intersection of the y-axis (assuming density and molar mass of the adsorbate are known). Another useful result is that adsorption data from Type I isotherms may produce a linear plot of the Langmuir equation. Further details of the Langmuir equation will be discussed in Section 1.3.14 (below), but it is worth mentioning at this point that the gradient of the Langmuir plot is equal to $1/n_m$ and can be used to calculate the gas sorption pore volume (Gregg and Sing, 1982), (where n_m is the maximum adsorption sites available on the adsorbent solid).

Type II isotherm are typical of macroporous and non-porous materials. It is a concave curve (relative to the pressure axis), followed by small linear region. The shape of this isotherm is due to the formation of a gas monolayer (the initial concave region), followed by multilayer surface coverage at higher relative pressure (Gregg and Sing, 1982),. The initial gas uptake in the concave section has a shallower gradient than in the equivalent part of a Type I isotherm (Toth, 2002). These isotherms are also known as "BET isotherms" (see Section 1.3.15, below) due to unrestricted multilayer formation in the second part of the isotherm. Type II isotherms are typical of low temperature nitrogen gas adsorption (-196^{o}C).

1.2.10 Capillary condensation and hysteresis loops of adsorption isotherms

In mesopores (2 nm to 50 nm), gas adsorption occurs by the capillary condensation mechanism (Toth, 2002). In the confined spaces of narrow capillary-like mesopores, the close proximity of the pore walls force gas phase molecules closely together, allowing the short range cohesive forces of attraction to condense gas molecules in to a liquid phase (or solid for CO_2) at temperatures above the boiling point (Gregg and Sing, 1982). The maximum temperature of capillary condensation is called the critical temperature (T_c), beyond which gas cannot be forced in to a condensed phase by confinement.

Capillary condensation does not occur in micropores or macropores (Rouquerol *et al*., 1999). In micropores (< 2 nm) the close proximity of the pore walls to each other results in a restricted volume, and gas adsorption occurs by a volume filling model (Dubinin and Radushkevich, 1947), rather than a capillary condensation mechanism. The volume filling mechanism occurs in micropores because the pore walls are close enough in proximity to facilitate an enhanced adsorption of gas molecules. In macropores (> 50 nm) gas adsorption only occurs by the formation of monolayers and multilayers, especially at higher relative pressures.

The capillary condensation mechanism of mesopores (2nm to 50nm) can be detected in porous materials as a hysteresis loop in the experimental gas isotherm (De Boer, 1958). Hysteresis is observed when the adsorption branch of an isotherm does not exactly overlay the desorption branch of the isotherm (over a specific pressure range). Hysteresis occurs in the isotherm when the mechanism of adsorption and desorption is different (Zsigmondy, 1911). Isotherm hysteresis is caused by the change in the contact angle between the meniscus and the pore wall during sorption. The size of hysteresis loops is temperature dependent, and it has been observed that the loops decrease in size with increasing temperature. Capillary condensation occurs because the localised vapour pressure above the surface meniscus of the confined liquid is reduced by the narrow diameter of a mesopore. The capillary condensation effect only occurs in mesopores (2 nm to 50 nm); in micropores (< 2 nm) the pore diameter is too small for a liquid meniscus to form, and in macropores (> 50 nm) the localised vapour pressure above the meniscus is almost equal to normal atmospheric conditions (Rouquerol *et al*., 1999).

Hysteresis loops are categorised into four groups (De Boer, 1958):

- Type H1
- Type H2
- Type H3
- Type H4

Type H1 hysteresis loops are characteristic of capillary condensation in open-ended cylindrical pores. It is a relatively narrow loop forming at high pressures, with a steep gradient on both the adsorption and desorption branches. Type H2 hysteresis loops are characteristic of trapped adsorbate within the porous structure of the sample. It is a broad loop which can form at both low and high pressures. Type H3 hysteresis loops are characteristic of slit shaped pores. It is a relatively narrow loop, and the adsorption branch does not reach plateau, even on approach to the adsorptive's saturated vapour pressure. The liquid meniscus in the mesopores does not form until a high relative pressure is reached. Type H4 hysteresis loops are characteristic of materials containing significant microporosity, and therefore observed with Type 1 isotherms (see above). It

is a relatively broad loop forming at high pressures, with a shallow gradient on both the adsorption and desorption branches

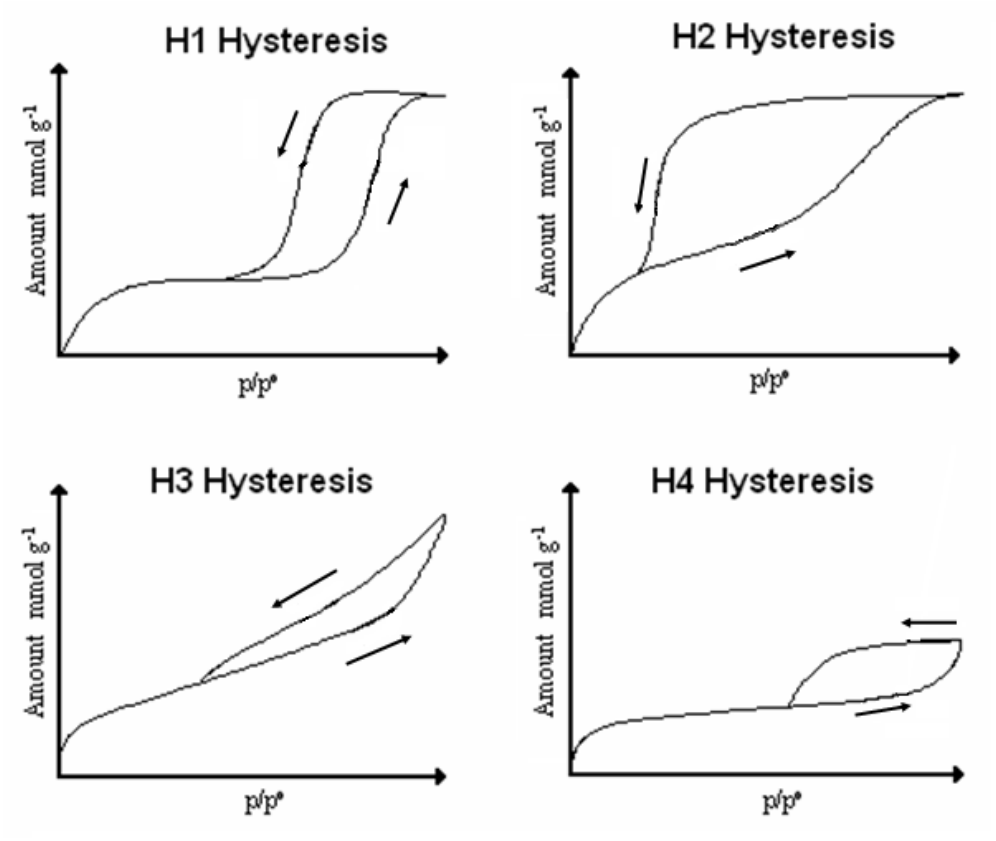

Figure 1.15: Four hysteresis loop types of the De Boer (1958) classification.

1.2.11 Interpretation and Analysis of Adsorption Isotherms

An experimentally measured gas adsorption isotherm for a geological sample can be interpreted using various mathematical models. These models are used to calculate key properties of the sample from the adsorption isotherms, such as 1) the maximum gas storage capacity, 2) the total pore volume of the porosity, 3) the pore size distribution, 4) specific surface areas, and 5) the micropore volume (Langmuir, 1918; Brunauer *et al.*, 1938; Dubinin and Radushkevic, 1947).

All isotherm models are based on the behaviour of gases interacting with solids:

1) Adsorption occurs when gas molecules collide with solid surfaces. This adsorption can be due to physisorption or chemisorption.

2) A physical equilibrium forms when the rate of gas molecules adsorbing to a surface is equal to the rate of gas molecules leaving the surface. The equilibrium position is affected by temperature (due to Le Chatelier's Principle).

3) The amount of adsorbed gas molecules is a function of pressure (at constant temperature).

4) At low pressures, all adsorption isotherms obey Henry's law

1.2.12 Henry's Law

Henry's Law is the fundamental starting point for all the mathematical models used for interpreting gas isotherms (Henry, 1803). Henry's law describes the empirical observation that at high temperatures and/ or very low pressures, the amount of gas adsorbed varies linearly with the equilibrium gas pressure (Henry, 1803). The equation for Henry's law is simply:

$$n = K_H\, p$$

(Equation 1.12)

where:
p = gas pressure,
n = amount adsorbed
K_H= Henry's constant (it depends on the interaction of the adsorbate and adsorbent)

All adsorption equations reduce to the Henry's law form in the very low pressure region of the gas isotherms (when gas uptake is low), (Henry, 1803).

1.2.13 Langmuir Model

The Langmuir equation (Langmuir, 1916; Langmuir, 1918) is probably the best known and most widely used model for interpreting sorption processes. It has been successfully used to interpret adsorption isotherms in geological materials (Clarkson and Bustin, 1996; Bustin and Clarkson, 1998; Crosdale *et al.*, 2008; Ross and Bustin, 2009; Gensterblum *et al.*, 2009).

The Langmuir equation models the adsorption process on an open surface, and is based on three assumptions (Langmuir, 1916; Langmuir, 1918):

1) An open surface has a 2-dimensional grid of energetically equal adsorption sites.

2) One gas molecule per site is the allowed adsorption limit, and maximum gas saturation occurs when the first monolayer has formed. There is no multilayer adsorption.

3) There are no electrostatic interactions or forces of attraction between the adsorbed molecules, hence adsorption is localised to the adsorption site on the open surface.

The standard form of the Langmuir equation is:

$$\frac{N}{N_m} = \frac{KP}{(1 + KP)}$$

(Equation 1.13)

Where N is the adsorption sites occupied by the gas molecules and N_m is the maximum adsorption sites available on the adsorbent solid, K is the equilibrium constant of the physical equilibrium, and P is the pressure of the gas (Langmuir, 1918).

The standard form of the Langmuir equation (Equation 1.13) can be rearranged in to a linear form (Gregg and Sing, 1982):

$$\frac{P}{N} = \frac{1}{N_m}.P + \frac{1}{KN_m}$$

(Equation 1.14)

Using the linear form of the standard Langmuir equation (equation 1.14), a plot of *P/N* against *P* gives a straight line with a gradient equal to 1/ N_m (the total uptake capacity) and an intercept equal to 1/ KN_m.

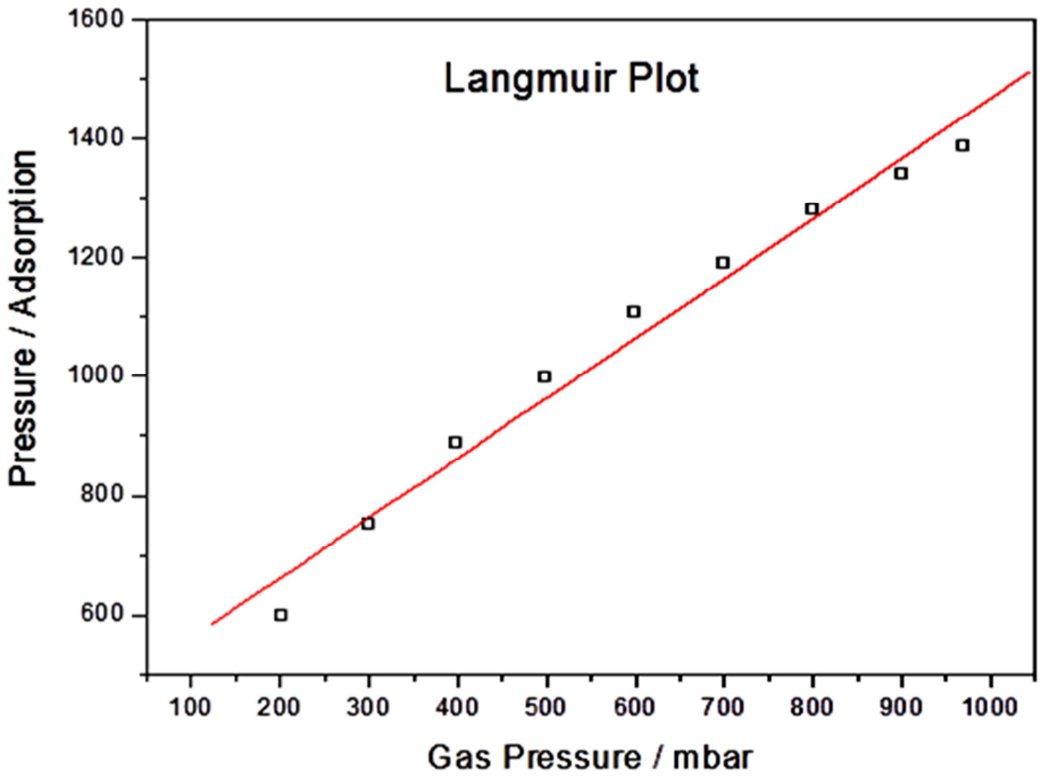

Figure 1.16: The Langmuir plot can be used to determine the total uptake capacity (N_m) from the inverse line gradient (Gregg and Sing, 1982),

The Langmuir model is widely used to determine the Gas In Place (GIP) in shale gas and coal bed methane plays. This is because the Langmuir model is a simple model that has a good fit empirically to many geological adsorption isotherms. It is often reported in the shale gas and coal bed methane literature in a modified form (e.g. Weniger *et al*., 2010):

$$N = \frac{N_m P}{P_L + P}$$

(Equation 1.15)

Where N_m is interpreted to be the maximum gas adsorption possible (and is sometimes referred to as the "Langmuir Volume" in studies using high pressure manometric equipment), (Gregg and Sing, 1982). The P_L is known as the "Langmuir Pressure", and it is the pressure value of the adsorption at half the maximum adsorption. This can be seen in Figure 1.17:

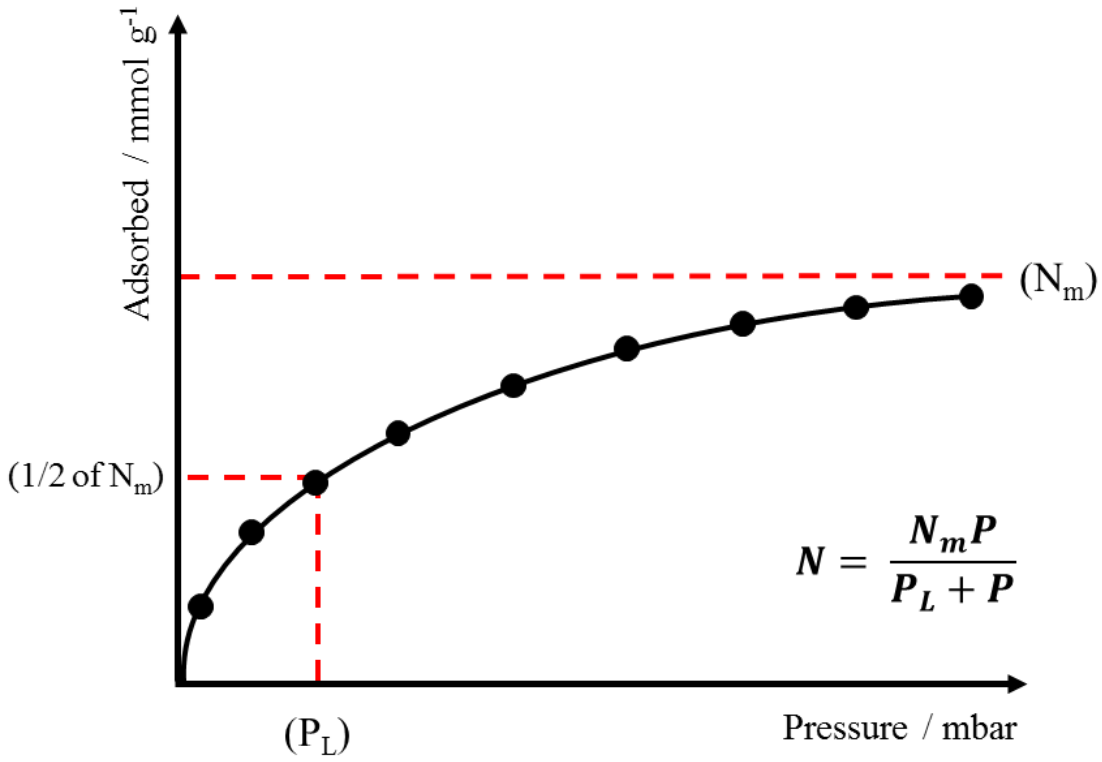

Figure 1.17: The modified Langmuir equation found in the shale gas and coal bed methane (CBM) literature (Ross and Bustin, 2007).

The experimentally obtained gas adsorption isotherm curves are fitted to the modified Langmuir equation using a computer software package (such as MATLAB™ or Origin™).

The maximum adsorption capacity (N_m) is dependent on the characteristics of the adsorbent and adsorbate, and the type of interaction existing between the gas molecule and the surface of the solid (Rouquerol *etal.*, 1999). It gives useful information about the nature of the geological sample, and can be used to calculate the GIP of a geological reservoir (Ross and Bustin, 2007).

1.2.14 Brunauer-Emmett-Teller (B.E.T) Model

The B.E.T. model extends the Langmuir model of gas adsorption from exclusively monolayer coverage to include the possibility of multilayer formation (Brunauer *et al.*, 1938). It has been successfully used in interpreting adsorption isotherms in geological materials. By removing the restrictive assumption of only forming monolayers during adsorption, the B.E.T. model can be used to calculate the surface areas of porous materials (Brunauer *et al.*, 1938).

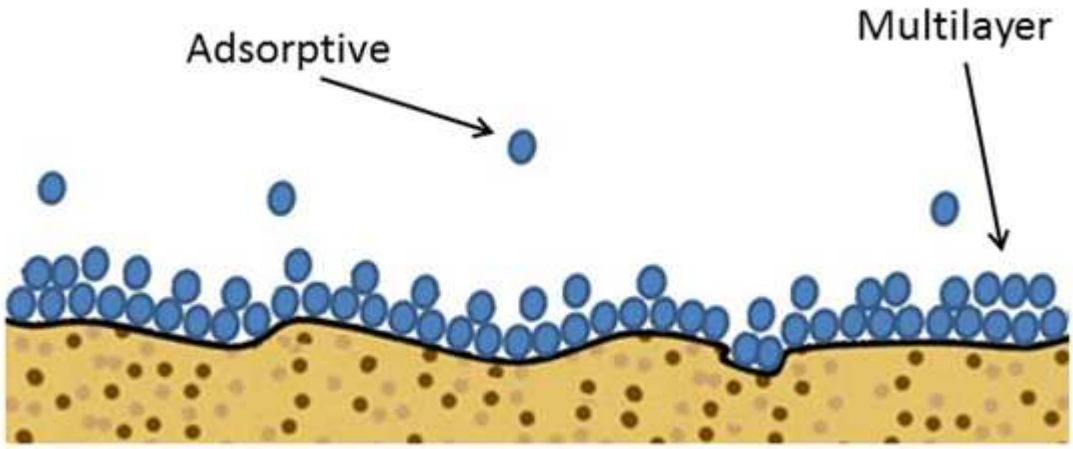

Figure 1.18: Multilayer adsorption of gas on adsorbent surface (schematic after Brunauer *et al*., 1938).

The B.E.T. model is based on the same 3 assumptions as the Langmuir equation (i.e. the first monolayer of adsorbed gas molecules occurs on uniform surface sites that are energetically equal) with the extra possibility of forming multilayers (Brunauer *et al*., 1938). The multilayer adsorption can occur because the first monolayer is a foundation site for gas molecules to continue physisorption. The adsorption in the multilayers is adsorbate-adsorbate interactions, and is similar to the type of physisorption interactions found during the condensation of a gas to a liquid (Brunauer *et al*., 1938).

The B.E.T. model can be applied to porous materials that do not reach a plateau at high relative pressures (which is due to monolayer saturation), but continues to rise until the isotherm has reached the maximum saturation vapour pressure of $p/p^o = 1$ (Gregg and Sing, 1982). The isotherm is able to continue to rise because monolayer saturation is not the limiting factor (as is the case of Type I isotherms), and the only restriction to amount of gas that can be adsorbed by multilayer adsorption is the total pore volume of the porosity (Gregg and Sing, 1982).

Isotherms that obey the B.E.T. model can be described by the linear form of the B.E.T. equation (Brunauer *et al*., 1938):

$$\frac{p}{n(p^\circ - p)} = \frac{1}{n_m c} + \frac{(c-1)}{n_m c} \cdot \frac{p}{p^\circ}$$

(Equation 1.16)

Where:
p^o = saturated vapour pressure
n = gas adsorbed
n_m= is monolayer coverage (mmol g^{-1})
c = constant

An example of a BET plot can be seen in Figure 1.19:

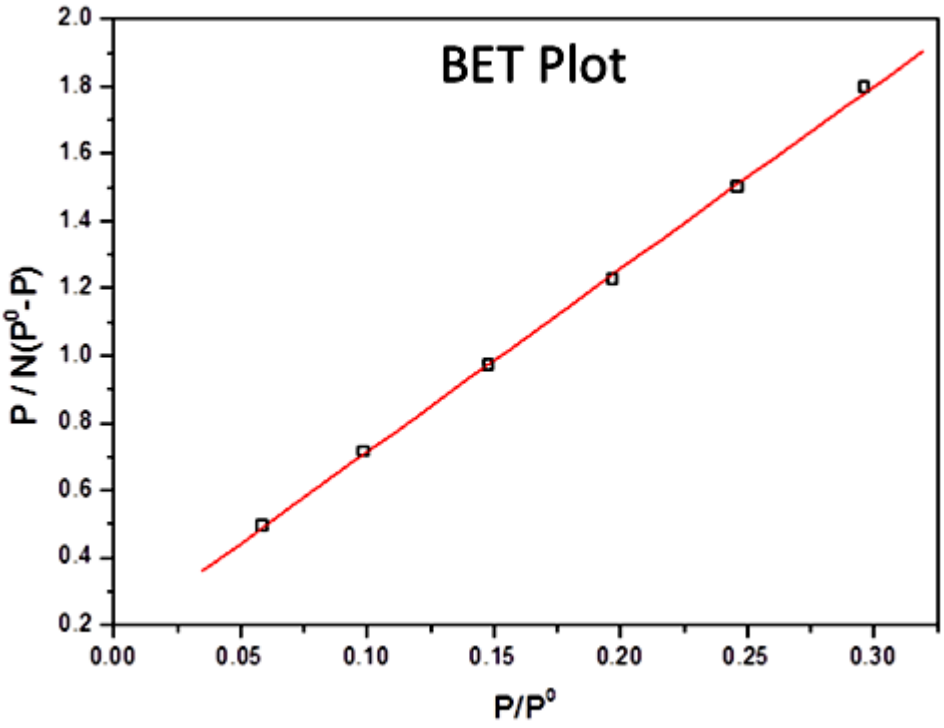

Figure 1.19: The BET plot, as described by the BET equation (after Brunauer *et al.*, 1938).

The linear form of the B.E.T. equation (see above, Equation 1.16) gives a linear relationship between relative pressures of p/p^{o} = 0.05 and 0.3, when $\frac{p}{n(p^{\circ}-p)}$ is plotted against $\frac{p}{p^{\circ}}$ on the pressure axis.

The gradient of the above graph (Figure 1.19) is equal to $\frac{(c-1)}{n_m c}$ and the intercept is equal to $\frac{1}{n_m c}$. The gradient and intercept can be used to calculate the monolayer coverage (n_m) and the constant (c) using:

$$n_m = \frac{1}{gradient + intercept}$$

(Equation 1.17)

and

$$c = 1 + \frac{gradient}{intercept}$$

(Equation 1.18)

Where the gradient and intercept is found from the B.E.T. plot shown in Figure 1.19, by linear regression.

Once the monolayer coverage (n_m) has been determined, it is possible to calculate the specific surface area (SSA) of the porous material. The effective cross sectional area (A_m) of the adsorbate gas molecule must be known, and it is usually taken as N_2 = 1.62 x $10^{-19}m^2$, and CO_2 = 1.9 x $10^{-19}m^2$ (Rouquerol *et al.*, 1999).

The specific surface area is calculated using the following equation (Rouquerol *et al*., 1999):

$$SSA = A_m . L . n_m$$

(Equation 1.19)

Where

SSA = specific surface area (m^2g^{-1})
A_m = effective cross sectional area (m^2)
L = Avogadro's number (mol^{-1})
n_m = monolayer coverage (mol g^{-1})

1.2.15 Dubinin-Radushkevich (D-R) Model

The Dubinin model of micropore filling is based on the observation that in constricted micropores (< 2nm), the close proximity of the pore walls causes the gas molecules to condense together and fill the pore volume, rather than adsorb layer by layer on the pore walls (Dubinin and Radushkevich, 1947; Dubinin, 1979).

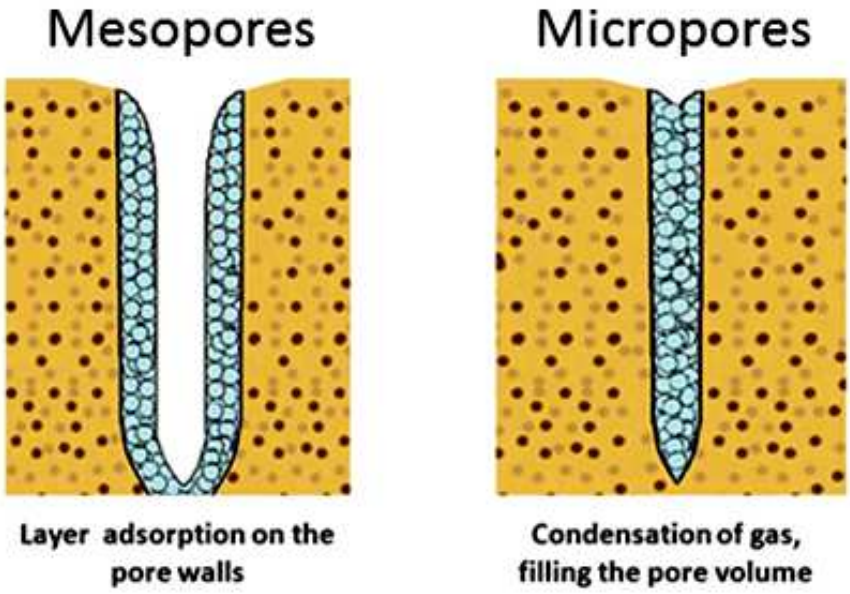

Figure 1.20: Filling of micropore volume by condensation of gas molecules

Geological samples may have significant amount of micropores, depending on the thermal maturity (Ross and Bustin, 2009). During gas adsorption experiments, the micropores are filled first at low pressures and the larger pores are subsequently filled at higher pressures.

The micropore volume can be calculated using the Dubinin-Radushkevich (D-R) equation:

$$\frac{W}{W_0} = exp\left[-B\left(\frac{T}{\beta}\right)^2\left(\log_{10}\frac{p^0}{p}\right)^2\right]$$

(Equation 1.20)

Where:

W = micropore volume filled at a chosen pressure
W_0 = total micropore volume ($cm^3\ g^{-1}$)
P = pressure
P^o = saturated vapour pressure
T = temperature
β = adsorbate affinity coefficient
$B = (2.3026R)^2k$

The linear form of the D-R equation is (Dubinin and Radushkevich, 1947):

$$\log_{10} W = \log_{10} W_0 - D \log_{10}{}^2 \left(\frac{p^0}{p}\right)$$

(Equation 1.21)

Where:

$$D = B\left(\frac{T}{\beta}\right)^2$$

(Equation 1.22)

The linear form of the D-R equation can be used to calculate the total micropore volume (W_0). When $\log_{10}(Con^c)$ is plotted against $\log_{10}{}^2$ (p^0/p), a straight line should be obtained, and the y-axis intercept is equal to the total micropore volume (in mmol g^{-1}, and needs to be converted to $cm^3\ g^{-1}$), (Dubinin and Radushkevich, 1947). The D-R equation is based on the assumption that there is a Gaussian distribution of micropore widths in the microporous material. The assumption is held to be true when a straight line is obtained from the plot of the linear form of the D-R equation (Equation 1.21), (Dubinin and Radushkevich, 1947).

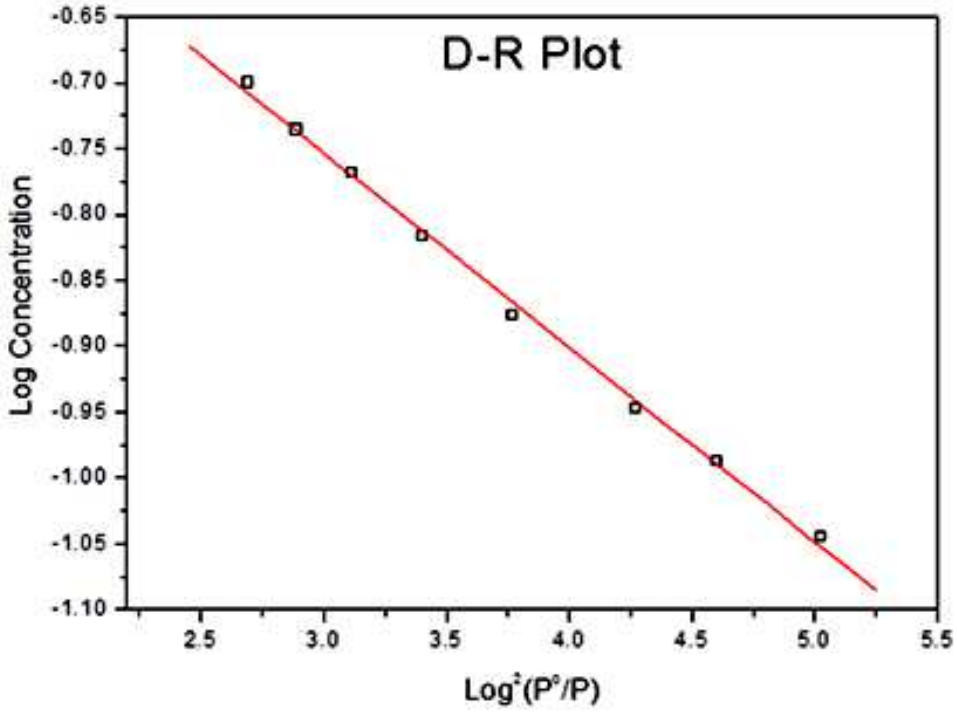

Figure 1.21: The D-R plot can be used to determine the micropore volume of a sample. This is calculated from the intercept, which is determined using linear regression (after Dubinin and Radushkevich, 1947).

1.2.16 Characterisation of pore volume.

The pore volumes of organic rich shales and kerogens can be determined using a combination of mercury intrusion porosimetry and gas adsorption analysis. Four measures of pore volume are obtained:

- Total pore volume
- Hg-macropore volume
- Gas sorption pore volume
- Micropore volume

The total pore volume and Hg-macropore volume are obtained from mercury intrusion porosimetry, as outlined above in section 1.2.6, above. The total pore volume is the maximum internal volume in a porous material. The Hg-macropore pore volume is the pore volume that is measurable with mercury intrusion porosimetry, but is not measurable by gas adsorption analysis. This equates to pore throats with diameters greater than 100 nm.

The gas sorption pore volume is determined using gas adsorption analysis performed at the gas condensation temperature point. The gas condensation point of CO_2 is -78^{o}C, and CO_2 adsorption isotherms performed at this temperature result in the formation of solid phase CO_2 in the confined pore spaces of the porous substance. This condensed phase adsorbate occupies a fixed volume (unlike a gas, which has a varying volume). The condensation of a fixed volume phase in the pores allows the internal volume of the pore body to be calculated. The maximum amount of gas adsorbed is converted to a gas sorption pore volume ($cm^3\ g^{-1}$) using the density of the adsorbate condensed phase. The density of solid CO_2 in confined pores is taken to be 1.032 gcm^{-3} at -78^{o}C, by convention. The formation of condensed phase gas adsorbate only occurs in pores up to ~ 100 nm in diameter (Diamond, 1970; Lowell and Shields, 1981; Westermarck, 1998; Groen *et al*., 2003; Lubda *et al*., 2005; Klobes *et al*., 2006; Bustin *et al*., 2008; Chalmers and Bustin, 2012; Kuila and Prasad, 2012).

An equivalent method is the adsorption of nitrogen gas at -196^{o}C to determine the internal pore volume of sub-100 nm pores using condensation. Unfortunately, at the very low temperature conditions of the experiment (-196^{o}C), the diffusion of nitrogen gas into the smallest pore spaces is impeded (Marsh, 1989). At this temperature nitrogen gas cannot enter the micropores (< 2 nm), and therefore the smallest pores accessible to nitrogen are the mesopores (> 2 nm), Ross and Bustin (2009). However, CO_2 at -78^{o}C has a higher kinetic energy and overcome the activated diffusional barriers in the pore system that nitrogen is hindered. Therefore, CO_2 at -78^{o}C can often give a more accurate measure of pore volume, especially in materials dominated by micropores (< 2nm).

The micropore volume (< 0.7 nm) is determined using CO_2 adsorption analysis performed at 0^{o}C. In micropores the close proximity of the pore walls to each other results in a restricted volume, and gas adsorption occurs by a volume filling model (Dubinin and Radushkevich, 1947; Dubinin and Stoeckli, 1980). The volume filling mechanism occurs in micropores because the pore walls are close enough in proximity to facilitate an enhanced adsorption of gas molecules. This enhanced adsorption cannot occur in larger pores because the CO_2 gas molecules have too much kinetic energy to adsorb when at a temperature of 0^{o}C (Gregg and Sing, 1982; Rouquerol *et al*., 1999).

Table 1.4: Pore volumes measurable using mercury intrusion porosimetry and gas adsorption analysis.

Pore Volume Measurement	Pore Range
Total pore volume	All accessible and blind pores
Hg-macropore volume	Pore volumes > 100 nm diameter
Gas sorption pore volume	Pore volumes < 100 nm diameter
Micropore volume	Pore volumes < 0.7 nm diameter

1.2.17: Determination of surface area

The surface area of the pore systems in organic rich shales and kerogens can be determined using mercury intrusion porosimetry and gas adsorption analysis (Ross and Bustin, 2009). A combination of the mercury intrusion, N_2 BET and CO_2 BET surface areas allow the 1) total surface area of open pores and 2) the distribution of surface areas to be calculated.

The mercury intrusion surface area is calculated using the R-P equation (Rootare and Prenzlow; 1967) in the low pressure region of the mercury intrusion curve (up to a pressure of 2500 psi). This low pressure region allows the surface area of the macropores to be determined (down to a limit of 100 nm in diameter). The surface area is determined from the integration of the area under the intrusion curve. Furthermore, although it is possible to apply the R-P equation to the full intrusion curve (thus determining the surface area of all pores down to the 3 nm limit), this is not recommended in compressible materials such as shales, because the high pressures can lead to damage of the pore systems and an over-estimation of surface areas (Rootare and Prenzlow, 1967).

The surface areas of the sub -100 nm pores are determined using gas adsorption analysis. The gas adsorption isotherms are fitted to the BET model (Brunauer *et al*., 1938). The BET surface area measurements are performed using nitrogen gas (at -196^{o}C) and CO_2 gas (at -78^{o}C) in the relative pressure range of p/p^{o} = 0.05 to 0.3. The nitrogen adsorption isotherms (-196^{o}C) cannot enter the micropores (< 2 nm), and the smallest pores accessible are mesopores (> 2 nm). The CO_2 adsorption isotherms at -78^{o}C contain a greater kinetic energy, and so the surface area of the full range of pores (macro-, meso-, and micropores) can be determined using CO_2 at -78^{o}C isotherms (Gregg and Sing, 1982; Rouquerol *et al*., 1999).

Each of the three experimental methods can measure the surface area for a different range of pore diameters. The range of each method is outlined in Figure 1.22. The mercury intrusion porosimetry (when applied up to 2500 psi) will measure the surface area of pores from the micrometre-scale down to a minimum diameter of 100 nm. The nitrogen gas adsorption (at -196^{o}C) will measure the surface area of pores from the micrometre-scale down to a minimum diameter of 2 nm. The CO_2 gas adsorption (at -78^{o}C) will measure the surface area of the full pore range, from the micrometre-scale pores down to the smallest pores that the CO_2 gas molecule can physically enter (the kinetic diameter of a CO_2 molecule is ~ 0.3 nm, Bustin *et al*., 2008). It is also worth remembering that the internal surface areas of any blind pores (which are inaccessible to these fluids) cannot be measured, and thus these three experimental methods are only measuring the surface area of the accessible open pore system.

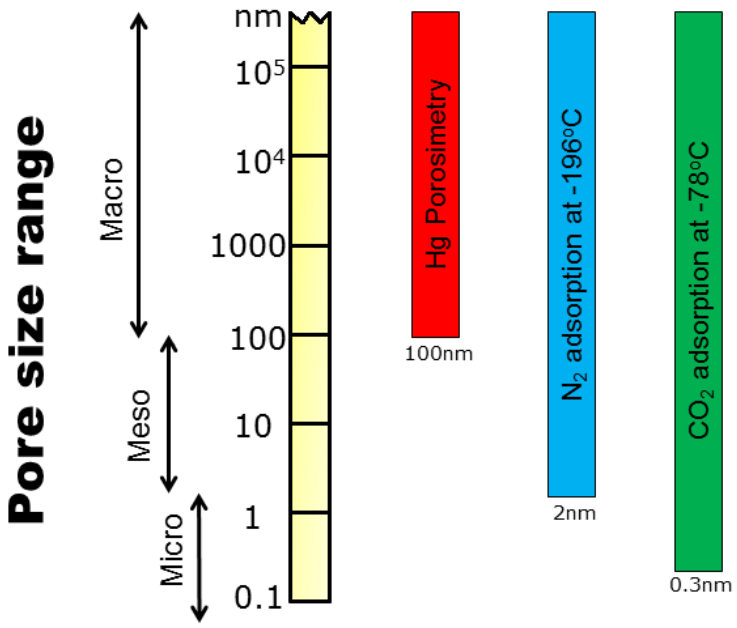

Figure 1.22: The pore ranges for which surface area can be determined using 1) mercury intrusion porosimetry, 2) nitrogen adsorption at -196°C, and 3) CO_2 adsorption at -78°C.

The pore system can be divided in to three pore ranges (Table 1.5), and the proportion of surface areas in each of these ranges can be determined using Equations 1.23 to 1.26:

Table 1.5: Pore system is divided in to three pore ranges for surface area analysis.

Surface Area	Pore Diameter
Macropores	> 100 nm
Mesopores	2 to 100 nm
Micropores	< 2 nm

For the micropores (< 2 nm), the surface area is:

$$A_{Micro} = A_{CO_2} - A_{N_2} \quad \text{(Equation 1.23)}$$

Where A_{Micro} = Surface area of the micropores (< 2nm) / $m^2 g^{-1}$
A_{CO2} = BET surface area determined from CO_2 at -78°C / $m^2 g^{-1}$
A_{N2} = BET surface area determined from N_2 at -196°C / $m^2 g^{-1}$

For the mesopores (2 to 100 nm), the surface area is:

$$A_{Meso} = A_{N2} - A_{Hg} \quad \text{(Equation 1.24)}$$

Where A_{Meso} = Surface area of the mesopores (2 to 100 nm) / $m^2 g^{-1}$
A_{N2} = BET surface area determined from N_2 at -196°C / $m^2 g^{-1}$
A_{Hg} = Mercury intrusion surface area / $m^2 g^{-1}$, using MIP up to 2500 psi pressure.

For the macropores (> 100 nm), the surface area is:

$$A_{Macro} = A_{Hg}$$

(Equation 1.25)

Where A_{Macro} = Surface area of the macropores (> 100 nm) / $m^2 g^{-1}$
A_{Hg} = Mercury intrusion surface area / $m^2 g^{-1}$, using MIP up to 2500 psi pressure.

The total surface area is:

$$A_{Total} = A_{Macro} + A_{Meso} + A_{Micro}$$

(Equation 1.26)

Where A_{Total} = Total surface area of accessible pores / $m^2 g^{-1}$
A_{Macro} = Surface area of the macropores (> 100 nm) / $m^2 g^{-1}$
A_{Meso} = Surface area of the mesopores (2 to 100 nm) / $m^2 g^{-1}$
A_{Micro} = Surface area of the micropores (< 2nm) / $m^2 g^{-1}$

1.3 Geological case studies

1.3.1 Geological setting of the Draupne Formation.

The Draupne Formation is the Norwegian nomenclature (Vollset and Doré, 1984; Keym *et al.*, 2006) used for the northern stratigraphic equivalent to the Kimmeridge Clay Formation (KCF). The DF is found in the northern sectors of the North Sea basin, above the present day latitude of 58^{o} N (Vollset and Doré, 1984) and was deposited at the same time and facies conditions as the KCF.

The Draupne Formation is part of the Viking Group, which also consists of the Heather Formation. This can be seen in the stratigraphic section of the Upper Jurassic in the northern sector of the North Sea basin, Figure 1.23:

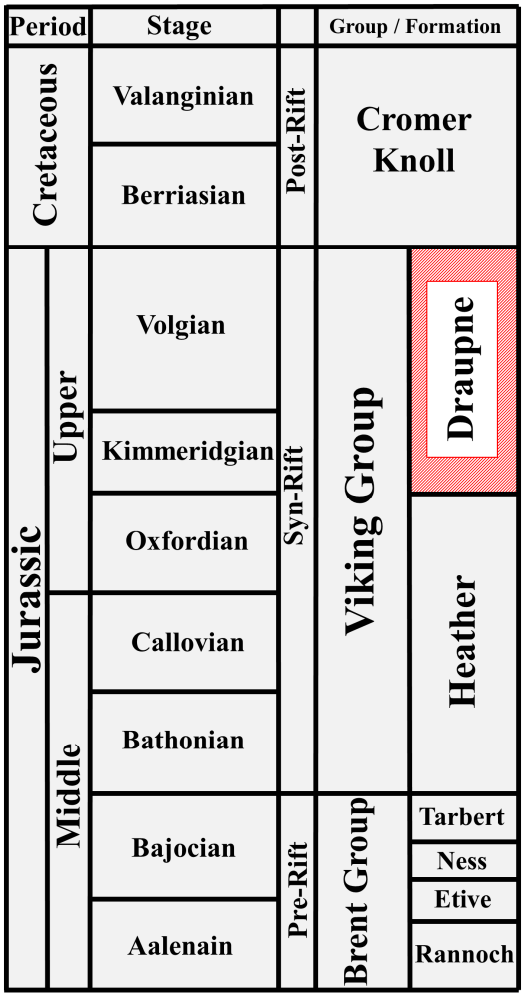

Figure 1.23: Stratigraphic section for the northern sector of the North Sea basin (Vollset and Doré, 1984).

The Draupne Formation was deposited during the Late Jurassic to the Early Cretaceous periods (Oxfordian to Berriasian ages), during a time of high global sea levels and significant marine transgression on to the land mass that is now north-west Europe. This can be seen in the paleogeographical map of Europe in the Late Jurassic, Figure 1.24:

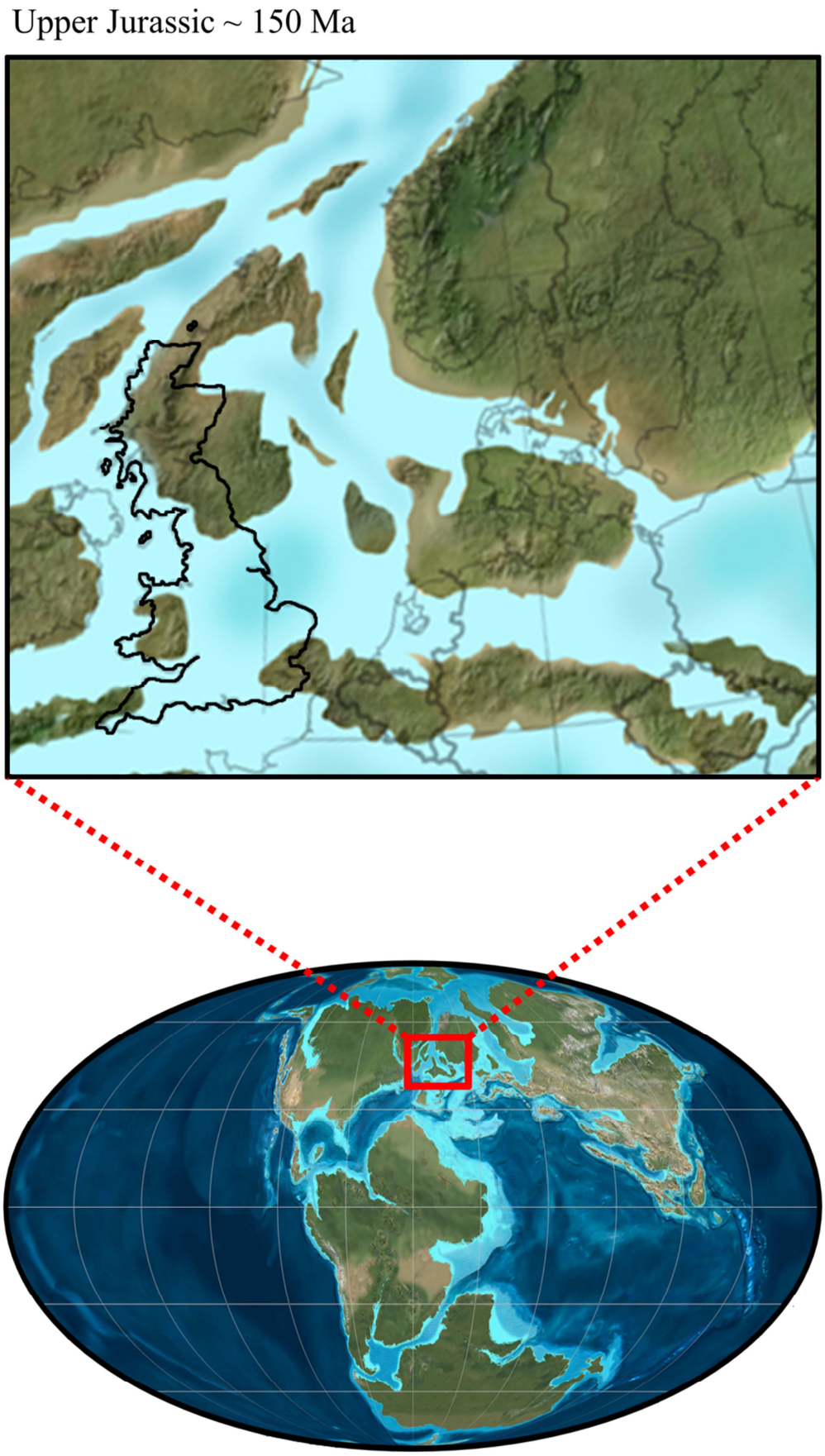

Figure 1.24: Global and European paleogeography in the Upper Jurassic period. The break-up of the super continent Pangea occurred at a time of high global sea-levels, with significant marine transgression in the region that is now North-West Europe
(figure modified from http://cpgeosystems.com/euromaps.html).

The Jurassic was a time of active geological rifting in the North Sea basin, and the Draupne Formation was rapidly deposited in the Late Jurassic during a time of major extensional faulting in the North Sea area (Færseth and Ravnås, 1998). The onset of this major rifting occurred during the middle Oxfordian to early Kimmeridgian (approximately 157 - 155 million years ago) (Underhill, 1991; Glennie and Underhill, 1998).

The extensional tectonic activity across the northern and central North Sea Basin created a triple junction of three connected rift systems: the Viking Graben, the Central Graben and the Moray Firth, as shown in Figure 1.25.

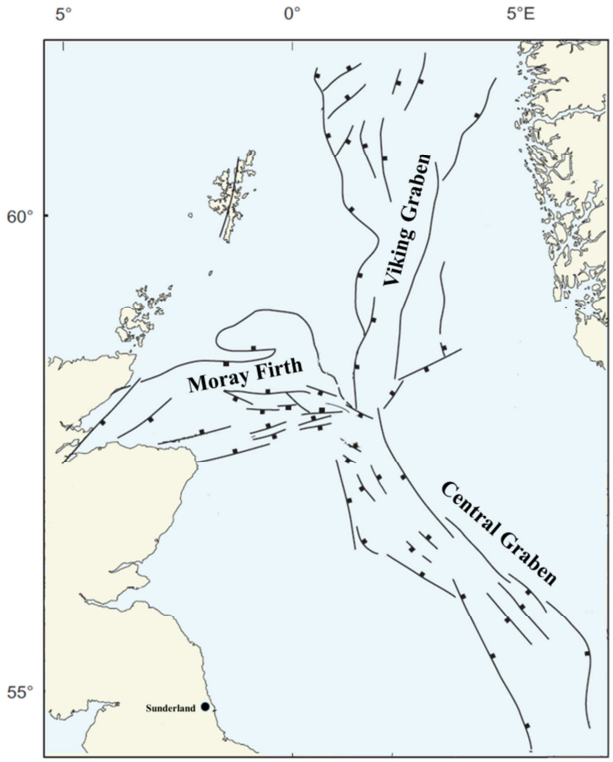

Figure 1.25: Jurassic extensional rifting of the North Sea Basin created the Viking Graben, the Central Graben and the Moray Firth rift systems.

The Draupne Formation was deposited in and around the Viking Graben area, in the northern North Sea sector between the Shetland Islands and Norway (Vollset and Doré, 1984). The Graben rift system created a partial barrier in the North Sea trough, isolating the seaway from the Tethys Ocean in the southeast. This isolation led to long periods of widespread anoxia, providing very favourable conditions for the generation of organic rich petroleum source rocks.

The extension of the North Sea Basin rift system ceased during the Early Cretaceous (Færseth and Ravnås, 1998), with the remainder of the Cretaceous and the Cenozoic experiencing little tectonic activity. The post Cretaceous subsidence and burial of the Draupne Formation has enabled this source rock to become thermally mature.

The combined events of the Jurassic marine transgression, the extensional rifting of the Graben system, and the post-Cretaceous subsidence controlled thermal maturation of the basin, has led to the Draupne Formation becoming the dominant petroleum source rock of the northern North Sea.

1.3.2 Geological setting of the Colorado group

The Colorado Group (CG) of the Western Canada Sedimentary Basin (WCSB) is a thick sequence of marine deposited, laterally extensive, Cretaceous shale and siltstone strata, which contain significant quantities of biogenic natural gas (Leckie *et al*., 2008). The WCSB is a foreland sedimentary basin that is adjacent to the Canadian Rocky Mountains; it is one of the largest foreland basins in the world, running parallel to the eastern flanks of the Cordillera (Macqueen and Leckie, 1992).

The Colorado Group was deposited during the Cretaceous (Cenomanian to Campanian ages), as global eustatic sea levels rose and the western region of the North American continent was subjected to a prolonged period of oceanic transgression. This time of high global sea levels led to a near continuous flooding of the WCSB basin, and the birth of the Western Interior Seaway (WIS), Figure 1.26:

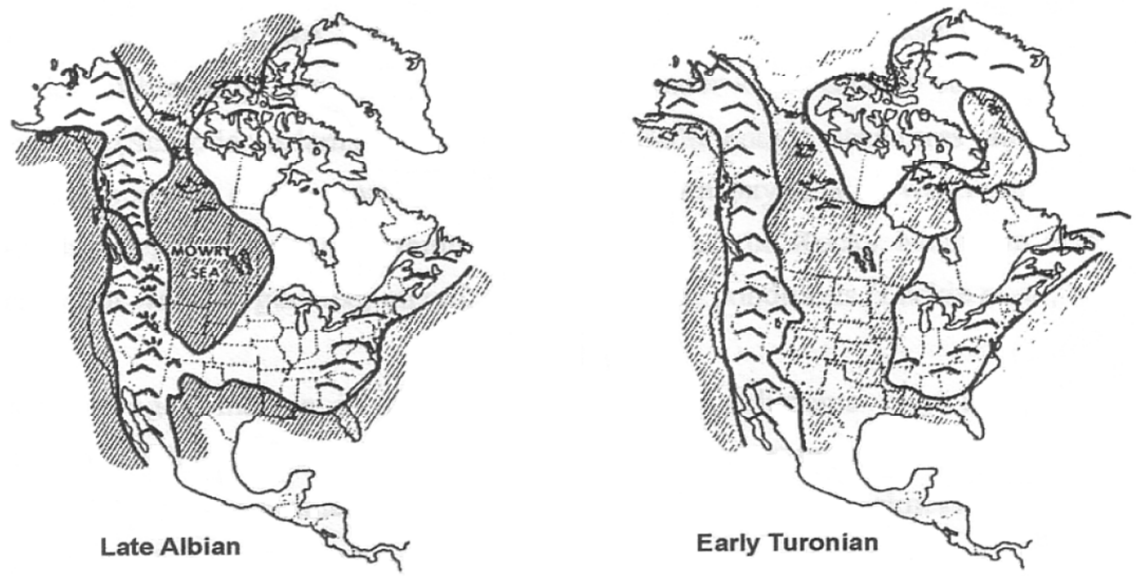

Figure 1.26: The Western Interior Seaway (WIS) led to the deposition of thick marine shales in the WCSB (after Kauffman, 1984)

The Western Interior Seaway was a vast, but shallow (100m to 400m), warm inland sea, which covered the western section of the North American continent during the Cretaceous period (Varban and Plint, 2008; Plint *et al*., 2009).

The WCSB was repeatedly flooded during the Cretaceous, and this (in conjunction with high sediment charge from the adjacent mountain chain) led to the deposition of thick marine shales, known as the Colorado Group. The high sedimentation rates led to the deposition of nearly 9 km of organic-rich mudstone and siltstone sequences in the foreland basin (Stott, 1993).

Stratigraphy of the Colorado Group

The nomenclature proposed by Nielsen (2003) and Nielsen *et al.* (2008) shall be used to define the stratigraphy of the Colorado Group in the Bigstick gas field.

The stratigraphy of the Colorado Group includes (from oldest to youngest) the Belle Fourche Formation, the Second White Specks Formation, the Carlile Formation (subdivided into lower, middle and upper units) and the Niobrara Formation (subdivided into the Verger Member, Medicine Hat Member and the First White Specks Member), as seen in Figure 1.27.

The biogenic gas produced from the Bigstick field is sourced in the Cretaceous aged Colorado Group (CG), mainly from the low permeability Belle Fourche Formation, with smaller contributions from the Niobrara Formation (Medicine Hat Member) and Milk River Formation (Leckie *et al*., 2008).

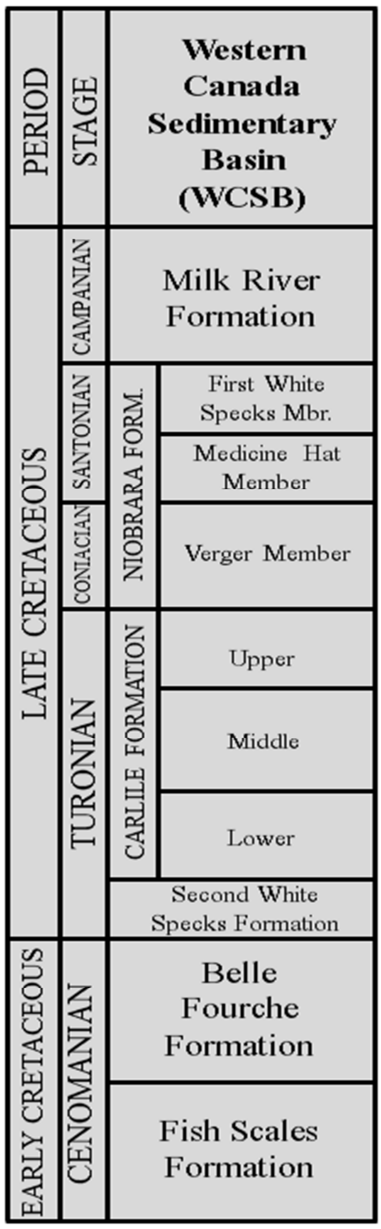

Figure 1.27: The stratigraphic Column of the Colorado Group in the Bigstick gas field area.

Historically, gas production in the wider region of the WCSB has been from the Belle Fourche Formation, the Second White Specks Formation, and the Medicine Hat Member of the Niobrara Formation.

1.4 Motivation for research into the pore structure of shales and kerogen

1.4.1 Outstanding issues for gas storage in shales

The nature of gas storage in gas shale pore systems is not fully understood. Identifying the relationships between porosity, pore structure, permeability and gas storage is fundamental to improving the effectiveness of gas appraisal and Gas In Place (GIP) determination. The low porosity and ultra-low permeability of shale sequences has a big impact on the efficiency of gas transport and production (Amann-Hildenbrand *et al*., 2012).

There has been an increased publication output of fundamental research in recent years (due to the economic success of shale gas in the USA), but there are still many outstanding questions (Amann-Hildenbrand *et al*., 2012). Most of the gas shale literature is centred on the USA experience of shale gas production, and a key example is the Barnett shale, Fort Worth, Texas. Unfortunately, the Barnett shale is atypical of most shale gas systems, and cannot be used as a general model (Montgomery *et al*., 2005). As the exploration for shale gas shifts towards Europe and Asia, new model(s) for the shale gas system will be needed.

There are unanswered questions about the nature of gas storage in these geological systems. It is usually assumed that a large amount of shale gas is stored in the pore network by adsorption (Bustin, 2005; Ross and Bustin, 2007; Chareonsuppanimit *et al*., 2012). This is because shales exhibit a considerable gas adsorption storage capacity, even at high temperatures (Amann-Hildenbrand, *et al*., 2012). It is uncertain whether this is premise is correct, and if so, under what specific geological conditions it is correct.

Another outstanding question is what happens when the pore network of the organic and mineral matrix is saturated with gas. This situation may occur when the shale rock has relatively high organic matter content, and has generated sufficient gas to cause saturation of the pore network (Lu *et al.*, 1995). Therefore, the organic matter type and content is of interest. Does low organic matter content mean that the excess gas that is not adsorbed to kerogen is stored as free gas in the pore space?

1.4.2 Research aim

The overall aim of the research project is to understand the nature of the pore system in organic rich shales and kerogens, and relate it to the gas storage capacity of gas bearing shales.

Characterisation of shale pore structure and porosity:

- To characterise the porosity and pores structures of organic-rich shales. Characterisation will be done using: 1) Scanning electron microscopy, 2) Mercury intrusion porosimetry, and 3) Gas adsorption. These three methods will be used in conjunction to give a complete pore characterisation for each geological sample.

- To characterise the origin and maturity of the organic matter fraction of the sample suite. This will be done using 1) TOC analysis, 2) Rock-Eval pyrolysis, 3) ATR-IR spectroscopy of kerogen, and 4) Pyrolysis GC-MS of kerogen 5) Solid State ^{13}C NMR spectroscopy of kerogen.

Gas storage potential of shale and kerogen samples:

- To investigate the relationships between in the gas storage potential of shales and isolated kerogen, with the properties of porosity, pore structure, organic richness and thermal maturity.

1.4.3. Research Hypotheses

The research hypotheses that are predicted for gas storage in gas bearing shales:

1. The total porosity will decrease with increasing burial depth (due to mechanical compaction and chemical diagenesis).

2. The pore size distribution of gas shales will be dependent on compaction, and will decrease with burial depth.

3. A large amount of shale gas is stored by adsorption (that is adsorbed molecules on the organic and mineral matter of shales).

4. The porosity content will be dependent on TOC content, and will increase with increasing TOC (%) value.

5. The microporosity of gas shales will be dependent on the shale maturity, and will increase with increasing shale maturity (as a portion of the total porosity).

6. The internal surface area of gas shale pore systems increases with microporosity content.

7. Gas storage in shales will be dependent on microporosity, and will increase with increasing microporosity.

1.5. Outline of thesis chapters

This research thesis contains the following chapters:

Chapter 1: The overall aim of this study is to investigate the nature of pores and porosity in organic rich shales and kerogens, and Chapter 1 is used to explain why research on this problem is required and to outline the current state of knowledge. The pore structures of shales and kerogens are poorly understood, and yet they are a principle location for natural gas storage. The gas shale hydrocarbon system is firstly introduced, and is compared to conventional petroleum systems. The mechanisms of gas storage in the pore systems of gas shales are described, with the partition of gas between different phases explained. The definition of pores and a porous system is discussed, with the various nomenclature used to define pores being introduced. After, the

experimental methods used to investigate pore systems are described in detail, with several approaches being outlined. The geological case studies used in this research is then presented. Finally, the research motivations, aim, objectives and hypotheses are outlined.

Chapter 2: The materials and methods used to investigate the research problem are described in Chapter 2. Firstly, the geological origin of the shale core samples is outlined, before an overview of the experimental methods and techniques utilised is given. The bulk geochemistry of the shale core samples was determined using TOC and Rock-Eval pyrolysis. The geochemistry of isolated kerogen samples was determined using Elemental Analysis, Pyrolysis GC MS, Solid state ^{13}C-NMR and ATR-FT-IR spectroscopy. The pore structures of the shale core and isolated kerogens was investigated using low pressure gas adsorption analysis, mercury intrusion porosimetry (MIP), and scanning electron microscopy (SEM).

Chapter 3: The Results and Discussion of the bulk geochemistry of the shale core and isolated kerogen concentrates is given in Chapter 3. This includes results for the TOC and Rock-Eval pyrolysis results of the shale core samples, as well as the geochemical results of the Elemental Analysis, Pyrolysis GC MS, Solid state ^{13}C-NMR and ATR-FT-IR spectroscopy of isolated kerogen samples.

Chapter 4: The Results and Discussion of the pore structure investigations of the Draupne Formation and Colorado Group shale cores is outlined in Chapter 4. The SEM images of shale cores are firstly presented, before the results of the mercury intrusion porosimetry and low pressure gas adsorption analysis are given. Finally, the experimental data and key results are analysed and interpreted in the Discussion, and the findings are related to other studies.

Chapter 5: The Results and Discussion of the pore structure investigations of isolated kerogen concentrates is presented in Chapter 5. Low pressure gas adsorption analysis is used to investigate the pore structure of isolated kerogen, before the key results are compared to the findings of the shale pore structure presented in Chapter 4. Finally, the experimental data and key results are analysed and interpreted in the Discussion, and the findings are related to other studies.

Chapter 6: The Results and Discussion of the high pressure methane adsorption of shales and the kerogen enthalpy of adsorption investigations are presented in Chapter 6. High pressure methane adsorption is used to determine the Langmuir Volume and Pressure of the DF and CG shales. The value of the enthalpy of adsorption for a DF kerogen is determined using gas adsorption uptakes measured at several temperatures.

Chapter 7: The Conclusions and Future Work are presented in Chapter 7. A summary of the key results and an interpretation is firstly offered, before discussing the findings in context of the hypotheses presented in Chapter 1. The Future Work section provides suggestions in how the research presented in this study could be continued by other researchers.

Chapter 2: Materials and Methods

2.1 Geological Samples

2.1.1 Draupne Formation Shales and kerogens

The Draupne Formation shales and kerogens used in this study were obtained from the shale core samples taken from the Draupne Formation (DF) in the northern sector of the North Sea Basin, Figure 2.1. The Draupne Formation shale samples are a suite of petroleum source rocks that have a range of thermal maturities.

The "hot shales" of the Draupne Formation are often mistakenly grouped together with the prolific Kimmeridge Clay Formation source rocks of the British sector of the North Sea basin (Doré *et al*., 1985; Keym *et al*., 2006). There are several key petrophysical properties (Vollset and Doré, 1984) that distinguish the Draupne Formation and the Kimmeridge Clay Formation, and hence the Draupne Formation nomenclature shall be used here.

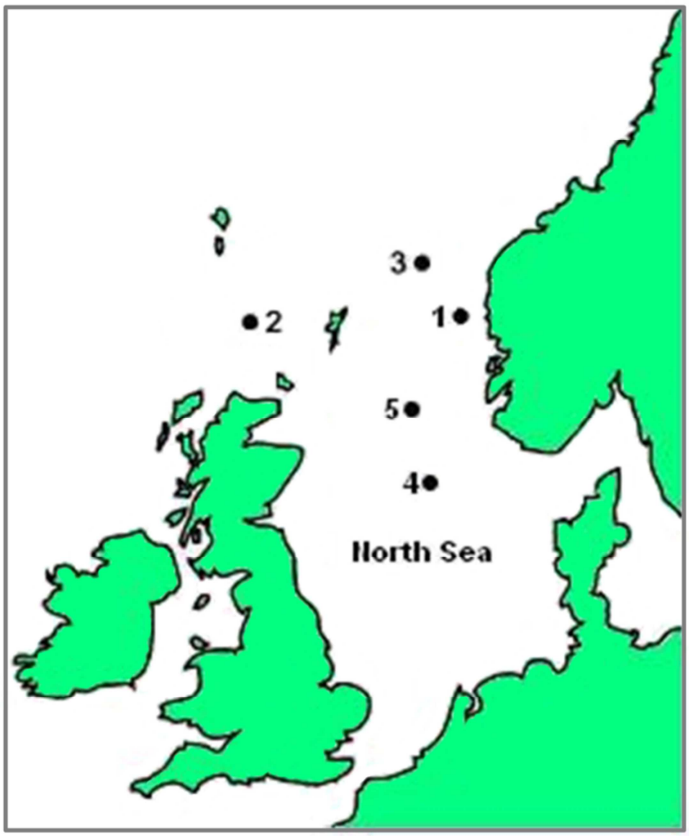

Figure 2.1: Location of Draupne Formation wellbores. The shale cores were obtained from the Northern sector of the North Sea Basin (Okiongbo *et al*., 2005).

The shale samples were obtained from offshore exploration boreholes (Figure 2.1) that were drilled by the British Petroleum and Statoil companies during the 1980's, and core samples were subsequently donated to the British Geological Survey.

Details of the shale core samples are listed in Table 2.1. Some core photographs are reported in Figure 2.2. The shale core samples were obtained from latitudes above 58^{o} North. The samples are all from the Draupne Formation, and have present day burial depths ranging from 2117.8 m to 4780.7 m.

Table 2.1: Draupne Formation shale samples

Sample	Well	Burial Depth / m	Field Name	Latitude / Longitude	Map Location
DF1	31/4-9	2117.8	Brage	60.533969, 3.090811	1
DF2	204/28-2	2325	West of Shetland	60.1342717, -4.5082935	2
DF3	30/9-14	2978.5	Oseberg Sor	60.386475, 2.705381	1
DF4	211/12A-M1	3124.7	Magnus	61.6199418, 1.3075294	3
DF5	211/12A-M16	3375.32	Magnus	61.6199923, 1.3075533	3
DF6	211/12A-M16	3400.4	Magnus	61.6199923, 1.3075533	3
DF7	16/7B-28B	4132.95	Miller	58.742972, 1.382361	4
DF8	3/29-2	4608.4	Rhum	60.1178145, 1.7229512	5
DF9	3/29A-4	4707.7	Rhum	60.1371486, 1.7138956	5
DF10	3/29A-4	4780.7	Rhum	60.1371486, 1.7138956	5

The Draupne Formation (DF) shales have the properties of high TOC, very high Gamma-ray readings (>100 API), and anomalously low seismic sonic velocities (Vollset and Doré, 1984). The DF core samples are typical organic-rich ‘black’ shales, usually occurring as laminated fissile clastic shale.

The DF suite of shale samples contains a high level of oil prone organic matter content, with a similar kerogen type and mineralogical content. The kerogen type of the DF shales are typically categorised as Type II oil-prone kerogen (Knudsen *et al.*, 1988). It is dominated by algal debris of marine planktonic origin, with variable amounts of degraded woody humic matter of terrigenous origin. The amorphous algal derived AOM is typically mixed with small amounts of particulate vitrinite and inertinite. Framboidal pyrite is commonly associated with kerogen, due to the action of sulfate reducing bacteria in anoxic bottom water conditions. Palynomorphs are only a trace fraction of the total kerogen. (Okiongbo *et al*., 2005).

DF4 shale core

DF5 shale core

DF6 shale core

DF7 shale core

DF8 shale core

DF9 shale core

DF10 shale core

Figure 2.2: Draupne Formation shale core photographs. (The JPEG photograph files of shales DF1 to DF3 were corrupted).

2.1.2 Colorado Group shales and kerogens

The Colorado Group shales and kerogens used in this study were obtained from the shale core samples taken from the onshore Bigstick gas field of the Western Canada Sedimentary Basin (WCSB), Figure 2.3. The Colorado Group is an organic rich Type II marine shale sequence that is thermally immature. The Colorado Group samples can be considered a scientific control group, where the pore structure of immature shales and kerogens are compared and contrasted to the thermally influenced changes observed in the Draupne Formation samples.

The 10 shale core samples used in this study were obtained from the Hatton 12-19-013-28W3 core, which is a long continuous drilling core approximately 240 metres in length. This core was obtained from the Bigstick gas field by Nexen Inc in 2007. The details are listed in Table 2.2. Some core photographs are reported in Figure 2.4.

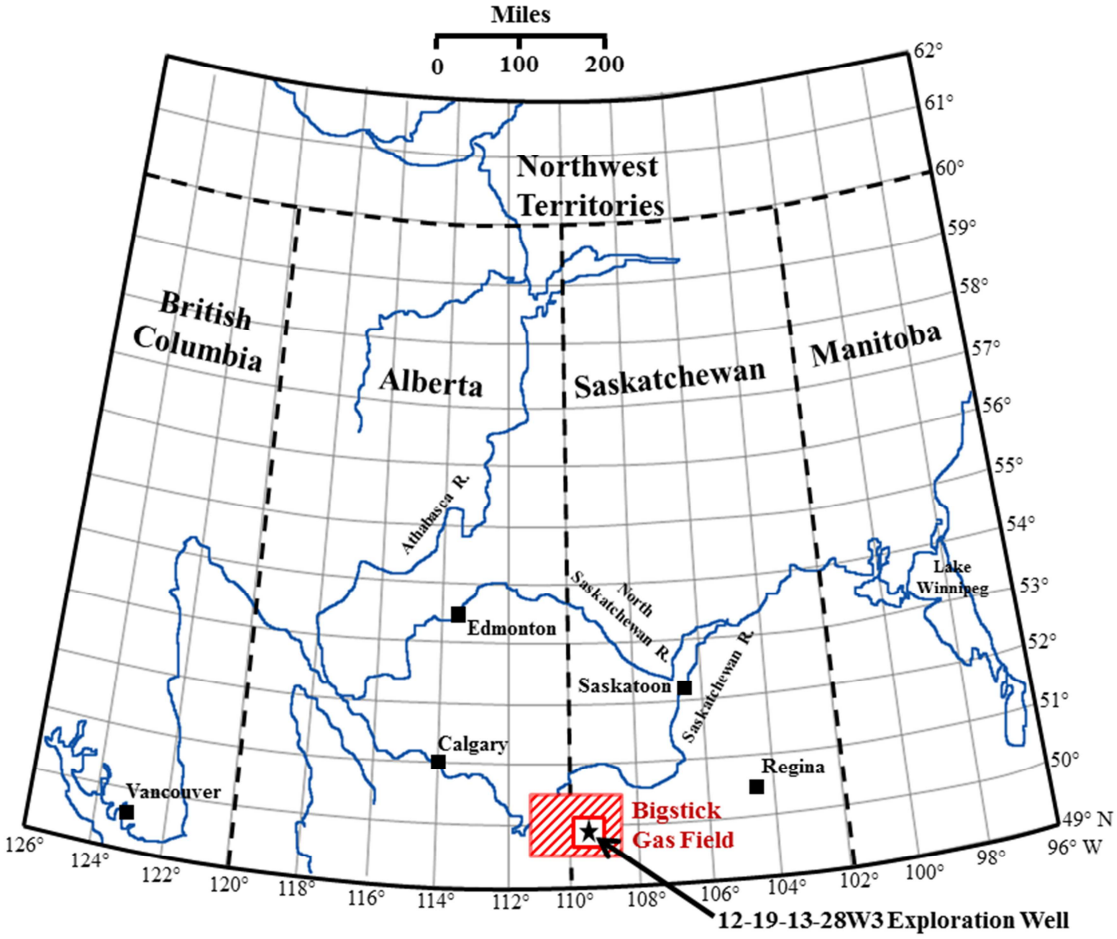

Figure 2.3: The Bigstick gas field (highlighted in the red box) is located in south-eastern Alberta and south-western Saskatchewan. The 12-19-13-28W3 well is indicated. (Base map redrawn from Mossop and Shetsen, 1994)

The Bigstick gas field produces biogenic natural gas from the thermally immature shale strata. The 10 samples chosen were selected on the basis of medium to high TOC contents (to facilitate the isolation of kerogen). The Bigstick gas field was discovered in 1980 (Leckie, 2008), and is located in western Canada, where it distributed between the provinces of Alberta and Saskatchewan.

Table 2.2: Burial depths and formations of the Colorado Group shales in this study.

Sample	Depth / m	Formation
C1	505.3	Medicine Hat
C2	506.55	Medicine Hat
C3	541	Medicine Hat
C4	546.3	Medicine Hat
C5	561.5	Verger
C6	642.1	2nd White Specks
C7	647.57	2nd White Specks
C8	651.75	2nd White Specks
C9	675.02	Belle Fourche
C10	684.61	Belle Fourche

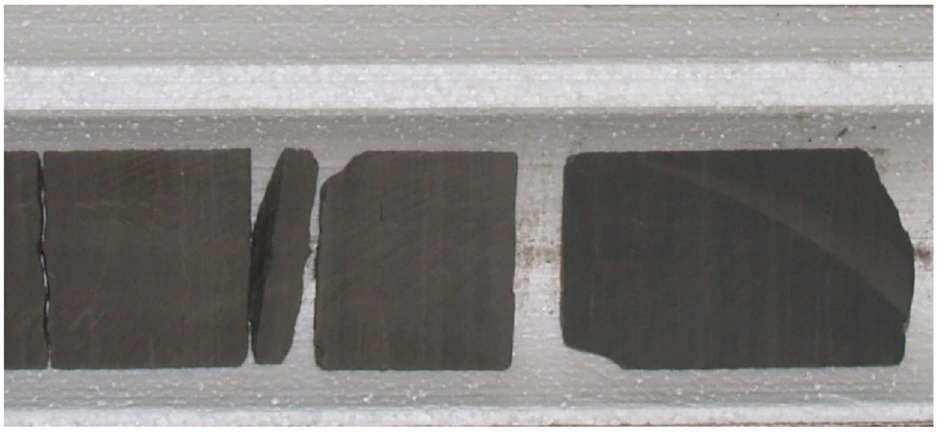

C1 shale core

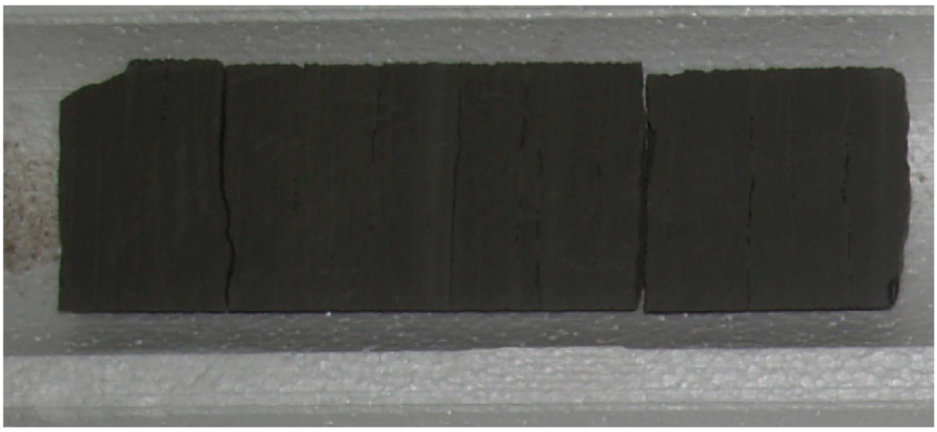

C2 shale core

Figure 2.4: Colorado Group shale core, C1 and C2

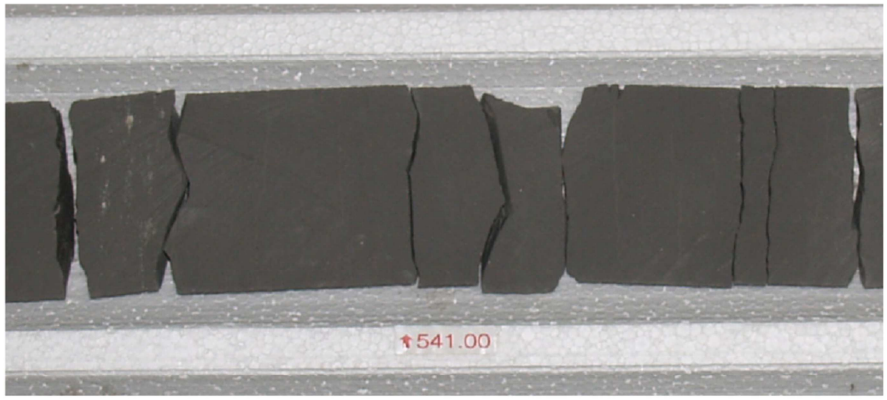

C3 shale core

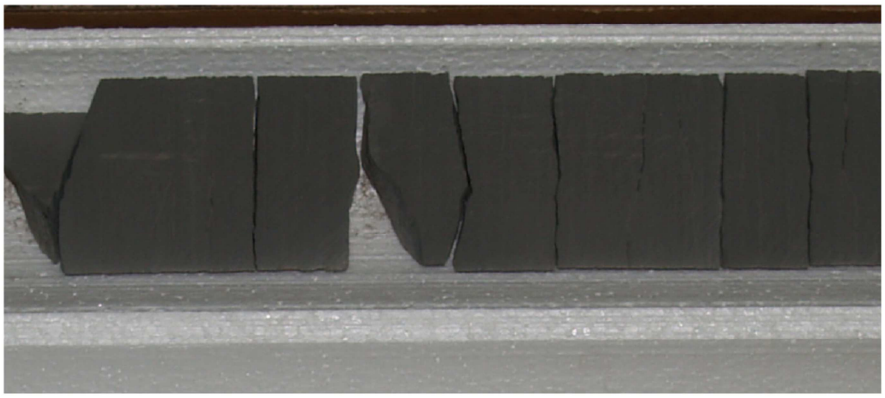

C4 shale core

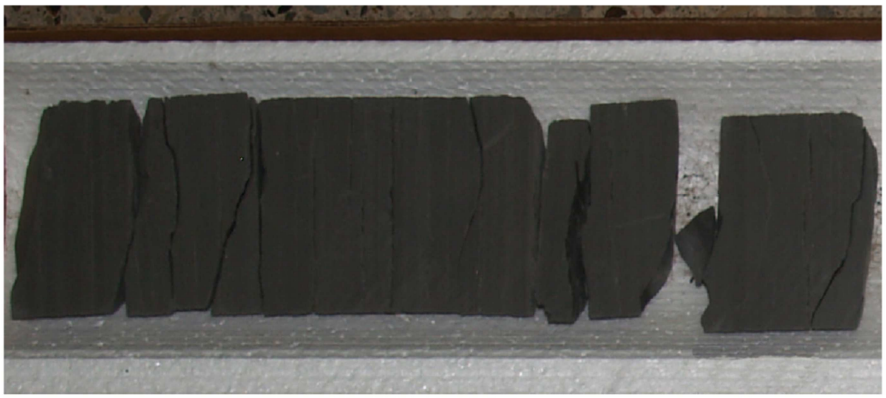

C5 shale core

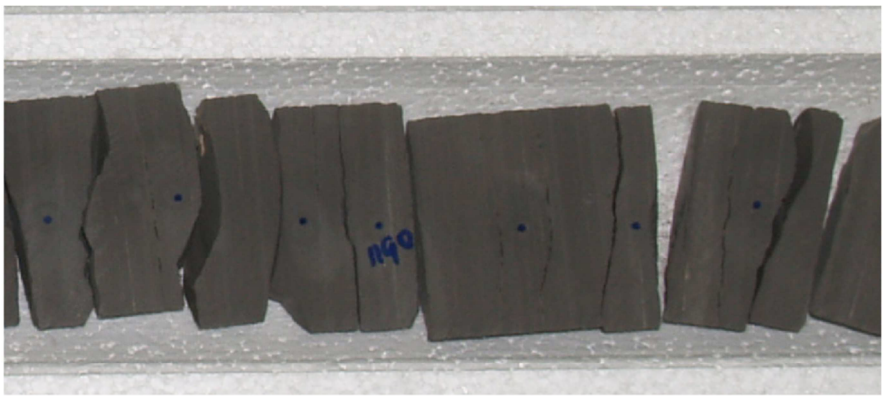

C6 shale core

Figure 2.4 (Continued): Colorado Group shale core, C3 to C6

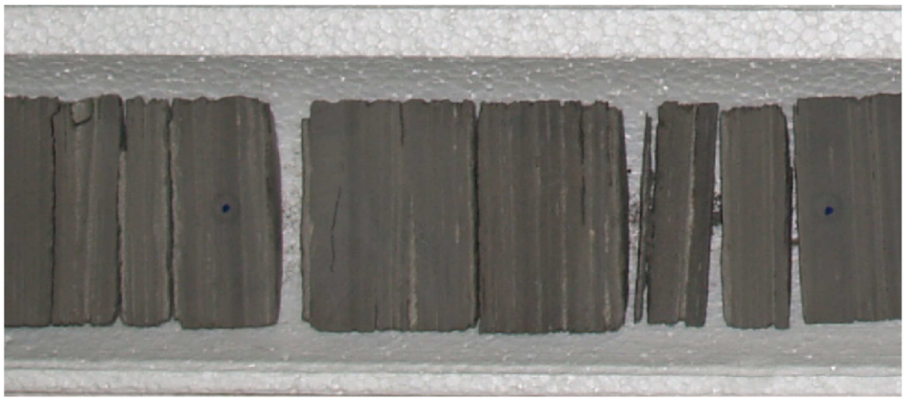

C7 shale core

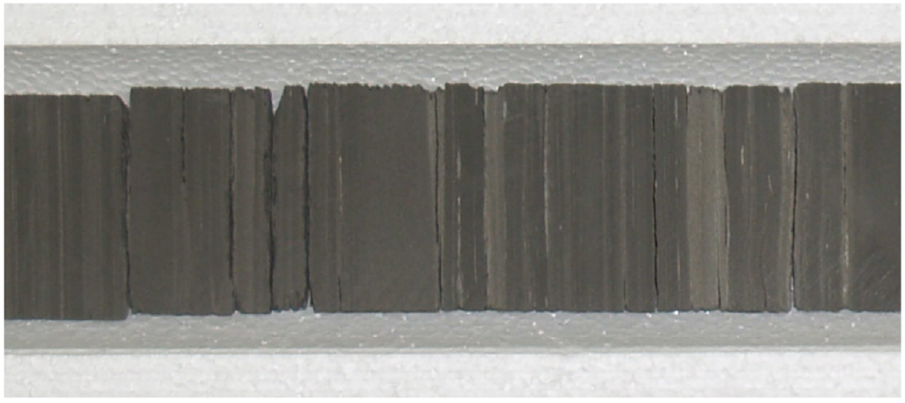

C8 shale core

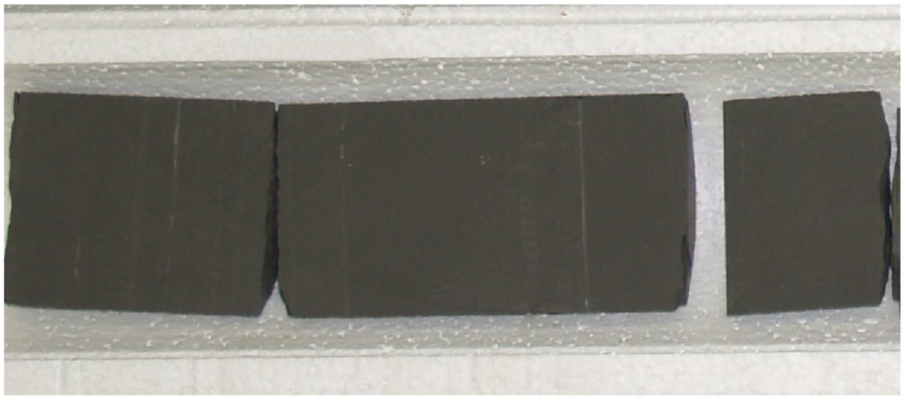

C9 shale core

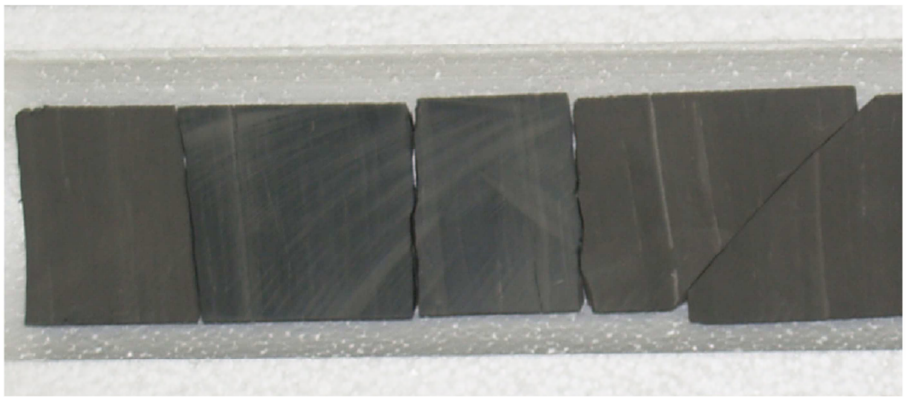

C10 shale core

Figure 2.4 (Continued): Colorado Group shale core, C7 to C10

2.2 Gases

The high pressure compressed gases used for gas adsorption work were supplied by BOC, UK. Research grade nitrogen, carbon dioxide and methane (99.9% purity) were used in all sorption work. The standard tabulated chemical and physical properties of gases used in this project are listed in Table 2.3:

Table 2.3: Chemical and physical properties of gases used in this study.

Gas	**N_2**	**CO_2**	**CH_4**
CAS Number	7727-37-9	124-38-9	74-82-8
Molecular weight, g mol^{-1}	28.0134	44.01	16.043
Liquid density, g cm^{-3}	0.8081 (at -195.8 °C)	1.032 (at 78°C and 0°C)	0.415 (at 30°C)
Boiling point, °C	-195.8 °C (101.3 kPa)	-78.5 °C (Sublimation)	-161.6 °C (101.3 kPa)
Critical temperature, °C	-147 °C	31.14 °C	-82.7°C
Critical pressure, bar	33.999	73.825	45.96
Saturated Vapour Pressure at temperature of use	1013.25 mbar at -195.8°C	34860.6 mbar at 0°C and 1013.25 mbar at -78.5°C	No vapour phase exists at 30°C

Data obtained from the CRC Handbook of Chemistry and Physics, 74th Edition, ISBN-0-8493-0474-1

2.3 Overview of Experimental Techniques

A flow diagram of the experimental techniques used in the project can be seen in Figure 2.5:

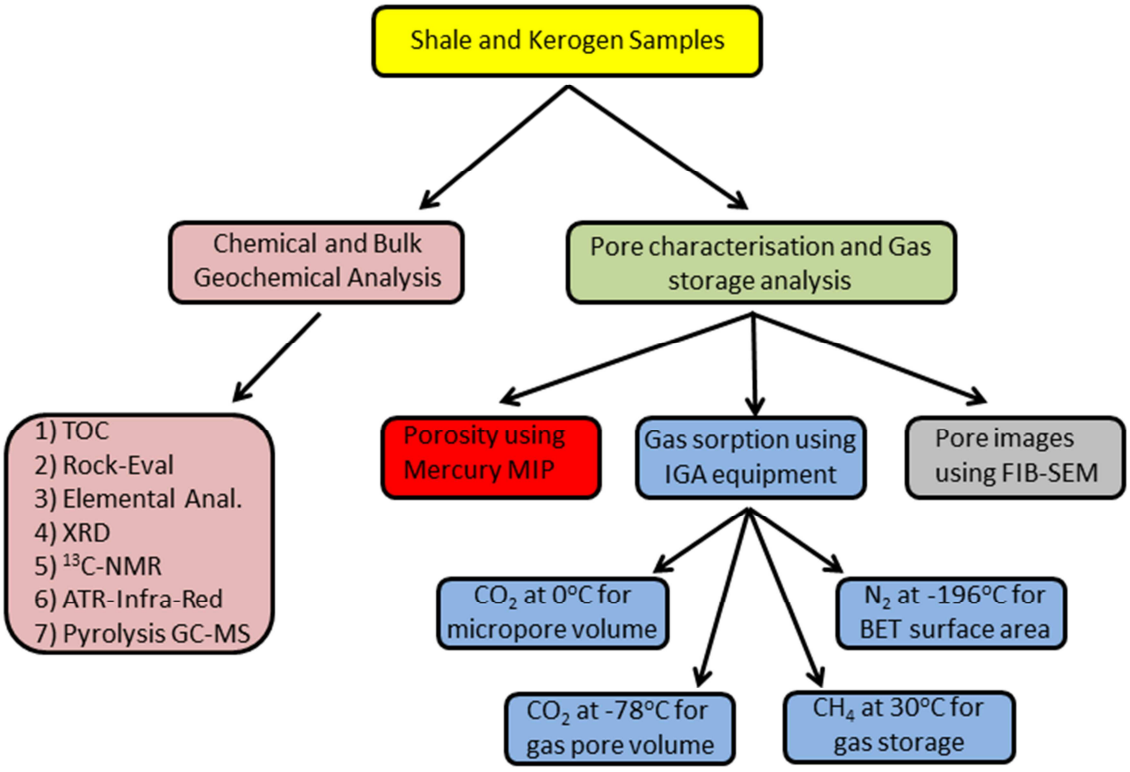

Figure 2.5: Schematic flow diagram of experimental techniques used in this study.

Two types of geological samples were used during this study: 1) shale core, and 2) kerogen. The details of the shale cores can be found in Sections 2.1.1 (DF) and 2.1.3 (CG). The isolated kerogen was obtained by demineralising and depyritising aliquots of the shales (see Sections 2.11 and 2.12 for details).

The experimental methods used can be placed in two categories: 1) chemical and geochemical analysis, and 2) porosity, pore characterisation and gas storage analysis.

Chemical and Geochemical characterisation of shale and kerogen samples:

- The bulk geochemistry and thermal maturity of the geological samples were determined using: 1) TOC analysis of shale, 2) Rock-Eval pyrolysis of shale, 3), Solid State ^{13}C-NMR spectroscopy of isolated kerogen, 4) Infra-Red spectroscopy of isolated kerogen, and 5) pyrolysis GC-MS of isolated kerogen, 6) powder X-Ray diffraction (XRD) for isolated kerogen.

Porosity, pore characterisation, gas sorption and storage:

- The porosity and pore size distribution of the geological samples were characterised using 1) SEM and FIB-SEM images for visual analysis of pores, 2) Mercury Intrusion Porosimetry (MIP) for total porosity and pore radii distributions, 3) CO_2 gas adsorption at -78^{o}C for total gas sorption pore volumes, 4) CO_2 gas adsorption at 0^{o}C for micropore volume, and 5) N_2 gas at -196^{o}C for specific surface areas.

2.4 Shale preparation

The shale core and archived ditch cuttings were crushed to a fine powder, using a TEMA™ laboratory disc mill. The shale powder was sieved through a 0.5 mm mesh geological sieve to remove coarser grain sizes.

2.5 Total Organic Carbon determination

The Total Organic Carbon (TOC, in weight %) was determined by analysing approximately 100 mg of the powdered shale rock. The sample was accurately weighed into a porous ceramic crucible, and aqueous hydrochloric acid (1 mL, 4 M) was added. The acid was used to remove unwanted calcium carbonate (calcite) mineral from the shale that may contribute to the total carbon content of the sample. The acid was allowed to react for 6 hours, and then the crucibles were placed into a drying oven overnight (at 60^{o}C). The next morning, a small amount of tungsten and iron chip accelerators was added to crucibles.

The TOC was determined using a LECO® HF-100 induction furnace that was connected to a LECO® CS-244 Carbon Sulfur Determinator, as depicted in Figure 2.6. The LECO® equipment uses a strong electromagnet to induce rapid heating in the magnetic metal chips, which causes the rock powder to combust. The sample crucibles were inserted into the LECO® HF-100 furnace and individually combusted at 1500 ^{o}C for approximately 1 minute. The carbon dioxide gas that is released is detected by an Infra-Red spectrometer in the LECO® CS-244 Carbon Sulfur Determinator. The signal magnitude of the IR adsorption is used to calculate the TOC of the rock sample.

Figure 2.6: LECO HF-100 induction furnace (left hand side) and LECO LS-244 Carbon Sulfur Determinator (right hand side) used for TOC analysis of shales

2.6 Rock-Eval pyrolysis

The Rock-Eval type pyrolysis of powdered shale rocks was performed using a Delsi Oil Show Analyser, as depicted in Figure 2.7. About 100 mg of powdered shale rock was accurately weighed into stainless steel crucibles. The samples were subjected to the heating program depicted in Figure 2.8. Initially the furnace temperature is set to 100 ^{o}C and held constant for 60 seconds. During the 2nd phase, the furnace temperature was heated to 300 ^{o}C at a rate of 25 ^{o}C/min, and held constant for 2 minutes. During the 3rd phase, the furnace temperature is increased at 25 ^{o}C/min to 550 ^{o}C and held for 90 seconds.

During the initial phase of the heating program the volatile gaseous hydrocarbons are released to give the S0 peak. During the second phase, the light free liquid hydrocarbons are vaporised and released to give the S1 peak (which is measured in milligrams of hydrocarbons per gram of rock). During the third phase, the non-volatile rock kerogen, resin and asphaltenes are pyrolysed to heavier liquid hydrocarbons (which replicates subsurface maturation of petroleum source rocks), to give the S2 peak (which is measured in milligrams of hydrocarbons per gram of rock), (Peters, 1986).

The T_{max} value corresponds to the maximum intensity of the S2 peak, and it is a maturity parameter that represents the point when the maximum rate of kerogen cracking occurs. It is know that shales in the “oil window” typically have T_{max} values between 435^{o}C and 470^{o}C (Peters, 1986).

The sample analyses took about 20 minutes per sample, and the S0, S1, S2 and T_{max} values were reported for each sample set.

Figure 2.7: Delsi Oil Show Analyser used for Rock-Eval pyrolysis of shales

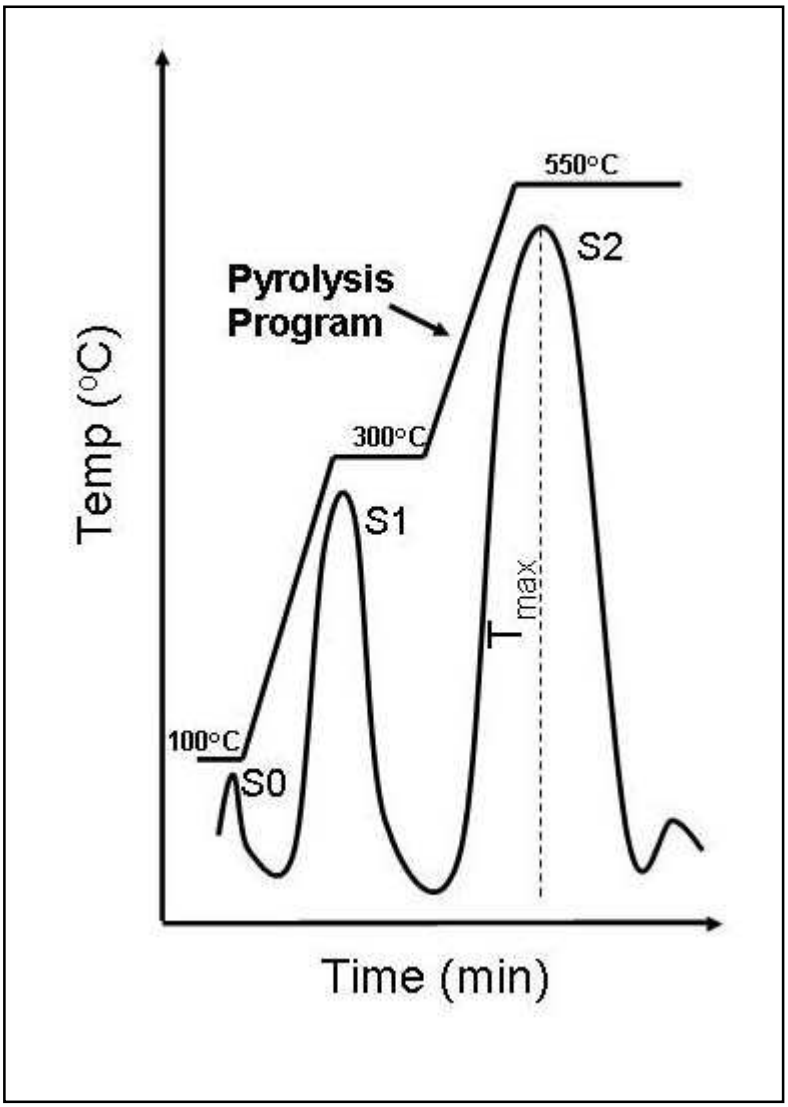

Figure 2.8: Schematic of the pyrolysis program temperature steps and the order of hydrocarbon peaks.

2.7 Electron Microscopy (SEM) of shale porosity

The pore structures of the shale samples were imaged using the Scanning Electron Microscopy (SEM) technique. The electron microscope used was a FEI Nova 200 Nanolab dual beam FIB-SEM, hosted at Leeds University's LEMAS facility, as depicted in Figure 2.9. Samples were prepared by mounting onto a standard SEM specimen stub. The shales were then coated with a 10 nm layer of platinum. The platinum surface coating is required because non-electrically conducting surfaces produce scanning faults and image anomalies.

The microscope was operated at 30 kV, and beam currents between 5 and 0.3 nA were used. The FIB used a high energy focused beam of gallium ions (Ga) to mill the surface of the sample. A second layer of platinum (a 1.5 μm thick) was locally deposited over the target area prior to milling. This was used to stop the sides of the wedge from caving in on themselves.

The highest energy 5 nA beam current was used to remove the initial trench and reveal the cross section area, and then lower beam currents were used to clean the area and reveal the microstructure of the shale.

Both Secondary (SE) and Back Scattered (BSE) Electron micrograph images were recorded of the cross sectioned area.

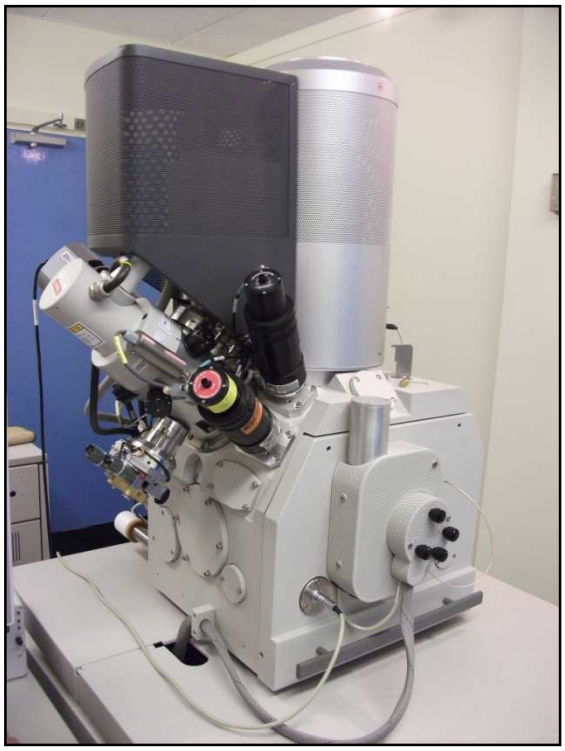

Figure 2.9: The FEI Nova 200 Nanolab FIB-SEM at Leeds University

2.8 Mercury intrusion porosimetry (MIP)

Mercury Intrusion Porosimetry (MIP) analysis of the shale cores was performed using an Autopore II 9220 Porosimeter (Figure 2.10), manufactured by the Micromeritics Corporation, Norcross, Georgia, USA. It generates a series of pressures from 3 psi (0.2 bar) to 39,000 psi (2690 bar), with a pressure resolution of ± 0.1% of the target pressure. The minimum pore "throat" radius that can be accessed by MIP is 3nm, when the pressure is at the maximum of 39 000 psi (2690 bar). The porosimeter has a low pressure chamber (up to 14.5 psi/1 bar) and a high pressure chamber (up to 39 000 psi/2690 bar).

Figure 2.10: The Autopore II 9220 Porosimeter used in the MIP analysis of the shales

The porosimeter determines the volume of mercury that has been intruded in to the sample at each pressure step by measuring the electrical capacitance of the column of mercury in the penetrometer capillary stem. The penetrometers (Figure 2.11) have an accurately known volume (with a capacity of 5 mL), with an associated experimental error of ± 1%. The measurement resolution of the experimental data is ± 0.1 μL, over the full mercury intrusion range

Figure 2.11: An MIP penetrometer, consisting of a sample cup connected to a metal-encased glass capillary stem.

Firstly, cubes of shale core (approx. 1 g) were freeze dried for 1 day and then oven dried to constant mass, to remove fluids (such as water) from the pore spaces. The completely dry, weighed samples were loaded into one of the MIP penetrometers.

The penetrometer (plus sample) was introduced to the low pressure port of the porosimeter, and was outgassed to a near vacuum. The evacuation of the sample is required to remove entrapped air from the pores, as this air can produce a resistant back pressure that impedes the intrusion of mercury.

After outgassing the sample, liquid mercury is flooded into the penetrometer. A series of low pressures steps (from near vacuum up to 1 bar/ 14.5 psi) were applied to the mercury. On completion of the low pressure run, the penetrometer (including the sample intruded with mercury) was removed from the porosimeter and the total weight was recorded. This total weight is used to calculate the bulk density (ρ) of the sample.

The penetrometer (plus mercury and sample) was transferred to the high pressure chamber of the porosimeter, and a series of high pressure steps (between 1 bar to 2690 bar) were applied to the mercury. The incremental increase in mercury volume relative to the pressure allows the pore size distribution to be determined using the Washburn equation (1921).

2.9 Determination of grain density.

The grain density (often referred to as the particle density or skeletal density) is the mass of rock divided by the volume of the solid rock material, without the volume of any internal pores or voids included. It is the density that a rock would have if it was compressed until it was completely non-porous, and no volume was occupied by voids in the internal structure (Masuda *et al*., 2006).

The total porosity of a shale sample is determined using both the grain density and the bulk density. Since the bulk density includes the internal volume occupied by the pores and voids, the value of the bulk density is always lower than the corresponding grain density for the same sample.

The grain densities of the shale samples were determined using a liquid pycnometer (Barbosa-Cánovas *et al*., 2006). The pycnometer method is based on Archimedes' Principle of fluid displacement due to the immersion of a solid into a liquid contained in a fixed volume (Masuda *et al*., 2006).

The pycnometer is a volumetric glass flask with a close-fitting ground glass stopper that has a capillary hole through the centre. This fine hole in the stopper releases excess liquid after closing the top of the pycnometer, so that the volume of liquid contained within is known with high accuracy. The Wadon-type pycnometer used to determine the grain densities in this study is shown in Figure 2.12:

Figure 2.12: The Wadon-type pycnometer used for measuring the grain density of shale samples.

To begin, finely powdered shale rock was oven dried overnight at 105^{o}C, to remove moisture from the porous structure.

Firstly, the mass of the empty pycnometer (with the stopper) was measured (m_0). Then, the dried shale powder was added to the pycnometer, and the new mass of the combined shale powder and pycnometer was measured (m_s).

Next, a small amount of distilled water was added to the density bottle, just enough to cover the shale powder. The mixture was shaken gently, and allowed to stand for 1 hour to allow the water to enter the porous structure of the shale.

The pycnometer was then filled to the top with distilled water (until a few drops escape from the capillary hole in the stopper). The combined mass of the shale, water and pycnometer was measured (m_{sw}).

Finally, the pycnometer was emptied and thoroughly washed, and the pycnometer was again completely filled with distilled water only. The combined mass of the pycnometer and distilled water only (m_w) was determined.

The grain density of the shale was calculated using Equation 2.1 (after Masuda *et al*., 2006; Barbosa-Cánovas *et al*., 2006).

$$\rho_g = \frac{(m_s - m_0)\rho_w}{[(m_w - m_0) - (m_{sw} - m_s)]}$$

Equation 2.1

Where ρ_g = grain density of shale
m_0 = mass of empty pycnometer
m_s = mass of pycnometer and dry shale powder
m_{sw} = mass of pycnometer with shale powder and distilled water
m_w = mass of pycnometer with distilled water only
ρ_w = density of distilled water (= 0.998 gcm^{-3} at 20^{oC} and 0.997 gcm^{-3} at 25^{o}C)

2.10 Gas Adsorption Analysis

The sorption of carbon dioxide, nitrogen and methane gases into shale and kerogen samples were investigated using the Intelligent Gravimetric Analyser (Benham and Ross, 1989), manufactured by Hiden Isochema Ltd, Warrington, UK. The IGA system generates sorption isotherms using a gravimetric approach, and can determine the gas sorption equilibrium point for each chosen pressure.

Figure 2.13: Hiden IGA system, for gravimetric gas sorption in shales and kerogen

2.10.1 IGA system hardware

The IGA system is automated and controlled using the IGASwin© software for personal computers. The IGA system's hardware consists of:

- High performance microbalance: the microbalance is used to accurately measure small mass changes. The microbalance has a long-term stability of ± 1 μg, with a weighing resolution of $\pm$ 0.2 μg.

- Temperature regulation system: the cabinet of the IGA is maintained to isothermal conditions using a sophisticated array of fans and heaters.

- Pressure control system: the IGA has a high precision gas admit and exhaust system. Two separate IGA machines were used. The standard IGA equipment's pressure transducer has a pressure range of 0 to 1 bar. The high pressure IGA has three pressure transducers, giving a pressure range between 0 to 20 bar. The IGA system can control the pressure set point to an accuracy of 0.02 % of the desired value. The gas admittance system also controls the rate of gas entrance into the vacuum chamber (the microbalance is extremely sensitive to sudden bursts of gas).

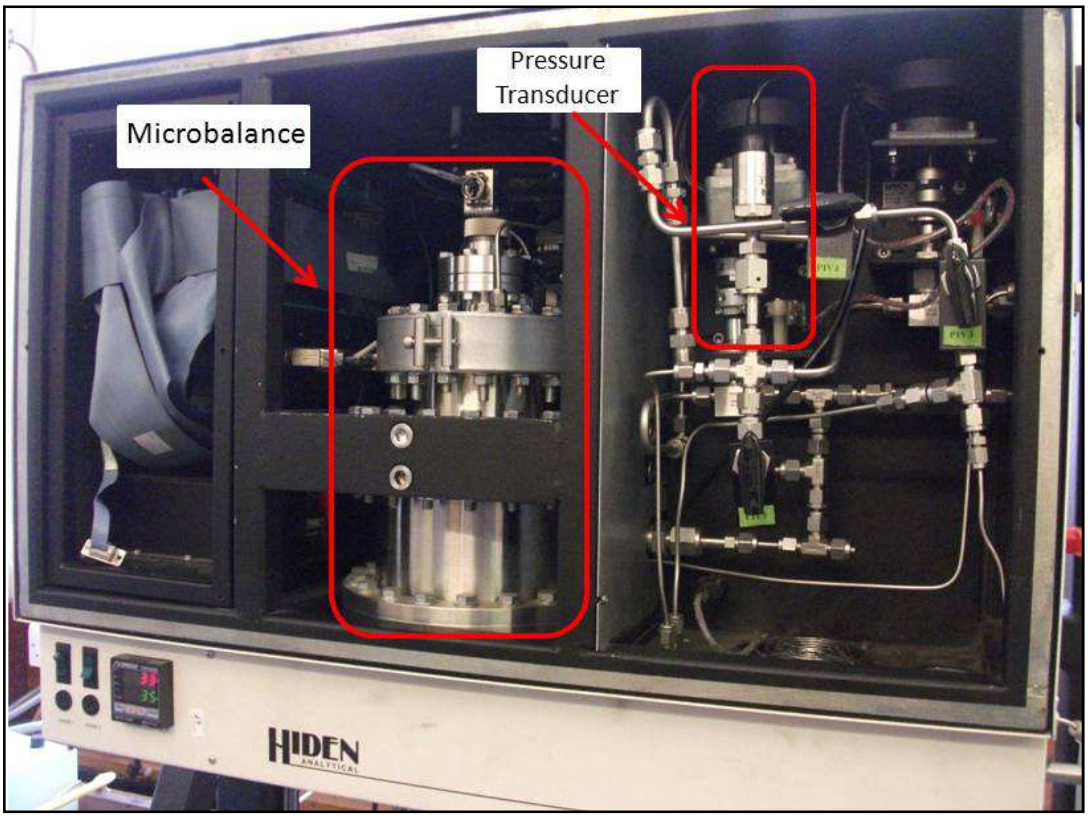

Figure 2.14: Hiden IGA system hardware, highlighting the microbalance housed in a vacuum chamber and the pressure transducer connected to the gas pipework.

2.10.2 IGA system operation

The operation of the IGA is done in a series of stages. A schematic of the process is shown in Figure 2.15:

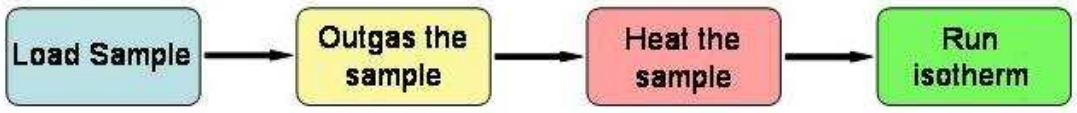

Figure 2.15: Schematic flow diagram of IGA operation.

Stage 1: The geological sample is loaded into a glass sample bucket, which is attached to the microbalance by a free hanging tungsten chain (Figure 2.16)

Stage 2: The sample is sealed in the tubular steel sample chamber using a copper gasket ring and bolted flanges to give a gas tight seal that is capable of achieving an ultra high vacuum (UHV). The sample needs to be evacuated to an UHV before any isotherm experiments can be conducted: atmospheric air is outgassed from the sample chamber down to a pressure of less than 10^{-5} mbar. It is imperative to avoid any leaks or cross-contamination of gases across the seal.

Stage 3: Once the sample chamber is fully outgassed to UHV, it is heated to a high temperature to remove volatile material from the pores of the geological sample (such as trace water). This is important because other studies in the field have shown that moisture in the pores of geological materials substantially reduces the maximum sorption capacity (Krooss *et al.*, 2002; Crosdale *et al.*, 2008; Weniger *et al.*, 2010). The shales were heated to 200°C, and the kerogens were heated to 105°C. These temperatures were chosen to minimise any thermal alteration to the chemical structure of the geological samples. The decrease in sample mass is recorded throughout the outgassing and heating process until a constant mass is achieved (Figure 2.17).

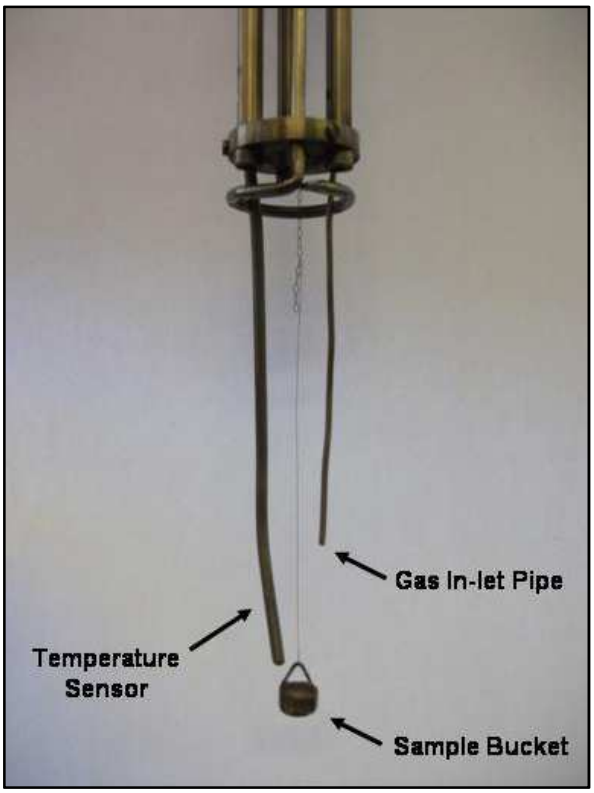

Figure 2.16: The geological sample is held in the sample bucket and sealed in to the sample chamber.

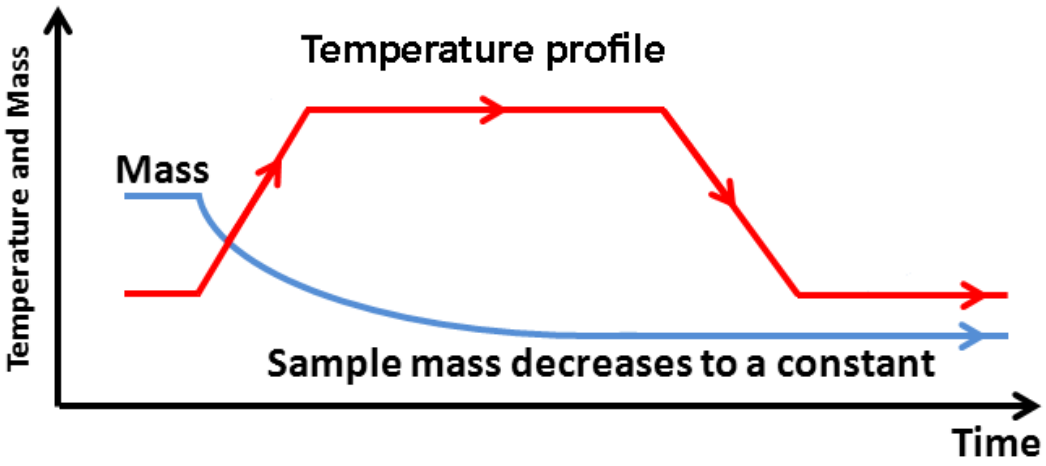

Figure 2.17: Schematic diagram of mass loss due to heat treatment of sample

Stage 4: After the sample heating has finished, the gas sorption experiment can be conducted. The experiment is done under isothermal conditions (the temperature is accurately controlled). This is so that gas pressure is the only experiment variable affecting the amount of gas adsorbed. The temperature of the sample chamber is controlled by either Dewar flask or by a Grant Optima waterbath, depending on the desired temperature. The CO_2 isotherms at 0^oC (273K) and the CH_4 isotherms at 30^oC (303K) have the sample temperature controlled to an accuracy of ± 0.05 K using the waterbath, which circulates a 1:1 mixture of water and ethylene glycol (Anti-Freeze). The CO_2 isotherms at -78^oC (195K) have the sample temperature controlled by a Dewar flask containing solid dry ice and acetone. The N_2 isotherms at -196^oC (77K) have the sample temperature controlled by a Dewar flask containing liquid nitrogen.

2.10.3 Real Time Processor (RTP) analysis of kinetic sorption-time data

During the sorption experiment, the uptake of gas is measured by recording the change in mass of the sample as a function of time (the gravimetric method). The sample mass increases with gas adsorption, and decreases with gas desorption. The approach of the sorption-time curve to the equilibrium point (at that specific pressure) is monitored by the IGASWin software's Real Time Processor (RTP).

The RTP uses least-squares non-linear regression to extrapolate a value of the asymptote and predict the adsorption equilibrium point (in real time using the sorption-time curve kinetic profile). This is done using a simple empirical mass relaxation model for equilibration, based on the following first order reaction kinetics equation:

$$\frac{M_t}{M_e} = \frac{M_t}{M_1 - M_0} = [1 - e^{-kt}]$$

(Equation 2.2)

where

M_t = mass at time (t)
M_e = mass at equilibrium
M_1 = final mass
M_0 = initial mass
t = time
k = rate constant (s^{-1})

Once 99% of the predicted adsorption equilibrium point was reached, the gas pressure was increased to the next pressure step, and gas uptake was again monitored until the new adsorption equilibrium had been established. A schematic diagram of this process is shown in Figure 2.18:

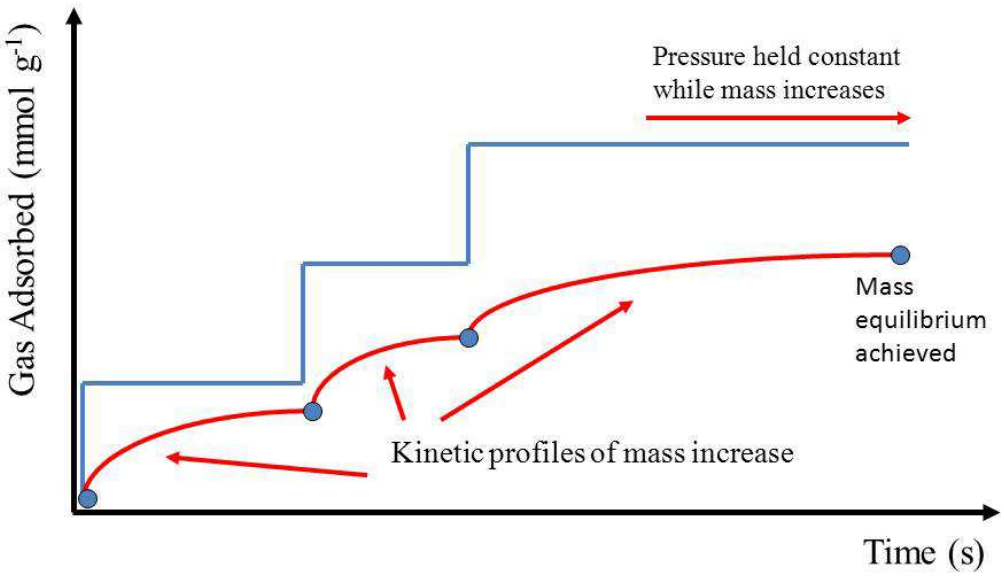

Figure 2.18: Schematic diagram of isotherm pressure steps and mass relaxation

2.11 Kerogen Preparation and Analysis

The kerogen was isolated from the shales in the following way:

1) Shale rock milled to a powder using a TEMA™ laboratory mill
2) Demineralised using hydrochloric and hydrofluoric acids
3) Depyritised using acidified chromous chloride extraction.

2.12 Acid digestion of shale to obtain kerogen

The acid digestion of the shale to isolated kerogen was performed using the procedure described in Vandenbroucke and Largeau (2007). Firstly, the powdered shale samples (approximately 10 g per sample) were suspended in distilled water (50 mL per sample). Then hydrochloric acid (4 M) was added (100 mL). The HCl is used to dissolve calcium carbonate (calcite). Hydrofluoric acid was then added (100 mL per sample), and allowed to digest the shale for two days in a fume cupboard. The acidified suspension was then neutralised by repeated dilutions using distilled water (10 times). Each time the fresh distilled water was added, the suspended kerogen took one day to re-settle to the bottom of the PTFE beakers. The suspension was tested for neutrality using litmus paper.

2.13 Chromous Chloride $CrCl_2$ pyrite reduction

Iron Pyrite (FeS_2) is an inorganic sulfur containing mineral that accumulates in sedimentary rocks during sediment diagenesis (Hurlbut and Klein, 1985). Pyrite is not digested by strong mineral acids, such as HCl and HF. It is an unwanted contaminant in the extracted kerogens. It has a particularly high density of 5.02 g cm^{-3}, and has the potential of introducing experimental errors in to subsequent measurements.

The majority of pyrite in the demineralised kerogens was removed by extracting the chromium reducible sulphur (CRS) using the acidic chromous chloride reduction developed by Canfield *et al.* (1986).

The glassware/equipment used is reported in Figure 2.19. The reaction was conducted in a 3-neck 100 mL round bottomed flask. The first side arm was used as a nitrogen gas inlet. The second side arm was sealed with a glass stopper. The top neck was connected to a Graham condenser that carries the H_2S gas to the aqueous silver nitrate $AgNO_3$ bubbler trap (1.5 mL of aqueous 1 M $AgNO_3$ in approximately 20 mL of distilled water).

The demineralised kerogens (approximately 1 g per sample) was added to the 3-neck round bottomed flasks. Then 50% aqueous hydrochloric acid (8 mL) was added to the flask. Pre-prepared dark green 4.33 M acidic chromous chloride solution (16 mL), was then added (it was prepared using 533 g of $CrCl_2$ per litre in aqueous 10% HCl solution). The reaction mixture was heated on full power using a laboratory heating mantle for one hour. The generated H_2S gas was transported to the aqueous silver nitrate $AgNO_3$ bubbler trap (via the Graham condenser) where it reacted to form a dark brown silver sulfide (Ag_2S) precipitate in the bubbler traps. The chromous chloride extractions were repeated a further two times to ensure removing as much pyrite as possible.

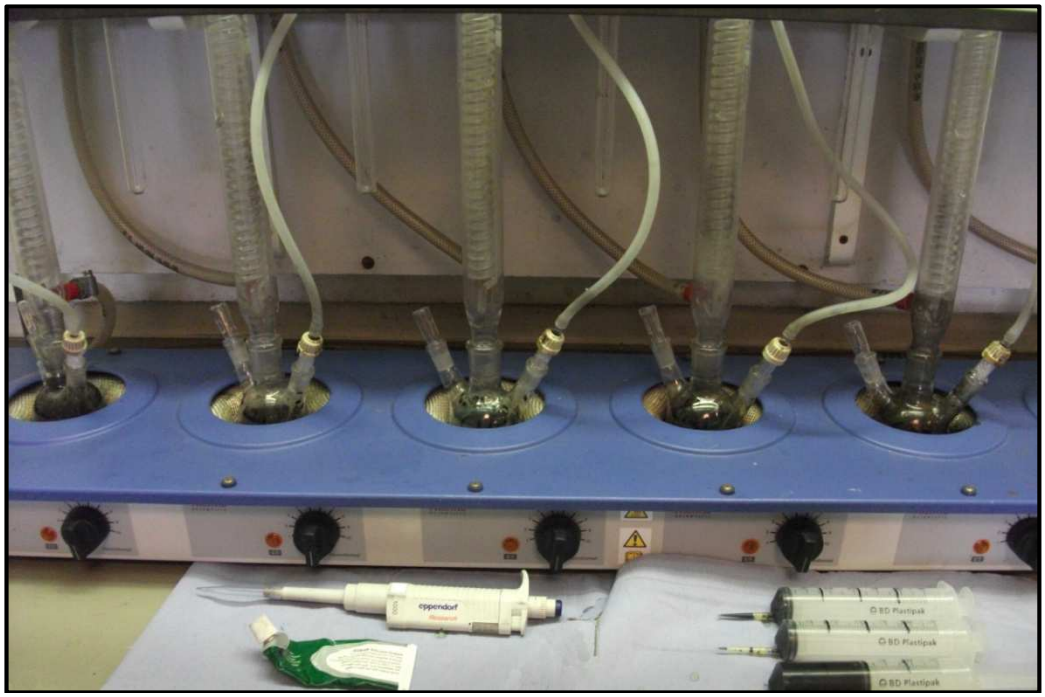

Figure 2.19: The chromous chloride extraction to remove iron pyrite from samples

2.14 Powder X-ray diffraction (XRD) of shale and kerogen

The mineralogy of the shales and the purity of the demineralised and depyritised kerogens were determined using powder X-ray diffraction (XRD). Powder XRD is a robust method for identifying and characterising crystalline minerals (such as quartz, clays, carbonates and pyrite).

The X-ray diffractograms of the shale and isolated kerogen samples were obtained using a PANalytical X'Pert Pro MPD, which is hosted at Newcastle University's powder XRD facility, as depicted in Figure 2.20. This instrument was fitted with an optional X'Celerator unit to increase data acquisition times, and a secondary monochromator to improve the peak to background measurement ratio. The scans were done using a Cu anode supplied with a voltage of 40 kV and a current of 40 mA to generate Cu-Kα radiation (λ = 1.54180 Å). The data were collected over a range of 2-70^{o} 2θ-angle with a nominal step size of 0.0167^{o} 2θ-angle and nominal time per step of 100 seconds (which is approximately equivalent to a counting time of 1 second per step on an older style diffractometer). Fixed anti-scatter and divergence slits of 1/4^{o} were used together with a beam mask of 10mm. All scans were carried out in 'continuous' mode using the X'Celerator RTMS detector.

Powdered shale (~ 500 mg) and isolated kerogen (~ 200mg) samples were mixed with a corundum mineral standard in a 80:20 %wt ratio, respectively. The mixtures were packed into steel sample holders (with 16 mm diameter wells) and loaded into the diffractometer. A spinning stage was used during sample analysis to maximise the randomisation of crystallites contributing to the diffraction pattern. Data collection involved the measurement of total X-ray counts over a 2-theta angle range.

Figure 2.20: PANalytical X'Pert Pro MPD X-Ray diffractometer

2.15 Elemental analysis of isolated kerogens

The elemental composition of the isolated kerogens was determined using a Carlo Erba EA-1108 CHNSO Element Analyser, as depicted in Figure 2.21. The kerogens were analysed twice: the first analysis was to determine the carbon, hydrogen, nitrogen and sulfur (CHNS) elemental composition, and the second analysis was to determine the oxygen content, using a modified equipment setup.

The CHNS composition of the kerogens was determined first. The dry powdered kerogen sample was accurately weighed (2 to 3 mg) into a tin crucible. It was placed in to the combustion oven and rapidly heated to 1020 °C in a pure stream of compressed oxygen gas. The combustion of kerogen generated CO_2, H_2O, NO_x, and SO_x gaseous combustion products. These combustion gases were carried to a gas chromatograph using a carrier stream of pure helium gas (unreacted oxygen gas was removed using a gas scrubber packed with a copper catalyst). The detection of the combustion gases were detected using the GC's thermal conductivity detector (TCD), and the CHNS elemental composition quantified.

Secondly, the oxygen elemental composition of the kerogens was determined. The analysis was performed as before, except that the kerogen sample was pyrolysed at 1070^{o}C in a pure stream of compressed helium gas. The pyrolysis of kerogen generated carbon monoxide gas, which is detected using the TCD, and the oxygen content quantified.

Calibration runs were performed with a standard (sulfanile amide), and blanks were also run with empty tin crucibles. The analytical error on the reported data is ± 0.01%

Figure 2.21: Carlo Erba EA-1108 CHNSO Element Analyser

2.16 Infra-Red spectroscopy of isolated kerogens

The organic functional groups present in the isolated kerogens were analysed using Fourier-Transform Infra-Red (FT-IR) spectroscopy. The organic functional groups absorb Infra-Red radiation, and undergo several vibrational stretching and bending motions. The wavelength of Infra-Red radiation absorbed is unique to each organic functional group (Williams and Fleming, 1995).

The machine used (Figure 2.22) had an Attenuated Total Reflection (ATR) attachment, which allows the sample to be analysed quickly and directly (usually taking a few minutes per sample). The ATR attachment only requires a very small amount of sample (~ 2 mg). The benefit of the ATR device is that it removes the need to process the sample in to potassium bromide (KBr) discs or a Nujol mull (Williams and Fleming, 1995). The details of the IR spectrometer used are listed in Table 2.4:

Table 2.4: Details of the ATR FT-IR spectrometer used to analyse the functional groups of the kerogens

MACHINE SPECIFICATIONS
Instrument: Thermo Nicolet 6700 FTIR ESP spectrometer
Spectrum range: Mid-IR (4000 to 600 cm^{-1})
Accessory: ATR; Attenuated Total Reflection
Scans: 32
Resolution: 4 cm^{-1}
Background scans co-added: 32
Detector: DTGS ambient (internal)
Mode of detection: Infra-Red Absorption

Figure 2.22: The ATR-FTIR spectrometer used to determine the functional groups in the kerogens.

2.17 Solid-State Nuclear Magnetic Resonance spectroscopy of kerogens

Solid state ^{13}C-NMR analyses of the kerogen samples were obtained by Durham University using their Varian VNMRS spectrometer (Figure 2.23) operating at 100.56 MHz for ^{13}C (399.88 MHz for 1H or a 9.4 T field) and a 6 mm magic-angle spinning (MAS) probe. The unwanted sidebands were suppressed using "TOSS" spinning sideband suppression, mostly from the aromatic signals in the spectra. Solid-state ^{13}C-NMR spins the sample on its magic-angle spinning (MAS) axis at extremely fast speeds (several kilohertz), to allow the average isotropic chemical shift values to be determined.

Solid-state ^{13}C-NMR analysis is required for kerogens because they do not dissolve into the deuterated organic solvents required by the more commonly used solution phase NMR. Solid state ^{13}C-NMR can be used for analysing the chemical structure and bonding of the kerogen carbon framework. It can identify the presence of organic functional groups, the degree of aromatization, and the level of cracking of aliphatic side chains.

Figure 2.23: Varian VNMRS spectrometer for solid-state NMR at Durham University

2.18 Pyrolysis GC-MS of isolated kerogens

The pyrolysis GC-MS analysis of the isolated kerogens was performed using a CDS Pyroprobe 1000 coupled to a Hewlett-Packard 6890 Gas Chromatograph (Figure 2.24). Helium gas was used as the carrier gas (constant flow 1 ml/min, initial pressure of 110 kPa, split at 30 ml / min). Separation was performed on a fused silica capillary column (60m x 0.25mm i.d) coated with 0.25 µm 5% phenyl methyl silicone (HP-5MS).

A Hewlett-Packard 5973MSD mass spectrometer was linked to the gas chromatograph, via a split injector (320°C). The mass spectrometer operated under the conditions of electron voltage 70eV, emission current 35µA, source temperature 230°C, quadrupole temperature 150°C, multiplier voltage 2200V, interface temperature 320°C. The data acquisition was controlled by the Agilent MSD Chemstation software, in full scan mode (50-650 amu).

The isolated kerogens were accurately weighed (~2mg) and packed into quartz pyrolysis tubes with glass wool end plugs. A sample tube was placed into the pyroprobe platinum heating coil and rapidly pyrolysed at 611°C (ramped at 10C/ms) for 10 seconds with the GC split open. The GC was initially held at 40°c for 4 min, before being ramped at 4 ^{o}C/min from 40 ^{o}C to 90 ^{o}C. The GC programme was then ramped at 2 ^{o}C/min to 150 ^{o}C, before finally increased at 4.5 ^{o}C/min to 320 ^{o}C where it was held for 6 min. The pyrolysate compound identification was done using the ion fragmentation patterns identified using the NIST98 spectral library.

Figure 2.24: The py-GC-MS instrument used to analyse the kerogens.

Chapter 3: Geochemical analysis of organic rich shales and isolated kerogens

3.1 Introduction

3.1.1 Organic matter content and thermal maturity of source rocks.

Geochemical analysis of shale core is performed to determine the organic richness and thermal maturity of a source rock. A potential source rock must contain enough organic matter to generate hydrocarbons upon thermal maturation, otherwise insufficient quantities of hydrocarbons may be generated to be expelled and migrate from the source rock to a nearby reservoir rock (Tissot and Welte, 1984). However, in the case of gas shales, the shale formation is both the source and the reservoir, so the expulsion and migration of hydrocarbons does not need to be considered (Curtis, 2002; Bowker, 2007; Hill *et al.*, 2007).

The abundance of organic matter in a shale formation is determined from a Total Organic Carbon (TOC) analysis. Shales with organic matter contents above 2% have good hydrocarbon generating potential, and TOC's above 4% are considered excellent (Tissot and Welte, 1984). It is important to note, however, that TOC content is not the only control on the hydrocarbon potential of a source rock, as the organic matter type (the kerogen quality) and level of thermal maturity must also be considered before a conclusion on source potential can be made.

The level of thermal maturation of a source rock is often determined using either optical microscopy (i.e. visual kerogen analysis, vitrinite reflectance, kerogen fluorescence and Thermal Alteration Index), or bulk geochemical methods (i.e. Rock-Eval Pyrolysis, Elemental Analysis, solvent extractable Biomarker Analysis). Maturation of the source rock affects the interpretation of TOC contents, as hydrocarbon generation causes the TOC values to decrease (relative to the original TOC of the immature shale). The Rock-Eval pyrolysis of shale core can also determine the geochemical Type of the kerogen, and thus the likely hydrocarbon products upon maturation (Langford and Blanc-Valleron, 1990). This is done using the Tmax of the S2 pyrolysis peak, and the Hydrogen and Oxygen Indices in the form of a pseudo-van Krevelen diagram.

3.1.2. The geochemical composition and structure of kerogen.

Kerogen is the high molecular weight organic geopolymer that is widely dispersed throughout the matrix of sedimentary rocks. It is insoluble in organic solvents (such as dichloromethane), and is often closely associated with bitumen, the low molecular weight organic matter that is soluble in organic solvents (Durand, 1980). Kerogen is the primary source of hydrocarbons in petroleum source rocks, when subjected to the correct temperature and pressure conditions (Tissot and Welte, 1984).

The structure and composition of kerogen is characterised using geochemical techniques such as Elemental Analysis, py-GC-MS, solid state NMR spectroscopy and Infra-Red spectroscopy. Optical microscopic examination of kerogen concentrates is also a key analytical technique used to identify the maceral composition and the trace presence of structured organic fragments (i.e. algae, spores, pollen).

The geochemical composition of kerogen depends upon the nature of the precursor organic matter incorporated into the sediments. The chemical composition of kerogen is therefore highly variable, and is dependent on the numerous biological inputs that may be included into the preserved sedimentary organic matter. Pyrite (FeS_2) is often a major constituent of kerogen, as pyrite is embedded in to the kerogen, especially in marine sedimentary rocks deposited under anoxic conditions. Pyrite can amount to more than 40 wt% of isolated kerogen (Vandenbroucke and Largeau, 2007). Several organic macerals are also commonly identified in kerogen (Stopes, 1935; Killops and Killops, 2005). The alginite maceral (from algaenan) is derived from the cell walls of marine and freshwater algae, and consists of long chain *n*-alkyl groups (Goth *et al*. 1988), which may contain significant polyester linkages (Allard *et al*. 2002). The cutinite maceral (from cutan) is derived from the waxy plant cuticles of terrestrial higher plants. The suberinite maceral (from suberan) is derived from cork tissues of terrestrial higher plants, e.g. bark and root walls. The vitrinite maceral is derived from macromolecular aromatic lignin found the woody xylem tissue in higher terrestrial plants (Teichmüller, 1989), Figure 3.1:

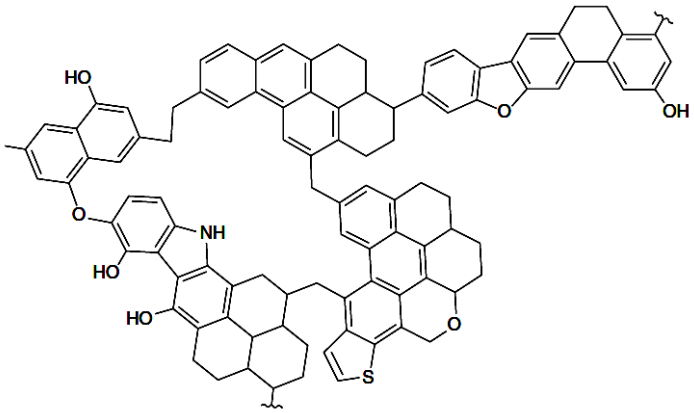

Figure 3.1: Geochemical structure of the vitrinite maceral. It is a highly aromatic interconnected carbon skeleton, containing thiophene and furan heteroatom rings (Heredy and Wender, 1980).

Kerogen is categorised (Tissot *et al*. 1974; Tissot and Welte 1984) in to geochemical types based on composition. The Type I kerogen group is typically formed from fresh water algal material (e.g. Botryococcus) that is deposition in the shallow fresh water anoxic muds of lakes and lagoons. Type I kerogen is usually comprised mostly of liptinite macerals, and is generally quite rare (Tissot and Welte, 1984). It contains significant amounts of lipid materials, especially long-chain aliphatics. The lipids of Type I kerogen are mainly derived from the alginite maceral, although bacterial lipids may be an important contributor (Tissot *et al*., 1978).

The Type II kerogen group is formed in low oxygen marine settings from a mixture of phytoplankton and terrestrial higher plant material. Type II kerogen is more common than Type I and is the source of hydrocarbons in many oil and gas fields (Tissot and Welte 1984). Type II kerogens usually comprise of a carbon skeleton of aromatic sheet units interlinked by ketone, carboxylic acid and ester bonding groups. Significant amount of aliphatic side chains may be bonded to the aromatic carbon skeleton, and these aliphatic chains are generally of moderate length (up to ~ C_{25}). Type II kerogen is often associated with significant amounts of pyrite.

The Type III kerogen group is common, and is formed from the vascular tissues of higher terrestrial plants, with the vitrinite maceral dominating the composition (Durand and Monin, 1980). The aromatic biopolymer lignin and its derivatives are a major component to Type III kerogens, and are a significant contributor to the aromatic nature of Type III kerogen. It is dominated by polycyclic aromatic hydrocarbons and oxygen functional groups (Tyson, 1995), Unlike Type II kerogen, Type III kerogen contains very few ester bonding linkages, and only minor amounts of aliphatic side chain groups, those of which are dominated by methyl and other short chain alkyl groups (not the longer alkyl chains of Type II kerogen), (Killops and Killops, 2005).

The Type IV kerogen group is dominated by the inertinite maceral group, with a minor amount of vitrinite (Killops and Killops, 2005). The Type IV kerogen group comprises black opaque debris under optical microscopic examination (Powell and Snowdon, 1980). It is dominated by polycyclic aromatic carbon atoms (Tyson, 1995), with negligible amounts of hydrogen (Tissot *et al*., 1980), and is considered to have a graphite-like in structure; the lack of hydrogen results in Type IV kerogen having no hydrocarbon generation potential. It is formed from severely oxidised higher plant matter that has been oxidised in subaerial environments and/or recycled from older thermally mature sediments (Tissot *et al*., 1980; Tyson, 1995).

The elemental analysis of isolated kerogen has identified carbon, hydrogen and oxygen as the main atomic elements in kerogen, with minor amounts sulfur sometimes present (Tissot and Welte 1984). Type I kerogen has a high H/C ratio ($\geq$1.5) and a low O/C ratio (<0.1), (Tissot and Welte 1984). Type II kerogen has relatively high H/C H/C ratio (~ 1.2) and low O/C ratios, being lower that Type I kerogen (Tyson, 1995). Type III kerogen has a low H/C (<1.0) and a high O/C ratio (up to 0.3), (Powell and Snowdon, 1980). The ratios of H/C and O/C can be plotted on the van Krevelen diagram to determine the kerogen type from the elemental analysis (Tyson, 1995). As Type I and IV kerogens are rare, most kerogens fall between Types II and III on the van Krevelen diagram (Killops and Killops, 2005).

The structure of kerogen is formed from a three-dimensional macromolecular carbon skeleton of aromatic units (known as the carbon nuclei), that are linked together by aliphatic carbon chains (Vandenbroucke and Largeau, 2007). The aliphatic cross-linkages may contain various functional groups, including carboxylic acids, alcohols, esters, and amides (Killops and Killops, 2005). The aromatic carbon units (the nuclei) take the form of flat aromatic sheets, often with aliphatic *n*-alkyl side chains bonded to them, and may also have heteroatoms (i.e. nitrogen, oxygen and sulphur) incorporated into the aromatic ring structures(Killops and Killops, 2005). Lipids can be trapped within the three-dimensional kerogen matrix. An idealised structure of Type II kerogen is reported in Figure 3.2:

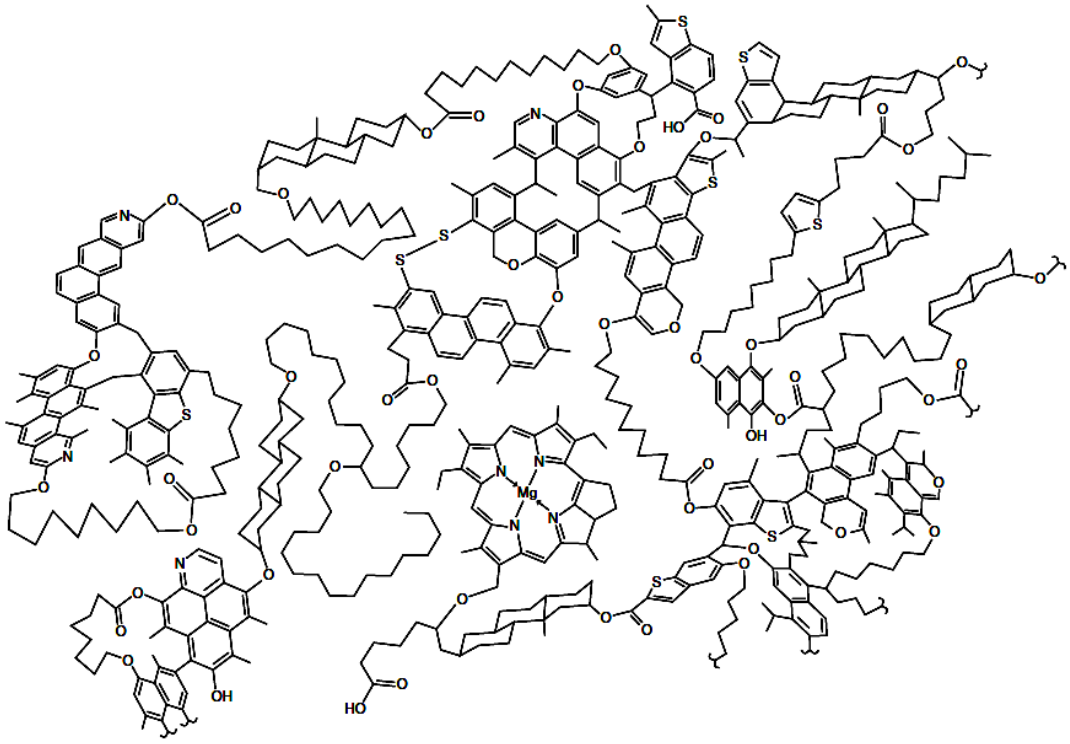

Figure 3.2: The structure of Type II kerogen (after Béhar and Vandenbroucke, 1987)

3.1.3 Maturity related changes to kerogen structure and composition

The structure and composition of immature kerogen is very stable over long periods; even in ancient sediments, the structure of immature kerogen will remain relatively unchanged (Killops and Killops, 2005). Significant compositional changes to the kerogen geopolymer will only occur from being subjected to thermal maturation. During catagenesis, the increased temperature and pressure conditions cause the 3-D structure of immature kerogen to rearrange to form a more ordered and compact structure (Vandenbroucke and Largeau, 2007). This rearrangement of the kerogen structure is an attempt to reduce the increasing molecular strain on the structure of the geopolymer. The bulky *n*-alkyl side chains sterically hinder the close packing of the carbon skeletal nuclei, so they are cleaved from the periphery of the macro-structure and eliminated as hydrocarbons. The loss of hydrogen atoms from the skeletal nuclei results in the aromatisation of the carbon skeleton, thus regaining the energetic stability that is lost by the ejection of the aliphatic *n*-alkyl groups (Vandenbroucke and Largeau, 2007).

The increased maturation of kerogen also leads to the progressive elimination of organic functional groups (such as aldehydes and esters), as they are mainly located on the ejected aliphatic side chains. The aromatic carbon skeletal nuclei units increasingly become cross-linked together (Larsen *et al.*, 2002). Furthermore, the progressive elimination of bulky peripheral groups results in a change in the elemental composition of the kerogen. The ejected compounds contain mostly C, H and O atoms, so the relative abundance of these elements in the kerogen changes with maturation. The loss of hydrogen results in the H/C ratio of the kerogen to decrease with the generation and release of hydrocarbons (acyclic and cyclic). The H/C ratios may decrease significantly in Type I and Type II kerogens (from around 1.5 and 1.2, respectively, down to 0.5). The decrease in the H/C ratio of type III kerogens is usually lower though, reflecting their smaller starting potential for hydrocarbon generation (Killops and Killops, 2005).

The aromaticity of kerogen increases significantly during thermal maturation, as a result of both the expulsion of aliphatic hydrocarbons and the increasing aromatization cyclic rings in the kerogen structure (i.e. aliphatic cyclohexyl- rings becoming aromatic benzene rings; Killops and Killops, 2005). The methyl group (CH_3-) content of the kerogen also increases during thermal maturation, as long-chain aliphatic components are removed, leaving behind a lone methyl group at the point where the aliphatic chain was cleaved from the carbon skeletal structure (Killops and Killops, 2005).

At advanced stages of thermal maturation, the chemical composition of all three kerogen types become increasingly alike, reaching an unchanging H/C ratio of less than 0.5, with up to 80% of the original carbon content being lost to expulsion (Killops and Killops, 2005). During the extreme conditions of metagenesis, the carbon content of kerogens is greater than 90%, with negligible amounts of other elements left in the kerogen structure (Killops and Killops, 2005). In mature source rocks, the original Type of a mature kerogen may be difficult to determine using bulk geochemical analyses only (Vandenbroucke and Largeau, 2007). Mature kerogen often has the characteristics of a geochemical Type III kerogen (i.e. high aromaticity, low Hydrogen Index, low elemental H/C ratios). If it is uncertain whether a mature kerogen originated from a Type II or Type III kerogen, the mineralogy of the source rock may be used to reconstruct the origin of a kerogen (Huc, 1990). The associated mineral fraction of a source rock gives an indication of the environmental conditions of kerogen deposition (the organo-facies), and thus the likely initial kerogen Type (Huc, 1990).

3.2 Results

3.2.1 Total Organic Carbon (TOC) content of shale

The organic carbon content (in weight %) of the Draupne Formation and Colorado Group shales were determined using the procedures described in chapter two, section 2.5. The DF shale samples have excellent organic matter contents (Table 3.1), with a range between 2.96 % to 10.75%, and a mean average of 7.24 % ± 2.33 %. The CG shale samples have good organic matter contents (Table 3.1), with a range between 2.02% and 3.68%, and an average of 2.74 % ± 0.57 %.

Table 3.1: Total Organic Carbon (TOC) Content of the Draupne Formation and Colorado Group shales.

Sample	Burial Depth / m	TOC / %	Sample	Burial Depth / m	TOC / %
DF1	2117.8	8.53	C1	505.3	2.54
DF2	2325	10.37	C2	506.55	2.51
DF3	2978.5	2.96	C3	541	2.46
DF4	3124.7	7.68	C4	546.3	2.42
DF5	3375.32	10.75	C5	561.5	3.15
DF6	3400.4	7.74	C6	642.1	3.33
DF7	4132.95	7.01	C7	647.57	3.68
DF8	4608.4	5.69	C8	651.75	3.28
DF9	4707.7	5.60	C9	675.02	2.05
DF10	4780.7	6.10	C10	684.61	2.02

3.2.2 Rock-Eval Pyrolysis of shale

Thermal maturity and hydrocarbon content/generation potential of the Draupne Formation and Colorado Group shale sample suites were determined using Rock-Eval Pyrolysis (after Espitalié *et al.*, 1977). The Rock-Eval pyrolysis was performed using the procedure described in chapter two, section 2.6. The results for the DF and CG shales are listed in Table 3.2.

For the DF shale samples, the S1 pyrolysis peak ranged between 1.00 mg g^{-1} to 4.70 mg g^{-1}, with an average of 2.46 mg g^{-1} ± 1.41 mg g^{-1}. The S2 pyrolysis peak ranged between 1.40 mg g^{-1} to 41.16 mg g^{-1}, with an average of 17.08 mg g^{-1} ± 13.94 mg g^{-1}. The Tmax temperature ranged between 416 ^{o}C to 463 ^{o}C, with a mean average of 440 ^{o}C ± 17 ^{o}C. The Hydrogen Index ranged between 24.6 mg and 419.7 HC g^{-1} TOC, with an average of 214.8 ± 138.4 mg HC g^{-1} TOC.

For the CG shales samples, the S1 pyrolysis peak ranged between 0.27 mg g^{-1} to 2.39 mg g^{-1}, with an average of 1.15 mg g^{-1} ± 0.74 mg g^{-1}. The S2 pyrolysis peak ranged between 3.33 mg g^{-1} to 12.79 mg g^{-1}, with an average of 8.10 mg g^{-1} ± 3.33 mg g^{-1}. The Tmax temperature ranged between 405 ^{o}C to 432 ^{o}C, with an average of 420 ^{o}C ± 8 ^{o}C. The Hydrogen Index ranged between 164.85 and 384.08 mg HC g^{-1} TOC, with an average of 284.40 ± 65.26 mg HC g^{-1} TOC.

The vitrinite reflectance (VR_c) maturity parameter was calculated using the Jarvie equation (Jarvie *et al*., 2001; Jarvie *et al*., 2007; Modica and Lapierre, 2012; Zhang *et al*., 2012). The strong linear relationship between the Tmax maturity parameter and the vitrinite reflectance (VR_o) maturity parameter is calculated as: $VR_c = (0.018 \times Tmax) - 7.16$. The correlation coefficient is R^2 =0.79, with n=179 data points (Jarvie *et al*., 2001).

For the DF shale samples, the S2 peak decreases with increasing burial depth, and the Tmax values increase with increasing burial depth. The correlation between Tmax and Hydrogen Index with increasing burial depth is reported in Figure 3.3. There is an excellent positive correlation between increasing burial depth and Tmax. The correlation coefficient for the linear regression is R^2 = 0.98. The Hydrogen Index (HI) is strongly negatively correlated to increasing burial depth, with a correlation coefficient of R^2 = 0.97.

For the CG shale samples, there is no observable trend in the S2, Tmax or HI with burial depth. The Second White Specks shale samples (C6, C7 and C8) have the highest Hydrogen Index values (average 357.44 ± 23.1 mg HC g^{-1} TOC), indicating a high hydrocarbon generating potential within this strata.

Table 3.2: Rock-Eval pyrolysis of Draupne Formation and Colorado Group shales.

Sample	**Burial Depth / m**	**S1** (Average) mg g^{-1}	**S2** (Average) mg g^{-1}	**Tmax** (Average) / ^{o}C	**Hydrogen Index** (Average) mg HC g^{-1} TOC	**Calculated Vitrinite Reflectance** VR_c / %
DF1	2117.8	1.9 ± 0.09	35.8 ± 4.0	416 ± 15.6	419.7 ± 47.2	0.33
DF2	2325	3.3 ± 0.2	40.3 ± 0.2	418 ± 0.7	388.6 ± 2.1	0.36
DF3	2978.5	2.1 ± 0.8	7.5 ± 0.09	436 ± 0.0	253.2 ± 3.1	0.69
DF4	3124.7	3.9 ± 0.06	23.6 ± 0.09	431 ± 1.4	307.0 ± 1.2	0.60
DF5	3375.32	4.7 ± 0.5	25.5 ± 0.6	432 ± 1.1	237.2 ± 5.8	0.62
DF6	3400.4	2.7 ± 0.3	17.5 ± 0.3	434 ± 8.5	225.7 ± 3.8	0.65
DF7	4132.95	3.5 ± 0.06	13.1 ± 8.3	452 ± 16.9	186.9 ± 119.0	0.98
DF8	4608.4	0.4 ± 0.06	1.4 ± 0.07	455 ± 5.7	24.6 ± 1.2	1.03
DF9	4707.7	1.0 ± 0.0	2.9 ± 0.09	460 ± 0.0	51.3 ± 1.5	1.12
DF10	4780.7	1.0 ± 0.0	3.3 ± 0.1	463 ± 1.4	53.7 ± 1.7	1.17
C1	505.3	1.3 ± 0.04	5.9 ± 0.5	419 ± 2.8	233.9 ± 17.8	0.38
C2	506.55	0.9 ± 0.03	6.9 ± 0.1	419 ± 1.4	275.3 ± 4.5	0.38
C3	541	0.6 ± 0.1	7.3 ± 0.3	423 ± 2.8	297.6 ± 12.1	0.45
C4	546.3	1.1 ± 0.1	6.2 ± 0.6	422 ± 0.0	255.8 ± 26.3	0.44
C5	561.5	1.0 ± 0.04	9.8 ± 0.4	417 ± 2.8	311.1 ± 13.0	0.35
C6	642.1	1.4 ± 0.09	12.8 ± 0.2	405 ± 1.4	384.1 ± 4.7	0.13
C7	647.57	2.4 ± 0.1	12.8 ± 0.3	412 ± 1.4	346.5 ± 7.3	0.26
C8	651.75	2.3 ± 0.16	11.2 ± 0.4	418 ± 2.8	341.8 ± 11.6	0.36
C9	675.02	0.3 ± 0.3	4.8 ± 0.2	430 ± 1.4	233.2 ± 9.7	0.58
C10	684.61	0.3 ± 0.1	3.3 ± 0.3	432 ± 2.8	164.9 ± 12.6	0.62

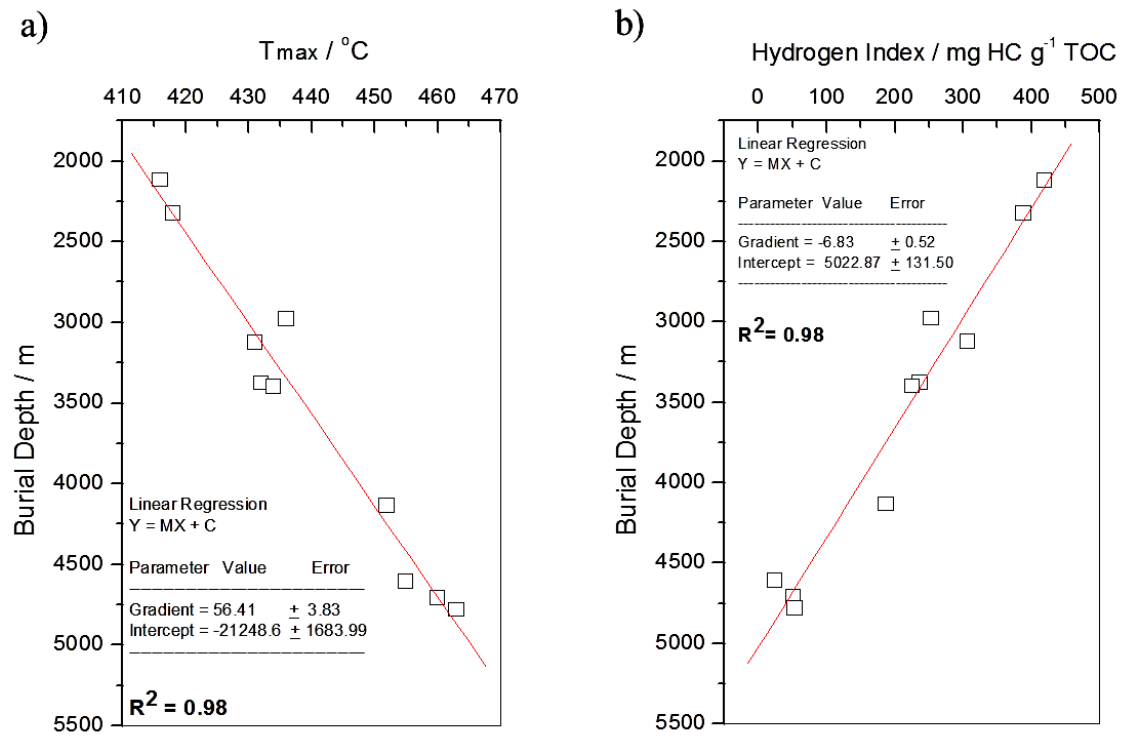

Figure 3.3: Correlation of the Draupne Formation shales with burial depth. In part a) there is an excellent positive correlation between increasing burial depth and Tmax. In part b) there is an excellent negative correlation between increasing burial depth and Hydrogen Index.

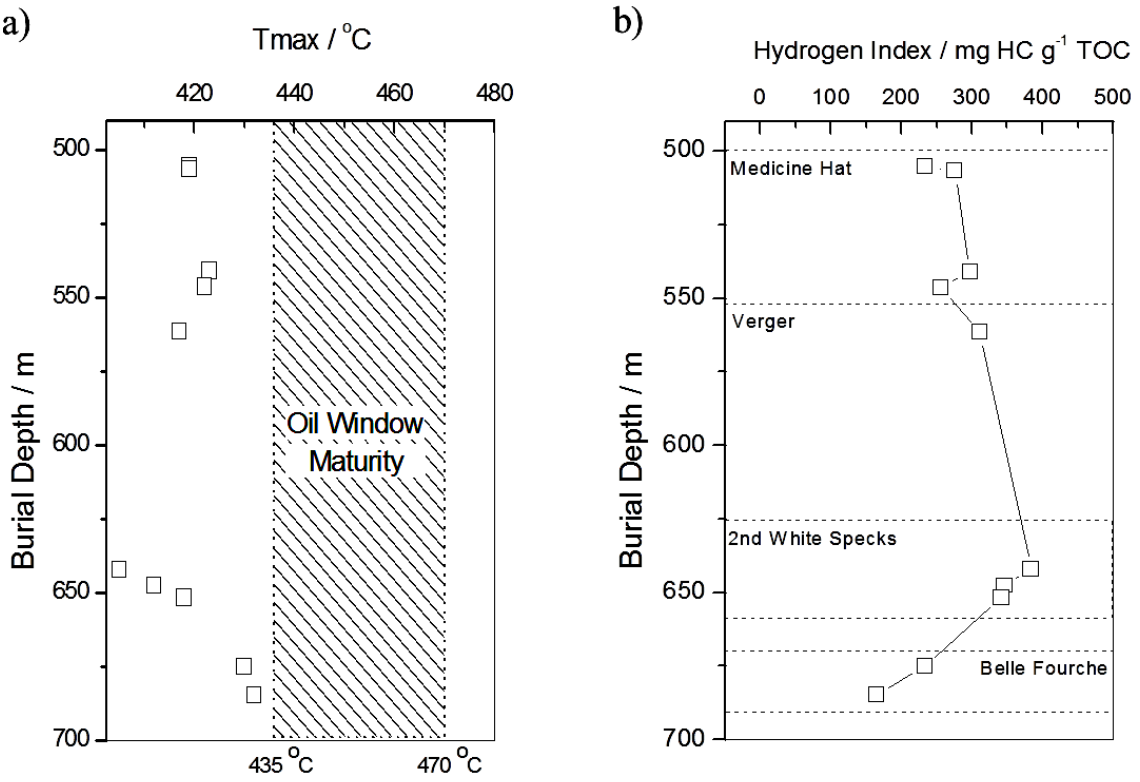

Figure 3.4: No correlation of the Colorado Group shales and burial depth.

3.2.3 Purity analysis of isolated kerogens

The isolated Draupne Formation and Colorado Group kerogens were tested for mineral purity using powder X-Ray diffraction. The powder XRD was performed using the procedure described in chapter two, section 2.14. There are no characteristic peaks in the low angle region (< 25 ^{o}) of the kerogen diffractograms for quartz, carbonates or clay minerals, as demonstrated for kerogen DF4 in Figure 3.5. This indicates a low level of contamination of these minerals in the isolated kerogens. The characteristic 9 peaks of the pyrite "fingerprint" pattern can be observed in the diffractogram of the DF4 kerogen, indicating that pyrite is present. All the diffractograms for the Draupne Formation and Colorado Group kerogens are reported in Figure 3.6 and Figure 3.7, respectively.

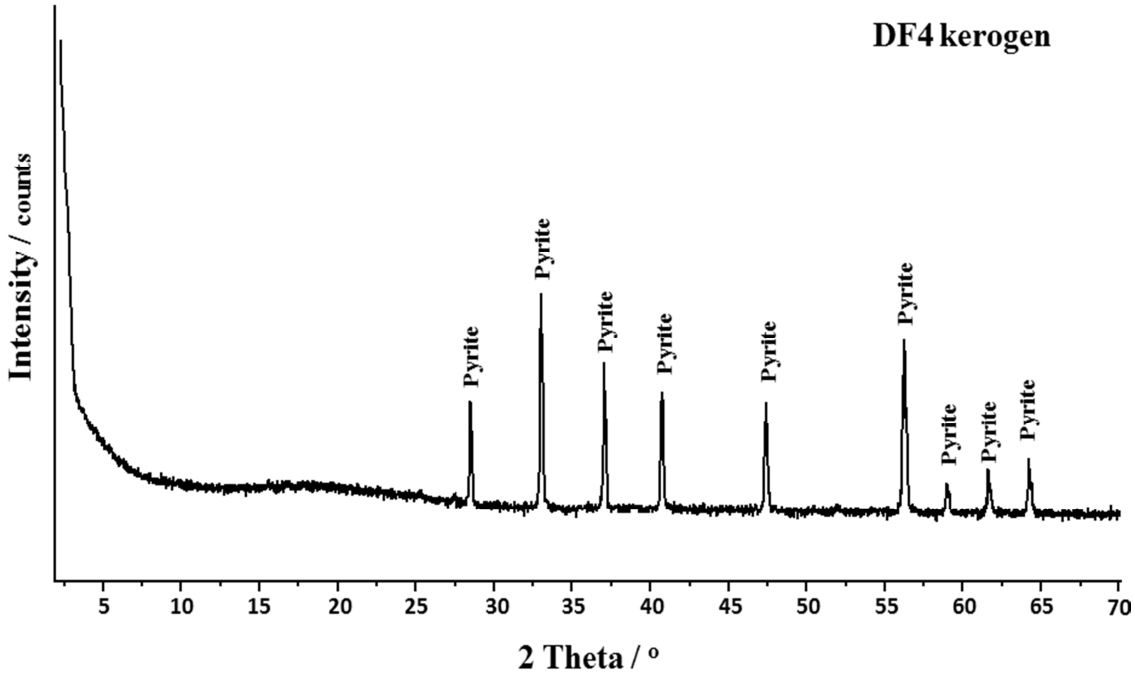

Figure 3.5: Powder XRD diffractograms of the DF4 kerogen. It shows the presence of pyrite (FeS_2), but no peaks associated with other shale minerals are present, indicating the absence of other minerals in the extracted kerogens.

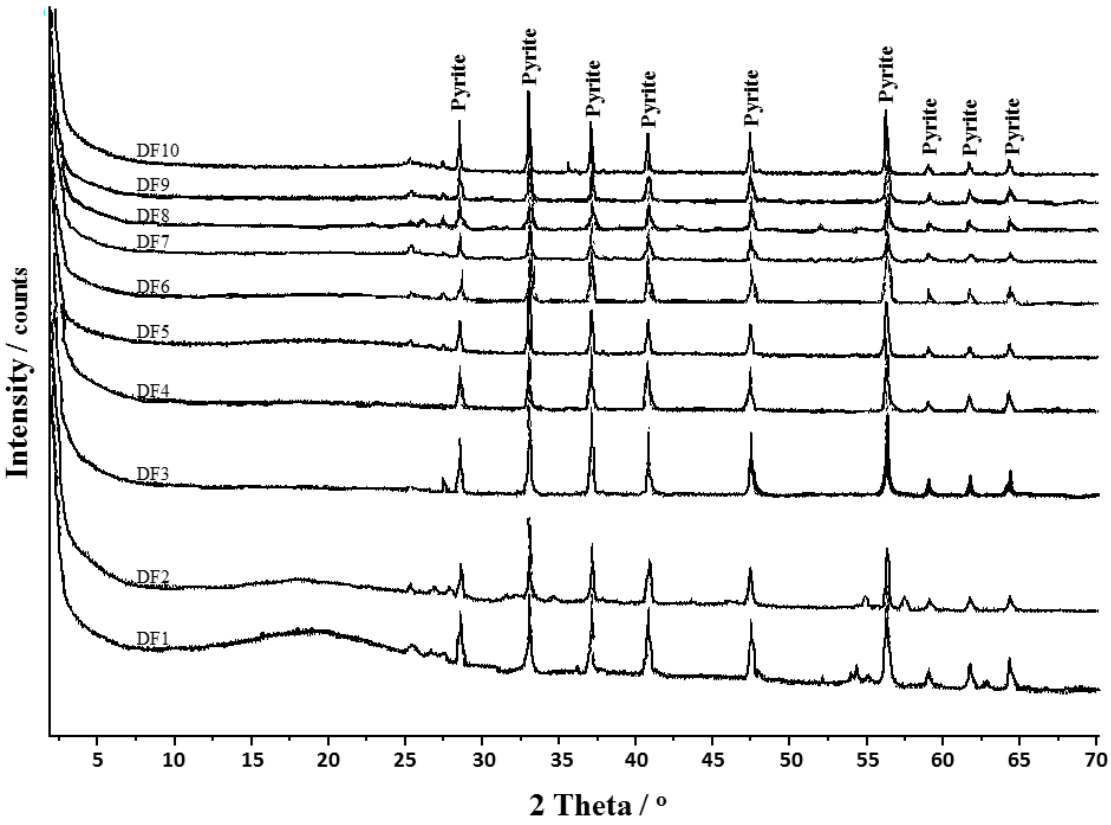

Figure 3.6: Powder XRD diffractograms for the Draupne Formation kerogens, showing a low level of contamination of shale minerals (other than pyrite).

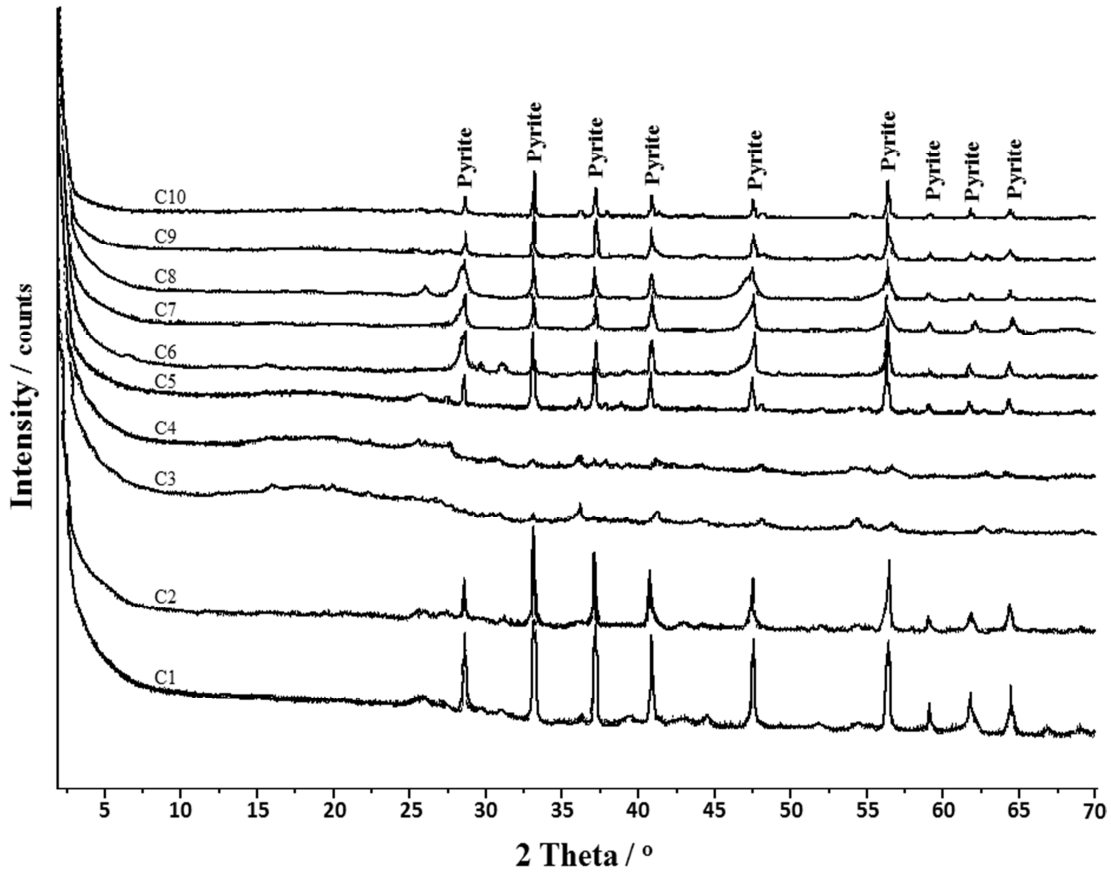

Figure 3.7: Powder XRD diffractograms for the Colorado Group kerogens, showing a low level of contamination of shale minerals (other than pyrite).

3.2.4 Elemental analysis of isolated kerogens

The elemental composition of the Draupne Formation and Colorado Group kerogens was determined by combustion, according to the method described in section 2.15 of chapter 2. The elemental analysis data is listed in Table 3.3. The carbon, hydrogen and oxygen contents of the Draupne Formation kerogens decrease with increased burial depth, whilst the Colorado Group kerogens exhibit no observable trend in elemental contents versus depth.

The raw data are given, without any correction for inorganic pyrite content. The carbon contents are therefore lower than expected (~75% to 80%), and the sulfur content is higher than expected (~ 2 to 6%). The high sulfur content is due to inorganic sulfur in the iron pyrite (FeS_2).

Table 3.3: Elemental analysis results for the Draupne Formation and Colorado Group isolated kerogens.

	C / %	H / %	N / %	S / %	O / %
DF1	61.74	5.57	1.36	10.39	6.47
DF2	53.72	4.64	1.10	15.24	4.83
DF3	43.89	3.88	0.83	20.44	3.55
DF4	64.31	5.28	1.21	12.30	5.11
DF5	56.16	4.25	1.15	14.04	4.33
DF6	50.38	3.80	0.92	17.69	3.95
DF7	42.31	2.68	0.69	24.08	2.61
DF8	57.14	4.03	0.80	16.27	3.84
DF9	45.47	3.22	0.96	23.62	3.39
DF10	43.28	2.62	0.16	24.25	2.51
C1	38.33	4.40	1.23	7.93	12.55
C2	35.52	4.21	1.30	7.75	11.74
C3	63.30	7.38	1.88	11.17	4.08
C4	62.73	7.36	1.95	12.17	3.75
C5	55.92	6.22	1.82	11.69	10.94
C6	21.09	2.30	0.51	4.77	10.86
C7	23.05	2.55	0.60	4.60	14.51
C8	21.93	2.58	0.48	4.96	10.14
C9	50.08	5.49	1.26	9.81	13.46
C10	41.30	4.73	1.00	8.37	12.07

3.2.5 Infra-Red spectroscopy of isolated kerogens

The infra-red spectral analysis of the Draupne Formation and Colorado Group isolated kerogens were obtained using the method described in section 2.16 of chapter 2. Unlike synthetic materials, kerogen IR spectra contain broad absorbance peaks due to the heterogeneous carbon skeleton of its natural geo-polymeric structure. The broad absorbance peaks are the averaged combination of many similar functional groups, and therefore the assignment of these broad peaks to individual functional groups is difficult. The normalisation of the peak intensities allows the aromaticity of the kerogens to be determined.

A representative FT-IR absorption spectrum for the kerogen DF1 is reported in Figure 3.8. Two broad absorbance peaks at approximately 2800-3000 cm^{-1} and 1600 cm^{-1} are observed, which are characteristic of aliphatic C-H bonds (at ~ 3000 cm^{-1}) and aromatic C=C bonds (at 1600 cm^{-1}), respectively. In Figure 3.9, the shallow, middle and deep Draupne Formation kerogen samples are overlain. The absorbance peak for the aliphatic C-H stretch at ~ 3000 cm^{-1} decreases with increasing burial depth for the three kerogens. The normalised absorbance peak for DF1 is larger than for DF5, and the DF10 kerogen has the lowest absorbance intensity. In Figure 3.10, the shallow, middle and deep Colorado Group kerogen samples are overlain The absorbance peak for the aliphatic C-H stretch at ~ 3000 cm^{-1} are identical for the three kerogens; there is no observable difference.

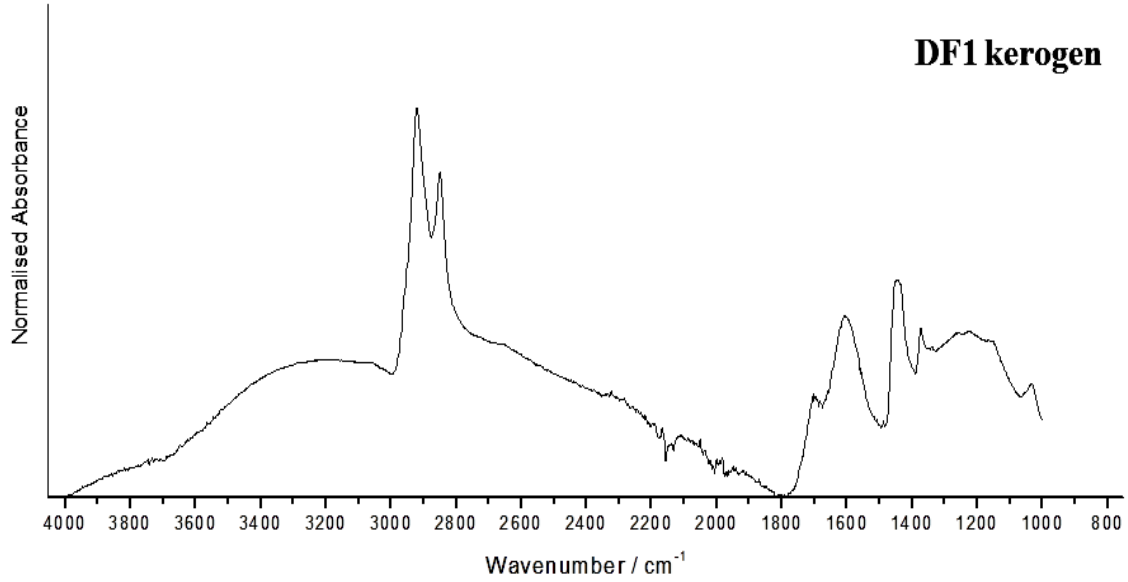

Figure 3.8: Representative example of the FT-IR spectra of isolated kerogens. A strong absorbance peak is observed between 2800 cm^{-1} and 3000 cm^{-1}.

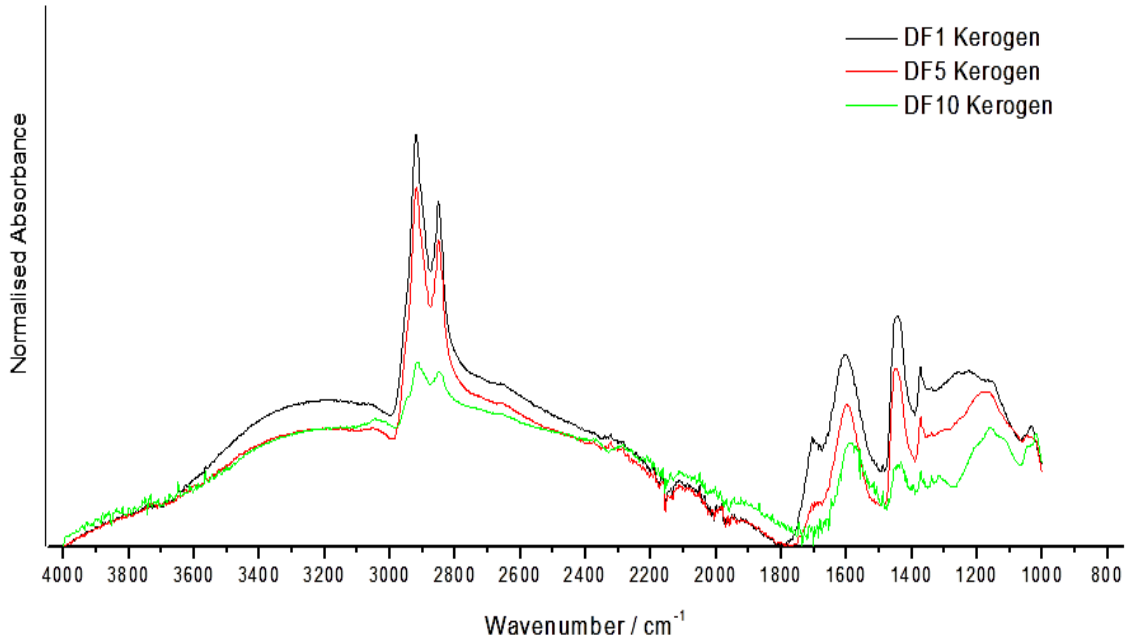

Figure 3.9: Normalised and overlain FT-IR spectra of the shallow, middle and deep Draupne Formation kerogens. The intensity of the alkyl group resonance decreases and the intensity of the aromatic group resonance increases. This is an indicator of the shift in the chemistry of the kerogens from a hydrogen-rich aliphatic structure to a polymerised aromatic hydrogen-poor structure.

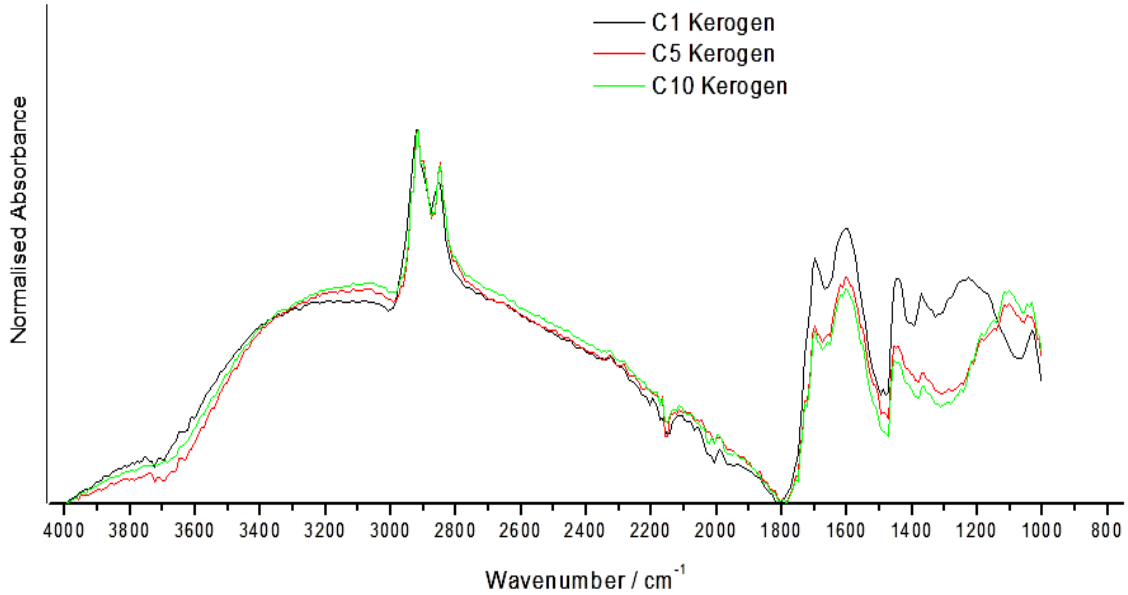

Figure 3.10: Normalised and overlain FT-IR spectra of the shallow, middle and deep Colorado Group kerogens. The intensity of the alkyl group resonance peaks is very similar, as indicated by the identical aliphatic C-H absorbance peak at 2800-3000 cm^{-1}.

3.2.6 Nuclear Magnetic Resonance spectroscopy of isolated kerogens

The solid-state ^{13}C-NMR spectra of the Draupne Formation and Colorado Group kerogens were obtained using the method described in section 2.17 of chapter 2. A representative example of a ^{13}C-NMR spectrum for kerogen DF5 is reported in Figure 3.11. Two broad resonance peaks at approximately at 30 ppm and 130-145 ppm are observed, which are characteristic of aliphatic methylene carbons (CH_2) (at 30 ppm) and the aromatic kerogen skeletal structure (130-145 ppm), respectively.

In Figure 3.12, the shallow, middle and deep Draupne Formation kerogen samples are overlain. The DF1 kerogen is the shallowest sample, and has the largest aliphatic 30ppm resonance peak of the 3 kerogens, with the aromatic signal at 130-145 ppm being the lowest intensity aromatic peak. The DF5 kerogen is the middle burial depth sample, and has a similar ^{13}C-NMR spectrum to the DF1 kerogen, with the same broad signals at ~ 15 to 30 ppm and ~130 ppm. However, the intensity of aromatic peak at ~130 ppm has increased in intensity, relative to the DF1 kerogen. The aliphatic signal at 30ppm has not changed much relative to the DF1 kerogen. The DF10 kerogen is the deepest buried sample. It also has the same aliphatic signal at ~ 15 to 30 ppm and the aromatic signal at ~130 ppm as the two previous samples. The main difference is the intensity of aromatic peak at ~130 ppm has significantly increased, and the intensity of aliphatic peak at ~15 to 30 ppm has significantly decreased. The aromaticity of the DF10 kerogen is estimated to be ~ 85 % (or more), as determined from the integrated intensity information given by the short direct-polarisation (pulse-acquire) experiment performed on the sample.

In Figure 3.13, the shallow, middle and deep Colorado Group kerogen samples are overlain. The C1 kerogen is the shallowest sample, the C6 kerogen is the middle burial depth, and the C10 is the deepest sample. In all 3 kerogens, the aliphatic peaks at 30ppm have the same intensity, indicating that they share identical concentrations of aliphatic alkyl groups. The combined aliphatic peak at 30 ppm is much more intense than the combined aromatic signal at 130-145 ppm. The aromatic signal at 130-145 ppm varies between the 3 kerogens, with the C1 being most aromatic, and C10 being the least aromatic.

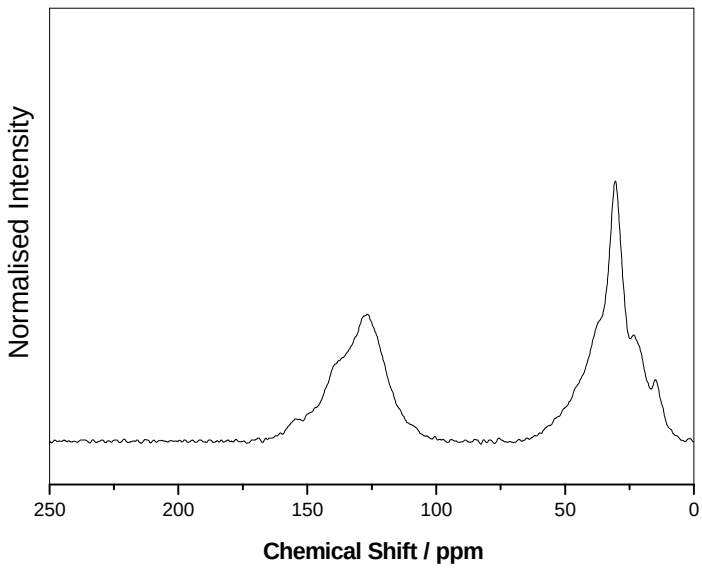

Figure 3.11: ^{13}C-NMR spectra of DF5 kerogen. The characteristic aliphatic alkyl peak is found at 30 ppm, and the characteristic aromatic kerogen skeletal peak is found at 130 -145 ppm.

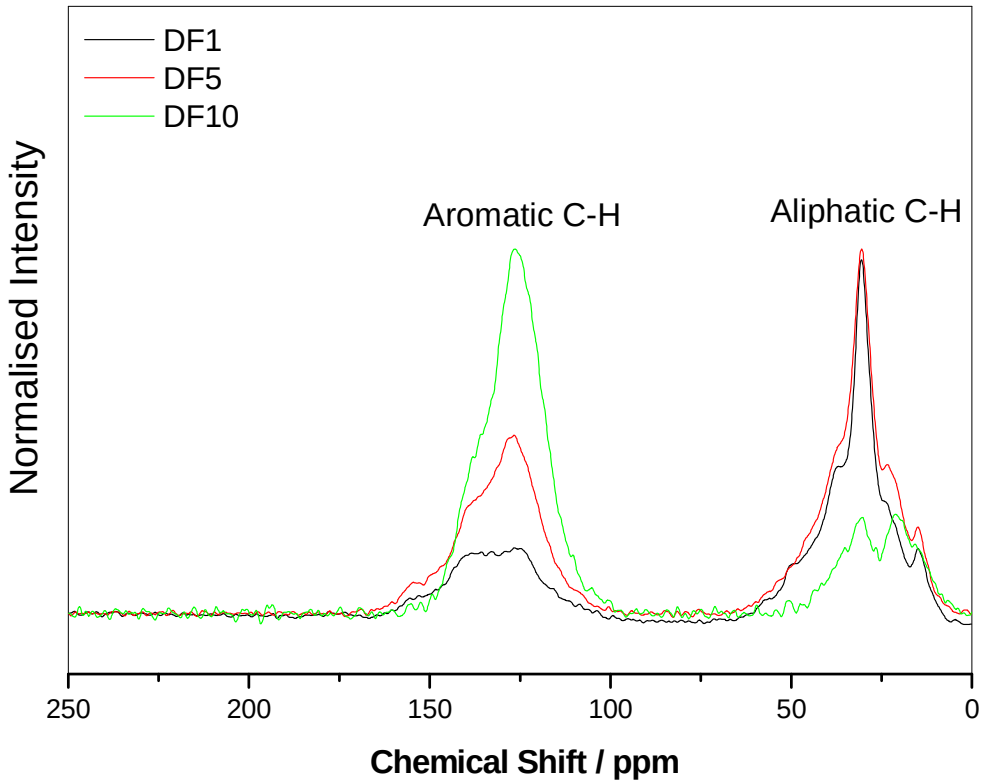

Figure 3.12: ^{13}C - NMR spectra of the 3 Draupne Formation kerogens overlaid to highlight changes with depth. The aromatic C-H peak increases in relative intensity with increased thermal maturity.

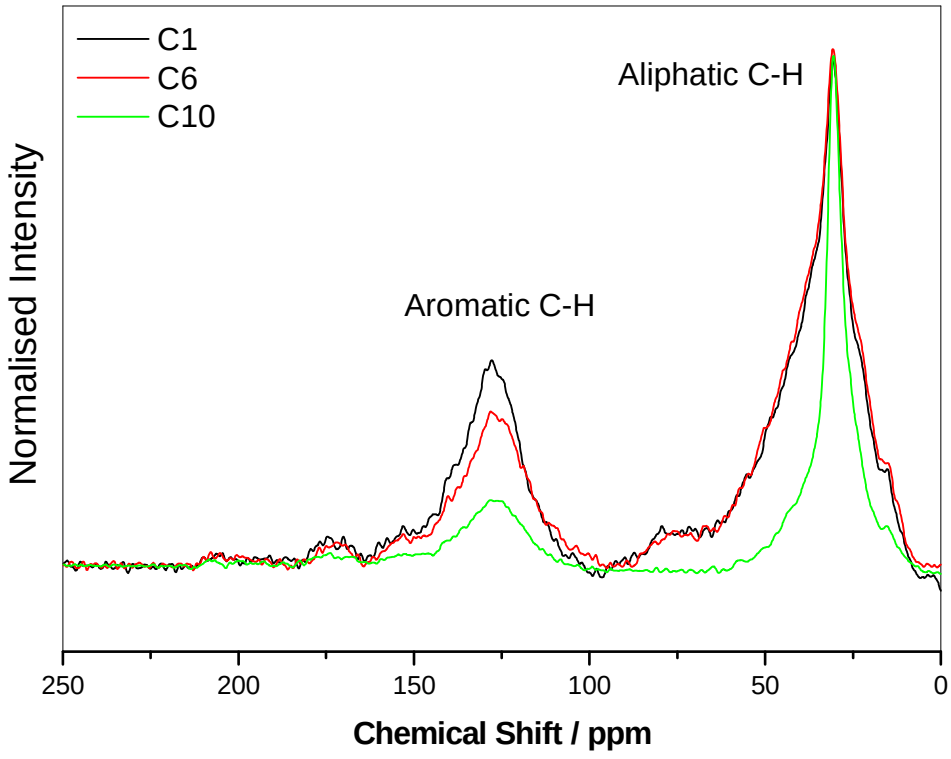

Figure 3.13: ^{13}C - NMR spectra of the 3 Colorado Group kerogens overlaid to highlight changes with depth. The aliphatic C-H peak is larger than the aromatic peak, and has a constant relative intensity.

3.2.7 Pyrolysis Gas Chromatography Mass Spectrometry (py-GC-MS) of isolated kerogens

The pyrolysis gas chromatography mass spectrometry (py-GC-MS) of the Draupne Formation and Colorado Group kerogens were obtained using the method described in section 2.18 of chapter 2. A shallow, middle and a deeply buried sample from both samples suites were chosen.

In Figure 3.14, the total ion chromatograms (TIC) of the shallow, middle and deep Draupne Formation kerogen samples are reported. In Figure 3.15, the TIC of the shallow, middle and deep Colorado Group kerogen samples is reported. The y-axis scales are normalised to 1 x 10^7 intensity units. The pyrolysate compounds released using pyrolysis GC-MS were dominated with alkane and alkene straight chain hydrocarbons, with small amounts of low molecular weight aromatic benzene derivatives (including toluene, xylene, ethylbenzene, 1,3,5-trihydroxybenzene, and mono-lignols derived from lignin pyrolysis). The dominant peaks were the *n*-alkane and *n*-alkene doublets, ranging from C_9 to C_{32}.

In Figure 3.14 the variation between the total ion chromatograms (TIC) of the Draupne Formation kerogens can be observed. The DF1 and DF5 kerogens have very similar TIC spectra, being rich in *n*-alkane and *n*-alkene doublets. The DF10 kerogen is visibly different, having a significantly reduced *n*-alkane and *n*-alkene doublet abundance. In Figure 3.15 the TIC of the Colorado Group kerogens are reported. The three Colorado Group kerogens have very similar chromatograms, indicating a large abundance of aliphatic alkyl groups being present in the kerogen.

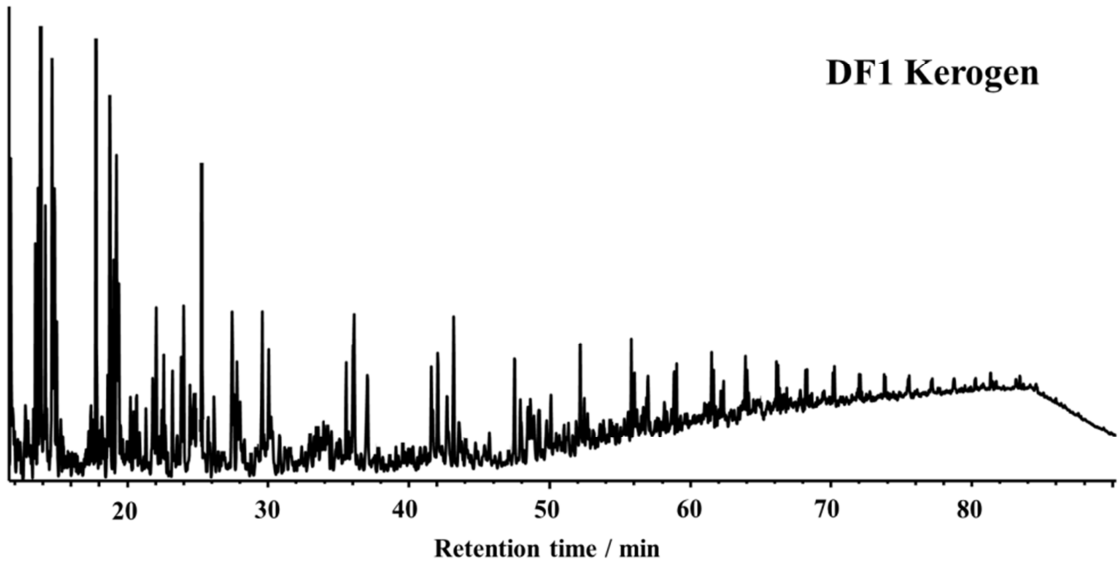

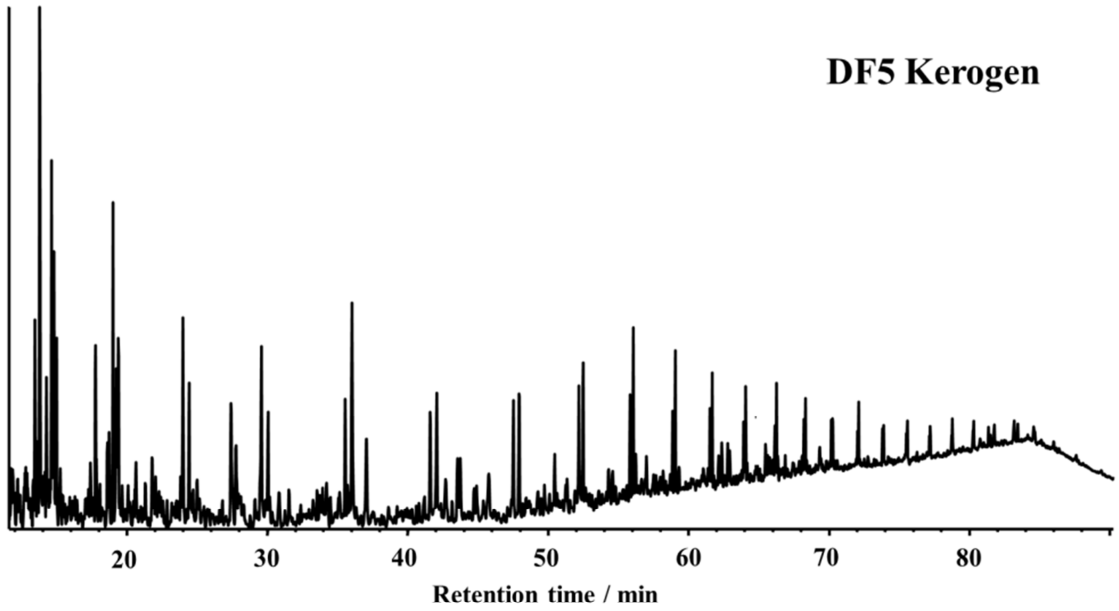

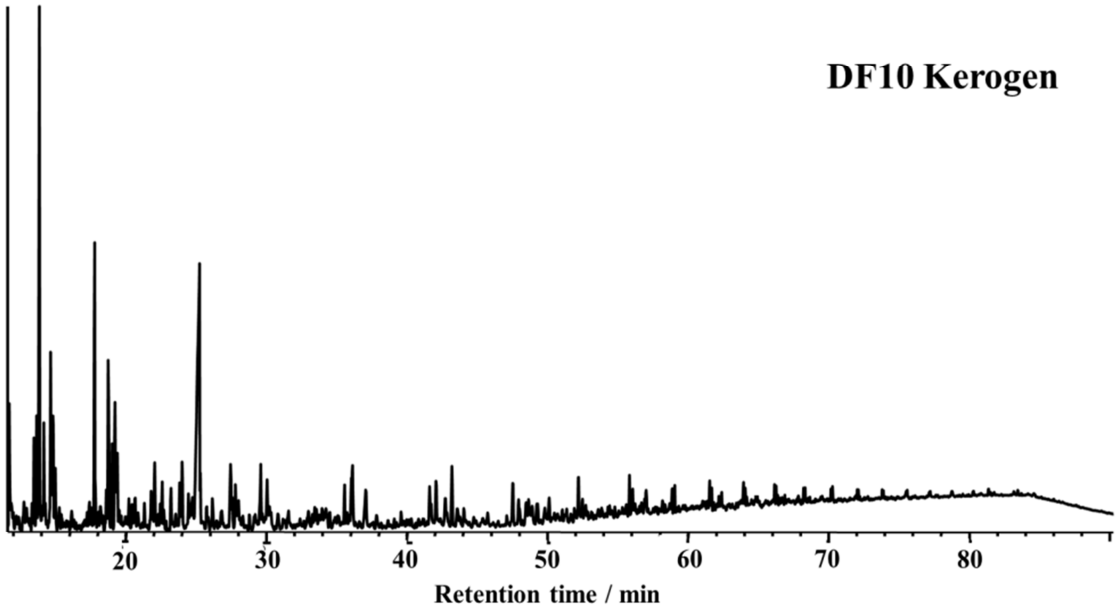

Figure 3.14: Total Ion Chromatogram (TIC) of the Draupne Formation isolated kerogens. The DF10 kerogen has reduced alkane and alkene double potential, relative to the DF1 and DF5 kerogens.

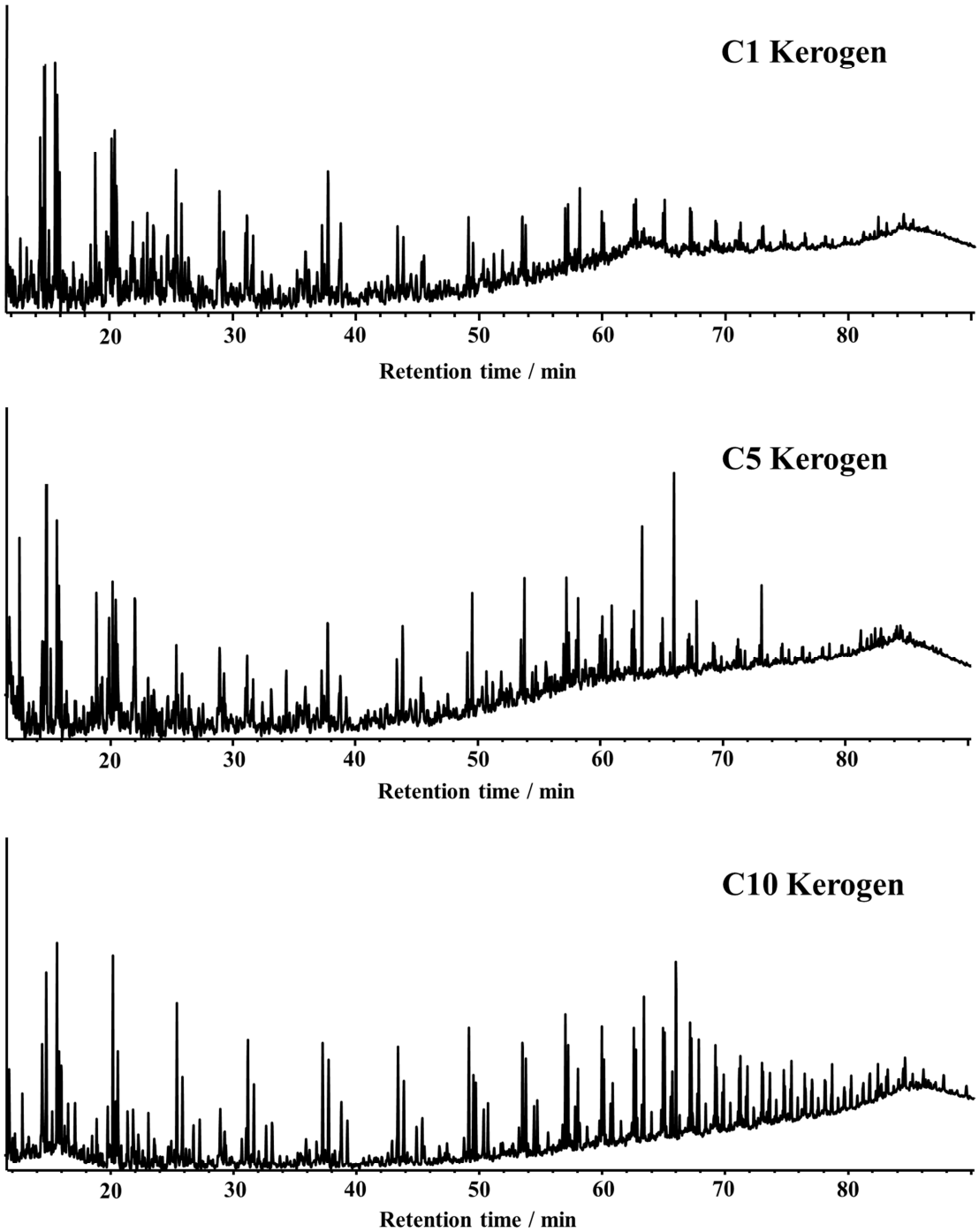

Figure 3.15: Total Ion Chromatogram (TIC) of the Colorado Group isolated kerogens.

3.3 Discussion

3.3.1 Organic matter type and content

The Draupne Formation and Colorado Group shales are organic rich, with the DF shale having an average TOC of 7.24 %, and the CG shale samples having an average of 2.74 %. Tissot and Welte (1984) have demonstrated that shales with organic matter contents above 2% have good hydrocarbon generating potential, and TOC's above 4% are considered excellent, suggesting that the Draupne Formation and Colorado Group shales have the potential to be prolific hydrocarbon source rocks. This interpretation is supported by the work of Justwan and Dahl (2005), who estimated gas reserves of 15,000 BCF in the Viking Graben sector of the Draupne Formation, and also by Bustin (2005) who estimated gas reserves > 1000 TCF in the Colorado Group of WCSB.

The Draupne Formation shales have a spread of TOC content values, whilst the Colorado Group shales have a narrow range of values. The DF shales exhibit a general trend of TOC reduction with increasing burial depth, as reported in Figure 3.16. The DF3 shale sample (TOC 2.96%) appears to be an outlier from the main group. In contrast, the Colorado Group shales appear to have no overall trend between TOC content and increased burial depth. This is expected, as there is only ~ 180 m difference between the shallowest and deepest sample in the CG sample suite. However, a localised variation in the TOC contents between the different shale formations exists for the Colorado Group. The Second White Specks shale samples (C6 to C8) have almost double the TOC contents of the Medicine Hat and Belle Fourche shale strata.

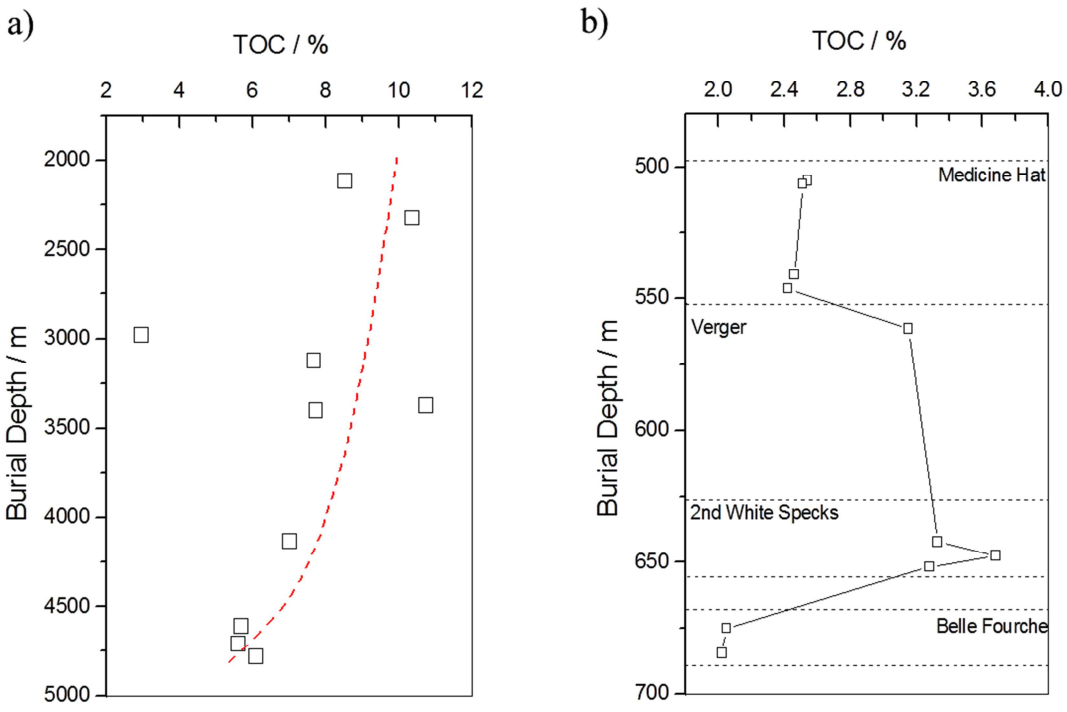

Figure 3.16: Variation of TOC with burial depth in the a) Draupne Formation, and b) Colorado Group shale suites. The DF shales decrease in TOC with increasing burial depth, whilst the CG shales have no observable trend with depth, with the TOC content varying instead according to the formations within the stratigraphic column of the Colorado Group.

The Draupne Formation isolated kerogens and shales are interpreted as being Type II, using both the van Krevelen diagram (van Krevelen, 1950) and the S2 against TOC plot (after Langford and Blanc-Valleron, 1990). Using the elemental analysis data from the isolated kerogens, the van Krevelen diagram (Figure 3.17, part a) demonstrates that the DF kerogens have the elemental ratios characteristic of Type II kerogen. The S2 vs TOC plot from the whole shale Rock-Eval pyrolysis data reports that the majority of the DF samples have geochemical characteristics of oil-prone Type II kerogen, as reported in Figure 3.18, part a. This interpretation of the Draupne Formation consisting of Type II kerogen is supported by the work of Knudsen *et al*., (1988) and Dahl (2004), who both identified Type II kerogen present in the Draupne Formation. Three samples (DF8, DF9 and DF10) have geochemical characteristics of gas prone Type III kerogen. These three samples have a significant reduction in hydrocarbon potential (due to oil generation as a consequence of thermal maturation), and now have gas prone Type III recalcitrant kerogen remaining. Moreover, the Colorado Group isolated kerogens and shales are also categorised as geochemical Type II kerogen, as determined using the van Krevelen diagram and plot of S2 against TOC, as reported in part b's of Figures 3.17 and 3.18, respectively. The CG shales have the geochemical characteristics of oil-prone Type II kerogen, and have the potential for oil generation, once they have become thermally mature. This interpretation is supported by the work of Taylor (2011), who found that the Colorado Group is dominantly Type II kerogen, with a minor type III component in the Lower Carlile member (a formation of the CG not investigated in this study).

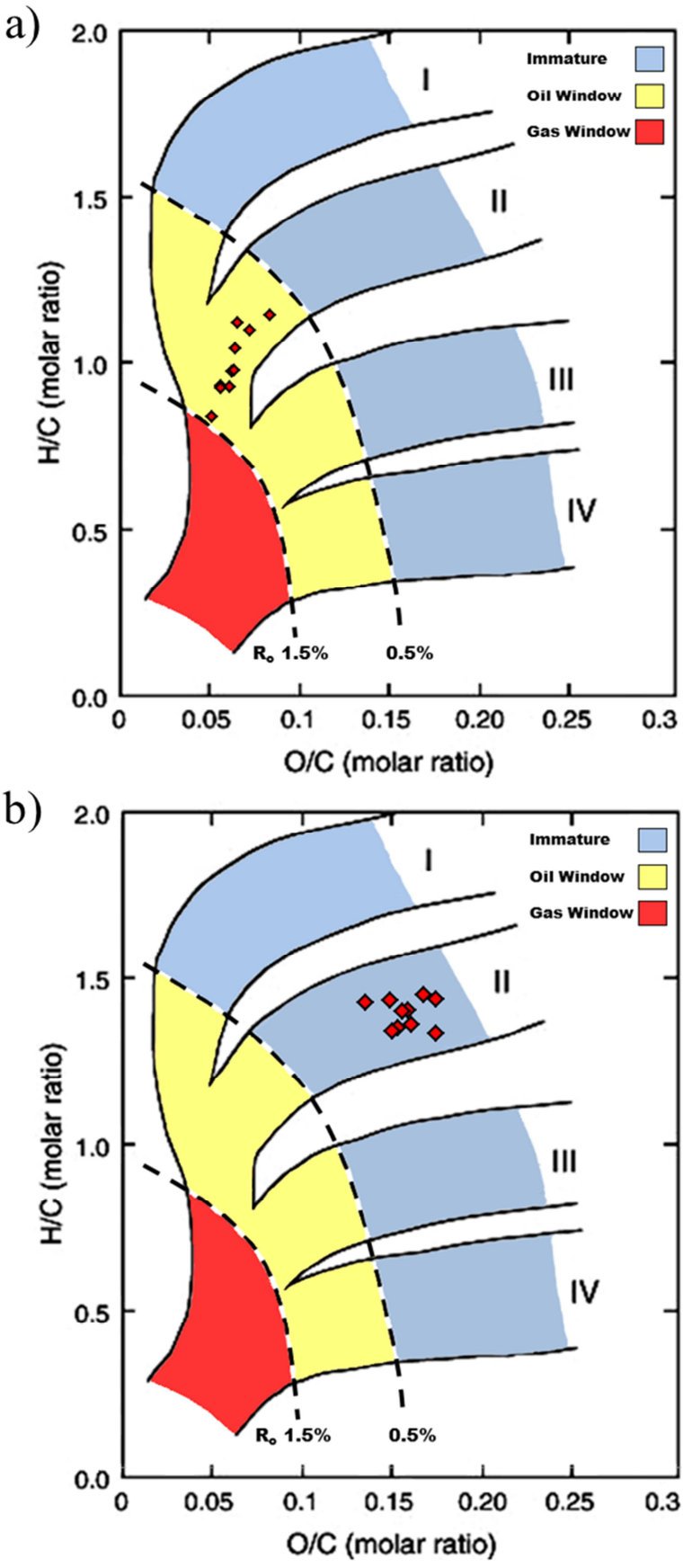

Figure 3.17: van Krevelen diagram for the elemental composition of the isolated kerogens (background image modified after Seewald, 2003). In part a), the Draupne Formation kerogens are within the Type II group and are in the lower to middle oil window. In part b), the Colorado Group kerogens are in the Type II group and are thermally immature.

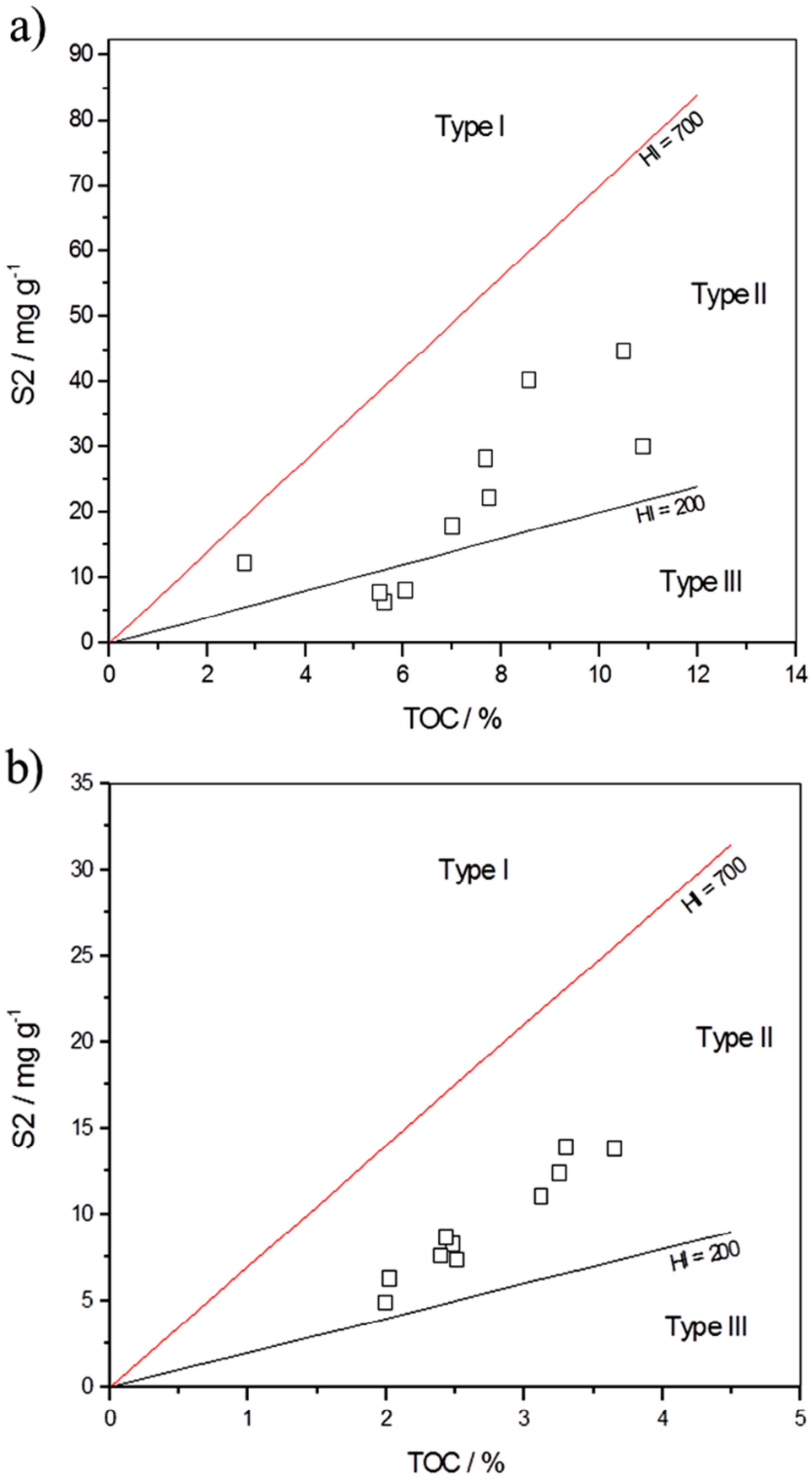

Figure 3.18: Plot of S2 vs TOC (after Langford and Blanc-Valleron, 1990). In part a), the Draupne Formation shales are mostly Type II kerogen, with the three mature samples exhibiting geochemical characteristics of Type III kerogen. In part b), the Colorado Group shales contain Type II organic matter.

The ^{13}C-NMR spectra of the Draupne Formation and Colorado Group contain two broad resonance peaks that are characteristic of Type II marine algal kerogens (Bharati *et al*., 1995). The resonance peak at 30 ppm is consistent with methylene carbons (CH_2) being the dominant alkyl carbon type in Type II algal kerogens (Bharati *et al*., 1995). The signal at 15 ppm (the "shoulder" on the 30 ppm peak) is typical of a methyl (CH_3) group at the end of the hydrocarbon chain. Type II marine algal kerogens have high concentrations of aldehyde (CHO) and alcohol (H_xC-OH) functional groups (Bharati *et al*., 1995). The resonance peak at 130-145 ppm range is consistent with the aromatic kerogen skeletal structure. Aromatic signals in the 130-145 ppm range are characteristic of a high proportion of quaternary carbon environments, i.e. carbons that are not bonded to any hydrogen atoms, which are characteristic of aromatic systems). Algal kerogens are rich in branched aromatics (Ar-C-C) and protonated aromatics (Ar-CH) (Mann *et al*., 1991; Patience *et al*. 1992). There is also a minor shoulder/hump at ~150 ppm, which is characteristic of nitrogen hetero-atoms involved in aromatic bonding environments (the presence of nitrogen in kerogen could be due to the biological origin of the kerogen geo-polymer).

The py-GC-MS total ion chromatograms of the Draupne Formation and Colorado Group kerogen samples have the characteristic carbon number distribution of Type II kerogen. The largest abundance *n*-alkane/*n*-alkenes are those with less than 20 carbon atoms (C_{20}), which is in agreement with the findings of Leplat and Vandenbroucke, 1993). As the molecular weight of the *n*-alkanes/*n*-alkenes increases, the relative abundance of the peaks decreases, with the heaver alkanes alkenes (> C_{25}) having a low intensity. This characteristic chromatogram trace pattern for Type II kerogen is in agreement with published kerogen characterisations (Larter, 1984; Horsfield, 1989).

3.3.2 Thermal maturity of shale and kerogens – Draupne Formation

The Rock-Eval pyrolysis indicates that the Draupne Formation shales have a range of thermal maturities, from immature up to oil generation maturity (catagenesis). Both the S2 and Hydrogen Index values decrease with increasing burial depth, whilst the Tmax values increase with increasing burial depth. Excellent linear correlations between burial depth, Tmax and HI are reported in Figure 3.3, with coefficients of $R^2 = 0.98$ and $R^2 = 0.98$, respectively. These correlations are characteristic of increasing thermal maturation, with the generation of hydrocarbons. The Tmax value is the temperature of maximum S2 peak generation, and indicates that the DF samples are within the oil window maturity range (Tmax range of 435^{o}C to 470^{o}C), but not in the gas window for Type II kerogen (> 470^{o}C). The Hydrogen Index is a measure of the hydrocarbon generating potential of the kerogen, and so a decrease in the HI value is a strong indicator of the thermal maturation history of the shale. In Figure 3.19, the maturity range of the Draupne Formation sample suite is identified using the plot of Hydrogen Index against Tmax (after Espitalié, 1986). The HI vs Tmax plot demonstrates that the DF samples are either immature or in the oil window, with no gas window maturity samples in the suite.

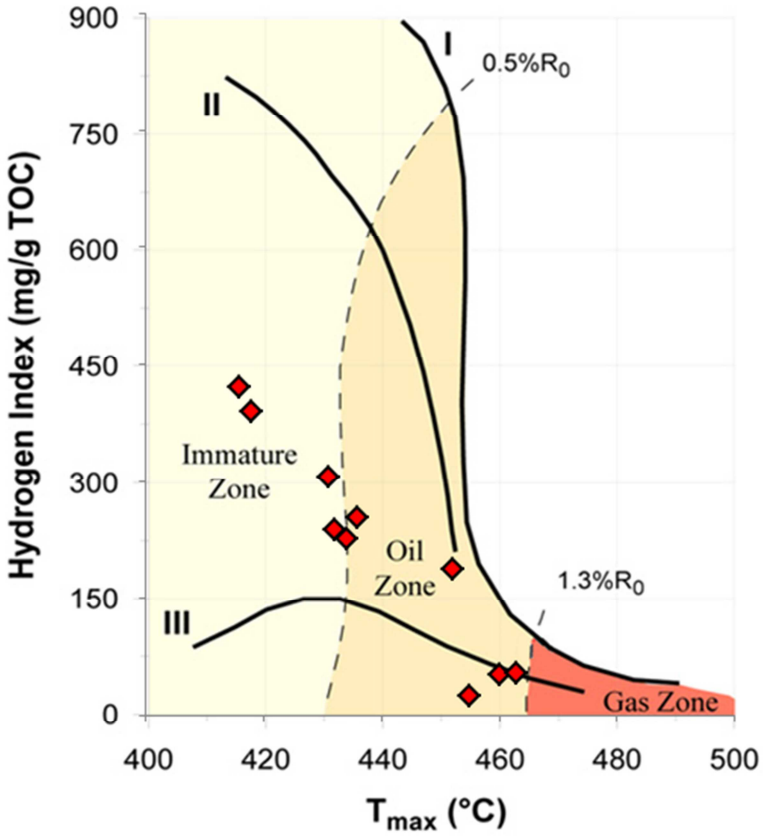

Figure 3.19: Plot of T_{max} vs. HI, (after Espitalié, 1986) for the Draupne Formation shale suite. The maturity of the shales range from immature to oil window; no samples are in the gas window.

The elemental analysis of the isolated Draupne Formation kerogens show that the carbon, hydrogen and oxygen contents decrease with increased burial depth. The van Krevelen diagram (Figure 3.17) identifies the DF kerogens as falling within the oil window maturity zone, with no gas window maturity kerogens identified. The spread of the data points is due to a range of thermal maturities within the oil window.

The overlain FT-IR spectra of the shallow, middle and deep Draupne Formation kerogen samples shows the absorbance peak for the aliphatic C-H stretch at ~ 3000 cm^{-1} decreasing with increasing burial depth. This indicates that the concentrations aliphatic C-H bond concentrations are changing with the maturity level of the kerogens. This is a strong indicator of the changes that thermal maturity has on the aliphatic alkyl carbon content of kerogen composition.

Significant changes in the chemical bonding and structure of the Draupne Formation kerogens were observed in the solid-state ^{13}C-NMR spectra due to increasing maturity. The DF1 kerogen was the lowest maturity sample, and had the largest aliphatic resonance signal (30ppm) and the lowest intensity aromatic peak (130-145 ppm) of the 3 kerogens. The DF10 kerogen was the highest maturity sample and the intensity of aromatic peak at ~130ppm had significantly increased, and the intensity of aliphatic peak at ~15 to 30ppm has significantly decreased. The aromaticity of the DF10 kerogen is ~ 85 % or more (as estimated from the short direct-polarisation integral of spectra intensity). This suggests that the DF10 kerogen has an aromatic structure that is much more condensed and less alkylated than the lower maturity samples. These changes in chemical structure from a predominantly aliphatic structure to a highly aromatic structure closely agree with the published work of Gonzalez-Vila *et al*., (2001).

The aromaticity of the kerogen increases, at the expense of the aliphatic hydrocarbon side-chains attached to the main carbon skeleton. Thermal maturation causes the chemical structure of kerogen to become compacted and to rearrange, with the carbon side chains polymerising to cyclic aromatic rings (Killops and Killops, 2005). Rearrangement and polymerisation to aromatic rings occurs because they occupy less space and are more thermally stable than saturated hydrocarbon chains. The hydrogen atoms attached to the carbon skeleton begin to migrate to the alkyl side chains, thus generating hydrocarbon fluids (Patience *et al*., 1992).

The influence of maturity on the Draupne Formation kerogens was observed in the py-GC-MS total ion chromatograms, as reported in Figure 3.14. The DF1 and DF5 kerogens have very similar TIC spectra, being rich in *n*-alkane and *n*-alkene doublets, whereas the DF10 kerogen has a significantly reduced *n*-alkane and *n*-alkene doublet abundance (relative to DF1 and DF5). This is characteristic of thermal maturation and the generation of hydrocarbons; the DF10 kerogen aliphatic alkyl content has been converted to petroleum, and thus has become exhausted (Gonzalez-Vila *et al*., 2001). The influence of maturity can be more clearly observed in the Selected Ion Monitoring (SIM) mode of the py-GC-MS chromatograms. The $^{m}/_{z}$ 57 ion fragment in the mass spectrum is characteristic of *n*-alkane and *n*-alkene and is used to separate out and identify the presence of alkane / alkene doublets in the kerogen TIC chromatograms. The SIM traces in Figure 3.20 also in agreement with the interpretation that the DF1 and DF5 kerogens are very similar in *n*-alkane and *n*-alkene content, and that the oil window DF10 kerogen has become exhausted in the aliphatic content, due to thermal maturity and generation of hydrocarbons (Gonzalez-Vila *et al*., 2001).

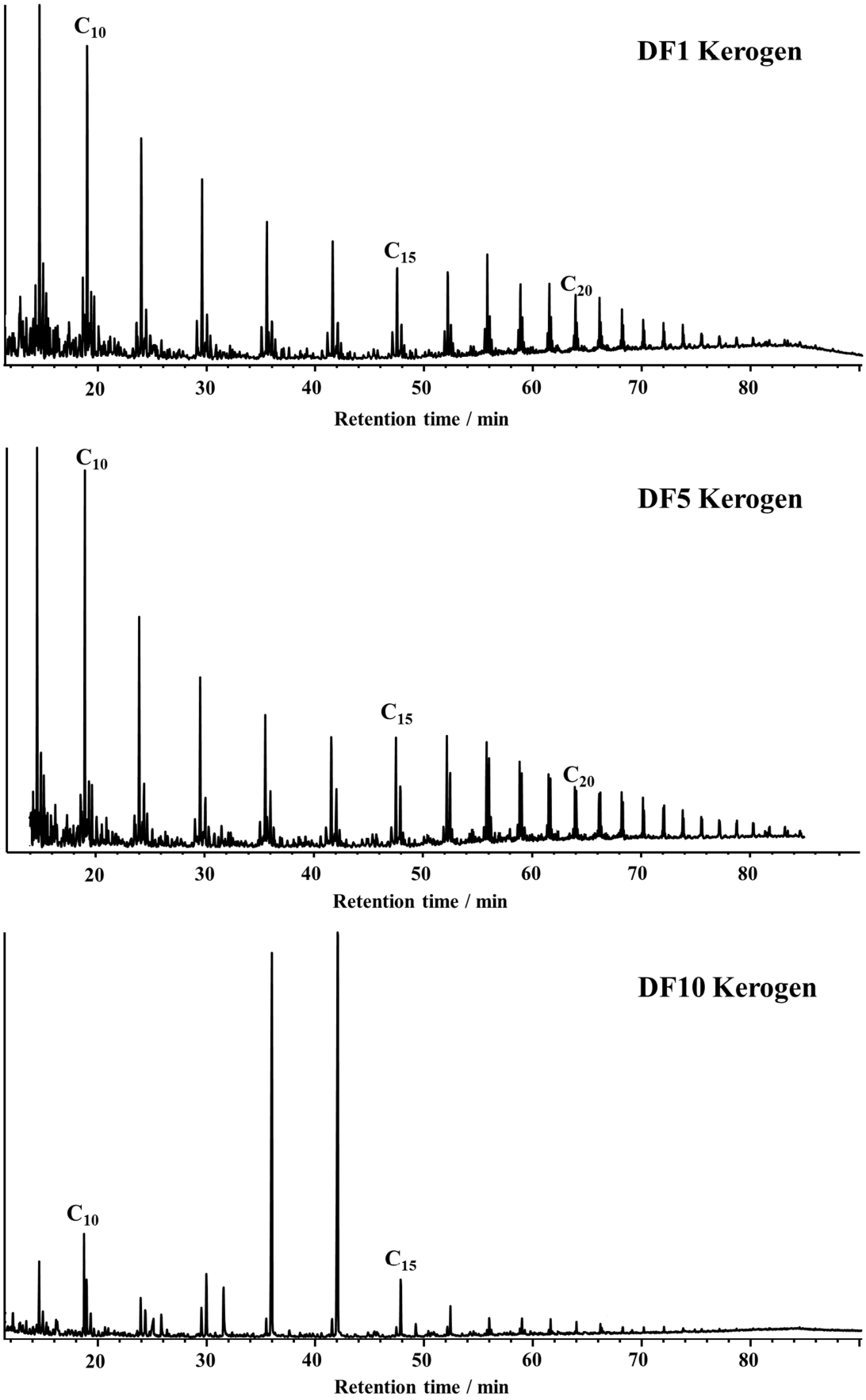

Figure 3.20: Selected Ion Monitoring (SIM) pyrograms of the Draupne Formation isolated kerogens. This is the $^{m}/_{z}$ 57 ion for the presence of *n*-alkane / *n*-alkene doublets.

3.3.3 Thermal maturity of shale and kerogens – Colorado Group

The Rock-Eval pyrolysis indicates that the Colorado Group shales they are thermally immature. The S2, Hydrogen Index and Tmax values exhibit no observable trends with burial depth, demonstrating that there is no change in maturity within the stratigraphic column. The Tmax temperature has a range between 405 ^{o}C to 432 ^{o}C, with an average of 420 ^{o}C. Therefore, the CG shales are thermally immature, as indicated by the Tmax temperatures below the start of the oil window (435^{o}C). In Figure 3.21, the maturity level of the Colorado Group suite is identified using the plot of Hydrogen Index against Tmax (after Espitalié, 1986). The HI vs Tmax plot demonstrates that the CG samples are immature, with no oil window or gas window maturity samples in the suite.

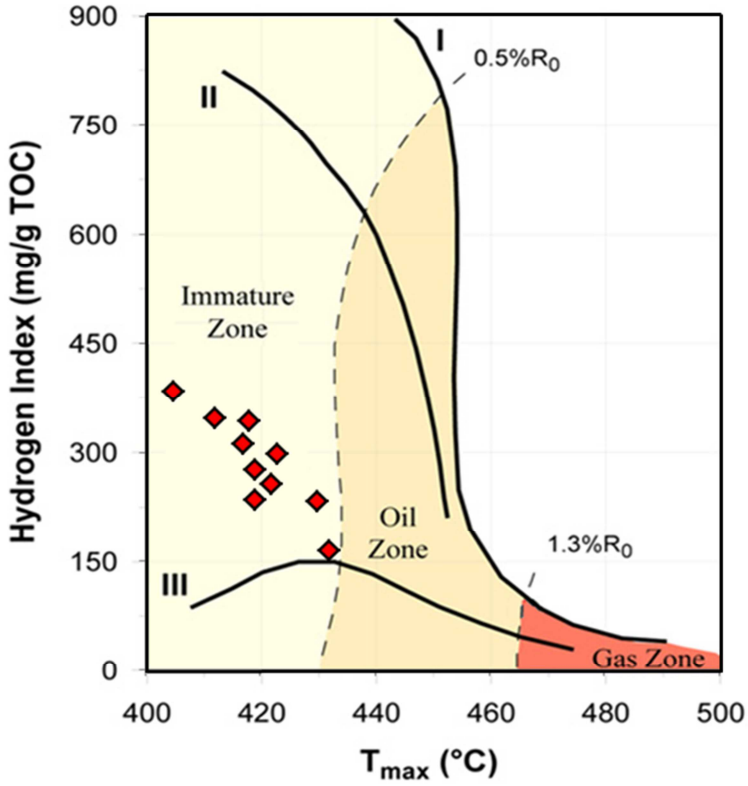

Figure 3.21: Plot of T_{max} vs. HI, (after Espitalié, 1986) for the Colorado Group shale suite. The shales are all immature, with no oil window or gas window maturity samples.

The elemental analysis of the isolated Colorado Group kerogens shows that the carbon, hydrogen and oxygen contents have no observable trend with burial depth. The van Krevelen diagram (Figure 3.17) identifies the CG kerogens as falling within the immature zone, with no oil window or gas window maturity kerogens identified. The spread of the data points is due to a range of thermal maturities within the oil window.

The FT-IR spectra of the shallow, middle and deep Colorado Group kerogen samples reports that there is no observable difference between the absorbance peak for the aliphatic C-H stretch at ~ 3000 cm^{-1} for the three kerogens. This indicates that the kerogens have very similar C-H bond concentrations, and that the maturity level of the kerogens is very similar (as maturity changes the hydrogen content of kerogen). The aliphatic C-H stretch at ~ 3000 cm^{-1} is significantly more intense than the aromatic peak at 1600 cm^{-1}, indicating that the Colorado Groups kerogens are thermally immature.

The solid-state ^{13}C-NMR spectra of the Colorado Group kerogens are thermally immature, as shown by the significantly larger aliphatic peak relative to the aromatic peak. The combined aliphatic peaks for the 3 kerogens have identical normalised intensities, which indicate that the samples have a consistent level of maturity throughout the stratigraphic column.

The immaturity on the Colorado Group kerogens was observed in the total ion chromatograms, as reported in Figure 3.15. The TIC of the three Colorado Group kerogens are very similar, with the large abundance of aliphatic alkyl groups indicating that the CG kerogens have the same level of maturity (i.e. immature), and have not begun to generate hydrocarbons. This interpretation is supported by the SIM chromatograms in Figure 3.22, where the large abundance of aliphatic doublets supports the immaturity assessment of the Colorado Group kerogens.

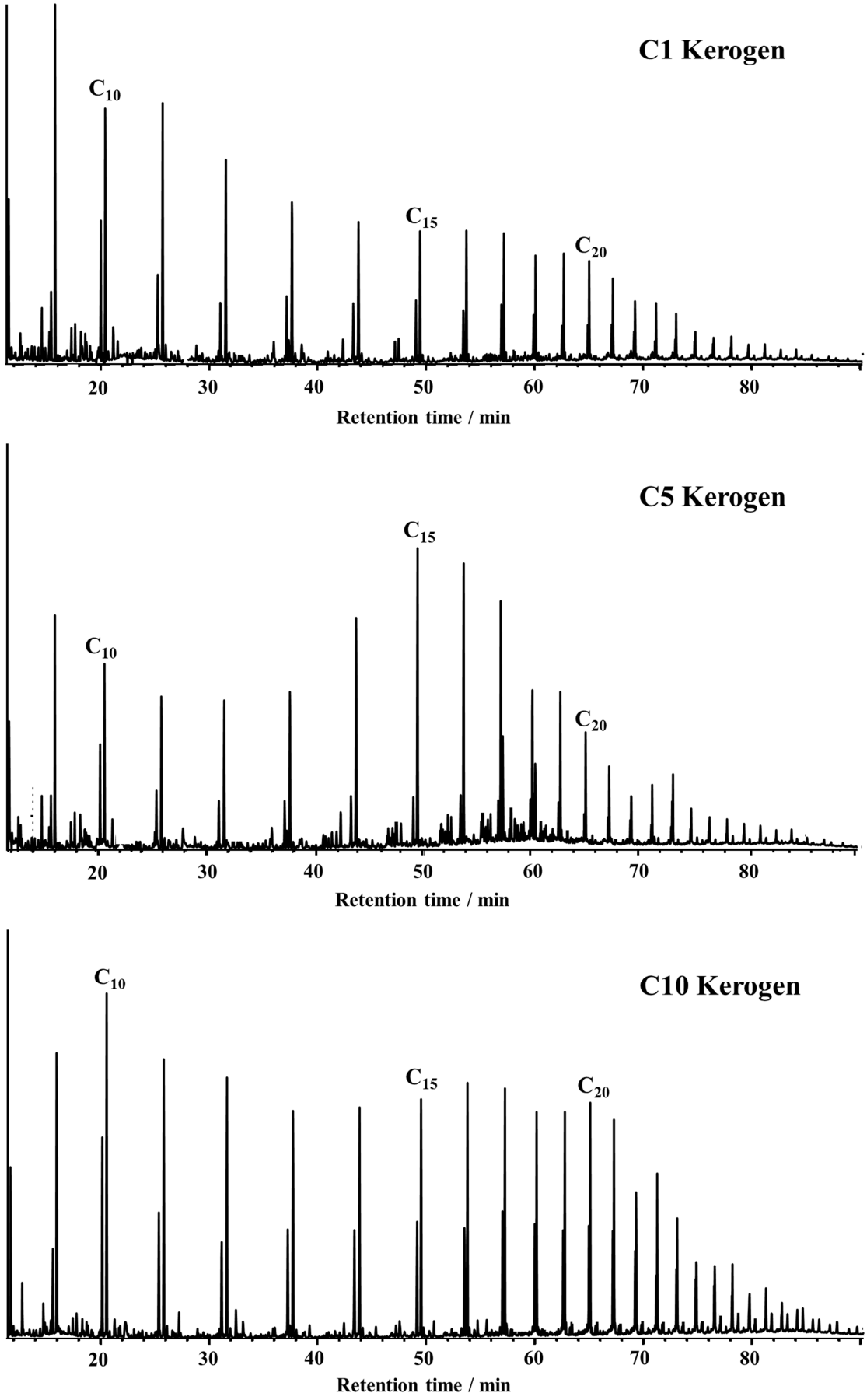

Figure 3.22: Selected Ion Monitoring (SIM) pyrograms of the Colorado Group isolated kerogens. This is the m/z 57 ion for the presence of alkane / alkene doublets.

3.4 Conclusions

The major findings and implications of Chapter 3 are:

- The Draupne Formation and Colorado Group shales are organic rich, and have good to excellent source rock potential. This is demonstrated by average TOC values of 7.24 % and 2.74 %, respectively, which are greater than the 2% threshold suggested by Tissot and Welte (1984).

- The Draupne Formation and Colorado Group shales contain Type II marine kerogens, as identified by the Rock-Eval pyrolysis data plotted on the S2 vs TOC diagram, and the elemental analysis data plotted on the van Krevelen diagram. The ^{13}C-NMR spectra of the isolated kerogens also contain aliphatic and aromatic resonance peaks that are characteristic of Type II marine algal kerogens, and the py-GC-MS total ion chromatograms have alkane/alkene distribution patterns characteristic of Type II kerogens.

- The Draupne Formation shales have a range of thermal maturities, from immature up to oil generation maturity (catagenesis). The S2 and Hydrogen Index values decreased with increasing maturity, and the Tmax values increased with increasing maturity. In addition, the carbon, hydrogen and oxygen contents of the isolated kerogens decreased with increasing maturity. The FT-IR spectra and the solid-state ^{13}C-NMR spectra also indicated that significant structural and bonding changes were occurring due to increased thermal maturity.

- The Colorado Group shales are both immature and iso-mature. This was indicated by very similar data values for the Rock-Eval pyrolysis and elemental analysis. The FT IR spectra and the solid-state ^{13}C-NMR spectra also presented very little difference between samples.

Chapter 4: Pore structure of organic rich shales

4.1 Introduction

4.1.1 Pore structure of organic rich shales

Understanding the pore structure of gas shales, and its control of gas storage is crucial for the prediction of Gas In Place (Pollastro *et al.*, 2007; Ross and Bustin, 2009; Loucks *et al.*, 2009; Bernard *et al.*, 2010; Bustin *et al.*, 2010). Pores in shales can be either inter-granular or intra-granular (Loucks *et al.*, 2011). The inter-granular pores in shales arise because clastic and biogenic sediment particles may not pack together perfectly, leaving space between the grains. Intra-granular pores in shales can occur inside sediment particles, being accessible from the surface. The shale pore system is filled with a fluid, such as water, oil or gas (Crosdale *et al.*, 2008)

Porous geological materials (such as coals and shales) are dominated by networks of slit-like pores which are interconnected by narrow capillary-like constrictions (Marsh, 1987). The shape of these pores is often likened to "ink-bottles", with narrow constrictions at the pore entrance that lead to a wide pore body. The narrow, constricted nature of the gas shale pore structure means that pore accessibility by gas is affected (Ross and Bustin, 2007). The geometry of the pore-throats and pore-bodies means that gas diffusion to the sites of adsorption is kinetically restricted (Ross and Bustin, 2007).

Shales have a wide pore size distribution, spanning nearly 5 orders of magnitude (10^5) from visible macropores (>10 mm) through to sub-nanometre pores (<0.7 nm) (Clarkson *et al.*, 2012). The pore size distribution of mudstones is strongly dependent on average grain size and mineralogy (Aplin and Macquaker, 2011), so that fine grained clay-rich shales have a smaller average pore size range than coarser grained silty shales.

The pores in gas bearing shale rocks are dominantly nanometre in scale (Loucks *et al.*, 2009; Modica and Lapierre, 2012), and the modal pore size is typically 100 nm in size (Loucks *et al.*, 2009; Zhang *et al.*, 2012). The presence and abundance of microporosity (< 2nm) is particularly significant, as this is the primary site for gas adsorption in shales (Bae *et al.*, 2009).

The total porosity of geological material evolves throughout burial history. The interconnected pore system of shales is subject to substantial changes during burial and compactional processes (Amann-Hildenbrand *et al.*, 2012). Newly deposited, unconsolidated sediment can have an initial porosity of ~ 80-90%, which is usually filled with electrolyte-rich pore water. After being deeply buried and compacted, the total porosity of lithified shales can be < 10% (Aplin and Macquaker, 2011). This major reduction in overall total porosity is the result of diagenetic processes (Amann-Hildenbrand *et al.*, 2012).

During early diagenesis of shales, redox processes occur in the pore water of the first few metres of sediment. These redox reactions lead to the formation and precipitation of diagenetic minerals (Curtis *et al.*, 1986). These diagenetic minerals (such as calcite, pyrite and clay minerals) precipitate as microcrystalline cements that in-fills the pore spaces between deposited clastic particles, thus reducing overall sediment porosity (Aplin and Macquaker, 2011).

In the later stages of diagenesis, burial and mechanical compaction is a key control on pore structure and total porosity. The shale matrix pore volume decrease with depth of burial, due to compaction and cementation (Modica and Lapierre, 2012). Compaction is a mechanical process driven by an increase in effective stress. This effective stress is the difference between the overburden (produced by overlying sediment), and the average pore pressure of the shale. The mechanical compaction of sediment is a strong driver of porosity reduction (Skempton, 1970). The rate of compaction is influenced by: 1) the average sediment grain size (Aplin *et al*., 1995), and 2) the permeability of the shale. Permeability determines the rate of pore water expulsion from the compressed shales (Aplin and Macquaker, 2011).

The increased effective stress and temperature during burial also leads to chemical diagenesis, where porosity is reduced due to thermodynamically unstable minerals converting to more stable analogues. An example of this is the inter-conversion of biogenic Opal A to quartz (Behl, 1999). Opal-rich shales exhibit very high porosities during early diagenesis (Volpi *et al.*, 2003), but the thermodynamic conversion to quartz leads to significant porosity reduction during burial diagenesis (Isaacs, 1981).

Shales can be subject to thermal maturation by geological processes occurring in sedimentary basins, and this can have a significant effect on the pore structure and porosity of shales (Loucks *et al.*, 2009; Zhang *et al.*, 2012). Thermal maturation occurs when an organic rich shale formation is subjected to large geological pressures and temperatures during catagenesis, usually from several kilometres of overbearing sediments. These conditions can lead to significant alteration of the overall pore structure and porosity of a shale sequence (Loucks *et al.*, 2009). It is suggested that these nano-scale pores are formed during the generation of hydrocarbons (Curtis *et al*., 2011).

The relationship between the shale pore system and the level of maturity has been attributed to changes in the porosity and pore structure of kerogen (Chalmers and Bustin, 2007; Bae *et al.*, 2009; Loucks *et al.*, 2009). It is well established that thermal maturation of geological samples causes an increase in the abundance of microporosity in the organic component of sedimentary rocks (Gan *et al*., 1972; Clarkson and Bustin, 1996; Bustin and Clarkson 1998; Prinz *et al.*, 2004; Prinz and Littke, 2005; Ross and Bustin, 2009). The increase in the relative abundance of micropores occurs at the expense of the macropore and mesopore content (Crosdale *et al.*, 1998). Over-maturity can have a negative impact on porosity though; the secondary cracking of liquid petroleum to methane-rich gas can form significant amounts of solid pyrobitumen residue in the shale pores that in-fills and occludes porosity (Muscio and Horsfield, 1996; Modica and Lapierre, 2012).

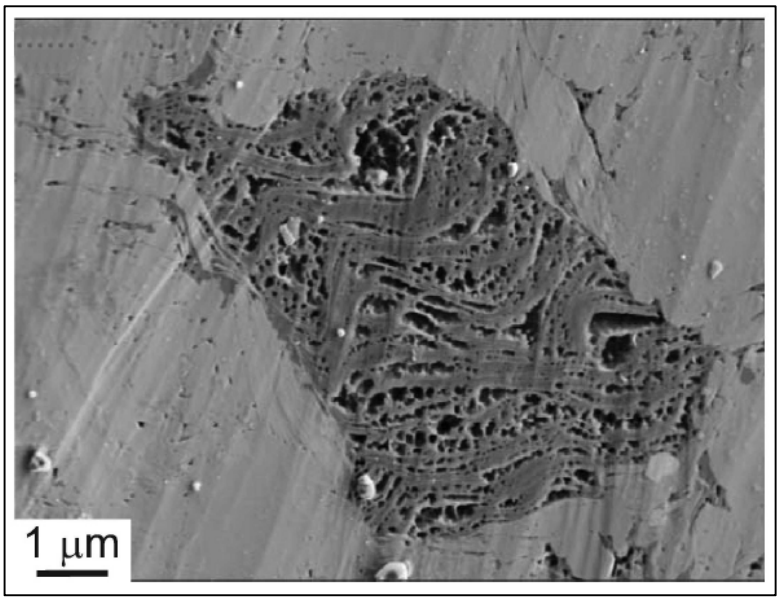

Figure 4.1: The presence of nanometre scale pores in the particle of kerogen can be seen in this FIB-SEM image of a high maturity (VR_0 = 1.6%) Barnett shale sample. There are minimal nanometre scale pores in the surrounding light grey shale clay matrix (after Loucks *et al.*, 2009).

The organic matter richness of a shale has a strong influence on the presence and abundance of microporosity (Beamish and Crosdale, 1995; Ross and Bustin, 2009). As the organic matter content increases, the overall micropore volume of the shale increases (shown in Figure 4.2). In addition, organic-rich shales may contain a heterogeneous mixture of different organic matter types that is highly variable on the bulk and molecular scale (Vandenbroucke and Largeau, 2007). The organic maceral with the highest micropore volume is vitrinite (Unsworth *et al*., 1989; Lamberson and Bustin; Chalmers and Bustin, 2007).

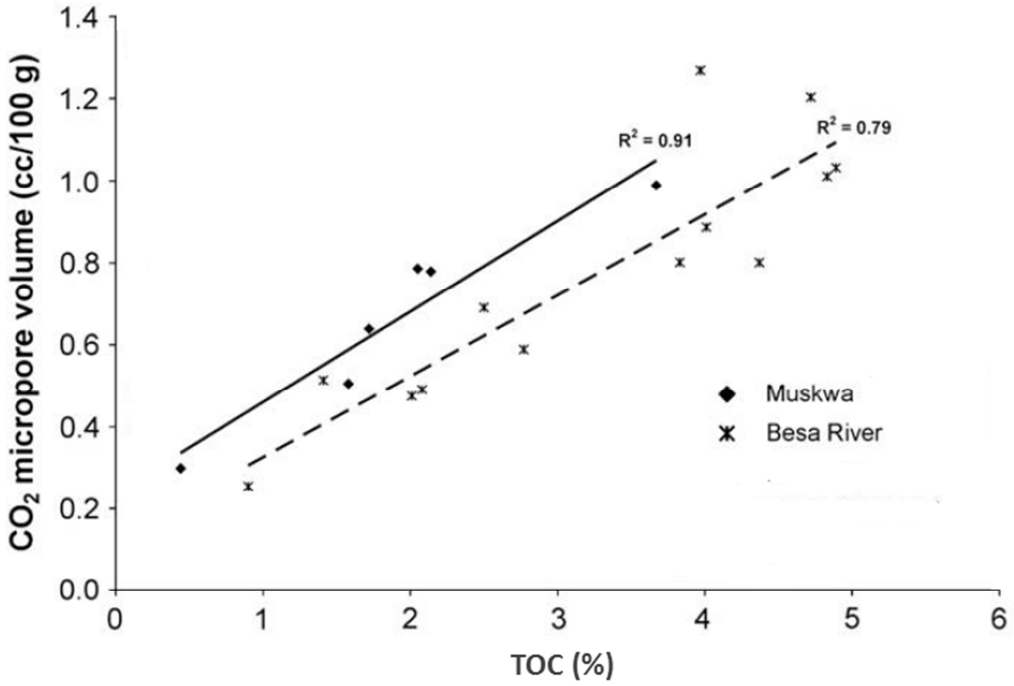

Figure 4.2: A strong positive correlation between micropore volume and organic matter content suggests that organic matter is the primary location of micropores in organic rich shales (modified after Ross and Bustin, 2009).

Mineralogy is a key factor in the origin and nature of the porous structure in shales (Aplin and Macquaker, 2011). Shales often contain more than 90% inorganic mineral matter, mostly consisting of silicates (quartz) and clays, with some carbonate minerals being present. Also, organic rich shales (> 2% TOC) may contain significant amounts of iron pyrite (FeS_2). This is because pyrite is precipitated and deposited from sea water in relatively permanent bottom-water anoxic-dysoxic oxygen regimes.

A positive correlation was observed between clay content and total porosity of some Muskwa Formation shales (Bustin *et al*., 2008). They observed that clay-rich shales have a higher porosity and permeability than silica-rich shales or carbonate-rich shales (Bustin *et al.*, 2008). This is explained by the presence of microporosity associated with the clay mineral matrix, which has a predominance of pores in the 1 and 2 nm ranges (Ross and Bustin, 2007). As the silica content of shales increases (and therefore the clay content decreases), there is a proportional decrease in meso- and micro-porosity (Bustin *et al*., 2008). The positive correlation between clay content and total porosity can be seen in Figure 4.3. It has also been shown that the origin of the quartz in the shale has an effect on the total porosity. Shales rich in detrital quartz have a higher porosity than shales rich in biogenic quartz (Bustin *et al.*, 2008). This is because there are insignificant amounts of microporosity in biogenic silica (Ross and Bustin, 2009).

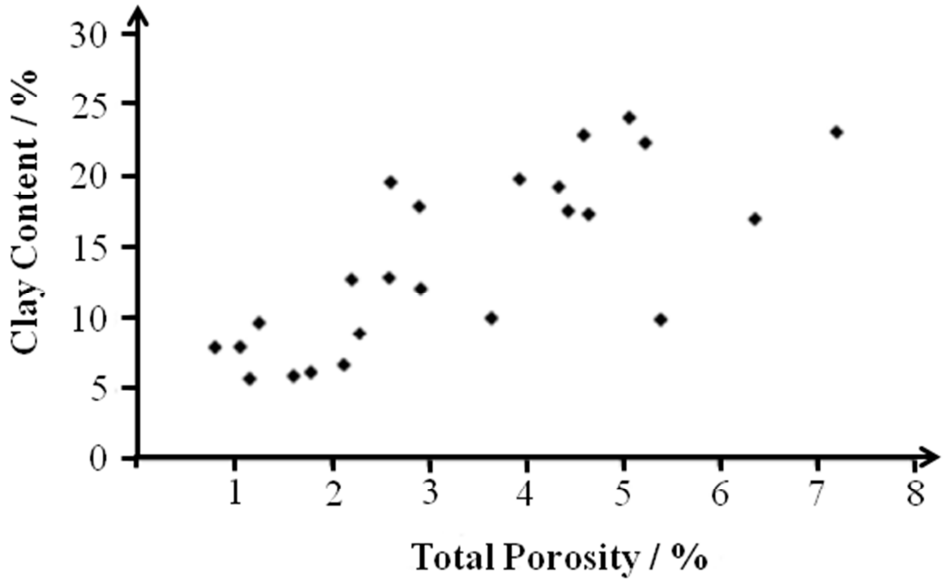

Figure 4.3: There is a positive correlation between clay content and total porosity (after Bustin *et al.*, 2008)

In the subsurface, the porosity and pore structures of shales are filled with interstitial pore fluid. The fluids are typically natural gas and/or formation water (Crosdale *et al*., 2008). Pore structure influences the relative amount of moisture adsorbed by shales (Modica and Lapierre, 2012). It has been shown that samples dominated by mesopores retain more water than samples which are microporous in nature (Day *et al*., 2008). This has been demonstrated by a strong hysteresis curve between the moisture adsorption and desorption isotherms in coals (Allardice, 1991; Allardice *et al*., 2003). The hysteresis curve is due to the capillary condensation effect of water in mesopores (Crosdale *et al*., 2008). As the microporosity of coal increases (and the mesoporosity decreases), the hysteresis loop becomes less prominent, and the shape of the curve changes (Bustin and Clarkson, 1998).

4.2 Results

4.2.1 Location and geometry of pores in the Draupne Formation and Colorado Group shales.

The location and shape of pores in the Draupne Formation and Colorado Group shales were investigated using scanning electron microscopy, using the procedures described in chapter 2, section 2.7. The SEM imaging of the shales was performed using Secondary Electron (SE), Backscatter Electron (BSE) and Focussed Ion Beam (FIB-SEM) techniques. The FIB is used to mill down in to the surface of the shale sample, and image the 3-D structure of the shale matrix at the nanometre scale.

The electron micrograph images of the Draupne Formation and Colorado Group shales (Figures 4.4 to 4.9) indicate that they consist of quartz grains (medium grey), phyllosilicate clay minerals, streaks of organic matter (black) and framboidal pyrite (white). A selection of Draupne Formation and Colorado Group shales were investigated using the FIB-SEM technique. For the Draupne Formation, an immature sample (DF1), a middle maturity shale (DF5), and a mature shale (DF10) were investigated. For the Colorado Group, the shales have equivalent maturity, so a shallow sample from the Medicine Hat formation (C1), a middle depth sample from the Second White Specks formation (C6), and a deep shale sample from the Belle Fourche formation (C10) were investigated.

The DF1 shale is the least mature shale sample, with a burial depth of 2117.8 m. This shale is essentially non-porous on the micrometre scale. No inter-granular pores can be seen in the shale matrix, and no intra-granular pores can be seen in organic matter particles. This finding suggests that low maturity shales may not have well defined pore structures on the micrometre scale.

The DF5 shale is beginning to enter the oil window (Tmax = 432 ^{o}C, VR_c = 0.62 %), at a burial depth of 3375.32 m. This shale does not have micrometre scale pores within organic matter particles, although there is some evidence of inter-granular pores in the shale matrix (above some clay mineral packages). This inter-granular pore structure in the shale matrix could be due to inefficient packing of the mineral matrix, or it could indicate the generation of liquid hydrocarbon, that has created a pore space by fluid expansion.

The DF10 shale is towards the top end of the oil window (Tmax = 463 ^{o}C, VR_c = 1.17 %), at a burial depth of 4780.7 m. This shale does not have visible micrometre scale pores within organic matter particles, but the FIB-SEM image shows a well-developed network of pore structures in the clay matrix. Pores can be seen around the fine silt grains and between clay particles. It is unlikely these pore structures are due to inefficient packing of shale minerals (at a burial depth of ~ 5km), and it could indicate the pore spaces have been forced open due to the generation and migration of liquid hydrocarbons.

The C1 shale had a present day burial depth of 505.3 m. This Medicine Hat formation shale sample had no intra-granular pores within the organic matter particles, but there was some inter-granular porosity between a group of poorly packed carbonate mineral grains, with some well-defined elliptical pore structures visible.

The C6 shale had a present day burial depth of 642.1 m. This Second White Specks shale sample had numerous thin streaks of organic matter dispersed within the carbonate rich shale matrix. There was some evidence of nanometer scale porosity within the shale matrix.

The C10 shale had a present day burial depth of 684.61 m. This Belle Fourche shale sample had some long thin cracks/pores within the clay matrix, and some nanometer scale circular pores within a localized area of organic matter.

SEM microscopy of shale DF1

Shale sample DF1 is the shallowest buried shale in the Draupne Formation suite (at a depth of 2117.8m), and is thermally immature.

In Figure 4.4, part a) a low magnification BSE micrograph can be seen. It shows a visibly non-porous block of organic matter in the centre (black), dispersed within a shale matrix of quartz grains, pyrite framboids/cubes and clay mineral packages.

In Figure 4.4, part b) a low magnification SE micrograph can be seen. The left-hand side of the image consists of a large organic particle (dark grey). There appears to be no visible porosity at the surface of the organic particle or the adjacent clay matrix.

In Figure 4.4, part c) a low magnification BSE micrograph can be seen. A rectangular organic particle is found in the centre of the image. There appears to be no visible pore structure within the rectangular particle, or surrounding shale matrix.

In Figure 4.4, part d) a low magnification BSE micrograph can be seen. There is no visible porosity or pore structure can be seen in the shale matrix.

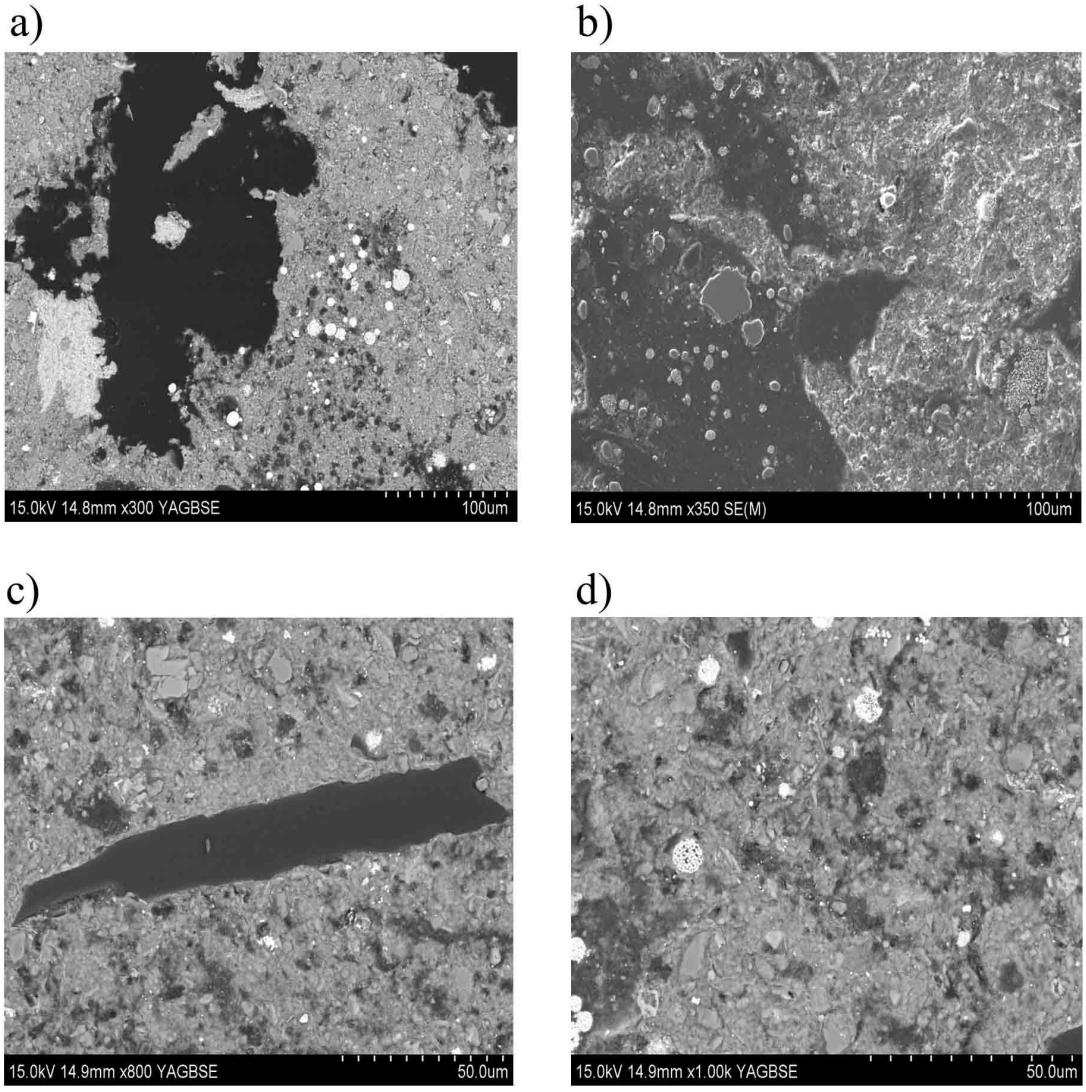

Figure 4.4: Unlabelled SEM micrographs of DF1 shale.

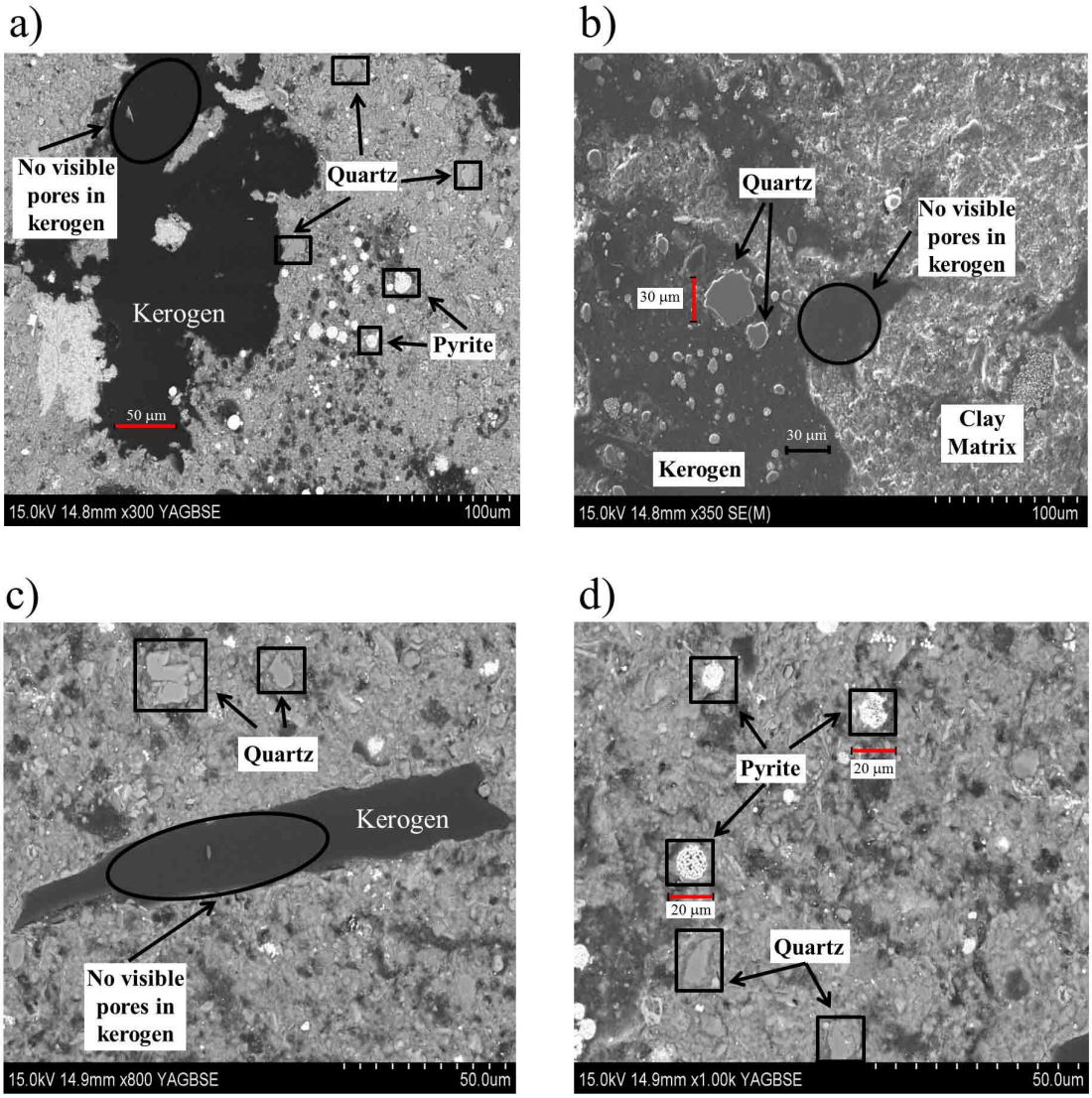

Figure 4.4 (continued): Labelled SEM micrographs of DF1 shale.

SEM microscopy of shale DF5

Shale sample DF5 is at a medium burial depth for the Draupne Formation suite (at a depth of 3400.4m), and is beginning to enter the oil window maturity. In Figure 4.5, part a) a high magnification FIB-SEM micrograph can be seen. On the vertical back wall of the trench, a streak of organic matter can be seen to run down the centre. There are not visible pore structures in this streak of organic matter.

In Figure 4.5, part b) a very high magnification FIB-SEM micrograph image of open porosity can be seen in the clay matrix above the streak of organic matter. These elongate pores are on the micrometre scale lengthways, but are nanometre scale width ways. It appears that these adjacent pores may be interconnected.

In Figure 4.5, part c) a very high magnification FIB-SEM micrograph image of a small number of oval shaped pores can be seen at the edge of the streak of organic matter. The majority of the area is essentially non porous on the micrometre scale.

In Figure 4.5, part d) a very high magnification BSE micrograph image of a particle of organic matter adjacent to wispy clay mineral packages can be seen.

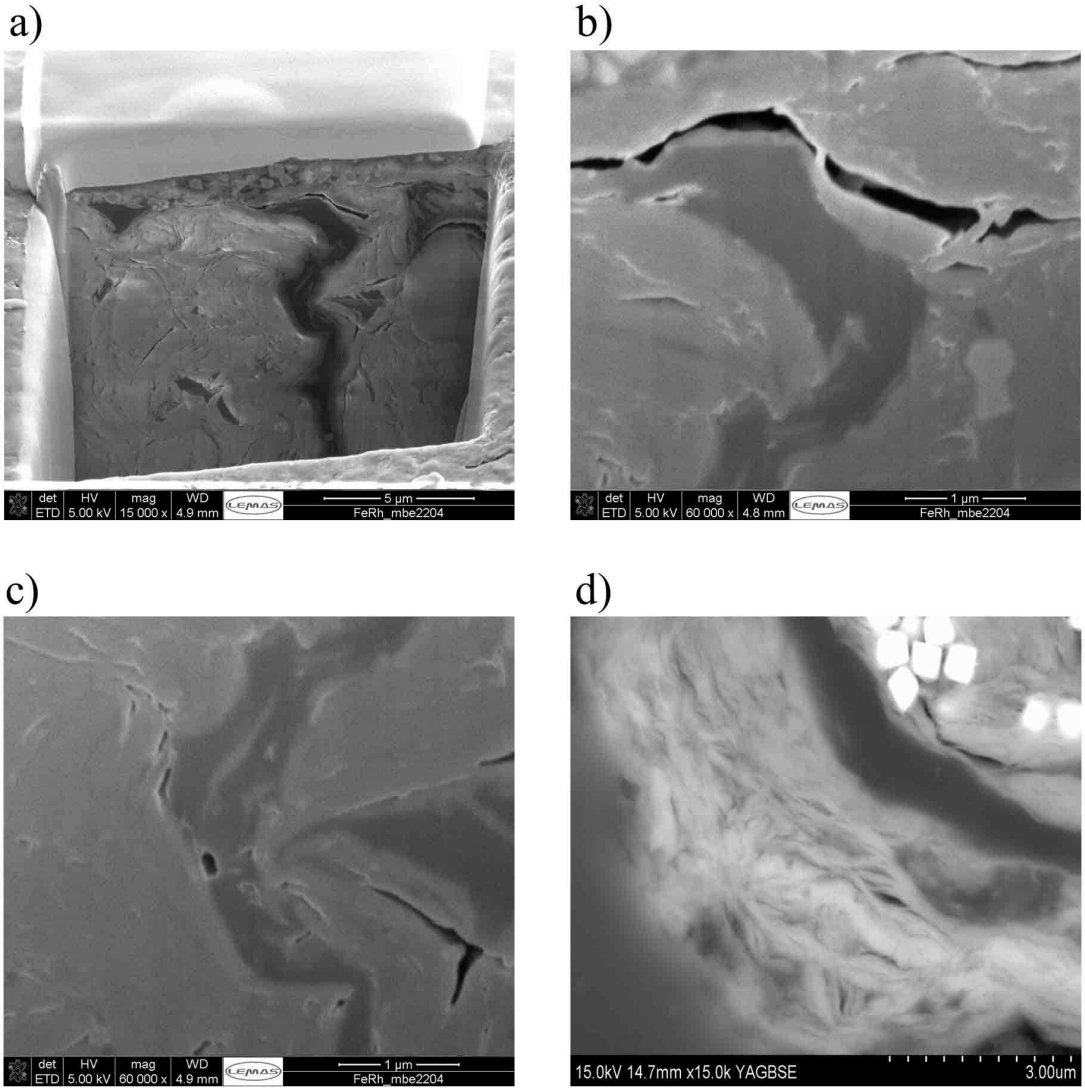

Figure 4.5: Unlabelled SEM micrographs of DF5 shale.

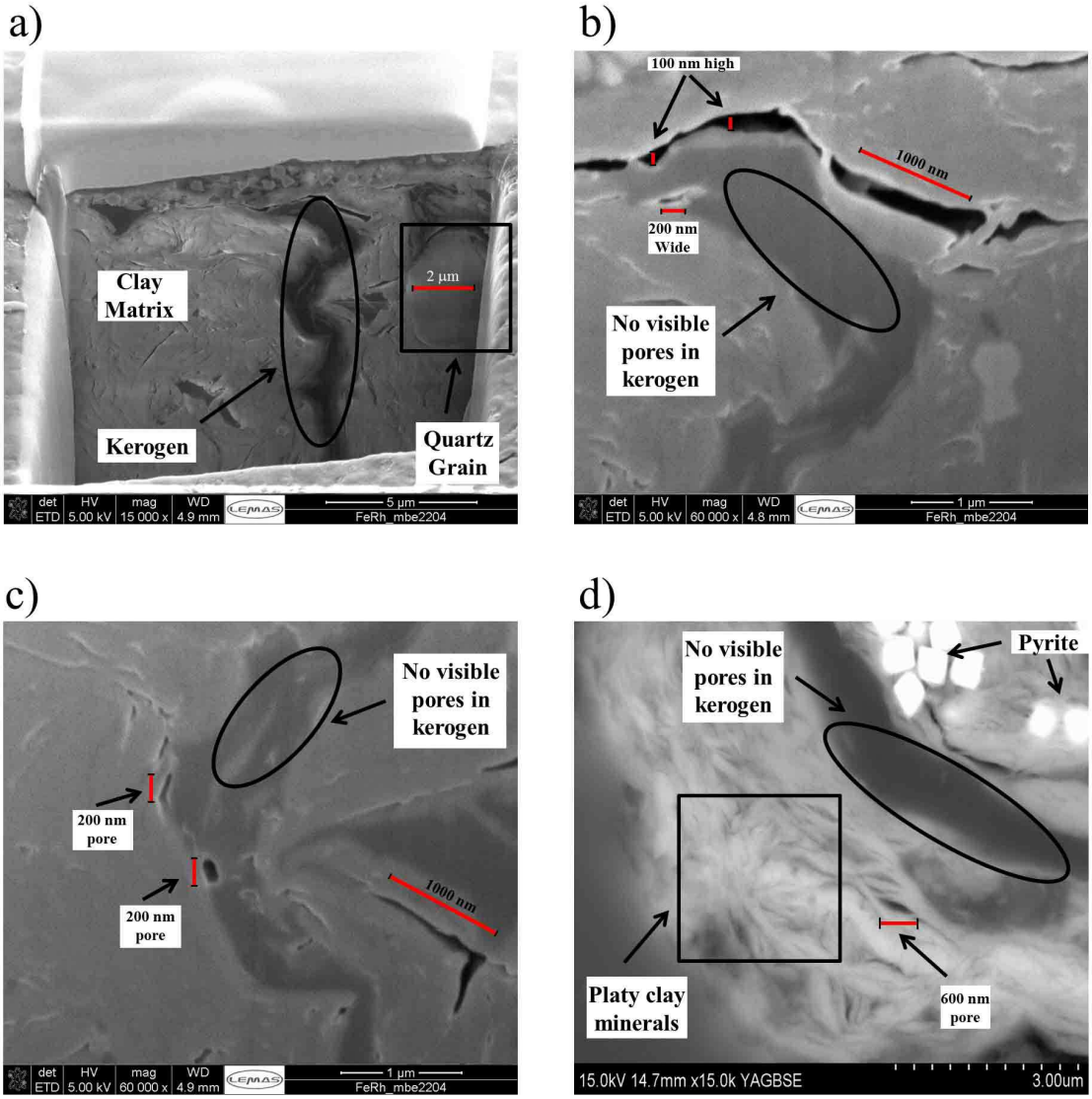

Figure 4.5 (continued): Labelled SEM micrographs of DF5 shale.

SEM microscopy of shale DF10

Shale sample DF10 is the deepest buried sample in the Draupne Formation suite (at a depth of 4780.7m), and is at the upper boundary of the oil window maturity.

In Figure 4.6, part a) a low magnification BSE micrograph can be seen. It shows a blocky particle of organic matter in the centre (black), dispersed within a shale matrix of quartz grains, pyrite framboids and clay mineral packages.

In Figure 4.6, part b) a high magnification SE micrograph of the organic particle in the centre of Figure 3.10, part a) can be seen. The centre of image consists of a surface image of the organic particle (dark grey). There appears to be no visible micrometre scale porosity at the surface of the organic particle or the adjacent clay matrix.

In Figure 4.6, part c) a very high magnification FIB-SEM micrograph image can be seen. On the vertical back wall of the trench, a significant amount of slit-shaped and oval shaped pore structures can be seen in the shale matrix.

In Figure 4.6, part d) a very high magnification FIB-SEM micrograph image of porosity in the shale matrix can be seen. Pores can be seen around fine silt grains and between clay particles. These pores are nanometre in scale.

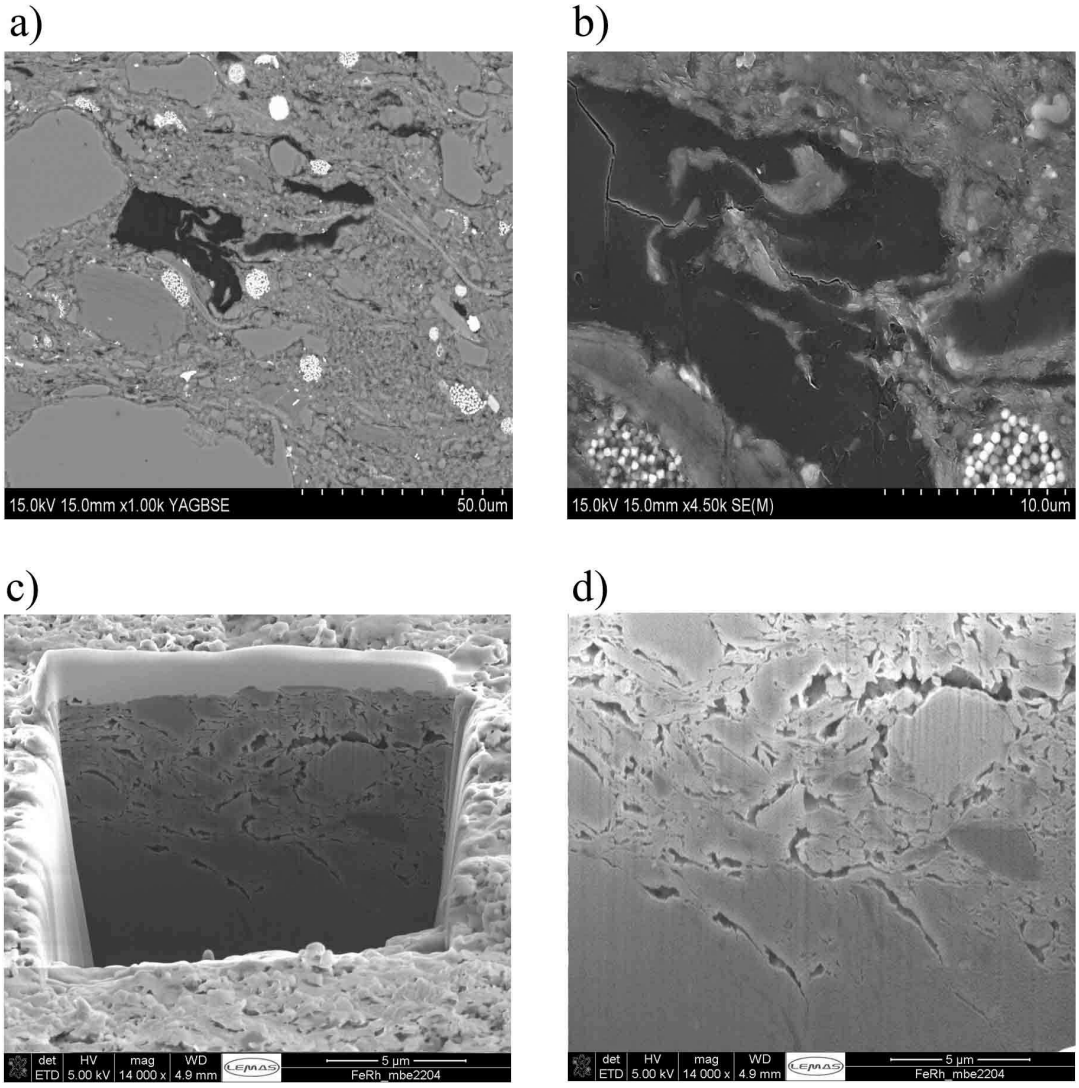

Figure 4.6: Unlabelled SEM micrographs of DF10 shale.

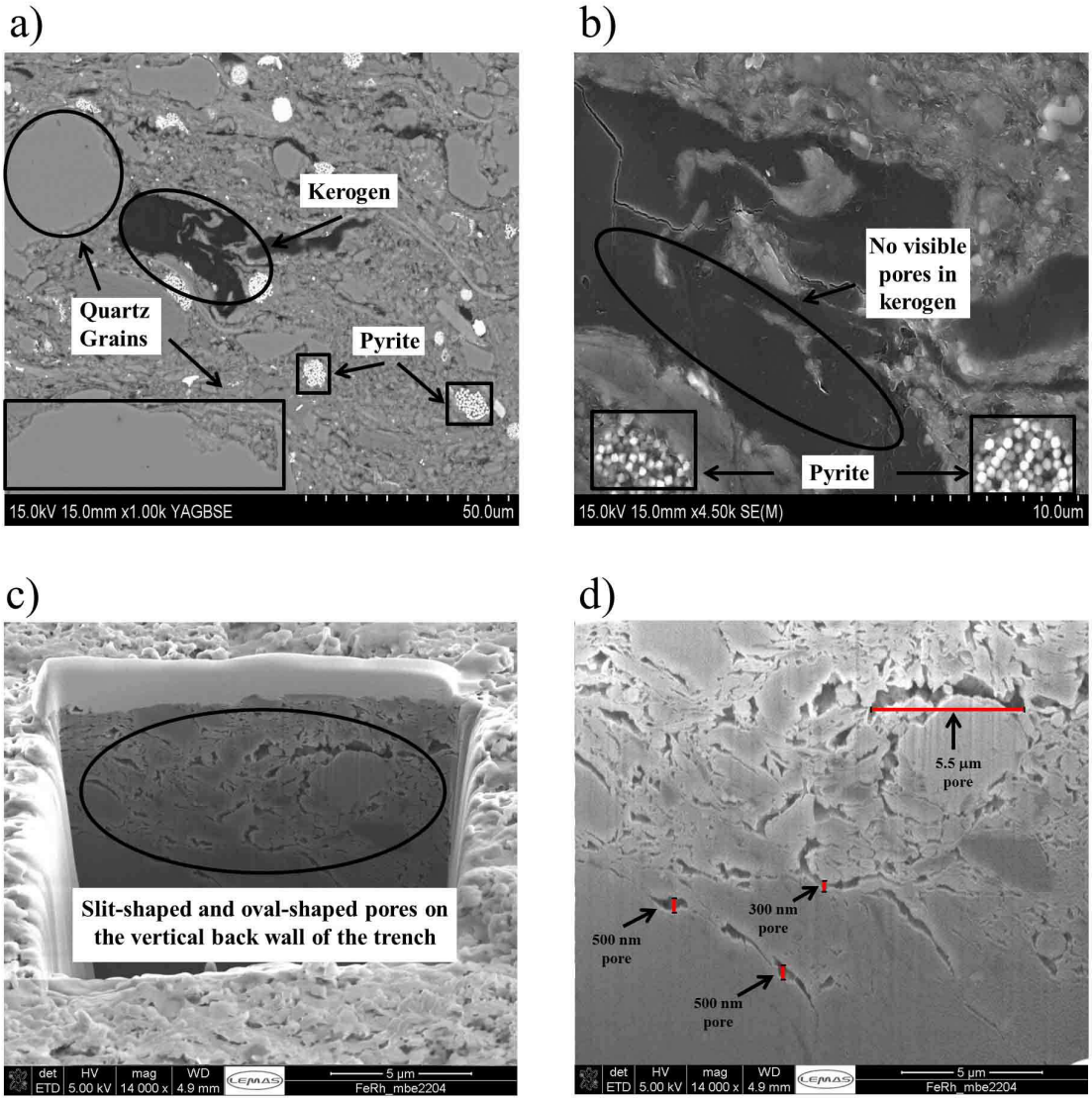

Figure 4.6 (Continued): Labelled SEM micrographs of DF10 shale.

SEM microscopy of shale C1

In Figure 4.7, part A) a low magnification BSE micrograph can be seen. It shows that the dominant components in sample C1 are detrital quartz grains, with unconnected blocky particulate organic matter dispersed within the clay mineral packages.

In Figure 4.7, part B) it can be seen in the higher magnification BSE image that an elliptical particle of organic matter is present in the centre of the image, and that it has no visible pore structures present in the organic matter.

In Figure 4.7, part C) a high magnification FIB-SEM micrograph can be seen. On the vertical back wall of the trench, a region of visible micrometre-scale porosity can be seen, that is associated with a group of poorly packed carbonate mineral grains. There is no in-fill of this porosity by diagenetic minerals or by amorphous/gelatinous organic matter.

In Figure 4.7, part D) a very high magnification FIB-SEM micrograph image of nanometre scale open porosity can be seen in the clay mineral packages. These nanometre scale elliptical pores would act as transport porosity for any bulk gas phase that may be present.

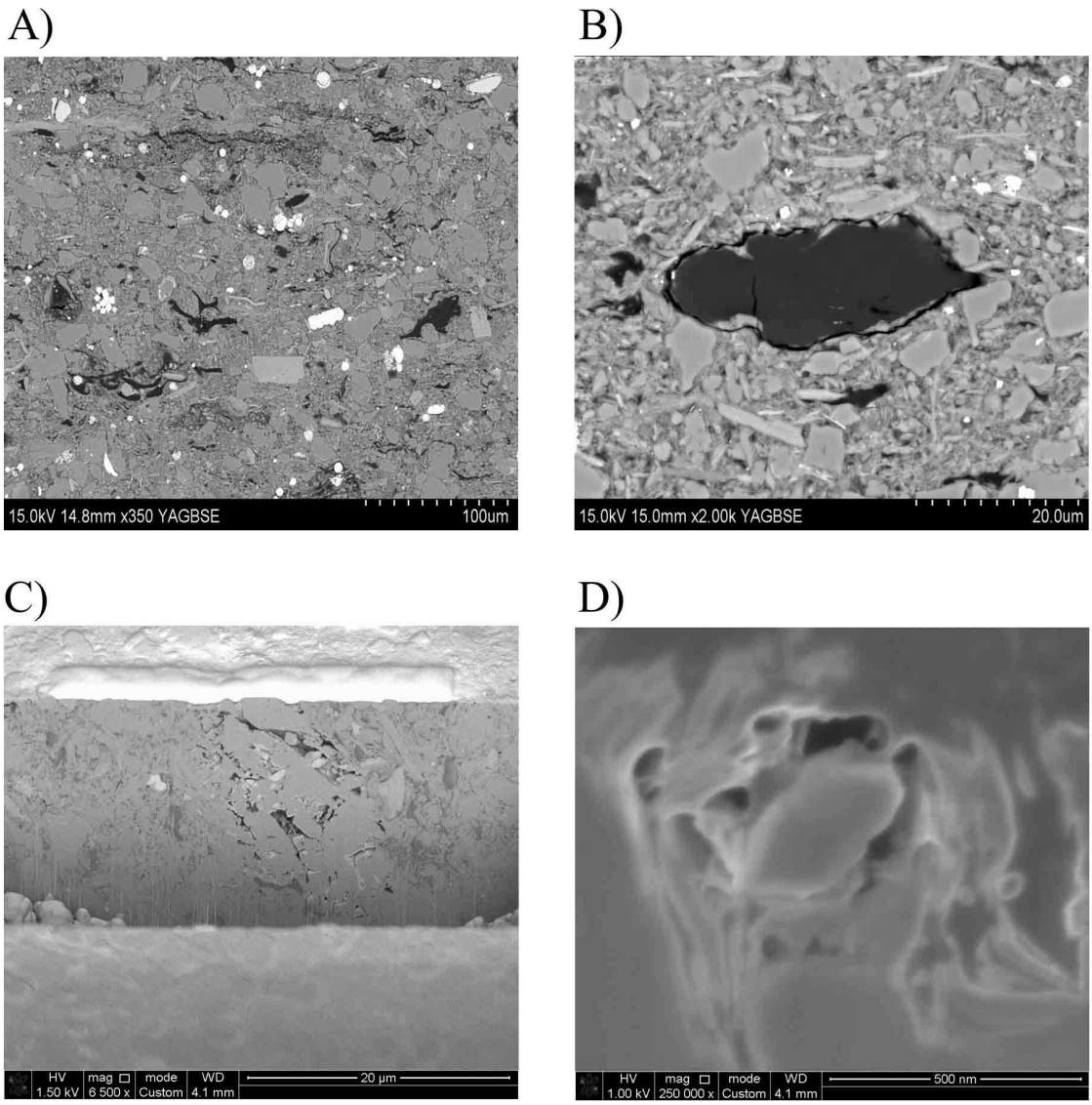

Figure 4.7: Unlabelled SEM micrographs of Colorado Group shale C1.

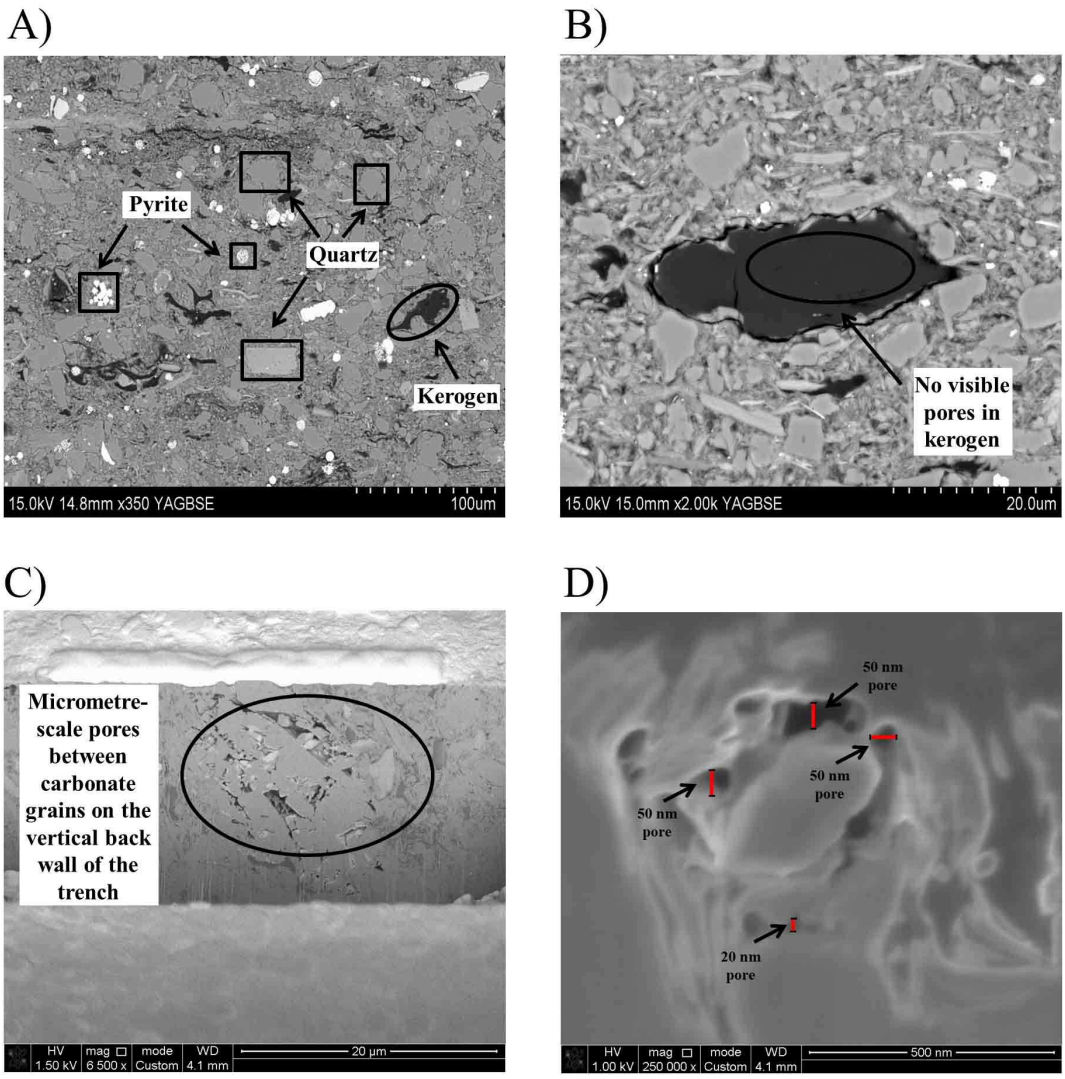

Figure 4.7 (Continued): Labelled SEM micrographs of Colorado Group shale C1.

SEM microscopy of shale C6

In Figure 4.8, part A) a low magnification BSE micrograph can be seen that shows areas of thin streaks of organic matter which are tens of micrometres in length, in the presence of carbonate (medium grey) and framboidal pyrite (white). The laminar organic matter does not appear to be inter-connected.

In Figure 4.8, part B) a high magnification FIB-SEM micrograph image can be seen. On the vertical back wall of the trench, a mixture of organic matter (dark) and carbonate can be seen on the left-hand side, whilst quartz/clay (grey) and pyrite (white) can be seen on the right-hand side. There is no micrometre-scale pore structure visible.

In Figure 4.8, part C) a higher magnification of the left-hand area of Figure 5.8, part b) can be seen. There is negligible evidence of visible porosity in either the organic or carbonate mineral phases.

In Figure 4.8, part D) a high magnification FIB-SEM image indicates the presence of a small amount of nanometre scale elongate pores in the clay mineral matrix.

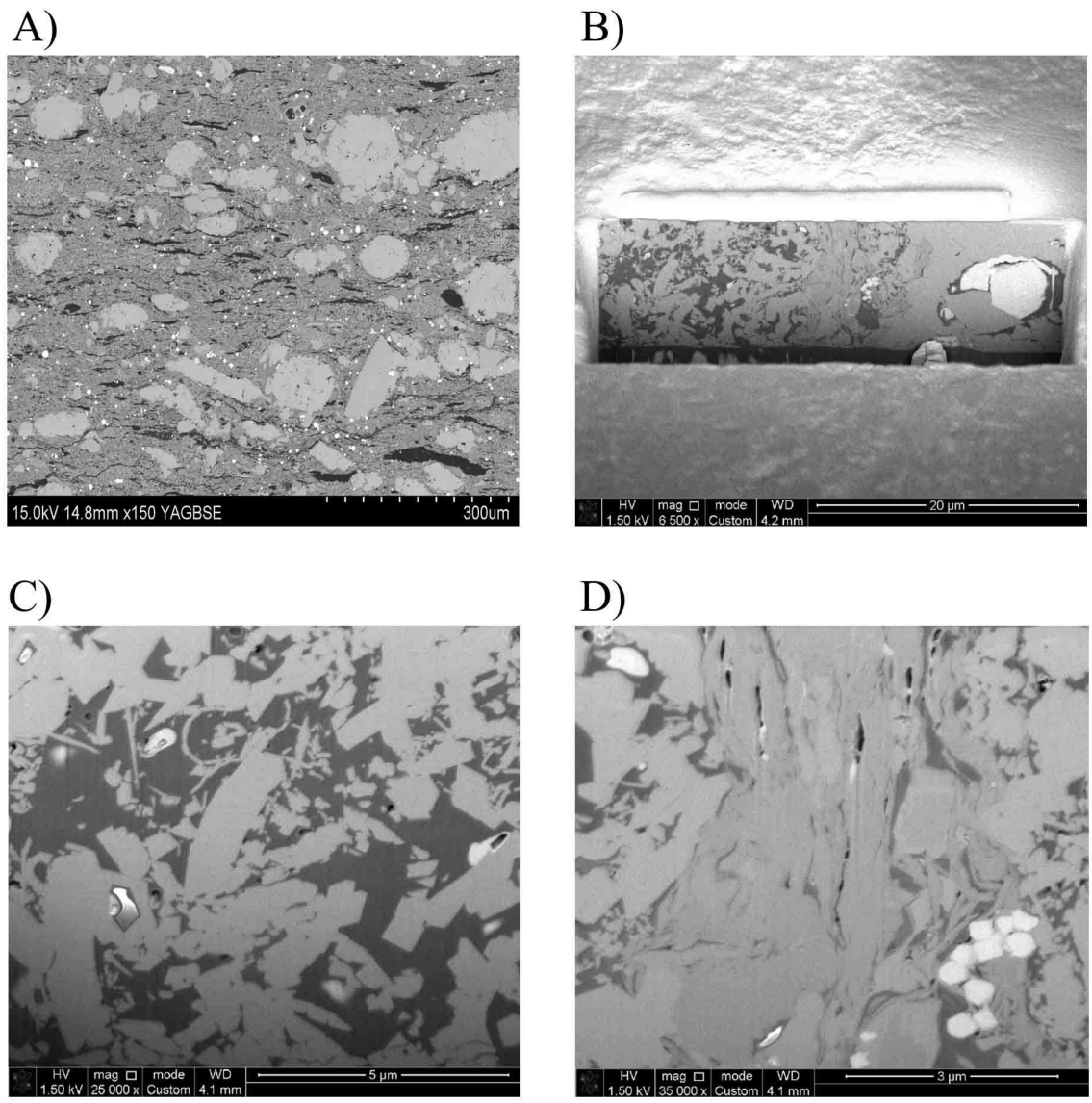

Figure 4.8: Unlabelled SEM micrographs of Colorado Group shale C6

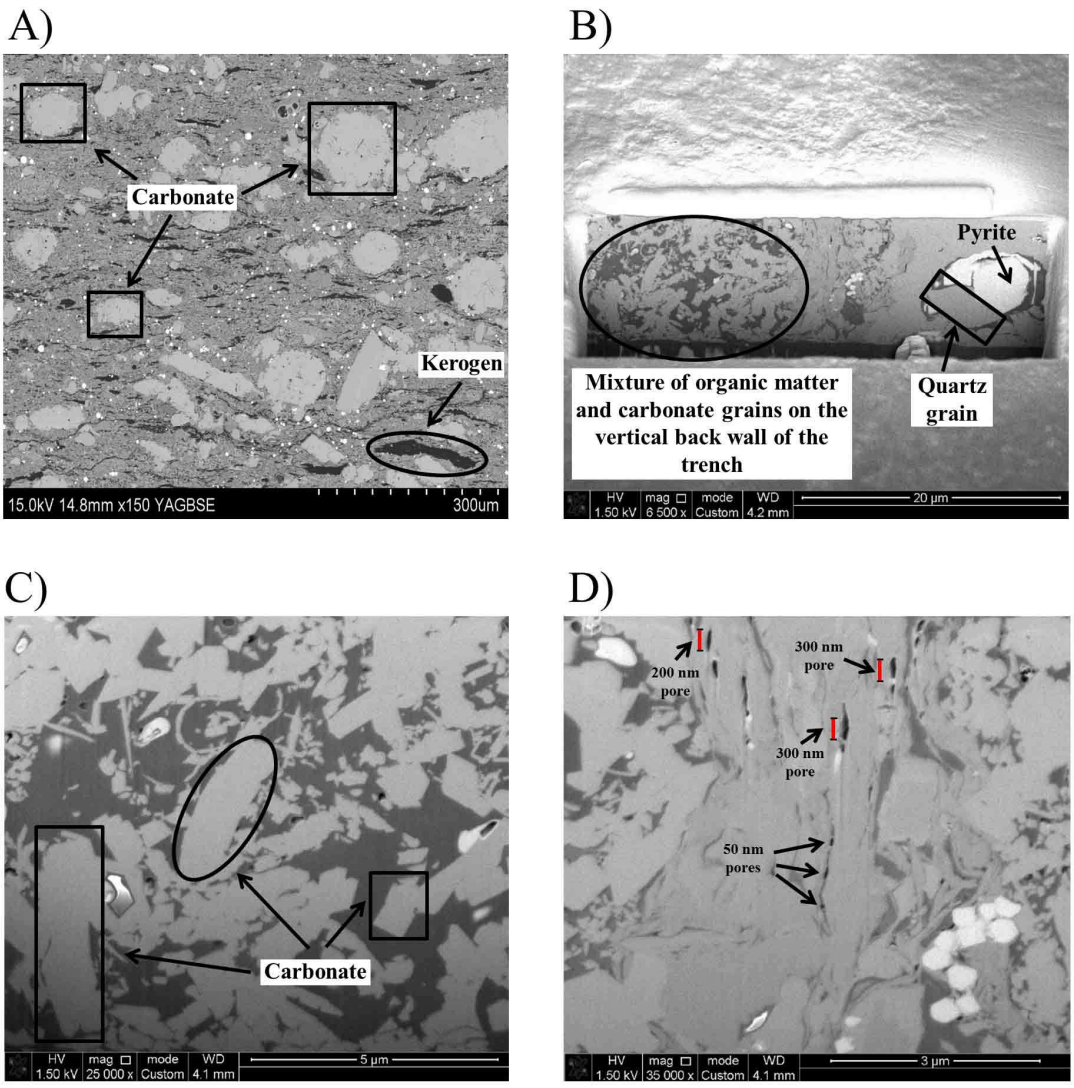

Figure 4.8 (Continued): Labelled SEM micrographs of Colorado Group shale C6

SEM microscopy of shale C10

In Figure 4.9, part A) low magnification BSE micrograph can be seen that indicates the quartz rich nature of this shale. There are negligible amounts of organic matter visible within the clay matrix, and there are long thin cracks/pores (which are tens of micrometres in length) within the clay matrix (this could be an artefact of decompaction after the reduction of overburden stress).

In Figure 4.9, part B) a high magnification FIB-SEM micrograph image can be seen. On the vertical back wall, a micrometre-scale pore network can be seen in the clay matrix. There does not appear to be a porous structure in the streaks of organic matter (black).

In Figure 4.9, part C) a very high magnification BSE micrograph can be seen that shows the absence of a visible pore structure in the streak of organic matter (black).

In Figure 4.9, part D) very high magnification secondary electron micrograph of the Figure in part C. Some nanometre scale circular pores can be seen at the top of the upward “fold” in the organic matter (in the centre of the image).

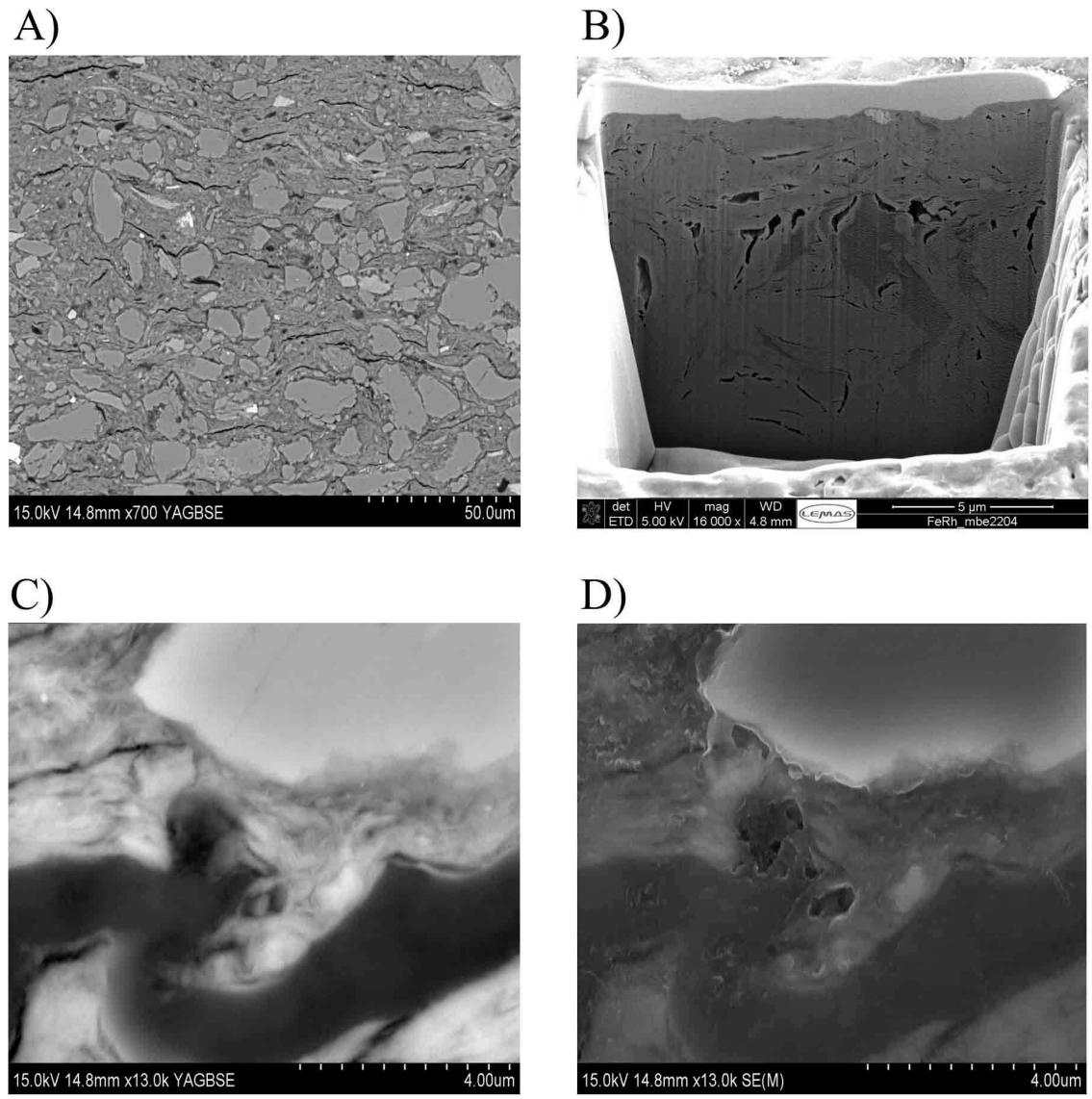

Figure 4.9: The SEM micrographs of Colorado Group shale C10.

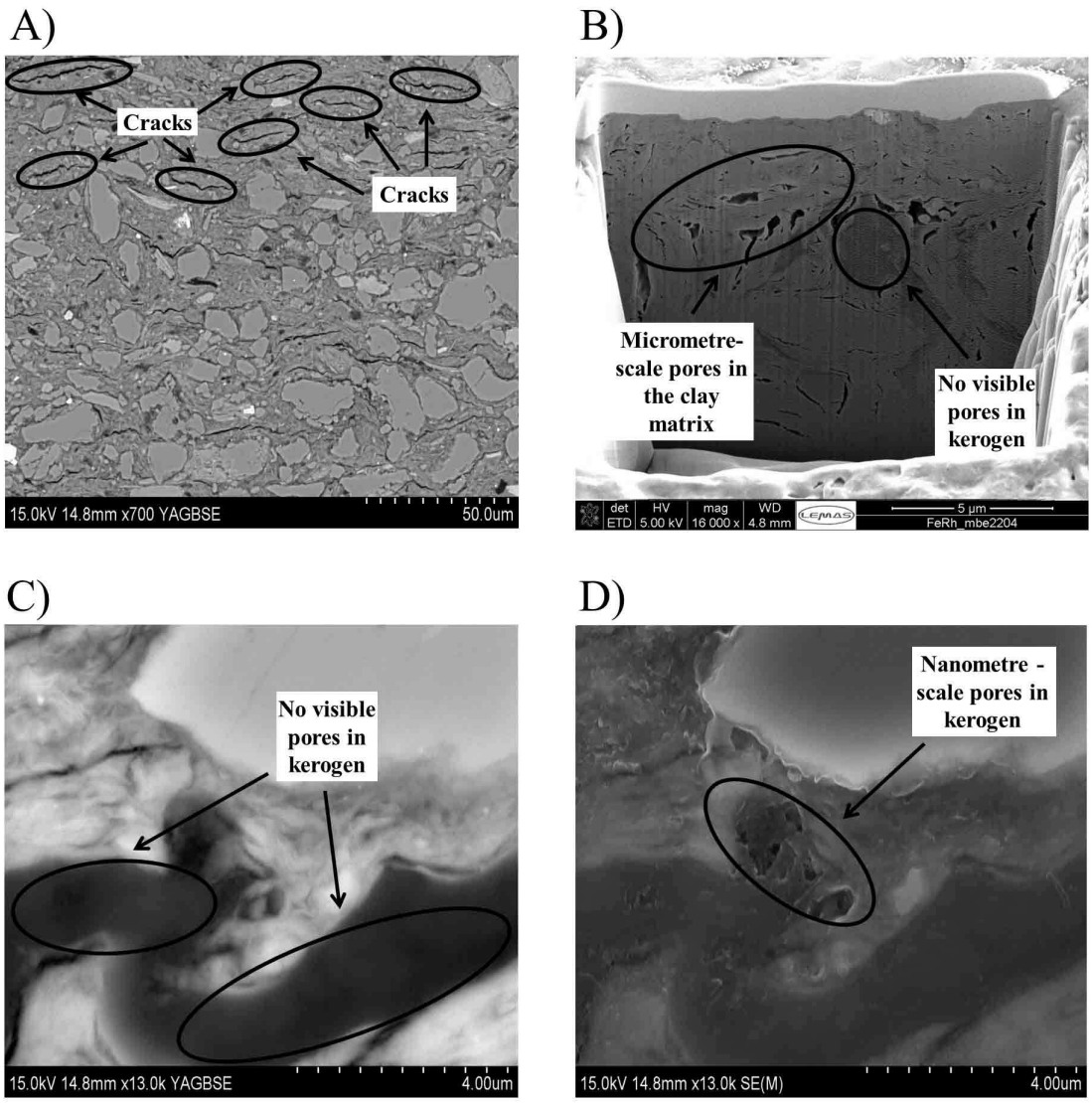

Figure 4.9 (Continued): Labelled SEM micrographs of Colorado Group shale C10.

4.2.2 Pore Size Distribution (PSD) of the Draupne Formation and Colorado Group shales.

The Pore Size Distribution (PSD) of the Draupne Formation and Colorado Group shales were investigated using mercury intrusion porosimetry (MIP), using the procedure described in chapter 2, section 2.8. The MIP technique investigates the pore size distribution of porous materials. The MIP cumulative intrusion curves for the DF shale suite are reported in Figure 4.10, part a. The MIP cumulative intrusion curves for the Colorado Group shales are reported in Figure 4.10, part b. For the Draupne Formation shales, the maximum amount of mercury intrusion ranged from 0.008 $cm^3\ g^{-1}$ to 0.071 $cm^3\ g^{-1}$, with an average value of 0.036 ± 0.024 $cm^3\ g^{-1}$. For the Colorado Group shales, the maximum amount of mercury intrusion ranged from 0.054 $cm^3\ g^{-1}$ to 0.066 $cm^3\ g^{-1}$, with an average of 0.059 ± 0.005 $cm^3\ g^{-1}$. For both sample suites, very little mercury intrusion occurred at low pressure, and the majority of mercury intrusion occurred at pressures of ~50 MPa and above. A pressure value of 50 MPa equates to a pore throat constriction diameter of ~ 35 nm or less (using the Washburn equation). The experimental value of 50 MPa agrees with the findings of Akkutlu *et al*., (2011) who observed that significant mercury intrusion begun in shales at ~ 10 000 psi (= 70 MPa).

The pore size distributions of the Draupne Formation and Colorado Group shales were determined using the Washburn equation (1921). Each of the DF and CG shales has a pore size distribution determined from MIP, which is reported in Figure 4.11. Pore size distributions for the DF and CG shales are predominantly unimodal, with the shale median pore throat range = 10 to 20 nm. The majority of the pore spaces in the DF and CG shales have a diameter of 100 nm or less in the pore size distribution curves. Most of the mercury accessible porosity is within this pore range, and it can be seen from these distributions that the mercury accessible porosity is dominated by pores in the nanometre scale range.

Some of the samples, notably DF4, DF5 and DF6, do have some mercury intrusion occurring at high pore size ranges (10's of microns scale), giving a bimodal pore size distribution. These three samples are from the Magnus oilfield, where the Draupne Formation is slightly siltier in grain size than in other sectors of the northern North Sea basin; the bimodal pore size distribution reflects this mixture of clay and silt size materials.

The pore size distribution curves in Figures 4.11 indicate that the majority of the pores in the DF and CG shales have diameters less than 100 nm. The cumulative mercury intrusion curves (Figure 4.10, above) allow the relative percentage of pores in < 100 nm range to be quantified. In Table 4.1 the amount of mercury intruded in the < 100 nm pore size range is reported. For the Draupne Formation the percentage of pores in the < 100 nm category ranges from 41.3 to 74.3 %, with an average of 56.9 ± 11.6 %. The < 100 nm pore range is a large percentage of the total pores size distribution (PSD), and a significant proportion of the pores in the DF shales have a diameter < 100 nm. For the Colorado Group the percentage of pores in the < 100 nm category ranges from 81.1 % to 97.8 %, with an average of 92.0 ± 4.9 %. The < 100 nm is therefore the majority for each of the pores size distributions (PSD), with the pores in the CG shales being dominated by nanometre scale pores.

The < 100 nm pore range was sub-divided in to smaller pore range categories, and the relative proportion of each determined. This is reported in Table 4.2 and Figure 4.12. For the Draupne Formation, the 10 nm to 3 nm pore category is the dominant pore size within the < 100 nm range. The 10 nm to 3 nm sized pores ranged from 47.0 to 92.6%, with an average of 71.5 ± 17.3 % of the <100 nm pores being in the10 nm to 3 nm category. The pore category of 25 nm to 10 nm is the second most common pore size, with a range of 3.8 to 37.2%, with an average of 15.6 ± 9.9 % of the < 100 nm pores being in the 25 nm to 10 nm category. In total, these two pore categories represent an average of 87.1% of all the pores in the dominant < 100 nm pore range of the shales, and a significant average of 49.9% of all the pores detected by mercury porosimetry. This indicates that half of all the pores in the full pore system in the Draupne Formation shales are < 25nm in size. The dominance of these two pore categories is reported in Figure 4.13.

For the Colorado Group, the pore category of 25 nm to 10 nm is the dominant pore size within the < 100 nm range. The 25 nm to 10 nm sized pores ranges from 21.0 to 67.6 %, with an average of 56.1 ± 13.6 %. The pore category of 10 nm to 3 nm is the second most common pore size, with a range of 23.1 to 69.3 %, with a mean average of 36.0 ± 13.2 %. In total, these two pore categories represent an average of 92.1% of all the pores in the dominant < 100 nm pore range of the shales, and a significant average of 84.7 % of all the pores detected by mercury porosimetry. This means that 84.7 % of all the pores in the full pore system in the Colorado Group shales are < 25nm in size. The dominance of these two pore categories is reported in Figure 4.14.

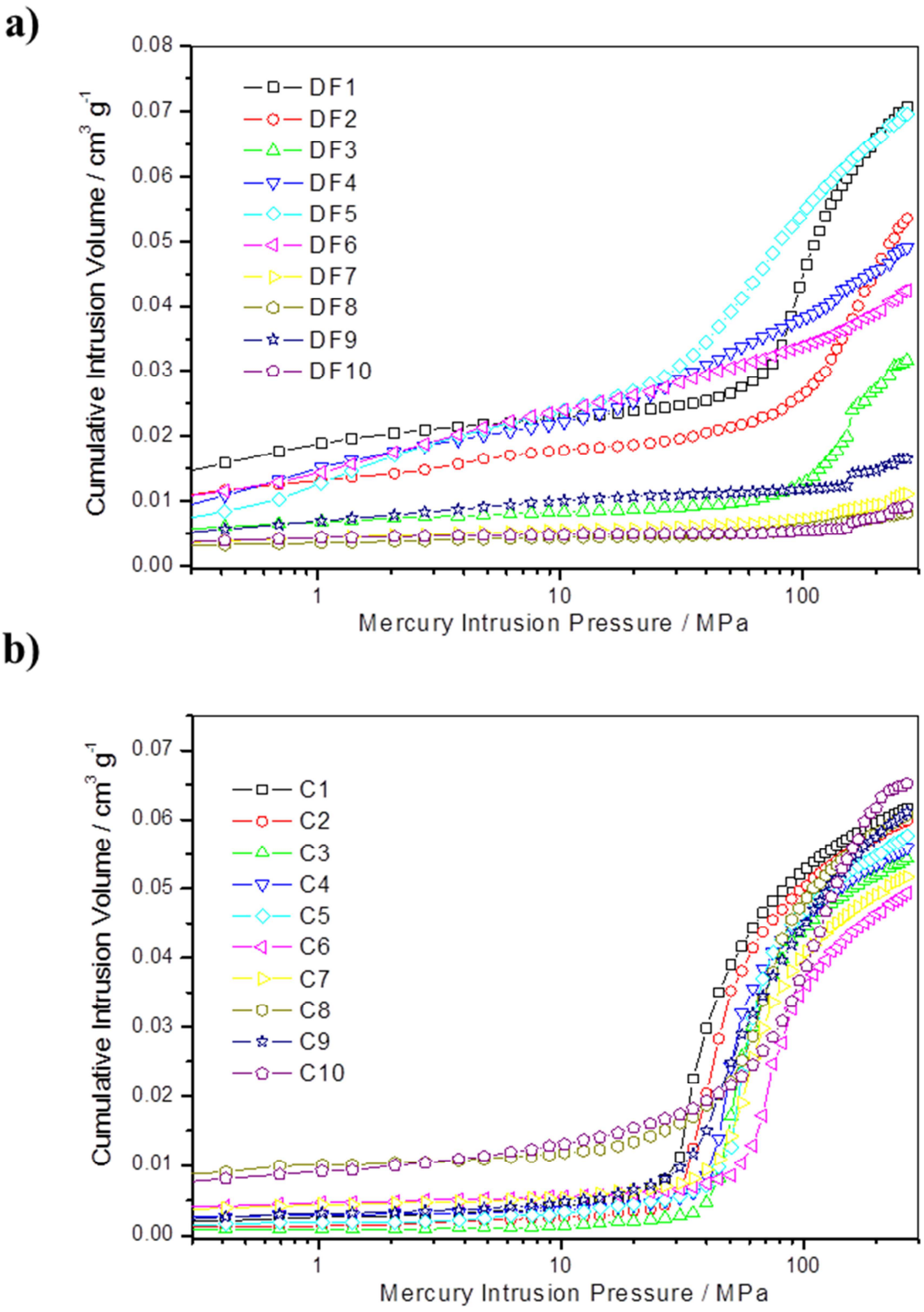

Figure 4.10: Cumulative mercury intrusion curves for a) Draupne Formation shales and b) Colorado Group shales. Very little mercury intrusion occurs at low pressure, with significant mercury intrusion only occurring above 50 MPa pressure.

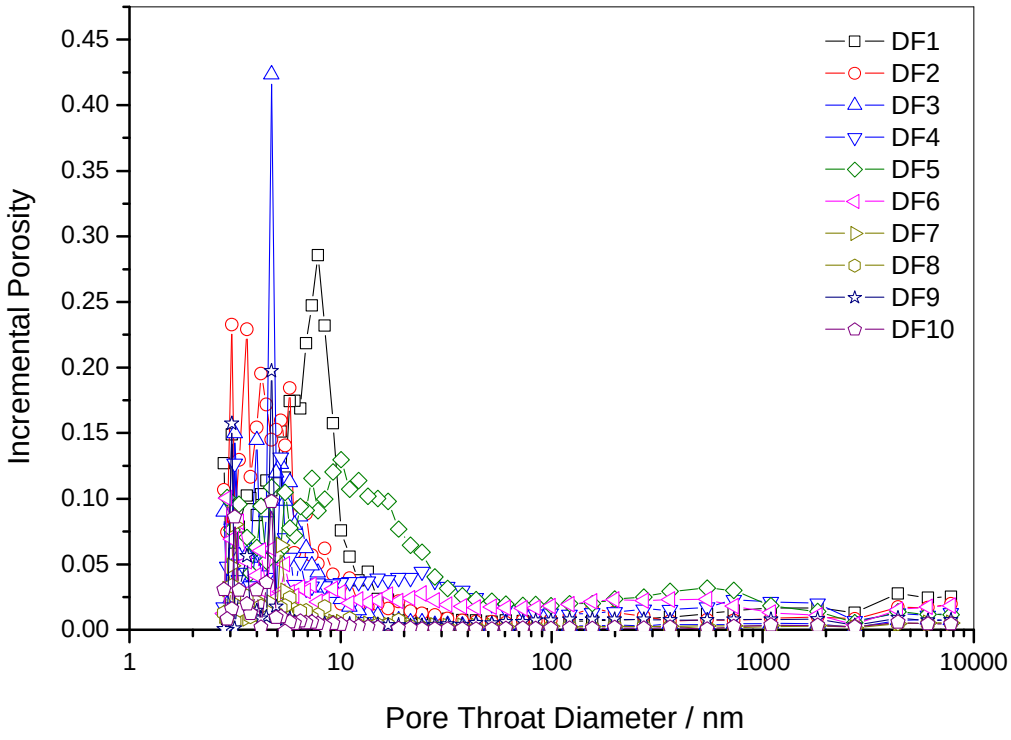

Figure 4.11, part a): Pore Size Distribution (PSD) curves for the Draupne Formation shales. Nearly all of the mercury intrusion occurs in pores below 10 nm in diameter, with very little mercury intrusion occurring in pores > 100 nm.

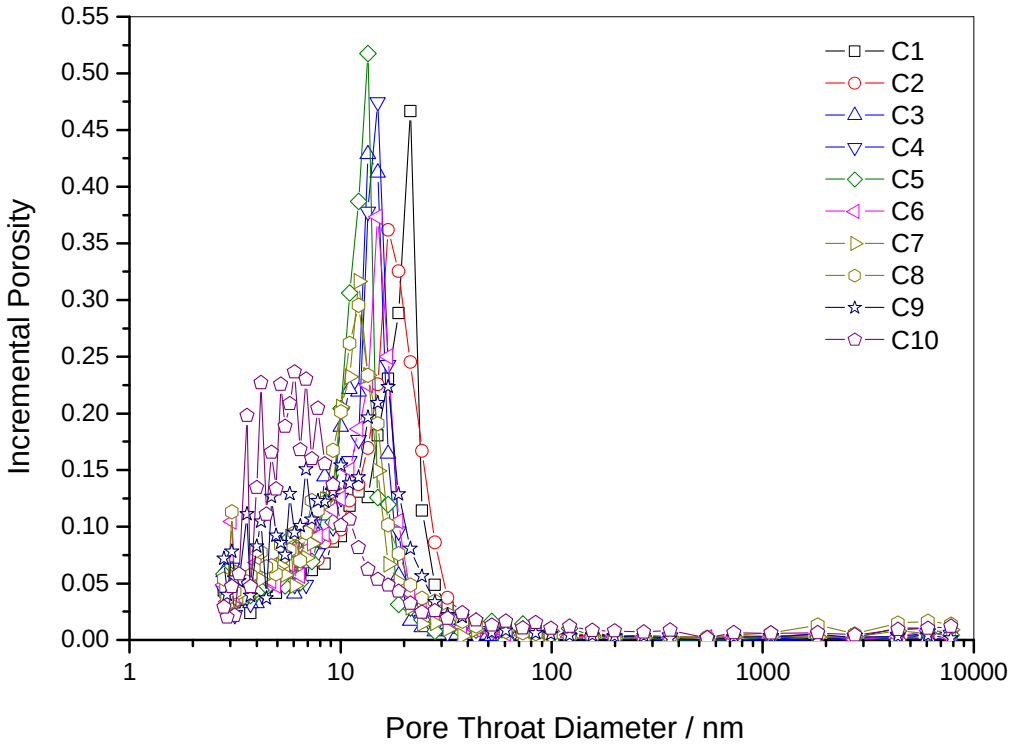

Figure 4.11, part b): Pore Size Distribution (PSD) curves for the Colorado Group shales. Nearly all of the mercury intrusion occurs in pores below 30 nm in diameter, with very little mercury intrusion occurring in pores > 100 nm.

Table 4.1: Percentage of total mercury intruded in the sub-100 nm pore range.

Sample	Mercury intruded in sub-100 nm pores / $cm^3\ g^{-1}$	Percentage of total PSD / %
DF1	0.048	68.3
DF2	0.036	67.6
DF3	0.024	74.3
DF4	0.028	56.6
DF5	0.047	67.3
DF6	0.019	45.8
DF7	0.006	52.3
DF8	0.004	47.9
DF9	0.007	41.3
DF10	0.004	47.7
C1	0.0579	94.0
C2	0.063	95.3
C3	0.053	97.8
C4	0.052	93.7
C5	0.055	95.0
C6	0.051	93.7
C7	0.046	89.8
C8	0.054	86.5
C9	0.057	93.0
C10	0.053	81.1

a)

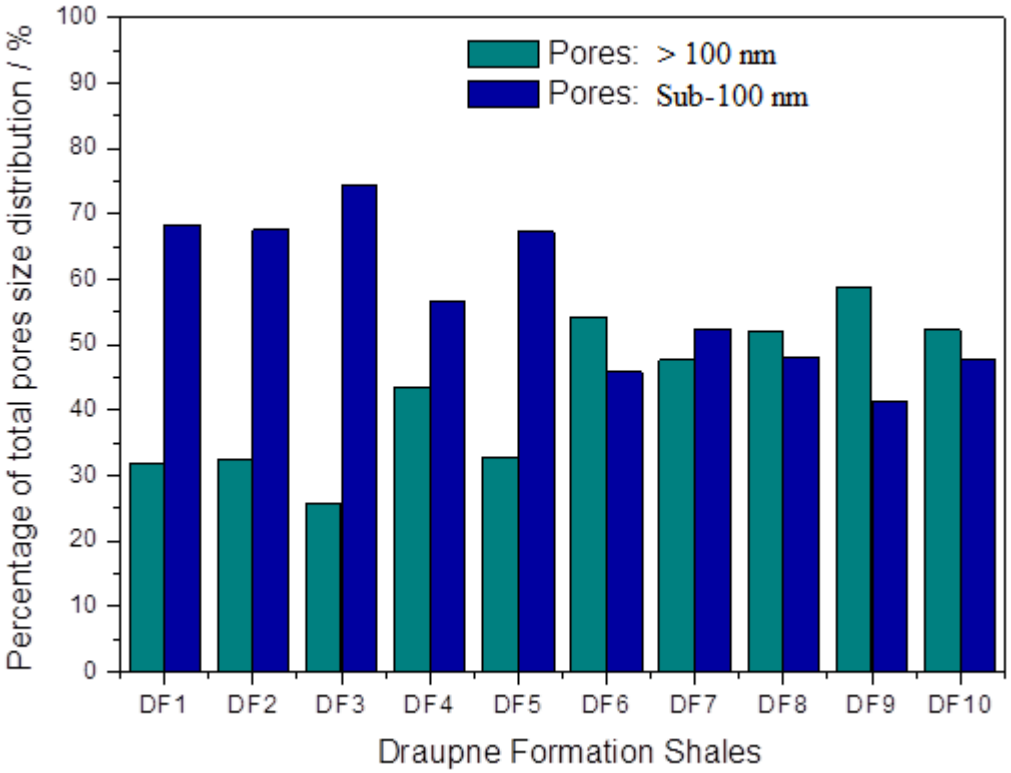

b)

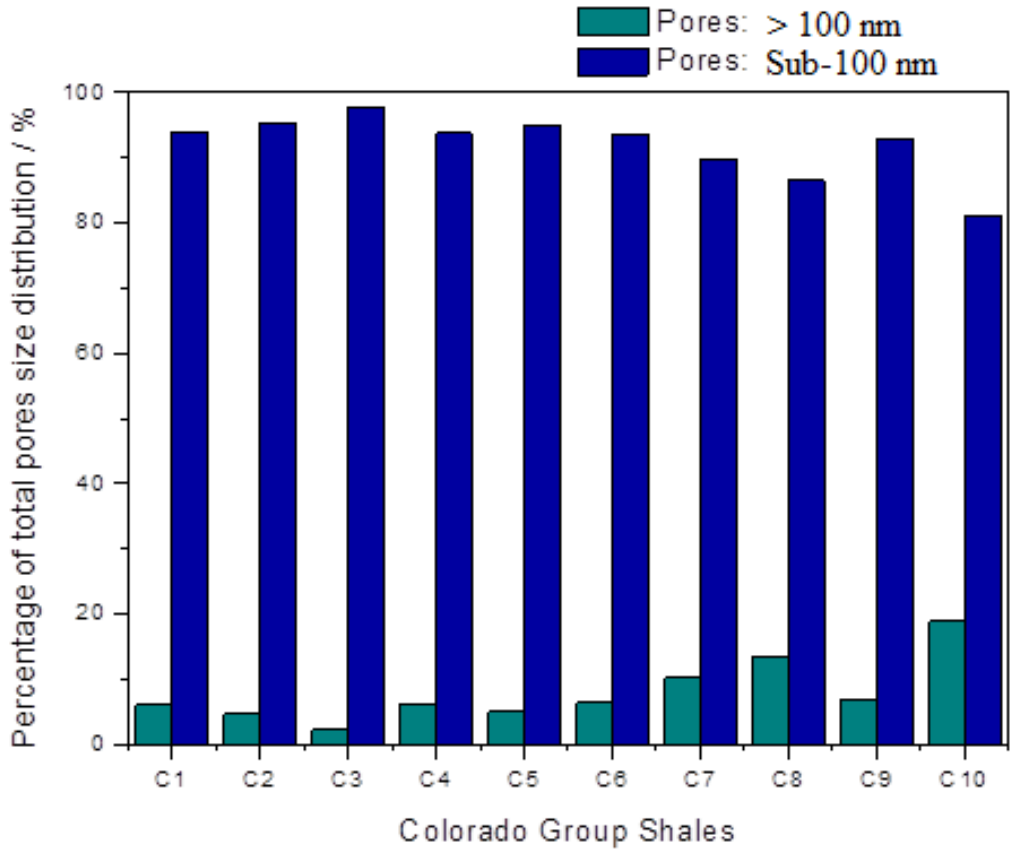

Figure 4.12: Majority of the pores in the Draupne Formation shale (a) and Colorado Group (b) shales have a diameter less than 100nm.

Table 4.2: Relative proportion of each pore range below 100 nm

Sample	Depth / m	Pore Range 100 nm to 50nm / %	Pore Range 50nm to 25nm / %	Pore Range 25nm to 10nm / %	Pore Range 10nm to 3nm / %
DF1	2117.8	1.9	2.9	13.2	82.09
DF2	2325	2.3	3.9	10.3	83.52
DF3	2978.5	1.5	2.4	7.6	88.54
DF4	3124.7	7.8	19.5	25.7	47.04
DF5	3375.32	5.6	11.7	37.2	45.53
DF6	3400.4	11.1	16.0	21.2	51.69
DF7	4132.95	5.2	7.9	12.4	75.39
DF8	4608.4	4.3	3.9	16.1	75.79
DF9	4707.7	10.3	8.2	8.5	73.03
DF10	4780.7	2.0	1.5	3.8	92.64
C1	505.3	1.9	10.9	64.9	23.1
C2	506.55	1.8	14.8	59.9	23.6
C3	541	0.9	2.1	65.4	31.6
C4	546.3	1.0	2.7	67.6	28.8
C5	561.5	1.8	3.1	64.2	30.8
C6	642.1	1.3	4.8	60.5	33.5
C7	647.57	1.3	3.2	56.5	39.0
C8	651.75	1.7	6.5	53.3	38.5
C9	675.02	1.8	7.8	48.8	41.7
C10	684.61	3.4	6.3	21.0	69.3

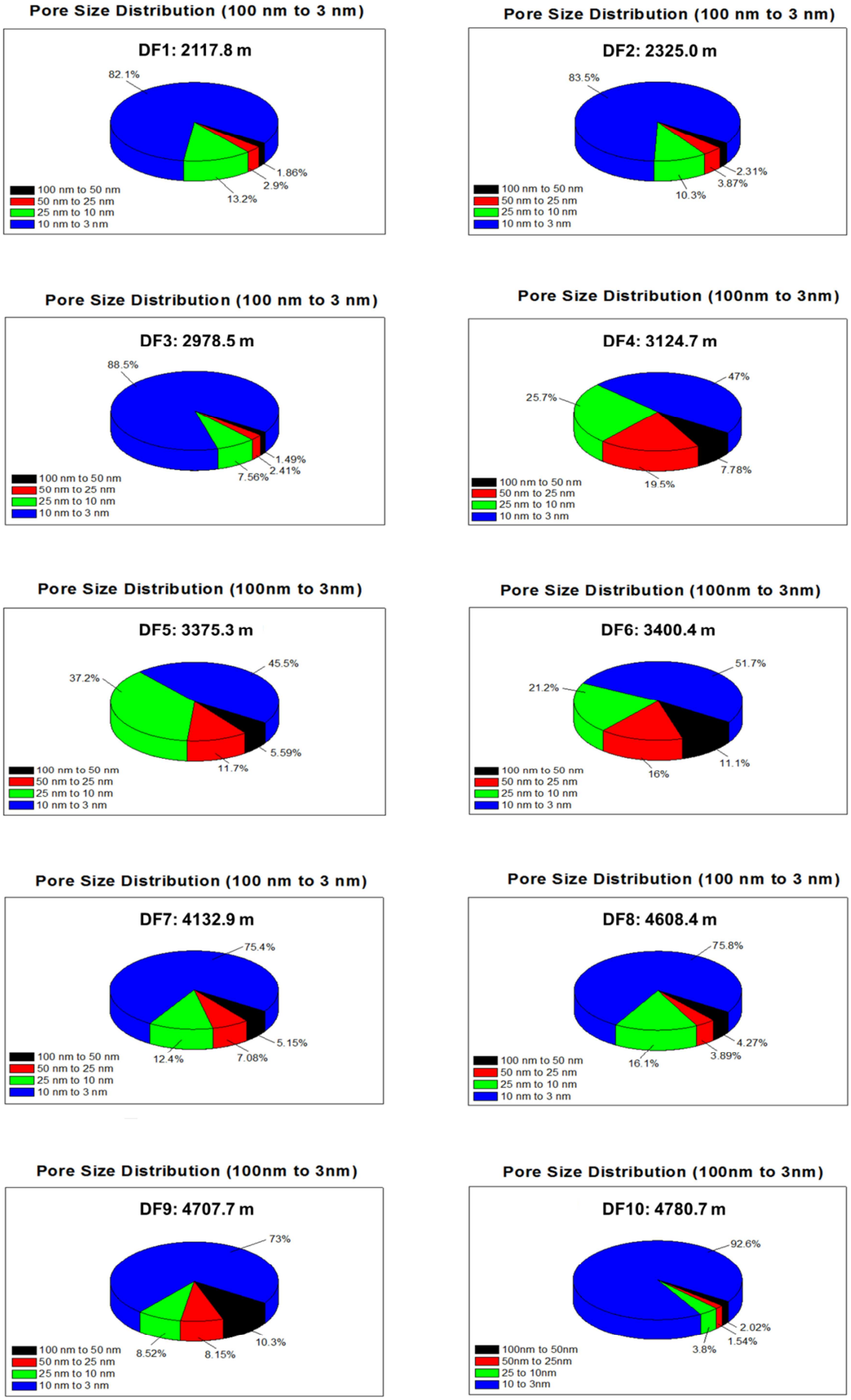

Figure 4.13: Relative distribution of pore sizes within the <100 nm pore range. The 10 nm to 3nm range is the dominant pore size in the < 100nm range for the Draupne Formation.

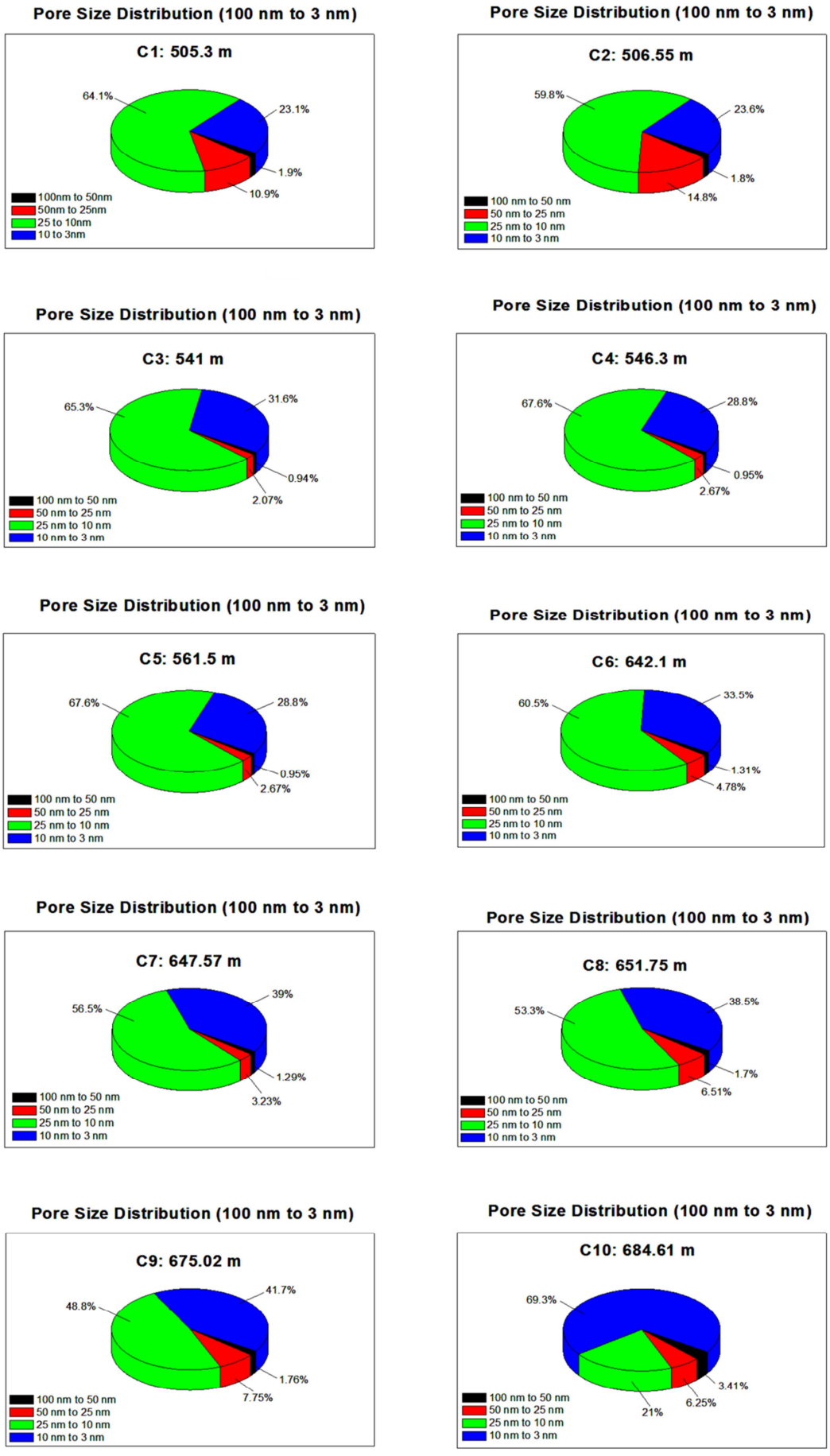

Figure 4.14: The nanometre scale pores of the Colorado Group are dominated by sub-25 nm scale pores.

4.2.3 Pore volumes of the Draupne Formation and Colorado Group shales.

The pore volumes of the Draupne Formation and Colorado Group shales were determined using the mercury intrusion porosimetry and gas adsorption analysis. The total pore volume and the Hg-macropore volume of the DF and CG shales were determined from the MIP intrusion curves (Figures 4.10), and are listed in Table 4.3. The total pore volume is the maximum pore space present, and includes both the open pores (that are accessible to probe molecules), and closed pores (that are completely isolated and inaccessible). The total pore volume of the Draupne Formation shales had a range of 0.0210 to 0.0828 $cm^3\ g^{-1}$, with an average value of 0.0517 ± 0.0219 $cm^3\ g^{-1}$. The total pore volume of the Colorado Group shales had a range of 0.0630 to 0.0980 $cm^3\ g^{-1}$, with an average value of 0.0766 ± 0.0096 $cm^3\ g^{-1}$. This finding indicates that the total pore volume of the Colorado Group shales is larger than that of the Draupne Formation shales.

The Hg-macropore volume is the shale pore volume that is detectable by mercury intrusion, but is not measurable by gas adsorption methods. The Hg-macropore volume is the volume of pores with diameters greater than 100 nm. These larger Hg-macropores are intruded with mercury at lower pressures to reduce the damage caused to the pore structures at higher intrusion pressures (Giesche, 2006). The Hg-macropore volume of the Draupne Formation shales had a range of 0.0045 to 0.0262 $cm^3\ g^{-1}$, with an average value of 0.0153 ± 0.0093 $cm^3\ g^{-1}$. The Hg-macropore volume of the Colorado Group shales had a range of 0.002 $cm^3\ g^{-1}$ to 0.0147 $cm^3\ g^{-1}$, with an average of 0.0061 ± 0.0036 $cm^3\ g^{-1}$.

Low pressure gas adsorption analysis was used to investigate the nanometre scale pore structure of the Draupne Formation and Colorado Group shales. Gas adsorption analysis can access the smallest pores present in shales, allowing the pore volume be determined (Greg and Sing, 1982). The condensation point of gaseous CO_2 is -78^oC, and CO_2 adsorption isotherms performed at this temperature result in the formation of solid phase CO_2 in the confined pore spaces of the porous substance.

A representative gas adsorption-desorption isotherm for the DF1 shale, using CO_2 at -78^oC (195K) is reported Figure 4.15. The DF1 shale has a Type I / Type II hybrid adsorption curve, with an initially steep uptake in the low pressure region, followed by a shallower uptake at higher pressure, before failing to reach a horizontal plateau at 1000 mbar pressure. The shape of the adsorption isotherm indicates that the shale pore structure is heterogeneous, with the presence of a pore size distribution. The Type I aspect of the adsorption isotherm indicates the presence of micropores (< 2 nm), and the Type II nature of the adsorption isotherm indicates the presence of macropores (> 50 nm).

The hysteresis loop of the DF1 isotherm is categorised as a H4 desorption curve, using the de Boer/IUPAC system. This is because there is no characteristic flat plateau at high relative pressure (as seen in H1 and H2 curves), and the adsorption – desorption curve does not rapidly curve upwards at high relative pressure (as seen in H3 curves). The H4 hysteresis loop indicates that the adsorbent (i.e. shale) contains significant microporosity, which traps and retains the adsorbate (i.e. CO_2) within the micropore structure when the pressure is decreased.

The Draupne Formation and Colorado Group shales were analysed using CO_2 adsorption isotherms at -78^oC. Each sample was measured twice for reproducibility. In Figure 4.16, part a), all of the adsorption isotherms for the DF shales are reported. In Figure 4.16, part b), all of the adsorption isotherms for the Colorado Group shales are reported. The adsorption isotherms for the Draupne Formation and Colorado Group shales are very similar in shape, indicating that a common porous structure is shared. The isotherms do not overlap each other, instead having a distribution of adsorption uptakes.

The sorption pore volumes of the Draupne Formation and Colorado Group shales are listed in Table 4.4. The sorption pore volumes are determined from the maximum adsorption uptake of CO_2 at -78^oC by the Draupne Formation and Colorado Group shales. The sorption pore volumes of the DF shales have a range of 0.0081 to 0.0296 $cm^3\ g^{-1}$, with an average of 0.0171 ± 0.007 $cm^3 g^{-1}$. The sorption pore volumes of the CG shales have a range of 0.0141 to 0.0234 $cm^3\ g^{-1}$, with an average of 0.0184 ± 0.0031 $cm^3 g^{-1}$. The average sorption pore volumes of both the Draupne Formation and Colorado Group shales are very similar (0.0171 mmol g^{-1} vs 0.0184 mmol g^{-1}), indicating that these shales have similar pore structures. The sorption pore volume of the DF shales decreases as burial depth increases, as reported in Figure 4.17, part a. The correlation is very strong, with a correlation coefficient of $R^2 = 0.90$. For the Colorado Group shales, there is no apparent correlation between sorption pore volume and changing burial depth, as reported in Figure 4.17, part b.

The sorption pore volume of the DF shales increases as TOC content increases, as reported in Figure 4.18, part a). The correlation coefficient is $R^2 = 0.75$. The sorption pore volume of the CG shales shows an excellent negative correlation to organic matter content (TOC). The sorption pore volume decreases as TOC increases, as reported in Figure 4.18, part b). The correlation coefficient is $R^2 = 0.94$. To account for the influence of organic richness on the pore volume of shales, the sorption pore volumes are normalised to the TOC content in Figure 4.19. In part a), the strong negative correlation between TOC normalised sorption pore volume and vitrinite reflectance is reported. The correlation coefficient is $R^2 = 0.88$. In Figure 4.19 part b), the strong negative correlation between TOC normalised sorption pore volume and Hydrogen Index is reported. The correlation coefficient is $R^2 = 0.75$.

The sorption pore volume of the Draupne Formation shales exhibits a strong correlation to maturity. In Figure 4.20 part a), the strong negative correlation between sorption pore volume of shale and vitrinite reflectance is reported. The correlation coefficient is $R^2 = 0.90$. In Figure 4.20 part b), the strong negative correlation between sorption pore volume of shale and Hydrogen Index is reported. The correlation coefficient is $R^2 = 0.87$. A high level of maturity is represented by a low Hydrogen Index, as the atomic hydrogen content in the kerogen is reduced when maturation generates liquid hydrocarbons. Thermally mature shales are often subjected to significant mechanical compaction from overbearing strata, which may contribute to the reduction of the pore volume. Therefore, to account for the influence of compaction on pore volume reduction, the sorption pore volumes are normalised for burial depth. In Figure 4.21 part a), a strong negative correlation between depth normalised sorption pore volume and vitrinite reflectance is observed for the Draupne Formation shales. The correlation coefficient is $R^2 = 0.90$. However, the sorption pore volumes of the Colorado Group shales have no observable correlation to maturity. The normalised sorption pore volumes also show no observable correlation to maturity. This is agrees with the assessment of the Colorado Group shales as being thermally immature.

The micropore volumes of the Draupne Formation and Colorado Group shales were determined using CO_2 adsorption isotherms at 0^oC (= 273K). Under these conditions, CO_2 condenses in micropores with diameters less than 0.7 nm (Gregg and Sing, 1982). Characterisation of the micropores is performed using CO_2 adsorption isotherms in the relative pressure range of $p/p^o = 0$ to 0.03 (0 to 1 bar). The CO_2 adsorption isotherms for the DF shales are reported in Figure 4.22, part a). The gas adsorption isotherms for the CG shales are reported in Figure 4.22, part b). Each sample was repeated twice for precision. All the CO_2 at 0^oC isotherms are Type I/II is the IUPAC classification scheme, and do not plateau at 1000 mbar pressure. The isotherms all have the same shape, and do not overlap each, instead having a distribution of adsorption uptakes. The shale CO_2 isotherms at 0^oC have similar shaped isotherms (Type I/II) as the CO_2 at -78^oC isotherms. This indicates that the CO_2 is measuring the same heterogeneous pore size distribution of micropores and macropores.

The micropore volumes of the Draupne Formation and the Colorado Group shales were determined using the Dubinin-Radushkevic (D-R) equation. The D-R equation has been applied to the all of the CO_2 at 0^oC shale isotherms, and an example of a D-R plot for shale DF3 is reported in Figure 4.23. The D-R plot is an excellent straight line, and the y-axis intercept value is used to calculate the micropore volume. According to D-R theory, a straight line indicates that a Gaussian curve distribution of pore widths is present (for the micropore range of pores, < 2 nm).

The D-R plots of the Draupne Formation and Colorado Group shale isotherms are reported in Figure 4.24 and Figure 4.25. The D-R plots are all excellent straight lines, which indicate the shales have the same Gaussian distribution of shale micropore widths. The D-R micropore volumes for the Draupne Formation and Colorado Group shales are listed in Table 4.5. For the DF shales, the D-R micropore volumes have a range of 0.00557 to 0.01240 cm^3g^{-1}, with an average of 0.00901 ± 0.0026 cm^{-3} g^{-1}. For the CG shales, the D-R micropore volumes have a range of 0.0049 to 0.0092 cm^3g^{-1}, with an average of 0.0066 ± 0.0014 cm^{-3} g^{-1}. The Draupne Formation shales have similar average micropore volumes to those of the Colorado Group shales. These micropore volumes for shales are lower than the typical value for microporous activated carbons, ~ 0.2 cm^3 g^{-1} (Bell *et al*., 2011).

The D-R micropore volume of the DF shales is positively correlated to TOC content, as reported in Figure 4.27. The correlation coefficient is $R^2 = 0.81$. This suggests that the primary location for micropores is the organic matter component of the shales. Conversely, the micropore volumes of the Colorado Group are negatively correlated to the TOC content, as reported in Figure 4.28. The correlation coefficient is $R^2 = 0.80$.

The D-R micropore volumes of the Draupne Formation shales exhibit a strong correlation to maturity, as reported in Figure 4.29. The correlation coefficient is R^2 = 0.73. Conversely, for the Colorado Group shales, the D-R micropore volumes do not change with maturity (either VRc or Hydrogen Index). To account for the influence of burial compaction on pore volume of the Draupne Formation shales, the D-R micropore volumes are normalised to burial depth in Figure 4.30. In part a), the strong negative correlation between depth normalised micropore volumes and vitrinite reflectance is reported. The correlation coefficient is $R^2 = 0.96$. For the Colorado Group shales, in Figure 4.30 part b), no observable correlation is present.

A summary of the pore volume data is listed in Table 4.6 and Table 4.7. These pore volumes were determined using the experimental methods outlined above and the equations in chapter 1. The Draupne Formation shales have a range of 0.056 to 0.0124 $cm^3 g^{-1}$ for the < 0.7 nm pore volumes, with an average of 0.0090 ± 0.0026 $cm^3 g^{-1}$. This accounts for 19.4 % of the total pore volume. The 0.7 to 100 nm pore volumes had a range of 0.0004 to 0.0198 $cm^3 g^{-1}$, with an average of 0.0080 ± 0.0059 $cm^3 g^{-1}$. This accounts for 14.6 % of the total pore volume. The > 100 nm pore volumes had a range of 0.0045 to 0.0262 $cm^3 g^{-1}$, with an average of 0.0153 ± 0.0092 $cm^3 g^{-1}$. This accounts for 27.9 % of the total pore volume. For the Colorado Group, the < 0.7 nm pore volumes had a range of 0.0047 to 0.0092 $cm^3 g^{-1}$, with an average of 0.0066 ± 0.0014 $cm^3 g^{-1}$. This accounts for 8.4 % of the total pore volume. The 0.7 to 100 nm pore volumes had a range of 0.0094 to 0.0148 $cm^3 g^{-1}$, with an average of 0.0118 ± 0.0021 $cm^3 g^{-1}$. This accounts for 15.6 % of the total pore volume. The > 100 nm pore volumes had a range of 0.0020 to 0.0147 $cm^3 g^{-1}$, with an average of 0.0061 ± 0.0036 $cm^3 g^{-1}$. This accounts for 7.8 % of the total pore volume.

Table 4.3: The total pore volumes and Hg-macropore volumes of the Draupne Formation and Colorado Group shales.

Sample	Burial Depth / m	Total Pore Volume / $cm^3 g^{-1}$	Hg-Macropore Volume (> 100 nm) / $cm^3 g^{-1}$
DF1	2117.8	0.0828	0.0236
DF2	2325	0.0648	0.0184
DF3	2978.5	0.0505	0.0086
DF4	3124.7	0.0818	0.0244
DF5	3375.32	0.0619	0.0262
DF6	3400.4	0.0580	0.0258
DF7	4132.95	0.0210	0.0057
DF8	4608.4	0.0304	0.0045
DF9	4707.7	0.0341	0.0106
DF10	4780.7	0.0315	0.0049
C1	505.3	0.0791	0.0052
C2	506.55	0.0774	0.0048
C3	541	0.0630	0.0020
C4	546.3	0.0707	0.0041
C5	561.5	0.0805	0.0042
C6	642.1	0.0680	0.0044
C7	647.57	0.0738	0.0062
C8	651.75	0.0724	0.0098
C9	675.02	0.0827	0.0059
C10	684.61	0.0980	0.0147

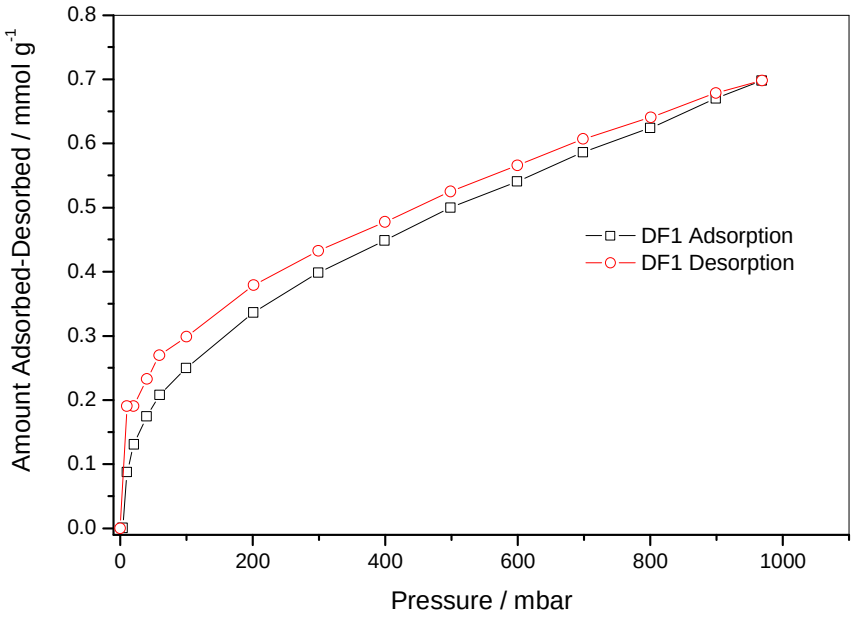

Figure 4.15: The DF shale exhibits a Type I/II hybrid adsorption isotherm curve, with a H4 desorption curve, as defined by the IUPAC isotherm system (see Chapter 1 for more details).

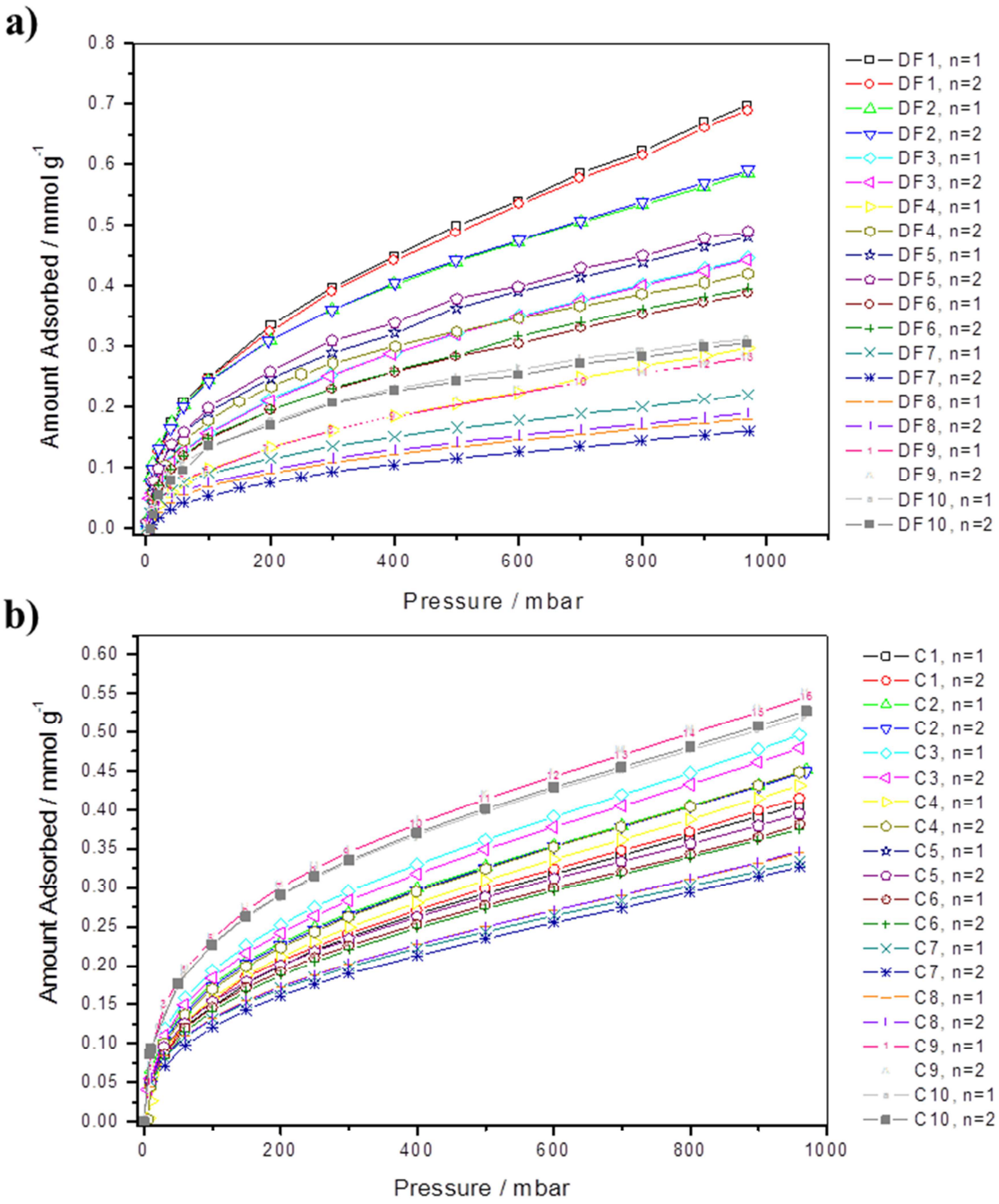

Figure 4.16: CO_2 at -78°C low pressure shale isotherms of the Draupne Formation (in part A), and the Colorado Group (in part B).

Table 4.4: Gas sorption pore volumes of the Draupne Formation and Colorado Group shales.

Sample	Maximum CO_2 adsorption / mmol g^{-1}	Sorption Pore Volume / cm^3 g^{-1}	Depth Normalised Sorption Pore Volume / cm^3 g^{-1} m^{-1}	TOC Normalised Sorption Pore Volume / cm^3 g^{-1} $\%^{-1}$
DF1	0.694 ± 0.006	0.0296 ± 0.0003	0.0000140	0.00347
DF2	0.589 ± 0.004	0.0251 ± 0.0001	0.0000108	0.00242
DF3	0.446 ± 0.002	0.0190 ± 0.0001	0.0000064	0.00643
DF4	0.421 ± 0.000	0.0180 ± 0.0000	0.0000058	0.00235
DF5	0.488 ± 0.008	0.0208 ± 0.0003	0.0000062	0.00194
DF6	0.393 ± 0.006	0.0168 ± 0.0002	0.0000049	0.00217
DF7	0.191 ± 0.042	0.0081 ± 0.0018	0.0000020	0.00116
DF8	0.185 ± 0.006	0.0079 ± 0.0002	0.0000017	0.00139
DF9	0.285 ± 0.003	0.0122 ± 0.0001	0.0000026	0.00218
DF10	0.310 ± 0.006	0.0132 ± 0.0002	0.0000028	0.00216
C1	0.411 ± 0.006	0.0175 ± 0.00024	0.0000346	0.00689
C2	0.450 ± 0.002	0.0192 ± 0.00007	0.0000379	0.00765
C3	0.488 ± 0.012	0.0208 ± 0.00052	0.0000384	0.00846
C4	0.440 ± 0.012	0.0188 ± 0.00052	0.0000344	0.00777
C5	0.395 ± 0.000	0.0168 ± 0.00000	0.0000299	0.00533
C6	0.378 ± 0.004	0.0161 ± 0.00017	0.0000251	0.00483
C7	0.330 ± 0.005	0.0141 ± 0.00021	0.0000218	0.00383
C8	0.346 ± 0.001	0.0148 ± 0.00005	0.0000227	0.00451
C9	0.548 ± 0.003	0.0234 ± 0.00015	0.0000347	0.01141
C10	0.524 ± 0.004	0.0224 ± 0.00019	0.0000327	0.01109

(c.f. density of CO_2 at -78°C = 1.032 g cm^{-3}. Each sample was measured twice for repeatability).

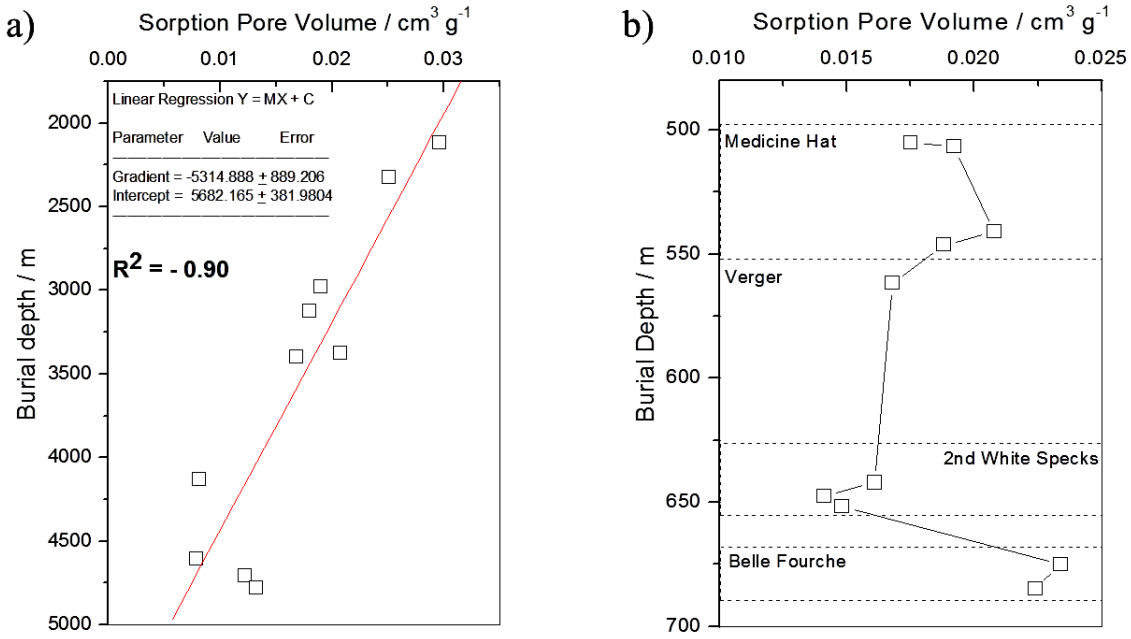

Figure 4.17: Sorption Pore Volumes against burial depth. For the Draupne Formation, the sorption pore volumes decrease as burial depth increases. For the Colorado Group shales, there is no apparent correlation between sorption pore volumes and changing burial depth.

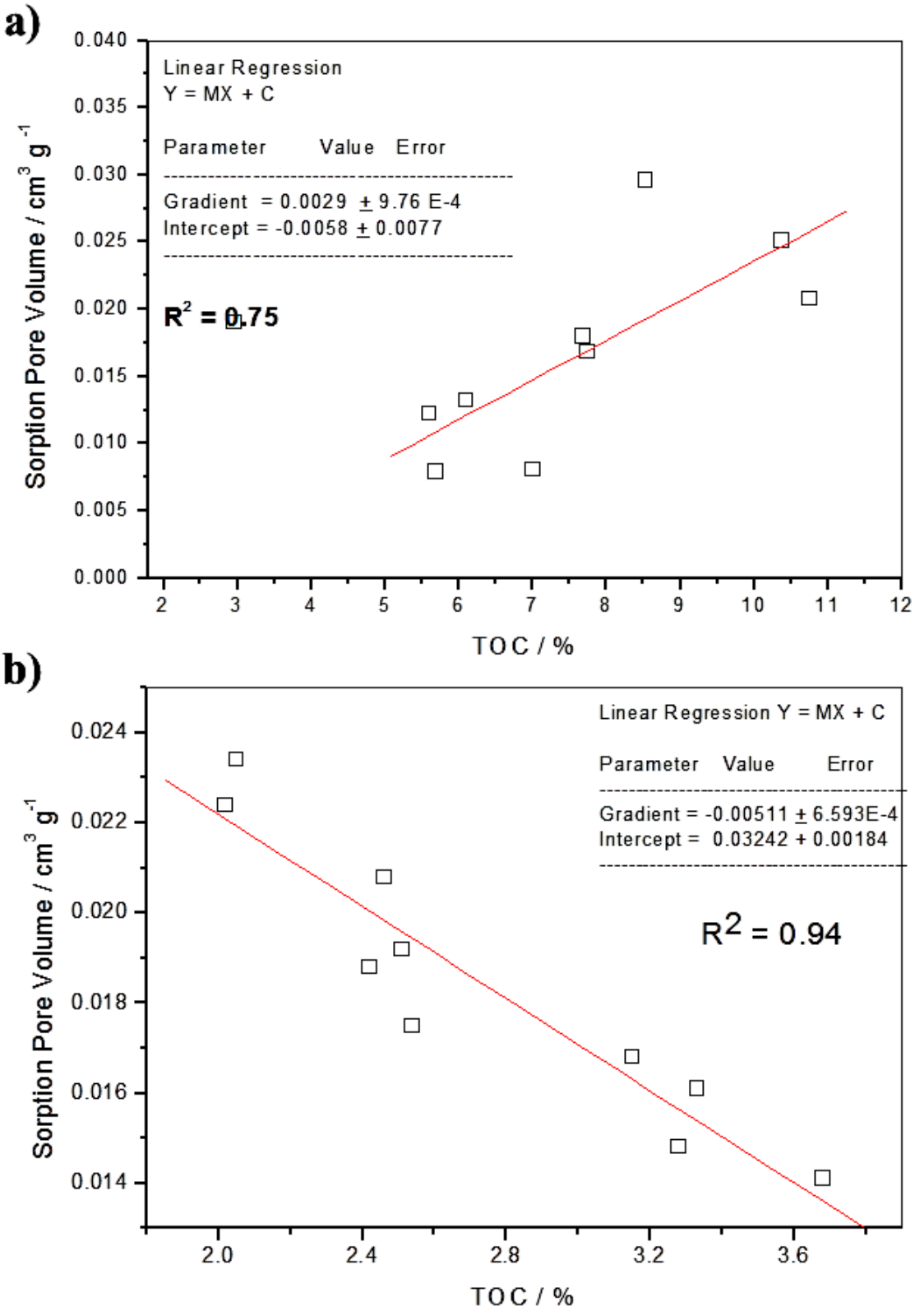

Figure 4.18: Sorption Pore Volume and TOC. In part a), there is medium strength positive correlation of R^2 = 0.75 for the Draupne Formation shales. In part b), an excellent negative correlation exists between sorption pore volume and TOC content for the Colorado Group shales.

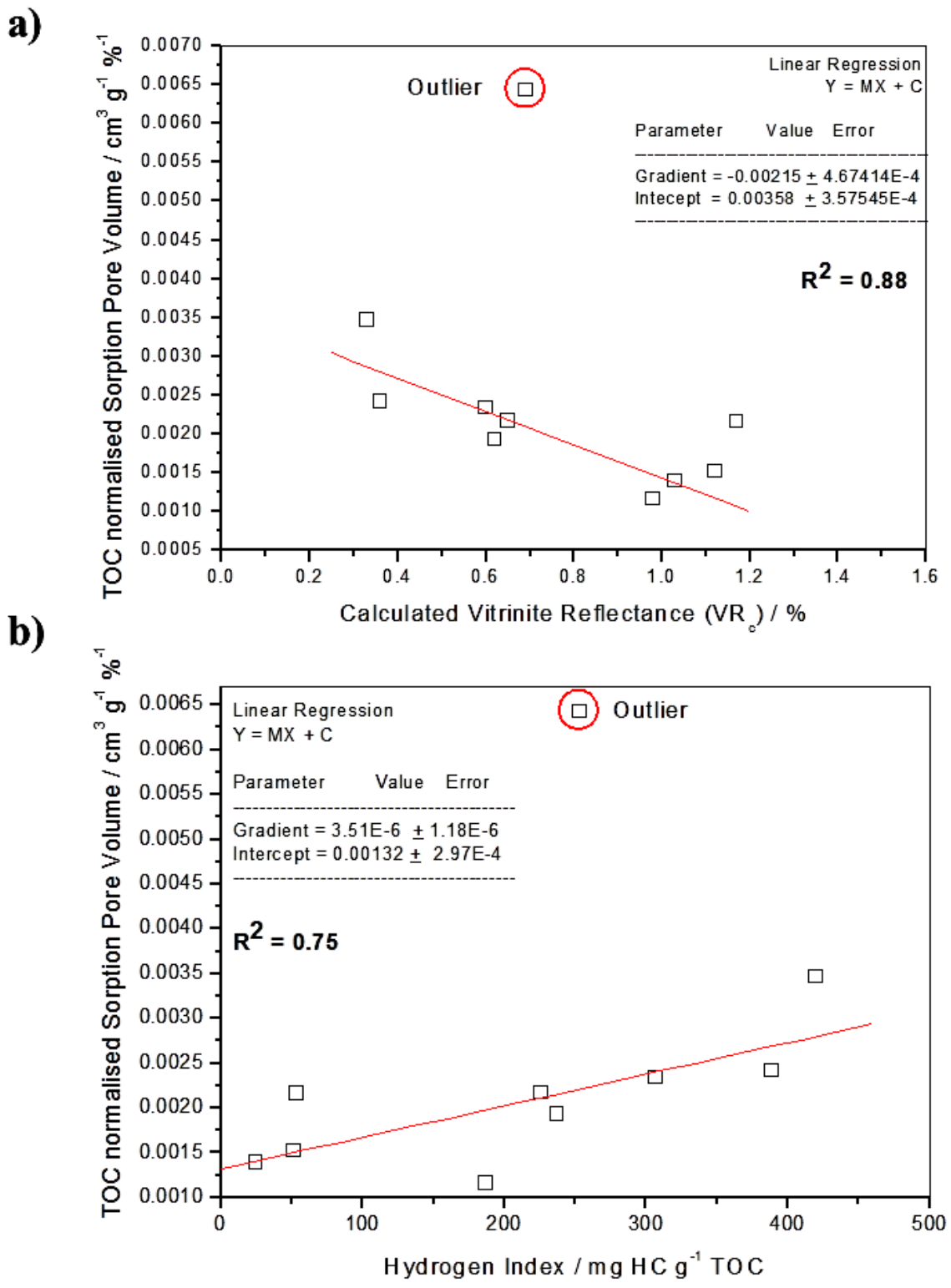

Figure 4.19: Plot of TOC normalised sorption pore volume vs maturity for the Draupne Formation shales. In part a), a strong negative correlation between TOC normalised sorption pore volume of DF shale and vitrinite reflectance. In part b), the TOC normalised sorption pore volume decreases as Hydrogen Index decreases (= maturity increases).

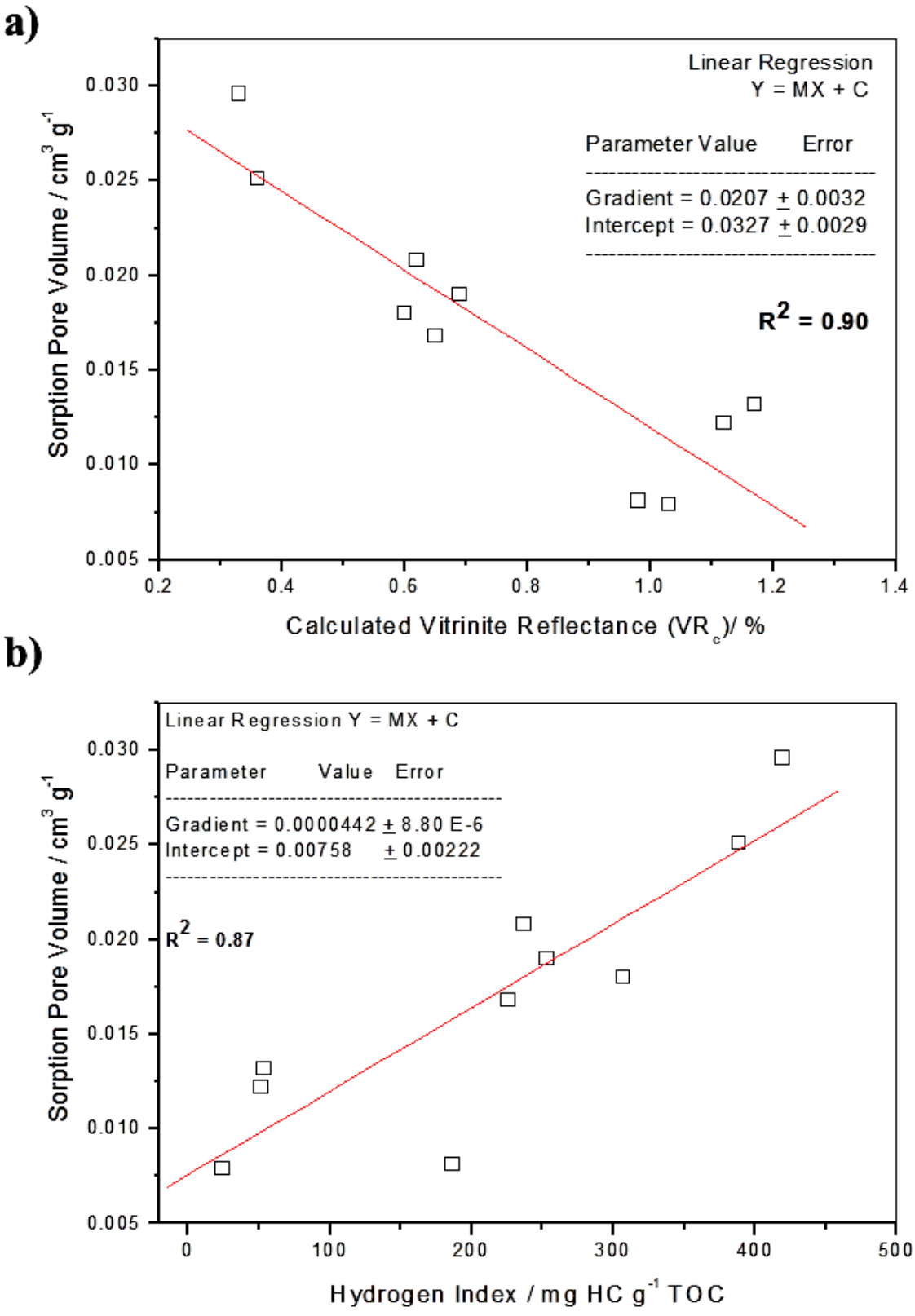

Figure 4.20: Plot of sorption pore volume vs maturity for the Draupne Formation shales. In part a), a strong negative correlation between gas sorption pore volume of DF shale and vitrinite reflectance. In part b), the sorption pore volume decreases as Hydrogen Index decreases (= maturity increases).

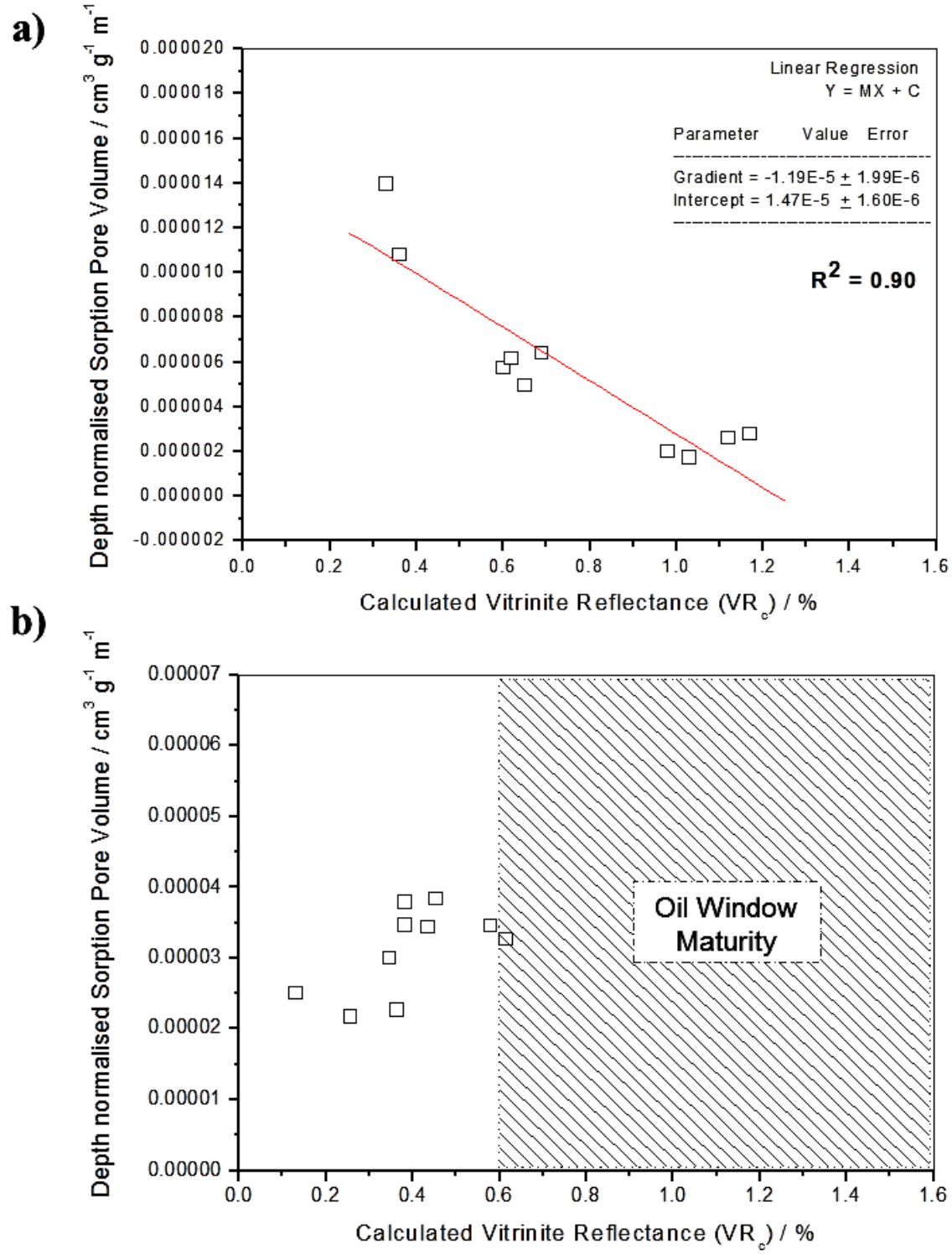

Figure 4.21: Plot of depth normalised sorption pore volume against maturity for the Draupne Formation and Colorado Group shales. In part a), a strong negative correlation between normalised sorption pore volume of DF shale and vitrinite reflectance. In part b), no observable correlation is present for the Colorado Group shales.

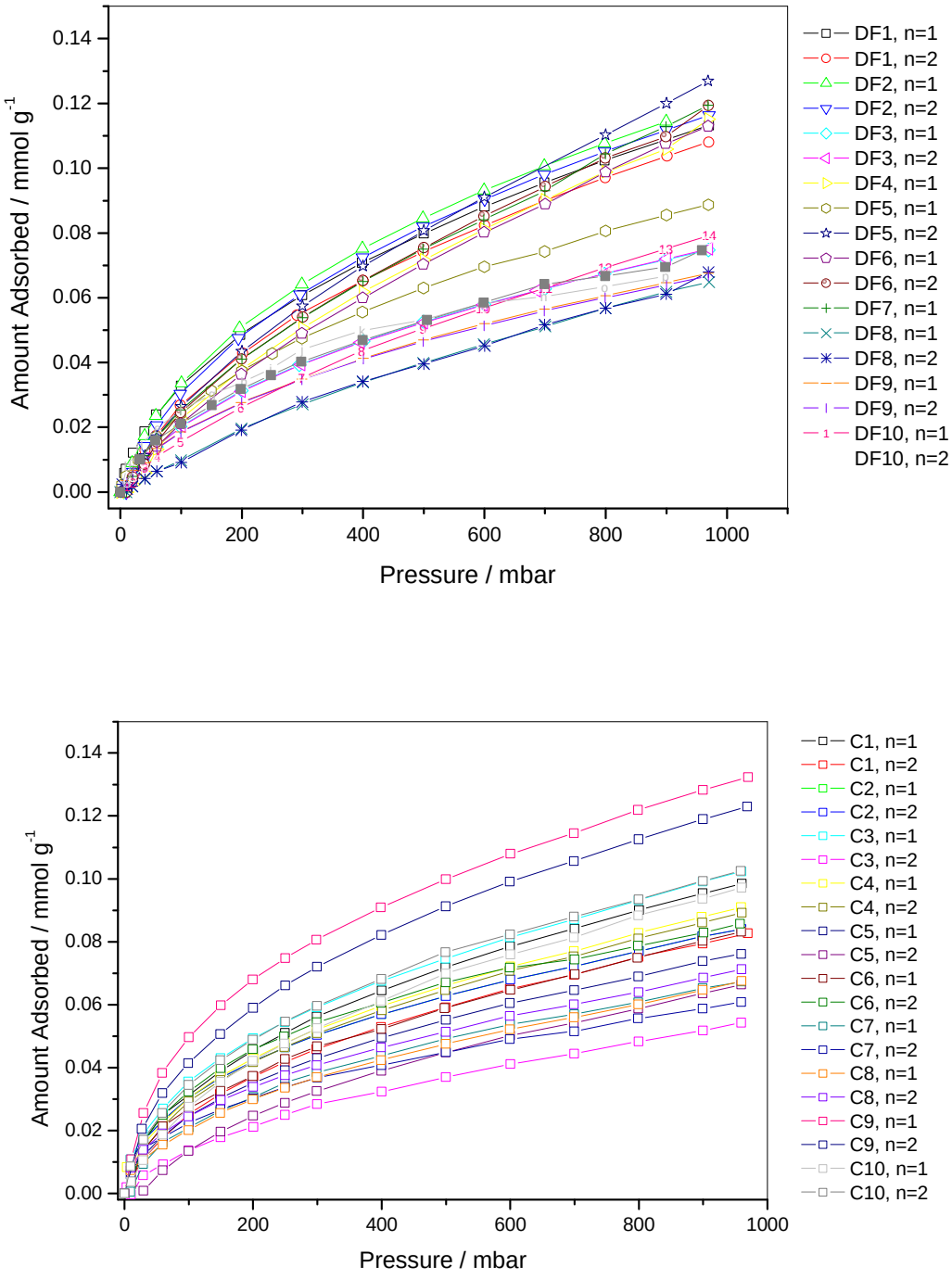

Figure 4.22: CO_2 isotherms at 0^oC for the Colorado Group shales.

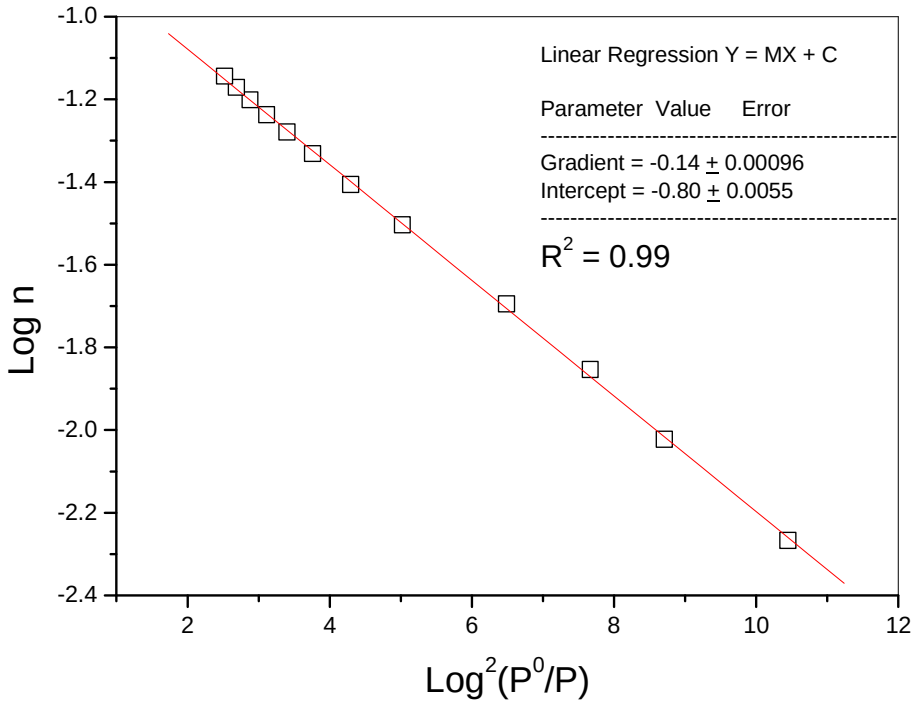

Figure 4.23: Example of a D-R plot for the CO_2 at 0°C isotherm for shale DF3. A linear plot indicates a Gaussian distribution of micropore widths. The micropore volume is calculated from the intercept value of the linear regression.

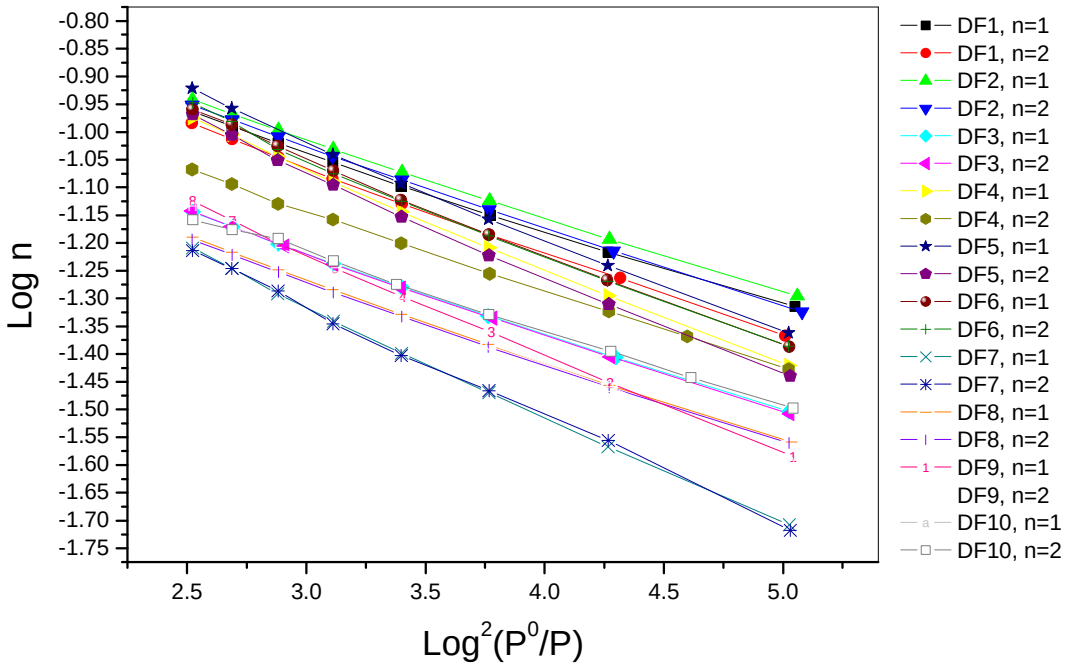

Figure 4.24: D-R plots of the Draupne Formation CO_2 isotherms at 0°C.

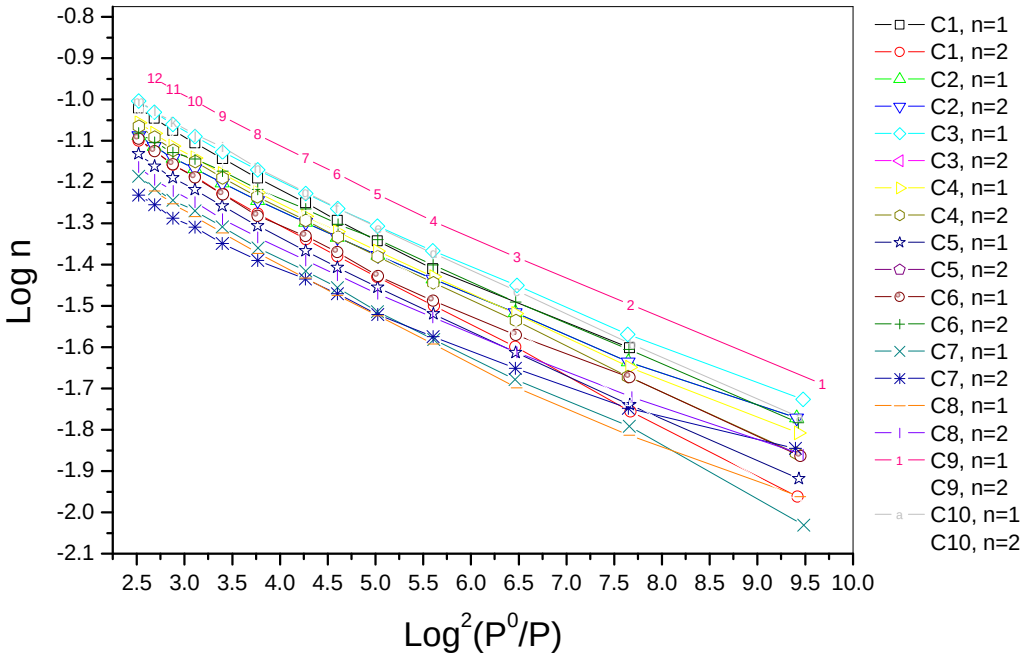

Figure 4.25: D-R plots of the Colorado Group CO_2 isotherms at 0°C.

Table 4.5: Maximum adsorption uptakes of CO_2 at 0°C and the D-R micropore volumes of the Draupne Formation and Colorado Group shales.

Sample	Depth / m	Maximum CO_2 adsorption / mmol g^{-1}	D-R Micropore Volume / cm^3 g^{-1}
DF1	2117.8	0.106 ± 0.0036	0.00982 ± 0.00139
DF2	2325	0.113 ± 0.0018	0.01100 ± 0.00085
DF3	2978.5	0.072 ± 0.0002	0.00680 ± 0.00002
DF4	3124.7	0.096 ± 0.0144	0.01143 ± 0.00519
DF5	3375.32	0.114 ± 0.0088	0.01240 ± 0.00042
DF6	3400.4	0.111 ± 0.0021	0.01195 ± 0.00092
DF7	4132.95	0.062 ± 0.0005	0.00771 ± 0.00005
DF8	4608.4	0.064 ± 0.0005	0.00563 ± 0.00028
DF9	4707.7	0.074 ± 0.0010	0.00779 ± 0.0006
DF10	4780.7	0.068 ± 0.0019	0.00557 ± 0.00079
C1	505.3	0.0874 ± 0.011	0.00717 ± 0.0006
C2	506.55	0.0818 ± 0.000	0.00590 ± 0.0000
C3	541	0.0754 ± 0.033	0.00599 ± 0.0018
C4	546.3	0.0870 ± 0.001	0.00676 ± 0.0001
C5	561.5	0.0687 ± 0.007	0.00670 ± 0.0013
C6	642.1	0.0816 ± 0.002	0.00613 ± 0.0002
C7	647.57	0.0619 ± 0.005	0.00465 ± 0.0010
C8	651.75	0.0667 ± 0.003	0.00491 ± 0.0001
C9	675.02	0.1236 ± 0.007	0.00922 ± 0.0003
C10	684.61	0.0965 ± 0.004	0.00816 ± 0.0006

(Each sample was measured twice for repeatability, n = 2)

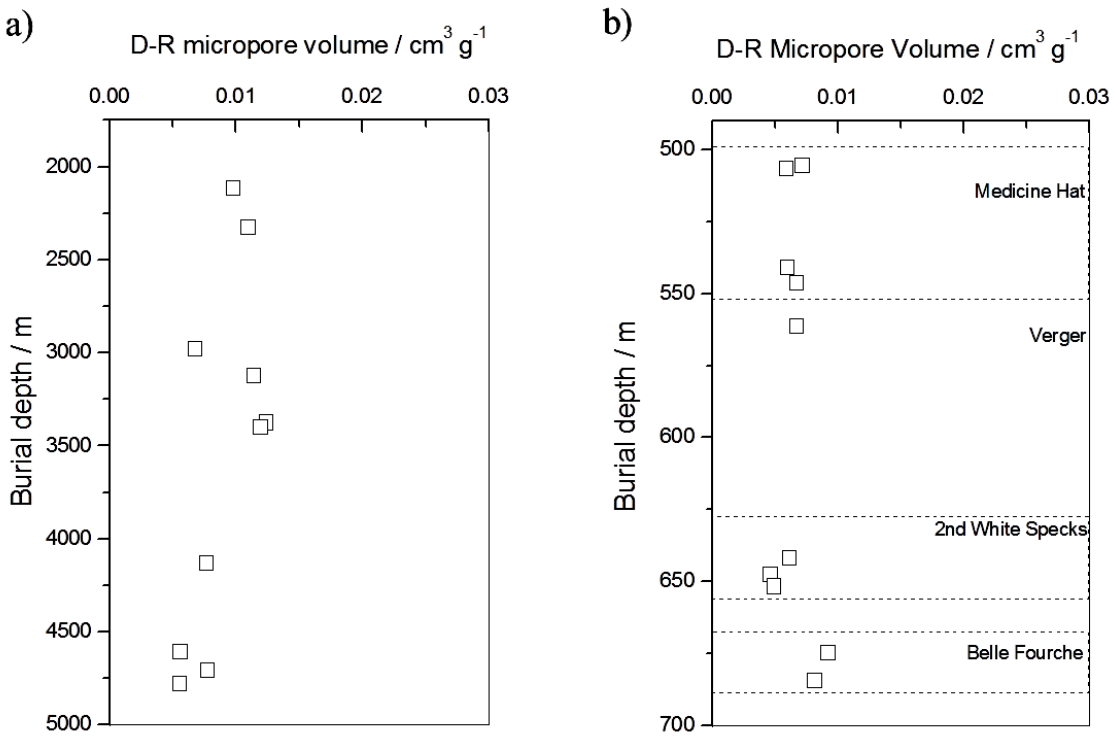

Figure 4.26: D-R micropore volumes against depth. There is no apparent correlation between the micropore volume and burial depth for either the a) Draupne Formation shales or b) Colorado Group.

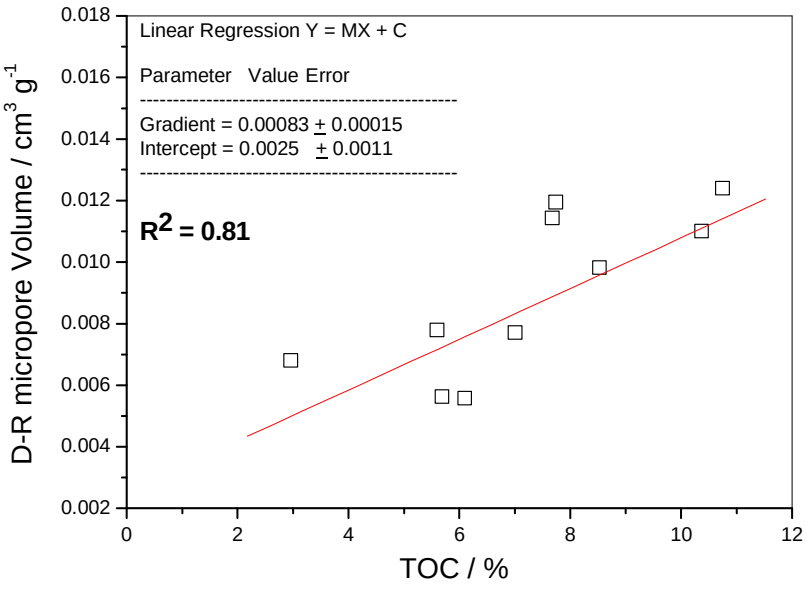

Figure 4.27: Good positive correlation of D-R micropore volume with organic matter content (TOC) for the Draupne Formation shales.

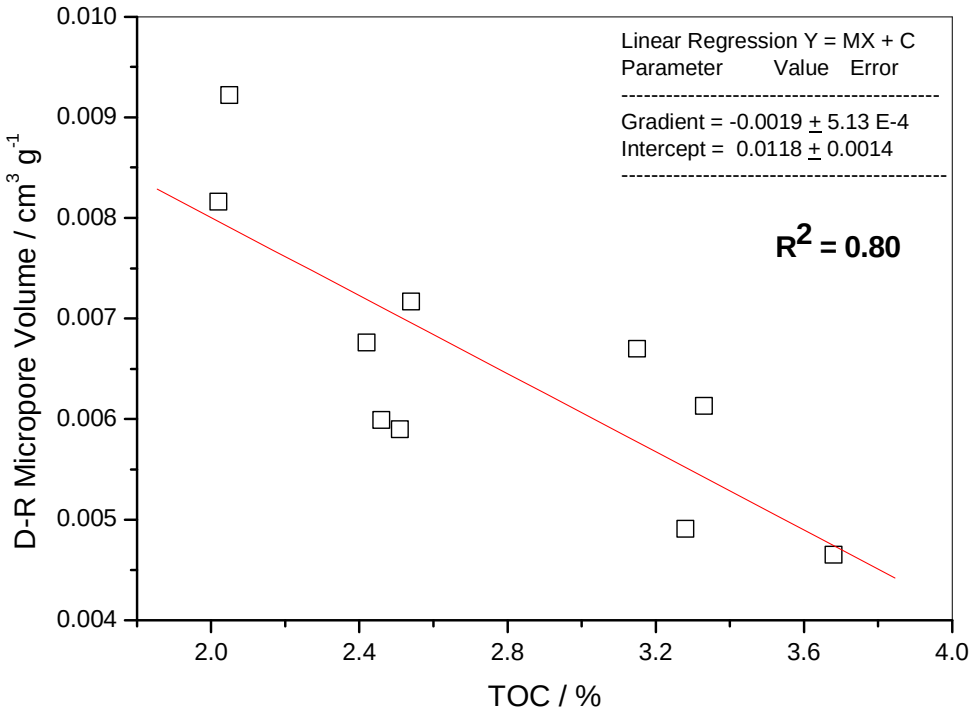

Figure 4.28: Good negative correlation between micropore volumes and organic matter content (TOC) for the Colorado Group shales.

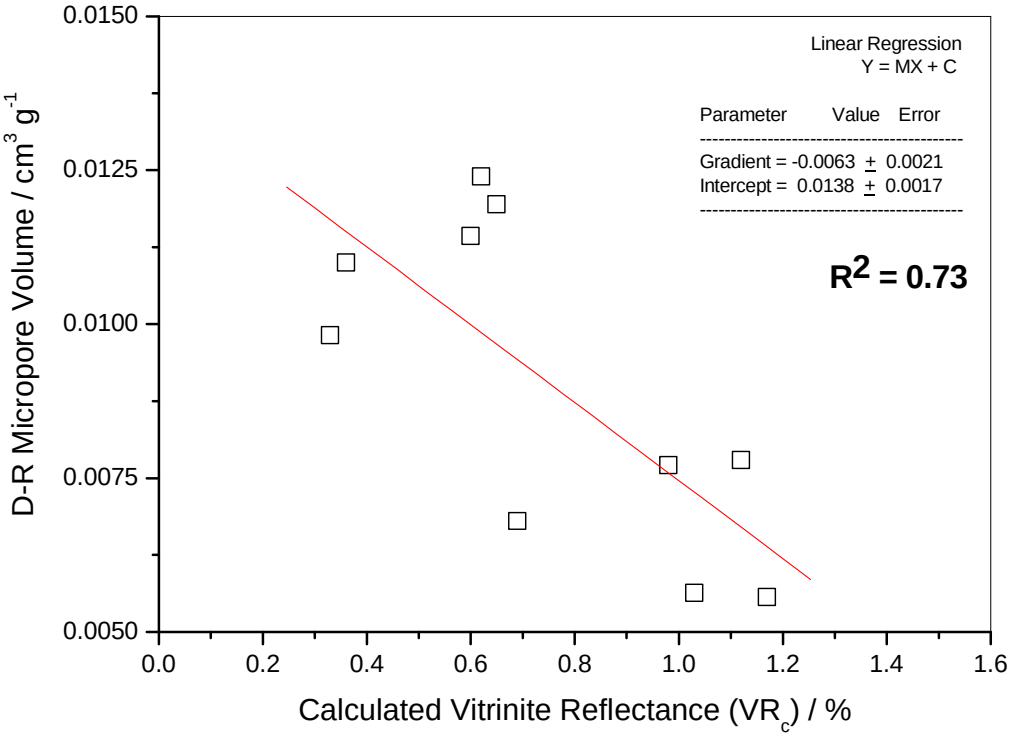

Figure 4.29: Plot of D-R micropore volume against maturity for the Draupne Formation shales. A good negative correlation between D-R micropore volume and vitrinite reflectance exists.

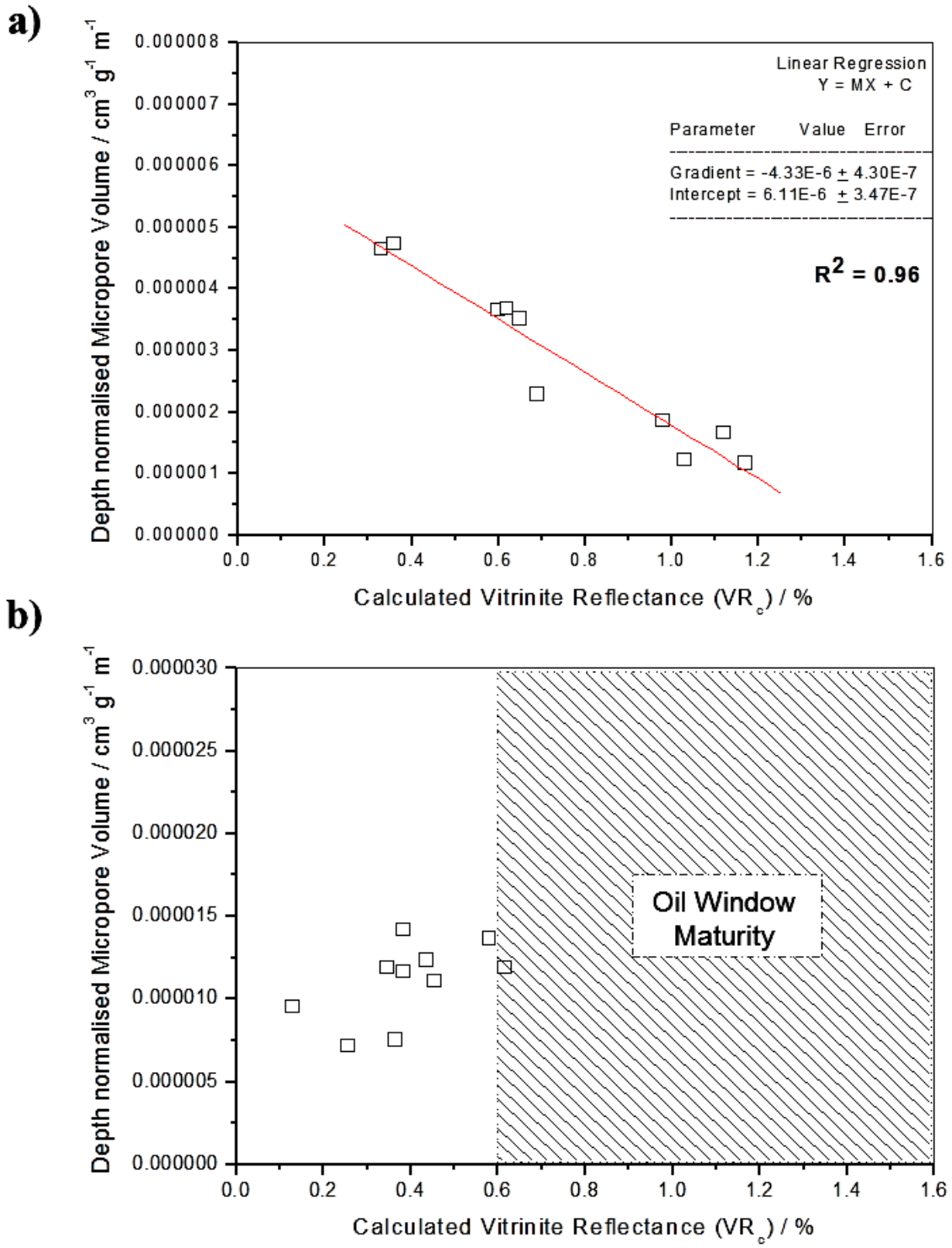

Figure 4.30: Plot of depth normalised micropore volume against maturity for the Draupne Formation and Colorado Group shales. In part a), a strong negative correlation between normalised micropore volume of DF shale and vitrinite reflectance. In part b), no observable correlation is present for the Colorado Group shales.

Table 4.6: Summary of the pore volumes for each pore size range of the Draupne Formation and Colorado Group shales.

Sample	Total Pore Volume / $cm^3\ g^{-1}$	Open Pore Volume / $cm^3\ g^{-1}$	0.7 to 100 nm Pore Volume / $cm^3\ g^{-1}$	> 100 nm Pore Volume / $cm^3\ g^{-1}$	< 0.7 nm Pore Volume / $cm^3\ g^{-1}$
DF1	0.0828	0.0532	0.0098	0.0198	0.0236
DF2	0.0648	0.0436	0.0110	0.0141	0.0184
DF3	0.0505	0.0276	0.0068	0.0122	0.0086
DF4	0.0818	0.0423	0.0114	0.0065	0.0244
DF5	0.0619	0.0470	0.0124	0.0084	0.0262
DF6	0.0580	0.0425	0.0120	0.0048	0.0258
DF7	0.0210	0.0138	0.0077	0.0004	0.0057
DF8	0.0304	0.0124	0.0056	0.0023	0.0045
DF9	0.0341	0.0227	0.0078	0.0044	0.0106
DF10	0.0315	0.0181	0.0056	0.0076	0.0049
C1	0.0791	0.0227	0.0072	0.0104	0.0052
C2	0.0774	0.0240	0.0059	0.0133	0.0048
C3	0.0630	0.0228	0.0060	0.0148	0.0020
C4	0.0707	0.0229	0.0068	0.0120	0.0041
C5	0.0805	0.0210	0.0067	0.0101	0.0042
C6	0.0680	0.0205	0.0061	0.0100	0.0044
C7	0.0738	0.0203	0.0047	0.0094	0.0062
C8	0.0724	0.0245	0.0049	0.0098	0.0098
C9	0.0827	0.0293	0.0092	0.0141	0.0059
C10	0.0980	0.0371	0.0082	0.0142	0.0147

Table 4.7: Summary of the percentages of pore volume in each pore size range for the DF and CG shales (where the total pore volume of the sample = 100 % pore volume).

Sample	Open Pore Volume / %	> 100 nm Pore Volume / %	0.7 to 100 nm Pore Volume / %	< 0.7 nm Pore Volume / %
DF1	64.2	28.5	23.9	11.9
DF2	67.2	28.5	21.8	17.0
DF3	54.7	17.1	24.2	13.5
DF4	51.8	29.8	8.0	14.0
DF5	75.9	42.3	13.5	20.0
DF6	73.4	44.5	8.3	20.6
DF7	65.9	27.1	2.1	36.8
DF8	40.7	14.7	7.4	18.5
DF9	66.5	30.9	12.8	22.8
DF10	57.6	15.6	24.2	17.7
C1	28.7	6.6	13.1	9.1
C2	31.0	6.2	17.2	7.6
C3	36.2	3.2	23.5	9.5
C4	32.3	5.8	17.0	9.6
C5	26.1	5.2	12.6	8.3
C6	30.2	6.5	14.7	9.0
C7	27.5	8.4	12.8	6.3
C8	33.9	13.5	13.6	6.8
C9	35.4	7.1	17.1	11.1
C10	37.8	15.0	14.5	8.3

4.2.4 Porosity of the Draupne Formation and Colorado Group shales.

The porosity of the Draupne Formation and Colorado Group shales was determined using mercury intrusion porosimetry and gas adsorption analysis. The total porosity and bulk density were determined from the MIP intrusion curves in Figure 4.10 (above), and are listed in Table 4.8. The total porosities of the DF shales had a range of 5.0 to 17.0 %, with an average of 11.4 ± 4.0 %. There is an overall trend of decreasing total porosities with increasing burial depth. The total porosities of the CG shales had a range of 14.4 to 21.5 %, with an average of 17.0 ± 1.9 %. For the Draupne Formation shales, a strong correlation exists between burial depth and total porosity (Figure 4.31, part a), whereas tor the Colorado Group, there is no observable correlation between burial depth and total porosity (Figure 4.31, part b). The correlation coefficient of the Draupne Formation is $R^2 = 0.84$ ($p = 0.00249$).

Gas adsorption analysis was used to determine the sub-100 nanometre-scale porosities of the Draupne Formation and Colorado Group shales. The gas sorption porosities of the Draupne Formation and Colorado Group shales were determined from the sorption pore volumes ($cm^3\ g^{-1}$) and the shale bulk densities ($g\ cm^{-3}$). The gas sorption porosity of the Draupne Formation shales had a range of 2.0 to 6.1%, with an average of 3.8 ± 3.1 %. The gas sorption porosity of the Colorado Group shales had a range of 3.14 to 5.11%, with an average of 4.09 ± 0.67 %. For the DF shales, a strong correlation is observed between the total porosity and sorption porosity, Figure 4.32. The correlation coefficient is $R^2 = 0.94$. The total porosity of the Colorado Group shales has no correlation to the sorption porosity, as reported in Figure 4.33.

The sorption porosities of the Draupne Formation shales exhibit a strong negative correlation to maturity. To account for the influence of burial compaction on pore volume, the sorption porosities are normalised to burial depth in Table 4.9 and in Figure 4.34. In Figure 4.34 part a), the strong negative correlation between depth normalised sorption porosities and vitrinite reflectance is reported. The correlation coefficient is $R^2 = 0.90$. In Figure 4.34 part b), the sorption porosities of the Colorado Group shales do not change with maturity (VR_c).

The microporosities of the Draupne Formation and Colorado Group shales were determined from the D-R micropore volumes ($cm^3\ g^{-1}$) and the shale bulk densities ($g\ cm^{-3}$). The gas sorption porosity of the Draupne Formation shales had a range of 1.4 to 2.7 %, with an average of 2.0 ± 0.5 %. The gas sorption porosity of the Colorado Group shales had a range of 3.14 to 5.11%, with an average of 4.09 ± 0.67 %.

The microporosities of the Draupne Formation shales are positively correlated to the organic matter content (TOC), as reported in Figure 4.35, part a). The correlation coefficient is $R^2 = 0.75$. The microporosity of the Colorado Group shales are negatively correlated to the organic matter content (TOC), as reported in Figure 4.35, part b). The correlation coefficient is $R^2 = 0.80$.

The distribution of porosities in each pore size range is listed in Table 4.10, with the average porosities reported in Figure 4.36. For the Draupne Formation shales, the open porosity has a range of 3.2 to 10.9 %, with an average of 7.1 ± 2.9 %. The > 100 nm porosity category has a range of 1.2 to 5.6 %, with an average of 3.2 ± 1.9 %. The 0.7 to 100 nm porosity has a range of 0.1 to 4.1 %, with an average of 1.8 ± 1.2 %. The < 0.7 nm porosity has a range of 1.4 to 2.6 %, with an average of 2.0 ± 0.5 %.

For the Colorado Group shales, the open porosity has a range of 4.5 to 8.1 %, with an average of 5.5 ± 1.1 %. The > 100 nm porosity category has a range of 0.5 to 3.2 %, with an average of 1.4 ± 0.8 %. The 0.7 to 100 nm porosity has a range of 2.1 to 3.4 %, with an average of 2.6 ± 0.5 %. The < 0.7 nm porosity has a range of 1.0 to 2.0 %, with an average of 1.5 ± 0.3 %.

Table 4.8: Densities and porosities of the Draupne Formation and Colorado Group shales, as measured using mercury intrusion porosimetry.

Sample	Burial Depth / m	Bulk Density / g cm^{-3}	Grain Density / g cm^{-3}	Total Porosity / %	Hg-Macroporosity / %
DF1	2117.8	2.049	2.467	17.0	4.8
DF2	2325	2.105	2.438	13.6	3.9
DF3	2978.5	2.331	2.642	11.8	2.0
DF4	3124.7	2.044	2.454	16.7	5.0
DF5	3375.32	2.138	2.465	13.2	5.6
DF6	3400.4	2.186	2.503	12.7	5.6
DF7	4132.95	2.397	2.523	5.0	1.4
DF8	4608.4	2.557	2.773	7.8	1.1
DF9	4707.7	2.436	2.656	8.3	2.6
DF10	4780.7	2.420	2.620	7.6	1.2
C1	505.3	2.219	2.691	17.5	1.2
C2	506.55	2.220	2.680	17.2	1.1
C3	541	2.280	2.663	14.4	0.5
C4	546.3	2.247	2.671	15.9	0.9
C5	561.5	2.214	2.694	17.8	0.9
C6	642.1	2.254	2.661	15.3	1.0
C7	647.57	2.228	2.666	16.4	1.4
C8	651.75	2.248	2.685	16.3	2.2
C9	675.02	2.190	2.675	18.1	1.3
C10	684.61	2.192	2.791	21.5	3.2

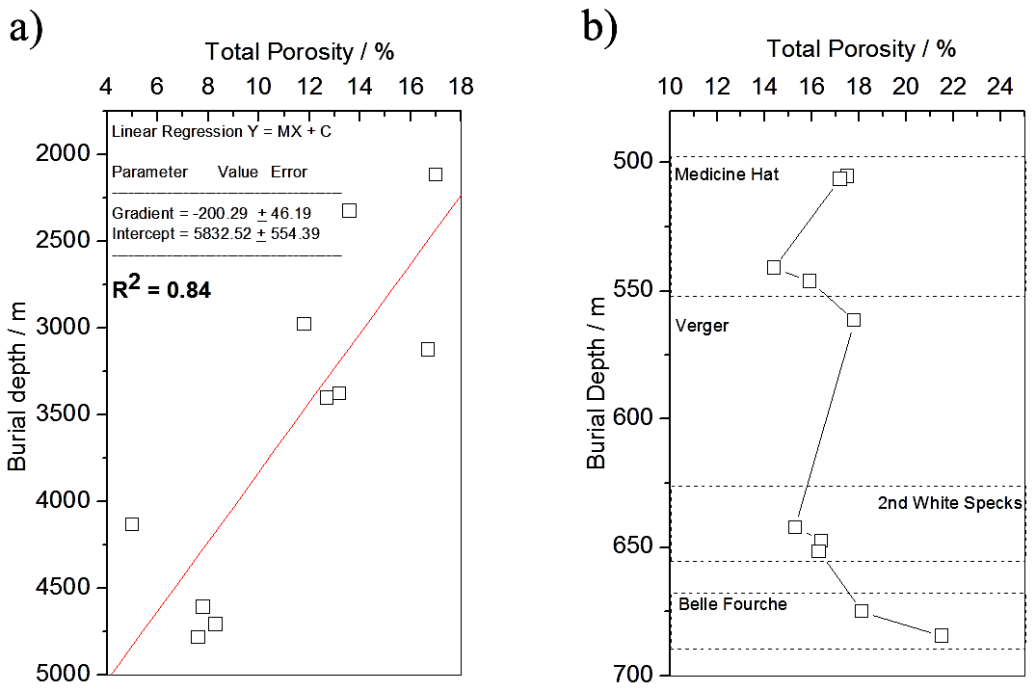

Figure 4.31: Total porosity against burial depth. In part a), a strong correlation is observed between total porosity and burial depth for the Draupne Formation shales, whereas in Part b), there is no observable correlation for the Colorado Group shales.

Table 4.9: Nanometre-scale porosities of the Draupne Formation and Colorado Group shales, as measured using gas adsorption.

Sample	Depth / m	Gas Sorption Porosity / %	Depth Normalised Gas Sorption Porosity / % m^{-1}	D-R Microporosity / %	Depth Normalised D-R Microporosity / % m^{-1}
DF1	2117.8	6.1	0.0029	2.0	0.0010
DF2	2325	5.3	0.0023	2.3	0.0010
DF3	2978.5	4.4	0.0015	1.6	0.0005
DF4	3124.7	3.7	0.0012	2.3	0.0007
DF5	3375.32	4.4	0.0013	2.7	0.0008
DF6	3400.4	3.7	0.0011	2.6	0.0008
DF7	4132.95	2.0	0.0005	1.8	0.0004
DF8	4608.4	2.0	0.0004	1.4	0.0003
DF9	4707.7	3.0	0.0006	1.9	0.0004
DF10	4780.7	3.2	0.0007	1.3	0.0003
C1	505.3	3.9	0.0077	1.6	0.0031
C2	506.55	4.3	0.0084	1.3	0.0026
C3	541	4.7	0.0088	1.4	0.0025
C4	546.3	4.2	0.0077	1.5	0.0028
C5	561.5	3.7	0.0066	1.5	0.0026
C6	642.1	3.6	0.0057	1.4	0.0022
C7	647.57	3.1	0.0048	1.0	0.0016
C8	651.75	3.3	0.0051	1.1	0.0017
C9	675.02	5.1	0.0076	2.0	0.0030
C10	684.61	4.9	0.0072	1.8	0.0026

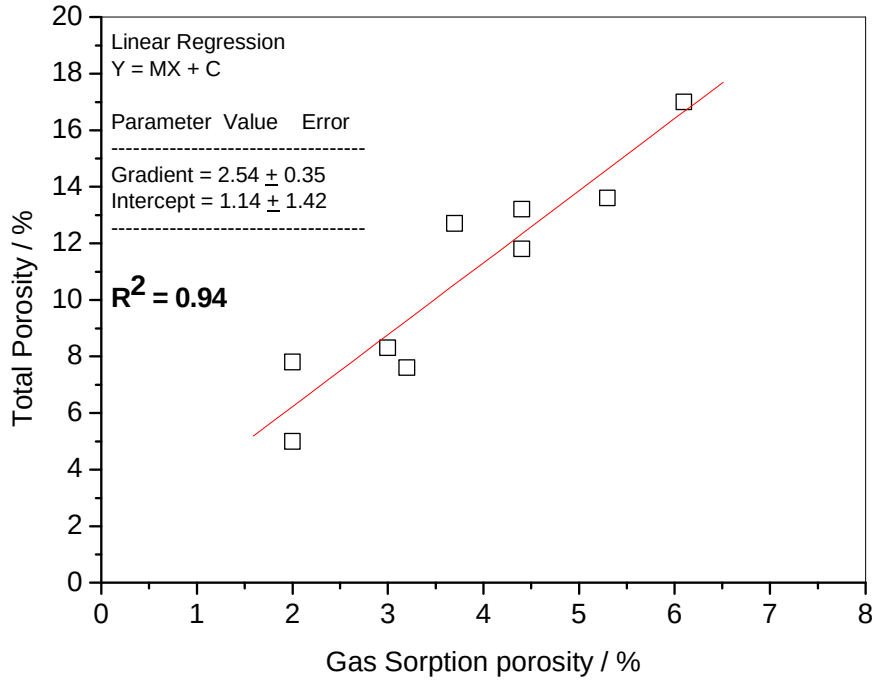

Figure 4.32: Total porosity and gas sorption porosity of the Draupne Formation shale. A strong correlation exists, indicating that gas sorption porosity (of the sub – 100 nm pores) is a controlling factor in the overall total porosity of the shale.

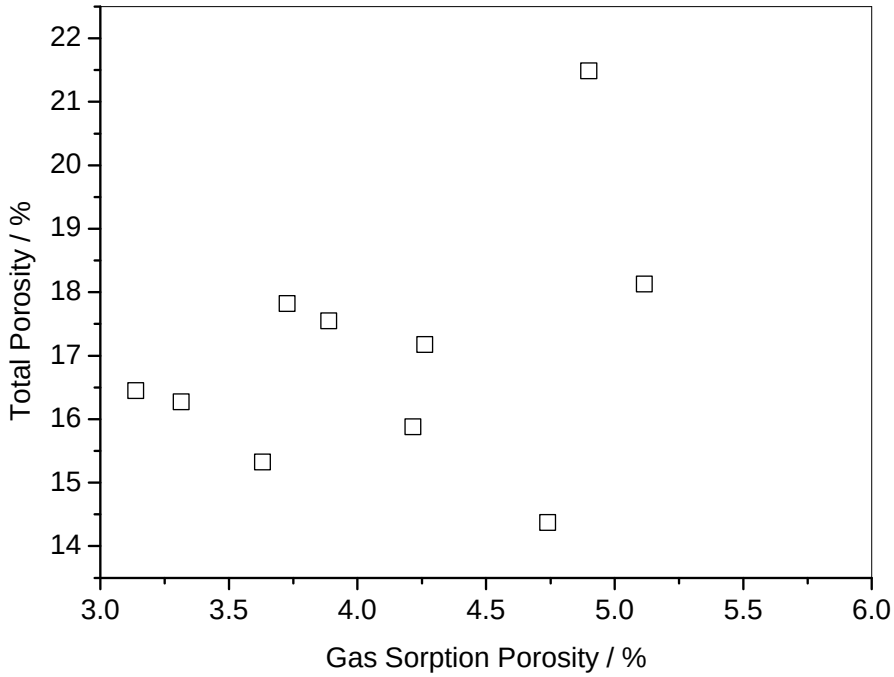

Figure 4.33: Total porosity and gas sorption porosity of the Colorado Group shale. No apparent correlation between total porosity and gas sorption porosity.

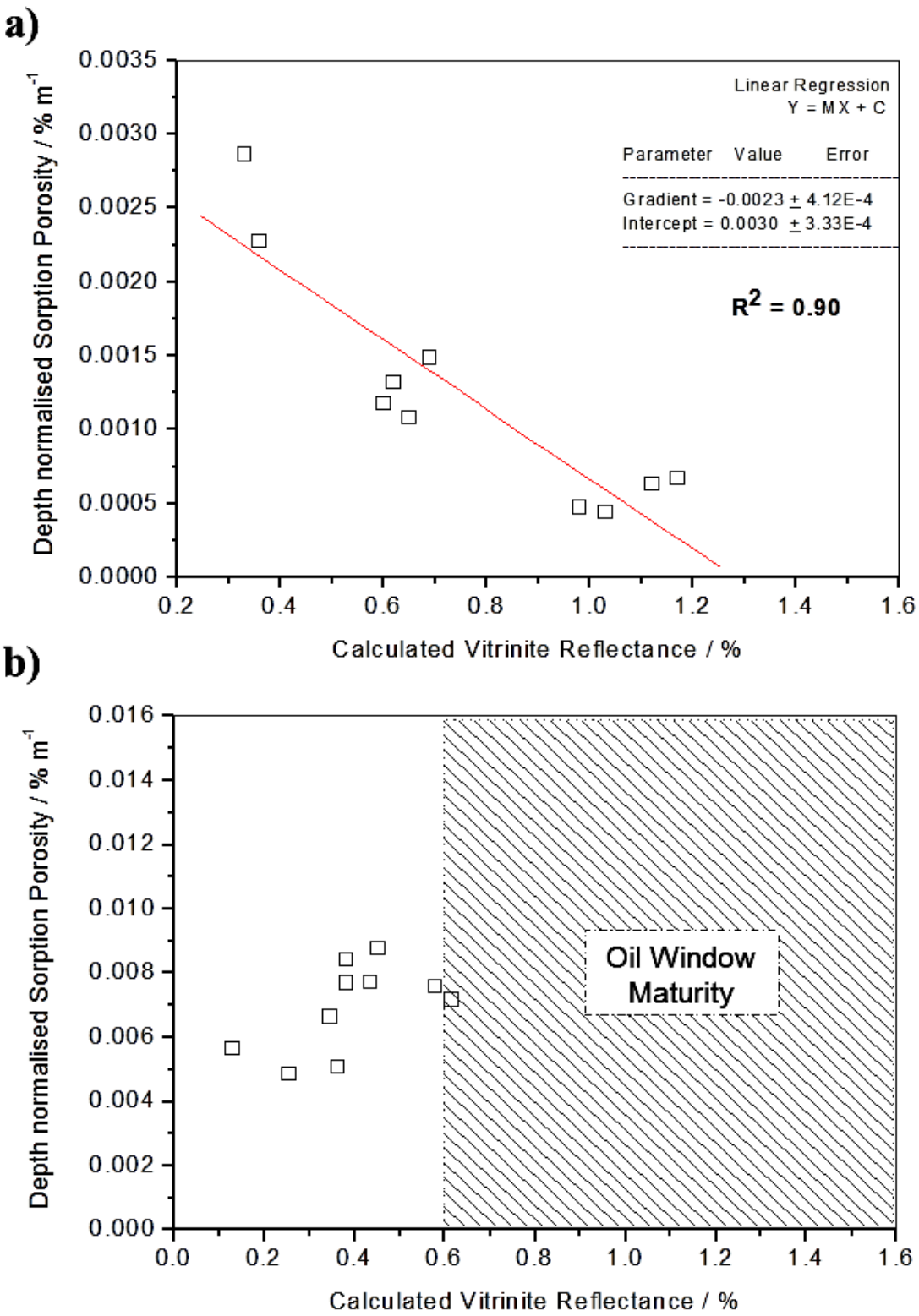

Figure 4.34: Plot of depth normalised sorption porosity against maturity. In part a), a strong negative correlation between normalised sorption pore volume of Draupne Formation shales and vitrinite reflectance. In part b), no observable correlation exists for the Colorado Group shales.

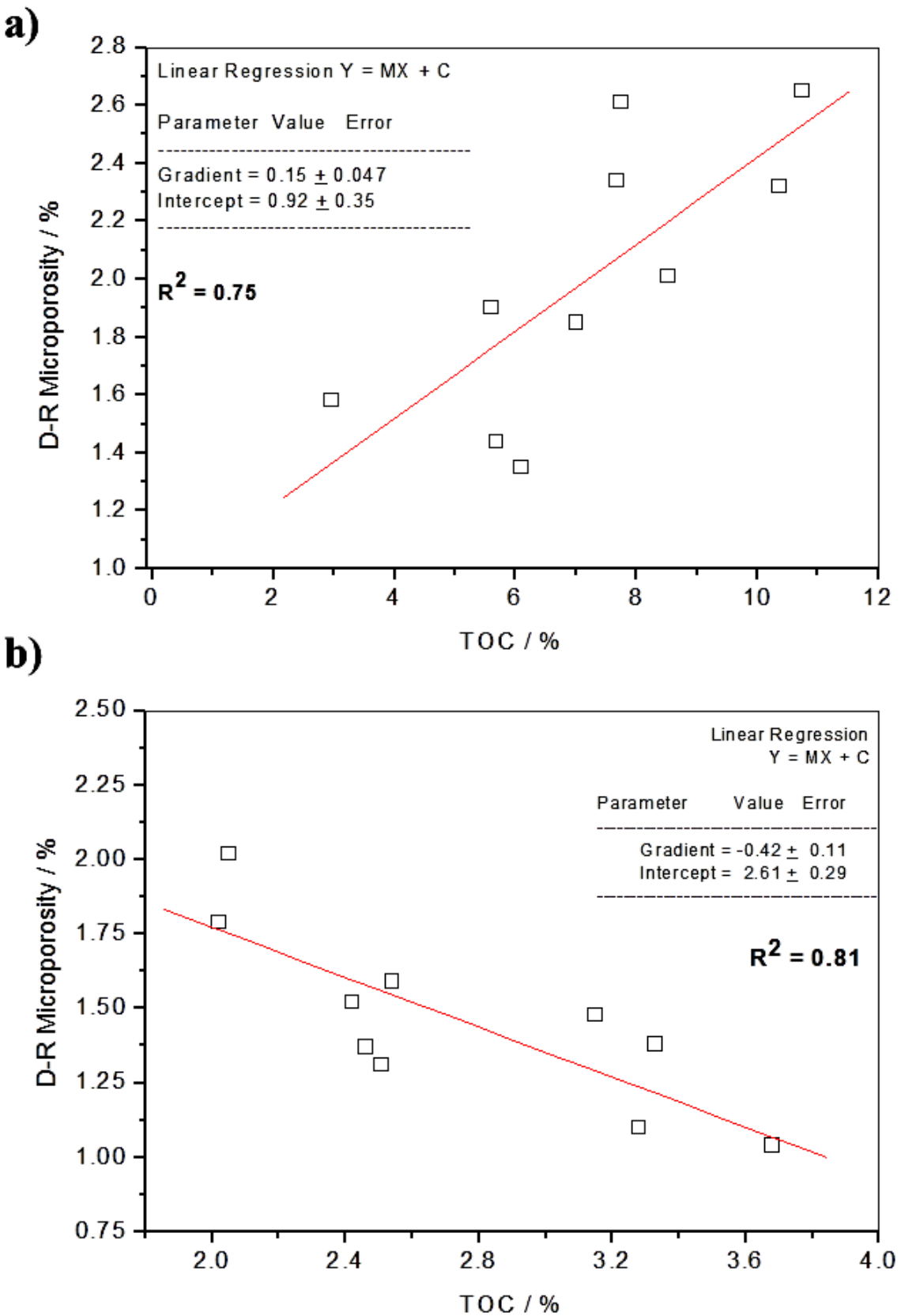

Figure 4.35: Microporosity and TOC content of the Draupne Formation and Colorado Group shales. In part a), a good positive correlation exists between microporosity and TOC content, indicating that organic matter is a primary location for microporosity in the Draupne Formation shales. In part b), a strong negative correlation exists between microporosity and TOC content for the Colorado Group shales.

Table 4.10: Shale porosities in each pore size range.

Sample	Total Porosity / %	Open Porosity / %	> 100 nm Porosity / %	0.7 to 100 nm Porosity / %	< 0.7 nm Porosity / %
DF1	17.0	10.9	4.8	4.1	2.0
DF2	13.6	9.1	3.9	3.0	2.3
DF3	11.8	6.5	2.0	2.9	1.6
DF4	16.7	8.6	5.0	1.3	2.3
DF5	13.2	10.0	5.6	1.8	2.6
DF6	12.7	9.3	5.6	1.1	2.6
DF7	5.0	3.3	1.4	0.1	1.8
DF8	7.8	3.2	1.2	0.6	1.4
DF9	8.3	5.5	2.6	1.1	1.9
DF10	7.6	4.4	1.2	1.8	1.3
C1	17.5	5.0	1.2	2.3	1.6
C2	17.2	5.3	1.1	3.0	1.3
C3	14.4	5.2	0.5	3.4	1.4
C4	15.9	5.1	0.9	2.7	1.5
C5	17.8	4.7	0.9	2.2	1.5
C6	15.3	4.6	1.0	2.2	1.4
C7	16.4	4.5	1.4	2.1	1.0
C8	16.3	5.5	2.2	2.2	1.1
C9	18.1	6.4	1.3	3.1	2.0
C10	21.5	8.1	3.2	3.1	1.8

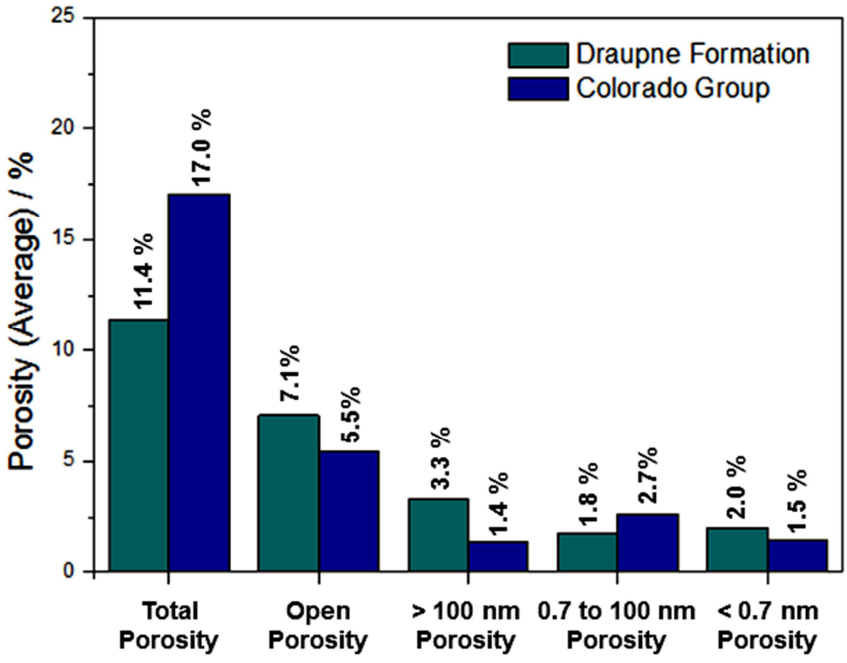

Figure 4.36: Average porosities of the Draupne Formation and Colorado Group shales in each pore size range.

4.2.5 Surface area of the Draupne Formation and Colorado Group shales.

The surface areas of the Draupne Formation and Colorado Group shales were determined using mercury intrusion porosimetry and gas adsorption analysis. The surface area measured by mercury intrusion was determined using the R-P equation (Rootare and Prenzlow, 1967) using the mercury intrusion curves presented in Figure 4.10 (above). The low pressure region of the mercury intrusion curve (up to a pressure of 2500 psi) allows the surface area of the macropores to be determined (up to a diameter of 100 nm). An example of a mercury intrusion curve in the low pressure region for the DF1 shale is reported in Figure 4.37. The surface area is determined from the area under the curve (using integration).

The BET surface areas of the Draupne Formation and Colorado Group shales were determined using gas adsorption analysis. The BET surface area measurements were performed using both nitrogen gas at -196^{o}C (= 77K) and CO_2 at -78^{o}C, and were determined in the relative pressure range of p/p^{o} = 0.05 to 0.3. An example of a full range nitrogen isotherm for shale DF10 is reported in Figure 4.38. The DF10 nitrogen isotherm has the characteristic Type II isotherm shape, with minimal amounts of gas adsorption uptake at low relative pressures, with a rapid upward increase in gas adsorption uptake at high relative pressures. This indicates that activated diffusion barriers are inhibiting the adsorption of N_2 in the shale at low pressures, only to rapidly increase as the N_2 pressure approaches the saturated vapour pressure of N_2 at 1 atm (i.e. 1013. 25 mbar).

The nitrogen adsorption isotherms for the Draupne Formation and Colorado Group shales (in the BET pressure range of 50 mbar to 300 mbar) are reported in Figure 4.39. The adsorption isotherms appear to be nearly linear in this low pressure region, with a low value gradient. There is a distribution of adsorption uptakes, with the isotherms appearing to be "stacked" on top of one another. There appears to be no crossing or overlap of the isotherms. The CO_2 isotherms at -78^{o}C for the Draupne Formation and Colorado Group shales were previously reported in Figure 4.14 (above).

The N_2 BET surface areas of the Draupne Formation and Colorado Group shales are listed in Table 4.11. The N_2 BET surface areas of the DF shales have a range of 1.23 to 16.52 $m^2\ g^{-1}$, with an average of 6.16 ± 5.8 $m^2\ g^{-1}$. The N_2 BET surface areas of the CG shales have a range of 8.37 to 26.33 $m^2\ g^{-1}$, with an average of 16.98 ± 5.93 $m^2\ g^{-1}$. The nitrogen BET surface areas of the Draupne Formation is significantly lower than the Colorado Group shales.

The CO_2 BET surface areas of the Draupne Formation and Colorado Group shales are listed in Table 4.11. For the DF shales, the CO_2 BET surface areas values have a range of 9.85 to 34.73 $m^2\ g^{-1}$, with an average of 20.70 ± 8.24 $m^2\ g^{-1}$. For the CG shales, the CO_2 BET surface areas values have a range of 17.01 to 30.06 $m^2\ g^{-1}$, with an average of 22.56 ± 4.19 $m^2\ g^{-1}$. The average CO_2 BET surface areas of the Draupne Formation and Colorado Group shales are similar in value (20.70 $m^2\ g^{-1}$ vs 22.56 $m^2\ g^{-1}$), indicating that these shales have full range pore structures (macro-, meso-, and micropores) with similar total surface areas.

The mercury intrusion, N_2 BET and CO_2 BET surface areas can be combined to determine the 1) total surface area and 2) the distribution of surface areas. This is done using the equations outlined in Chapter 1, section 1.2.17. The total surface areas are listed in Table 4.12. The Draupne Formation shales have a total surface area with a range of 9.85 to 34.73 $m^2 g^{-1}$, with an average of 20.70 ± 8.24 $m^2 g^{-1}$. The Colorado Group shales have a total surface area with a range of 17.01 to 30.06 $m^2 g^{-1}$, with an average of 22.56 ± 4.19 $m^2 g^{-1}$.

The distribution of surface areas for the Draupne Formation and Colorado Group shales are listed in Table 4.12 and summarised in Figure 4.40. The Draupne Formation shales have a macropore surface area (> 100 nm) with a range of 0.07 to 0.69 $m^2 g^{-1}$, with an average of 0.35 ± 0.24 $m^2 g^{-1}$. The Colorado Group shales have a macropore surface area (> 100 nm) with a range of 0.05 to 0.47 $m^2 g^{-1}$, with an average of 0.20 ± 0.14 $m^2 g^{-1}$. The Draupne Formation shales have a mesopore surface area (100 to 2 nm) with a range of 0.88 to 16.32 $m^2 g^{-1}$, with an average of 5.80 ± 5.81 $m^2 g^{-1}$. The Colorado Group shales have a mesopore surface area (100 to 2 nm) with a range of 8.17 to 25.87 $m^2 g^{-1}$, with an average of 16.77 ± 5.91 $m^2 g^{-1}$. The Draupne Formation shales have a micropore surface area (< 2 nm) with a range of 6.06 to 20.76 $m^2 g^{-1}$, with an average of 14.55 ± 5.50 $m^2 g^{-1}$. The Colorado Group shales have a micropore surface area (< 2 nm) with a range of 2.54 to 9.81 $m^2 g^{-1}$, with an average of 5.58 ± 2.58 $m^2 g^{-1}$.

The distribution of surface areas for the Draupne Formation and Colorado Group shales indicates that the macropores (> 100 nm) have very little internal surface areas (0.35 $m^2 g^{-1}$ vs 0.20 $m^2 g^{-1}$). The pores with diameters less than 100 nm are where the vast majority of the surface area is located. The Draupne Formation shales contain most of their surface areas within the micropores less than 2 nm (14.55 $m^2 g^{-1}$), whereas the Colorado Group shales contain most of their surface areas within the mesopores (100 nm to 2 nm), with an average of 16.77 $m^2 g^{-1}$.

The total surface areas of the Draupne Formation shales exhibit no correlation to TOC content. However, the micropore surface areas (< 2nm) of the DF shales have a strong positive correlation to TOC content, as reported in Figure 4.41, part a). The correlation coefficient is $R^2 = 0.87$. For the Colorado Group, the total surface areas are negatively correlated to the TOC content, as reported in Figure 4.41, part b). The correlation coefficient is $R^2 = 0.94$. This suggests that the primary location for internal surface area in the Colorado Group shales is not the organic matter component of the shales. The illite content of the Colorado Group shales has an excellent correlation with the total surface areas, as reported in Figure 4.42. The correlation is positive, with a correlation coefficient of $R^2 = 0.98$. This indicates that the primary location of the internal surface area in the immature Colorado Group shales is in the shale matrix, in the illite clay mineral assemblages. The decrease in illite content with increasing TOC is the underlying cause for the misleading negative correlation between total surface area and TOC in Figure 4.42.

The total surface areas of the Draupne Formation shales decrease with increasing burial depth, Figure 4.43. A strong correlation between total surface area and burial depth exists, with a correlation coefficient of $R^2 = 0.86$. This reduction of surface area is linked to the reduction of pore volume due to increasing thermal maturity, as reported in Figure 4.44. The correlation is strong, with a correlation coefficient of $R^2 = 0.93$. However, the Colorado Group shales have no apparent correlation between the decrease of total surface areas and burial depth, as reported in Figure 4.43. The Colorado Group shales have no apparent correlation between the total surface areas and maturity.

To account for the influence of burial compaction on pore volume, the total surface areas are normalised to burial depth in Figure 4.45. In part a), the strong negative correlation between depth normalised total surface areas and vitrinite reflectance of the Draupne Formation shales is reported. The correlation coefficient is $R^2 = 0.89$. In Figure 4.45 part b), the total surface areas of the Colorado Group shales do not change with maturity (VR_c).

The total surface areas of the Draupne Formation shales increase with increasing total porosity, as reported in Figure 4.46. The correlation is strong, with a correlation coefficient of $R^2 = 0.93$. Conversely, this suggests that the surface area of the pore system is decreasing with decreasing total porosity. This could be due mechanical compaction reducing pore volume. The Colorado Group shales have no apparent correlation between the total surface areas and total porosity. The correlation is strong, with a correlation coefficient of $R^2 = 0.93$.

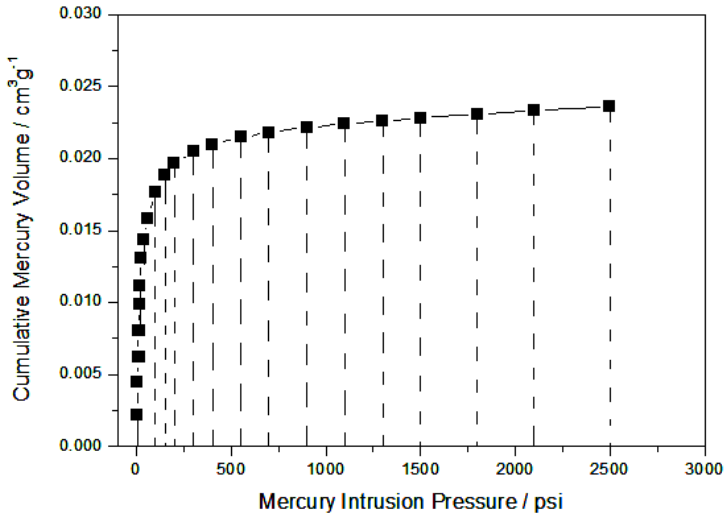

Figure 4.37: Mercury intrusion curve for sample DF1 in the low pressure region. The integration of the area under the intrusion curve is used to determine the surface area of the macropores (down to a limit of 100 nm).

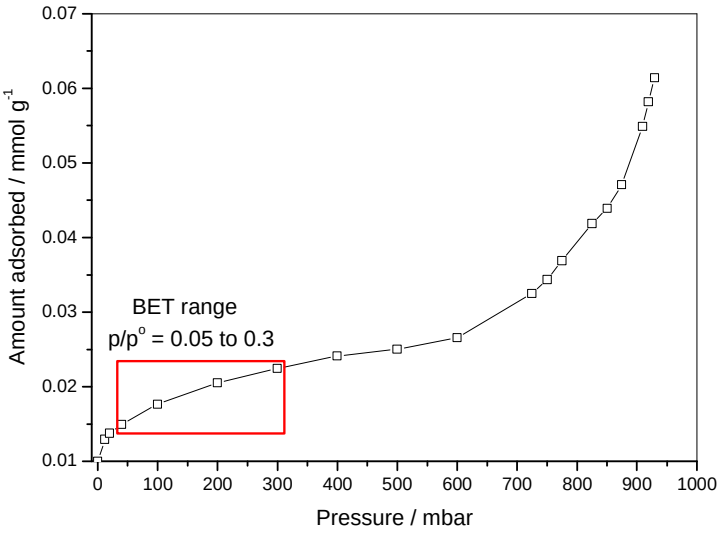

Figure 4.38: N_2 isotherm at -196°C for the DF10 shale. A characteristic Type II isotherm shape is exhibited, as defined by the IUPAC classification scheme..

a)

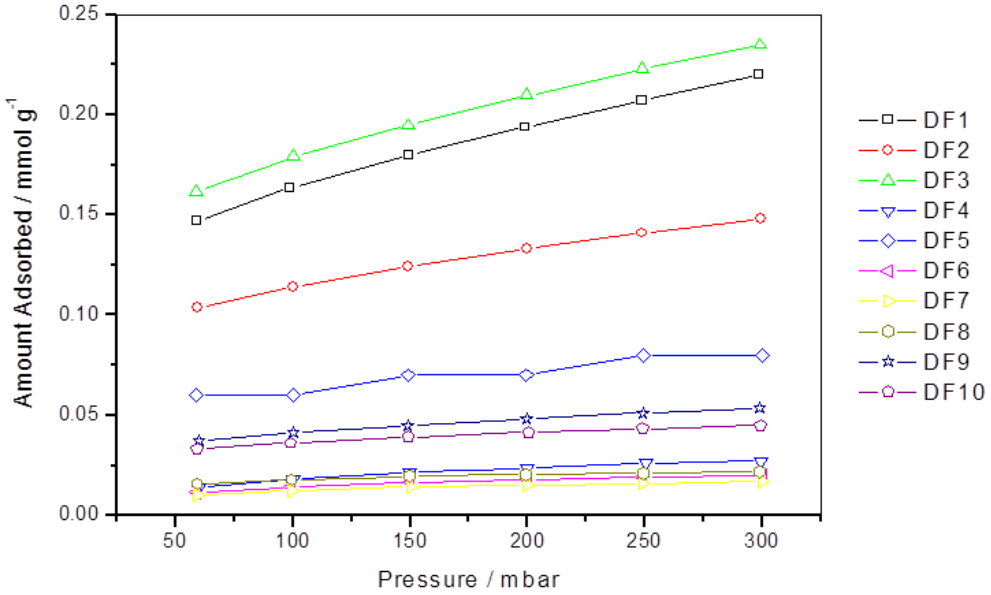

b)

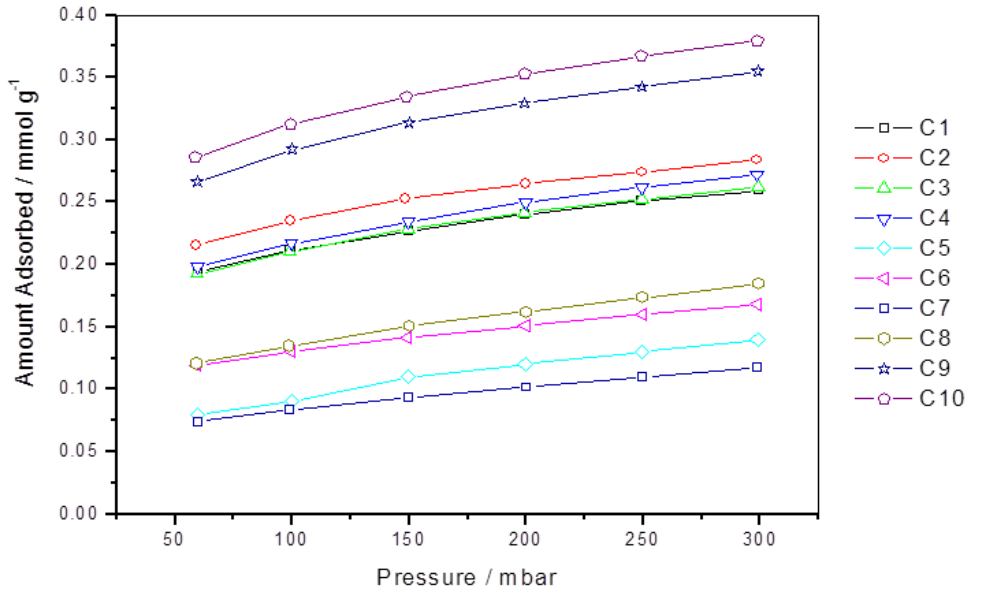

Figure 4.39: Nitrogen adsorption isotherms at -196oC in the relative pressure range of p/po = 0.05 to 0.3. In part a), the Draupne Formation shales isotherms are reported. In part b), the Colorado Group shale isotherms are reported.

Table 4.11: Surface areas of the Draupne Formation and Colorado Group shales, using mercury intrusion porosimetry, N_2 at -196°C, and CO_2 at -78°C.

Shale	Burial depth / m	Hg Intrusion Surface Area (> 100 nm) / $m^2\ g^{-1}$	N_2 BET Surface Area / $m^2\ g^{-1}$	CO_2 BET Surface Area / $m^2\ g^{-1}$
DF1	2117.80	0.60	15.56	34.73
DF2	2325.00	0.36	10.40	31.16
DF3	2978.50	0.20	16.52	22.58
DF4	3124.70	0.60	2.06	19.29
DF5	3375.32	0.69	5.87	25.99
DF6	3400.40	0.60	1.48	20.25
DF7	4132.95	0.08	1.23	10.19
DF8	4608.40	0.07	1.52	9.85
DF9	4707.70	0.23	3.77	14.57
DF10	4780.70	0.09	3.13	18.39
C1	505.30	0.15	18.03	20.93
C2	506.55	0.09	19.67	23.22
C3	541.00	0.05	18.26	25.32
C4	546.30	0.13	19.03	22.55
C5	561.50	0.11	10.61	20.42
C6	642.10	0.20	11.75	19.58
C7	647.57	0.20	8.37	17.01
C8	651.75	0.43	13.09	17.64
C9	675.02	0.17	24.61	30.06
C10	684.61	0.47	26.33	28.87

Table 4.12: The total surface area, the surface area of the macropores (> 100 nm), the 100 to 2 nm pores, and the micropores (< 2 nm) for the Draupne Formation and the Colorado Group shales.

Shale	Burial depth / m	Total surface area / $m^2 g^{-1}$	> 100 nm pores / $m^2 g^{-1}$	100 to 2 nm pores / $m^2 g^{-1}$	< 2 nm pores / $m^2 g^{-1}$
DF1	2117.80	34.73	0.60	14.96	19.17
DF2	2325.00	31.16	0.36	10.04	20.76
DF3	2978.50	22.58	0.20	16.32	6.06
DF4	3124.70	19.29	0.60	1.46	17.23
DF5	3375.32	25.99	0.69	5.18	20.12
DF6	3400.40	20.25	0.60	0.88	18.77
DF7	4132.95	10.19	0.08	1.15	8.96
DF8	4608.40	9.85	0.07	1.45	8.33
DF9	4707.70	14.57	0.23	3.54	10.80
DF10	4780.70	18.39	0.09	3.04	15.26
C1	505.30	20.93	0.15	17.88	2.90
C2	506.55	23.22	0.09	19.58	3.55
C3	541.00	25.32	0.05	18.21	7.06
C4	546.30	22.55	0.13	18.90	3.52
C5	561.50	20.42	0.11	10.50	9.81
C6	642.10	19.58	0.20	11.55	7.83
C7	647.57	17.01	0.20	8.17	8.64
C8	651.75	17.64	0.43	12.66	4.55
C9	675.02	30.06	0.17	24.44	5.45
C10	684.61	28.87	0.47	25.87	2.54

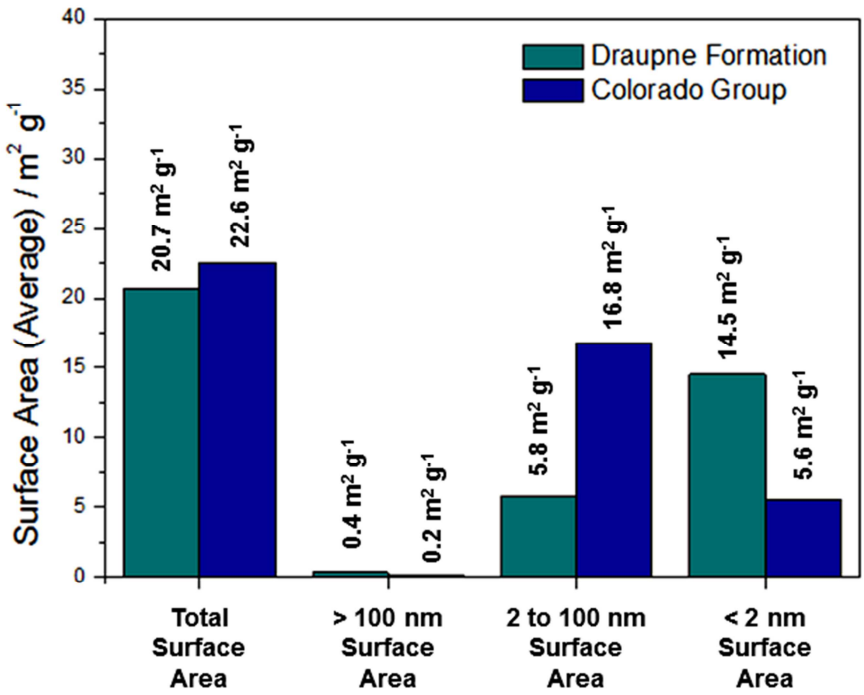

Figure 4.40: Average surface areas of the Draupne Formation and Colorado Group shales in each pore size range.

a)

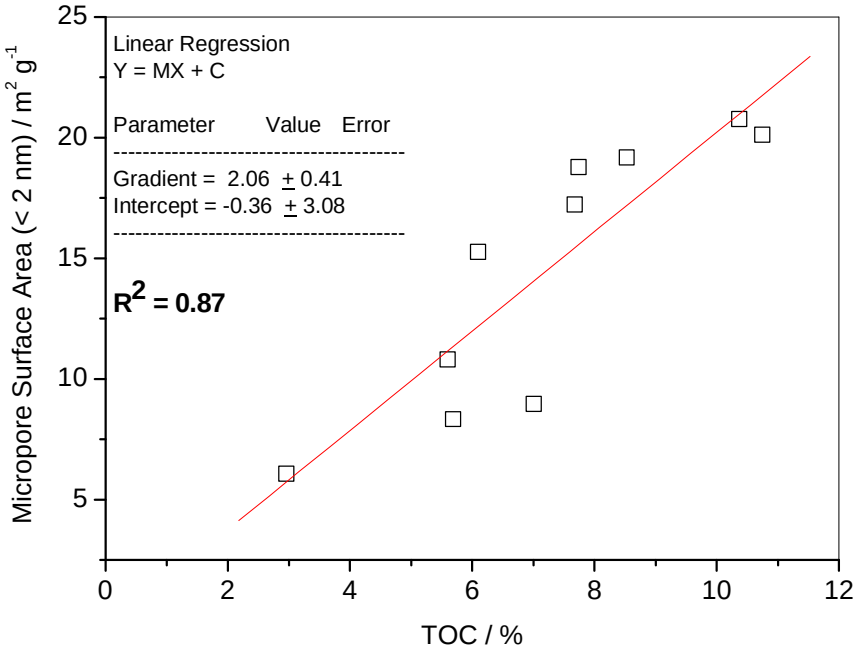

b)

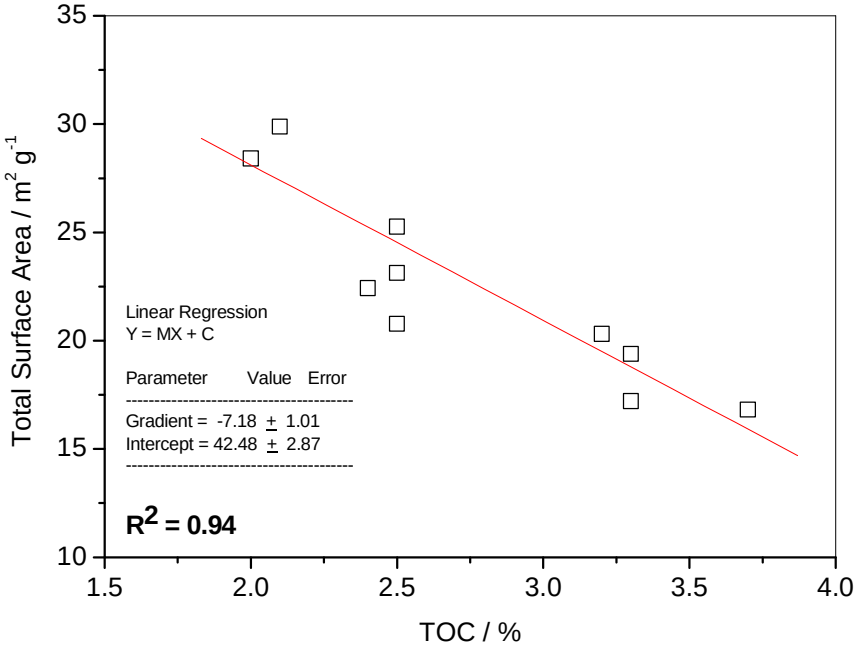

Figure 4.41: Total surface area against TOC. In part a), the micropore surface area exhibits a good positive correlation with increasing organic matter content for Draupne Formation shales. In part b), the surface area decreases with increasing organic matter content for the Colorado Group shales.

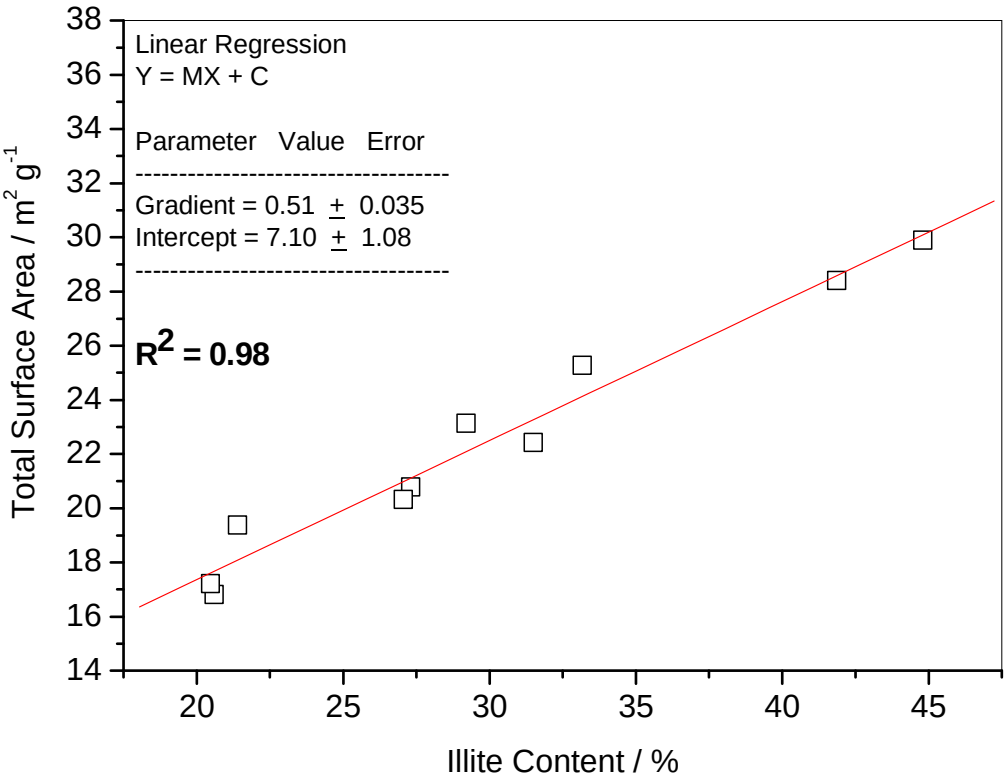

Figure 4.42: Total surface area against illite content. An excellent positive correlation exists between total surface area and illite content for the Colorado Group shales.

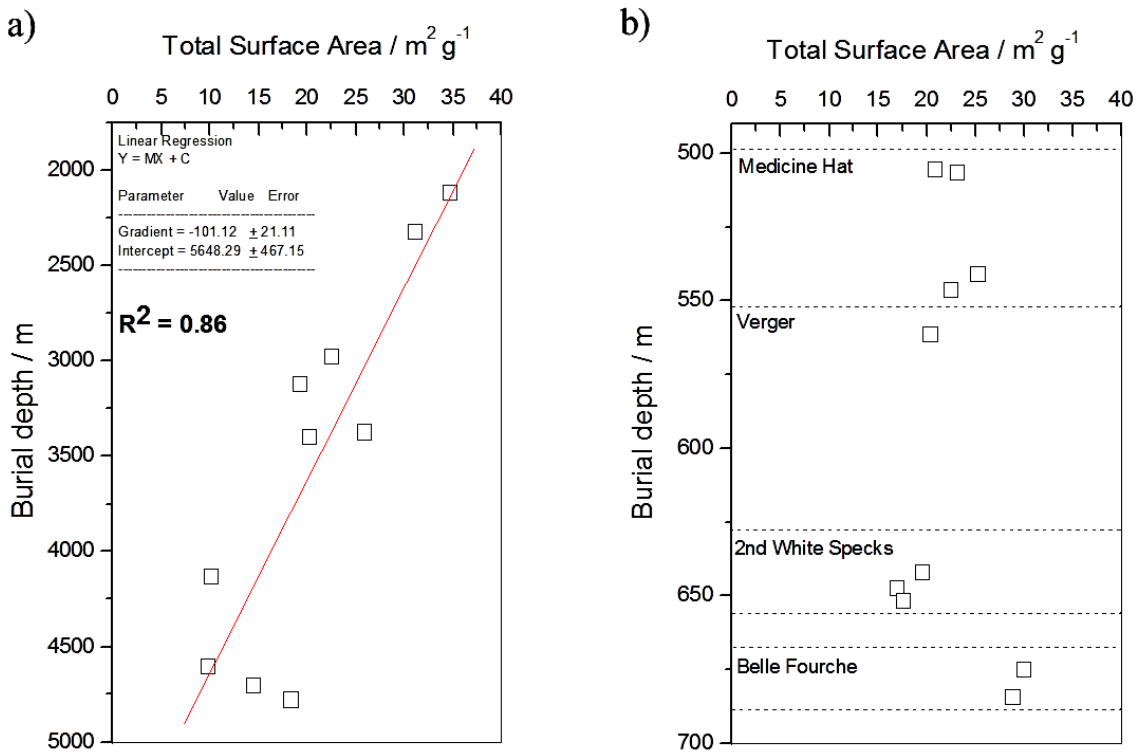

Figure 4.43: Total surface area against burial depth. In part a) the total surface area of the Draupne Formation shales decreases with increasing burial depth. In part b) there is no observable correlation between total surface area and burial depth for the Colorado Group shales.

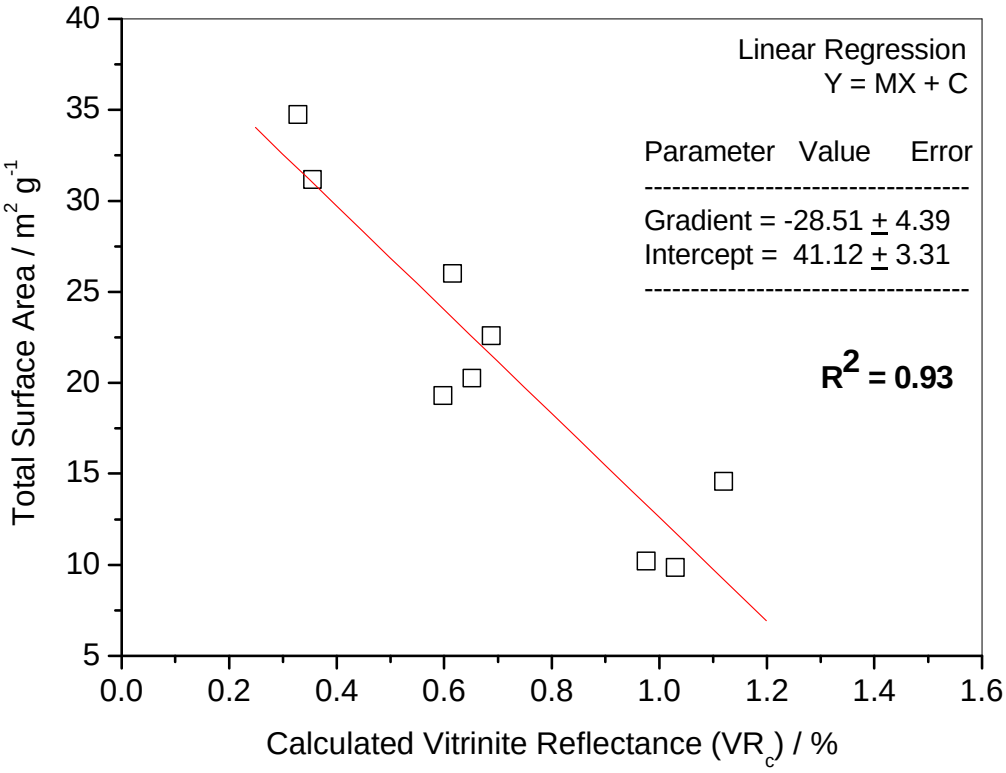

Figure 4.44: Total surface area against maturity. A strong negative correlation exists between total surface area and maturity for the Draupne Formation shales.

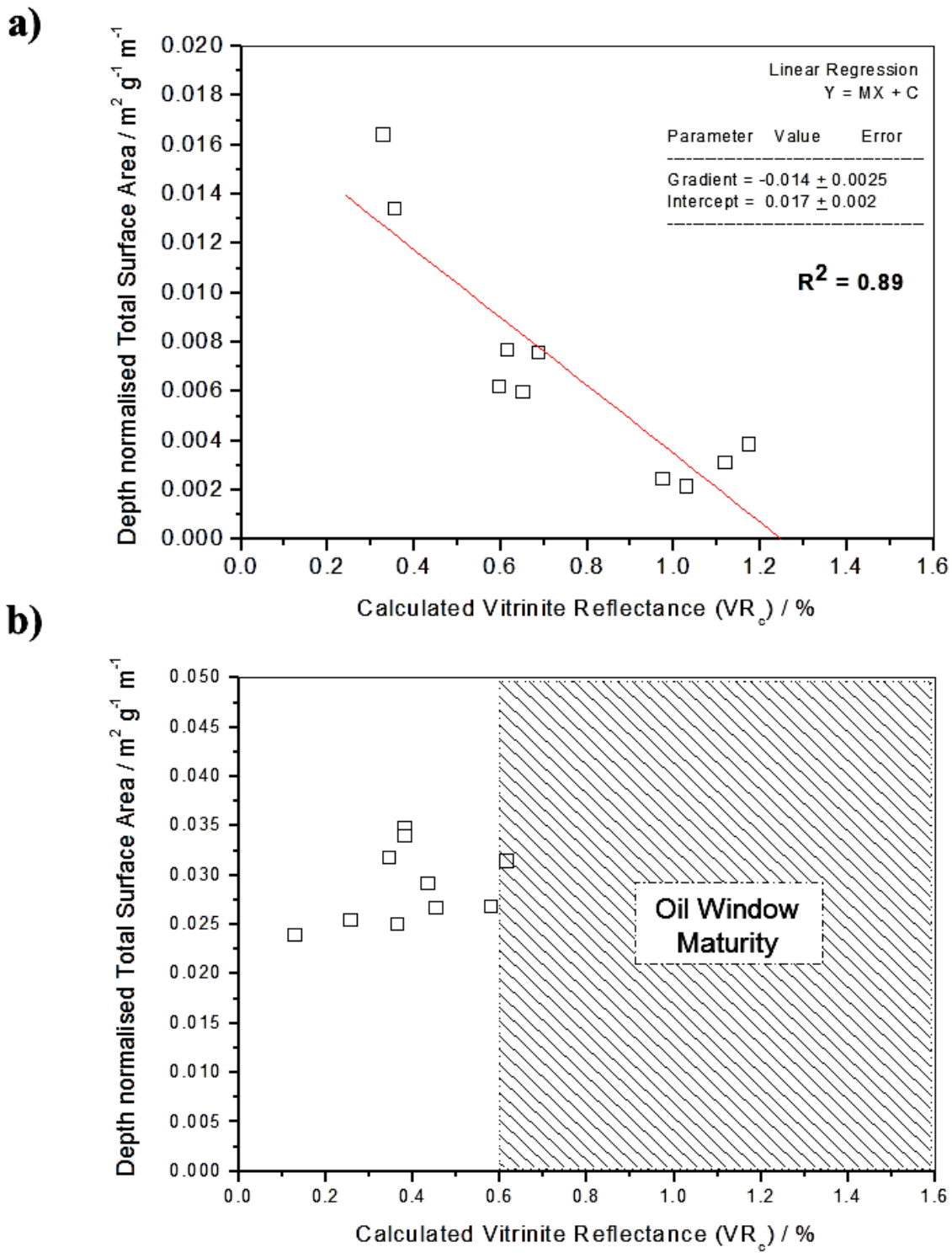

Figure 4.45: Plot of depth normalised total surface area against maturity. In part a), a strong negative correlation exists between normalised total surface area of Draupne Formation shales and vitrinite reflectance. In part b), no observable correlation exists for the Colorado Group shales.

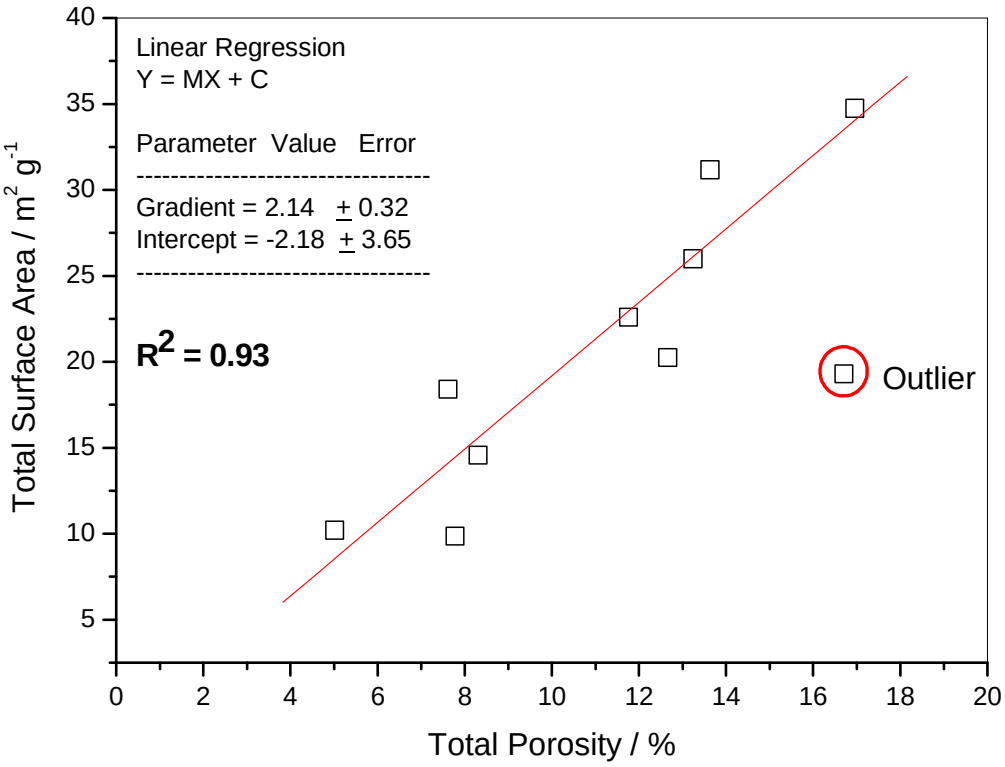

Figure 4.46: Total surface area against total porosity. A strong positive correlation exists between total surface area and total porosity for the Draupne Formation shales.

4.3 Discussion

The pore structure and porosity of the Draupne Formation and Colorado Group shales were investigated using a multi technique approach, which included electron microscopy, mercury intrusion porosimetry and gas adsorption analysis, as outlined in chapter 1. Electron microscopy was used to gather a visual analysis of the pore shape and location. The MIP was used to determine the total porosity and pore size distribution of pore structure over a 5 orders of magnitude size range (Clarkson *et al*., 2012). The gas adsorption analysis was used to characterise the nanometre scale pore volumes, porosities and surface areas.

4.3.1 Pore shape and locations in shale.

The SEM micrographs identified the presence of spherical and silt shaped pores in the Draupne Formation and Colorado Group shales. This is observed in Figures 4.4 and 4.9 (shales DF10 and C10, above). Silt-shaped pores are found in many porous systems (Marsh, 1987), and often take the form of "ink bottles", with a narrow slit-shape constriction at the entrance (the pore "throat") leading to a larger pore body.

The SEM micrographs indicate the presence of inter-particle (InterP) pores in the matrix of the Draupne Formation and Colorado Group shales, primarily between clay mineral packages and quartz grains, which agrees with the findings of Loucks *et al*., (2009). This is observed in Figures 4.5 and 4.6 (shales DF5 and DF10, above). In the Colorado Group shale, InterP pores were also observed between clusters of poorly packed carbonate mineral grains, and were elliptical in shape, Figure 4.7 (shale C1). InterP pores arise in shales because clastic and biogenic sediment particles may not pack together perfectly, leaving space between the grains.

The InterP pores of the DF and CG shales were typically slit shaped or long thin cracks within the clay matrix (which could be artefacts), and were tens of micrometres in length. Very few nanometre-scale InterP pores were observed. This finding does not agree with the work of Loucks *et al*., (2009) who found that pores in gas bearing shale rocks are dominated by nanometre-scale pores (Figure 4.47, below). A possible explanation for the difference between this work and that of Loucks *et al*., (2009) is that they focussed on gas window maturity shales, whilst this study investigates immature and oil window maturity shales.

Very few intra-particle (IntraP) pores were found in the organic matter particles of either the Draupne Formation or Colorado Group shales. The few IntraP pore present were often circular or oval in shape.

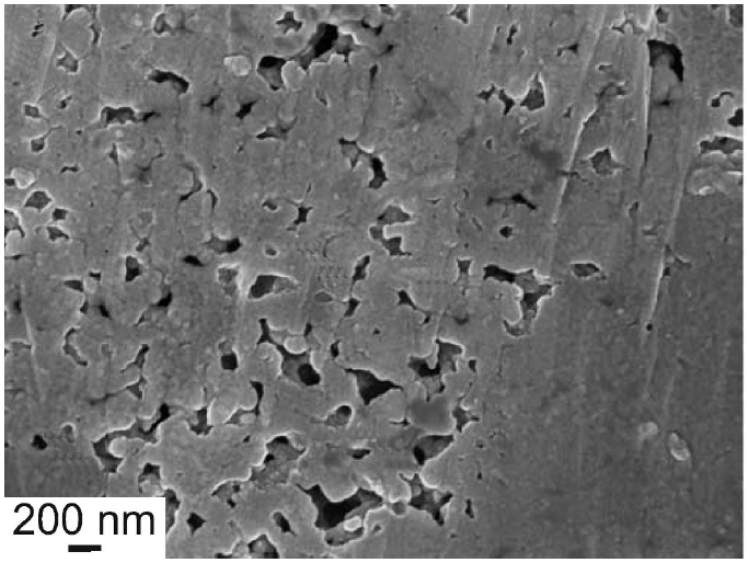

Figure 4.47: Nanometre scale pores are abundant in this SEM micrograph of a gas window maturity Barnett shale from Loucks *et al*., (2009).

4.3.2 Pore volumes and Pore Size Distributions (PSD) of the shales.

The pore size distributions of the Draupne Formation and Colorado Group shales are dominated by nanometre-sized pores, typically below 100 nm in diameter (Figures 4.11). The pore size distributions are predominantly unimodal, with a median pore throat width of 20 nm. This finding is supported by the work of Loucks *et al*., (2009), who identified that Barnett shale samples were dominated by nanometre-scale pores.

In the Draupne Formation, an average of 49.9% of all the pores in the mercury accessible pore size distribution was less than 25 nm in diameter. For the Colorado Group, this value was even higher, with an average of 84.7 % of all the pores measured by mercury intrusion being less than 25 nm in diameter. This is a significant result, demonstrating that shales are effectively "nanoporous" materials (using the terminology of Loucks *et al*., 2012). The higher percentage of sub-25 nm pores in the Colorado Group (84.7% compared to the Draupne Formation's 49.9%) is interpreted as being due to the Colorado Group's lower thermal maturity (further details of this is given in section 4.3.5, below).

Within the category of pores with diameters less than 100 nm, the most common pore size for the Draupne Formation shales was 10 nm to 3 nm, with an average value of 71.5 % of the pores in the 100 nm group. For the Colorado Group, the dominant pore size range was the 25 nm to 10 nm, with an average value of 56.1 % of the pores in the 100 nm category. This indicates that the Draupne Formation shales have nanometer-scale pores which are slightly narrower than those of the Colorado Group shales. This difference between the mesopore distributions is interpreted as being due to the mineralogy, especially the percentage of clay minerals. It was observed by Ross and Bustin (2009) in Devonian shales from British Columbia that clay-rich samples had unimodal mercury intrusion pore size distributions of less than 10 nm, whereas equivalent silica-rich Devonian shales were dominated by micrometer-scale pores. They noted that an increase in silica content resulted in a shift in the pore size distribution towards larger pore diameters. Their findings can be observed in Figure 4.48, where in

part a) the clay rich samples are dominated by nanometer scale pores, whereas in part b) the silica rich samples are dominated by micrometer-scale pores. The significant differences in the pore size distributions of clay-rich and silica-rich Devonian shales highlights the impact that mineralogy can have on the pore size distribution of shales, even for the Draupne Formation and Colorado Group shales, where the shift towards larger pore diameters is not as pronounced.

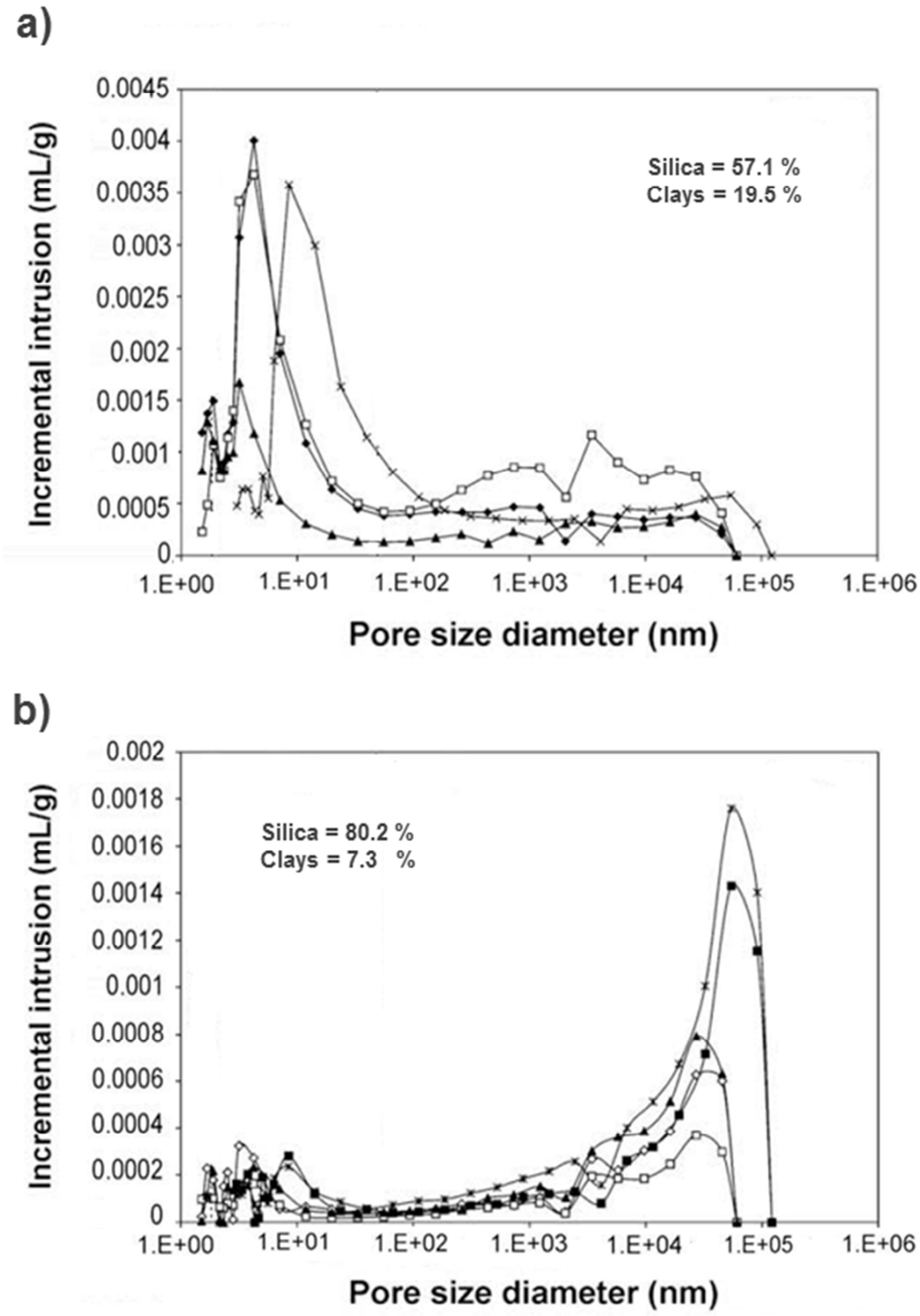

Figure 4.48: Mercury Intrusion Porosimetry pore size distribution (PSD) curves for Devonian shales from British Columbia (after Ross and Bustin, 2009). In part a) the clay-rich samples are dominated by nanometre-scale pores, whereas in part b) the silica-rich samples are dominated by micrometre-scale pores.

Although the majority of pores in the Draupne Formation and Colorado Group shales have diameters less than 25 nm, larger nanometre and micrometre pore sizes are still present, as reported in the mercury intrusion pore size distribution curves (Figure 4.10). The low pressure CO_2 adsorption isotherms at both -78^{o}C and 0^{o}C also indicate that some meso- and macropores are present, with the Type I / Type II hybrid adsorption curves being characteristic of gas adsorption occurring in micro-, meso- and macropores (Sing *et al*., 1985). The finding that a small abundance of micrometre-scale pores are present in the Draupne Formation and Colorado Group shales agree with the results of Ross and Bustin (2009) in Devonian shales from British Columbia. In Figure 4.48, part a) small volumes of mercury intrusion do occur above 1 x 10^3 nm (= 1 μm) in the clay-rich Devonian shales.

4.3.3 Pore volumes and porosities of the shales.

The average total pore volume of the Draupne Formation shales is smaller than the Colorado Group shales (0.0517 cm^3 g^{-1} vs 0.0766 cm^3 g^{-1}, respectively). This is interpreted as the Draupne Formation shales having a much deeper burial depth than the Colorado Group shales, and so being more compacted. The Hg-macropore volumes are determined at low intrusion pressures, and measure the pore volume of macropores > 100 nm in diameter. The average Hg-macropore volume of the Draupne Formation shales is 2.5 times larger than the Hg-macropore volume of the Colorado Group shales. This finding is interpreted as being due to the larger organic matter content of the Draupne Formation shales. In Figure 4.49, the percentage of Hg-macropore volumes in the shales increases as the TOC content increases for both the DF and CG shales. The correlation coefficient is R^2 = 0.86. The relationship between the percentage of macropores (> 100 nm) and the TOC can be explained as the macropores are primarily located in organic matter particles, and/or the organic matter disrupts the efficiency of the packing of the inorganic minerals thus forming larger pores in the shale matrix.

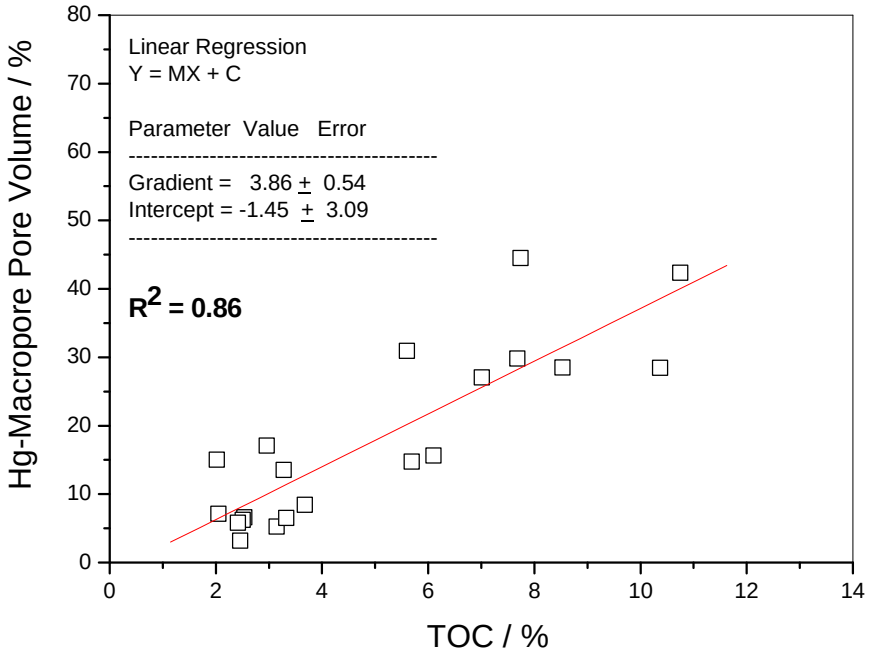

Figure 4.49 Hg-macropore volume against TOC for both the DF and CG shales. The percentage of the Hg-macropore volume increases as the TOC increases, indicating that the proportion of larger macropores (> 100 nm) is related to organic richness.

The sorption pore volume of the sub-100 nm diameter pores was determined using gas adsorption analysis. The pore volumes of these sub -100 nm pores are very similar in value for both sample suites, despite their different total porosities, thermal maturities and burial depths. The average sorption pore volume of the DF shales was 0.0171 cm^3g^{-1}, whilst the average sorption pore volume of the CG shales was 0.0184 cm^3g^{-1}. The commonality shared by these two shale suites is the organic-richness, and therefore the very similar pore volumes of the sub-100 nm pores is interpreted as being a property of Type II marine kerogen. This will be investigated further in Chapter 5.

The sorption pore volume of the Draupne Formation shales (average of 0.0171 cm^3g^{-1}) accounts for 33.0 % of the average total pore volume (average of 0.0517 cm^3 g^{-1}). For the Colorado Group, the average sorption pore volume (0.0184 cm^3g^{-1}) accounts for 24.0 % of the average total pore volume (0.0765 cm^3 g^{-1}). These percentages suggest that about a quarter to a third of the total pore volume is in sub-100 nm range. Two possible interpretations as to why the Draupne Formation has a larger percentage of sub-100 nm pores are: 1) the DF shales are more organic rich than the CG shales, and these sub-100 nm pores are located within the kerogen, and 2) the total pore volume of the DF shales is lower than the CG shales, because the DF shales have been subjected to increased compaction and cementation due to deeper burial depths.

The sorption pore volume of the Draupne Formation shales exhibits a good positive correlation to organic matter content (TOC), as reported in Figure 4.18 (above). This is typical of the correlations between pore volume and organic matter content found in the literature. However, in contrast the sorption pore volume of the Colorado Group shales exhibits a strong negative correlation to organic matter content (TOC). The amount adsorbed decreases as TOC increases, as reported in Figure 4.18 (above). The negative correlation of pore volume with TOC is counter-intuitive, as organic matter is a key site

for gas adsorption in shales, and positive correlations between TOC gas adsorption is often reported in the published literature. The negative correlation from organic matter content is probably a false correlation, due to an underlying effect that is masking the influence of organic matter in the Colorado Group shales. This factor is the mineralogy, as outlined below. The bulk mineralogy of the Colorado Group shales was obtained by a fellow PhD student who worked on the same CG samples. This mineralogical data is published in the thesis of Adamu (2012) and are reported in Table 4.13. The quartz content ranges from 28.08 to 47.27 %, with an average of 35.78 ± 7.92 %. The illite content ranges from 20.60 to 44.81 %, with an average of 29.74 ± 8.44 %. The carbonate content (calcite + dolomite) ranges from 1.00 to 14.69 %, with an average of 6.75 ± 4.70 %.

The illite content has an excellent correlation with the gas sorption pore volume of the Colorado Group shales, as reported in Figure 4.50. The correlation is positive, with a correlation coefficient of R^2 = 0.97. This indicates that the primary site of gas adsorption in the immature Colorado Group shales is in the pore structures of the shale matrix, in the illite clay mineral assemblages. Hence, an interpretation of this finding is that the illite content of the Colorado Group shales is the main controlling factor for pore volume, and organic matter content is secondary. The gas adsorption potential of the mineral illite was recognised by Ross and Bustin (2009).

When the sorption pore volume of the CG shales is normalised for illite content, an excellent correlation between sorption pore volume and TOC content is observed, as reported in Figure 4.51. The correlation coefficient is R^2 = 0.90. Once the abundance of illite in the Colorado Group shales is accounted for, the standard positive relationship between organic matter content and sorption pore volume is observed. Furthermore, the illite content of the CG shales is negatively correlated to the organic matter content, as reported in Figure 4.52. The correlation coefficient is R^2 = 0.92. The decrease in illite content with increasing TOC content is the underlying cause for decrease in sorption pore volume with increasing TOC content. The strong negative correlation between TOC and illite explains the unlikely correlation between sorption pore volume and TOC in Figure 4.18 (above). The overall conclusion is that the dominant control on the sorption pore volume in the Colorado Group shales is the illite content of the shale matrix, and the immature organic matter has a secondary role. This also agrees with the finding that the Colorado Group shales is dominated by isolated closed pores, that are not associated with organic matter (as outlined in Figure 4.56)

Table 4.13: Mineralogy of the Colorado Group shales.

Sample	Depth / m	Quartz / %	Illite / %	Carbonates / %
C1	505.3	39.4	27.3	5.2
C2	506.55	45.0	29.2	1.0
C3	541	47.2	33.1	4.2
C4	546.3	42.0	31.5	3.0
C5	561.5	37.0	26.0	7.0
C6	642.1	28.6	21.3	12.2
C7	647.57	35.0	19.6	12.4
C8	651.75	22.5	20.4	14.6
C9	675.02	28.0	44.8	3.6
C10	684.61	32.8	41.8	3.9

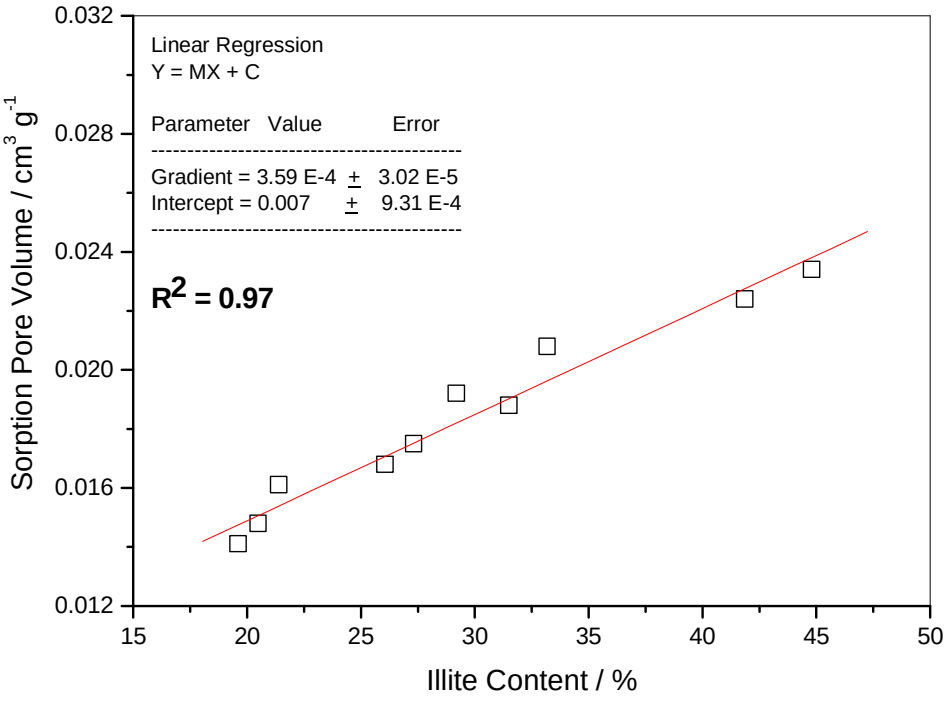

Figure 4.50: Sorption pore volume against illite wt.% content for the CG shales. The sorption pore volume exhibits an excellent positive correlated to illite content.

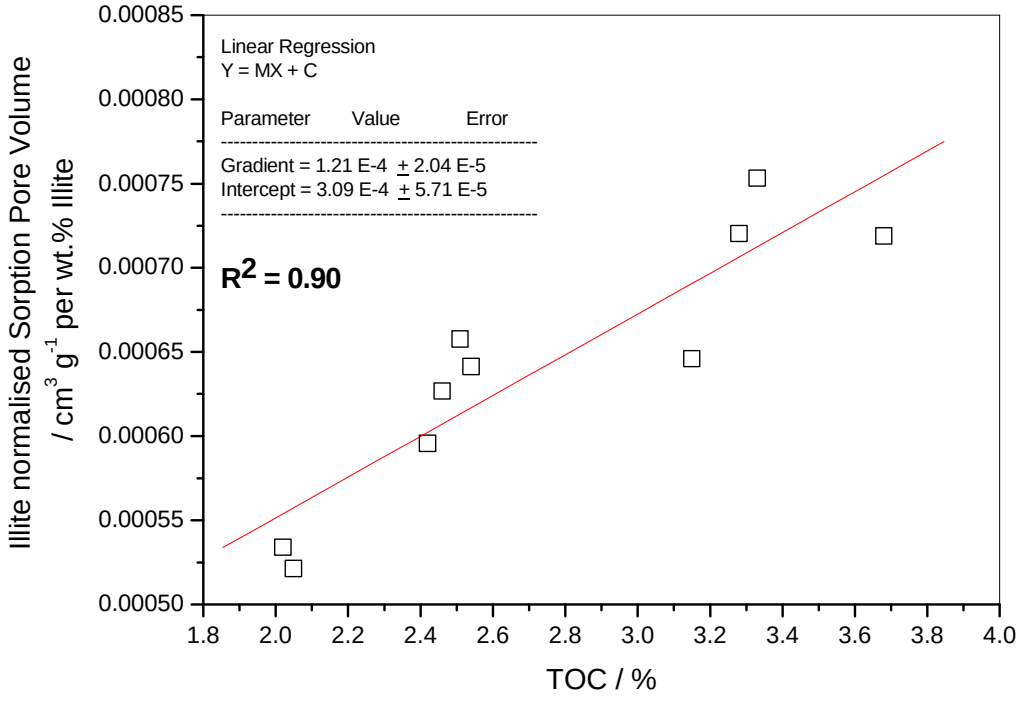

Figure 4.51: Normalised sorption pore volume (for illite) against TOC content for the CG shales. A strong correlation between illite normalised sorption pore volume and TOC is observed, indicating that pore volume occurs in the organic matter.

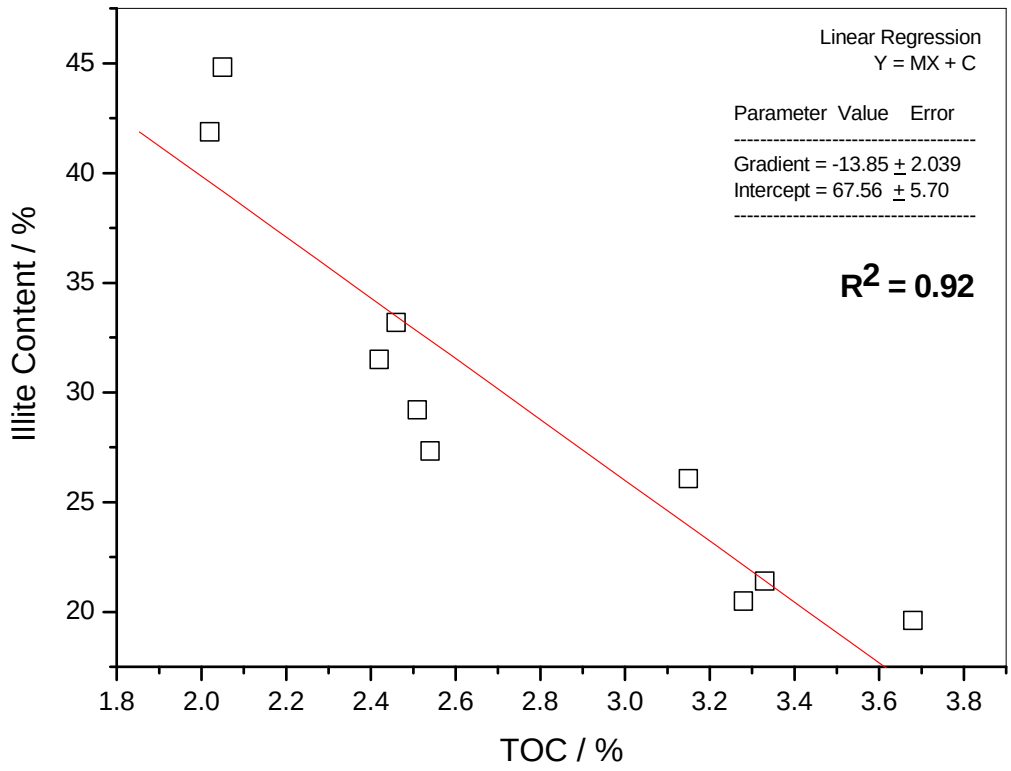

Figure 4.52: Illite against TOC content for the CG shales. The illite content is strongly negatively correlated to TOC content.

The micropore volume of < 0.7 nm diameter pores was determined using CO_2 adsorption at 0^oC. The micropore volume is a significant part of the sorption pore volume available to gas adsorption processes (i.e. pores that have up to 100 nm in diameter). The micropore volume of the Draupne Formation shales accounts for 52.3% of the gas sorption pore volume, and the micropore volume of the Colorado Group shales accounts for 35.9 % of the gas sorption pore volume. This finding indicates that the tiniest pores contribute significantly to the shale's pore volume; however, these pores maybe overlooked as they are not accessible to mercury intrusion porosimetry.

The micropore volumes of the Draupne Formation and the Colorado Group do not vary with increasing burial depth. This result is in contrast to the total pore volume, the Hg-macropore volume and the sorption pore volume, which to varying amounts, will decrease in pore volume with increasing burial depth. This finding suggests that micropores are not mechanically compressed during the compaction processes that occur during formation burial.

The micropore volumes of the Draupne Formation shales exhibit a good positive correlation to organic matter content (TOC), suggesting that organic matter is a key location of micropores in the Draupne Formation shales. Conversely, the micropore volumes of the Colorado Group are negatively correlated to the TOC content, this suggests that the primary location for micropores in the Colorado Group shales is not the organic matter component of the shales, but the mineral assemblages.

The illite content of the Colorado Group shales has an excellent correlation with the micropore volume, as reported in Figure 4.54. The correlation is positive, with a correlation coefficient of $R^2 = 0.88$. This result is interpreted as the illite minerals is the primary location of micropores in the immature Colorado Group shales is in the shale matrix, and organic matter content is a secondary location.

The normalisation of the Colorado Group shale micropore abundance for TOC content leads to an excellent correlation between micropore and illite content, as reported in Figure 4.55. The correlation coefficient of the normalised micropore volumes and illite is $R^2 = 0.96$. This positive correlation supports the interpretation that the micropores of the immature Colorado Group shales are primarily located in the inorganic mineral matrix.

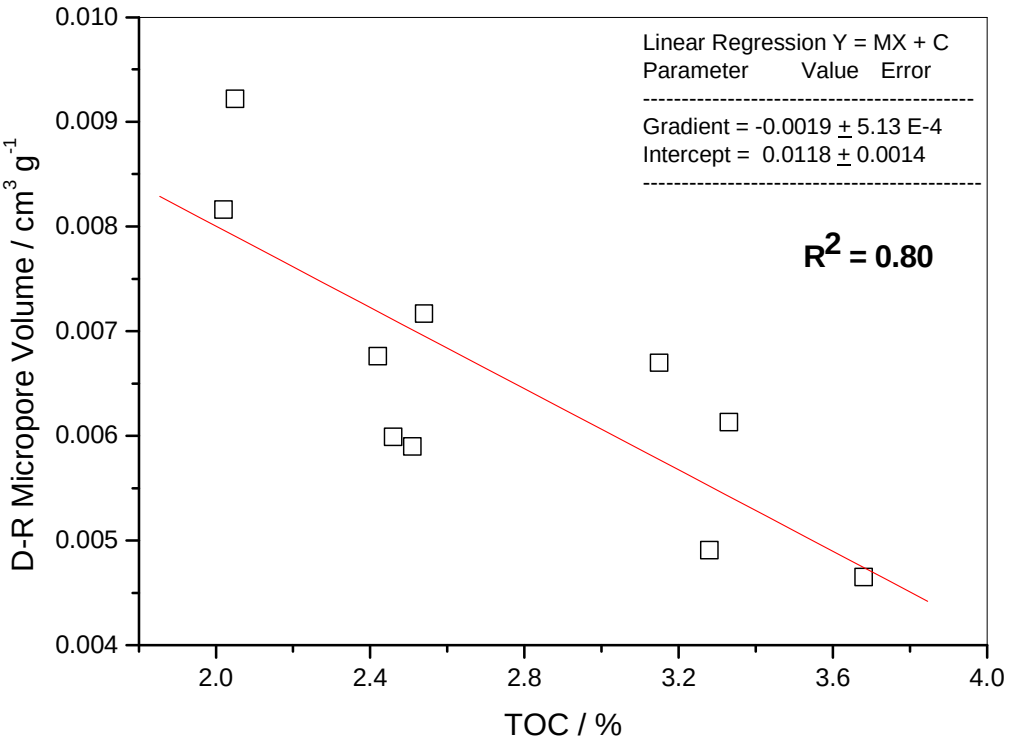

Figure 4.53: Micropore volume against TOC for the CG shales. There is a false negative correlation between micropore volumes and organic matter content (TOC).

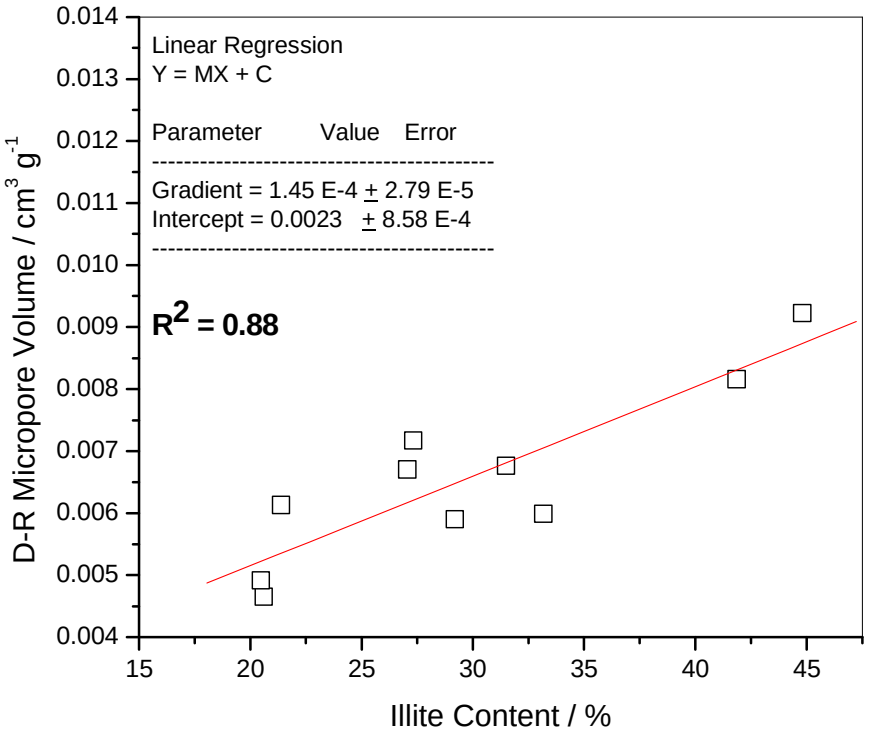

Figure 4.54: Micropore volume against illite wt.% for the CG shales. A strong correlation between micropore volumes and illite content exists.

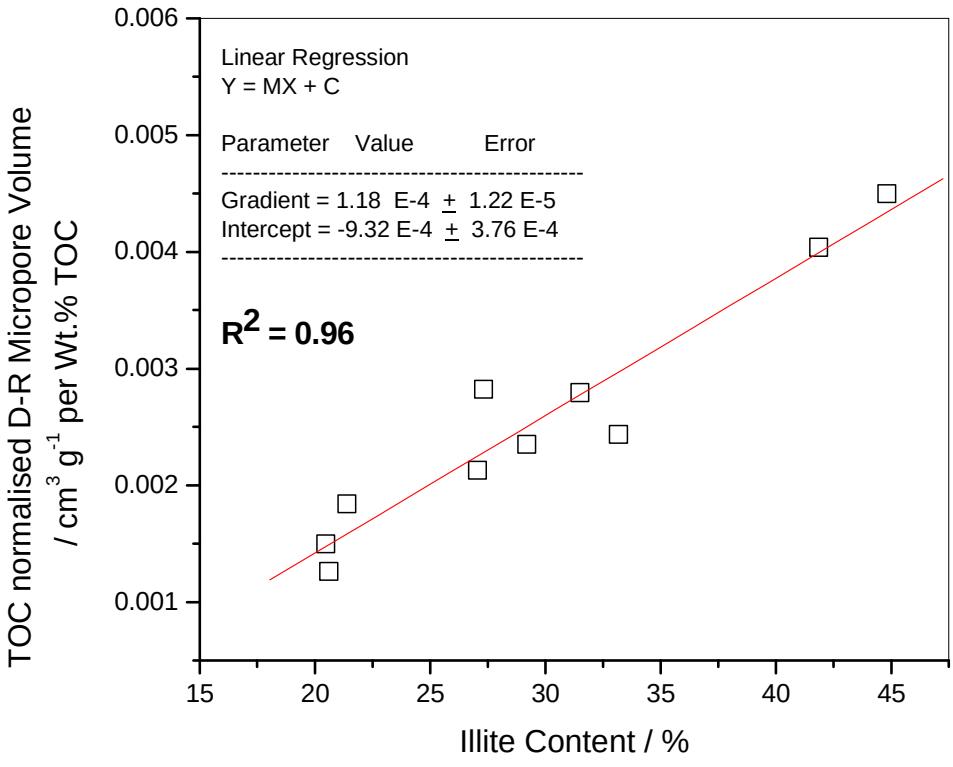

Figure 4.55: TOC normalized D-R micropore volume vs Illite content for the CG shales. An excellent correlation exists between the micropore volume and % illite after the effect of TOC is accounted for.

The proportion of pore volume in each of the three pore size ranges for the DF and CG shales were listed in Table 4.7 (above). The open pore volumes of the Draupne Formation shales accounted for 61.8 % of the total pore volume, whereas the open pore volume only accounts for 31.9% of the total pore volume in the Colorado Group shales. It is a significant finding that less than one third of the pore volume in the CG shales is accessible to mercury or gas adsorptives, with the remaining pore volume being completely isolated and inaccessible. This finding indicates that the pore system of the Colorado Group shales is much less open and interconnected than that of the Draupne Formation shales. The lower interconnectivity of the CG pore system is interpreted as being due to the lower organic matter content compared to the DF shales. It is reported in Figure 4.56 that as the TOC content of the shale samples increase, the accessible pore volume increases. This suggests that the organic matter is a primary location for open accessible pores, and the inorganic mineral matrix is host to closed inaccessible pores.

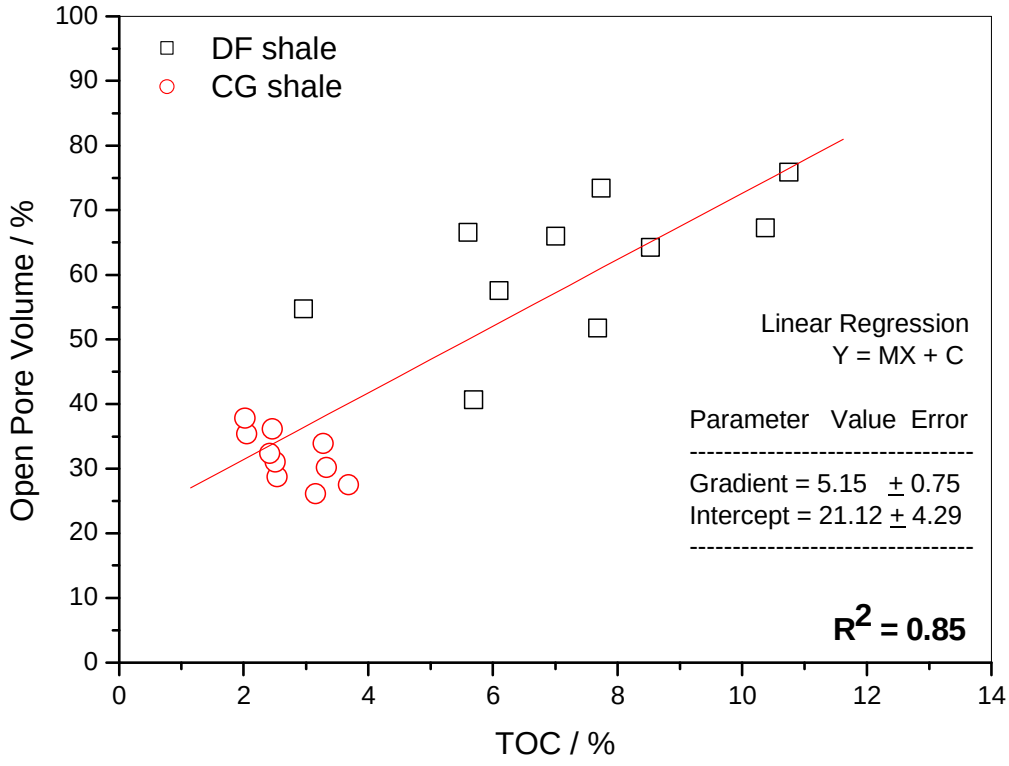

Figure 4.56: Open pore volume against TOC for both the DF and CG shales. The increase in accessible pore volume with increasing organic matter content indicates that the primary location for open accessible pores is in the organic matter, and the inorganic mineral matrix is host to closed inaccessible pores, for the Draupne Formation and Colorado Group shales.

The total porosity, the Hg-macroporosity, the gas sorption porosity and the D-R microporosity of the Draupne Formation and Colorado Group shales were determined from the corresponding pore volumes and the bulk density of the shale. The Draupne Formation shales exhibited a noticeable decrease in the total porosity with increasing burial depth, from 17% down to 5%. This pore volume reduction can be attributed to the mechanical compaction and lithification of the shale strata, and also to the cementation of pores due to precipitation of minerals that are dissolved in pore fluids. The Colorado Group shales exhibited no observable trend in total porosities with increasing burial depth (average total porosity = 17.0%). The total porosities of the CG shales are lower than would be expected for shales at burial depths of ~500 m, and this indicates that these shales have been buried to a deeper burial depth in the geological past, and then uplifted to their current depth.

The gas sorption porosity of Draupne Formation shales exhibits a strong correlation with total porosity (R^2 = 0.94). In contrast, the Hg-macroporosity and the D-R microporosity exhibit a weaker correlations to total porosity (R^2 = 0.6 and R^2 = 0.3, respectively). For the Colorado Group, the Hg-macroporosity, the sorption porosity and the D-R microporosity has no observable correlation to the total porosity of the shales. This indicates that the sub-100 nm porosity is a primary controlling factor on the total porosity of the Draupne Formation shales, with the macroporosity > 100 nm having a secondary influence. The interpretation of this finding is that the organic matter content of the Draupne Formation is larger than the Colorado Group shales, and the sub-100 nm porosity is located within the organic matter. This interpretation agrees with the positive correlation observed between D-R microporosity and TOC content for the Draupne Formation shales.

4.3.4 Surface areas of the shales.

A large proportion of the internal surface area of the Draupne Formation shales is located within micropores (< 2nm). The average N_2 BET surface area (6.16 m^2 g^{-1}) is much smaller than the average CO_2 BET surface area value (20.70 m^2 g^{-1}). As micropores are inaccessible to N_2 at -196^oC, the large difference is attributed to significant micropore surface area. Conversely, the average N_2 BET surface area (16.98 m^2 g^{-1}) of the Colorado Group shales is similar to the average CO_2 BET surface area value (22.56 m^2 g^{-1}). This suggests that a smaller proportion of internal surface area is located within the micropores (< 2 nm), and a larger proportion of the total surface area is located in mesopores and macropores.

The total surface areas of both the Draupne Formation and Colorado Group shales are very similar (average of 20.35 m^2 g^{-1} and 22.36 m^2 g^{-1}, respectively), indicating that these shales suites have similar pore structures. The total surface area of the shale pore system is almost exclusively found within the sub-100 nm pores, as reported by the excellent positive correlations in Figures 4.57 and 4.58. For the Draupne Formation, the correlation coefficient is R^2 = 0.99. For the Colorado Group, the correlation coefficient is R^2 = 0.99. The interpretation for this finding is that the macropores (> 100 nm) contribute very little to the total surface area of the shale pore system. This is supported by the very low macropore surface area values, which have an average of only 0.35 m^2 g^{-1} for the DF shales, and an average of 0.20 m^2 g^{-1} for the CG shales.

The primary location for surface area in the Draupne Formation shales is in the micropores of organic matter. A large proportion of the total surface area is located within the micropores (average = 73.7%), and the micropore surface areas of the DF shales are strongly correlated to organic matter content, as reported in Figure 4.59. The correlation coefficient between the micropore surface area and TOC content is R^2 = 0.87. Furthermore, in Figure 4.59 the percentage of micropore surface area in both the Draupne Formation and Colorado Group shales increases as TOC content increases, with an excellent positive correlation of R^2 = 0.96 (where the relative proportion of micropore surface area is out of the total surface area).

Conversely, the primary location for surface area in the Colorado Group shales is in the mesopores of shale matrix. The Colorado Group shales have a low percentage of micropore surface area (average = 26.4 %), which agrees with the similar values of BET surface area for both N_2 at -196°C and CO_2 at -78°C. The location of surface area in mesopores is interpreted as being due to the lower organic matter content of the CG shales, leading to fewer micropores in the CG shales compared to the organic rich DF shales. This finding is supported by the excellent positive correlation (R^2 = 0.96) between total surface area and illite wt% content.

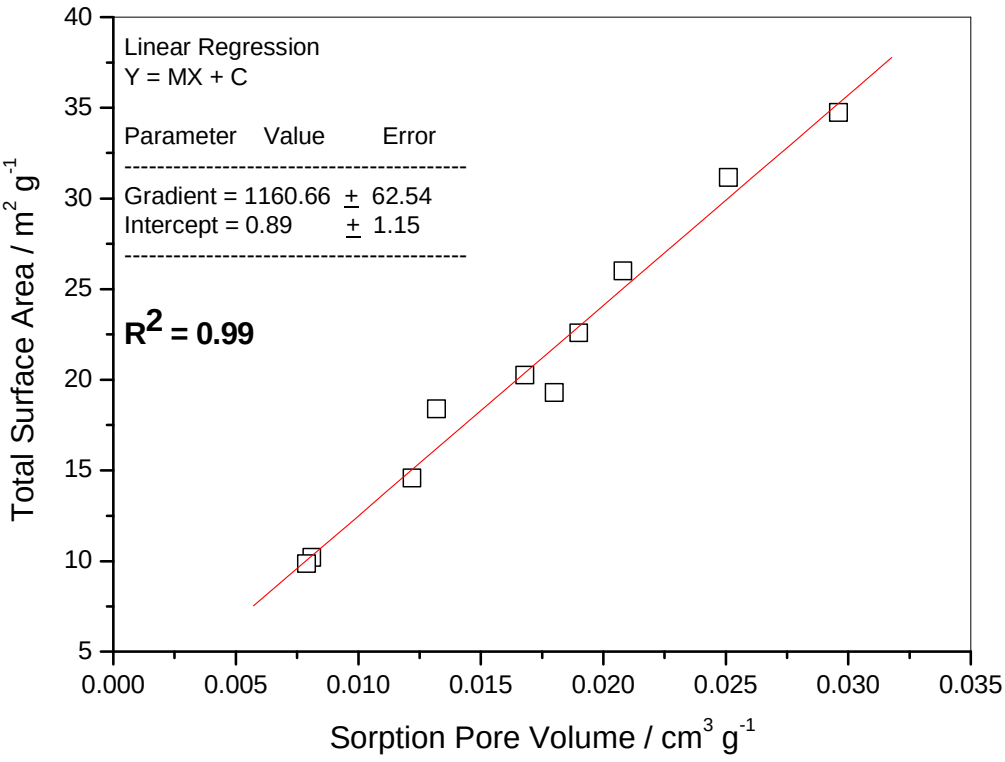

Figure 4.57: Total surface area against sorption pore volume for the Draupne Formation shales. The total surface area exhibits an excellent positive correlation to sorption pore volume, indicating that the surface area of the shales is almost wholly found within the sub-100 nm diameter pores.

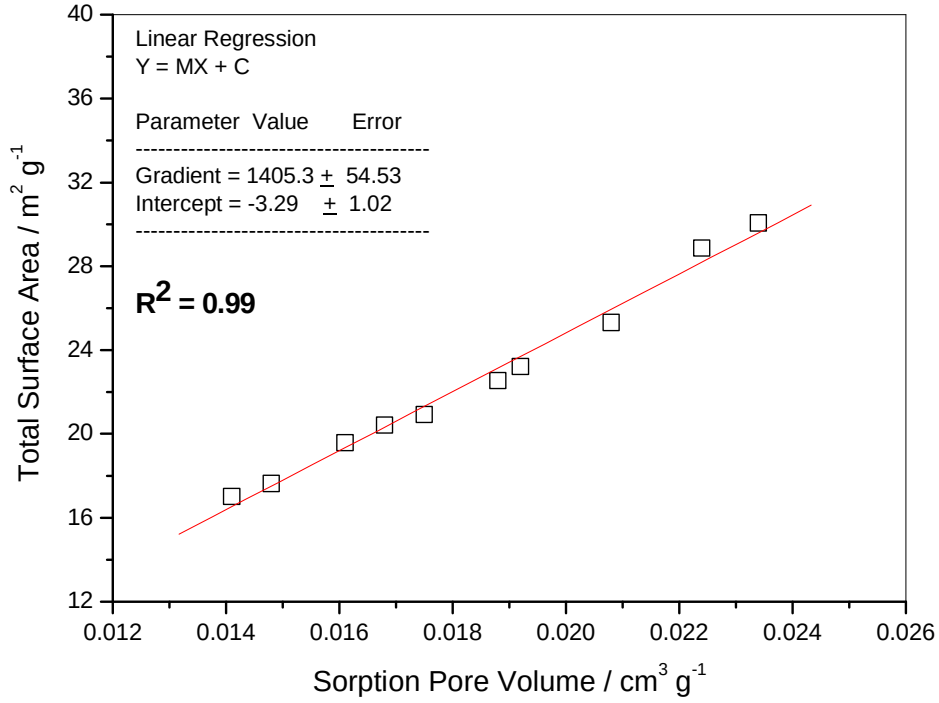

Figure 4.58: Total surface area against sorption pore volume for the Colorado Group shales. The total surface area exhibits an excellent positive correlation to sorption pore volume, indicating that the surface area of the shales is almost wholly found within the sub-100 nm diameter pores.

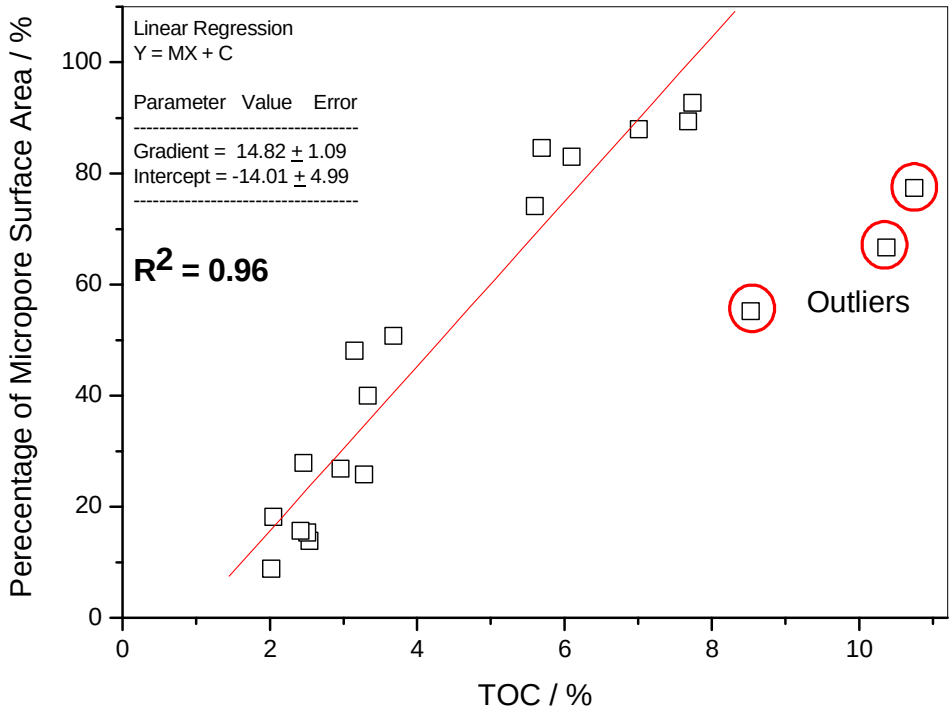

Figure 4.59: Percentage of micropore surface area against TOC. The percentage of micropore surface area in both the Draupne Formation and Colorado Group shales increases as TOC content increases,

4.3.5 Pore structure and thermal maturity

Thermal maturity has a significant influence on the pore structure of the Draupne Formation shales. The pore volumes of the sub-100 nm pores decreases as the thermal maturity of the shales increase. Evidence of the pore volume reduction of the sub- 100 nm pores can be observed in the sorption pore volumes, the D-R micropore volumes, the porosities and the surface areas of the Draupne Formation shales (see Figures above). The pore volume reduction of the sub- 100 nm pores can also be observed in the mercury intrusion Pore Size Distribution curves. The pore size distribution curves indicate that a significant decrease in the pore volume of the sub-100 nm pores occurred with increasing maturity. This is observed in Figure 4.60, where the pore volume decreases substantially with increasing maturity in the DF1, DF5 and DF10 shales. This finding agrees with Jarvie *et al.* (2012), who identified that oil window maturity shales are not as macroporous as gas window maturity shales. The reduction of pore volume in the sub-100 nm pores with maturation is interpreted as being due to changes in levels of aromaticity of the kerogen; this interpretation is discussed further in Chapter 5

The decrease in the pore volumes of the sub-100 nm pores of the Draupne Formation shales is atypical of the commonly observed maturity correlations in the literature (Gan *et al*., 1972; Clarkson and Bustin, 1996; Bustin and Clarkson 1998; Prinz *et al.*, 2004; Prinz and Littke, 2005; Ross and Bustin, 2009; Loucks *et al*., 2009; Zhang *et al*., 2012). Usually, thermal maturation of shales (and coals) is demonstrated to occur in tandem with an increase in the pore volume of the kerogen (Loucks *et al*., 2009), and especially in the pore volume of the micropores in the organic matter component (Clarkson and Bustin, 1996; Prinz and Littke, 2005; Ross and Bustin, 2009). Since the opposite effect is occurring in the Draupne Formation shales, it is interpreted that the limited maturity range of the DF sample suite is a factor. The geochemical analyses indicate that the Draupne Formation shales have a maturity range from immature up to oil generation maturity (catagenesis), with no gas window maturity (VR_c =1.4 %) shales being present. However, in nearly all of the studies that have identified an increase in the abundance of micropore volume (i.e. Prinz and Littke, 2005; Ross and Bustin, 2009), the sample suites have included shales of much high thermal maturity, generally in the gas maturity window (> 1.4%).

It is therefore suggested that the pore volume of immature and early oil window maturity shales initially decreases, until a minimum is reached at intermediate maturities, and then the pore volume begins to steadily increase again at higher maturity levels (as described in Figure 4.61). This “U” shaped maturity trend has been frequently observed in coal studies (Moffat and Weale, 1955; Yee *et al*., 1993; Levy *et al*., 1997; Bustin and Clarkson, 1998; Hildenbrand *et al*., 2006; Weniger, 2012), and it is suggested here that the same U-shaped maturity trend occurs in organic rich shales and kerogens. This interpretation of decreasing pore volumes in pre-gas window samples will be investigated further in Chapter 5 for isolated DF kerogen samples.

In contrast to the maturity correlations of the Draupne Formation shales, the Colorado Group shales do not exhibit any trends with increasing maturity. None of the sorption pore volumes, the D-R micropore volumes, the porosities and the surface areas of the Colorado Group shales exhibit any evidence of systematic change with increasing maturity. Even the depth normalised pore volume data exhibits no correlation to the variations in maturity. An interpretation of the cause behind this apparent lack of correlation will be discussed further in Chapter 5 for isolated CG kerogen samples.

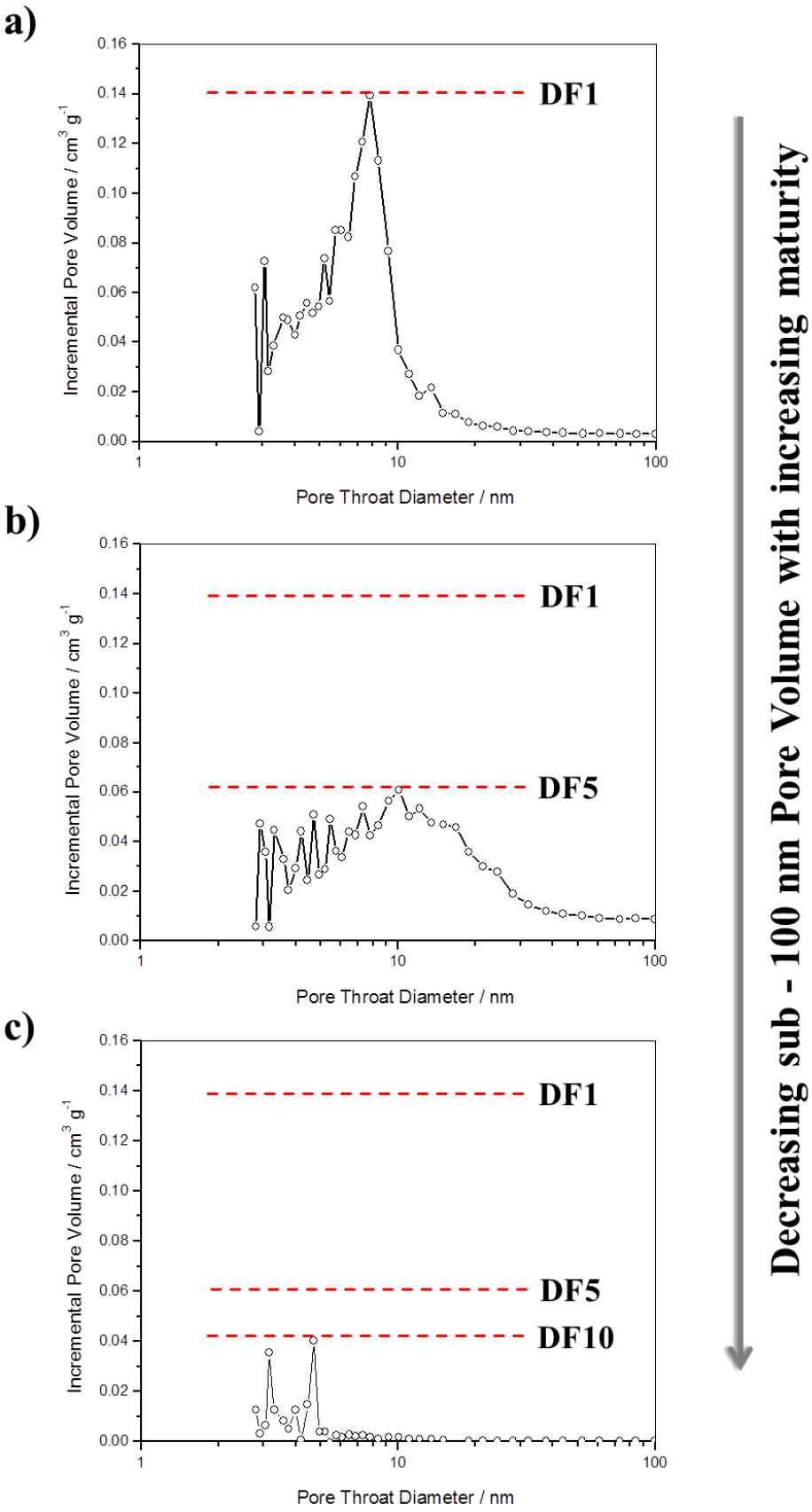

Figure 4.60: Pore Size Distribution curves (up to 100 nm) for the DF1, DF5 and DF10 shales. In part a), the pore volume of the immature DF1 shale is large. In part b), the pore volume of the medium maturity DF5 shale has decreased significantly. In part c), the oil window maturity DF10 shale is very low. This series of PSD curves indicate that the pore volume of the sub – 100 nm pores decreases significantly with increasing maturity.

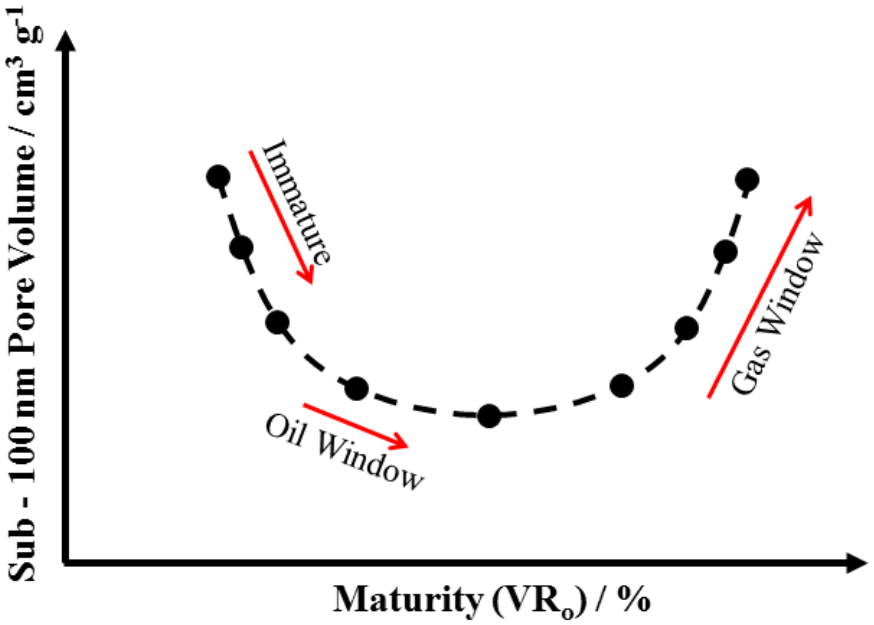

Figure 4.61: Sub-100 nm pore volume against maturity. It is suggested that the pore volume of immature and early oil window maturity shales initially decreases, until a minimum is reached, and the pore volume begins to steadily increase.

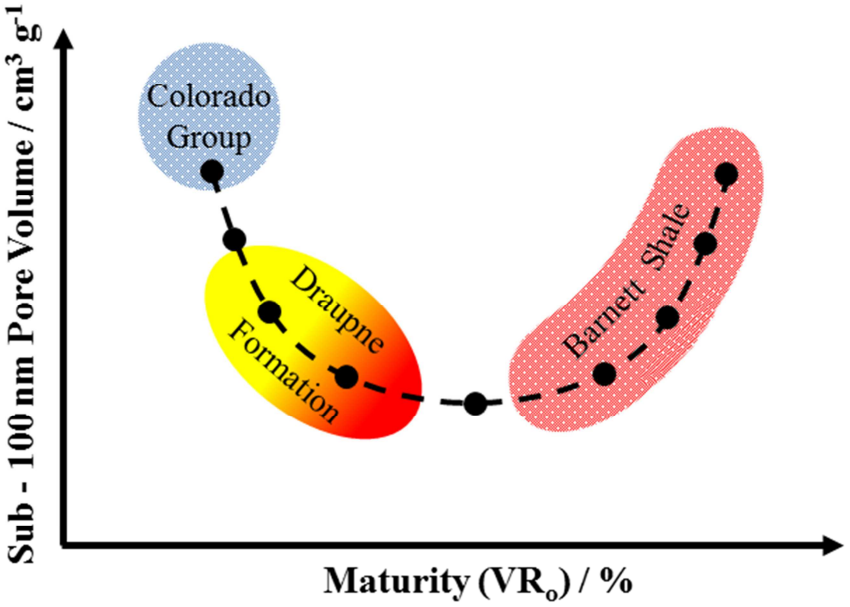

Figure 4.61 (Continued): Locations of DF and CG shales on the sub-100 nm pore volume against maturity schematic diagram. At the top left, the suggested location of the Colorado Group shales, which do not exhibit any evidence of systematic change with increasing maturity. The region is colour coded as blue, because the CG shales are immature. At the bottom left of the diagram, the suggested region for the Draupne Formation shales is located. The sub-100nm pore volumes of the DF shales decrease with increasing maturity. The region changes from yellow to orange to indicate increasing maturity. At the right of the schematic diagram, the suggested location for the Barnett shales is highlighted. The pore volume of the Barnett shale increases with thermal maturity (Loucks *et al.*, 2009). The region is colour-coded red, as the Barnett shale is in the gas window (> 1.6%).

4.4 Summary and Conclusions

The major findings of Chapter 4 are:

- Shales are effectively “nanoporous” materials, with the pore size distributions of the DF and CG shales being dominated by nanometre-sized pores, typically below 100 nm in diameter, with a median pore throat width of 20 nm.

- The open pore volume of shales is strongly positively correlated to the abundance of organic matter (TOC), indicating that the pore structures are more interconnected in kerogen than in inorganic shale minerals. The open (accessible) pore volumes of the DF shales accounts for 61.8 % of the total pore volume, whereas the open pore volume of the CG shales only accounts for 31.9 % of the total pore volume. Less than one third of the pore volume in the CG shales is accessible, with the remaining pore volume being completely isolated and inaccessible, and this could be due to the lower amounts of OM in the CG shales.

- The sorption pore volume of the Draupne Formation shales exhibits a good positive correlation to organic matter content (TOC), whereas the sorption pore volume of the Colorado Group shales exhibits a strong negative correlation to organic matter content (TOC). The CG shales are influenced by illite content.

- The micropore volume of the DF shales accounts for half of the gas sorption pore volume, whilst the micropore volume of the CG shales accounts for one third of the gas sorption pore volume. The micropore volumes of the DF shales exhibit a good positive correlation to organic matter content (TOC), whereas the micropore volumes of the CG are negatively correlated to the TOC content.

- A large proportion of the internal surface area of the DF shales is located within micropores (< 2nm). Conversely, a larger proportion of the total surface area of the CG shales is located in mesopores and macropores. The primary location for surface area in the DF shales is in the micropores of organic matter. Three quarters (75%) of the total surface area is located within the micropores, and the micropore surface areas are strongly correlated to organic matter content. Conversely, the primary location for surface area in the CG shales is in the mesopores of shale matrix, with only one quarter of the surface area being found in the micropores.

- Thermal maturity has a significant influence on the pore structure of the DF shales (but not in the CG shales). The pore volumes of the DF shales sub-100 nm pores decreases as the thermal maturity of the shales increase. Evidence of the pore volume reduction of the sub- 100 nm pores can be observed in the sorption pore volumes, the D-R micropore volumes, the porosities and the surface areas of the Draupne Formation shales, and correlates to maturity.

- A U-shaped maturity trend is suggested for organic rich shales, where the pore volume of immature and early oil window maturity shales initially decreases, until a minimum is reached at intermediate maturities, and then the pore volume begins to steadily increase again. This U-shaped maturity trend has been observed in coal studies, and may have a similar mechanism.

Chapter 5: Porous structure of kerogen

5.1 Introduction

5.1.1 Origin of kerogen

Kerogen is the most abundant form of organic matter in the geosphere, and is the dominant pool of carbon in the global carbon cycle; there is an estimated 10^{16} tons of kerogen stored in the Earth (Durand, 1980). Kerogen has a complex and varied biological origin; it is formed from the preservation of dead organic material as sedimentary organic matter (SOM). Typically, less than 1% of a dead organism's biomass is preserved in the sediment column (Tissot and Welte, 1978; Summons, 1993), with the vast majority of the organic tissue being rapidly remineralised by animal and microbial decomposers (Tyson, 1995). A range of bacteria are required to degrade organic matter, with each type having a particular role. The hydrolytic and fermentative bacterial groups are especially important, as they are the only types capable of degrading the larger biomacromolecules of fresh organic matter into the smaller monomer sub-units required by other bacteria (Tyson, 1995).

The small amount of organic matter that is deposited in to the sediment column is done so under the favourable conditions of high primary productivity, high sedimentation rates and oxygen deficient bottom waters (anoxia). The metabolic pathways of organic matter remineralisation (oxygen consumption, sulfate reduction, fermentation and methanogenesis, Heinrichs 1993), are disrupted under the conditions of high production of organic matter, high sedimentation rates and anoxia.

Kerogen is formed by a dual process of selective preservation of resistant biopolymers (such as lipids and lignin), and the formation of new geopolymers in the sediment column (Vandenbroucke and Largeau, 2007). These geopolymers are high molecular weight macromolecules that do not exist in living organisms, but are formed from the polymerisation and condensation reactions of chemically resistant low molecular weight biomolecules and humic substances (Vandenbroucke and Largeau, 2007).

During the early stages of diagenesis (in the first few meters of the sediment column), the more reactive biochemical constituents of organisms (such as the protein and carbohydrates) are rapidly consumed by microbial degradation (Tyson 1995). The more resistant organic constituents (i.e. lipids and lignins), will be selectively preserved, and concentrated within the sediments (even though their initial abundance in living organisms is low). At the end of diagenesis, sedimentary organic matter is composed mainly of kerogen and bitumen (Killops and Killops, 2005).

Quantitatively, the two most important contributors of organic matter to kerogen are algae and terrestrial higher plants (Peters *et al*, 2004). Some researchers have claimed that the contribution of bacterial organic matter to kerogen is minor (Hartgers *et al*., 1994), although this is still not widely accepted. The composition of kerogen is often dominated with amorphous organic matter (> 80 %), with only minor amounts of well-defined structured organic particles (e.g. spores, pollen) being found in kerogen (and these are usually well dispersed; Tyson, 1995).

The dominant biological tissues contributed to kerogen are algaenan, cutan, suberan and lignin. These tissues are resistant to oxidation and microbial degradation. The contribution of algaenan, cutan and suberan results in many kerogens being more aliphatic in nature than coals. These organic substances are highly aliphatic and insoluble lipid-derived biopolymers that resist microbial biodegradation. The structure of cutan and algaenan can be seen in Figure 5.1.

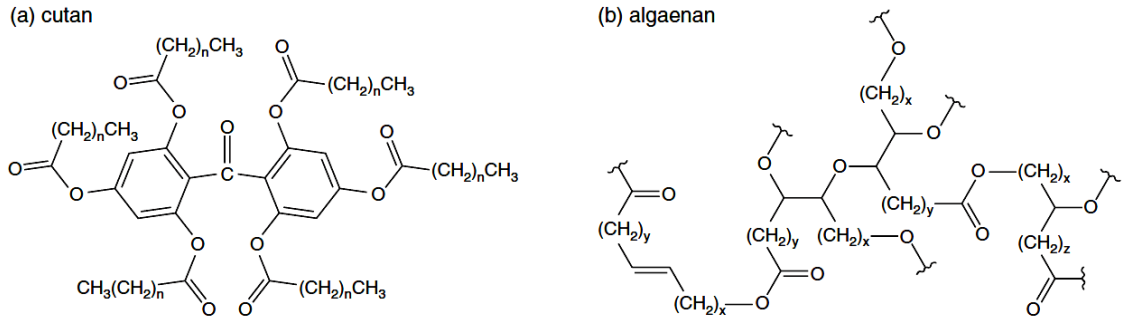

Figure 5.1: The structure of a) cutan, after McKinney *et al.* 1996, and the structure of b) algaenan, after Blokker *et al*. 1998.

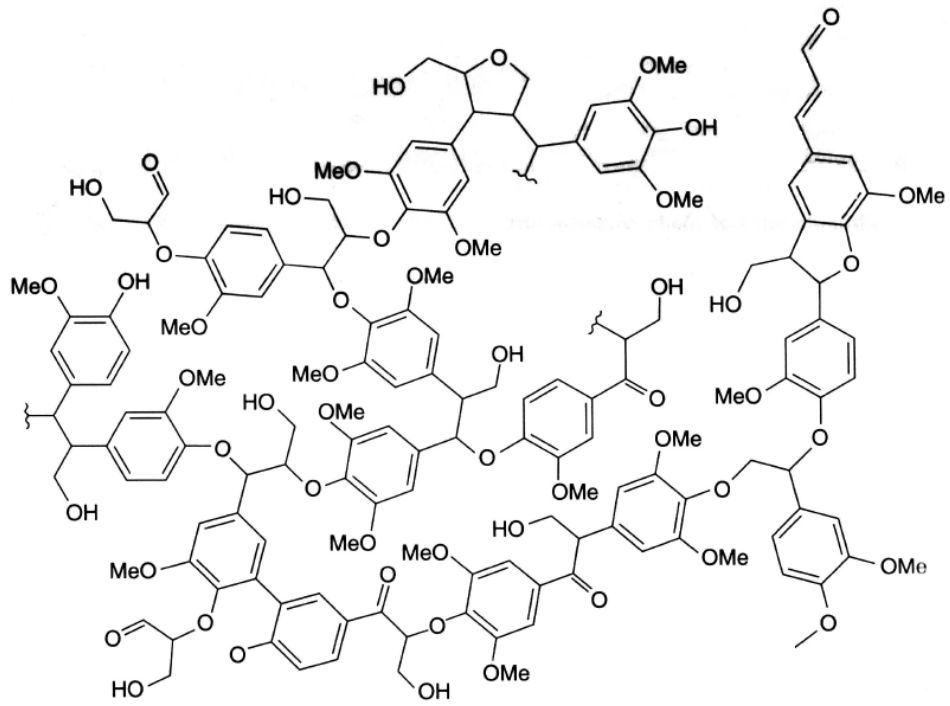

Figure 5.2: Structure of lignin, after Killops and Killops, 2005

5.1.2 Porous structure of kerogen

The pore structure of kerogen is not well understood, and very little research on the porous nature of isolated kerogen is available in the published literature. It is believed that the pore structure of kerogen is dominated by micropores (Clarkson *et al*., 2012, Amann-Hildenbrand *et al*., 2012), with lesser amounts of meso- and macropores (Passey *et al*., 2010). It is also believed that the pore size distribution of kerogen is influenced by geochemical composition and thermal maturity.

The closest analogue to kerogen is coal, and in the coal literature it is well established that vitrinite is the most microporous maceral. Vitrinite has a higher methane storage capacity than either inertinite (Unsworth *et al*., 1989; Lamberson and Bustin, 1993), or liptinite (Chalmers and Bustin, 2007). High inertinite content results in insignificant levels of microporosity (Clarkson and Bustin, 1999). Liptinite has also been found to contain very little microporosity (Chalmers and Bustin, 2007). A transmission electron microscope (TEM) study (Harris and Yust, 1976) confirmed that vitrinite in coal is mainly micro- and mesoporous, that inertinite is mainly mesoporous, and liptinite is mainly macroporous.

Terrestrial derived Type III woody kerogen (equivalent to vitrinite) has the highest gas storage capacity of the kerogen groupings (Noble *et al*., 1997; Jarvie, 2005; Zhang *et al*., 2012). This is shown in Figure 5.3:

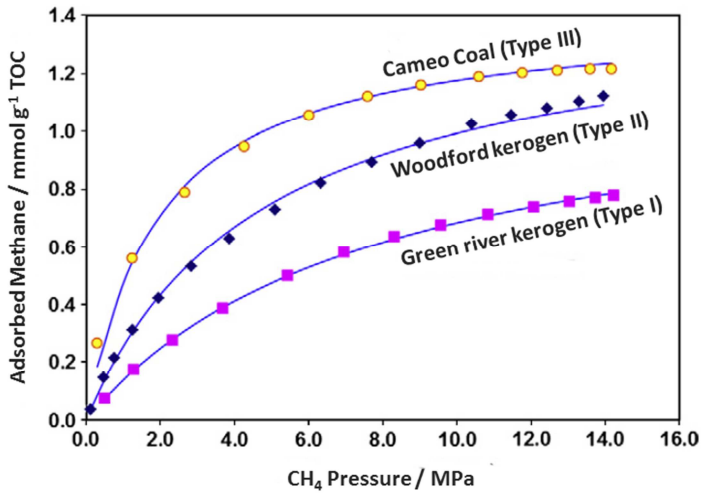

Figure 5.3: Methane adsorption by isolated kerogens shows that wood terrestrial Type III kerogens exhibit the highest gas adsorption potential (after Zhang *et al*., 2012)

Type III woody terrestrial kerogen has the highest inherent gas storage capacity, but the majority of shale gas produced in the USA comes from gas bearing shales containing Type II marine algal kerogen (Glorioso and Rattia, 2012). For example, the Barnett shale of the Fort Worth basin, and the Marcellus shale of the Appalachian basin are both of Type II marine kerogen in origin.

The porosity of organic matter dispersed in shale changes with compaction and thermal maturation (Loucks *et al*., 2009). Thermal maturation can cause an increase in the abundance of microporosity in the organic component of sedimentary rocks (Gan *et al*., 1972; Clarkson and Bustin, 1996; Bustin and Clarkson 1998; Prinz *et al.*, 2004; Prinz and Littke, 2005; Ross and Bustin, 2009). In kerogen, the increase in the relative abundance of micropores occurs at the expense of the macropore and mesopore content (Crosdale *et al.*, 1998).

The porosity and pore size distribution of kerogen is greatly altered in highly mature shales (Loucks *et al*., 2009; Passey *et al*., 2010). Whilst thermal maturity increases kerogen microporosity significantly (with large internal surface areas available for gas adsorption, Amann-Hildenbrand *et al*., 2012), the actual pore volumes of kerogen micropores are small, and it is estimated that total kerogen porosity is never usually more than 3% of bulk rock volume (Modica and Lapierre, 2012). This thermal maturity driven porosity change is due to the aromatization of the kerogen, with the rearrangement and loss of alkyl side chains (Killops and Killops, 2005). The maceral composition has a greater impact on microporosity capacity in higher rank coals than in lower rank coals (Chalmers and Bustin, 2007)

It has been shown that different types of organic material exhibits different levels of porosity, even though the thermal maturity is the same. This is because the tendency to form pores is dependent on the origin of the organic matter, even when subjected to the same level of thermal maturation (Curtis *et al*., 2011). It was observed that adjacent kerogens exposed to the same thermal environment within a distance of several microns from each other showed significant differences in porosity (Curtis *et al*., 2011). It is reported in Figure 5.4 that three different kerogens 12μm apart in the same high maturity Woodford shale sample had different levels of porosity:

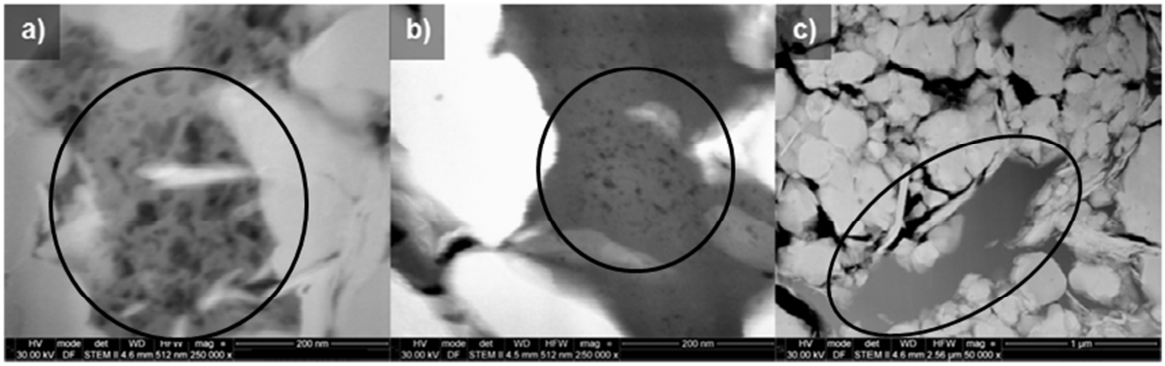

Figure 5.4: FIB-SEM images of porosity in kerogens. These three kerogen particles were 12 μm apart in the same Woodford shale sample. The difference in porosity is attributed to variable origin of kerogen (after Curtis *et al*., 2011).

5.2 Results

5.2.1 Influence of pyrite on gas adsorption isotherms of isolated kerogen.

The nanometre scale pore structure of the Draupne Formation and Colorado Group kerogens were investigated using low pressure gas adsorption isotherms. The isolated kerogen adsorption isotherms needed to be normalised and corrected for the presence of iron pyrite in the kerogen samples. Gas adsorption isotherms obtained from the gravimetric IGA system are a relative measurement of the absolute amount of gas adsorbed. The amount of sample used is typically ~ 100 mg, so the absolute amount of gas adsorbed is scaled up to a relative "per gram" basis (i.e. mmol g^{-1}). Iron pyrite is a dense component of kerogen (~ 5 g cm^{-3}), and therefore even a trace amount of iron pyrite in the kerogen sample contributes to the total mass being analysed, and thus changes the relative "per gram" amount of gas being reported in the isotherm . This problem is corrected by determining the weight percent of pyrite in each sample, and then normalising the kerogen isotherm data up to the amount of adsorption that would be obtained if the kerogen was 100% pure organic matter.

Firstly, the gas adsorption uptake capacity of iron pyrite was measured, as this data could not be found in the literature. This was done to determine if pyrite had an adsorption potential that would adversely impact the gas adsorption experiments of the isolated kerogens. Therefore, a series of gas adsorption isotherms for a certified mineral standard of pyrite were performed to investigate the adsorption potential of pure iron pyrite. The pyrite mineral standard was obtained from the Clay Minerals Society repository, with all standards having a percentage purity of 99.7% or higher. The gas adsorption isotherms were obtained under identical experimental conditions and procedures as the kerogens to ensure the validity of the comparison to the isolated kerogen isotherm data.

A 100 mg of finely crushed iron pyrite mineral standard was used to obtain the experimental data using the IGA system adsorption equipment. The CO_2 adsorption isotherms at -78^oC for a mineral standard of iron pyrite are reported in Figure 5.5. The iron pyrite has negligible gas adsorption uptake, with the pyrite adsorption isotherms tracing along the x-axis, reaching a maximum adsorption uptake of only 0.002 mmol g^{-1}. In the inset box of Figure 5.5, a magnification of the isotherms is reported, showing that the isotherms have a Type I shaped curve, according to the IUPAC system. It can also be observed that the two replicates have good repeatability.

The adsorption value of 0.002 mmol g^{-1} for a mineral standard of iron pyrite indicates that negligible amounts of gas is being adsorbed by pores in the 100 nm or less scale, and that in terms of adsorption isotherms on isolated kerogen, iron pyrite is not a site for adsorption. It will be shown below that isolated kerogen has a typical maximum adsorption value of about ~ 1 to 2 mmol g^{-1} for CO_2 at -78^oC, and consequently a value of 0.002 mmol g^{-1} for pyrite accounts for only 0.1% to 0.2% of the total adsorption uptake by kerogens. As these values are within the experimental error range for the adsorption measurements, it is acceptable to conclude that the presence of pyrite in the isolated kerogens will not adversely impact their adsorption isotherms.

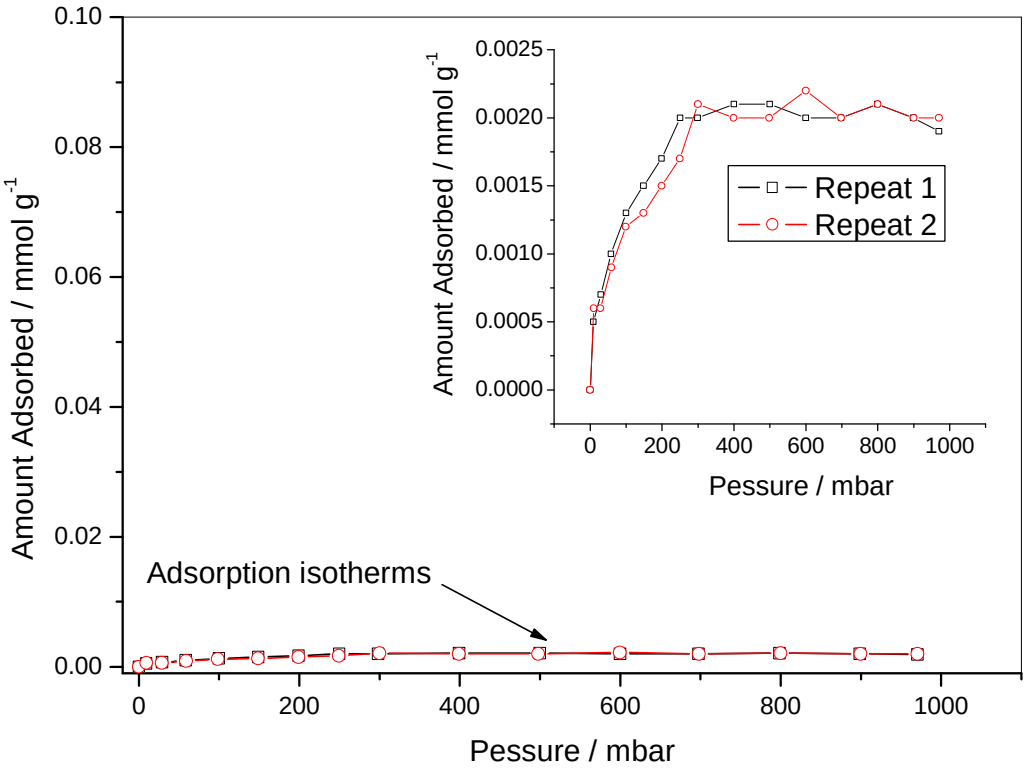

Figure 5.5: Negligible amount of CO_2 is adsorbed by a pyrite mineral standard. The presence of iron pyrite in the isolated kerogens will not adversely impact the kerogen adsorption isotherms.

The amount of pyrite in each kerogen sample was determined using two independent experimental methods:

- Elemental analysis of isolated kerogen.
- Quantitative powder X-Ray Diffraction (XRD).

Method 1: The elemental analysis of the isolated kerogens was obtained, and the full dataset has been presented in Table 3.3 (Section 3.2.4). The weight percents of sulfur obtained from the elemental analysis were used to calculate the amount of pyrite in the kerogens. The only caveat is the assumption that all the sulfur is from pyrite, and there is no organic sulfur contributing to the elemental analysis.

The weight percent of elemental sulfur in iron pyrite (FeS_2) is 53.45% (i.e. 64.14 $gmol^{-1}$ ÷ 119.98 $gmol^{-1}$ = 0.5345). Therefore, the weight percent of iron pyrite in the kerogens is determined from the elemental analysis by dividing the weight percent of sulfur by 0.5345. The results are reported in Table 5.1.

Method 2: The quantitative XRD analysis of the isolated kerogens was performed. A mixture of 20 % to 80 % ratio of corundum and kerogen (respectively) was prepared for each kerogen sample (i.e. 40 mg to 160 mg was made up to 200 mg in total). The intensities of the pyrite peaks in the diffractograms were converted to weight percents of pyrite, using the peak intensities of the known mass of the corundum standard (Al_2O_3).The weight percents of pyrite in each kerogen sample are reported in Table 5.2.

Table 5.1: The pyrite content derived from the sulfur elemental analysis.

Sample	Sulfur / wt%	Pyrite / wt%
DF1	10.39	19.44
DF2	15.24	28.51
DF3	20.44	38.24
DF4	12.3	23.01
DF5	14.04	26.27
DF6	17.69	33.1
DF7	24.08	45.05
DF8	16.27	30.44
DF9	23.62	44.19
DF10	24.25	45.37

Sample	Sulfur / wt%	Pyrite / wt%
C1	12.55	23.48
C2	11.74	21.96
C3	4.079	7.63
C4	3.745	7.01
C5	10.94	20.47
C6	10.86	20.32
C7	14.51	27.15
C8	10.14	18.97
C9	13.46	25.18
C10	12.07	22.58

Table 5.2: The pyrite (wt %) of each kerogen sample, measured by Q-XRD

Sample	Pyrite / wt%
DF1	14.5
DF2	27.6
DF3	40.6
DF4	20.8
DF5	16.6
DF6	31.3
DF7	35.9
DF8	22.6
DF9	44.7
DF10	49.0

Sample	Pyrite / wt%
C1	27.6
C2	13.3
C3	0.0
C4	0.6
C5	19.2
C6	15.1
C7	22.6
C8	13.9
C9	22.6
C10	32.6

The pyrite contents (wt %) reported from both independent methods can be compared:

Table 5.3: The pyrite contents from elemental analysis and Q-XRD compared

	Elemental Analysis	Q-XRD
Sample	Pyrite / wt%	Pyrite / wt%
DF1	19.44	14.5
DF2	28.51	27.6
DF3	38.24	40.6
DF4	23.01	20.8
DF5	26.27	16.6
DF6	33.1	31.3
DF7	45.05	35.9
DF8	30.44	22.6
DF9	44.19	44.7
DF10	45.37	49

	Elemental Analysis	Q-XRD
Sample	Pyrite / wt%	Pyrite / wt%
C1	23.48	27.6
C2	21.96	13.3
C3	7.63	0
C4	7.01	0.62
C5	20.47	19.2
C6	20.32	15.1
C7	27.15	22.6
C8	18.97	13.9
C9	25.18	22.6
C10	22.58	32.6

The values obtained from the two independent methods closely agree. A cross-plot is reported in Figure 5.6. The correlation coefficient is R^2= 0.92. The statistical significance of the agreement between the results is tested using a paired means Students t-Test, and is listed in Table 5.4. The p-value is 0.011, and at the 95% confidence level, the agreement between the experimental data is statistically significant, and therefore unlikely to be due to random chance.

The average of the pyrite (%) from both methods is listed in Table 5.5. The average pyrite contents for all the kerogens (except C3 and C4) are listed. The average values for C3 and C4 have not been reported because it is unlikely that the Q-XRD pyrite contents = 0 % are correct. A small aliquot was taken from the bulk, and it is more likely that these aliquots did not represent the bulk of the kerogen (due to the heterogeneous nature of geological samples). The experimental values obtained from the elemental analysis presented instead.

The average values listed in Table 5.5 are used to normalise all of the kerogen isotherm data shown in the subsequent sections. The raw data, before normalisation, are reported in the Appendix. A representative example of the isotherm normalisation process is reported in Figure 5.7, where the CO_2 at -78^{o}C isotherm for the Draupne Formation kerogen (DF1) has been normalised by its pyrite content of 16.97 %. It is observed that the amount adsorbed at each pressure step has increased, after the isotherm normalisation.

The average pyrite values listed in Table 5.5 are also used to correct the raw carbon elemental analysis data previously present in Chapter 3, section 3.2.4. This correction allows the TOC of the kerogen to be determined. The corrected organic carbon contents (the TOC) for the kerogens are listed in Table 5.6. For the Draupne Formation kerogens, the TOC has a range of 71.08 to 82.35 %, with an average of 76.23 ± 4.43 %. For the Colorado Group kerogens, the TOC has a range of 72.81 to 75.60 %, with an average of 74.20 ± 0.88 %.

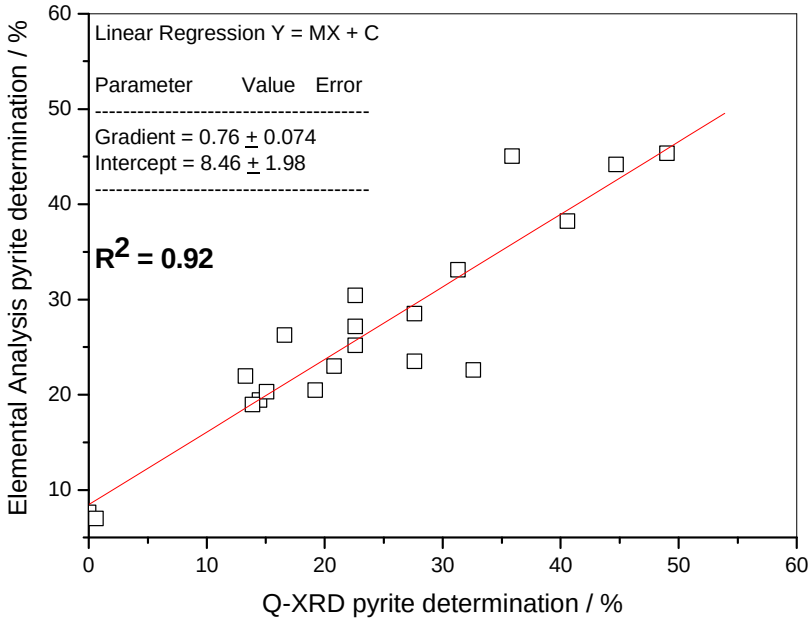

Figure 5.6: Cross-plot of the pyrite (wt %) from the independent methods. There is close agreement between the reported values.

Table 5.4: The paired means Student's t-Test of the correlation of the elemental and XRD pyrite contents.

Pair t-Test for sample means	*Elemental method*	*Q-XRD method*
Mean Average	26.418	23.556
Variance s^2	115.293	169.599
R^2	0.92	
t - statistic	-2.494	
P value	0.011	

Table 5.5: The mean averages of the pyrite weight percents for the kerogens.

Sample	Mean Average Pyrite / wt%	Sample	Mean Average Pyrite / wt%
DF1	16.97 ± 3.49	C1	25.54 ± 2.91
DF2	28.06 ± 0.65	C2	17.63 ± 6.13
DF3	39.42 ± 1.67	C3	7.63 ± 0.00
DF4	21.91 ± 1.56	C4	7.01 ± 0.00
DF5	21.43 ± 6.84	C5	19.83 ± 0.90
DF6	32.20 ± 1.27	C6	17.71 ± 3.69
DF7	40.48 ± 6.47	C7	24.87 ± 3.22
DF8	26.52 ± 5.54	C8	16.44 ± 3.59
DF9	44.45 ± 0.36	C9	23.89 ± 1.83
DF10	47.18 ± 2.57	C10	27.59 ± 7.08

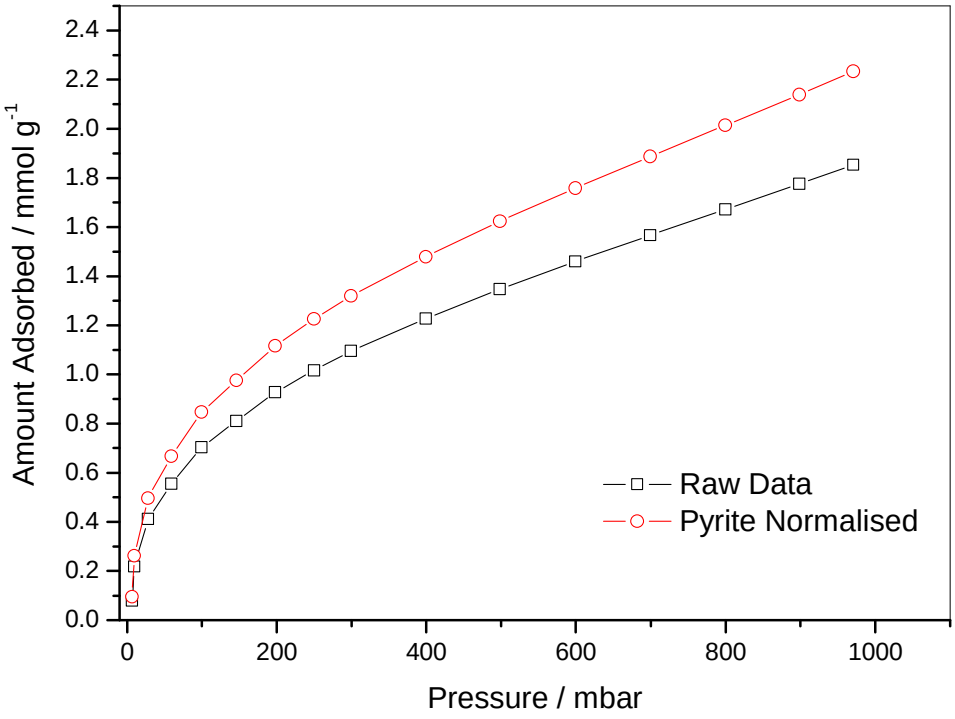

Figure 5.7: The raw and pyrite normalised adsorption isotherm for kerogen DF1, using CO_2 at -78°C.

Table 5.6: The raw Elemental Analysis carbon data, and the corrected organic carbon (TOC) contents for the kerogens.

Sample	Elemental Carbon / %	Kerogen TOC / %
DF1	61.74	74.36
DF2	53.72	74.68
DF3	43.89	72.44
DF4	64.31	82.35
DF5	56.16	71.48
DF6	50.38	74.31
DF7	42.31	71.08
DF8	57.14	77.76
DF9	45.47	81.85
DF10	43.28	81.93

Sample	Elemental Carbon / %	Kerogen TOC / %
C1	38.33	73.88
C2	35.52	72.81
C3	63.3	75.60
C4	62.73	74.49
C5	55.92	73.91
C6	21.09	73.57
C7	23.05	74.85
C8	21.93	73.21
C9	50.08	75.15
C10	41.3	74.55

5.2.2 Pore volumes of the Draupne Formation and Colorado Group kerogens.

The sub-100 nm pore volumes of the Draupne Formation and Colorado Group isolated kerogens was investigated using gas adsorption analysis. Adsorbate gas can access the smallest pores present in kerogens, thus allowing the nanometre scale pore structure to be characterised. The isolated kerogens were analysed using CO_2 adsorption isotherms at -78^oC, up to 1 bar pressure. Each sample was measured twice for repeatability. In Figure 5.8, all of the adsorption isotherms for the isolated kerogen isotherms are reported. The kerogen isotherms have a Type I / Type II hybrid adsorption curve, with an initially steep uptake in the low pressure region, followed by a shallower uptake at higher pressure, before failing to reach a horizontal plateau at 1000 mbar pressure. The shape of the adsorption isotherm indicates that the kerogen pore structure is heterogeneous, with the presence of a pore size distribution. The Type I aspect of the adsorption isotherm indicates the presence of micropores (< 2 nm), and the Type II nature of the adsorption isotherm indicates the presence of mesopores and macropores (> 50 nm). The adsorption isotherms for both the Draupne Formation and Colorado Group kerogens are very similar in shape, indicating that a common porous structure is shared by the Type II kerogens.

The sorption pore volumes of the Draupne Formation and Colorado Group kerogens are listed in Table 5.7. The sorption pore volumes of the DF kerogens have a range of 0.0732 to 0.0949 $cm^3\ g^{-1}$, with an average of 0.0816 ± 0.009 cm^3g^{-1}. The DF kerogen sorption pore volume average is larger than the equivalent DF shale sorption pore volume average (0.0816 cm^3g^{-1} vs 0.0171 cm^3g^{-1}). The sorption pore volumes of the CG kerogens have a range of 0.0552 to 0.1143 $cm^3\ g^{-1}$, with an average of 0.0834 ± 0.0213 cm^3g^{-1}. The CG kerogen sorption pore volume average is larger than the equivalent CG shale sorption pore volume average (0.0834 cm^3g^{-1} vs 0.0184 cm^3g^{-1}). Furthermore, the average kerogen sorption pore volumes are very similar (0.0816 cm^3g^{-1} vs 0.0834 cm^3g^{-1}) for the Draupne Formation and Colorado Group shales.

The sorption pore volumes of the Draupne Formation kerogens decreases as burial depth increases, as reported in Figure 5.9, part a. The correlation is very strong, with a correlation coefficient of $R^2 = 0.91$. For the Colorado Group isolated kerogens, there is no observable correlation between kerogen sorption pore volume and burial depth. as reported in Figure 5.9, part b.

The sorption pore volumes of the Draupne Formation isolated kerogens exhibit a strong correlation to maturity, with an increase of maturity resulting in a decrease of sorption pore volume. In Figure 5.10 part a), the strong negative correlation between sorption pore volume of shale and calculated vitrinite reflectance is reported. The correlation coefficient is $R^2 = 0.93$. In Figure 5.10 part b), the strong negative correlation between sorption pore volume of shale and Hydrogen Index is reported. The correlation coefficient is $R^2 = 0.91$. For the Colorado Group kerogens, the sorption pore volumes show no observable correlation to maturity, as indicated by VR_c (in Figure 5.11), or Hydrogen Index (in Figure 5.11). This agrees with the assessment of the Colorado Group kerogens as being thermally immature.

The sorption pore volumes of the Draupne Formation isolated kerogens are strongly correlated to the sorption pore volumes of the Draupne Formation shales (before acidic extraction of kerogen). The kerogen sorption pore volumes are positively correlated to the shale sorption pore volumes, as reported in Figure 5.12, part a. The correlation coefficient is R^2 = 0.91. However, the sorption pore volumes of the Colorado Group isolated kerogens exhibit no observable correlation to the sorption pore volumes of the shales, as reported in Figure 5.12, part b).

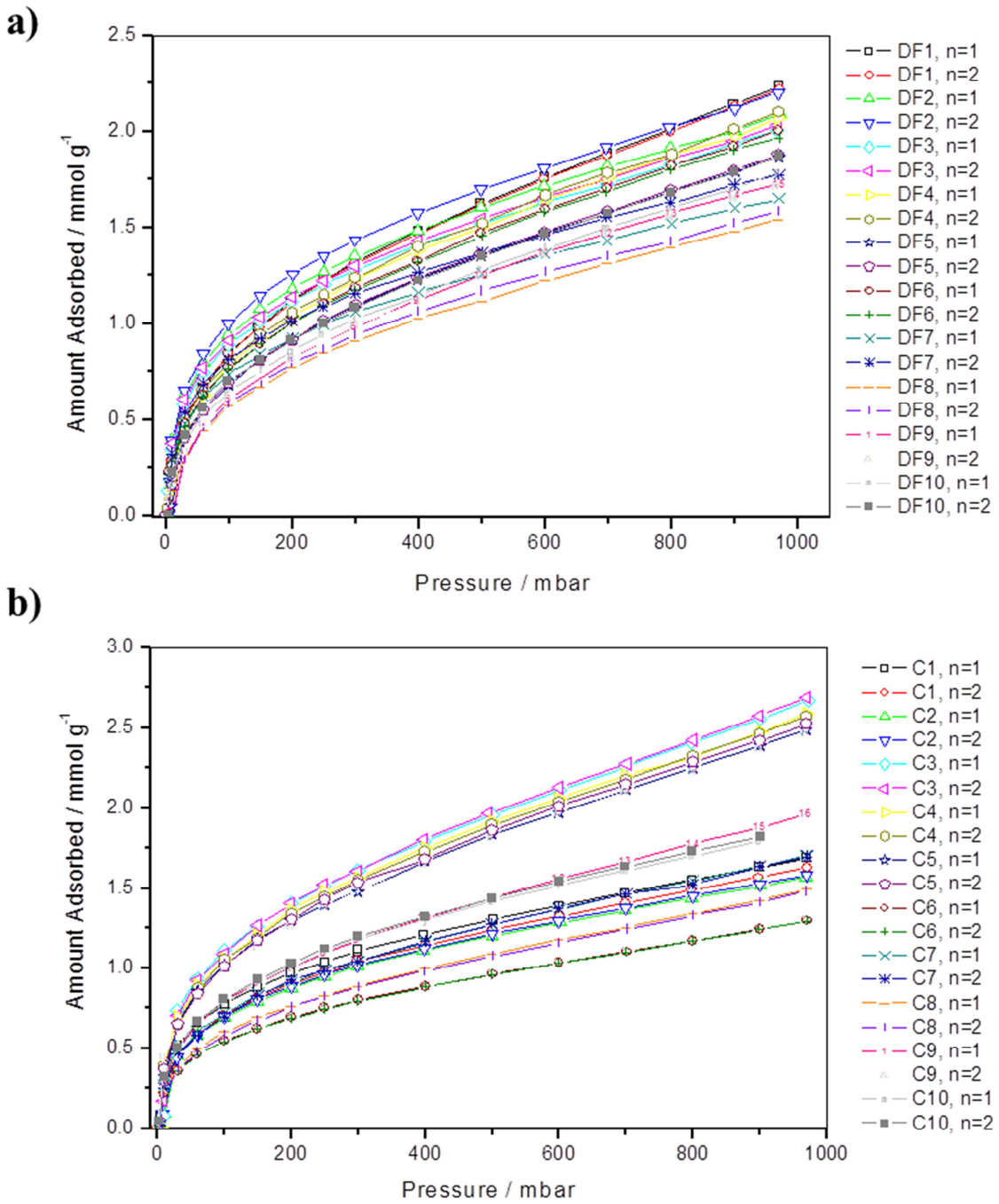

Figure 5.8: CO_2 adsorption isotherms at -78°C for the Draupne Formation (a) and Colorado Group (b) isolated kerogens. The adsorption uptakes of the isolated kerogen isotherms are significantly larger than the shale.

Table 5.7: Adsorption uptakes of CO_2 at -78°C, and gas sorption pore volumes of the Draupne Formation and Colorado Group isolated kerogens.

Sample	Depth / m	Average CO_2 adsorption at -78°C / mmol g^{-1}	Sorption Pore Volume / cm^3 g^{-1}
DF1	2117.8	2.226 ± 0.01	0.0949 ± 0.0005
DF2	2325	2.145 ± 0.08	0.0915 ± 0.003
DF3	2978.5	2.019 ± 0.02	0.0861 ± 0.0008
DF4	3124.7	2.083 ± 0.02	0.0888 ± 0.001
DF5	3375.32	1.869 ± 0.008	0.0797 ± 0.0003
DF6	3400.4	1.984 ± 0.03	0.0846 ± 0.001
DF7	4132.95	1.709 ± 0.09	0.0729 ± 0.004
DF8	4608.4	1.562 ± 0.03	0.0666 ± 0.001
DF9	4707.7	1.717 ± 0.01	0.0732 ± 0.0004
DF10	4780.7	1.825 ± 0.06	0.0778 ± 0.0027
C1	505.3	1.659 ± 0.04	0.0707 ± 0.002
C2	506.55	1.577 ± 0.008	0.0673 ± 0.0004
C3	541	2.679 ± 0.01	0.1143 ± 0.0006
C4	546.3	2.579 ± 0.01	0.1099 ± 0.0005
C5	561.5	2.506 ± 0.03	0.1069 ± 0.001
C6	642.1	1.294 ± 0.001	0.0552 ± 0.0006
C7	647.57	1.699 ± 0.002	0.0725 ± 0.0008
C8	651.75	1.488 ± 0.01	0.0634 ± 0.0004
C9	675.02	2.215 ± 0.4	0.0945 ± 0.02
C10	684.61	1.851 ± 0.08	0.0789 ± 0.004

(c.f. density of CO_2 at -78°C = 1.032 g cm^{-3})

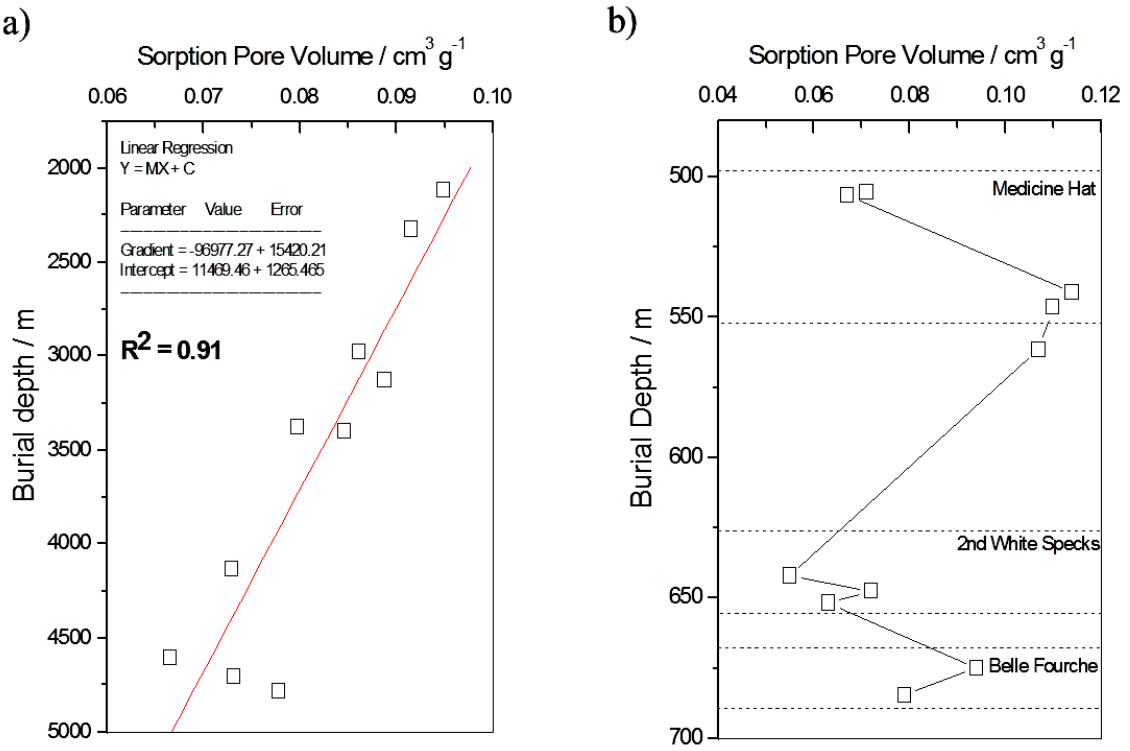

Figure 5.9: Sorption pore volume against burial depth. In part a) the sorption pore volume decreases linearly with burial depth for the Draupne Formation kerogens. In part b) the sorption volume varies with burial depth for the Colorado Group.

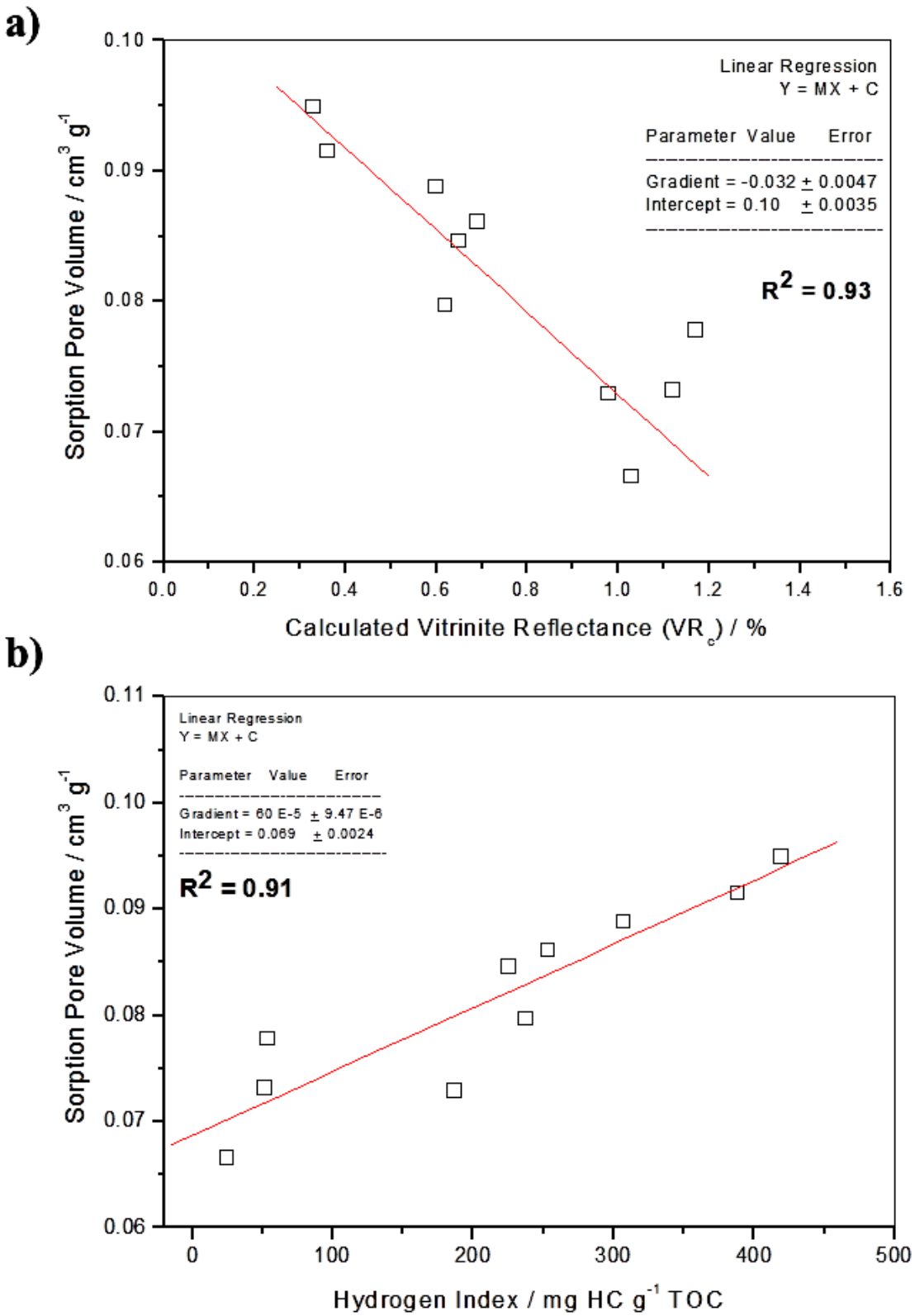

Figure 5.10: Draupne Formation kerogens exhibit a strong correlation between sorption pore volume and the thermal maturity, as indicated by calculated Vitrinite Reflectance and Hydrogen Index. In Part A) the sorption pore volume of the kerogen decreases as maturity increases (VR_c). In Part B), a high maturity is represented by a low Hydrogen Index, as the hydrocarbon generation potential of the kerogen is reduced due to liquid hydrocarbon generation.

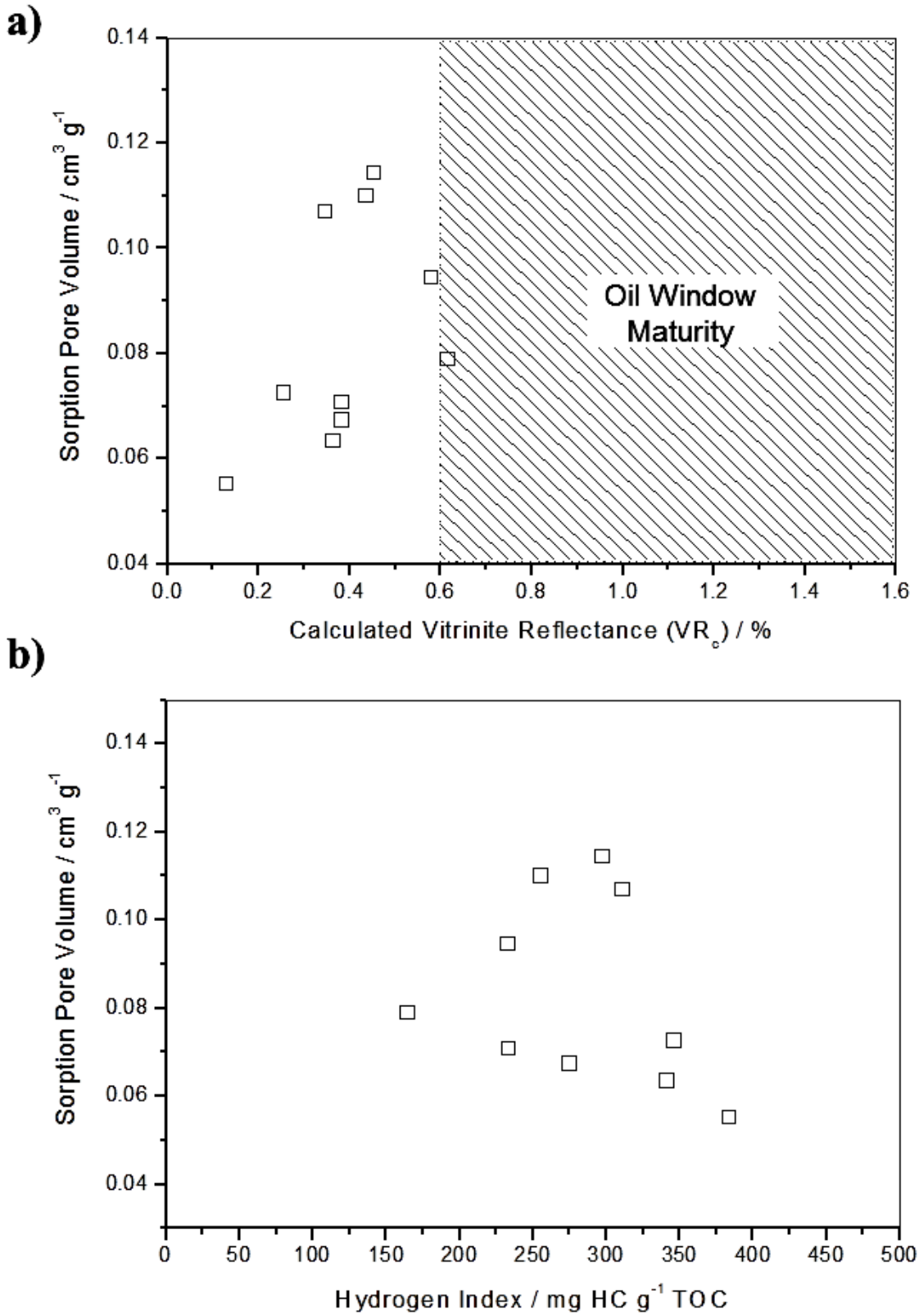

Figure 5.11: Colorado Group kerogens have no apparent correlation between sorption pore volume and the thermal maturity, as indicated by calculated vitrinite reflectance (part A) or Hydrogen Index (part B).

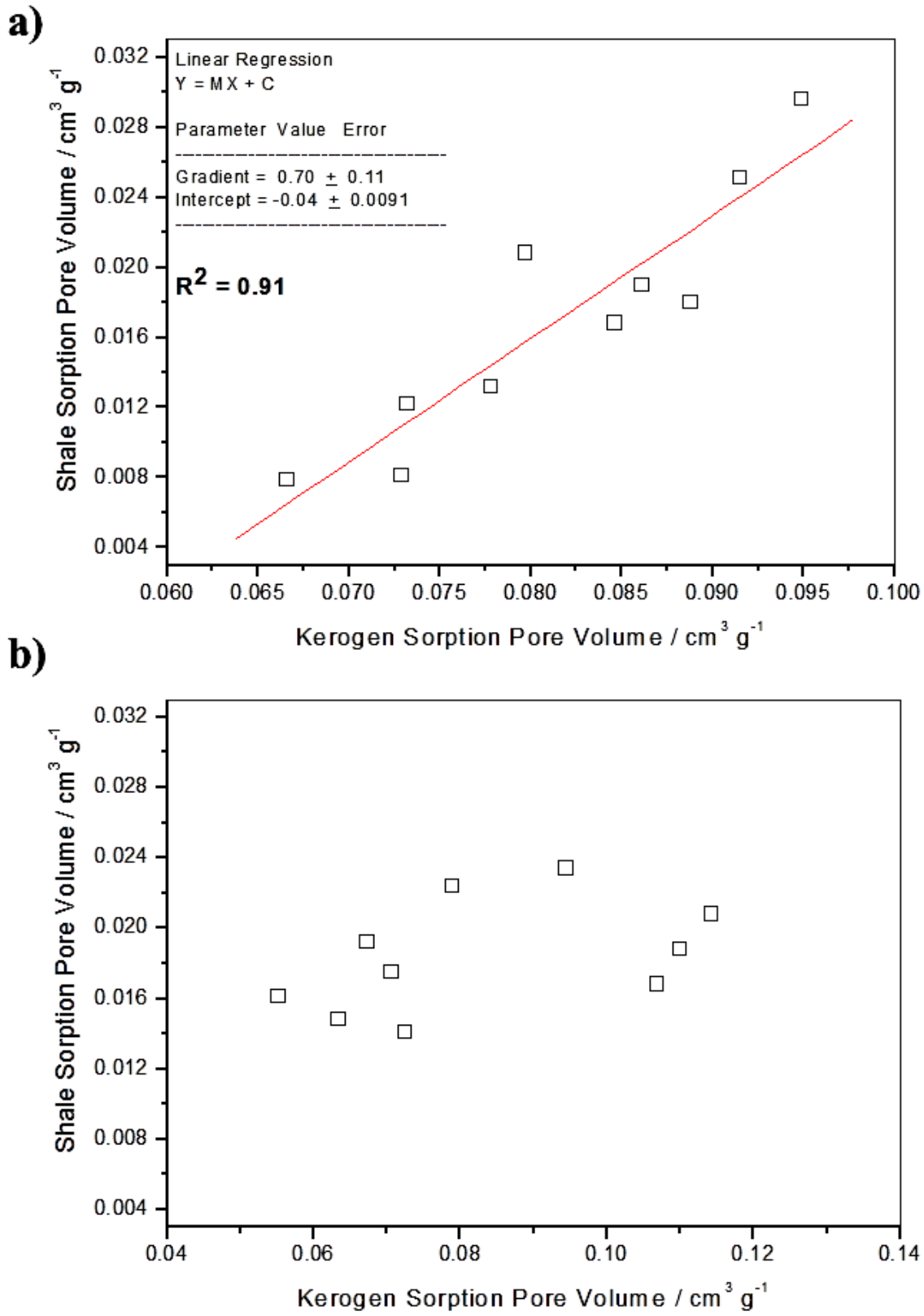

Figure 5.12: Comparison of kerogen sorption pore volume and shale sorption pore volume. In part a), the kerogen sorption pore volume is strongly correlated to the shale sorption pore volume for the Draupne Formation samples. In part b), the kerogen sorption pore volume and the shale sorption pore volume exhibit no observable correlation for the Colorado Group samples.

The micropore volume (< 0.7 nm) of Draupne Formation and Colorado Group isolated kerogens were determined using CO_2 adsorption isotherms at 0^oC (273K). The adsorption isotherms covered the relative pressure range of p/p^o = 0 to 0.03 (0 to 1 bar). The gas adsorption isotherms for the DF and CG kerogens are reported in Figure 5.13. Each sample was repeated twice for precision. The isotherms are Type I/II, and do not plateau at 1000 mbar pressure. The isotherms exhibit a similar shape, and do not overlap each, having a distribution of adsorption uptakes. The kerogen CO_2 isotherms at 0^oC have similar shaped isotherms as the CO_2 at -78^oC kerogen isotherms, indicating that the same heterogeneous pore size distribution of micropores and macropores is being characterised at both temperatures.

The micropore volumes of the Draupne Formation and Colorado Group isolated kerogens were determined using the Dubinin-Radushkevic (D-R) equation, with the y-axis intercept of the D-R plot being used to calculate the micropore volume. The D-R plots of the Draupne Formation kerogen isotherms are reported in Figure 5.14, part a, and the D-R plots of the Colorado Group kerogen isotherms are reported in Figure 5.14, part b. The D-R plots consist of excellent straight lines, indicating that a Gaussian curve distribution of pore widths is present.

The D-R micropore volumes, (calculated from the intercept of the D-R plots), for the Draupne Formation and Colorado Group kerogens are listed in Table 5.8. For the DF kerogens, the D-R micropore volumes have a range of 0.0267 to 0.0452 cm^3g^{-1}, with an average of 0.0335 ± 0.0061 cm^{-3} g^{-1}. For the CG kerogens, the D-R micropore volumes have a range of 0.0224 to 0.0400 cm^3g^{-1}, with an average of 0.0307 ± 0.0059 cm^{-3} g^{-1}. The D-R micropore volumes are very similar for both suites of kerogens (0.0335 mmol g^{-1} vs 0.0307 mmol g^{-1}).

The D-R micropore volumes of the Draupne Formation and Colorado Group kerogens do not appear to vary with burial depth, as reported in Figure 5.15. Furthermore, there is no observable correlation between D-R micropore volumes and maturity. This suggests that the sub-0.7 nm micropores are relatively stable against the effects of burial compaction and thermal maturation.

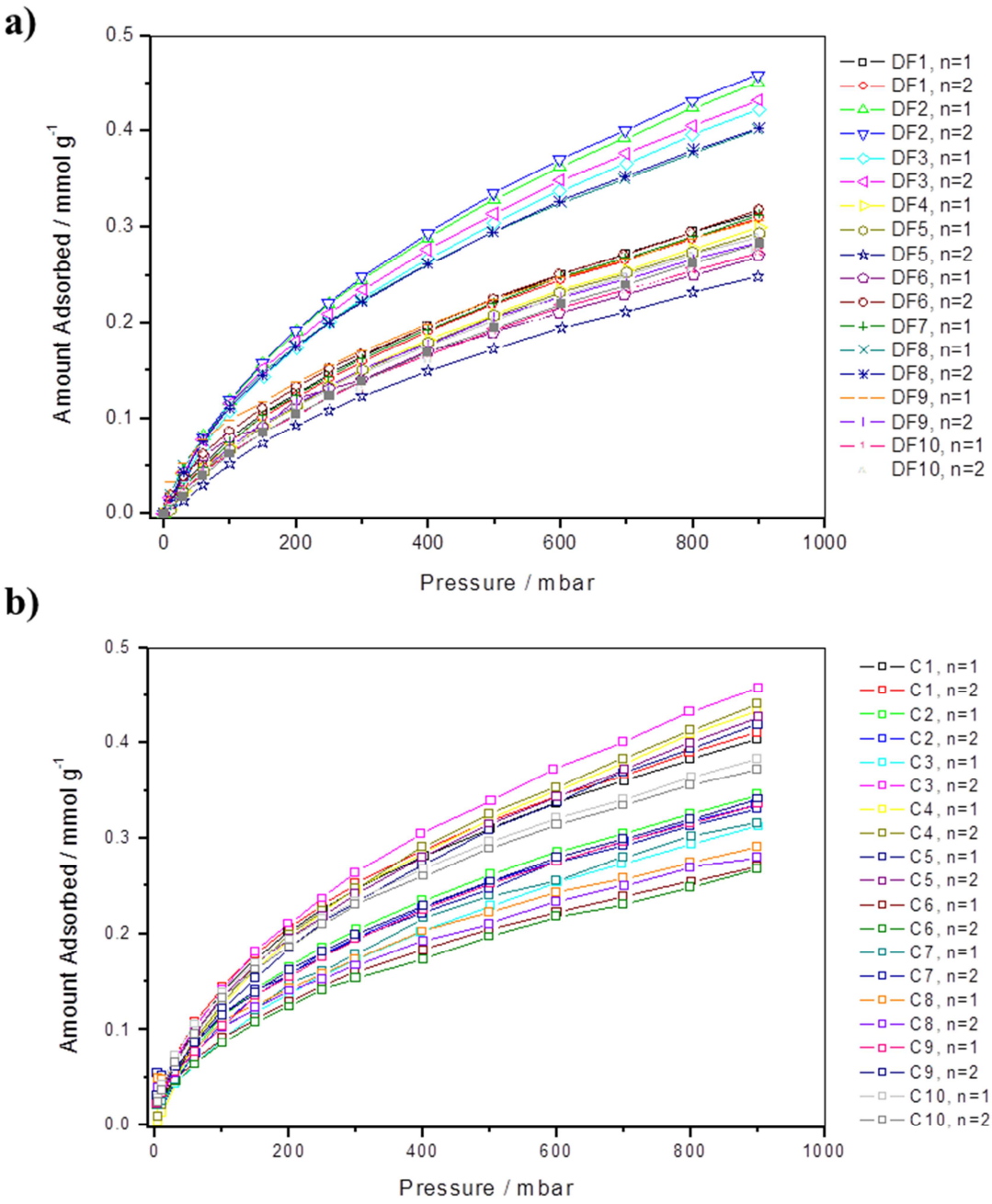

Figure 5.13: CO_2 adsorption isotherms at 0°C for the Draupne Formation (part a), and for the Colorado Group kerogens (part b).

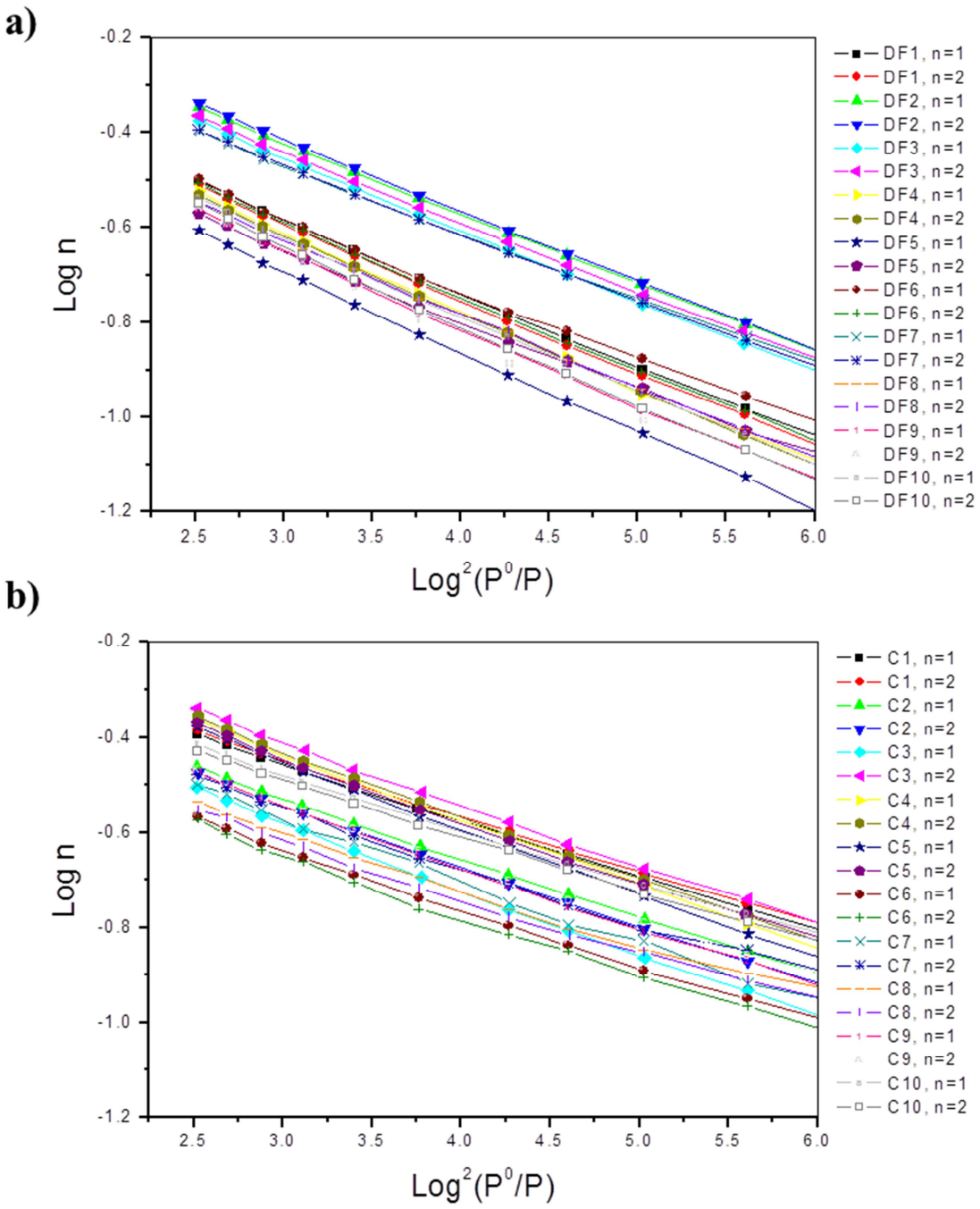

Figure 5.14: D-R plots for the CO_2 isotherms of the DF and CG kerogens at 0°C. The D-R plots are excellent straight lines, indicating that a Gaussian curve distribution of pore widths is present.

Table 5.8: Maximum adsorption uptakes of CO_2 at 0°C and the D-R micropore volumes, for the Draupne Formation and Colorado Group kerogens.

Sample	Depth / m	Maximum CO_2 adsorption / mmol g^{-1}	D-R Micropore Volume / cm^3 g^{-1}
DF1	2117.8	0.31243 ± 0.00344	0.0320 ± 0.00006
DF2	2325	0.45550 ± 0.00584	0.0452 ± 0.00101
DF3	2978.5	0.42743 ± 0.00727	0.0423 ± 0.00005
DF4	3124.7	0.29670 ± 0.00427	0.0317 ± 0.00010
DF5	3375.32	0.25857 ± 0.01463	0.0267 ± 0.00198
DF6	3400.4	0.31534 ± 0.00352	0.0310 ± 0.00162
DF7	4132.95	0.40259 ± 0.00124	0.0379 ± 0.00093
DF8	4608.4	0.29593 ± 0.01672	0.0277 ± 0.00192
DF9	4707.7	0.27553 ± 0.00207	0.0299 ± 0.00091
DF10	4780.7	0.28654 ± 0.00517	0.0308 ± 0.00003
C1	505.3	0.40748 ± 0.00496	0.0334 ± 0.00022
C2	506.55	0.34029 ± 0.00743	0.0293 ± 0.00018
C3	541	0.38528 ± 0.10296	0.0345 ± 0.00808
C4	546.3	0.43682 ± 0.00503	0.0400 ± 0.00003
C5	561.5	0.42311 ± 0.00535	0.0379 ± 0.00130
C6	642.1	0.26896 ± 0.0223	0.0224 ± 0.00011
C7	647.57	0.32397 ± 0.28557	0.0272 ± 0.00053
C8	651.75	0.28557 ± 0.00832	0.0225 ± 0.00039
C9	675.02	0.33856 ±0.00386	0.0289 ± 0.00083
C10	684.61	0.37746 ± 0.00832	0.0305 ± 0.00020

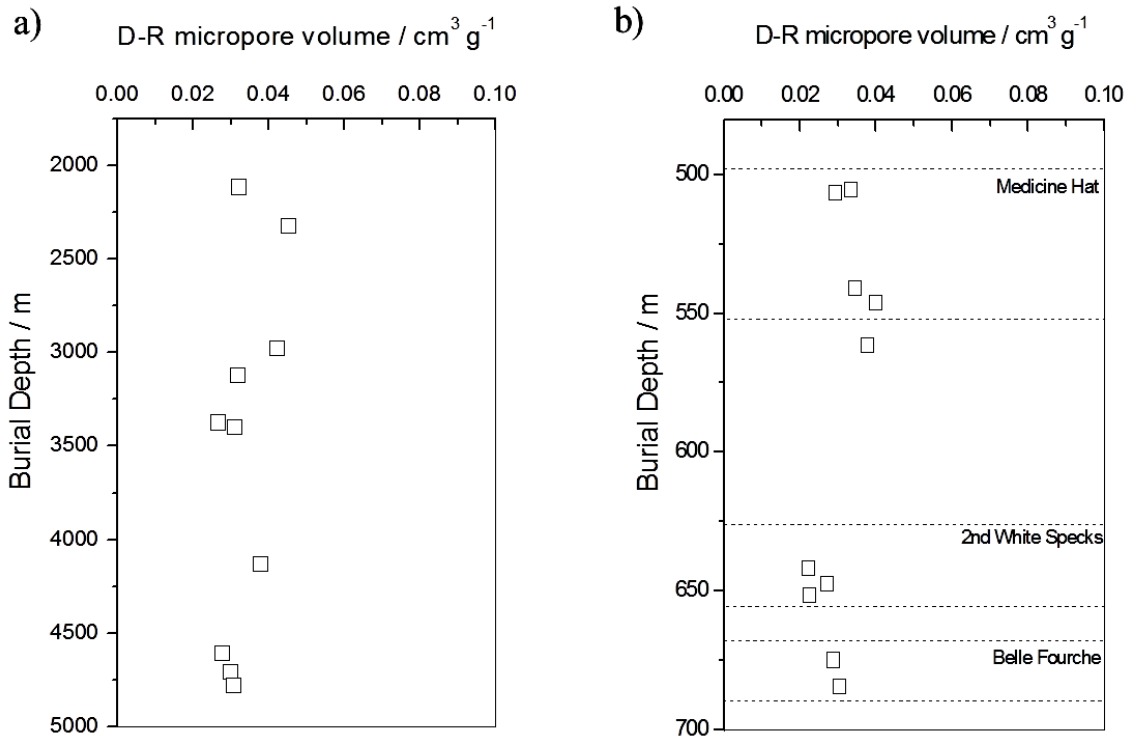

Figure 5.15: D-R micropore volume against burial depth. There is no observable correlation for a) the Draupne Formation kerogens, or b) the Colorado Group kerogens. The kerogen micropore volumes remain constant with increasing burial depth.

5.2.2 Porosity of the Draupne Formation and Colorado Group kerogens.

Gas adsorption analysis was used to determine the sub-100 nanometre-scale porosities of the Draupne Formation and Colorado Group kerogens. The kerogen sorption porosities were determined from the bulk density of the kerogen. The bulk densities of the kerogens are unknown, so are estimated to be 1.25 g cm^{-3} (the average kerogen density value of immature and oil window shales, as published in Okiongbo *et al*., 2005). The sorption porosities of the Draupne Formation and Colorado Group isolated kerogens are reported in Table 5.9. The DF kerogen sorption porosities range from 8.3 to 11.8 %, with an average of 10.2 ± 1.1 %, whilst the CG kerogen sorption porosities range from 7.9 to 14.3 %, with an average of 10.4 ± 2.6 %. For the DF kerogen, a strong correlation is observed between the sorption porosity of the kerogen and the total porosity of the shale, as reported in Figure 5.16, part a. The correlation coefficient is R^2 = 0.87. The sorption porosity of the Colorado Group kerogen has no correlation to the total porosity of the shale, as reported in Figure 5.16, part b.

The sorption porosities of the Draupne Formation kerogens exhibit a strong negative correlation to maturity, as reported in Figure 5.17. In part a), the strong negative correlation between sorption porosities and calculated vitrinite reflectance is reported. The correlation coefficient is R^2 = 0.88. In Figure 5.17 part b), the sorption porosities of the Colorado Group shales do not change with maturity (VR_C).

The sorption porosities of the Draupne Formation isolated kerogens are strongly correlated to the sorption porosities of the Draupne Formation shales (before acidic extraction of kerogen). The kerogen sorption porosities are positively correlated to the shale sorption porosities, as reported in Figure 5.18, part a. The correlation coefficient is R^2 = 0.90. However, the sorption porosities of the Colorado Group isolated kerogens exhibit no observable correlation to the sorption porosities of the shales, as reported in Figure 5.18, part b).

The microporosities of the Draupne Formation and Colorado Group kerogens were determined from the D-R micropore volumes ($cm^3\ g^{-1}$) and the assumed kerogen bulk density of 1.25 g cm^{-3}. The microporosities of the Draupne Formation kerogens had a range of 3.3 to 5.7 %, with an average of 4.2 ± 0.8 %. The microporosities of the Colorado Group shales had a range of 2.8 to 5.0 %, with an average of 3.8 ± 0.7 %.

Table 5.9: Nanometre-scale porosities of the Draupne Formation and Colorado Group kerogens, as measured using gas adsorption.

Sample	Depth / m	Sorption Porosity / %	D-R Microporosity / %
DF1	2117.8	11.43	4.0
DF2	2325	11.2	5.7
DF3	2978.5	10.3	5.3
DF4	3124.7	10.7	4.0
DF5	3375.32	9.9	3.3
DF6	3400.4	10.3	3.9
DF7	4132.95	9.1	4.8
DF8	4608.4	9.2	3.5
DF9	4707.7	10.0	3.7
DF10	4780.7	10.5	3.9
C1	505.3	8.5	4.2
C2	506.55	8.1	3.7
C3	541	13.7	4.3
C4	546.3	13.2	5.0
C5	561.5	12.8	4.7
C6	642.1	6.6	2.8
C7	647.57	8.7	3.4
C8	651.75	7.6	2.8
C9	675.02	11.3	3.6
C10	684.61	9.5	3.8

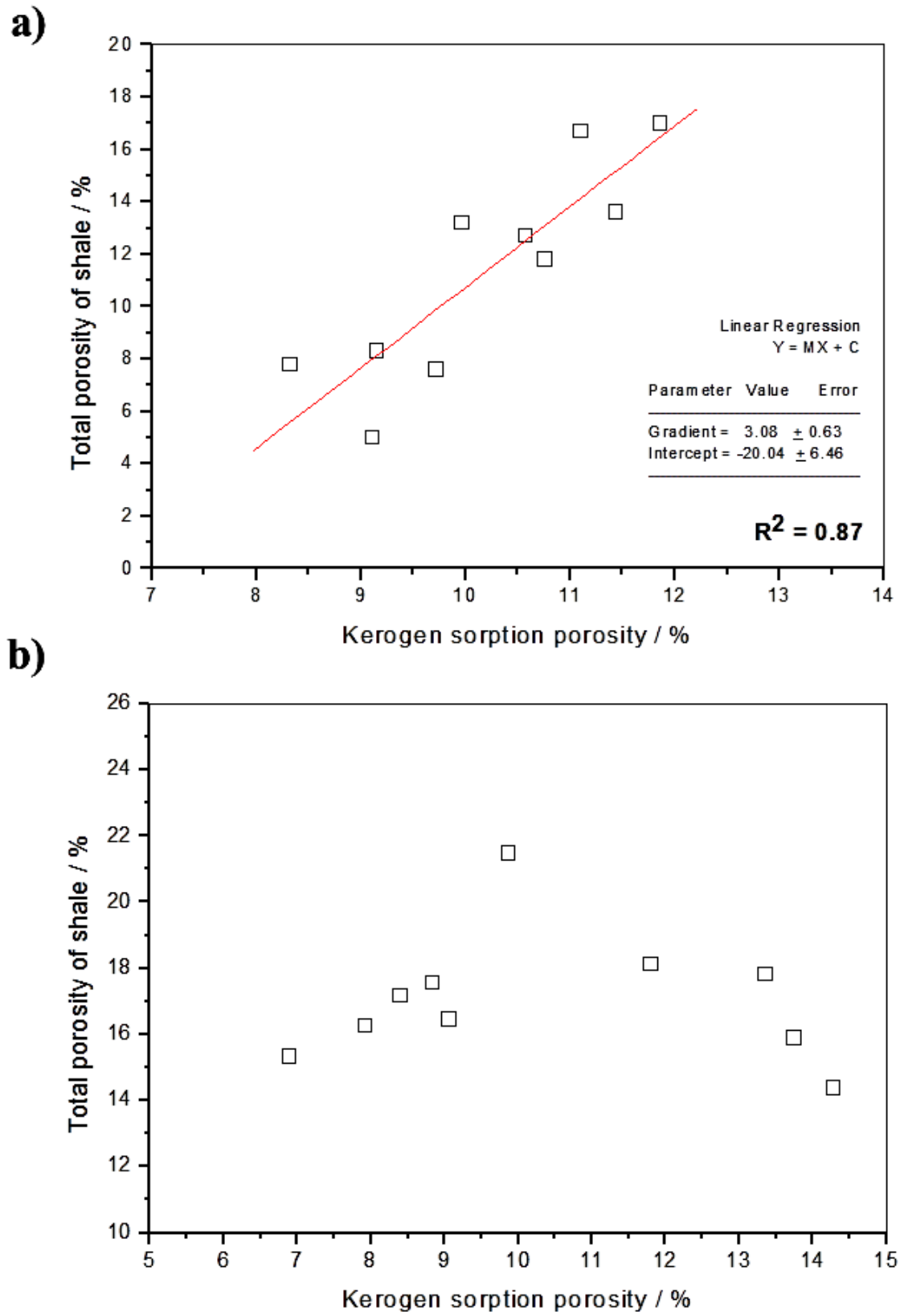

Figure 5.16: Total porosity of shale against sorption porosity of isolated kerogen. In part a), a strong correlation exists for the Draupne Formation, indicating that sorption porosity of the kerogen (of the sub – 100 nm pores) is a controlling factor in the overall total porosity of the shale. In part b), no observable correlation exists for the Colorado Group.

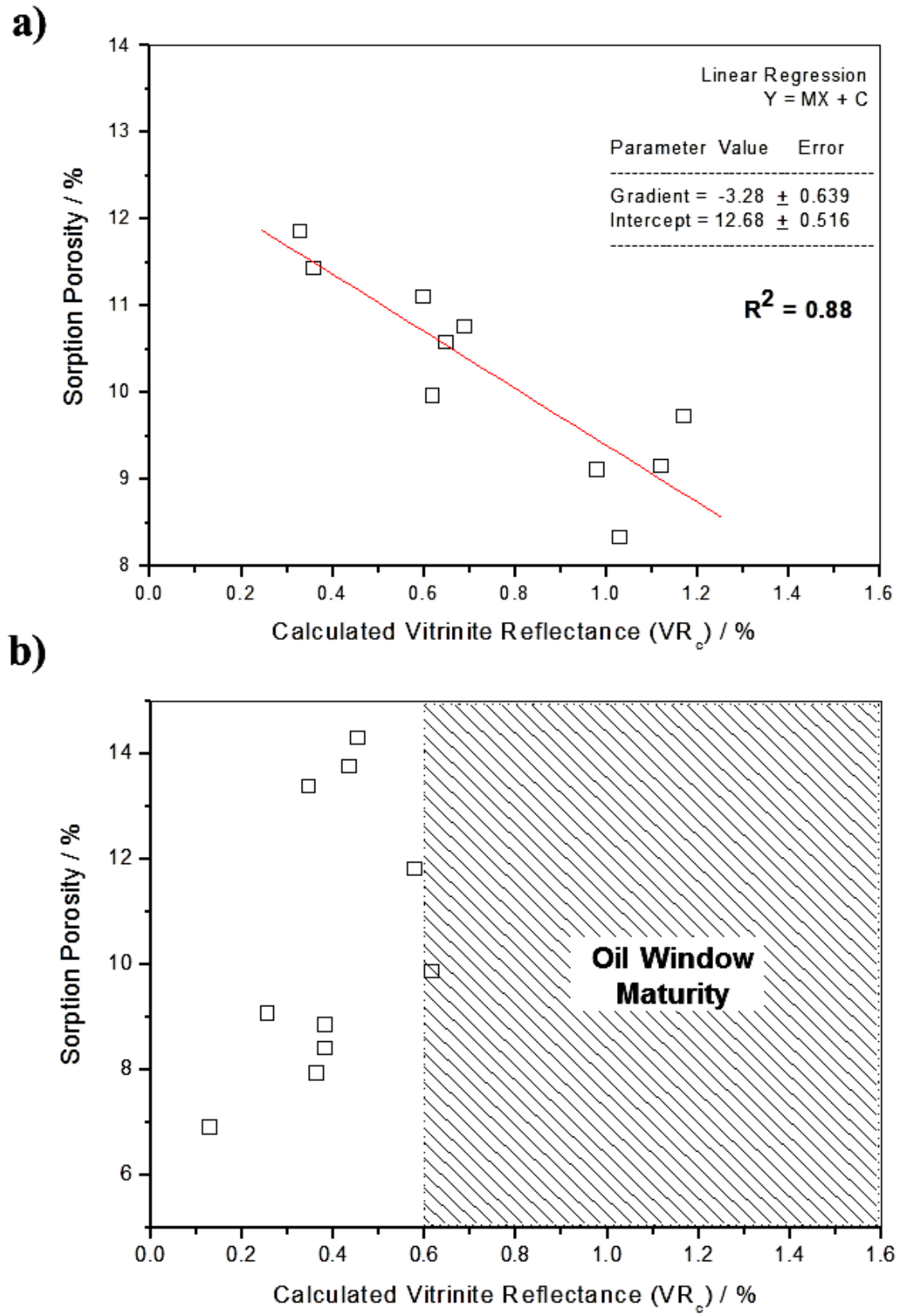

Figure 5.17: Plot of sorption porosity against maturity. In part a), a strong negative correlation between sorption pore volume of Draupne Formation kerogens and calculated vitrinite reflectance. In part b), no observable maturity correlation exists for the Colorado Group kerogens.

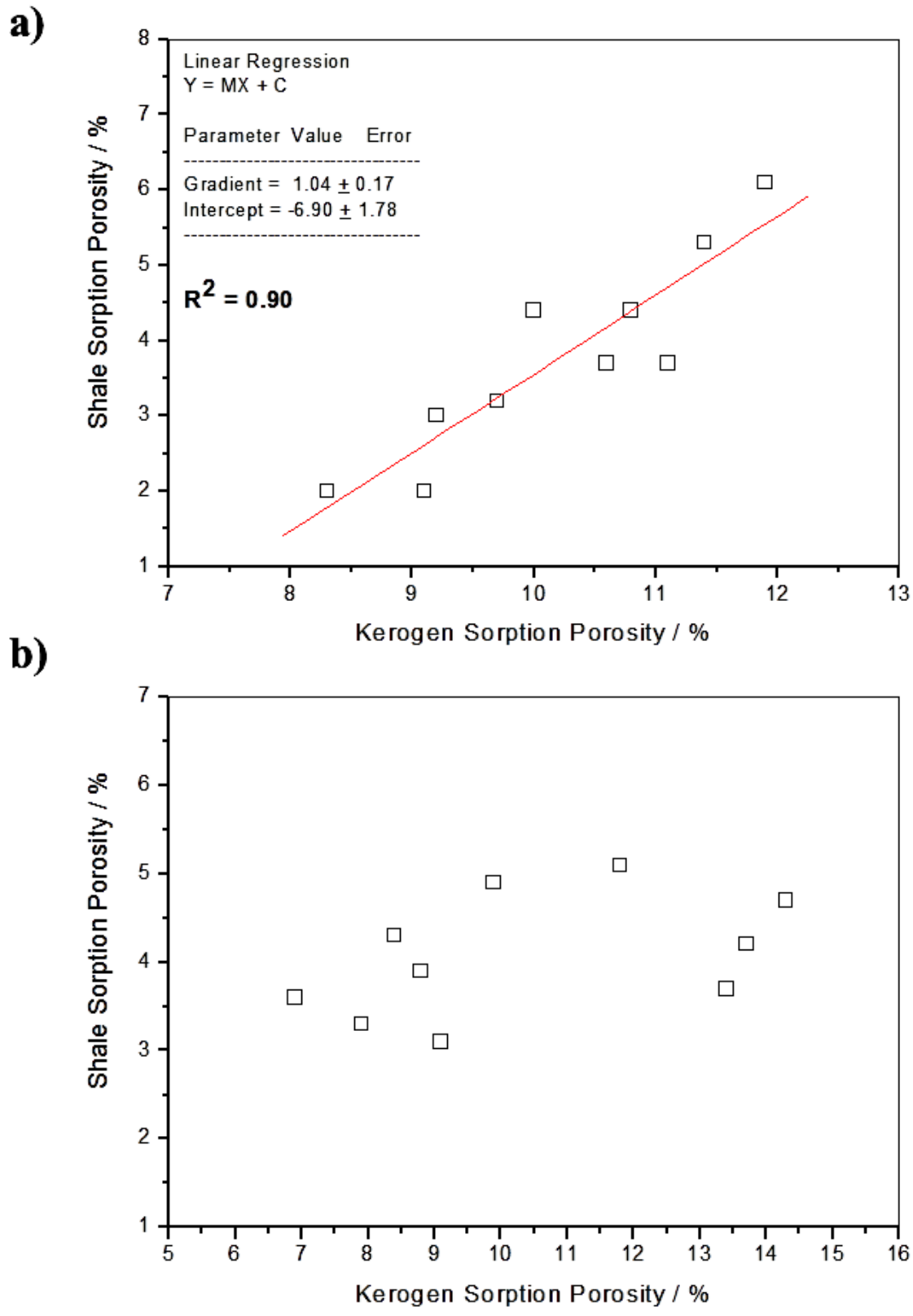

Figure 5.18: Comparison of kerogen sorption porosity and shale sorption porosity. In part a), the kerogen sorption porosity is strongly correlated to the shale sorption porosity for the Draupne Formation samples. In part b), the kerogen sorption porosity and the shale sorption porosity exhibit no observable correlation for the Colorado Group samples.

5.2.3 Surface area of the Draupne Formation and Colorado Group kerogens.

The surface areas of the Draupne Formation and Colorado Group kerogens were determined using the adsorption of N_2 at -196^{o}C and CO_2 at -78^{o}C in the BET pressure range of 50 mbar to 300 mbar. The nitrogen adsorption isotherms for the Draupne Formation and Colorado Group kerogens are reported in Figure 5.19. The adsorption isotherms for the isolated kerogens are linear in this low pressure region, with a low value gradient. There is a distribution of adsorption uptakes, with the isotherms appearing to be "stacked" on top of one another. There appears to be no crossing or overlap of the isotherms. The CO_2 isotherms at -78^{o}C for the Draupne Formation and Colorado Group shales were previously reported in Figure 5.8.

The N_2 BET surface areas of the isolated kerogens are determined from the BET plots in Figure 5.20. The BET plots have good linearity. The N_2 BET surface areas of the DF and CG kerogens (as measured using N_2 at -196^{o}C) are reported in Table 5.10. For the DF kerogens, the values have a range of 12.74 to 51.98 $m^2 g^{-1}$, with an average of 26.43 ± 12.28 $m^2 g^{-1}$. For the CG kerogens, the values have a range of 15.31 to 58.78 $m^2 g^{-1}$, with an average of 28.13 ± 12.39 $m^2 g^{-1}$. The average N_2 BET surface area values for the two samples suites closely agree (26.43 vs 28.13 $m^2 g^{-1}$), indicating that a common mesopore and macropore structure is shared by the Type II kerogens.

The CO_2 BET surface areas of the DF and CG kerogens using CO_2 at -78^{o}C were determined from the kerogen adsorption isotherms reported in Figure 5.8 (the CO_2 -78^{o}C above). The CO_2 BET plots are presented in Figure 5.21: The BET plots of both the DF and CG kerogens have good linearity. The CO_2 BET surface areas are reported in Table 5.10. For the DF kerogens, the CO_2 BET surface area values range from 82.98 to 109.99 $m^2 g^{-1}$, with an average of 101.24 ± 12.09 $m^2 g^{-1}$. For the CG kerogens, the CO_2 BET surface area values range from 68.27 to 139.00 $m^2 g^{-1}$, with an average of 103.54 ± 25.08 $m^2 g^{-1}$. The average CO_2 BET surface area values for the two samples suites closely agree (101.2 $m^2 g^{-1}$ vs 103.54 $m^2 g^{-1}$), indicating that these shales have full range pore structures (macro-, meso-, and micropores) with similar total surface areas. The average CO_2 BET surface area values are significantly larger than the values obtained using N_2 at -196^{o}C. This is due to CO_2 at -78^{o}C having larger kinetic energy available to access the full pore size distribution, including the micropores (< 2 nm). However, N_2 adsorption at -196^{o}C is restricted to only the mesopores and macropores (> 2 nm), due to activated diffusion. The larger BET surface area measurements of CO_2 at -78^{o}C suggests that a significant amount of surface area is located on the internal surfaces of micropores.

The N_2 BET and CO_2 BET surface areas allow the 1) total surface area and 2) the micropore surface area of the isolated kerogens to be determined. This is done using the equations outlined in Chapter 1, section 1.2.17. The total surface areas and the micropore surface areas are listed in Table 5.11. The Draupne Formation kerogens have a total surface area with a range from 82.98 to 109.99 $m^2 g^{-1}$, with an average of 101.24 ± 12.09 $m^2 g^{-1}$. The Colorado Group kerogens have a total surface area with a range from 68.27 to 139.00 $m^2 g^{-1}$, with an average of 103.54 ± 25.08 $m^2 g^{-1}$. The Draupne Formation kerogens have micropore surface areas (< 2 nm) with a range of 55.71 to 97.72 $m^2 g^{-1}$, with an average of 74.77 ± 12.48 $m^2 g^{-1}$. The Colorado Group kerogens have micropore surface areas (< 2 nm) with a range of 32.75 to 105.40 $m^2 g^{-1}$, with an average of 75.40 ± 26.44 $m^2 g^{-1}$.

The micropore surface areas are a significant percentage of the total surface areas of both the Draupne Formation and Colorado Group kerogens. The micropore surface area consists of an average of 74.2 % of the DF kerogen surface area. The micropore surface area consists of an average of 71.7 % of the CG kerogen surface area micropores. This agrees with the experimental finding that the CO_2 BET surface area values are significantly larger than the values obtained using N_2 at -196^{o}C.

The total surface areas of the DF kerogens decrease with increasing burial depth. There is an excellent correlation between total surface area and burial depth, with a correlation coefficient of $R^2 = 0.95$. This is reported in Figure 5.22, part a). The total surface area values of the Colorado Group kerogens vary between shale stratigraphic formations, as reported in Figure 5.22, part b). There is no observable correlation between total surface areas and maturity. This is agrees with the assessment of the Colorado Group kerogens as being thermally immature.

The total surface areas of the DF kerogens decrease with increasing thermal maturity. In Figure 5.23, part A), there is a strong correlation between total surface area and calculated vitrinite reflectance of the DF kerogens. The correlation coefficient is $R^2 = 0.92$. For the Colorado Group kerogens, there is no observable correlation between total surface area and maturity, as reported in Figure 5.23, part b).

The total surface areas of the Draupne Formation isolated kerogens are strongly correlated to the total surface areas of the Draupne Formation whole shales. The kerogen total surface areas are positively correlated to the shale total surface areas, as reported in Figure 5.24, part a. The correlation coefficient is $R^2 = 0.84$. However, the total surface areas of the Colorado Group isolated kerogens exhibit no observable correlation to the total surface areas of the shales, as reported in Figure 5.24, part b).

The micropore surface areas of the DF kerogens is positively correlated to the total porosity of the shale, with a correlation coefficient of $R^2 = 0.87$. This is reported in Figure 5.25, part a). For the CG kerogens, the micropore surface area has no observable correlation to the total porosity of the shale, as reported in Figure 5.25, part b).

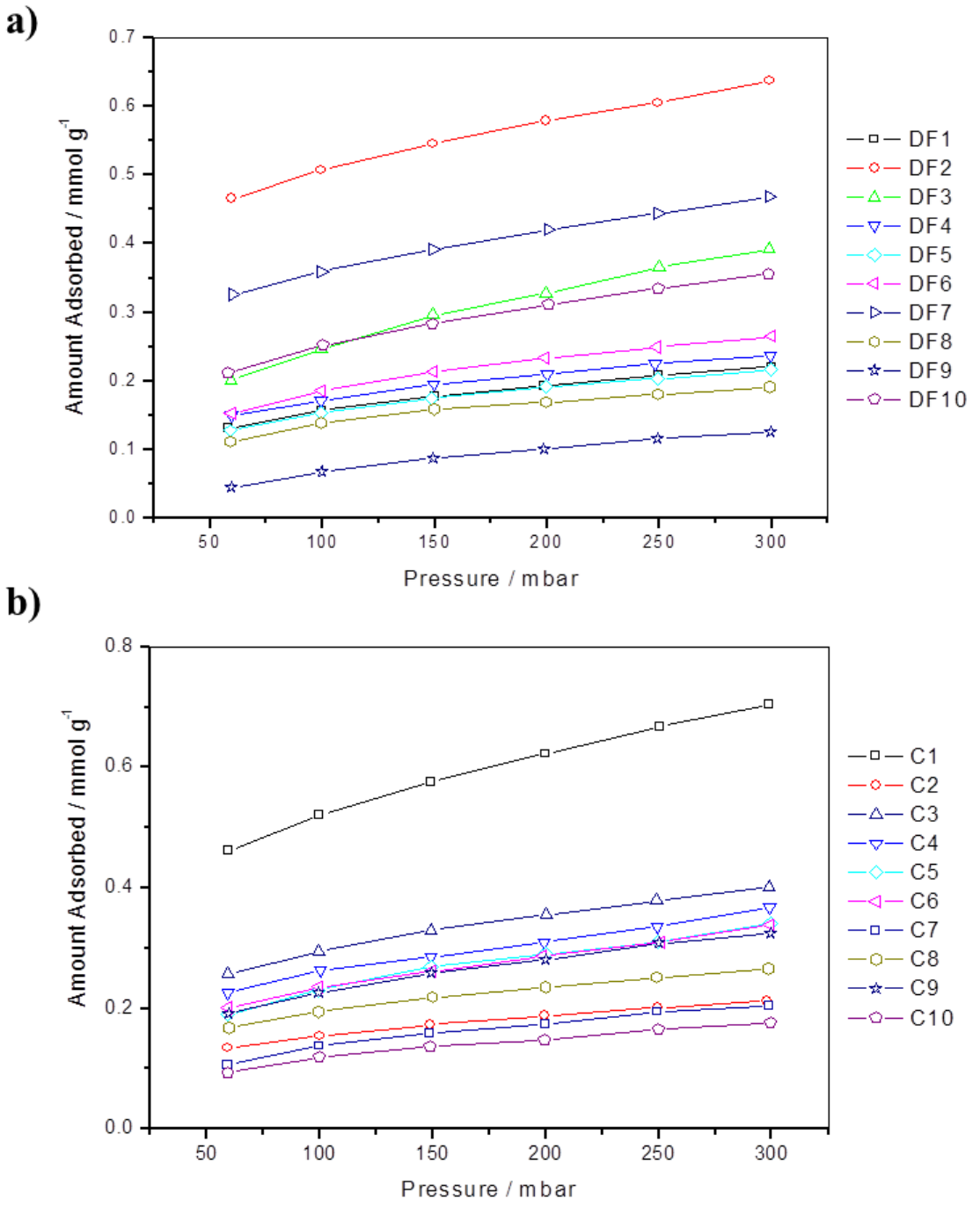

Figure 5.19: Nitrogen adsorption isotherms (at -196°C) for the a) Draupne Formation and b) Colorado Group kerogens. The isotherms are typically linear in this low pressure range.

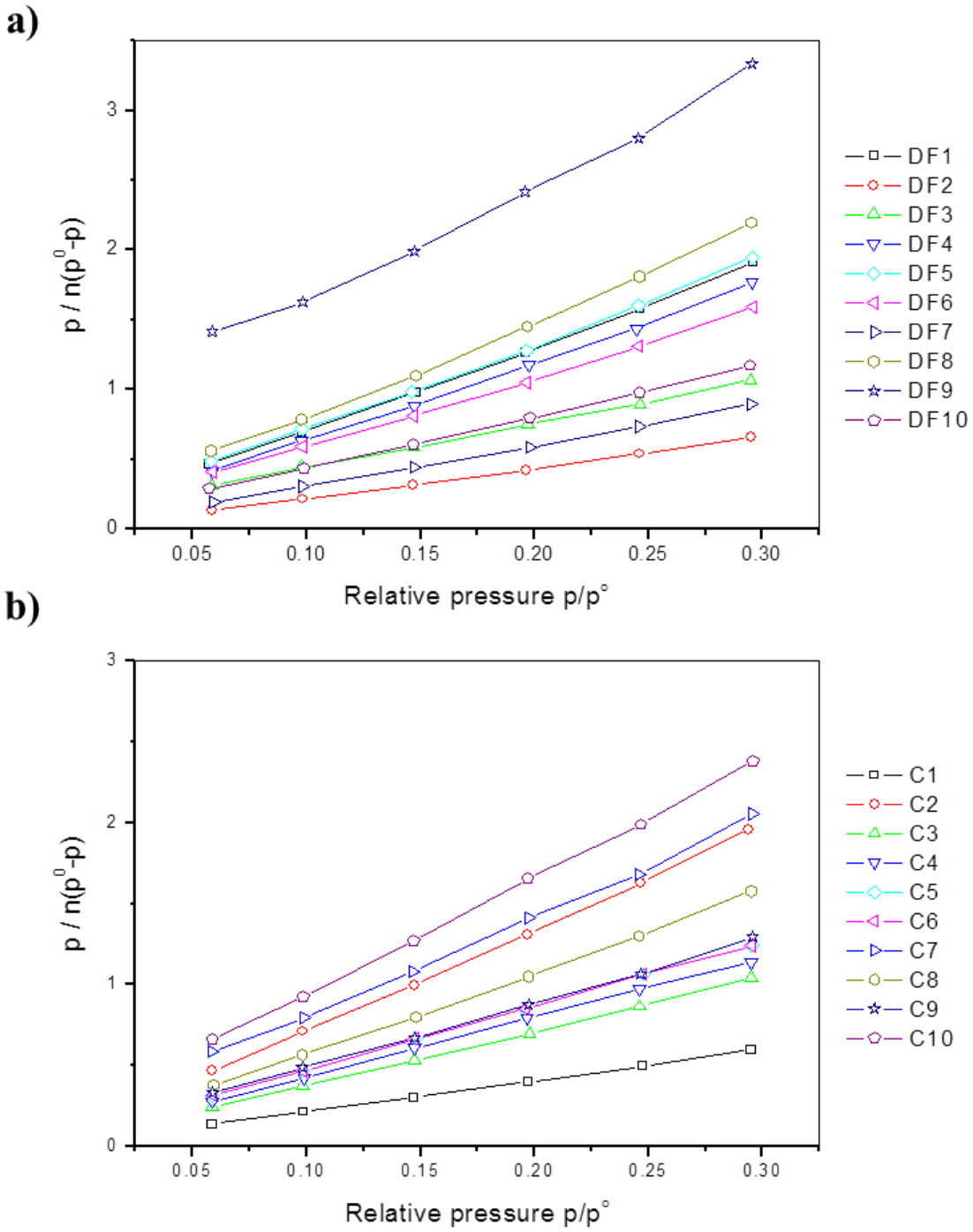

Figure 5.20: Nitrogen BET plots for the a) Draupne Formation and b) Colorado Group kerogens.

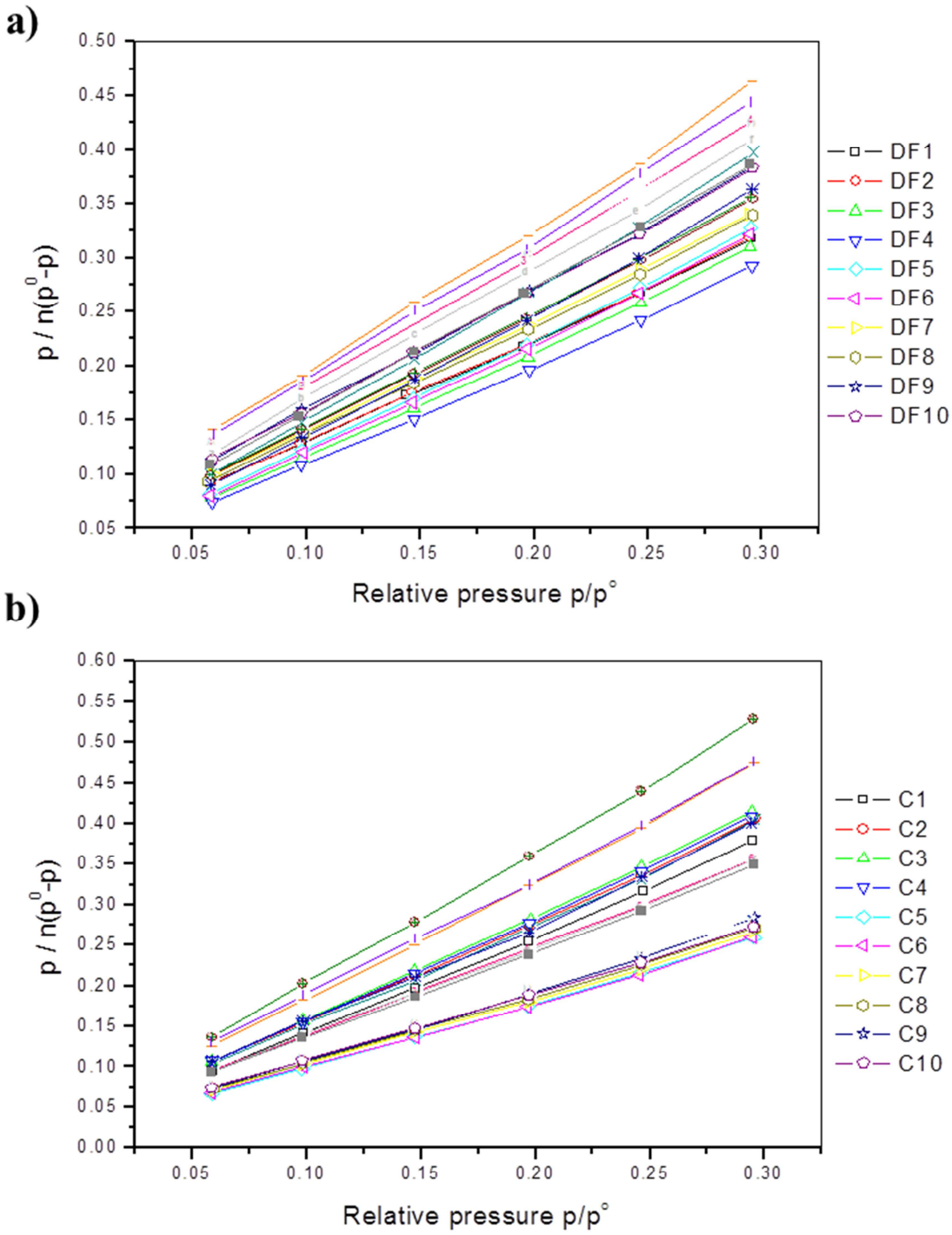

Figure 5.21: Nitrogen BET plots for the a) Draupne Formation and b) Colorado Group kerogens.

Table 5.10: BET surface areas of Draupne Formation and Colorado Group kerogens using N_2 at -196°C and CO_2 at -78°C.

Sample	Burial depth / m	N_2 BET Surface Area / $m^2\ g^{-1}$	CO_2 BET Surface Area / $m^2\ g^{-1}$
DF1	2117.8	18.68 ± 0.30	116.40 ± 0.52
DF2	2325	51.98 ± 0.88	118.90 ± 5.16
DF3	2978.5	34.76 ± 0.45	109.99 ± 1.10
DF4	3124.7	20.00 ± 0.40	108.21 ± 0.27
DF5	3375.32	18.38 ± 0.41	97.15 ± 0.22
DF6	3400.4	22.65 ± 0.50	103.30 ± 0.46
DF7	4132.95	38.59 ± 0.55	94.30 ± 5.62
DF8	4608.4	16.25 ± 0.44	82.98 ± 2.14
DF9	4707.7	12.74 ± 0.53	88.14 ± 0.65
DF10	4780.7	30.27 ± 0.37	92.67 ± 2.99
C1	505.3	58.78 ± 0.70	91.52 ± 3.36
C2	506.55	17.90 ± 0.24	87.08 ± 0.86
C3	541	33.60 ± 0.47	139.00 ± 0.70
C4	546.3	30.60 ± 0.32	134.91 ± 1.66
C5	561.5	28.67 ± 0.36	130.30 ± 4.54
C6	642.1	28.43 ± 0.16	68.27 ±0.28
C7	647.57	17.95 ± 0.46	90.03 ± 1.12
C8	651.75	22.32 ± 0.37	76.50 ± 0.58
C9	675.02	27.77 ± 0.45	114.99 ± 19.4
C10	684.61	15.31 ± 0.20	102.78 ± 1.22

Table 5.11: Total surface areas and micropore surface areas (< 2nm) of the Draupne Formation and Colorado Group kerogens.

Sample	Burial depth / m	Total Surface Area / $m^2 g^{-1}$	Micropore surface area / m2 g-1
DF1	2117.8	116.40 ± 0.52	97.72 ± 0.60
DF2	2325	118.90 ± 5.16	66.92 ± 5.23
DF3	2978.5	109.99 ± 1.10	75.23 ± 1.19
DF4	3124.7	108.21 ± 0.27	88.21 ± 0.48
DF5	3375.32	97.15 ± 0.22	78.77 ± 0.47
DF6	3400.4	103.30 ± 0.46	80.65 ± 0.68
DF7	4132.95	94.30 ± 5.62	55.71 ± 5.65
DF8	4608.4	82.98 ± 2.14	66.73 ± 2.18
DF9	4707.7	88.14 ± 0.65	75.4 ± 0.84
DF10	4780.7	92.67 ± 2.99	62.4 ± 3.01
C1	505.3	91.52 ± 3.36	32.74 ± 3.43
C2	506.55	87.08 ± 0.86	69.18 ± 0.89
C3	541	139.00 ± 0.70	105.4 ± 0.84
C4	546.3	134.91 ± 1.66	104.31 ± 1.69
C5	561.5	130.30 ± 4.54	101.63 ± 4.55
C6	642.1	68.27 ±0.28	39.84 ± 0.32
C7	647.57	90.03 ± 1.12	72.08 ± 1.21
C8	651.75	76.50 ± 0.58	54.18 ± 0.69
C9	675.02	114.99 ± 19.4	87.22 ± 19.39
C10	684.61	102.78 ± 1.22	87.47 ± 1.21

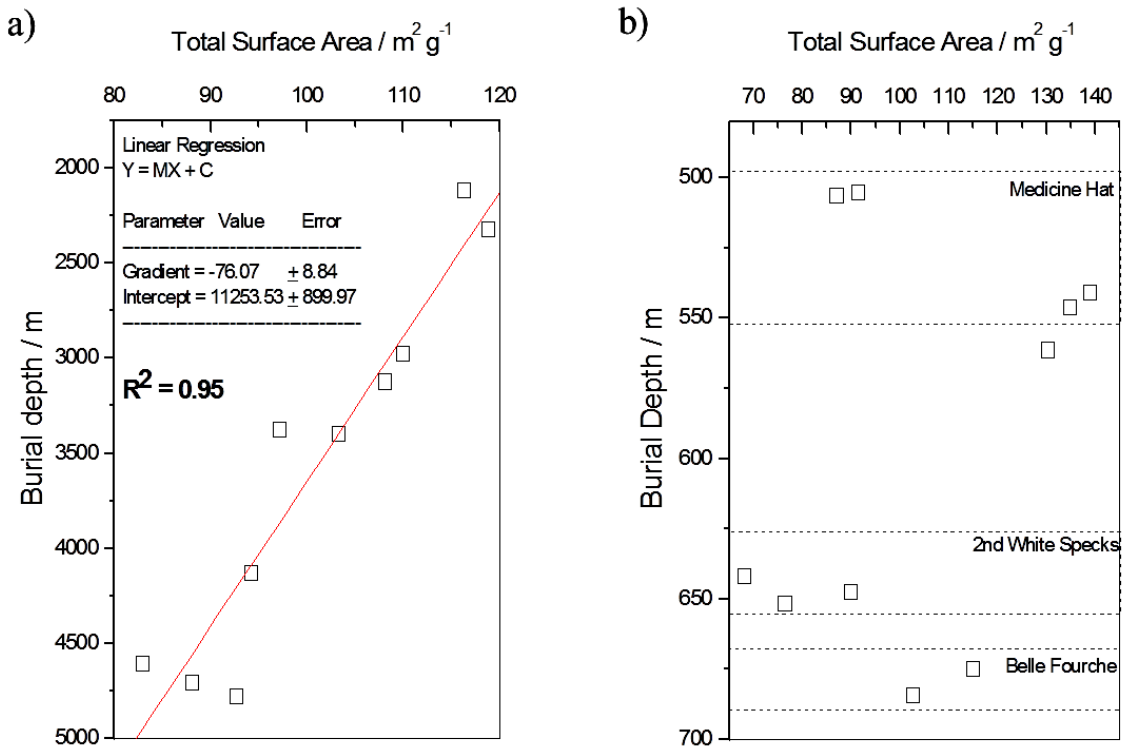

Figure 5.22: Total surface area against burial depth. In part a) the total surface area of the Draupne Formation kerogens decreases with increasing burial depth. In part b) there is no observable correlation between total surface area and burial depth for the Colorado Group kerogens.

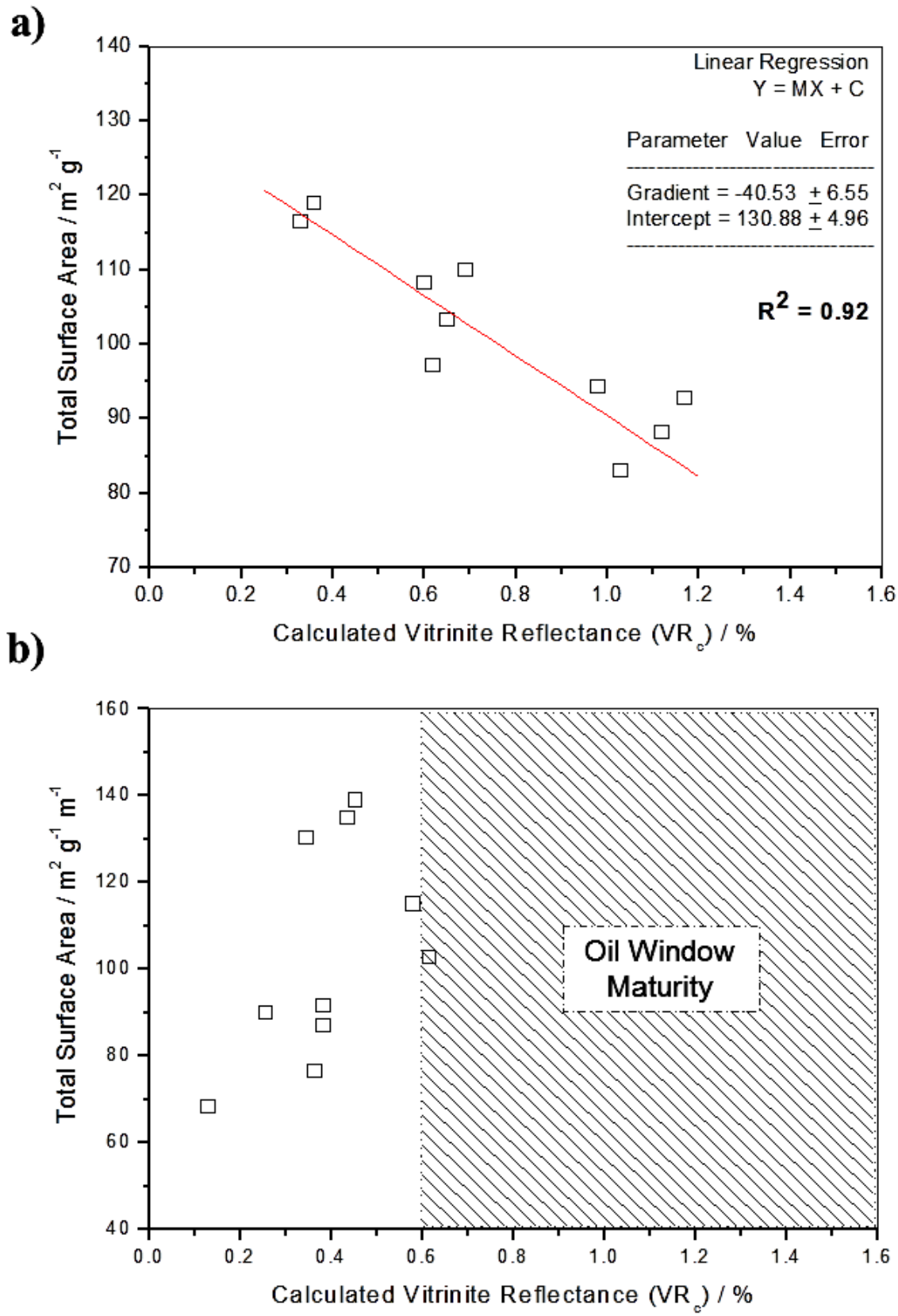

Figure 5.23: Total surface area against maturity. In part a), a strong negative correlation between total surface area and calculated vitrinite reflectance exists for the Draupne Formation kerogens. In part b), no observable correlation exists for the Colorado Group kerogens.

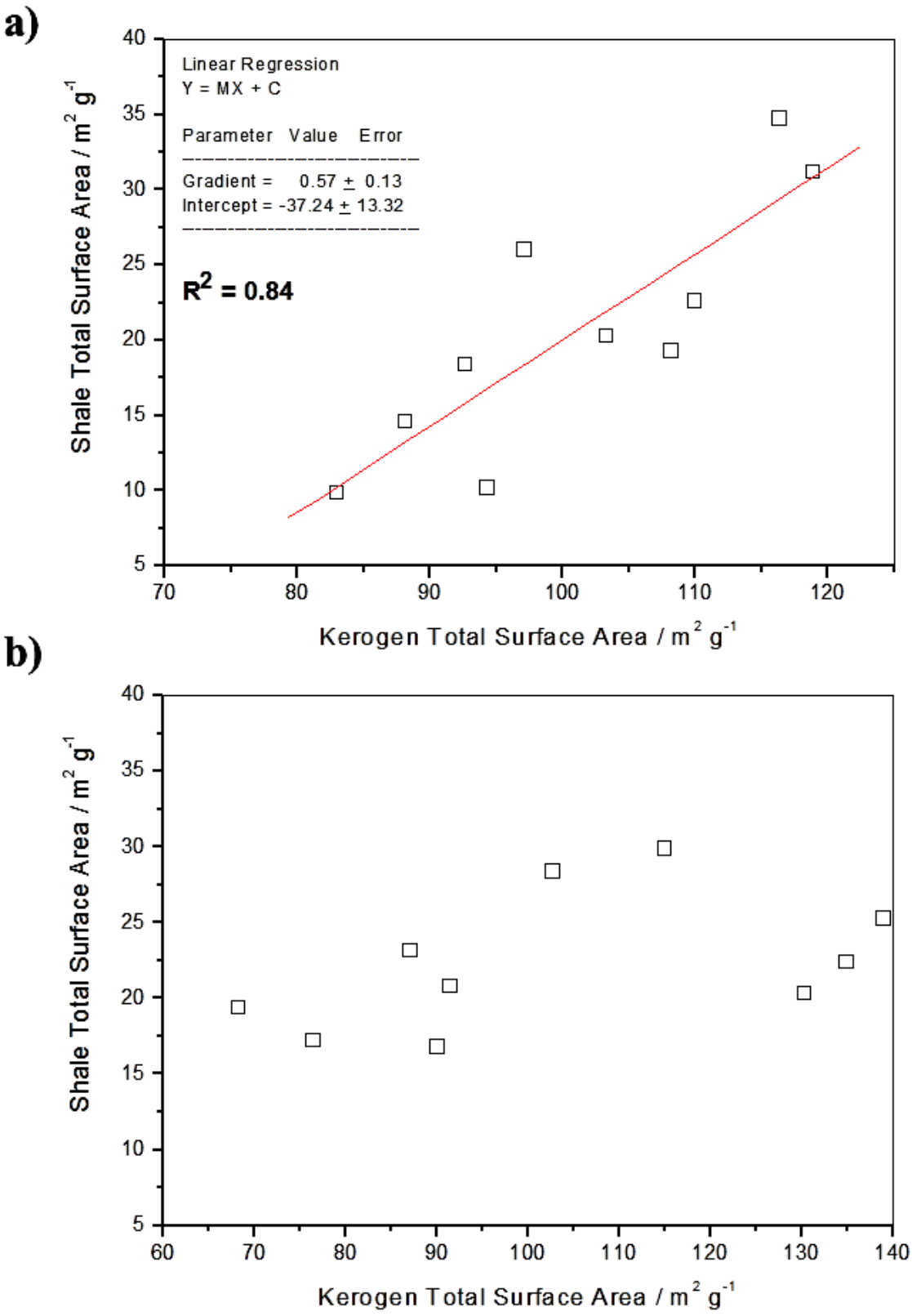

Figure 5.24: Comparison of kerogen total surface area and shale total surface area. In part a), the kerogen total surface area is correlated to the shale total surface area for the Draupne Formation samples. In part b), the kerogen total surface area and the shale total surface area exhibit no observable correlation for the Colorado Group samples.

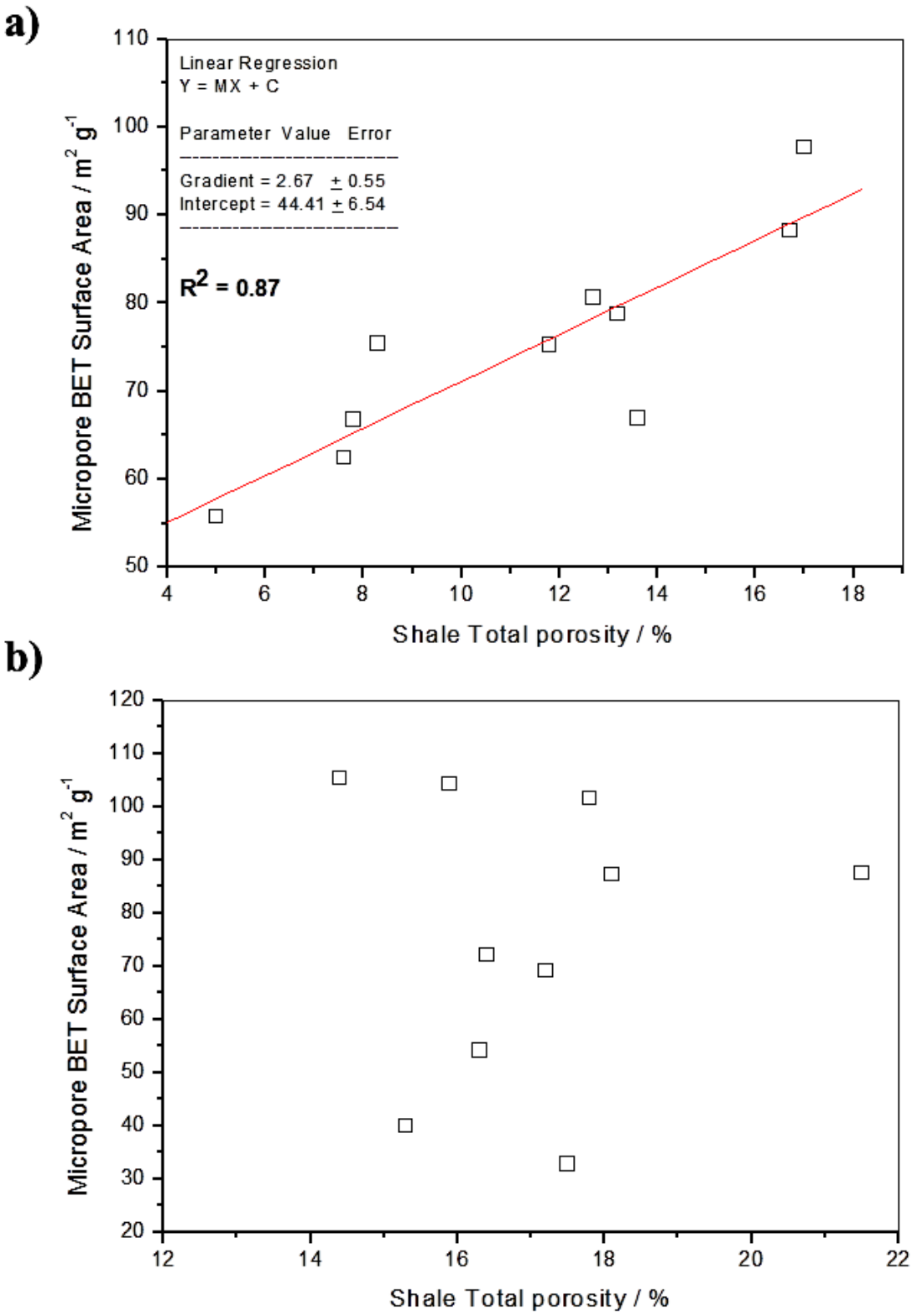

Figure 5.25: Kerogen micropore surface area against shale total porosity. In part a) a strong positive correlation between micropore surface area and shale total porosity exists for the Draupne Formation. In part b), there is no observable correlation between micropore surface area and shale total porosity for the Colorado Group.

5.3 Discussion

5.3.1 Influence of pyrite on gas adsorption isotherms of isolated kerogen.

The adsorption uptake of an iron pyrite standard was shown to be negligible in Figure 5.5 (above). To ensure that pyrite does not have an influence on the pore measurements of the Draupne Formation and Colorado Group kerogens, the weight percent of pyrite in each kerogen is plotted against: 1) sorption pore volume, 2) microporosity, and 3) total surface area. It can be observed in Figure 5.26, that there is no correlation to any of the pore measurements and iron pyrite content for the Draupne Formation and Colorado Group kerogens.

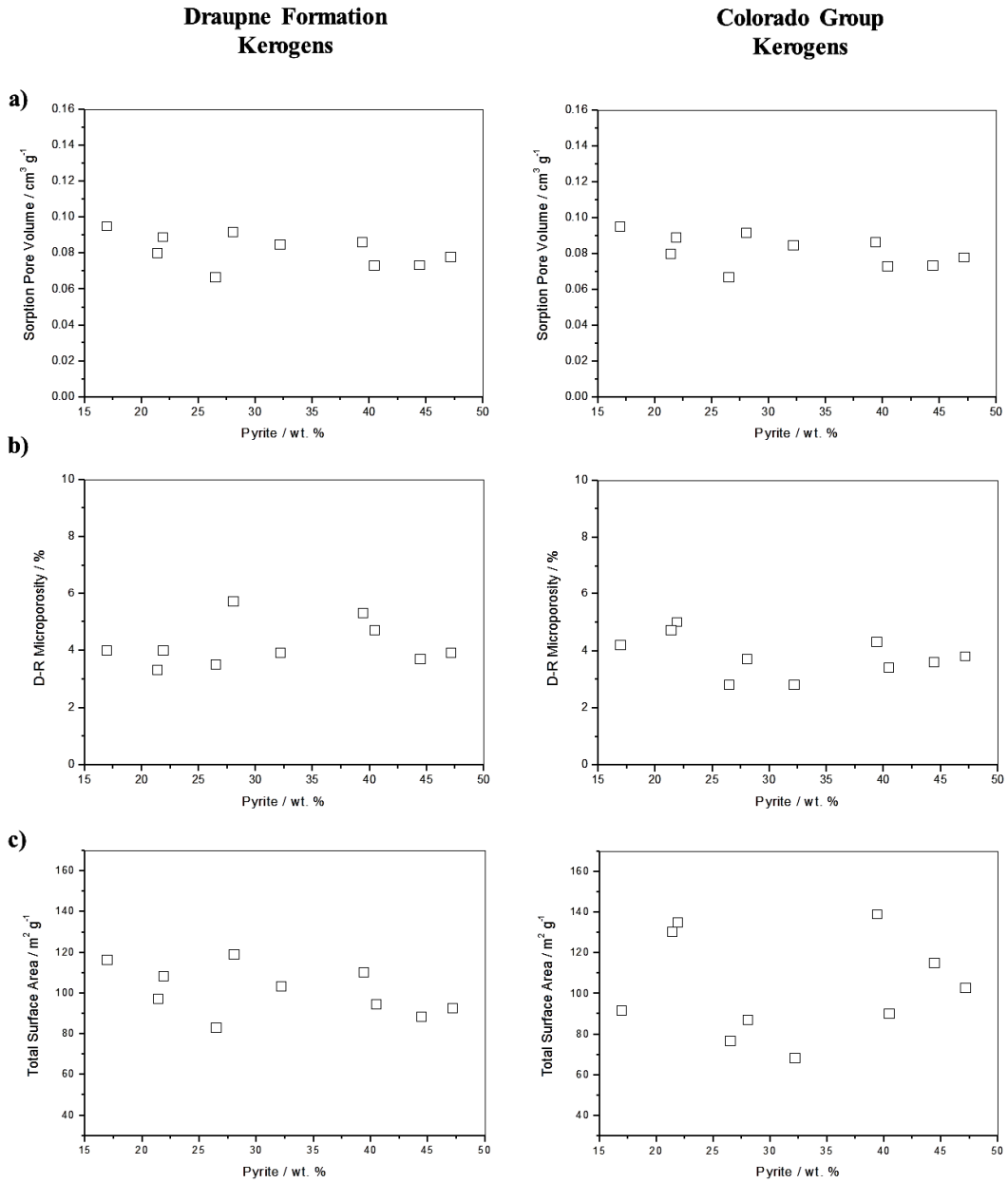

Figure 5.26: Pyrite content against sorption pore volume, microporosity and total surface area for the Draupne Formation and Colorado Group kerogens. The wt.% of pyrite has no influence on the pore measurements of the kerogens. In part a), the pyrite content has no correlation to sorption pore volume. In part b), the pyrite content has no correlation to D-R microporosity. In part c), the pyrite content has no correlation to total surface area.

5.3.2 Pore volumes and porosities of the kerogens.

The average sorption pore volumes of the sub-100 nm diameter pores are very similar in value for both sets of kerogens (0.0816 cm^3g^{-1} vs 0.0834 cm^3g^{-1}), despite their different levels of thermal maturity. This suggests that the typical sorption pore volume of a Type II kerogen is around ~ 0.1 $cm^3\ g^{-1}$, and that Type II kerogen sorption pore volumes are lower than other carbonaceous materials. For example, the commercially available Chemviron and Norit-Supra activated carbons have sorption pore volumes (measured using CO_2 at -78^oC) of 0.391 and 0.282 $cm^3\ g^{-1}$, respectively (Gavrilov and Zakharov, 2010). Furthermore, the similarity of the average sorption pore volumes of the DF and CG kerogens (0.0816 cm^3g^{-1} vs 0.0834 cm^3g^{-1}) mirrors the similarity observed in the sorption pore volumes of the pre-extraction shales (0.0171 cm^3g^{-1} vs 0.0184 cm^3g^{-1}), as reported in Chapter 4. In the case of the shales, the similar sorption pore volume values were interpreted as being a property of Type II marine kerogen, as the DF and CG shales have different total porosities, thermal maturities and burial depths, and the commonality shared by these two shale suites was the organic-richness.

The sorption pore volumes of the Draupne Formation isolated kerogens are strongly correlated to the sorption pore volumes of the Draupne Formation whole shales. This is suggests that organic matter is a primary location for sub-100 nm pores in the Draupne Formation shales. However, the sorption pore volumes of the Colorado Group isolated kerogens exhibit no observable correlation to the sorption pore volumes of the shales. The explanation for the difference between the Draupne Formation and the Colorado Group shales is the level of organic matter content. The DF shales are much more organic rich than the Colorado Group shales, and this is the suggested reason why the sorption pore volumes of the Draupne Formation shales is dependent on the sorption pore volumes of the kerogens.

There is significant variation in the sorption pore volumes of the Colorado kerogens. It is suspected that this spread in sorption pore volumes is due to the natural variability of the organic composition of the immature kerogen; it has been shown that kerogens which have a high abundance of woody Type III vitrinite macerals have an increased gas adsorption capacity, as reported by Zhang *et al*., (2012). Unfortunately, the optical microscopy examination of the Colorado Group kerogens was not performed to support this interpretation of the data.

The micropore volume of < 0.7 nm diameter pores was determined using CO_2 adsorption at 0^oC. The micropore volume is a significant part of the sorption pore volume available to gas adsorption processes (i.e. pores that have up to 100 nm in diameter). The micropore volume of the Draupne Formation kerogens accounts for 41.1% of the gas sorption pore volume, and the micropore volume of the Colorado Group kerogens accounts for 36.8 % of the gas sorption pore volume. This finding indicates that the tiniest pores contribute significantly to the kerogen's pore volume. Furthermore, the average percentage of micropores in both the Colorado Group shales and kerogens are very similar in value (35.9% vs 36.8%). In the Draupne Formation, this trend is not repeated, with the average percentage of micropores in both the shale being larger than in the kerogen (52.3 % vs 41.1%).These correlations suggest that micropores (< 0.7nm) are a significant proportion of the sub-100 nm pore volume.

The micropore volumes of the Draupne Formation and the Colorado Group kerogens do not vary with increasing burial depth. This result is in contrast to the sorption pore volume, which decreases in pore volume with increasing burial depth. This finding suggests that micropores are not mechanically compressed during the compaction processes that occur during formation burial.

The gas sorption porosity and the D-R microporosity of the Draupne Formation and Colorado Group kerogens were determined from the corresponding pore volumes and the estimated bulk density of the kerogen. The gas sorption porosity of Draupne Formation kerogens exhibits a strong correlation with total porosity ($R^2 = 0.87$). For the Colorado Group kerogens, the sorption porosity and the D-R microporosity has no observable correlation to the total porosity of the shales. This indicates that the sub-100 nm porosity of the kerogens is a primary controlling factor on the total porosity of the Draupne Formation shales. The interpretation of this finding is that the organic matter content of the Draupne Formation is larger than the Colorado Group shales, and the sub-100 nm porosity is located within the organic matter.

The sorption porosities of the isolated Draupne Formation kerogens are significantly higher than the kerogen porosity values estimated by Modica and Lapierre (2012) for kerogen dispersed in some Mowry Shale core samples. Modica and Lapierre (2012) used a mass balance approach to calculate the maximum porosity of kerogen in the Mowry Shale, which is based on the relationship of initial TOC, the Transformation Ratio (from the Rock-Eval S2 parameter) and the ratio of shale density to kerogen density. They calculate that kerogen porosity increases exponentially with increasing thermal maturity, until a maturity of Ro = 0.9% is reached, and then the porosity of the kerogen gradually becomes constant. They calculate that the maximum porosity of kerogen in the Mowry Shale reaches a constant porosity of between 2.5 and 3.3% for gas window maturity shales. Using this figure, they estimate that kerogen porosity does not increase beyond ~ 3%.

5.3.3 Surface areas of the shales.

A large proportion of the internal surface area of the Draupne Formation kerogens is located within micropores (< 2nm). The average N_2 BET surface area (26.43 $m^2\ g^{-1}$) is much smaller than the average CO_2 BET surface area value (101.24 $m^2\ g^{-1}$). As micropores are inaccessible to N_2 at -196^oC, the large difference is attributed to significant micropore surface area. Similarly, the average N_2 BET surface area (28.13 $m^2\ g^{-1}$) of the Colorado Group shales is much smaller than the average CO_2 BET surface area value (103.54 $m^2\ g^{-1}$). Again, this suggests that a large proportion of surface area is located within the micropores (< 2 nm) for the Colorado Group kerogens.

The total surface areas of both the Draupne Formation and Colorado Group kerogens are very similar (average of 101.24 $m^2\ g^{-1}$ and 103.54 $m^2\ g^{-1}$, respectively), indicating that these Type II kerogens have similar pore structures. The total surface areas of the Draupne Formation isolated kerogens are strongly correlated to the total surface areas of the Draupne Formation whole shales. However, the total surface areas of the Colorado Group isolated kerogens exhibit no observable correlation to the total surface areas of the shales.

Furthermore, the primary location for surface area in the Draupne Formation and Colorado Group kerogens is in the micropores (< 2 nm). The micropore surface area of the DF kerogens consists of an average of 74.2 % of the total surface area. The micropore surface area of the CG kerogens consists of an average of 71.7 % of the total surface area. The micropore surface areas of the DF kerogens is positively correlated to the total porosity of the shale, suggesting that the kerogen micropores (< 2nm) are a significant control on the overall porosity of the shale.

5.3.4 Pore structure and thermal maturity

Thermal maturity has a significant influence on the pore structure of the Draupne Formation kerogens. The pore volumes of the sub-100 nm pores decreases as the thermal maturity of the kerogens increase. Evidence of the pore volume reduction of the sub- 100 nm pores can be observed in the sorption pore volumes, the D-R micropore volumes, the porosities and the surface areas of the Draupne Formation kerogens (see Figures above). A decrease in sorption pore volume with increasing thermal maturity has been previously observed in coal (Bustin and Clarkson 1998), where the relationship between gas adsorption and thermal maturity is 'U' shaped, and the pore volume initially decreases with maturity before increasing at high maturity (Bustin and Clarkson, 1998).

The reduction of pore volume in the sub-100 nm pores with maturation is interpreted as being due to changes in levels of aromaticity of the kerogen. It is well established that thermal maturation has a significant effect on the pore structure of organic matter (Loucks *et al*., 2009; Zhang *et al*., 2012, and references there in). The relationship between the pore volume of shales and the level of maturity is often attributed to changes in the pore structure of the kerogen (Chalmers and Bustin, 2007; Bae *et al.*, 2009; Loucks *et al.*, 2009). It is also known that thermal maturation causes the 3-D structure of immature kerogen to rearrange to a more ordered and compacted highly aromatic structure. As the aromaticity increases, the mature organic matter occupies less space than the immature organic matter, and the bulk volume of the kerogen decreases.

Therefore, the interpretation suggested is that the aromatisation process causes the decrease in the volume of the Draupne Formation sub-100 pores with increasing thermal maturation. Evidence of the significant changes in the structure of the Draupne Formation kerogens was observed in the geochemical analyses. The FT-IR spectra, solid-state ^{13}C-NMR spectra and pyrolysis GC-MS determined that the aliphatic alkyl carbon content of kerogens decreased, and the aromatic carbon content significantly increased with maturation (the aromaticity of the DF10 kerogen is greater than 85 %). This aromatisation process is suggested as the cause of the trends in pore volume data of the Draupne Formation kerogens. This interpretation of the maturity trend agrees with that of Chalmers and Bustin (2012) and Loucks *et al*., (2009), who observed significant changes in pore structure of shale organic matter with increasing thermal maturity.

In contrast to the maturity correlations of the Draupne Formation shales, the Colorado Group shales do not exhibit any trends with increasing maturity. This is supported by the geochemical analyses of the organic matter, which is primarily aliphatic in nature, with minimal levels of aromaticity. As with the Draupne Formation samples, the level of aromaticity (or the lack of) is interpreted as being the controlling factor for the pore volumes of the Colorado Group kerogens.

5.3.5 Distribution of pore volumes and surface areas between organic matter and inorganic matrix.

The average total organic carbon (TOC) content of the Draupne Formation shales is 7.2%, and the average TOC of the Colorado Group shales is 2.7%. Consequently, over 90 wt.% of the whole shale is mineral matter. As with the kerogen, this inorganic shale matrix will contain pores and porosity, so an important proportion of the surface area and pore volumes measured for the whole shales (in Chapter 4) will be attributed to this inorganic shale matrix.

The surface areas and pore volumes of the DF and CG shales were determined prior to acidic extraction of their kerogens (reported in chapter 4). Since the surface areas and pore volumes of the DF and CG kerogens were subsequently determined after isolation, it is possible to calculate the surface areas and pore volumes of the in-situ shale organic matter component (prior to kerogen extraction). This is done by normalising the isolated kerogen's experimental surface area and pore volume data down by the initial organic matter content of the whole shales. Furthermore, as the surface area and pore volumes of the organic matter component must be less than the values for the whole shale, the difference between these values is the surface area and pore volumes of the inorganic mineral matrix of the shale. It is important to note, however, that during the scaling down of the kerogen data to the levels of organic matter in the whole shale, an implicit assumption is being made that the pore structure of the organic matter is not changed during the acidic kerogen extraction process.

The sorption pore volume of the in-situ organic matter for the Draupne Formation had a range of 18.5 to 88.2 %, with an average of 49.7 %. The sorption pore volume of the inorganic mineral matrix for the Draupne Formation had a range of 11.8 to 81.5 %, with an average of 50.3 %. The sorption pore volume of the in-situ organic matter for the Colorado Group had a range of 9.6 to 27.1 %, with an average of 17.1 %. The sorption pore volume of the inorganic mineral matrix for the Colorado Group had a range of 72.9 to 90.4 %, with an average of 82.9 %. These finding indicate that the majority of sub-100 nm pore volume in the Colorado Group shales are located within the inorganic mineral matrix (82.9 %). This agrees with the finding that the Colorado Group sorption pore volumes are strongly correlated to the illite content.

The micropore volume of the in-situ organic matter for the Draupne Formation had a range of 25.4 to 57.1 %, with an average of 35.7 %. The micropore volume of the inorganic mineral matrix for the Draupne Formation had a range of 42.9 to 74.6 %, with an average of 64.3 %. The micropore volume of the in-situ organic matter for the Colorado Group had a range of 8.6 to 28.8 %, with an average of 18.0 %. The micropore volume of the inorganic mineral matrix for the Colorado Group had a range of 71.2 to 91.4 %, with an average of 82.0 %. These finding indicate that the majority of the micropore volume in the Colorado Group shales are located within the inorganic mineral matrix (82.0 %). This agrees with the finding that the Colorado Group sorption pore volumes are strongly correlated to the illite content.

The total surface area of the in-situ organic matter for the Draupne Formation had a range of 19.9 to 91.2 %, with an average of 50.3 %. The total surface area of the inorganic mineral matrix for the Draupne Formation had a range of 8.8 to 80.1 %, with an average of 49.7 %. The total surface area of the in-situ organic matter for the Colorado Group had a range of 9.6 to 27.2 %, with an average of 17.4 %. The total surface area of the inorganic mineral matrix for the Colorado Group had a range of 72.8 to 90.4 %, with an average of 82.6 %.

The organic matter normalised kerogen values are the experimental kerogen values that have been scaled down to fit with the amount of organic matter in the whole shale. The weight percent of organic matter (OM wt.%) is found by dividing the shale TOC content (%)by the elemental carbon content the kerogen (wt.%), which were determined using Elemental Analysis.

Table 5.12: Sorption Pore Volumes of the in-situ organic matter and inorganic mineral matrix in whole shale.

Sample	Kerogen Sorption Pore volume / $cm^3\ g^{-1}$	OM Normalised Kerogen Sorption Pore Volume / $cm^3\ g^{-1}\ wt\ \%^{-1}$	Whole Shale Sorption Pore volume / $cm^3\ g^{-1}$	Sorption Pore Volume of In-situ Organic Matter / %	Sorption Pore Volume of Inorganic Shale Matter / %
DF1	0.0949	0.0109	0.0296	36.8	63.2
DF2	0.0915	0.0127	0.0251	50.6	49.4
DF3	0.0861	0.0035	0.0190	18.5	81.5
DF4	0.0888	0.0083	0.0180	46.1	53.9
DF5	0.0797	0.0120	0.0208	57.6	42.4
DF6	0.0846	0.0088	0.0168	52.6	47.4
DF7	0.0729	0.0072	0.0081	88.2	11.8
DF8	0.0666	0.0049	0.0079	61.8	38.2
DF9	0.0732	0.0050	0.0122	41.2	58.8
DF10	0.0778	0.0058	0.0132	43.9	56.1
C1	0.0707	0.0175	0.0175	13.9	86.1
C2	0.0673	0.0192	0.0192	12.1	87.9
C3	0.1143	0.0208	0.0208	17.9	82.1
C4	0.1100	0.0188	0.0188	19.0	81.0
C5	0.1069	0.0168	0.0168	27.1	72.9
C6	0.0552	0.0161	0.0161	15.5	84.5
C7	0.0725	0.0141	0.0141	25.3	74.7
C8	0.0634	0.0148	0.0148	19.3	80.7
C9	0.0945	0.0234	0.0234	11.0	89.0
C10	0.0789	0.0224	0.0224	9.6	90.4

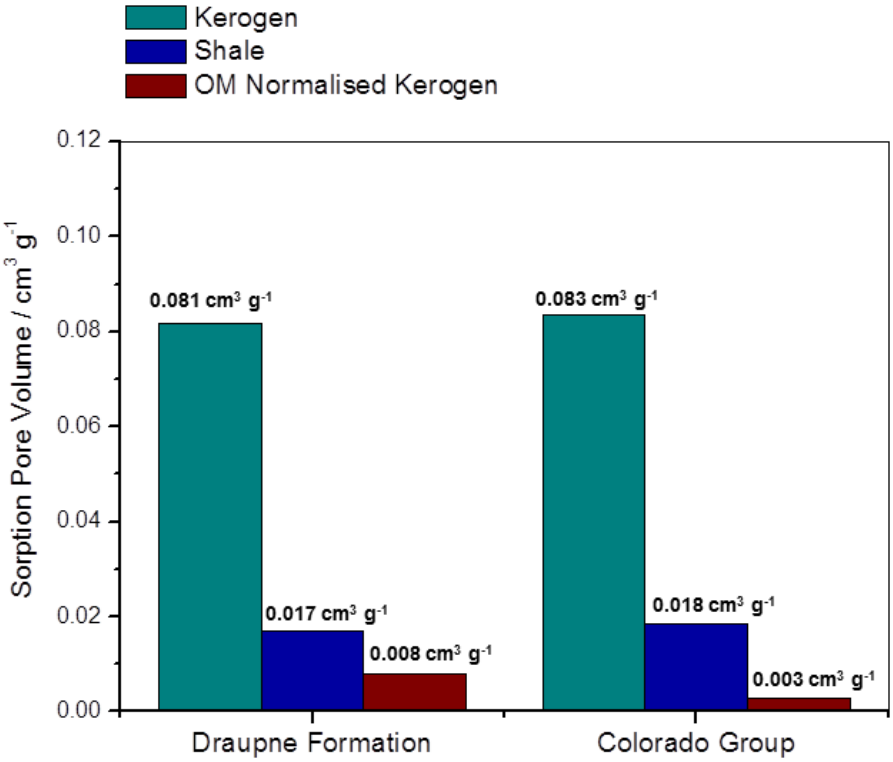

Figure 5.27: Average sorption pore volumes for the a) kerogens, b), shales, and c) organic matter (OM) normalised kerogens.

Table 5.13: Micropore Volumes of the in-situ organic matter and inorganic mineral matrix in whole shale.

Sample	Kerogen Micropore Volume / $cm^3\ g^{-1}$	OM Normalised Kerogen Micropore Volume / $cm^3\ g^{-1}\ wt\ \%^{-1}$	Whole Shale Micropore Volume / $cm^3\ g^{-1}$	Micropore Volume of In-situ Organic Matter / %	Micropore Volume of In-situ Organic Matter / %
DF1	0.0320	0.00367	0.00982	37.4	62.6
DF2	0.0452	0.00628	0.011	57.1	42.9
DF3	0.0423	0.00172	0.006795	25.4	74.6
DF4	0.0317	0.00295	0.01143	25.8	74.2
DF5	0.0267	0.00402	0.0124	32.4	67.6
DF6	0.0310	0.00323	0.01195	27.0	73.0
DF7	0.0379	0.00374	0.007705	48.5	51.5
DF8	0.0277	0.00203	0.00563	36.0	64.0
DF9	0.0299	0.00205	0.007785	26.3	73.7
DF10	0.0308	0.00229	0.00557	41.2	58.8
C1	0.0334	0.00115	0.00717	16.0	84.0
C2	0.0293	0.00101	0.00590	17.1	82.9
C3	0.0345	0.00112	0.00599	18.7	81.3
C4	0.0400	0.00130	0.00676	19.2	80.8
C5	0.0379	0.00161	0.00670	24.1	75.9
C6	0.0224	0.00101	0.00613	16.6	83.4
C7	0.0272	0.00134	0.00465	28.8	71.2
C8	0.0225	0.00101	0.00491	20.6	79.4
C9	0.0289	0.00079	0.00922	8.6	91.4
C10	0.0305	0.00083	0.00816	10.1	89.9

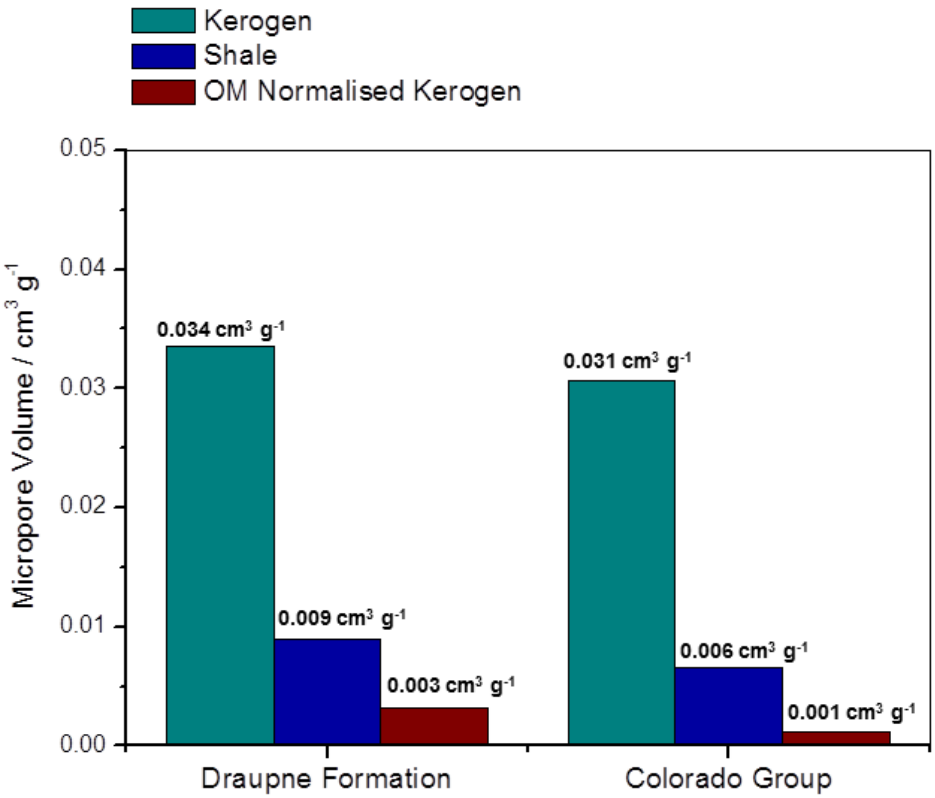

Figure 5.28: Average micropore volumes for the a) kerogens, b), shales, and c) organic matter (OM) normalised kerogens.

Table 5.14: Total surface areas of the in-situ organic matter and inorganic mineral matrix in whole shale.

Sample	Kerogen Total surface areas / $m^2\ g^{-1}$	OM Normalised Kerogen Total Surface Area / $m^2\ g^{-1}$ wt $\%^{-1}$	Whole Shale Total Surface Area / $m^2\ g^{-1}$	Total Surface Area of In-situ Organic Matter / %	Total Surface Area of Inorganic Shale Matter / %
DF1	116.40	13.36	34.73	38.5	61.5
DF2	118.90	16.52	31.16	53.0	47.0
DF3	109.99	4.49	22.58	19.9	80.1
DF4	108.21	10.09	19.29	52.3	47.7
DF5	97.15	14.60	25.99	56.2	43.8
DF6	103.30	10.76	20.25	53.1	46.9
DF7	94.30	9.29	10.19	91.2	8.8
DF8	82.98	6.07	9.85	61.6	38.4
DF9	88.14	6.03	14.57	41.4	58.6
DF10	92.67	6.90	18.39	37.5	62.5
C1	91.52	3.15	20.93	15.0	85.0
C2	87.08	3.00	23.22	12.9	87.1
C3	139.00	4.52	25.32	17.9	82.1
C4	134.91	4.38	22.55	19.4	80.6
C5	130.30	5.55	20.42	27.2	72.8
C6	68.27	3.09	19.58	15.8	84.2
C7	90.03	4.43	17.01	26.0	74.0
C8	76.50	3.43	17.64	19.4	80.6
C9	114.99	3.14	30.06	10.4	89.6
C10	102.78	2.78	28.87	9.6	90.4

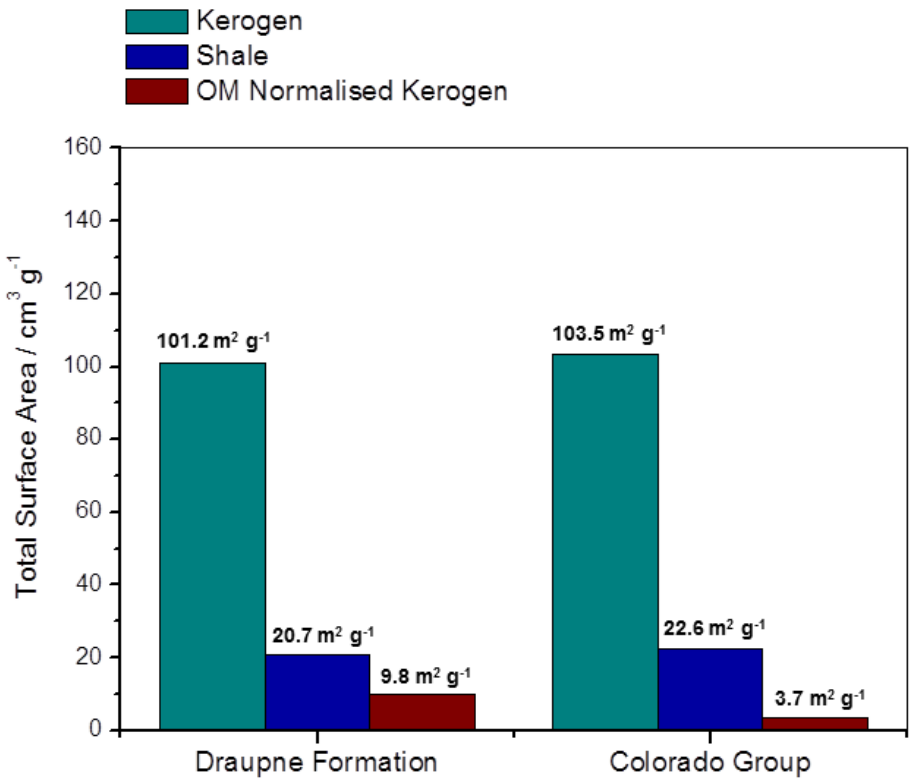

Figure 5.29: Total surface areas for the a) kerogens, b), shales, and c) organic matter (OM) normalised kerogens.

5.4 Summary and Conclusions

The major findings and implications of Chapter 5 are:

- Pyrite in the kerogen concentrates is not a site for gas adsorption, and has negligible influence on the gas adsorption uptakes by kerogen. The presence of non-adsorbing pyrite can be corrected for by mass normalising the gas adsorption isotherms.

- The typical sorption pore volume of Type II kerogen is around ~ 0.1 cm3 g-1, which is approximately one order of magnitude (x 10) more than that of the sorption pore volumes of shale.

- The average sorption porosity of Type II kerogen is 10%. The sorption porosity of the DF kerogen is strongly correlated to the total porosity of the shale. This suggests that the nanometre-scale porosity of the organic matter fraction is an important influence on the overall total porosity of the shale.

- The total surface areas of kerogens are significantly larger than that of whole shale samples, suggesting that organic matter is a key site for gas storage by adsorption. The DF and CG kerogens have very similar total surface areas (101.24 m2 g-1 vs 103.54 m2 g-1, respectively), indicating that Type II kerogens have similar pore structures. In addition, a large proportion of the total surface area of kerogens is located within micropores (< 2nm), nearly three quarters (74 %) for the DF kerogens.

- The sorption pore volumes, the porosities and the surface areas of the DF kerogens strongly decrease with increasing thermal maturity. These pore structural changes are interpreted to being due to changes in levels of aromaticity of the kerogen with maturity. However, the micropore volumes of kerogens are relatively stable against the effects of burial compaction and thermal maturation. The CG kerogens do not shown any maturity affects.

- Using a mass balance approach, the pore structure measurement of the whole shale in Chapter 4 can be partitioned between the organic kerogen, and the inorganic shale mineral matrix. The average sorption pore volume of the inorganic mineral fraction of the DF shales is 50.3 %, whereas the average sorption pore volume of the inorganic mineral fraction of the CG shales is 82.9 %, indicating that shale mineral porosity is important in the CG shales. This supports the finding that the CG sorption pore volumes are strongly influenced by illite mineral content.

Chapter 6: Gas adsorption in shales and kerogens.

6.1 Introduction

6.1.1 Methane adsorption capacity of shales.

To understand and predict the behaviour of shale gas in geological formations it is necessary to perform methane storage experiments under geological pressure and temperature conditions (Chalmers and Bustin, 2007; Ross and Bustin, 2009; Weniger *et al.* 2010; Zhang *et al*., 2012). Under these conditions, gas experiences significant compression, which results in a higher density and occupying a smaller volume than equivalent gas would exhibit at surface standard pressure and temperature (Krooss *et al*., 2002).

Geological physical conditions cause the shale gas to partition between three phases (i.e. free, adsorbed and dissolved), and a chemical equilibrium between the phases is established (Zhang *et al*., 2012). The position of the equilibrium is dynamic and can be altered (as explained by Le Chatelier's Principle), and the relative distribution of gas molecules between the adsorbed phase and the free gas phase will change as the pressure and temperature conditions change (Krooss *et al*., 2002).

The presence and abundance of microporosity in shales is a primary control on the storage of gas by adsorption (Bae *et al.*, 2009; Ross and Bustin, 2009). The large internal surface area of micropores provides the necessary sites for gas adsorption in the porous structure of gas shales (Zhang *et al*., 2012). Several important factors influence the gas adsorption processes of organic rich shales, and subsequently the amount of gas that is stored (GIP):

- Burial and compaction
- Thermal maturity
- Organic matter type and richness
- Amount and type of mineral matter
- Moisture content

Burial and compaction: There is an empirical relationship between the burial depth and gas storage capacity of shales and coals (Bustin and Clarkson 1998, Bustin and Bustin, 2008; Hackley *et al*., 2007). Generally, as burial depth increases, gas storage capacity increases. This relationship is explained by a simultaneous increase in the pressure and the thermal maturity of the shale formation, when being subjected to deep burial. An important consideration is that current present day burial depth may not be the same as the maximum paleo-burial depth (as geological formations can be uplifted or rapidly buried due to subsidence). For this reason, it is probable that current burial depth is not a reliable indicator of gas storage potential. What is known is that that the reduction of pressure caused by geological uplift actually causes gas to be desorbed and be liberated, thus reducing the amount of gas stored as adsorbed gas (Bustin and Bustin, 2008).

Thermal maturity: The thermal maturity of shales and coals has been shown to be a significant factor in the amount of gas that can be stored. An increase in the methane storage by adsorption occurs when the thermal maturity increases, and this relationship is attributed to the increase in the microporosity of the samples with increased maturity (Yee *et al.*, 1993; Levy *et al.*, 1997; Clarkson and Bustin, 1999; Chalmers and Bustin, 2007). The presence and abundance of microporosity is known to be a key factor in the storage of gas by adsorption (Bae *et al.*, 2009; Ross and Bustin, 2009). This is because micropores have much larger internal surface areas than mesopore and macropores, and this larger surface area provides significantly increased amounts of adsorption sites in the pores. It was observed by Ross and Bustin (2009) that physical/chemical alterations had occurred in a suite of high maturity shales, with the creation and expansion of microporosity, relative to equivalent low maturity shales from the same sedimentary basin. It was also noticed that the same high maturity shales had a higher methane sorption capacity than the low maturity shales at the same weight percent (TOC%) organic matter content.

Organic matter content and type: It is well established that organic richness of the shale is a dominant factor in the gas storage capacity (Lu *et al.*, 1995, Ross and Bustin, 2009; Weniger *et al.* 2010; Zhang *et al.*, 2012). This is because a significant proportion of the gas storage capacity is contained within the kerogen pore networks (Modica and Lapierre, 2012). Petroleum source rocks often contain more than 2% total organic carbon (Tyson, 1995), with values up to 20% to 30% being possible (Aplin and Macquaker, 2011). It has been shown that as the amount of organic matter (the TOC) increases, the gas storage capacity of shales increases (Chalmers and Bustin, 2007; Ross and Bustin 2009). This is reported in Figure 6.1, where an excellent positive correlation exists between methane adsorbed and TOC. It was found by Ross and Bustin (2009) that the gas adsorption capacity of a suite of organic rich shales increased with both increasing TOC and micropore volume (Ross and Bustin 2009).

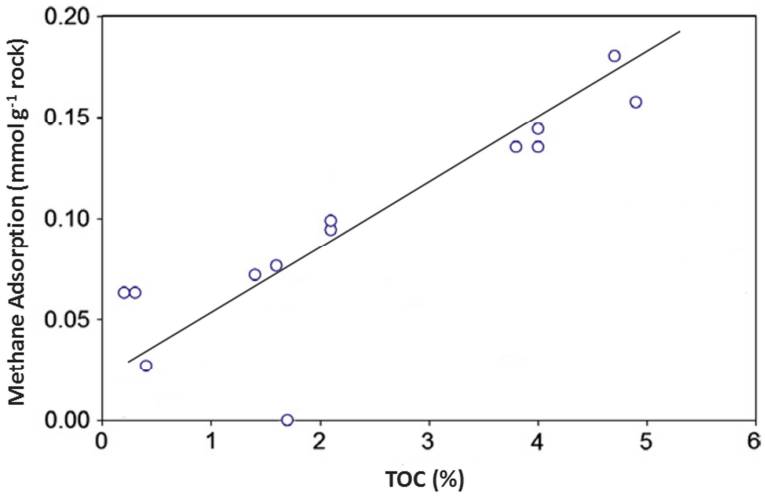

Figure 6.1: There is a strong positive correlation between organic matter content of shales and the methane adsorption capacity (modified after Zhang *et al.*, 2012)

Mineralogy: In terms of overall gas storage capacity of shales, it has been found that the bulk mineral matter content has a detrimental effect to gas adsorption uptake (Chareonsuppanimit *et al*., 2012). The ash content of coals has a strong negative impact on methane adsorption capacity (Faiz *et al*., 1992; Yee *et al.*, 1993; Crosdale *et al*., 1998; Clarkson and Bustin, 1999; Laxminarayana and Crosdale, 1999, Chalmers and Bustin, 2007). This is shown in Figure 6.2.

It has been found that the ash/mineral matter is very weakly adsorbing of gas, and acts as a bulk diluent to the more strongly gas adsorbing organic matter (Crosdale *et al*., 1998, Weniger *et al*., 2010, Gasparik, *et al*., 2013). It is shown in Figure 6.3 that as the ash content of Brazilian coals and shales increases, the methane adsorption capacity decreases. The gas adsorption uptake of pure clay minerals standards is low relative to pure organic matter (Ross and Bustin, 2009; Ji *et al*., 2012; Gasparik, *et al*., 2013). It is shown in Figure 6.4 that the methane adsorption uptakes of illite, montmorillonite and kaolinite minerals are less than 3 cm^3 g^{-1}, whereas isolated kerogen concentrates can have adsorption uptakes of more than 22 cm^3 g^{-1} (i.e. 1 mmol g^{-1}; Zhang *et al.*, 2012). It was also noted by Gasparik *et al*., (2013) that in high maturity gas window shales, most of the smectite mineral content will have been converted to illite (or illite/smectite mixed layer), thus increasing the gas storage capacity of this mineral fraction (as illite has a larger sorption capacity, Ross and Bustin (2009), as shown in Figure 6.4)

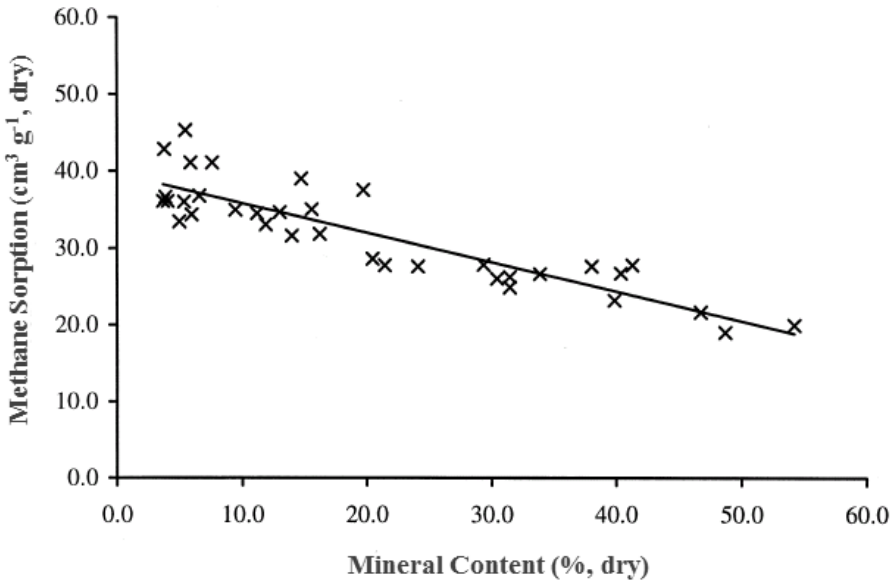

Figure 6.2: Mineral matter in geological materials can be detrimental to gas adsorption uptake, having a negative impact on methane adsorption capacity (modified after Laxminarayana and Crosdale, 1999).

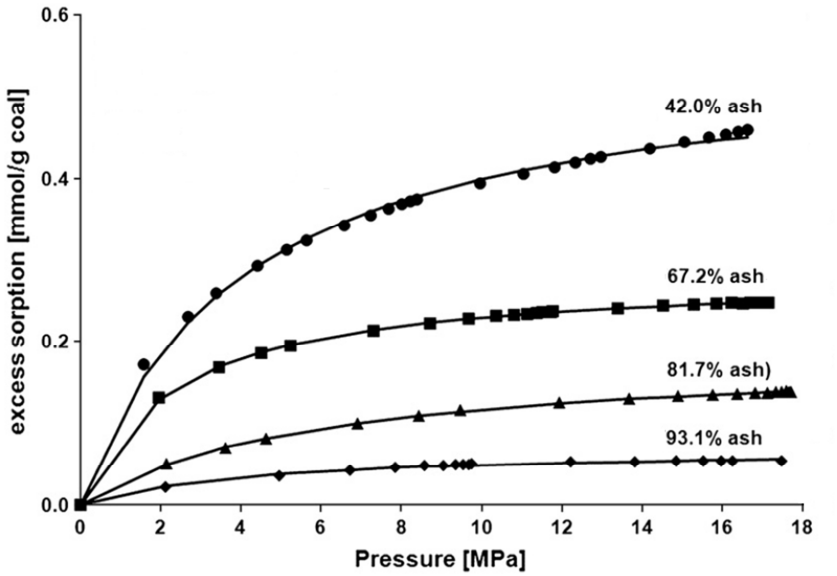

Figure 6.3: The high pressure methane adsorption uptake (at 45°C) is adversely affected by the mineral matter (ash) content of these Brazilian coals and shales (after Weniger *et al*., 2010).

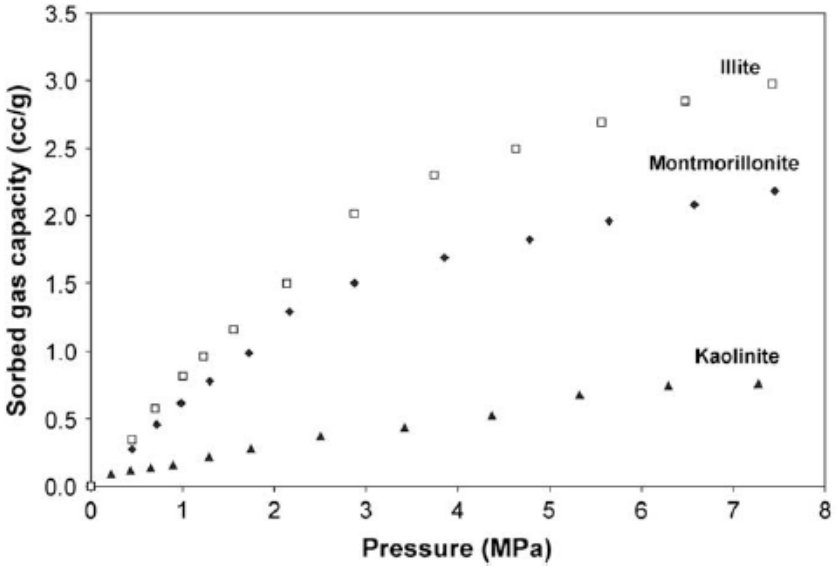

Figure 6.4: Pure clay mineral standards have a small but important gas adsorption uptake for CH_4 at 30°C, as shown by these adsorption isotherms (after Ross and Bustin, 2009)

Moisture: The moisture content is a key factor when evaluating the overall methane storage capacity (Crosdale *et al*., 2008). Pore structure is a key control in the retention of water in the pores, and this pore moisture determines the amount of gas that can be stored by adsorption (Krooss *et al.*, 2002; Bae and Bhatia, 2006; Day *et al*., 2008; Modica and Lapierre, 2012). This moisture dependence has been termed the 'moisture saturation effect', and is attributed to a "pore blocking" mechanism, where the water molecules compete with gas molecules for adsorption sites in the pore structures (Busch *et al*., 2007; Crosdale *et al*., 2008; Hackley *et al*., 2007). The pores of clay minerals are a key adsorption site for moisture (Ross and Bustin, 2009), and easily blocked by water (Ji *et al*., 2012; Rexer *et al*., 2013), and as a consequence, organic-rich shales typically possess a larger methane adsorption capacity than organic lean, clay-dominated shales (Ji *et al*., 2012).

It has long been established that gas storage in coal is a function of water content (Joubert *et al*., 1973; Joubert *et al*., 1974). The effect of moisture in coal is shown in Figure 6.5. The moisture saturation effect is controlled by the nature of the adsorption sites in the pore structure. These adsorption sites include: 1) free water in macropores and interstitial spaces, 2) as a meniscus in slit shaped pores, and 3) as mono- and multilayers on pore walls (Allardice and Evans, 1978).

It is claimed that there is a linear relationship between water saturation and methane adsorption capacity at constant pressure (Joubert *et al*., 1974; Levy *et al*., 1997). An example of a linear relationship between moisture and gas sorption is shown in Figure 6.6. This claim is in contention though, as Crosdale *et al*., (2008) found a non-linear relationship.

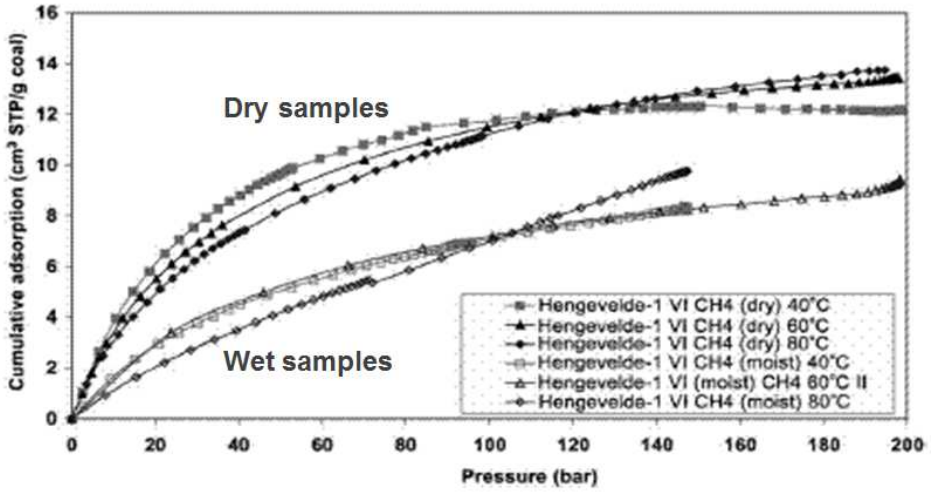

Figure 6.5: Pore moisture results in an observable decrease in the methane sorption capacity of coal, with the moisture equilibrated samples having a reduced storage capacity relative to the dry samples (after Krooss *et al*., 2002)

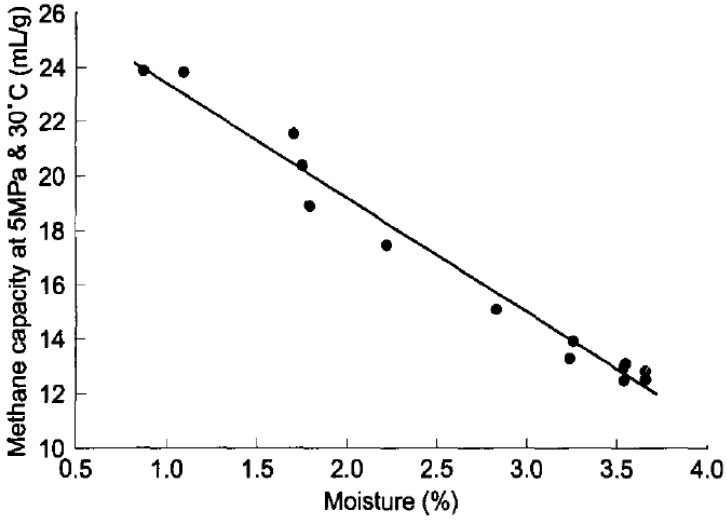

Figure 6.6: A negative linear relationship exists between moisture content and gas storage capacity (after Levy *et al*., 1997).

6.1.2 Isosteric enthalpy of adsorption (ΔH_{ads}) of isolated kerogens

Gas adsorption is an exothermic process, and heat energy is released when free gas enters the adsorbed phase (Gregg and Sing, 1982). The amount of heat released during gas adsorption, known as the enthalpy of adsorption (ΔH_{ads}), is a fundamental property of the chemical equilibrium system. It is a measure of the strength of the non-covalent physisorption bond that forms when a gas molecule interacts with a surface (or another molecule; Gregg and Sing, 1982; Rexer *et al*., 2013).

The enthalpy of adsorption (ΔH_{ads}) has important practical applications in gas shale reservoirs. The enthalpy of adsorption gives an indication of the ease of gas desorption from a material; and a low enthalpy of adsorption value results in favourable desorption process. The smaller the enthalpy of adsorption, the more of the adsorbed phase gas can be recovered from a shale gas reservoir.

The Virial equation is used to determine the enthalpy of adsorption at zero surface coverage, and the van't Hoff isochore equation is used to determine the enthalpy of adsorption as function of amount adsorbed (Rexer *et al*., 2013).

Enthalpy of Adsorption (Q_{st}) at Zero Surface Coverage: The isosteric enthalpy of adsorption at zero surface coverage (Q_{st}) is a fundamental measurement of the interaction of the adsorbate and adsorbent. It is a measure of the strength of the physisorption bond between the gas molecules and the surfaces (Gregg and Sing, 1982).

The Virial equation is applied to the low relative pressure region of the gas adsorption isotherm (Avgul *et al*., 1973), ideally no more than about 100 mbar. This is the region where Henry's law is obeyed and the isotherms are close to linearity.

The linear form (Cole *et al*., 1974) of the Virial equation is:

$$ln\left(\frac{n}{p}\right) = A_0 + A_1 n + A_2 n^2 + \ ...$$

(Equation 6.1)

Where:

n = gas adsorption (mol g^{-1})
p = pressure (Pa)
A_0, A_1, A_2 =Virial coefficients

The … ellipsis symbol is used to indicate that the equation continues in a power series to infinity. The 'A_0' Virial coefficient represents the strength of the adsorbate-adsorbent bonding interactions, and is related to the Henry's Law constant (K_H), by the $K_H = \exp(A_0)$. The 'A_1' Virial coefficient represents the strength of the adsorbate-adsorbate bonding interactions.

The A_0 and A_1 Virial coefficients are determined from the linear regression of the plot of $ln\left(\frac{n}{p}\right)$ against 'n'. The isosteric (constant mass) enthalpy of adsorption at zero surface coverage (Q_{st}) can then be determined from the 'A_0' Virial coefficient by plotting 'A_0' against 1/ T for a series of isotherms at different temperatures (Zhao *et al*., 2005).

Enthalpy of Adsorption (ΔH_{ads}) as function of amount adsorbed: The enthalpy of adsorption may vary with the amount of gas that is adsorbed by a material. The strength of the physisorption bond is different for gas-adsorbate interactions as opposed to gas-gas interactions. At high relative pressures, significant multilayers of adsorbed gas may have formed on the adsorbent material, and therefore there is a higher chance of a free gas molecule interacting with another gas molecule in an adsorbed multilayer, rather than with a bare surface of the adsorbent. This change in the interaction type that occurs during adsorption results in the enthalpy of adsorption being dependent on the amount of gas that is adsorbed.

The differential enthalpy of adsorption for the kerogen was calculated as a function of amount adsorbed (n) using the van't Hoff isochore:

$$ln(p)_n = \frac{\Delta H_n}{RT} - \frac{\Delta S}{R}$$

(Equation 6.2)

Where p_n = Pressure, in Pa, at 'n' amount adsorbed
ΔH_n = Enthalpy of adsorption, J mol^{-1}, at 'n' amount adsorbed
T = Temperature, in K
ΔS = Entropy of adsorption in J K^{-1}
R = Molar gas constant = 8.3145 J K^{-1} mol^{-1}

The van't Hoff isochore is based on the relationship between the gas pressure and the temperature, at a constant amount of adsorbed gas (Rexer *et al.*, 2013). The experimental pressure required to achieve a desired adsorption amount increases with increasing temperature, due to the temperature sensitivity of gas adsorption equilibrium processes (Zhang *et al.*, 2012).

A plot of $ln(p)$ against 1/T at constant amount adsorbed allows the differential enthalpy to be determined, where the gradient = $\Delta H/R$. The entropy of adsorption (ΔS) is determined from the y-axis intercept of the $ln(p)$ against 1/T plot, where the y-axis intercept = - $\Delta S/R$.

6.2 Results

6.2.1 Methane adsorption capacity of the DF and CG shales.

The gas adsorption capacity of shales needs to be measured to allow the calculation of the Gas In Place (GIP) in the gas shale formation. The methane adsorption capacity of the Draupne Formation and Colorado Group shales was determined using methane adsorption isotherms at 10 bars (1 MPa) and 30°C. This was done using an upgraded gravimetric IGA analyser, similar to the type used for the low pressure CO_2 work. The methane isotherms for both the Draupne Formation and Colorado Group shales are shown in Figure 6.7, with the amount adsorbed in mmol g^{-1} on the left-hand side y-axis, and the amount adsorbed in scf ton^{-1} on the right-hand side y-axis.

All of the methane isotherms are Type I/II in the IUPAC classification scheme, and do not plateau at 10 bar pressure. The isotherms all have a similar shape, with a distribution of adsorption uptakes. The shape of the methane isotherms is similar to the Type I/II isotherms generated by low pressure CO_2 at -78^oC and CO_2 at 0^oC isotherms. This indicates that the methane gas is adsorbing in similar pore structures as the low pressure CO_2., because it is the structure of the pore system that determines the shape of the isotherm curve (Sing *et al*., 1985).

The maximum adsorption uptakes of the methane adsorption isotherms are listed in Table 6.1. The adsorption uptakes of the Draupne Formation shales range from 0.0298 to 0.0717 mmol g^{-1}, with an average of 0.0501 ± 0.0214 mmol g^{-1}, whilst the adsorption uptakes of the Colorado Group shales range from 0.0282 to 0.0436 mmol g^{-1}, with an average of 0.0319 ± 0.049 mmol g^{-1}.

Strong positive correlations between the methane adsorption uptake and organic matter content (TOC) of the Draupne Formation and Colorado Group shales are observed in Figure 6.8. The correlation coefficient of the Draupne Formation is R^2 = 0.84, and the correlation coefficient of the Colorado Group is R^2 = 0.85.

A good correlation between maximum methane adsorption uptake and thermal maturity of the Draupne Formation shales exists, as shown in Figure 6.9. The correlation between methane adsorption and maturity is a negative correlation, where gas storage capacity decreases with increasing thermal maturity. The correlation coefficient between CH_4 adsorption and calculated vitrinite reflectance is R^2 = 0.94, and the correlation coefficient between CH_4 adsorption and Hydrogen Index is R^2 = 0.91. For the Colorado Group shales, there is no observable correlation between maximum methane adsorption and thermal maturity, as reported in Figure 6.10.

To account for the influence of burial compaction on pore volume, the amounts of methane adsorbed are normalised to burial depth in Figure 6.11. In part a), the strong negative correlation between depth normalised methane adsorption and calculated vitrinite reflectance of the Draupne Formation shales is shown. The correlation coefficient is R^2 = 0.89. In Figure 6.11 part b), the methane adsorption of the Colorado Group shales do not change with maturity (VR_c).

The Langmuir equation was applied to the methane adsorption isotherms of the DF and CG shales (in Figure 6.7) to determine the maximum adsorption capacity (N_m) and the Langmuir pressure (P_L). These Langmuir constants are used to predict the adsorption properties of shale methane isotherms under different pressure and temperature conditions. The maximum adsorption capacity (N_m) is obtained from the reciprocal of the gradient of a Langmuir plot (p/n vs p). An example of a Langmuir plot is given in Figure 6.12.

The Langmuir parameters calculated from the Langmuir plots of the DF and CG shales are listed in Table 6.2. The maximum adsorption capacity (N_m) of the Draupne Formation shales ranges from 0.0344 to 0.2459 mmol g^{-1}, with an average of 0.1465 ± 0.0629 mmol g^{-1}. The Langmuir Pressure (P_L) of the Draupne Formation shales ranges from 13812 to 34602 mbar, with an average of 19834 ± 7461 mbar. The maximum adsorption capacity (N_m) of the Colorado Group shales ranges from 0.0577 to 0.1808 mmol g^{-1}, with an average of 0.0956 ± 0.0477 mmol g^{-1}. The Langmuir Pressure (P_L) of the Colorado Group shales ranges from 8862 to 41023 mbar, with an average of 18974 ± 10924 mbar.

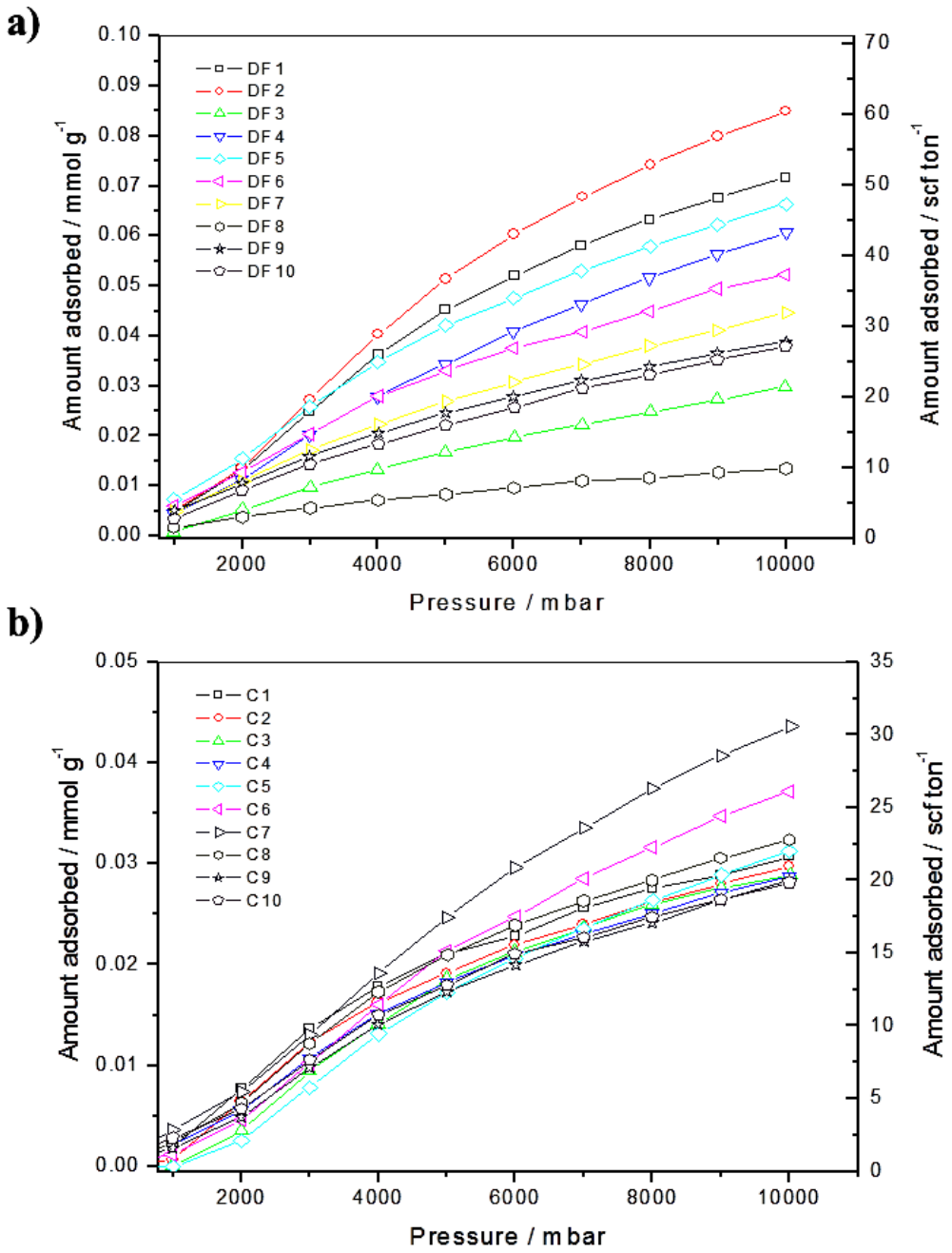

Figure 6.7: Methane adsorption isotherms. In part a), the Draupne Formation shales isotherms, and in part b) the Colorado Group shale isotherms are given. The isotherms are reported in the adsorption units of mmolg^{-1} on the left-hand side y-axis, and in the adsorption units of scf ton^{-1} on the right-hand side y-axis (The conversion factor is 1 mmol g^{-1} is equal to 711.42 scf ton^{-1}, Zhang *et al*., 2012; Ji *et al*., 2012).

Table 6.1: Maximum adsorption uptakes of CH_4 at 30°C for the DF and CG shales

Sample	Burial Depth / m	CH_4 Adsorption / mmol g^{-1}	CH_4 Adsorption / scf ton^{-1}
DF1	2117.8	0.0717	51.002
DF2	2325	0.0850	60.459
DF3	2978.5	0.0298	21.215
DF4	3124.7	0.0607	43.214
DF5	3375.32	0.0665	47.305
DF6	3400.4	0.0523	37.203
DF7	4132.95	0.0446	31.754
DF8	4608.4	0.0134	9.559
DF9	4707.7	0.0389	27.643
DF10	4780.7	0.0378	26.895
C1	505.3	0.0307	21.848
C2	506.55	0.0297	21.162
C3	541	0.0289	20.576
C4	546.3	0.0287	20.423
C5	561.5	0.0312	22.211
C6	642.1	0.0372	26.430
C7	647.57	0.0436	31.024
C8	651.75	0.0324	23.023
C9	675.02	0.0284	20.182
C10	684.61	0.0282	20.031

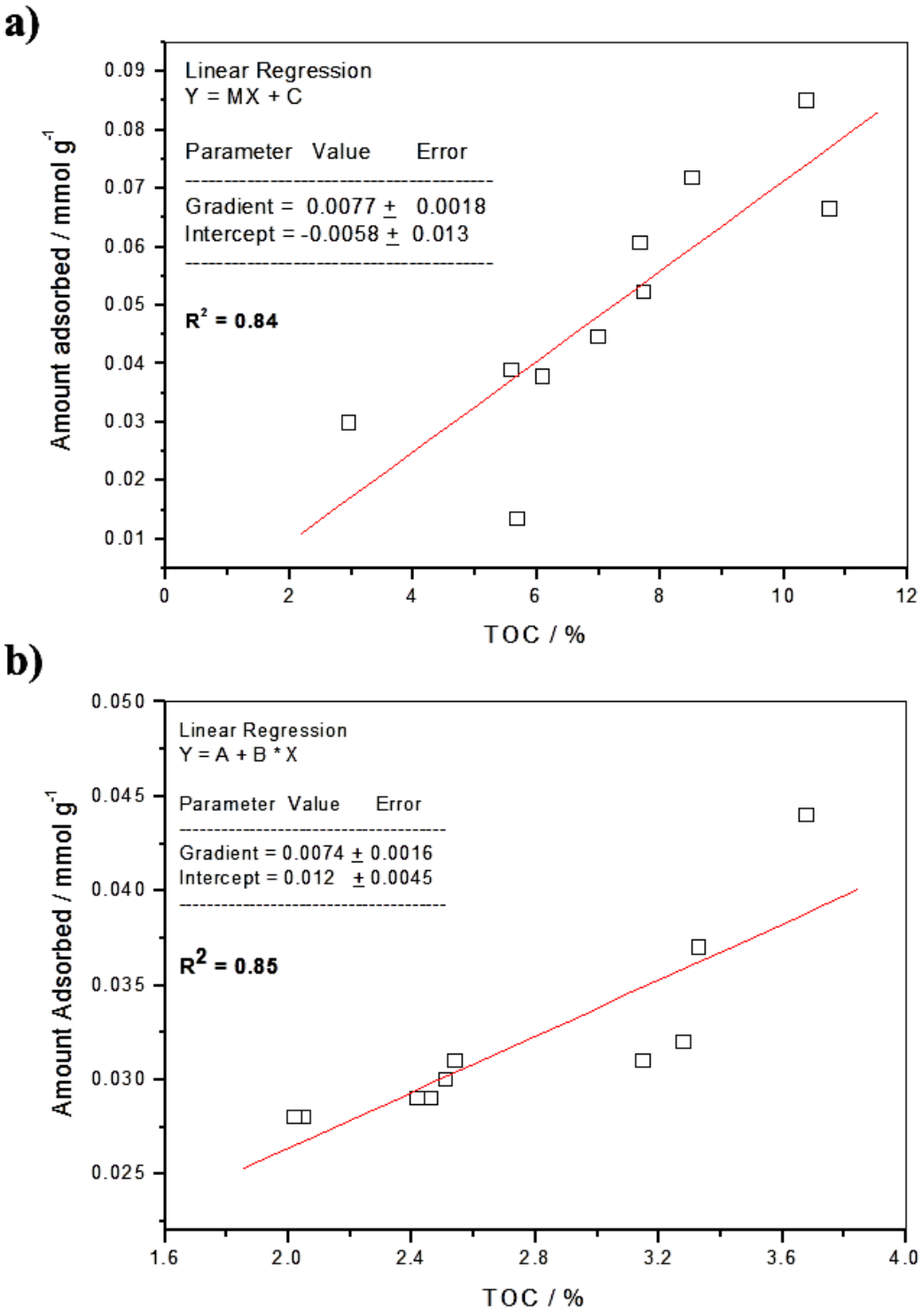

Figure 6.8: Strong positive correlations between maximum methane adsorption and organic matter content (TOC) are observed for the Draupne Formation (part a), and the Colorado Group shales (part b).

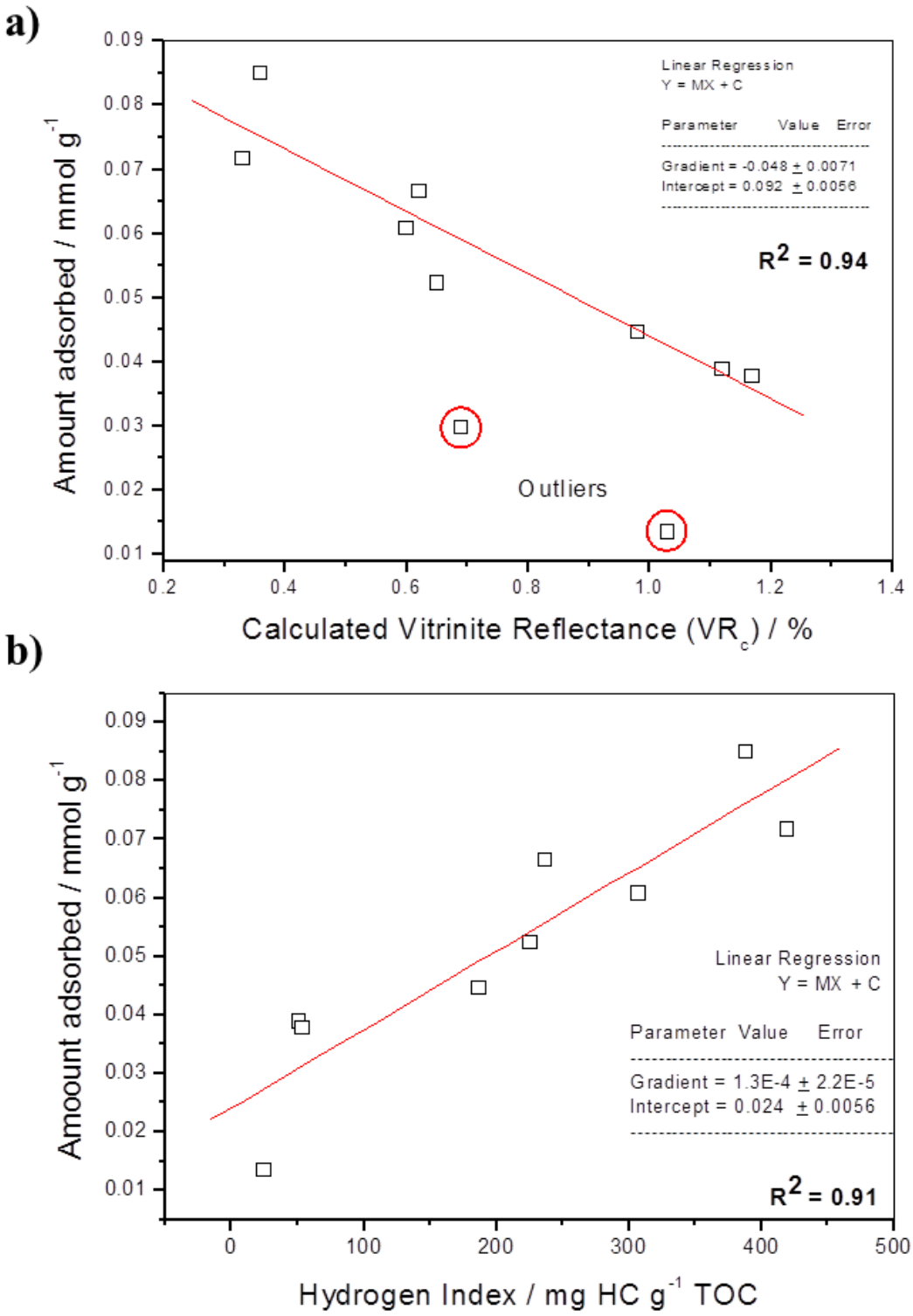

Figure 6.9: Methane adsorption vs maturity for the Draupne Formation shales. In part a), a strong negative correlation between maximum methane adsorption and calculated vitrinite reflectance exists, and in part b), a strong correlation between methane adsorption and Hydrogen Index is indicative of hydrocarbon generation due to thermal maturity.

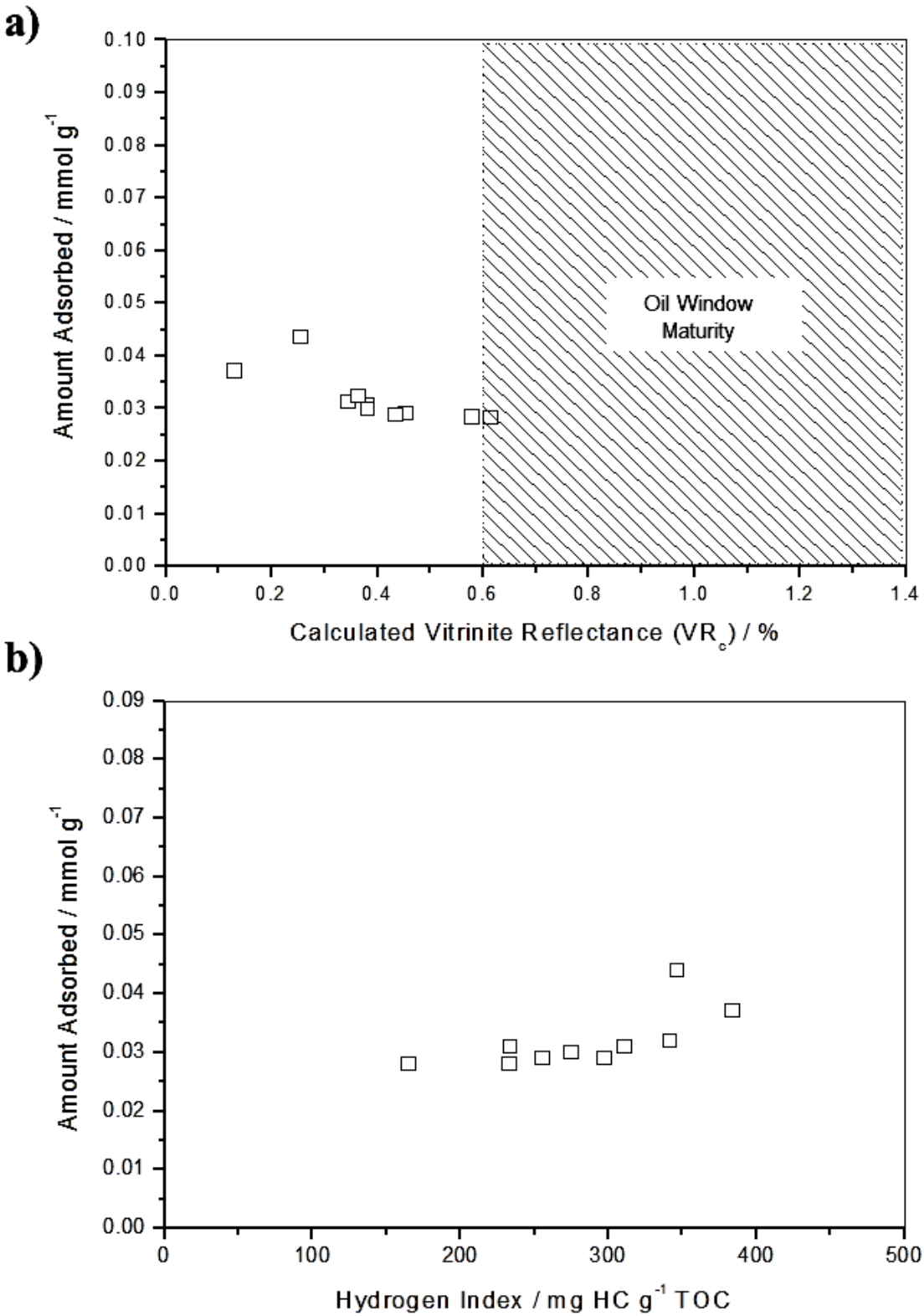

Figure 6.10: Methane adsorption vs maturity for the Colorado Group shales. There is no observable correlation between methane adsorption uptake and calculated vitrinite reflectance (part a), or with Hydrogen Index (part b).

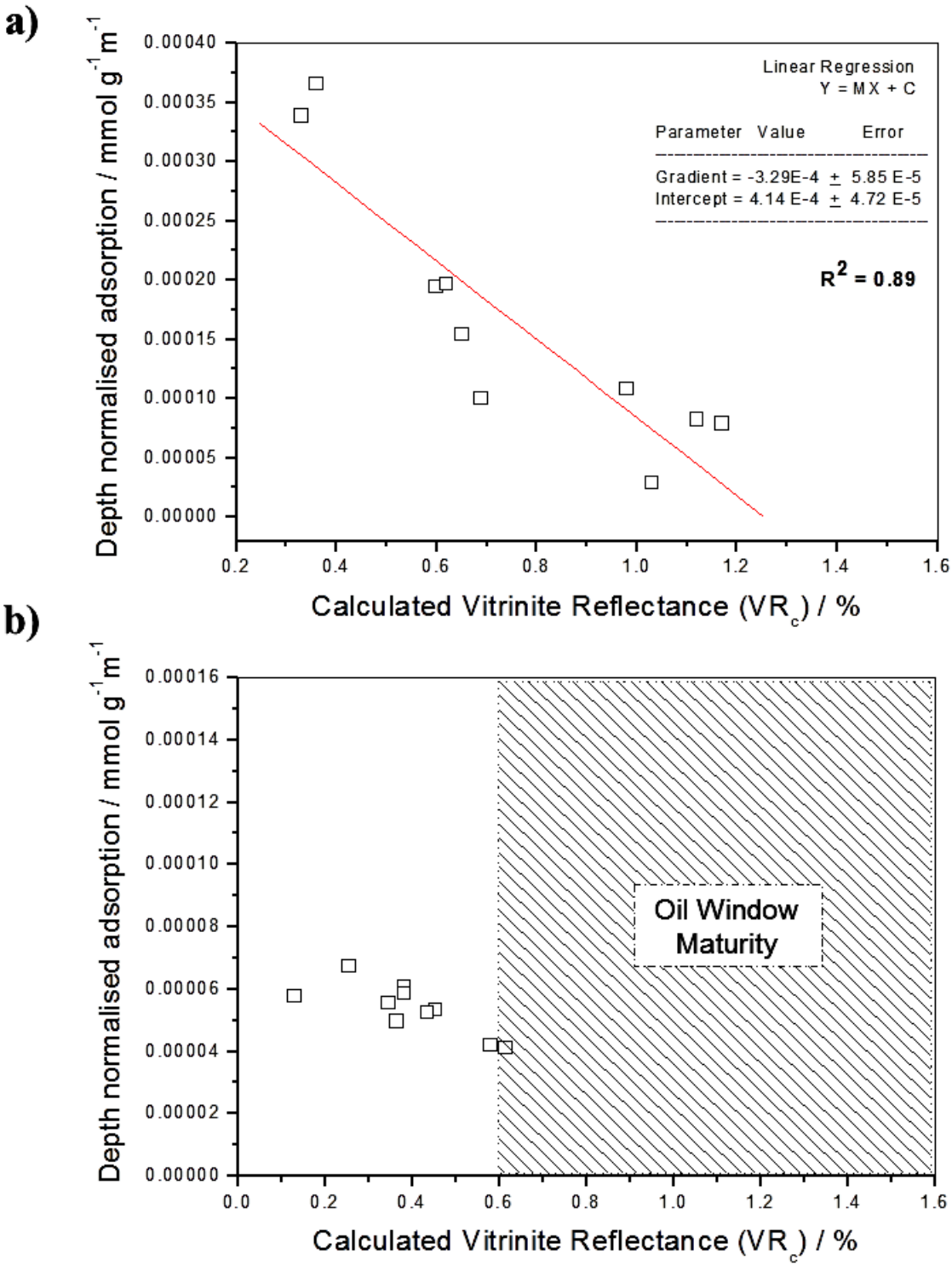

Figure 6.11: Plot of depth normalised methane adsorption against maturity. In part a), a strong negative correlation exists between normalised methane adsorption of Draupne Formation shales and vitrinite reflectance. In part b), no observable correlation exists for the Colorado Group shales.

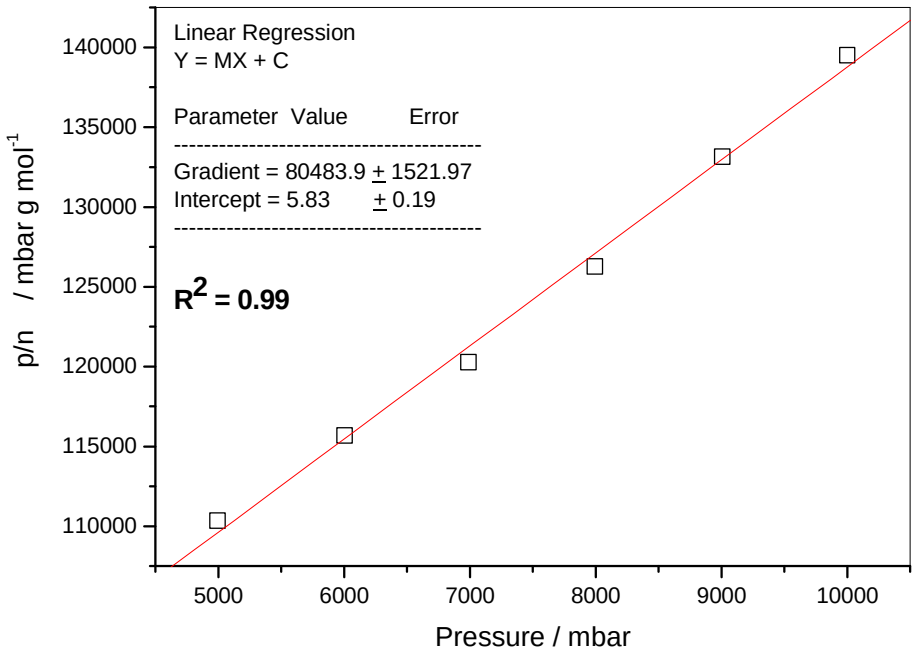

Figure 6.12: The Langmuir plot for the DF1 shale methane isotherm. The maximum adsorption capacity (N_m) can be determined from the reciprocal of the gradient.

Table 6.2: The maximum adsorption capacity (N_m) and Langmuir pressure (P_L) of the DF and CG shales.

Sample	Burial Depth / m	Maximum Adsorption Capacity / N_m	Langmuir Constant / K	Langmuir Pressure / P_L	Correlation Coefficient / R^2
DF1	2117.8	0.1715	0.0000724	13812.155	0.9954
DF2	2325	0.2387	0.0000559	17889.088	0.9867
DF3	2978.5	0.1325	0.0000289	34602.076	0.9925
DF4	3124.7	0.2459	0.0000330	30303.030	0.9823
DF5	3375.32	0.1598	0.0000711	14064.698	0.9933
DF6	3400.4	0.1284	0.0000685	14598.540	0.9816
DF7	4132.95	0.1300	0.0000518	19305.019	0.9948
DF8	4608.4	0.0344	0.0000647	15455.951	0.9717
DF9	4707.7	0.0936	0.0000712	14044.944	0.9992
DF10	4780.7	0.1302	0.0000412	24271.845	0.9914
C1	505.3	0.0577	0.0001128	8862.758	0.9897
C2	506.55	0.0658	0.0000826	12106.266	0.9978
C3	541	0.0661	0.0000793	12614.574	0.9905
C4	546.3	0.0671	0.0000749	13345.066	0.9986
C5	561.5	0.1606	0.0000244	41023.346	0.9431
C6	642.1	0.1493	0.0000335	29871.879	0.9819
C7	647.57	0.1808	0.0000323	31004.602	0.9448
C8	651.75	0.0703	0.0000852	11739.886	0.9993
C9	675.02	0.0764	0.0000586	17053.958	0.9931
C10	684.61	0.0622	0.0000825	12124.486	0.9887

Table 6.3: Mean average of the maximum adsorption capacity (N_m) for the DF and CG shales.

Sample	Burial Depth / m	CH_4 adsorption / mmol g^{-1}	Maximum CH_4 Adsorption Capacity (N_m) / mmol g^{-1}	% of maximum adsorption / N_m
DF1	2117.8	0.0717	0.1772	40.5
DF2	2325	0.085	0.2439	34.9
DF3	2978.5	0.0298	0.1334	22.3
DF4	3124.7	0.0607	0.2418	25.1
DF5	3375.32	0.0665	0.155	42.9
DF6	3400.4	0.0523	0.1329	39.4
DF7	4132.95	0.0446	0.1263	35.31
DF8	4608.4	0.0134	0.0334	40.1
DF9	4707.7	0.0389	0.0988	39.4
DF10	4780.7	0.0378	0.1255	30.1
C1	505.3	0.030711	0.0588	52.2
C2	506.55	0.029746	0.0676	44.0
C3	541	0.028923	0.0634	45.6
C4	546.3	0.028707	0.0698	41.1
C5	561.5	0.03122	0.1631	19.1
C6	642.1	0.037151	0.1515	24.5
C7	647.57	0.043609	0.1845	23.6
C8	651.75	0.032362	0.072	44.9
C9	675.02	0.028369	0.0782	36.3
C10	684.61	0.028156	0.0616	45.7

6.2.2 Relationship between pore structure and methane adsorption capacity for the DF and CG shales.

The relationship between the pore structure and the methane adsorption capacities of the DF and CG shales is investigated using the pore characterisation data reported in Chapter 4. The methane adsorption capacities are cross-plotted against the 1) sorption pore volumes, 2) the D-R micropore volumes, 3) the total surface areas, and 4) the micropore surface areas. In Chapter 4, the sorption pore volumes are listed in Table 4.4, the D-R micropore volumes are listed in Table 4.5, and the total and micropore surface areas are listed in Table 4.12.

The methane adsorption capacity of the DF shales increases as sorption pore volume increases, as shown in Figure 6.13, part a. The correlation is good, with a correlation coefficient of $R^2 = 0.79$. For the Colorado Group shales, there is no apparent correlation between methane adsorption capacity and sorption pore volume, as shown in Figure 6.13, part b. The methane adsorption capacity of the DF shales increases as D-R micropore volume increases, as shown in Figure 6.14, part a. The correlation is good, with a correlation coefficient of $R^2 = 0.80$. For the Colorado Group shales, there is no apparent correlation between methane adsorption capacity and D-R micropore volume, as shown in Figure 6.14, part b.

The methane adsorption capacity of the DF shales increases as total surface area increases, as shown in Figure 6.15, part a. The correlation is good, with a correlation coefficient of $R^2 = 0.79$. For the Colorado Group shales, there is no apparent correlation between methane adsorption capacity and total surface area, as shown in Figure 6.15, part b. The methane adsorption capacity of the DF shales increases as micropore surface area increases, as shown in Figure 6.16, part a. The correlation is strong, with a correlation coefficient of $R^2 = 0.86$. For the Colorado Group shales, there is no apparent correlation between methane adsorption capacity and micropore surface area, as shown in Figure 6.16, part b.

Furthermore, there is no apparent correlation between the total porosity of the DF and CG shales and the methane adsorption capacity, as shown in Figure 6.17. The total porosity was determined using mercury intrusion porosimetry, and the measurement data were previously reported in Table 4.8, Chapter 4.

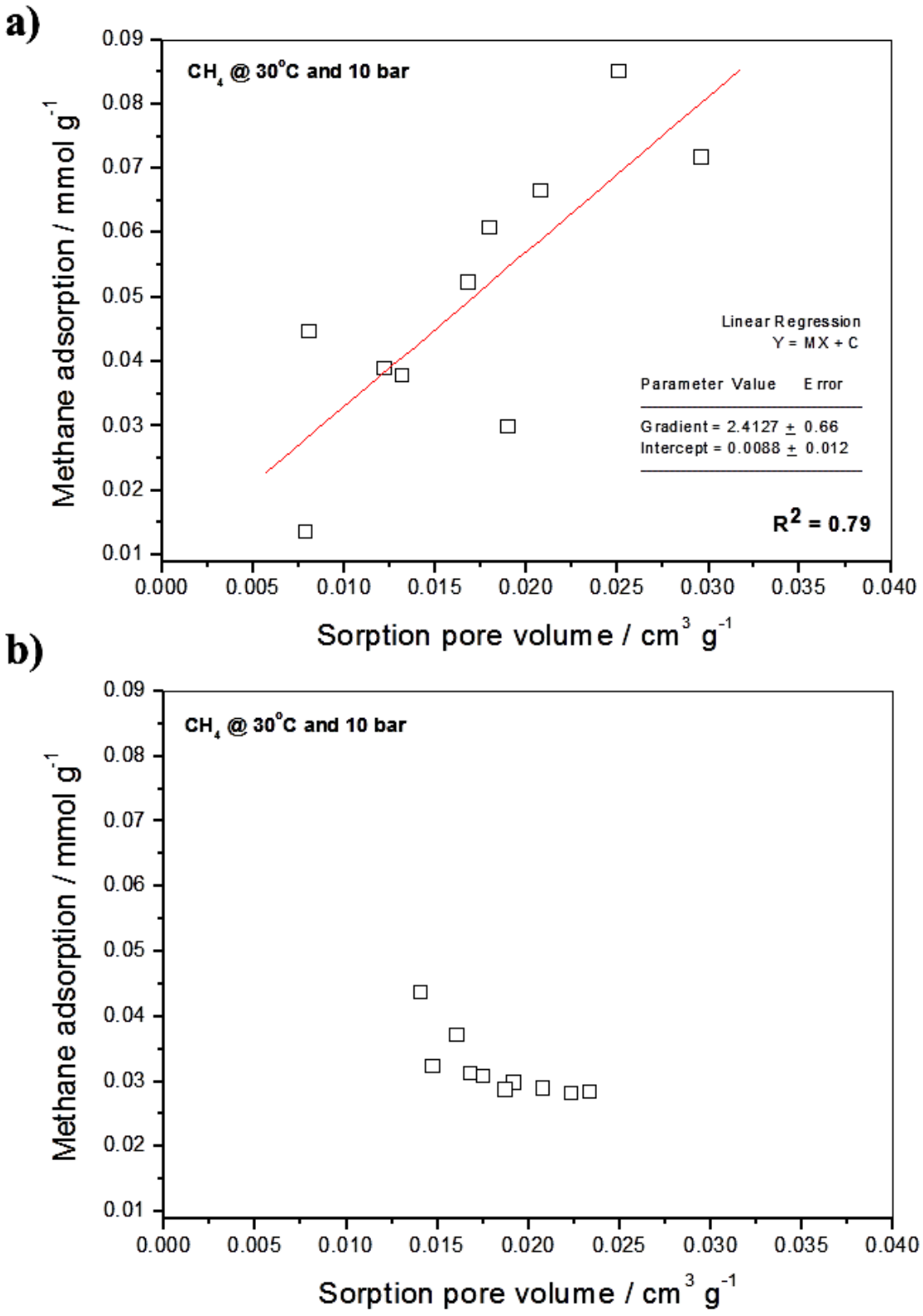

Figure 6.13: Methane adsorption against sorption pore volume the Draupne Formation and Colorado Group shales. In part a), a good positive correlation between the methane adsorption uptake of DF shale and sorption pore volume exists. In part b), no observable correlation is present for the Colorado Group shales.

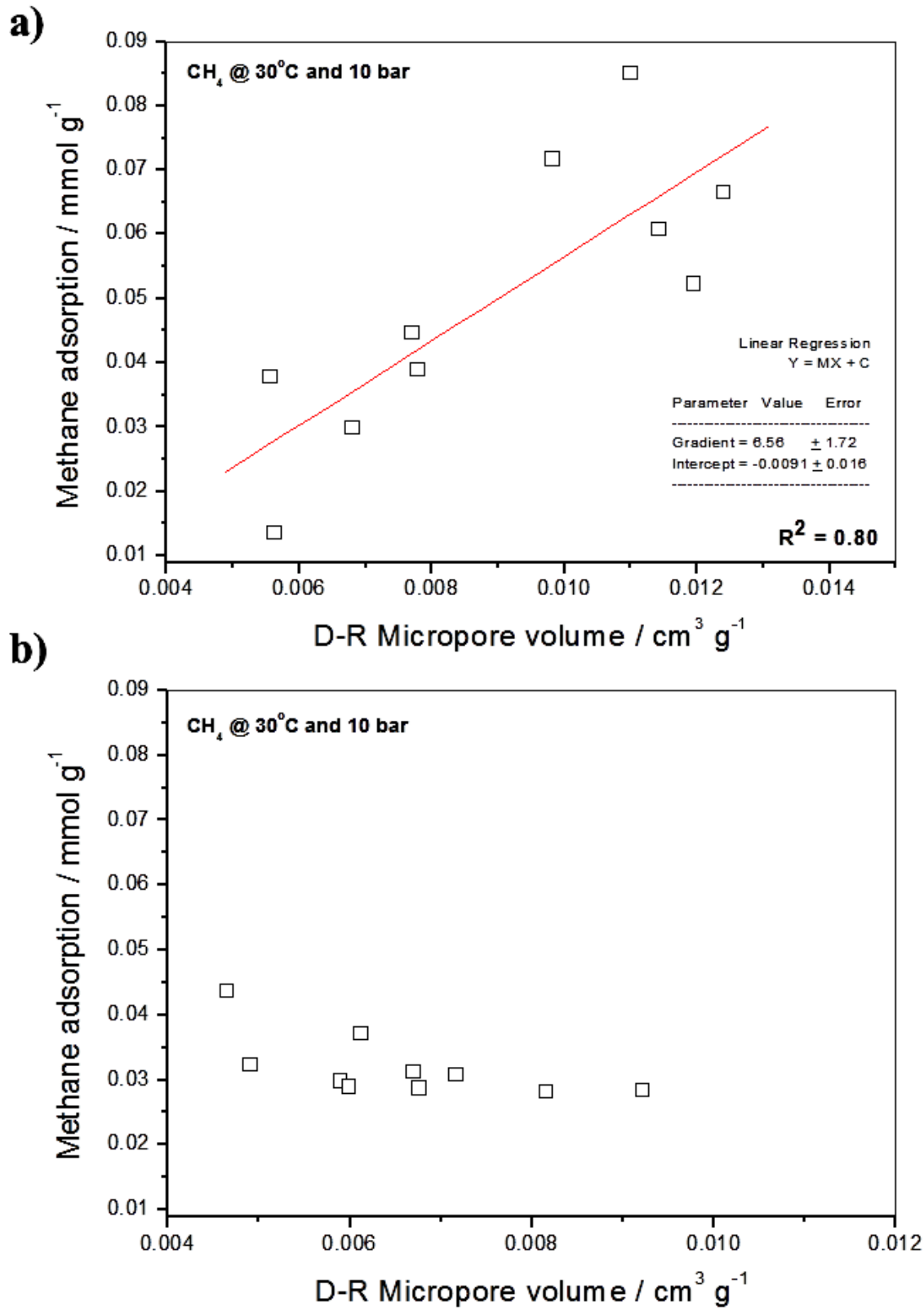

Figure 6.14: Methane adsorption against D-R micropore volume the Draupne Formation and Colorado Group shales. In part a), a good positive correlation between the methane adsorption uptake of DF shale and D-R micropore exists. In part b), no observable correlation is present for the Colorado Group shales.

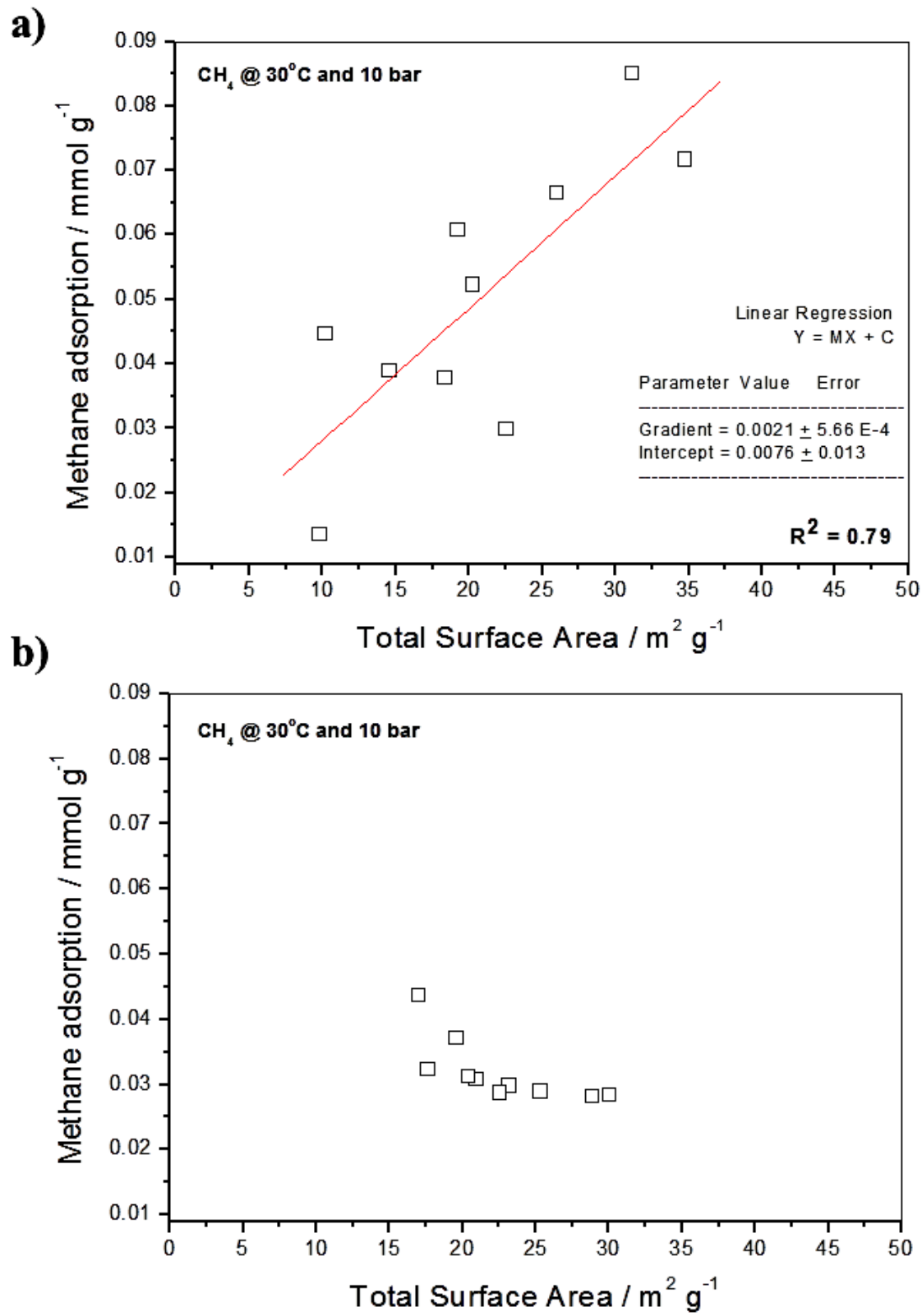

Figure 6.15: Methane adsorption against total surface area of the Draupne Formation and Colorado Group shales. In part a), a good positive correlation between the methane adsorption uptake of DF shale and total surface area exists. In part b), no observable correlation is present for the Colorado Group shales.

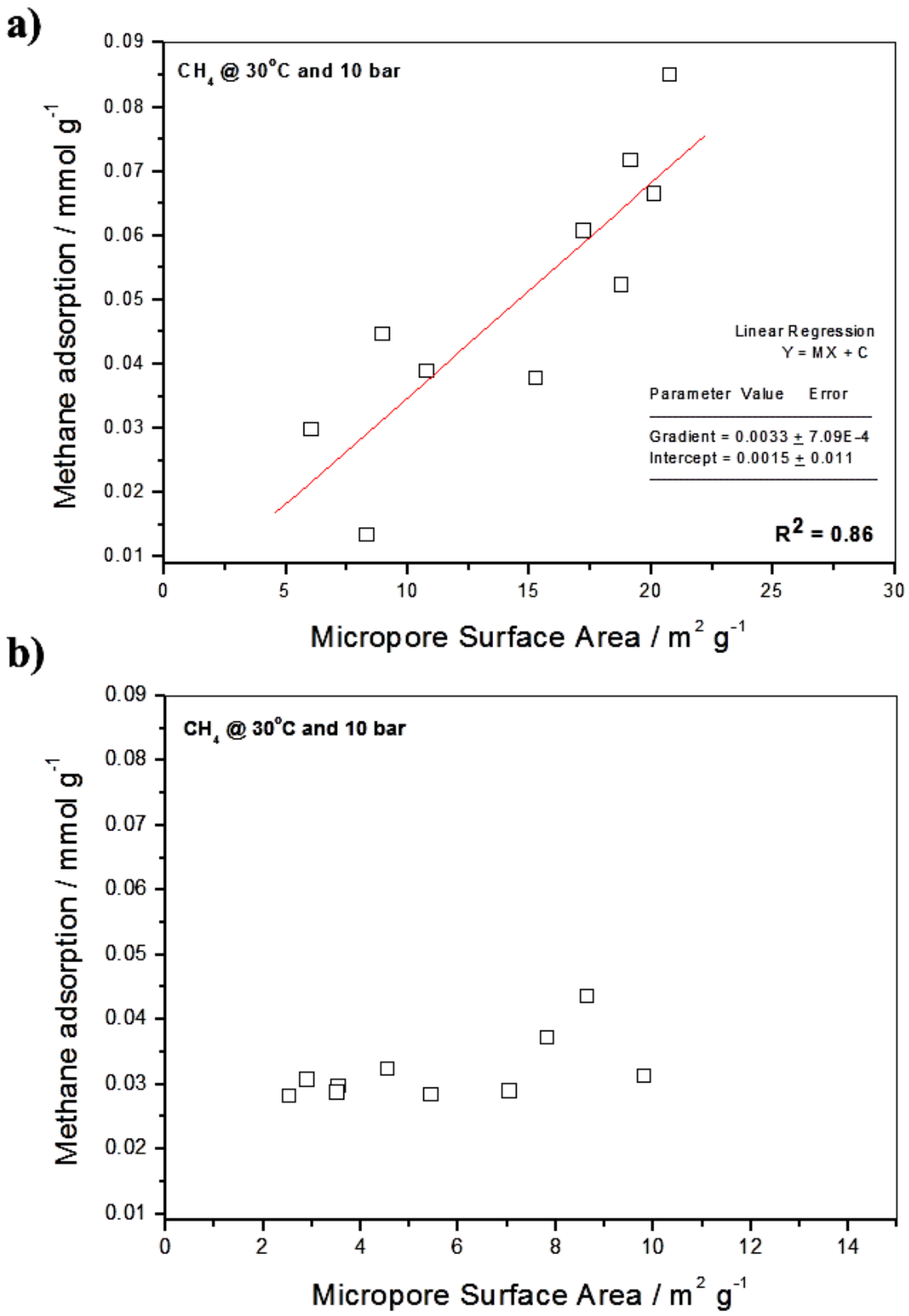

Figure 6.16: Methane adsorption against micropore surface area of the Draupne Formation and Colorado Group shales. In part a), a good positive correlation between the methane adsorption uptake of DF shale and micropore surface area exists. In part b), no observable correlation is present for the Colorado Group shales.

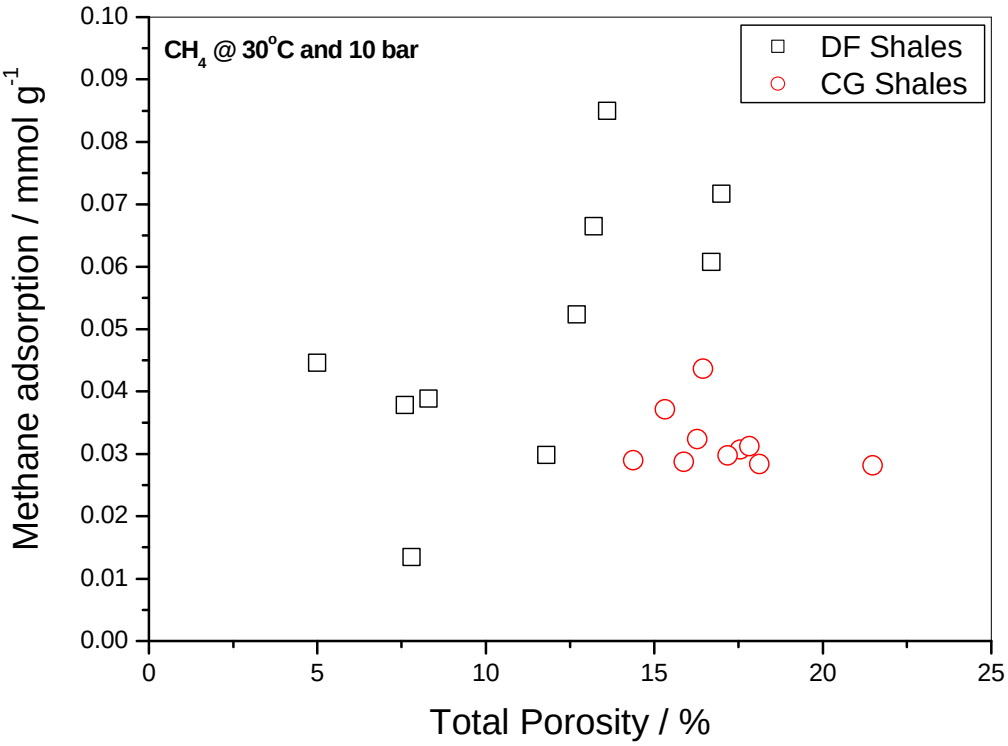

Figure 6.17: Methane adsorption against total porosity of the Draupne Formation and Colorado Group shales. In part a), a good positive correlation between the methane adsorption uptake of DF shale and micropore surface area exists. In part b), no observable correlation is present for the Colorado Group shales.

6.2.3 Thermodynamics of gas adsorption in kerogens.

Gas adsorption isotherms were measured on the Draupne Formation DF1 kerogen sample at 5 different temperatures. The gravimetric IGA equipment was used to determine CO_2 isotherms at the following temperatures: 10°C, 5°C, 0°C, -5°C and -10°C. The DF1 kerogen sample was chosen because it is the least mature sample in the Draupne Formation sample suite, and therefore less likely to have adverse maturity affects influencing the enthalpy of adsorption values obtained.

The 5 gas adsorption isotherms obtained for the DF1 kerogen are shown in Figure 6.18. As the temperature of the adsorption measurements increases in Figure 6.18, the absolute amount of gas adsorbed decreases. It is noteworthy that there is a large number (10) of isotherm points below 100 mbar. The amount of gas adsorbed as a function of pressure is approximately linear at low pressures, but deviations from linearity are observed as pressure increases above 100 mbar.

Using the adsorption isotherms reported in Figure 6.18, the enthalpies of adsorption for the DF1 kerogen was determined using both the Virial equation (Avgul *et al.*, 1973; Cole *et al.*, 1974; Reid and Thomas, 1999) and the van't Hoff isochore equation (Bell *et al.*, 2011). The Virial equation is used to determine the enthalpy of adsorption at zero surface coverage, and the van't Hoff isochore equation is used to determine the enthalpy of adsorption as function of amount adsorbed (see Section 6.1.2, above).

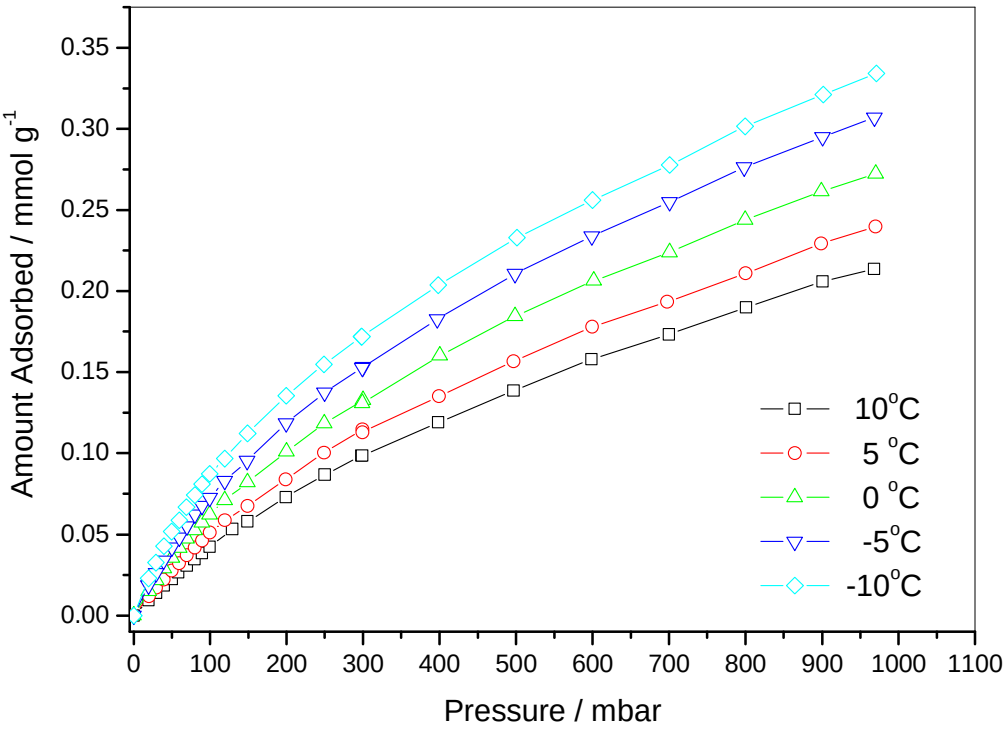

Figure 6.18: Gas adsorption isotherms for CO_2 at 5 temperatures on kerogen DF1.

6.2.4 Enthalpy of Adsorption (Q_{st}) at Zero Surface Coverage

The Q_{st} of the DF1 kerogen was determined using the Virial equation method. The low pressure region (<100mbar) of the 5 gas adsorptions are reported in Figure 6.19. The low pressure isotherm points were used to form a Virial plot, where the $ln\left(\frac{n}{p}\right)$ is plotted against gas adsorption 'n'. The Virial plot of the DF1 kerogen at 5 temperatures is show in Figure 6.20. The low pressure isotherm points fit the Virial equation closely, and excellent straight lines are obtained. These straight lines allow the determination of the A_0 and A_1 Virial coefficients using linear regression.

The data is reported in Table 6.4. The values for the gradient Virial parameter (A_1) increased with increasing temperature (i.e. became less negative), whilst the values of the y-axis intercept Virial parameter (A_0) decreased with increasing isotherm temperature (became more negative). The Henry's Law constant (K_H) also decreased with increasing temperature, as it is related to the (A_0) value. The decrease of K_H with increasing temperature is consistent with the physisorption mechanism, as weaker adsorbate-adsorbent interactions occur at higher temperatures.

The (A_0) intercept for the isotherm conducted at -10°C was -18.16 ± 0.007. The intercept for the isotherm conducted at -5°C was -18.42 ± 0.009. The intercept for the isotherm conducted at 0°C was -18.64 ± 0.012. The intercept for the isotherm conducted at 5°C was -18.92 ± 0.008. The intercept for the isotherm conducted at 10°C was -19.13 ± 0.004. These y-axis values are used to calculate the isosteric enthalpy of adsorption.

The value of Q_{st} for kerogen DF1 was determined by plotting the y-axis intercept (A_0) against the reciprocal of temperature, 1/T (where temperature is in the units of Kelvins), and determining the gradient of the straight line (Zhao *et al*., 2005). This is shown in Figure 6.21.

The gradient of the straight line in Figure 6.21 is equal to $\Delta H_{ads}/R$, where R is the molar gas constant 8.3145 J K^{-1} mol^{-1}. The isosteric enthalpy of adsorption at zero surface coverage for kerogen DF1 is:

$$Q_{st} = (3633.51 \times 8.3145 \text{ J K}^{-1} \text{ mol}^{-1})/1000$$
$$= 30.2 \text{ kJ mol}^{-1}$$

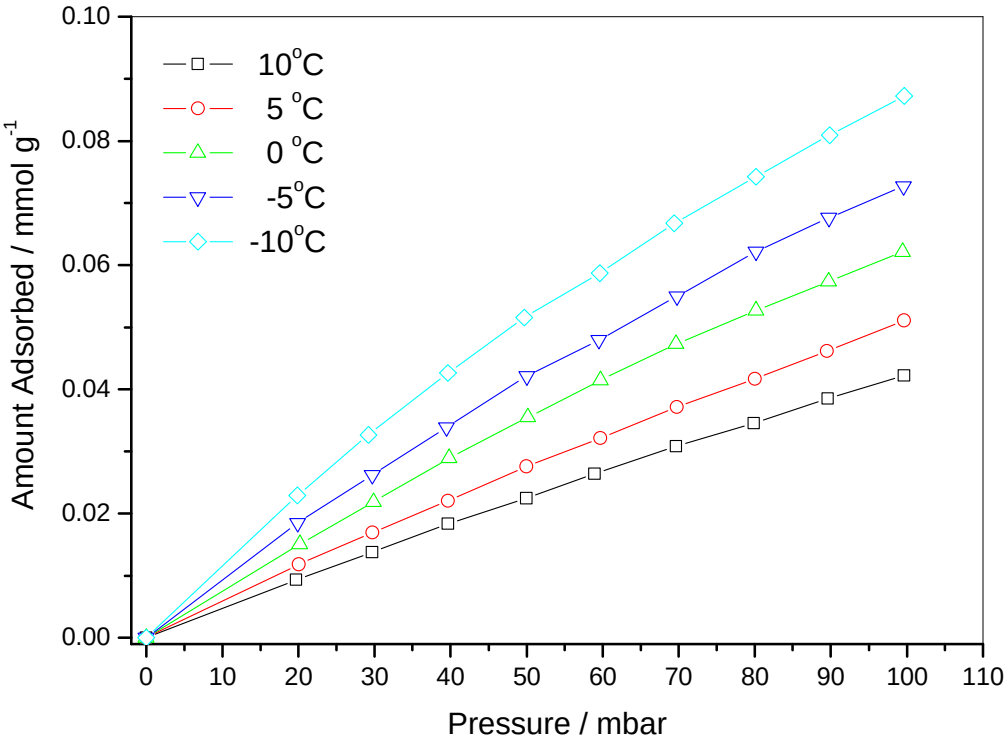

Figure 6.19: The isotherms are approximately linear at low pressures, in the region where Henry's law is obeyed.

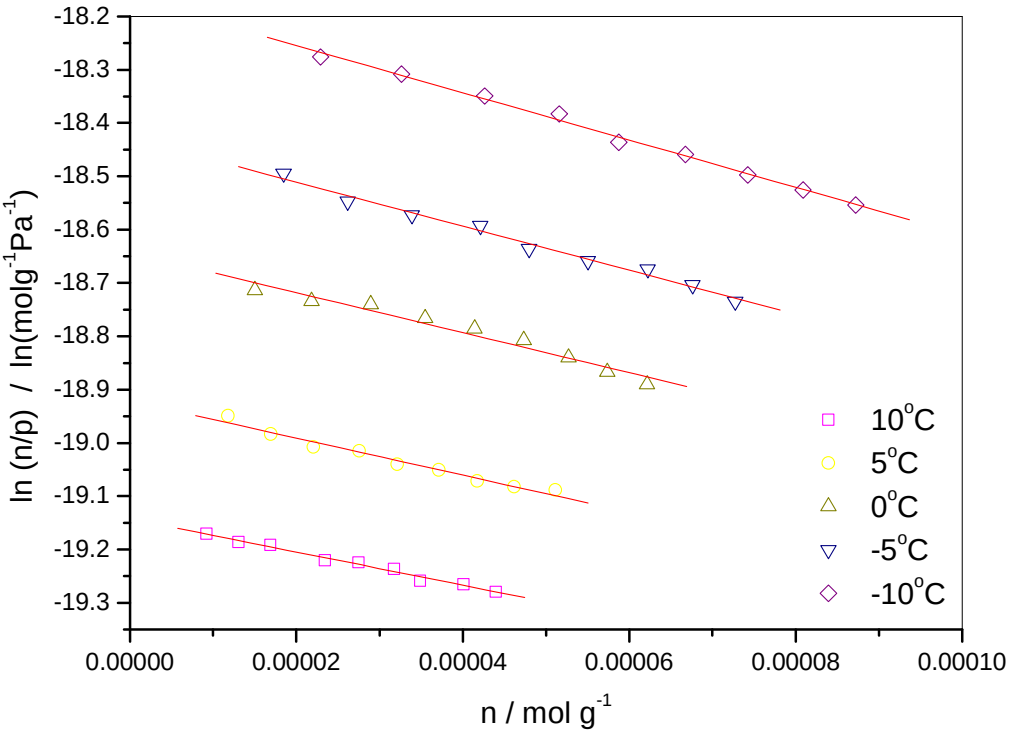

Figure 6.20: The Virial plot of the 5 low pressure adsorption isotherms of kerogen DF1.

Table 6.4: The linear regression Virial constants from the Virial plot.

Temperature / °C	Gradient / A_1	Intercept / A_0 ln(molg^{-1}Pa^{-1})	K_H (x10^{-8}) / mol g^{-1} Pa^{-1}	R^2
-10	-4434.4 ± 1.1	-18.16 ± 0.007	1.290	0.997
-5	-4131.2 ± 1.7	-18.42 ± 0.009	0.926	0.994
0	-3749.6 ± 2.8	-18.64 ± 0.012	0.801	0.981
5	-3473.8 ± 2.2	-18.92 ± 0.008	0.606	0.986
10	-3333.0 ±1.6	-19.13 ± 0.004	0.487	0.992

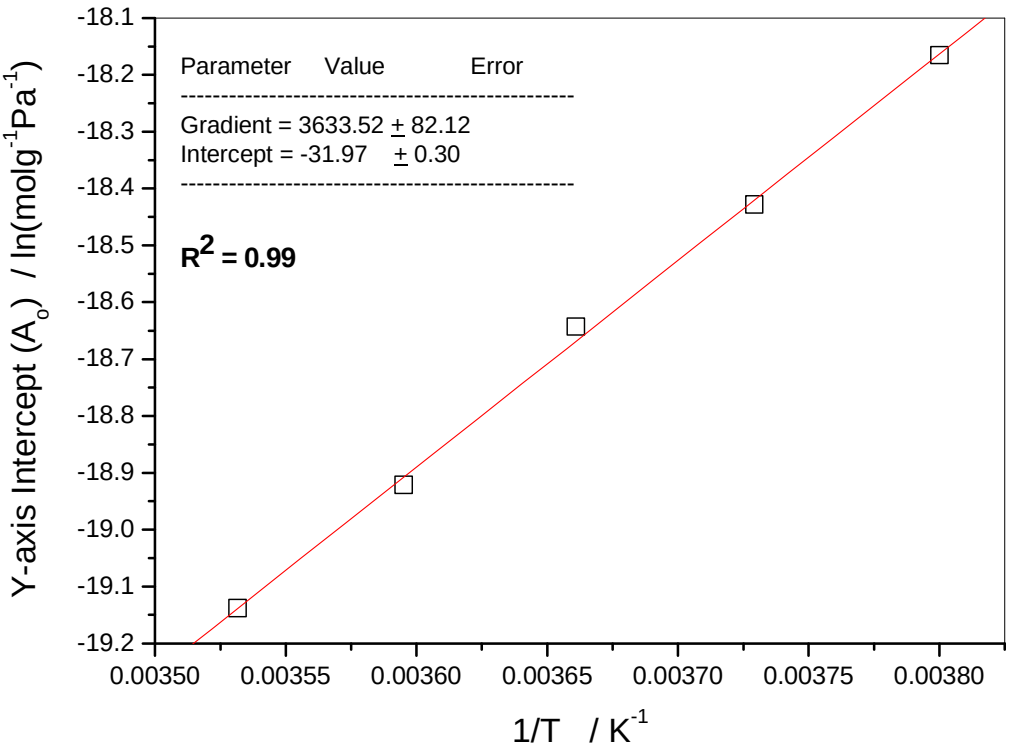

Figure 6.21: The plot of A_0 against 1/T, giving the gradient of the line as 3663.5

6.2.5 Enthalpy of Adsorption (ΔH_{ads}) as function of amount adsorbed

The enthalpy of adsorption as function of amount adsorbed (ΔH_{ads}) was determined for the DF1 isolated kerogen using the van't Hoff Isochore. An example of the pressure variation that occurs with increasing temperature is shown in Figure 6.22, where the pressure required to reach 0.15 mmol g^{-1} of adsorption is higher at increased temperatures.

The enthalpy of adsorption as function of amount adsorbed (ΔH_{ads}) for the DF1 kerogen was calculated using the 5 isotherms previously reported in Figure 6.18. The isotherm pressures required to achieve a constant adsorption amount with increasing temperature are reported in Table 6.5. The amounts of adsorption chosen to be constant were 0.1, 0.125, 0.15, 0.175 and 0.2 mmol g^{-1}.

The pressure required to achieve a constant mass progressively increases with increasing temperature. At 0.1 mmol g^{-1} of constant adsorption, the pressure ranges from 119.892 to 302.354 mbar with increasing temperature. At 0.125 mmol g^{-1} of constant adsorption, the pressure ranges from 178.651 to 429.150 mbar with increasing temperature. At 0.15 mmol g^{-1} of constant adsorption, the pressure ranges from 234.318 to 555.945 mbar with increasing temperature. At 0.175 mmol g^{-1} of constant adsorption, the pressure ranges from 311.632 to 716.759 mbar with increasing temperature. At 0.2 mmol g^{-1} of constant adsorption, the pressure ranges from 382.731 to 862.110 mbar with increasing temperature.

A plot of $ln(p)$ against 1/T at constant amount adsorbed allows the enthalpy of adsorption as function of amount adsorbed (ΔH_{ads}) to be determined, where the gradient of the linear regression = $\Delta H/R$. The data listed in Table 6.5 is plotted in Figure 6.23. The isochores are excellent straight lines, with pressure increasing with increasing temperature (from right to left on the x-axis). The lines of constant adsorption are stacked on top of each other, from 0.1 mmol g^{-1} at the bottom to 0.2 mmol g^{-1} at the top, with no overlap or crossing.

The gradient of the straight lines in Figure 6.23 are equal to $\Delta H_{ads}/R$, where R is the molar gas constant 8.3145 J K^{-1} mol^{-1}. The enthalpies of adsorption as a function of amount adsorbed for kerogen DF1 are reported in Table 6.6. The enthalpies of adsorption range from 25.90 to 28.34 kJ mol^{-1}.

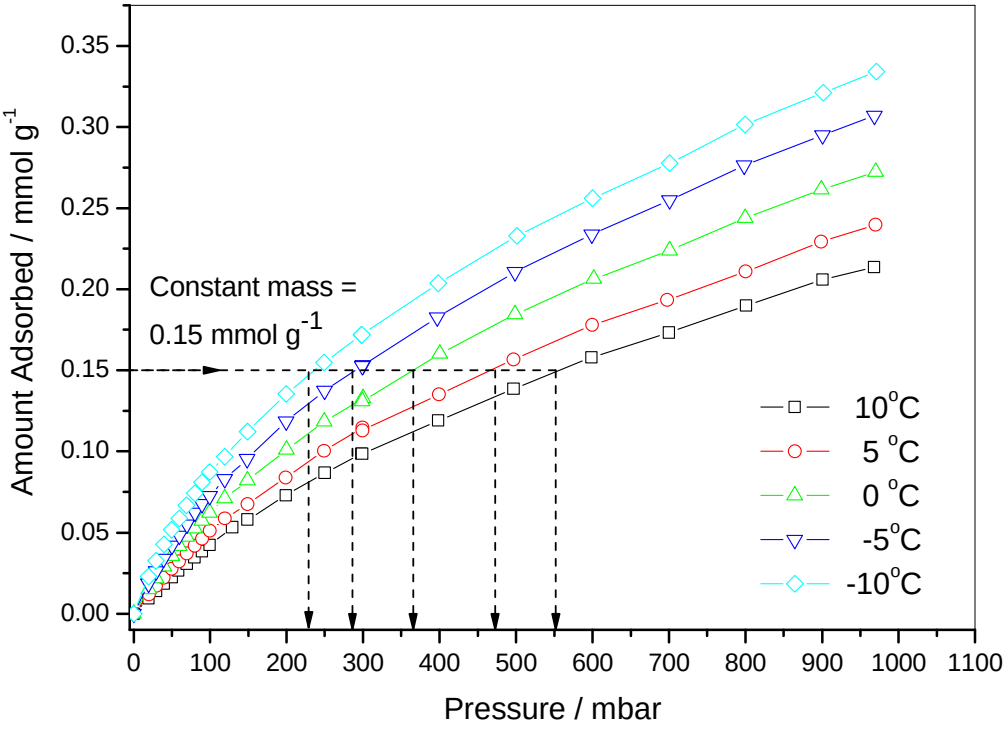

Figure 6.22: The pressure that the 5 isotherms intersect the constant mass line varies.

Table 6.5: The isotherm pressures required to achieve a constant adsorption amount at varying temperatures.

Constant amount adsorbed / mmol g^{-1}	0.100	0.125	0.150	0.175	0.200
Temperature / ^{o}C	Pressure / mbar	Pressure / mbar	Pressure / mbar	Pressure / mbar	Pressure / mbar
-10	119.892	178.651	234.318	311.632	382.761
-5	157.003	218.855	286.891	367.298	460.075
0	191.022	274.521	364.206	456.983	568.315
5	243.595	354.928	469.353	583.778	735.314
10	302.354	429.150	555.945	716.759	862.110

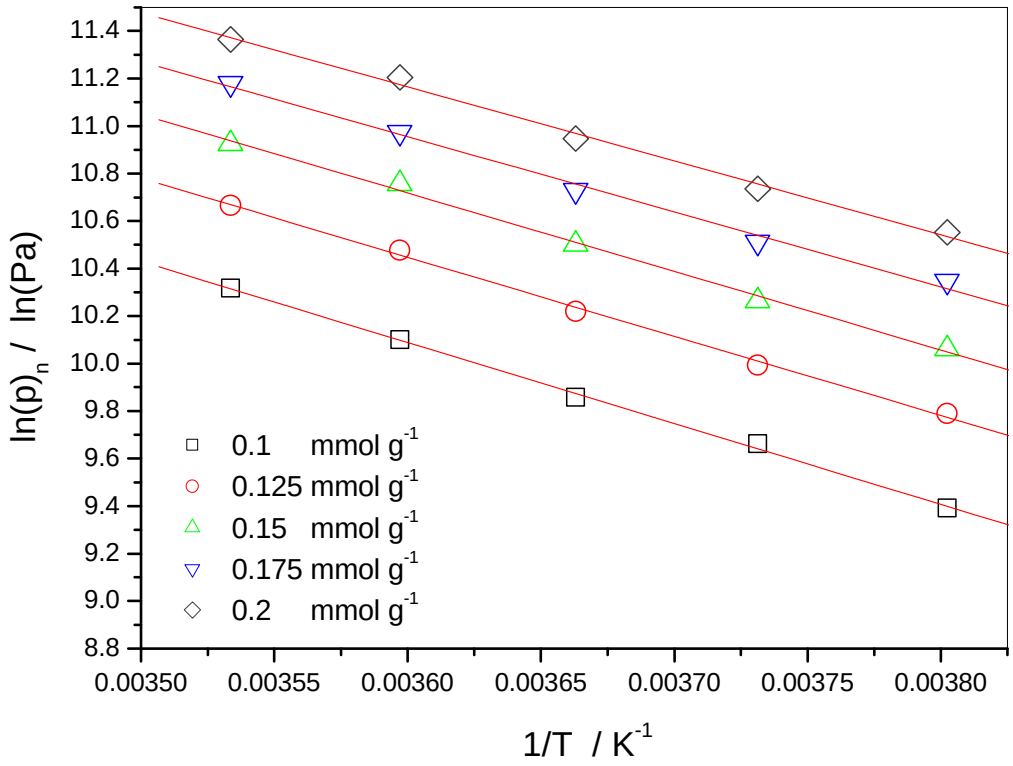

Figure 6.23: The van't Hoff isochores for the 5 adsorption isotherms of DF1 kerogen.

Table 6.6: Enthalpies of adsorption as a function of amount adsorbed (ΔH_{ads}).

Constant mass / mmol g^{-1}	ΔH / kJ mol^{-1}	R^2
0.100	28.34	0.999
0.125	27.67	0.998
0.150	27.48	0.998
0.175	26.32	0.996
0.200	25.90	0.997

6.3 Discussion

6.3.1 Methane adsorption and pore structure of shales.

The maximum adsorption uptakes of the methane adsorption isotherms are listed in Table 6.1. The Draupne Formation shales had an average methane adsorption capacity of 0.0501 mmol g^{-1}, which is 57% more methane storage than the Colorado Group shales (that had 0.0319 mmol g^{-1}). The average methane adsorption values of the DF and CG shales are very typical of the adsorption values reported in the literature for other gas shales (see Table 6.7).

Table 6.7: The methane adsorption uptakes of the DF and CG shales are similar to adsorption values reported in the literature for other gas shales.

Reference	Gas Shale	Methane Adsorbed / mmol g^{-1}
Nuttall *et al.*, 2005	New Albany Shale (Blocher Mbr.)	0.011
Paktinat *et al.*, 2009	Utica Shale	0.025
Zhang *et al.*, 2012	Green River Formation shale	0.034
Zhang *et al.*, 2012	Woodford Shale	0.038
Zhang *et al.*, 2012	Barnett Shale (Blakely #1)	0.046
This Study	Draupne Formation (Average)	0.050
This Study	Colorado Group (Average)	0.032

The methane adsorption capacities for both DF and CG shale suites are much lower than the adsorption values obtained for the CO_2 at-78^oC isotherms, even though the CO_2 isotherms were measured at low pressure (maximum of 1 bar) and the methane isotherms were at a higher pressure (10 bar). This indicates that methane has a lower adsorption energy in shales than CO_2. It is important to note that the large temperature difference between the two types of isotherm experiment could also be a factor.

Strong positive correlations between the methane adsorption uptake and organic matter content (TOC) of the Draupne Formation and Colorado Group shales were observed in Figure 6.8. These positive correlations are typical of previously published work (i.e. Chalmers and Bustin, 2007; Ross and Bustin 2009; Zhang *et al*., 2012), and supports the generally held view that the organic matter component of shales is an important location for the storage of methane.

A good correlation between maximum methane adsorption uptake and thermal maturity of the Draupne Formation shales was observed in Figure 6.9. The correlation between methane adsorption and maturity is a negative correlation, where gas storage capacity decreases with increasing thermal maturity. The negative maturity correlation is strong evidence that methane adsorption is occurring in the same pore structures as the low pressure CO_2 adsorption measurements, previously presented in Chapter 4. In contrast, the Colorado Group shales exhibit no observable correlation between maximum methane adsorption and thermal maturity, as shown in Figure 6.10. This supports the general finding that the Colorado Group shales are thermally immature.

The experimentally measured adsorption capacities of the Draupne Formation and Colorado Group shales are compared to the calculated maximums from the Langmuir equation in Table 6.3. The experimentally obtained values are, on average, one third (1/3) of the theoretical maximum value calculated with the Langmuir equation. The average value for Draupne Formation for the adsorption measurements as a percentage of the theoretical maximum is 34.99 % ± 6.98 %., and for the Colorado Group adsorption measurements as a percentage of the theoretical maximum is 37.72 % ± 11.35 %. These percentages indicates that at the conditions of 10 bar and 30^{o}C, both the DF and CG shales are under-saturated with adsorbed gas, and that under these conditions most of the gas in the shale sample would exist in the pore structure as a free gas phase.

The methane sorption capacity of the DF shales increases strongly with both the pore volumes and the total surface areas. This relationship agrees with the findings of Ross and Bustin (2009), who observed the same trend in Devonian–Mississippian shales from British Columbia, western Canada. This relationship is interpreted to be due to the greater adsorption energy of smaller pores within the organic fraction of the shales (Burggraaf, 1999; Ross and Bustin, 2009). It was previously shown in Chapter 4 that the pore volumes and surface areas of the DF shales were strongly correlated to organic matter content, and that the micropore volumes increased with TOC.

6.3.2 Enthalpy of Adsorption of isolated kerogen concentrates.

The isosteric enthalpy of adsorption at zero surface coverage **(**Q_{st}) for the DF1 isolated kerogen concentrate was 30.2 kJ mol^{-1}. This value agrees with the work of Zhang *et al*., (2012) who reported the enthalpy of adsorption **(**Q_{st}) for isolated kerogens in a range of 10.3 to 28.0 kJ mol^{-1}. In particular Zhang *et al*., (2012) reported a value of 21.9 kJ mol^{-1} for an immature (VR_o = 0.58 %) Type II kerogen from the Woodford gas shale of Oklahoma. As the Draupne Formation DF1 kerogen used in this study is also Type II and immature (VR_c = 0.33%) in nature, this suggests that the adsorptive gas used is significant. It is interpreted that carbon dioxide gas has a higher affinity for kerogen than methane gas; this interpretation is supported by the work of Mastalerz *et al*., (2004) who observed that the adsorbed amount of CO_2 is always higher than that of CH_4 in bituminous coals from Indiana. It was also reported by Bae and Bhatia (2006) that twice as much CO_2 was adsorbed (2:1 ratio) than methane in Australian Bowen Basin coals.

The Q_{st} value for the DF1 kerogen (30.2 kJ mol^{-1}) is larger than reported in the literature for both unaltered shale samples and for pure mineral samples. For example, Zhang *et al*., (2012) reported a value of 18 kJ mol^{-1} for a high maturity Barnett shale, and Rexer *et al*., (2013) reported a value of 19.2 kJ mol^{-1} for a high maturity Alum shale sample. For clay minerals, the Q_{st} value determined for montmorillonite, I–S mixed layer clay, illite, kaolinite and chlorite is 16.6, 14.6, 10.3, 9.6 and 9.4 kJ mol^{-1}, respectively (Ji *et al*., 2012).

After comparing the Q_{st} value for the DF1 kerogen with these other literature Q_{st} values, the data suggests that isolated kerogen concentrates have a higher affinity to gas adsorption than either pure minerals or whole shale samples; it is interesting to note that Zhang *et al*., (2012) also determined the Q_{st} for a Cameo coal sample as being 28.0 kJ mol^{-1}, which is very close to the Q_{st} value for the DF1 kerogen (30.2 kJ mol^{-1}). It is therefore suggested that isolated kerogen concentrates have adsorption potentials that are similar to those of coal. Assuming that this value of 30 kJ mol^{-1} for the DF1 kerogen

is representative for all the kerogens in this Draupne Formation sample suite (and further work would be required to confirm this), then the physisorption of CO_2 in the pore structures of kerogen is a highly favourable process. This has implications of a significant gas storage capacity in organic rich shales and mudstones, especially for Carbon Capture and Storage (CCS).

The enthalpies of adsorption as a function of amount adsorbed (ΔH_{ads}) decreases in value with increasing adsorption uptake. This is shown in Figure 6.24, which also includes the Q_{st} value (30.2 kJ mol^{-1}). The ΔH_{ads} for the DF1 kerogen has excellent linearity, and can be interpreted as the adsorbed gas phase being less favourable as the amount of gas adsorbed increases. After the initial surface has been covered, all further increases in gas adsorption cause a strong decrease in the enthalpy of adsorption. In other words, the energetic favourability of gas adsorption decreases as the adsorption sites on the bare surface become filled, and multilayers of gas molecules form. This fits with the Le Chatelier's principle of chemical equilibriums, where the system tries to maintain the position of the equilibrium by making additional changes less favourable when far away from the equilibrium position. This result has implications for the recovery of gas from shale reservoirs: at higher gas saturations, the desorption of gas is a more favourable process than at lower gas saturations.

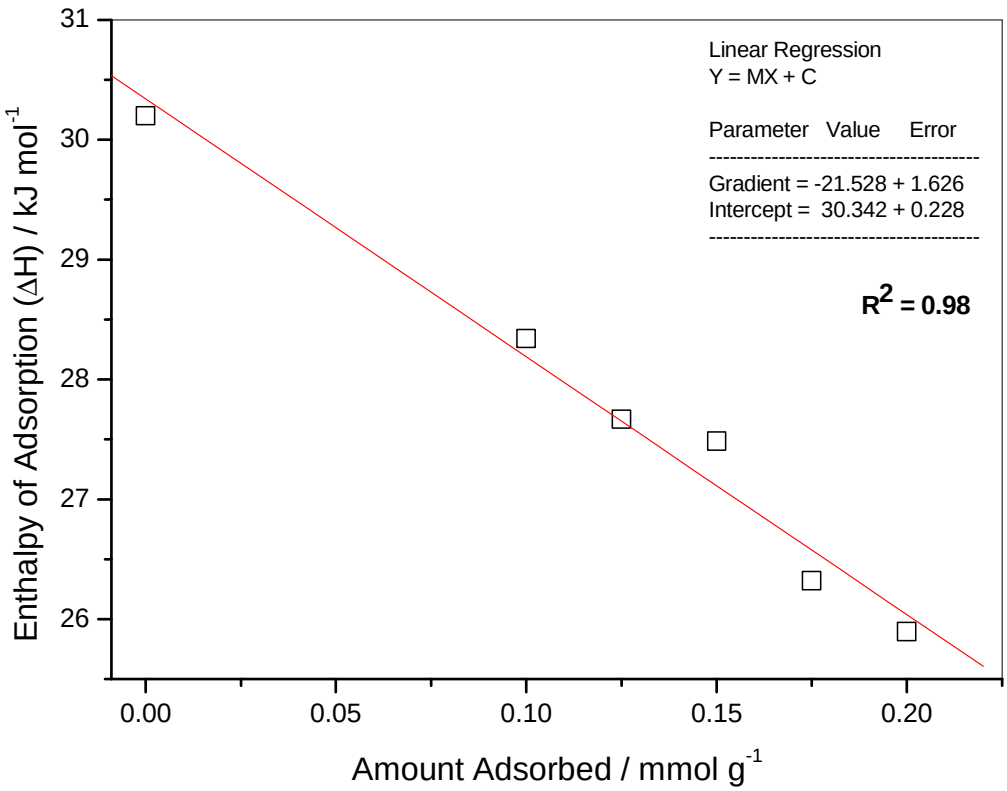

Figure 6.24: The variation of Enthalpy of Adsorption for the DF1 kerogen has excellent linearity, and decreases with increasing amount of gas adsorption.

6.4 Conclusions

The major findings and implications of Chapter 6 are:

- The methane adsorption capacity of shales is much lower than for CO_2 adsorption capacity, indicating that CO_2 gas has a higher affinity for shales than methane. The methane adsorption capacity is strongly correlated to TOC, which suggests that the organic matter component is a key site for methane storage in shales.

- A strong negative correlation between methane adsorption capacity and thermal maturity exists for the DF shales. This is consistent with the negative correlations between pore structure and maturity observed in Chapters 4 and 5. This suggests that pore structure and methane storage are closely dependent.

- The methane sorption capacity of the DF shales increases strongly with both the pore volumes and the total surface areas, demonstrating that pore structure is a key factor in the amount of methane that can be stored in shales by adsorption.

- The methane sorption capacity of the shales is one third (1/3) of the theoretical maximum value calculated with the Langmuir model. This indicates that at the conditions of 10 bar and 30^{o}C, the shales are under-saturated with adsorbed gas and most of the Gas In Place will be stored in the pore structure as free gas.

- The thermodynamics of gas adsorption in kerogens are highly favourable, with the isosteric enthalpy of adsorption at zero surface coverage (Q_{st}) for kerogen DF1 being 30.2 kJ mol^{-1}. This value is close to reported value for coals.

- The enthalpy of adsorption as function of amount adsorbed (ΔH_{ads}) decreases from 28.34 to 25.90 kJ mol^{-1} with increasing adsorption uptake. This result suggests that the production of shale gas will initially be energetically favourable, and gradually get increasingly less favourable as the gas is desorbed off from the surfaces. At low surface coverage, the affinity for gas adsorption will be large, making desorption of the last remaining gas highly unfavourable.

Chapter 7: Summary, conclusions and future work

7.1 Summary and Conclusions

The overall aim of the research project was to investigate the nature of the pore system of organic rich shales and kerogens, and to relate it to the gas storage capacity of gas bearing shales. This was done by characterising the pore volumes, porosities and surface areas of organic-rich shales and isolated kerogens, and then correlating them to the organic geochemical and petrophysical properties of the samples. The full range of pore sizes was investigated using a multi-technique approach, utilising scanning electron microscopy, mercury intrusion porosimetry, and gas adsorption analysis.

The Draupne Formation and Colorado Group shales were found to be organic rich, with average TOC values of 7.24 % and 2.74 %, respectively. The Draupne Formation shales have a spread of TOC content values, whilst the Colorado Group shales have a narrow range of values. The Draupne Formation and Colorado Group shales and isolated kerogens are interpreted as being Type II organic matter, using both the van Krevelen diagram and the S2 against TOC plot. This conclusion was supported by the ^{13}C-NMR spectra and py-GC-MS total ion chromatograms of the isolated kerogens.

The Draupne Formation shales have a range of thermal maturities, from immature up to oil generation maturity (catagenesis), whilst the Colorado Group shales are both immature and iso-mature. Excellent linear correlations between burial depth, Tmax and Hydrogen Index are observed for the Draupne Formation shales. The van Krevelen diagram identified the Draupne Formation kerogens as falling within the oil window maturity zone, with no gas window maturity kerogens identified. The overlain FT-IR spectra identified the concentrations aliphatic C-H bond concentrations decreasing with increasing thermal. In contrast, the Colorado Group shales display van Krevelen diagrams, ^{13}C-NMR spectra and FT-IR spectra consistent with thermally immature shale samples.

The SEM micrographs identified the presence of spherical and silt shaped pores in the Draupne Formation and Colorado Group shales, and the pore size distributions were dominated by nanometre-sized pores, typically below 100 nm in diameter. In the Draupne Formation, an average of 49.9% of all the pores in the mercury accessible pore size distribution was less than 25 nm in diameter. For the Colorado Group, this value was even higher, with an average of 84.7 % of all the pores measured by mercury intrusion being less than 25 nm in diameter. This is strong evidence suggesting the Draupne Formation and Colorado Group shales are “nanoporous” materials.

The organic matter of the Draupne Formation shales was a key location for pore volume, whereas the pore volume in the Colorado Group shales was primarily located in the shale clay matrix. The pore volumes of the macropores (> 100 nm) of the Draupne Formation shales was 2.5 times larger than the macropore volume of the Colorado Group shales, and this was found to be related to the organic richness (a strong positive correlation was observed). The sorption pore volume was strongly correlated to increasing organic matter content, as was the micropore volumes of the Draupne Formation shales.

The average total pore volumes of the Draupne Formation and Colorado Group shales were ~ 0.05 cm^3 g^{-1}. The total pore volume includes all pore space, both open and accessible pore volumes, and the completely isolated "blind" pores that are inaccessible to probe molecules. Furthermore, the pore system of the Colorado Group shales is much less open and interconnected than that of the Draupne Formation shales, where only 31.9% of the total pore volume in the Colorado Group shales is accessible to probe molecules. The lower interconnectivity of the Colorado Group pore system is interpreted as being due to pore volume being primarily located in the shale matrix and having a lower organic matter content compared to the Draupne Formation shales. It was found that as the TOC content of the shale samples increased, the accessible pore volume increased.

The average sorption pore volume of the Draupne Formation and Colorado Group shales sub-100 nm diameter pores were similar in value for both sample suites, despite their different total porosities, thermal maturities and burial depths. This suggests that marine black shales have a similar pore structure at the nanometre-scale. The sorption pore volume of the Draupne Formation shales accounted for 33.0 % of the average total pore volume (including the blind pores). For the Colorado Group shales, sorption pore volume accounted for 24.0 % of the average total pore volume. The difference in the share of sorption pore volume was attributed to the increased level of organic richness in the Draupne Formation, relative to the Colorado Group shales. The sorption pore volume of the Draupne Formation shales exhibited a strong positive correlation to organic matter content (TOC), whilst the Colorado Group shales exhibited an unexpected negative correlation to TOC. It was discovered that this negative correlation for the Colorado Group shales was due to the wt % of the mineral illite. The illite mass concentration was found to be controlling the sorption pore volume, indicating that the primary location of nanometre-scale pores in the CG shales was in the clay matrix.

The micropore volume (< 0.7 nm) accounts for a large percentage of the sorption pore volume (< 100 nm). The micropore volume of the Draupne Formation shales accounted for 52.3% of the gas sorption pore volume, and the micropore volume of the Colorado Group shales accounts for 35.9 % of the gas sorption pore volume. It appears that the smallest of sub-nanometre pores contribute significantly to the shale's pore volume. Unlike the total pore volume, the macropore volume and the sorption pore volume, the micropore volumes of the Draupne Formation and Colorado Group shales do not decrease with increasing burial depth. This suggests that they are not subject to mechanical compaction in the same way that the other pore volumes of the shales.

The total surface areas of both the Draupne Formation and Colorado Group shales are very similar, indicating that marine black shales have a similar internal pore structure. Furthermore, a large proportion of the internal surface area of the DF shales was located within micropores (< 2 nm), whereas the majority of surface area in the CG shales was located within the mesopores (2 – 50 nm). For the DF shales, it was found that the primary location for this micropore surface area was in the organic matter, as was indicated by the excellent positive correlation between the increasing percentage of micropore internal surface area and TOC. Conversely, for the CG shales an excellent correlation was found between the surface area and the illite concentration, indicating that the shale matrix is the primary location for surface area.

Thermal maturity has a significant influence on the pore structure of the Draupne Formation shales. The pore volumes of the sub-100 nm pores decreased as the thermal maturity of the shales increased. This was repeatedly demonstrated in sorption pore volumes, the D-R micropore volumes, the porosities and the surface areas of the Draupne Formation shales. This pore volume reduction with increasing maturity was also observed in the Pore Size Distribution curves of the Draupne Formation sub- 100 nm pores. The decrease in the pore volumes of the sub-100 nm pores of the Draupne Formation shales is unusual, as the majority of the commonly observed maturity correlations in the literature demonstrate an increase in nanometre-scale pore volume with increasing thermal maturity. It was suggested that the pore volume of immature and early oil window maturity shales initially decreases, until a minimum is reached, and then the pore volume begins to steadily increase again. This "U" shaped maturity trend has been observed in coal studies, and it is suggested that organic rich shales will also display this maturity trend, with sub-gas window maturity shales located on the downward section of the maturity curve. In contrast to the maturity correlations of the Draupne Formation shales, the Colorado Group shales do not exhibit any trends with increasing maturity. This agrees with the finding that the Colorado Group shales are both immature and iso-mature.

In Chapter 5 the isolated kerogens of the Draupne Formation and Colorado Group were analysed using the methods performed on the whole shale. This was done to obtain a "before and after" comparison of organic rich whole shale and its subsequent isolated kerogen concentrates. In general, the majority of the correlations found in Chapter 4 for the whole shales also were found to be present for the isolated kerogens. The same trends of decreasing pore volumes, porosities and surface areas with increasing thermal maturity were observed. This indicates that the pore structure of the organic matter within shales has a very significant influence on the pore structure of the whole shale. In general, the pore volumes, porosities and surface areas of the isolated kerogens were significantly larger than for the whole shale; however, when the experimental measurements for the isolated kerogens were scaled-down to normalise them for the amount of organic material in the whole shales, it was found that the kerogens contributed less than half of values for the whole shales. This indicates that the pore structures of the inorganic shale matrix still provide a major contribution to the overall pore structure of the whole shales, and pores in the organics is not the full story.

In Chapter 6 the methane adsorption capacities of the Draupne Formation and Colorado Group shale were determined using methane adsorption isotherms. In addition, the thermodynamics of gas adsorption for isolated kerogen concentrates was investigated. The methane adsorption capacity of the Draupne Formation shales was higher than the Colorado Group shales, and this was attributed to the difference in organic-richness. The methane adsorption uptakes of both the DF and CG shales are similar to other shales measured in the literature, and this suggests that methane adsorption in shales does not exhibit wide ranges in storage capacity. It is also noteworthy that organic rich shales have low gas adsorption capacities relative to coals, and this has been attributed to shales containing smaller amounts of microporosity than coals.

The methane adsorption capacities of the Draupne Formation and Colorado Group shale were strongly positively correlated to organic matter content, and this suggests that the organic matter component of shales is an important location for the storage of methane. The methane adsorption capacities of the Draupne Formation exhibited a negative correlation to thermal maturity, and the Colorado Group shales had no observable

correlations. This negative correlation of methane adsorption uptakes and thermal maturity was attributed to the decreasing pore volumes observed in Chapters 4 and 5.

The Langmuir volumes (V_L) was determined from the methane adsorption isotherms, and it was found that at the experimental conditions of 10 bar and 30^{o}C, only one third (1/3) of the maximum capacity was occupied by methane, suggesting that the DF and CG shales would be under-saturated, and the other two thirds (2/3) of the Gas In Place would exist as a free gas phase in the shale's gas saturated porosity.

The isosteric enthalpy of adsorption at zero surface coverage **(**Q_{st}) for the DF1 isolated kerogen concentrate was higher than other measured kerogens in the literature, and this was attributed to the use of CO_2 as the adsorptive gas. This is because carbon dioxide gas has a higher affinity for kerogen than methane gas, and up to twice as much CO_2 can be adsorbed. It was also observed that the isosteric enthalpy of adsorption at zero surface coverage **(**Q_{st}) for the DF1 isolated kerogen was much higher than pure minerals, and generally higher than for whole shales, suggesting that the organic matter fraction of shales is the most energetically favourable location for gas adsorption in shales. Furthermore, as the adsorption uptake increases, the favourability of additional adsorption decreases.

7.2 Future work

The research objectives of this study have been tightly focussed on the pore structures of organic-rich shales and kerogens, allowing the key research questions to be investigated within the time available. However, there are other fundamental aspects of gas storage in shales and kerogens that could have been investigated, and two possible areas of research that could have been undertaken to extend the scope of this project are:

- The use of manometric adsorption equipment to extend the experimental conditions of the methane adsorption to that of deep reservoir conditions.

- Determining the kinetic rates for gas desorption processes in shales and kerogens.

References

Adamu M., 2012, Mineralogical and petrophysical characterization of gas shales: Colorado Group, Western Canada Sedimentary Basin, PhD thesis submitted at Newcastle University.

Allard B., Rager M.-N., Templier J., 2002, Occurrence of high molecular weight lipids (C80+) in the trilaminar outer cell walls of some freshwater microalgae: A reappraisal of algaenan structure, *Organic Geochemistry*, **33**, 789-801.

Allardice, D.J., 1991, The water in brown coal. In: Durie, R.A. (Ed.), The Science of Victorian Brown Coal, Butterworth Heinmann, Oxford, pp. 104-150.

Allardice, D.J., Clemow, L.M., Favas, G., Jackson, W.R., Marshall, M., Sakurovs, R., 2003, The characterisation of different forms of water in low rank coals and some hydrothermally dried products, *Fuel*, **82**, 661-667.

Allardice, D.J., Evans, D.G.,1978, Moisture in coal, *In*: Karr Jr., C. (Ed.), Analytical Methods for Coal and Coal Products, vol. 1. Academic Press, New York, pp. 247–262.
Allen T., 1997, Particle size measurement, 5th Ed., Chapman & Hall, New York, USA, p. 251.

Amann-Hildenbrand A., Ghanizadeh A., Krooss B.M., 2012, Transport properties of unconventional gas systems, *Marine and Petroleum Geology*, **31**, 90-99.

Ambrose R.J., Hartman R.C., Diaz-Campos M., Akkutlu Y., Sondergeld C.H., 2010, New Pore-Scale Considerations for shale Gas In Place Calculations, *SPE 131772.*

Aplin A.C., Macquaker J.H.S., 2011, Mudstone diversity: Origin and implications for source, seal, and reservoir properties in petroleum systems, *AAPG Bulletin*, **95(12)**, 2031-2059.

Aplin, A. C., Yang Y. L., Hansen S., 1995, Assessment of beta, the compression coefficient of mudstones, and its relationship with detailed lithology, *Marine and Petroleum Geology*, **12**, 955-963.

Akkutlu I.Y., Fathi E., 2011, Multi-scale Gas Transport in Shales with Local Kerogen Heterogeneities, *SPE 146422*, 1 – 13.

Auvinet G., Bouvard D., 1989, Pore size distribution of granular media, powders and grains, *Biarez &Gourves (Eds.)*, Rotterdam, p.35-40.

Avgul N. N.; Bezus A. G.; Dobrova E. S.; Kiselev A. V., 1973, The Similarity of Gas Adsorption by Nonporous and Microporous Crystalline Adsorbents, *Journal of Colloid and Interface Science*, **42**, 486-495.

Bae J., and Bhatia S.K., 2006, High-Pressure Adsorption of Methane and Carbon Dioxide on Coal, *Energy and Fuels*, **20(6)**, 2599-2607.

Bae J.S., Bhatia S.K., Rudolph V., Massarotto P., 2009, Pore Accessibility of Methane and Carbon Dioxide in Coals, *Energy and Fuels*, **23**, 3319-3327.

Barbosa-Cánovas G.V., Ortega-Rivas E., Juliano P., Yan H., 2006, Food Powders: Physical Properties, Processing, and Functionality, *Springer*, pg 388, ISBN 0387276130

Beamish, B.B., Crosdale, P.J., 1995, The influence of maceral content on the sorption of gases by coal and the association with outbursting, International Symposium Cum Workshop on Management and Control of High Gas Emission and Outbursts, Wollongong, 20-24 March, 1995. Wollongong, Australia.

Behl R.J., 1999, Since Bramlette (1946): The Miocene Monterey Formation of California revisited, in Moores, E. M., Sloan, D., and Stout, D. L., eds., Classic Cordilleran Concepts: A View from California: Boulder, Colorado, *Geological Society of America*, Special Paper **338**, 301-313.

Bell J.G., Zhao X., Uygur Y., Thomas K.M., 2011, Adsorption of Chloroaromatic Models for Dioxins on Porous Carbons: The Influence of Adsorbate Structure and Surface Functional Groups on Surface Interactions and Adsorption Kinetics, *Journal of Physical Chemistry C*, **115**, 2776-2789.

Benham M.J. and Ross D.K., 1989, Experimental determination of absorption-desorption isotherm by computer controlled gravimetric analysis, Zeitschrift für physikalische chemie, **163(1)**, 25-32.

Bernard S., Horsfield B., Schulz H., Schreiber A., Wirth R., Vu T.T.A., Perssen F., Konitzer S., Volk H., Sherwood N., Fuentes D., 2010, Multi-scale detection of organic and inorganic signatures provides insights into gas shale properties and evolution, *Chemie der Erde*, **70(S3)**, 119–133.

Bharati S., Patience R., Larter S.R., Standen G., Poplett I.J.F., 1995, Elucidation of the Alum Shale kerogen structure using a multi-disciplinary approach, *Organic Geochemistry*, **23(12)**, 1043-1058.

Blokker P., Schouten S., van den Ende H., de Leeuw J.W., Hatcher P.G., Sinninghe Damste J.S., 1998, Chemical structure of algaenans from the fresh water algae Tetraedron minimum, Scenedesmus communis and Pediastrum boryanum, *Organic Geochemistry*, **29**, 1453-1468.

Bowker K.A., 2007, Barnett Shale gas production, Fort Worth Basin: Issues and discussion, *AAPG Bulletin*, **91(4)**, 523–533.

Bozzola J.J., Russell L.D., 1999, Electron Microscopy: Principles and Techniques for Biologists, Jones & Bartlett Learning, ISBN 0763701920, pp 670.

Braun R.L., Rothman A.J., 1975, Oil shale pyrolysis: kinetics and mechanism of oil production, *Fuel*, **54**, 129-131.

Brunauer S., Emmett P.H., Teller E., 1938, Adsorption of Gases in Multimolecular Layers, *Journal of the American Chemical Society*, **60(2)**, 309-319.

BS 1016-106.4.1, May 1993, Methods for analysis and testing of coal and coke. Ultimate analysis of coal and coke. Determination of total sulfur content. Eschka method, ISBN 0-580-21715-9.

Burggraaf A.J., 1999, Single gas permeation of thin zeolite (MFI) membranes: theory and analysis of experimental observations, *Journal of Membrane Science*, **155**, 45-65.

Busch A., Alles S., Gensterblum Y., Prinz D., Dewhurst D., Raven M., Stanjek H., Krooss B.M., 2008, Carbon dioxide storage potential of shales, *International Journal of Greenhouse Gas Control*, **2**, 297-308.

Busch A., Gensterblum Y., Krooss B.M., 2007, High-Pressure Sorption of Nitrogen, Carbon Dioxide, and their Mixtures on Argonne Premium Coals, *Energy Fuels*, **21(3)**, 1640-1645.

Bustin A.M., Cui X., Bustin R.M., 2010, Measurements of Gas Permeability and Diffusivity of Tight Reservoir Rocks: Different Approaches and their Applications, Search and Discovery Article #40479, AAPG Convention Denver, downloaded on the 1st Feb 2010 from:
http://www.searchanddiscovery.com/documents/2010/40479bustin/ndx_bustin.pdf.

Bustin A.M.M., Bustin R.M., 2008, Coal reservoir saturation: Impact of temperature and pressure, *AAPG Bulletin*, **92(1)**, 77-86.

Bustin R.M. Clarkson C.R., 1998, Geological controls on coalbed methane reservoir capacity and gas content, *International Journal of Coal Geology*, **3**8, 3-26.

Bustin R.M., 2005, Shales tapped for big play, *AAPG Explorer*, Feb 2005 Edition. Accessed on 01/02/12: http://www.aapg.org/explorer/divisions/2005/02emd.cfm

Bustin R.M., Bustin A.M.M., Cui X., Ross D.J.K., Murthy Pathi V.S., 2008, Impact of shale properties on pore structure and storage characteristics, *SPE 119892*.

Canfield D.E., Raiswell R., Westrich J.T., Reaves C.M., Berner R.A., 1986, The use of chromium reduction in the analysis of reduced inorganic sulfur in sediments and shales, *Chemical Geology*, **54**, 149-155.

Chalmers and Bustin, 2007, On the effects of petrographic composition on coalbed methane sorption, *International Journal of Coal Geology*, **69**, 288-304.

Chalmers G.R., Bustin, R.M., Power I.M., 2012, Characterization of gas shale pore systems by porosimetry, pynconmetry, surface area, and field emission scanning electron microscopy/transmission electron microscopy image analyses: Examples from the Barnett, Woodford, Haynesville, Marcellus, and Doig units, *American Association of Petroleum Geologists Bulletin*, **96**, 1099-1119.

Chalmers G.R.L., Bustin R.M., 2007, On the effects of petrographic composition on coalbed methane sorption, *International Journal of Coal Geology*, **69**, 288-304.

Chareonsuppanimit P,, Mohammad S.A., Robinson R.L., Gasem K.A.M., 2012, High-pressure adsorption of gases on shales: Measurements and modelling, *International Journal of Coal Geology*, **95**, 34-46.

Choquette P.W., Pray L.C., 1970, Geological nomenclature and classification of porosity in sedimentary carbonates, *AAPG Bulletin*, **54**, 207-244.

Clarkson C.R., and Bustin R.M., 1999, The effect of pore structure and gas pressure upon the transport properties of coal: a laboratory and modeling study. 1. Isotherms and pore volume distributions, *Fuel*, **78**, 1333-1344.

Clarkson C.R., Freeman M., Heb L., Agamalian M., Melnichenko Y.B., Mastalerz M., Bustin R.M., Radlinski A.P., Blach T.P., 2012, Characterization of tight gas reservoir pore structure using USANS/SANS and gas adsorption analysis, *Fuel*, **95**, 371-385.

Clarkson C.R., Solano N., Bustin R.M., Bustin A.M.M., Chalmers C.R.L., Hec L., Melnichenko Y.B., Radlin A.P., Blach T.P., 2013, Pore structure characterization of North American shale gas reservoirs using USANS/SANS, gas adsorption, and mercury intrusion, *Fuel*, **103**, 606-616.

Clarkson, C.R., Bustin, R.M., 1996, Variation in micropore capacity and size distribution with composition in bituminous coal in the western Canadian Sedimentary Basin: implications for coalbed methane potential, *Fuel*, **75**, 1483-1498.

Cole J. H., Everett D. H., Marshall C. T.; Paniego A. R.; Powl J. C.; Rodriquez-Reinoso F., 1974, Thermodynamics of the High Temperature Adsorption of some Permanent gases by Porous Carbons Journal of the Chemistry Society, *Faraday Transactions 1*, **70**, 2154-2169.

Conner W.C., Cevallos-Candau J.F., Weist E.L., 1986, Characterization of Pore Structure: Porosimetry and Sorption, *Langmuir*, **2**, 151-155.

Cramer D.D., 2008, Stimulating unconventional reservoirs: lessons learned, successful practices, areas for improvement, *Society of Petroleum Engineers, SPE 114172*.

Cranganu C., Villa M.A., Saramet M., Zakharova N., 2009, Petrophysical characterisation of source and reservoir rocks in the Histria Basin, Western Black Sea, *Journal of Petroleum Geology*, **32(4)**, 357-372.

Crosdale P., Moore T., Mares T., 2008, Influence of moisture content and temperature on methane adsorption isotherm analysis for coals from a low-rank biogenically sourced gas reservoir, *International Journal of Coal Geology*, **76**, 166–174.

Crosdale P.J., Beamish, B.B., Valix, M., 1998, Coalbed methane sorption related to coal composition, *International Journal Coal Geology*, **35**, 147-158.

Crosdale P.J., Moore T.A., Mares T.E., 2008, Influence of moisture content and temperature on methane adsorption isotherm analysis for coals from a low-rank, biogenically-sourced gas reservoir, *International Journal of Coal Geology*, **76**, 166-174.

Cui X., Bustin R.M., Dipple G., 2004, Selective transport of CO_2, CH_4, and N_2 in coals: insights from modelling of experimental gas adsorption data, *Fuel*, **83**, 293-303.

Curtis J.B., 2002, Fractured shale-gas systems, *AAPG Bulletin*, **86(11)**, 1921-1938.

Curtis M.E., Ambrose R.J., Sondergeld C.H., Rai C.S., 2011, Investigation of the Relationship between Organic Porosity and Thermal Maturity in the Marcellus Shale, *SPE 144370*.

Curtis, C. D., Coleman M.L., Love L.G., 1986, Pore water evolution during sediment burial from isotopic and mineral chemistry of calcite, dolomite and siderite concretions, *Geochimica et Cosmochimica Acta*, **50**, 2321-2334.

Dahl B., 2004, The use of bisnorhopane as a stratigraphic marker in the Oseberg Back Basin, North Viking Graben, Norwegian North Sea, *Organic Geochemistry*, **35**, 1551-1571.

Day S., Sakurovs R., Weir S., 2008, Supercritical gas sorption on moist coals, *International Journal of Coal Geology*, **74**, 203-214.

De Boer In: D.H. Everett and F.S. Stone, Editors, The Structure and Properties of Porous Materials, Butterworths, London (1958), p. 68.

Dees P.J., Polderman J., 1981, Mercury porosimetry in pharmaceutical technology, *Powder Technology*, **29**, 187-197.

Denoyel R., Llewellyn P., Beurroies I., Rouquerol J., Rouquerol F., Luciani L., 2004, Comparing the Basic Phenomena Involved in Three Methods of Pore-size Characterization: Gas Adsorption, Liquid Intrusion and Thermoporometry, *Particle and Particle Systems Characterisation*, **21**, 128-137.

Dewhurst D.N., Aplin A.C., Sarda J.P., Yang Y.L., 1998, Compaction-driven evolution of porosity and permeability in natural mudstones: An experimental study, *Journal of Geophysical Research*, **103**, 651-661.

Diamond S., 1970, Pore Size distributions in Clays, *Clays and Clay Minerals*, **18**, 7-23.

Do D.D., 1998, Adsorption Analysis: Equilibria and Kinetics, Chemical Engineer Series, Volume 2, ISBN-10: 1860941370.

Doré A.G., Vollset J., Hamar G.P., 1985, Correlation of the offshore sequences referred to the Kimmeridge Clay Formation – relevance to the Norwegian sector. In: Graham and Trotman, (Ed. 1985), *Geochemistry in Exploration of the Norwegian Shelf*, Norwegian Petroleum Society, 27 – 37.

Dubinin M. M., 1979, in: Gregg S.J., Sing K.S.W., Stoeckli H.F. (Editors), The Characterisation of Porous Solids, *Society of Chemical Industry*, London, pg 1–11.

Dubinin M. M., Stoeckli H.F., 1980, Homogeneous and Heterogeneous Micropore Structures in Carbonaceous Adsorbents, *Journal of Colloid and Interface Science*, **75(1)**, 34-42.

Dubinin M.M., and Radushkevich L.V., 1947, The Equation of the Characteristic Curve of Activated Charcoal, Doklady Akademii Nauk(Proceedings of the Russian Academy of Sciences), **55**, 327-329.

Dufek M., 2007, The Nova NanoSEM User Operation Manual, 1st Edition, FEI Company, 4022 290 31602, Accessed on the 17th August 2012 from: http://emu.uct.ac.za/wp-content/uploads/2013/06/Nova-NanoSEM-Operation-manual.pdf

Durand B., 1980, Kerogen: Insoluble Organic Matter from Sedimentary Rocks, Editions TECHNIP, pp 519, ISBN-10: 2710803712.

Egerton R.F., 2005, Physical Principles of Electron Microscopy: An Introduction to TEM, SEM, and AEM, Springer, ISBN 0387258000, pp 202.

Espitalié J., 1986, Use of Tmax as a Maturation Index for different types of organic matter: Comparison with vitrinite reflectance. In: Burrus J. (editor), *Thermal Modelling in Sedimentary Basins*, Editions Technip, 475 – 496.

Espitalié J., Laporte J.L., Madec M., Marquis F., Leplat P., Paulet J. and Boutefeu A., 1977, Methode rapide de characterization des roches meres de leur potentiel petrolier et de leur degre d'evolution (English: Rapid Method for Source Rocks Characterisation and for Determination of Petroleum Potential and Degree of Evolution), *Oil & Gas Science and Technology - Revue de l'Institut Francais du Petrole*, **32(1)**, 23 - 42.

Ettinger I., Eremin I., Zimakov B., Yanovskaya M., 1966, Natural factors influencing coal sorption properties. I. Petrography and sorption properties of coals, *Fuel*, **45**, 267 - 275.

Færseth R.B., Ravnås R., 1998, Evolution of the Oseberg Fault Block in context of the northern North Sea structural framework, *Marine and Petroleum Geology*, **15**, 467-490.

Faiz, M.M., Aziz, N.I., Hutton, A.C., Jones, B.G., 1992, Porosity and gas sorption capacity of some eastern Australian coals in relation to coal rank and composition, Coalbed Methane Symposium. Townsville, Townsville, Australia. 19–21 November, 1992.

Fischer C., Gaupp R., 2004, Multi-scale rock surface area quantification—a systematic method to evaluate the reactive surface area of rocks, *Chemie der Erde*, **64**, 241-2586.

Gan, H., Nandi, S.P., Walker Jr., P.L., 1972, Nature of porosity in American Coals, *Fuel*, **51**, 272-277.

Gasparik M., Bertier P., Gensterblum Y., Ghanizadeh A., Krooss B.M., Littke R., 2013, Geological controls on the methane storage capacity in organic-rich shales, International Journal of Coal Geology, http://dx.doi.org/10.1016/j.coal.2013.06.010. (at the time of writing, this journal paper was still an “Article In Press”, and had no volume or page numbers yet).

Gavrilov V.Y., Zakharov R.S., 2010, Carbon Dioxide Adsorption on Carbon Nanomaterials, *Kinetics and Catalysis*, **51(4)**, 609-614.

Giesche H., 2006, Mercury Porosimetry: A General (Practical) Overview, *Particle and Particle Systems Characterisation*, **23(1)**, 9-19.

Glennie K.W., Underhill J.R., 1998, Origin, development and evolution of structural styles. In: Glennie K.W. (editor), *Petroleum geology of the North Sea, basic concepts and recent advances*, 4th edition, Blackwell Science Limited, 42-84.

Glorioso J.C., Rattia A., 2012, Unconventional Reservoirs: Basic Petrophysical Concepts for Shale Gas, SPE 153004.

Gonzalez-Vila F.J., Ambles A., del Rio J.C., Grasset L., 2001, Characterisation and differentiation of kerogens by pyrolytic and chemical degradation techniques, *Journal of Analytical and Applied Pyrolysis*, **58-59**, 315-328.

Goth K., de Leeuw J.W., Püttmann W., Tegelaar E.W., 1988, Origin of Messel Oil Shale kerogen, *Nature*, **336**, 759-61.

Gregg S. J., Sing K.S.W., 1982, Adsorption, Surface Area and Porosity, 2nd ed; Academic Press: London, U.K.

Groen J.C., Peffer L.A.A., Perez-Ramirez J., 2003, Pore size determination in modified micro- and mesoporous materials: Pitfalls and limitations in gas adsorption data analysis, *Microporous and Mesoporous Materials*, **60**, 1-17.

Gutierrez M., Øilno L.E., Nygård, R., 2000, Stress-dependent permeability of a demineralised fracture in shale, *Marine and Petroleum Geology*, **17(8)**, 895-907.

Hackley P.C., Warwick P.D., Clayton Breland Jr F, 2007, Organic petrology and coalbed gas content, Wilcox Group (Paleocene–Eocene) northern Louisiana, *International Journal of Coal Geology*, **71**, 54-71.

Hao F., Zou H., Lu Y., 2013, Mechanisms of shale gas storage: Implications for shale gas exploration in China, *AAPG Bulletin*, **97(8)**, 1325 – 1346.

Harris, L. A. and Yust, C. S., 1976, Transmission electron microscope observations of porosity in coal, *Fuel*, **55**, 233.

Hartgers W.A., Sinninghe Damste J.S., Requejo A.G., Allan J., Hayes J.M., Ling Y., Xie T.M., Primack J., de Leeuw J.W., 1994, Evidence for only minor contribution from bacteria to sedimentary organic carbon, Nature, **369**, 224-227.

Hartwig A., Könitzer S., Boucsein B., Horsfield B., Schulz H., 2010, Applying classical shale gas evaluation concepts to Germany - Part II: Carboniferous in Northeast Germany, *Chemie der Erde*, **70(S3)**, 93-106.

Heinrichs S.M., 1993, Early diagenesis of organic matter: the dynamics (rates) of cycling of organic compounds, In: Engel, M.H., Macko, S.A. (Eds.), Organic Geochemistry – Principles and Applications. Plenum Press, New York.

Henry W., 1803, Experiments on the Quantity of Gases Absorbed by Water, at Different Temperatures, and under Different Pressures, *Philosophical Transactions of the Royal Society of London*, **93**, 29-42.

Heredy L.A.,Wender I., 1980, Model structure for a bituminous coal, *American Chemical Society Division of Fuel Chemistry Preprints*, **25**, 38-45.

Hildenbrand A., Krooss B.M., Busch A., Gaschnitz R., 2006, Evolution of methane sorption capacity of coal seams as a function of burial history - a case study from the Campine Basin, NE Belgium, *International Journal of Coal Geology*, **66(3)**, 179 – 203.

Hill R.J., Zhang E., Katz B.J., TangY., 2007, Modeling of gas generation from the Barnett Shale, Fort Worth Basin, Texas, *AAPG Bulletin*, **91(4)**, 501-521.

Hill D. G., Nelson C.R., 2000, Gas productive fractured shales - an overview and update, *GasTIPS*, **6(2)**, 4-13.

Horsfield B., 1989, Practical criteria for classifying kerogens – some observations from pyrolysis-gas chromatography, *Geochimica et Cosmochimica Acta*, **53(4)**, 891-901.

Huc A.Y., 1990, Understanding organic facies: a key to improved quantitative petroleum evaluation of sedimentary basins. In: Huc, A.Y. (Ed.), Deposition of Organic Facies, *AAPG Studies in Geology*, **30**, AAPG Publications, Tulsa, Oklahoma.

Huisman H.F., 1983, Contact Angle and the Rootare-Prenzlow Equation in Mercury Intrusion Porosimetry, *Journal of Colloid and Interface Science*, **94(1)**, 25-36.

Hunt J. M., 1996, Petroleum Geochemistry and Geology, 2nd ed.; W.H. Freeman: San Francisco, ISBN 0716724413.

Hurlbut. C.S. and Klein C., 1985, Manual of Mineralogy, 20th ed., John Wiley and Sons, New York, p 285-286, ISBN 0-471-80580-7.

Isaacs, C. M., 1981, Porosity reduction during diagenesis of the Monterey Formation, Santa Barbara coastal area, California, in *R. E. Garrison and R. G. Douglas, eds., The Monterey Formation and related siliceous rocks of California: Los Angeles*, SEPM Pacific Section, 257–271.

Jarvie D.M, 2011, Worldwide Shale Resource Plays and Potential, Search and Discovery Article #80144. Downloaded on the on 21/12/11 from:
http://www.searchanddiscovery.com/documents/2011/80144jarvie/ndx_jarvie.pdf

Jarvie D.M., 2005, Evaluating Shale Gas Plays using the Barnett Shale Model, oral presentation given at the Dallas SIPES Meeting, Oct 18, 2005. Downloaded 30/11/2011 from:
http://www.beg.utexas.edu/pttc/archive/oct05sipes/jarvie-sipesoct05.pdf.

Jarvie D.M., Claxton B., Henk B., Breyer J., 2001, Oil and Shale Gas from Barnett Shale Ft. Worth Basin Texas, *AAPG National Convention, Denver CO June 3-6*, pg 1-28.

Jarvie D.M., Hill R.J., Ruble T.E., Pollastro R.M., 2007, Unconventional shale-gas systems: the Mississippian Barnett Shale of north-central Texas as one model for thermogenic shale-gas assessment, *AAPG Bulletin*, **91(4)**, 475-499.

Javadpour F., Moravvej-Farshi M., Amrein M., 2012, Atomic-Force Microscopy: A New Tool for Gas-Shale Characterization, *Journal of Canadian Petroleum Technology*, **6**, 236-243.

Jenkins C., Boyer C., 2008, Coalbed and shale-gas reservoirs, *Journal of Petroleum Technology*, Distinguished Author Series, 92-99.

Ji L., Zhang T., Milliken K.L., Qu J., Zhang X., 2012, Experimental investigation of main controls to methane adsorption in clay-rich rocks, *Applied Geochemistry*, **27**, 2533 – 2545.

Joubert J.I., Grein C.T., Bienstock D., 1973, Sorption of methane on moist coal, *Fuel*, **52**, 181-185.

Joubert J.I., Grein C.T., Bienstock D., 1974, The effect of moisture on the methane capacity of American coals, *Fuel*, **53**, 186-191.

Joy D.C., Romig D.A., Goldstein J., 1986, Principles of Analytical Electron Microscopy, Springer, ISBN 0306423871, pp 448.

Justwan H., Dahl B., Isaksen G.H., Meisingset I., 2005, Late to Middle Jurassic source facies and quality variations, South Viking Graben, North Sea, *Journal of Petroleum Geology*, **28(3)**, 241-268.

Kang S.M., Fathi E., Ambrose R.J., Akkutlu I.Y., Sigal R.F., 2010, Carbon Dioxide Storage Capacity of Organic-rich Shales, *SPE 134583*.

Kauffman E.G., 1984, Paleobiogeography and evolutionary response dynamic in the Cretaceous Western Interior Seaway of North America. *In: Westermann G.E.G., (Editor), Jurassic-Cretaceous Biochronology and Paleogeography of North America, Geological Association of Canada Special Paper,* **27**, 273-306.

Kausik R., Minh C.C, Zielinski L., Vissapragada B., Akkurt R., Song Y., Liu C., Jones S., Blair E., 2011, Characterization of Gas Dynamics in Kerogen Nanopores by NMR, *SPE 147198*.

Keym M., Dieckmann V., Horsfield B., Erdmann M., Galimberti R., Kua C., Leith L., Podlaha O., 2006, Source rock heterogeneity of the Upper Jurassic Draupne Formation, North Viking Graben, and its relevance to petroleum generation studies, *Organic Geochemistry*, **37**, 220–243.

Killops S.D., Killops V.J., 2005, An Introduction to Organic Geochemistry, Wiley-Blackwell; 2nd Edition, ISBN 0632065044.

Klobes P., Meyer K., Munro R.G., 2006, Porosity and Specific Surface Area Measurements for Solid Materials, National Institute of Standards and Technology, Special Publication SP960-17, pp 87.

Knudsen K., Leythaeuser D., Dale B., Larter S.R., Dahl B., 1988, Variation in organic matter quality and maturity in Draupne Formation source rocks from the Oseberg Field region, offshore Norway, *Advances in Organic Geochemistry*, **13(4-6)**, 1051-1060.

Krooss B.M., van Bergen F., Gensterblum Y., Siemons N., Pagnier H.J.M., David P., 2002, High-pressure methane and carbon dioxide adsorption on dry and moisture-equilibrated Pennsylvanian coals, *International Journal of Coal Geology*, **51**, 69-92.

Kuila U., Prasad M., 2012, Surface Area and Pore-size Distribution of Clays and Shales, *SPE 146869*.

Lamberson, M.N., Bustin, R.M., 1993, Coalbed methane characteristics of Gates Formation Coals, Northeastern British Columbia: effect of maceral composition, *AAPG Bulletin*, **77**, 2062-2072.

Langford F.F., Blanc-Valleron M.M., 1990, Interpreting Rock-Eval data using graphs of pyrolyzable hydrocarbons vs total organic carbon, *American Association of Petroleum Geologists Bulletin,* **74(6)**, 799-804.

Langmuir I., 1916, The constitution and fundamental properties of solids and liquids - Part 1 Solids, *Journal of the American Chemical Society*, **38**, 2221-2295.

Langmuir I., 1918, The adsorption of gases on plane surfaces of glass, mica and platinum, *Journal of the American Chemical Society*, **40**, 1361-1403.

Laplace P.S., 1806, On several subjects relative to the system of the world, (Supplement to the tenth book): On capillary attraction, a supplement to the theory of capillary attraction, *Méchanique céleste,* 10th Edition.

Larsen J.W., Kidena K., Ashida R., Parikh H., 2005. Kerogen Chemistry 3 - Shale Elemental Analysis and Clay Dehydroxylation, *Energy & Fuels*, **19**, 1699-1703.

Larsen J.W., Parikh H., Michels R., 2002, Changes in the cross-link density of Paris Basin Toarcian kerogen during maturation, *Organic. Geochemis*try, **33**, 1143-1152.

Larter S.R., 1984, Application of analytical pyrolysis techniques to kerogen characterization and fossil fuel exploration/exploitation. In: Voorhees K. (ed.), Analytical Pyrolysis - Methods and Applications. Butterworth, London, pp. 212–275.

Law, B.E., Curtis, J.B., 2002, Introduction to petroleum systems, *AAPG Bulletin*, **86**, 1851-1852.

Laxminarayana, C., Crosdale, P.J., 1999, Role of coal type and rank on methane sorption characteristics of Bowen Basin, Australia coals, *International Journal of Coal Geology*, **40**, 309-325.

Leckie .D.A., Bhattacharya, J.P., Bloch, J., Gilboy, C.F., Norris B., 2008, Chapter 20: Cretaceous Colorado/Alberta Group of the Western Canada Sedimentary Basin. In: Geological Atlas of the Western Canada Sedimentary Basin. Mossop, G.D., and I. Shetsen (eds.). *Canadian Society of Petroleum Geologists and Alberta Research Council*, Special Report 4, URL http://www.ags.gov.ab.ca/publications/wcsb_atlas /atlas.html, accessed 15/04/12.

Leon C. A., 1998, New perspectives in mercury porosimetry, *Advances in Colloid and Interface Science*, **76-77**, 341-372.

Leplat P., Vandenbroucke M. 1993, Combined thermal extraction pyrolysis and gas chromatography, *In: Bordenave M.L. (Editor), Applied Petroleum Geochemistry, Editions Technip*, 262 – 270.

Levy J.H., Day S.J., Killingly J.S., 1997. Methane capacities of Bowen Basin coals related to coal properties, *Fuel*, **76**, 813–819.

Littke R., Krooss B., Uffmann A.K., Schulz H.-M., Horsfield B., 2011, Unconventional Gas Resources in the Paleozoic of Central Europe, *Oil and Gas Science and Technology*, **66(6)**, 953-978.

Loucks R. Reed R.M., Ruppel S.C., Jarvie D.M., 2009, Morphology, genesis, and distribution of nanometer-scale pores in siliceous mudstones of the Mississippian Barnett shale, *Journal of Sedimentary Research*, **79**, 848-861.

Loucks R.G., Reed R.M., Ruppel S.C., Hammes U., 2012, Spectrum of pore types and networks in Mudrocks and a descriptive classification for Matrix-related mudrock pores, *AAPG Bulletin*, **96(8)**, 1071-1098.

Loucks R.G., Ruppel S., Reed M., Hammes U., 2011, Origin and Classification of Pores in Mudstones from Shale-Gas Systems, Search and Discovery #40855, downloaded on 21/12/11:
http://www.searchanddiscovery.com/documents/2011/40855loucks/ndx_loucks.pdf.

Lowell S., Shields J.E., 1981, Influence of Contact Angle on Hysteresis in Mercury Porosimetry, *Journal of Colloid and Interface Science*, **80(1)**, 192-196.

Lu X., Li F., Watson A.T., 1995, Adsorption measurements in Devonian shales, *Fuel*, **74(4)**, 599-603.

Lubda D., Lindner W., Quaglia M., von Hohenesche C., Unger K.K., 2005, Comprehensive pore structure characterization of silica monoliths with controlled mesopore size and macropore size by nitrogen sorption, mercury porosimetry, transmission electron microscopy and inverse size exclusion chromatography, *Journal of Chromatography A*, **1083**, 14–22.

Macqueen R.W., Leckie D.A., 1992, Foreland Basins and Fold Belts, *American Association of Petroleum Geologists*, **55**, 457.

Magoon L. B., Dow W.G., 1994, The petroleum system, in L. B. Magoon and W. G. Dow, eds., The petroleum system - From source to trap: *AAPG Memoir*, **60**, 3 - 24.

Mann A. L., Patience R. L. and Poplett I. J. F., 1991, Determination of molecular structure of kerogens using ^{13}C NMR spectroscopy: I. Effects of variation in kerogen type, *Geochimica et Cosmochimica Acta*, **55**, 2259-2268.

Marsh H., 1987, Adsorption methods to study microporosity in coals and carbons -a critique, *Carbon*, **25**, 49-58.

Martini A. M., Walter L.M., Budai J.M., Ku T.C.W., Kaiser C.J., Schoell M., 1998, Genetic and temporal relations between formation waters and biogenic methane - Upper

Devonian Antrim Shale, Michigan basin, USA: *Geochimica et Cosmochimica Acta*, **62(10)**, 1699-1720.

Martini A.M., Walter L.M., Ku T.C.W, Budai J.M., McIntosh J.C., Schoell M., 2003, Microbial production and modification of gases in sedimentary basins: a geochemical case study from a Devonian shale gas play, Michigan Basin, *AAPG Bulletin*, **87(8)**, 1355-1375.

Mastalerz M., Gluskoter H., Rupp J., 2004, Carbon dioxide and methane sorption in high volatile bituminous coals from Indiana USA, *International Journal of Coal Geology*, **60**, 43 - 55.

Masuda H., Higashitani K., Yoshida H., 2006, Powder Technology: Fundamentals of Particles, Powder Beds, and Particle Generation, *CRC Press*, pp 536, ISBN 1420044117

McBain J. W., 1909, The mechanism of the adsorption ("sorption") of hydrogen by carbon, *Philosophical Magazine*, ***18(108),*** 916-935.

McKinney D.E., Bortiatynski J.M., Carson D.M., Clifford D.J., de Leeuw J.W., Hatcher P.G., 1996, Tetramethylammonium hydroxide (TMAH) thermochemolysis of the aliphatic biopolymer cutan: insights into the chemical structure, *Organic Geochemistry*, **24**, 641-650.

Modica C.J., Lapierre S.G., 2012, Estimation of kerogen porosity in source rocks as a function of thermal transformation: Example from the Mowry Shale in the Powder River Basin of Wyoming, *AAPG Bulletin*, **96(1)**, 87-108.

Moffat D.H., Weale K.E., 1955, Sorption by coal of methane at high-pressures, *Fuel*, **34**, 449-462.

Montgomery S.L., Jarvie D.M., Bowker K.A., Pollastro R.M., 2005, Mississippian Barnett Shale, Fort Worth basin, north-central Texas: Gas-shale play with multi–trillion cubic foot potential, *AAPG Bulletin*, **89(2)**, 155–175.

Mossop G., Shetson I., 1994, Geological Atlas of the Western Canada Sedimentary Basin, Canadian Society of Petroleum Geologists and the Alberta Research Council. Accessed on the 15/03/12 from:
http://www.ags.gov.ab.ca/publications/wcsb_atlas/atlas.html

Muscio G.P.A., Horsfield B., 1996, Neoformation of inert carbon during the natural maturation of a marine source rock: Bakken Shale, Williston Basin, *Energy and Fuels*, **10**, 10-18.

Nielsen K.S., Schröder-Adams C.J., Leckie D.A., 2003, A new stratigraphic framework for the Upper Colorado Group (Cretaceous) in southern Alberta and southwestern Saskatchewan, Canada, *Bulletin of Canadian Petroleum Geology*, **51(3)**, 304-346.

Nielsen K.S., Schröder-Adams C.J., Leckie D.A., Haggart J.W., Elberdak K., 2008, Turonian to Santonian paleoenvironmental changes in the Cretaceous Western Interior Sea: The Carlile and Niobrara formations in southern Alberta and southwestern Saskatchewan, Canada, *Palaeogeography, Palaeoclimatology, Palaoecology*, **270**, 64-91.

Noble R.A., Kaldi J.G., Atkinson C.D., 1997, Seals, Traps, and the Petroleum System - Chapter 2: Oil Saturation in Shales, Applications in Seal Evaluation, *AAPG Memoir*, **67**, 13-29.

Nuttall B.C., Eble C.F., Drahovzal J.A., Bustin R.M., 2005, Analysis of Devonian Black Shales in Kentucky for potential carbon dioxide sequestration and enhanced natural gas production, Kentucky Geological Survey, DE-FC26-02NT41442.

Okiongbo K.S., Aplin A.C., Larter S.R., 2005, Changes in Type II Kerogen Density as a Function of Maturity: Evidence from the Kimmeridge Clay Formation, *Energy & Fuels*, **19**, 2495-2499.

Paktinat J., Pinkhouse J., Fontaine J., Lash G., Penny G., 2009, Investigation of Methods to Improve Utica Shale Hydraulic Fracturing in the Appalachian Basin, *Search and Discovery*, Article 40391.

Passey Q. R., Bohacs K. M., Esch W. L., Klimentidis R., Sinha S., 2010, From oil-prone source rock to gas-producing shale reservoir: Geologic and petrophysical characterization of unconventional shale-gas reservoirs, *SPE 131350*, 29.

Patience R. L., Mann A. L., Poplett I. J. F., 1992, Determination of molecular structure of kerogens using ^{13}C NMR spectroscopy: II. The effects of thermal maturation on kerogens from marine sediments, *Geochimica et Cosmochimica Acta*, **56**, 2725-2742.

Peters K.E., 1986, Guidelines for evaluating petroleum source rocks using programmed pyrolysis, *American Association of Petroleum Geologists Bulletin*, **70**, 318-329.

Peters K.E., Walters C.C., Moldowan J.M., 2004, The Biomarker Guide, second ed. Cambridge University Press.

Plint A.G., Tyagi A., Hay M.J., Varban B.J., Zhang H., Roca X., 2009, Clinoforms, Paleobathymetry and mud dispersal across the western Canada Cretaceous foreland basin: evidence from the Cenomanian Dunvegan Formation and contiguous strata, *Journal of Sedimentary Research*, **79**, 144-161.

Pollastro R.M., Hill R.J., Jarvie D.M., Henry M.E., 2003, Assessing undiscovered resources of the Barnett–Paleozoic total petroleum system, Bend arch– Fort Worth basin province, Texas (abs.), *AAPG Southwest Section Convention*, 18.

Pollastro R.M., Jarvie D.M., Hill R.J., Adams C.W., 2007, Geologic framework of the Mississippian Barnett Shale, Barnett-Paleozoic total petroleum system, Bend arch-Fort Worth Basin, Texas, *AAPG Bulletin*, **91(4)**, 405–436.

Powell T.G., Snowdon L.R., 1980, Geochemical controls on hydrocarbon generation in Canadian sedimentary basins, in *Facts and Principles of World Petroleum Occurrence*, Editor A.D. Miall, *Canadian Society of Petroleum Geologists Memoir*, **6**, 421-446.

Prinz D., Littke R., 2005, Development of the micro- and ultramicroporous structure of coals with rank as deduced from the accessibility to water, *Fuel*, **84**, 1645–1652.

Prinz D., Pyckhout-Hintzen W., Littke R., 2004, Development of the meso- and macroporous structure of coals with rank as analysed with small angle neutron scattering and adsorption experiments, *Fuel*, **83**, 547–556.

Reid C. R.; Thomas K. M., 1999, Adsorption of Gases on a Carbon Molecular Sieve Used for Air Separation: Linear Adsorptives as Probes for Kinetic Selectivity, *Langmuir*, **15**, 3206-3218.

Reimer L., 1998, Scanning Electron Microscopy: Physics of Image Formation and Microanalysis, Springer Series in Optical Sciences, ISSN 0342-4111, 527.

Rexer T.F.T., Benham M.J., Aplin A.C., Thomas K.M., 2013, Methane Adsorption on Shale under Simulated Geological Temperature and Pressure Conditions, *Energy and Fuels*, **27**, 3099 – 3109.

Rigby S.P., Chigada P.I., Wang J., Wilkinson S.K., Bateman H., Al-Duri B., Wood J., Bakalis S., Miri T., 2011, Improving the interpretation of mercury porosimetry data using computerised X-ray tomography and mean-field DFT, *Chemical Engineering Science*, **66**, 2328-2339.

Ritter H.L., Drake L. C., 1945, Pore-Size Distribution in Porous Materials Pressure Porosimeter and Determination of Complete Macro pore size Distributions, *Industrial and Engineering Chemistry*, **17(12)**, 782-786.

Rokosh C.D., Pawlowicz J.G., Berhane H., Anderson S.D.A., Beaton A.P.,2009, What is Shale Gas? An Introduction to Shale-Gas Geology in Alberta, *Energy Resources Conservation Board Alberta Geological Survey, ERCB/AGS Open File Report*, 1-26.

Rootare H.M., Prenzlow C.F., 1967, Surface Areas from Mercury Porosimeter Measurements, *Journal of Physical Chemistry*, **71(8)**, 2733-2736.

Ross D.J.K., Bustin R. M., 2007, Impact of mass balance calculations on adsorption capacities in microporous shale gas reservoirs, *Fuel*, **86**, 2696-2706.

Ross D.J.K., Bustin R. M., 2008, Characterizing the shale gas resource potential of Devonian–Mississippian strata in the Western Canada sedimentary basin: Application of an integrated formation evaluation, *AAPG Bulletin*, **92(1)**, 87-125.

Ross D.J.K., Bustin R. M., 2009, The importance of shale composition and pore structure upon gas storage potential of shale gas reservoirs, *Marine and Petroleum Geology*, **26**, 916-927.

Rouquérol F., Rouquérol J., Sing K.S.W., 1999, Adsorption by Powders and Porous Solids: Principles, Methodology and Applications, ACADEMIC Press INC, pp 467, ISBN 0125989202.

Rouquerol J., Avnir D., Fairbridge C.W., Everett D.H., Haynes J.H., Pernicone N., Ramsay J.D.F., Sing K.S.W., Unger K.K., 1994, Recommendations for the Characterisation of Porous Solids, *Pure and Applied Chemistry*, **66(8)**, 1739-1758.

Seewald J.S., 2003, Organic–inorganic interactions in petroleum-producing sedimentary basins, *Nature*, **426**, 327 - 333.

Sevenster P.G., 1959, Diffusion of gases through coal, *Fuel*, **38**, 403 – 418.

Sing K.S.W., 2004, Characterization of porous materials: past, present and future, *Colloids and Surfaces A*, **241**, 3-7.

Sing K.S.W., Everett D.H., Haul R.A.W., Moscou L., Pierotti R.A., Rouquerol J., Siemieniewska T, 1985, Reporting physisorption data for gas/solid systems with special reference to the determination of surface area and porosity, *Pure and Applied Chemistry*, **57**, 603.

Skempton A. W., 1970, The consolidation of clays by gravitational compaction, *Quarterly Journal of the Geological Society of London*, **125**, 373-411.

Smolyaninov I.I., 2008, Optical microscopy beyond the diffraction limit, HFSP Journal, 2(3), 129 – 131.

Stopes M. C., 1935, On the petrology of banded bituminous coals, *Fuel*, **14**, 4-13.

Summons R.E., 1993, Biogeochemical cycles: A review of fundamental aspects of organic matter formation, preservation, and composition, *Topics in Geobiology*, **11**, 3-21.

Taylor S.E., 2011, Shale Gas Potential of the Late Cretaceous Upper Colorado Group; Bigstick Pool, Southeastern Alberta and Southwestern Saskatchewan, MSc Dissertation, Department of Geoscience, The University of Calgary.

Teichmuller M., 1989, The genesis of coal from the viewpoint of coal petrology, *International Journal of Coal Geology*, **12**, 1-87.

Tissot B., Demaison G., Masson P., Delteil J.R., Combaz A., 1980, Paleoenvironment and petroleum potential of Middle Cretaceous black shlaes in Atlantic Basins, *AAPG Bulletin*; **64**, 2051-2063.

Tissot B., Durand B., Espitalié J., Combaz A., 1974, Influence of the nature and diagenesis of organic matter in the formation of petroleum, *AAPG Bulletin*, **58**, 499-506.

Tissot B.P, Welte D.H., 1984, Petroleum formation and occurrence, *Springer-Verlag*, New York, ISBN-13: 978-0387132815.

Tissot B., Deroo G., Hood A., 1978, Geochemical study of the Uinta Basin: formation of petroleum from the Green River formation, *Geochimica et Cosmochimica Acta*, **42**, 1469-1485.

Toth J., 2002, Adsorption: Theory, Modeling and Analysis, CRC Press, pp 878, ISBN-10: 0824707478.

Tyson R. V., 1995, Sedimentary organic matter: Organic facies and palynofacies, London, Chapman and Hall. ISBN 041236350X.

Underhill J.R., 1991, Controls on Late Jurassic seismic sequences, Inner Moray Firth, UK North Sea: a critical test of a key segment of Exxon's original global cycle chart, *Basin Research*, **3**, 79-98.

Unsworth, J.F., Fowler, C.S., Jones, L.F., 1989. Moisture in coal: 2. Maceral effects on pore structure, *Fuel*, **68**, 18-26.

van Krevelen D.W., 1950, Graphical-statistical method for the study of structure and reaction processes of coal, *Fuel*, **29**, 269-284.

Vandenbroucke M., Largeau C., 2007, Kerogen origin, evolution and structure, *Organic Geochemistry*, **38**, 719 – 833.

Vanorsdale C. R., 1987, Evaluation of Devonian Shale Gas Reservoirs, SPE Reservoir Engineering, SPE 14446.

Varban B.L., Plint A.G., 2008, Palaeoenvironments, paleogeography, and physiogeography of a large, shallow muddy ramp; late Cenomanian-Turonian Kaskapau Formation, Western Canada foreland basin, *Sedimentology*, **55(1)**, 201-233.

Vollset J., Doré A.G., 1984, A revised Triassic and Jurassic lithostratigraphic nomenclature for the Norwegian North Sea, *NPD-Bulletin*, **3**, 1-62, ISBN 82-7257-155-2.

Volpi V., Camerlenghi A., Hillenbrand C.D., Rebesco M., Ivaldi R., 2003, Effects of biogenic silica on sediment compaction and slope stability on the Pacific margin of the Antarctic Peninsula, *Basin Research*, **15**, 339-363.

Walser D.W., Pursell D.A., 2008, Making mature shale gas plays commercial: process and natural parameters, *Society of Petroleum Engineers, SPE 110127*.

Washburn E.W., 1921, The Dynamics of Capillary Flow, *Physical Review*, **17**, 273–283.

Webb P.A., Orr C., 1997, Analytical methods in fine particle technology, *Micromeritics Instrument Corp., Norcross, GA, USA*, p. 301.

Weniger P., Kalkreuth W, Busch A, Krooss B.M., 2010, High-pressure methane and carbon dioxide sorption on coal and shale samples from the Paraná Basin, Brazil, *International Journal of Coal Geology*, **84**, 190–205.

Weniger P., 2012, Thermal and microbial gas generation, accumulation and dissipation in coal basins, PhD thesis from the Institute of Geology and Geochemistry of Petroleum and Coal, RWTH Aachen University. Available from http://d-nb.info/1030378045/34

Westermarck S., 2000, Use of Mercury Porosimetry and Nitrogen Adsorption in Characterisation of the Pore Structure of Mannitol and microcrystalline cellulose powders, granules and tablets, PhD Thesis, Department of Pharmacy, University of Helsinki (Finland).

Westermarck S., Juppo A.M., Kervinen L., Yliruusi J., 1998, Pore structure and surface area of mannitol powder, granules and tablets determined with mercury porosimetry and

nitrogen adsorption, *European Journal of Pharmaceutics and Biopharmaceutics*, **46**, 61–68.

Wickramaratne N.P., Jaroniec M., 2013, Activated Carbon Spheres for CO_2 Adsorption, *Applied Materials and Interfaces*, **5(5)**, 1849-1855.

Williams D.H., Fleming I., 1995, Spectroscopic Methods in Organic Chemistry, McGraw-Hill Higher Education, 5th Edition, pp 352, ISBN-10: 0077091477.

World Energy Council, 2012, Survey of Energy Resources: Shale Gas - What's New, ISBN 978 0 946121 05 2. Downloaded on the 31/05/12:
http://www.worldenergy.org/ documents/shalegasupdatejan2012.pdf.

Yee D., Seidle J.P., Hanson W.B., 1993, Gas sorption on coal and measurement of gas content. In: Law, B.E., Rice, D.D. (Eds.), Hydrocarbons from Coal. AAPG Studies in Geology, Chapter 9, AAPG, Tulsa, Oklahoma, 74101 USA, pp. 203–218.

Zhang T., Ellis G.S., Ruppel S.C., Milliken K., Yang R., 2012, Effect of organic-matter type and thermal maturity on methane adsorption in shale-gas systems, *Organic Geochemistry*, 47, 120-131.

Zhao X.B., Xiao B., Fletcher A.J., Thomas K.M., 2005, Hydrogen Adsorption on Functionalized Nanoporous Activated Carbons, *Journal of Physical Chemistry B*, **109**, 8880-8888.

Zsigmondy R. Z., 1911, Über die Struktur des Gels der Kieselsäure.Theorie der Entwässerung (About the structure of silica gel. Theory of drainage), *Zeitschriftfüranorganische und allgemeineChemie (Journal of Inorganic and General Chemistry)*, **71**, 365-377.